
On the Saharan Air Layer Aerosol and its Role as a Reservoir of Cloud Condensation Nuclei

Adrian Walser



München 2017

On the Saharan Air Layer Aerosol and its Role as a Reservoir of Cloud Condensation Nuclei

Adrian Walser

Dissertation
an der Fakultät für Physik
der Ludwig–Maximilians–Universität
München

vorgelegt von
Adrian Walser
aus Heidelberg

München, den 17. November 2017

Erstgutachter: Prof. Dr. Bernadett Weinzierl

Zweitgutachter: Prof. Dr. Bernhard Mayer

Tag der mündlichen Prüfung: 21. Dezember 2017

Contents

Abstract	xix
Zusammenfassung	xxi
1 Introduction	1
1.1 Atmospheric Aerosols and the Role of North African Mineral Dust . . .	1
1.2 Transatlantic Transport of North African Dust	4
1.3 Impact of North African Dust	6
1.4 The SALTRACE Campaign and Thesis Objectives	12
1.5 Thesis Structure	13
1.6 External Data	14
2 Theory	17
2.1 Nucleation and Köhler Theory	17
2.1.1 Homogeneous Nucleation	18
2.1.2 Heterogeneous Nucleation	21
2.1.3 Kappa-Köhler Theory	25
2.2 Scattering Theory	27
2.2.1 The Scattering Problem	28
2.2.2 Scattering by Spherical Particles	30
2.2.3 Scattering by Aspherical Particles	33
2.3 Aerosol Particle Size Distributions	34
2.4 Aerosol Mixing State and Volatility	38
2.5 Particle Sampling Losses	41
3 Methods	47
3.1 SALTRACE	47
3.1.1 Airborne Campaign	48
3.2 Instruments and Data	50
3.2.1 Auxiliary Devices	53
3.2.1.1 Differential Mobility Analyzer (DMA)	53
3.2.1.2 Thermodenuder (TD)	56
3.2.2 Main Instruments	58
3.2.2.1 Condensation Particle Counters (CPCs)	58
3.2.2.2 Optical Particle Counters (OPCs)	66
3.2.2.3 Cloud Condensation Nuclei Counter (CCNC)	80
3.2.3 Supplementary Instruments	89

3.2.3.1	Airborne Instruments	89
3.2.3.2	Ground-Based Instruments	91
3.3	Data Evaluation	93
3.3.1	Cloud Passage Masking	93
3.3.2	Size Distribution Retrieval	95
3.3.3	Derivation of Size-Dependent Volatility	103
3.3.4	Derivation of Effective Particle Hygroscopicity	104
3.3.5	Validation of Results	108
3.4	Additional Tools	115
4	Results	117
4.1	Intense Dust Event in the Caribbean	117
4.1.1	Vertical Profiles	119
4.1.1.1	Meteorological Parameters	119
4.1.1.2	Particle Concentrations and Total Particle Volatility	121
4.1.2	Comparison with Dust-Free Air Mass	124
4.1.3	Detailed Properties of the SAL Aerosol	126
4.2	Overall Picture of the SAL During SALTRACE	132
4.2.1	Entirety of Vertical Profiles in the Presence of the SAL	132
4.2.1.1	Caribbean	132
4.2.1.2	Northwest African Coast	137
4.2.2	Spatiotemporal Course of Observations	143
4.2.2.1	Complete Vertical Information from Airborne and Ground-Based Measurements	143
4.2.2.2	Aerosol Parameter Statistics for the SAL Flight Legs	148
4.2.2.3	Horizontal Variability of Particle Concentrations in the SAL	152
4.2.3	SAL Aerosol Composition and NSD Before and After Long-Range Transport	154
5	Discussion	161
5.1	The SAL as a Separated Particle Reservoir	161
5.2	Overlay of the SAL by UT Aerosol	163
5.3	Internal Structure of the SAL	163
5.3.1	Vertical Heterogeneity	163
5.3.2	Horizontal Homogeneity	164
5.4	Vertical Aerosol Exchange Between the SAL and the Adjacent Troposphere	165
5.4.1	Entrainment of UT Aerosol	165
5.4.2	SAL Aerosol Presence in the Lower Troposphere	167
5.5	CCN Properties of the SAL Aerosol in the Context of Particle Composition	168
5.5.1	Role of Soluble Sulfates	168
5.5.2	Impact of UT Aerosol Entrainment	170
5.5.3	Role of Mineral Dust	171
5.6	Modification of the SAL Aerosol with Transatlantic Transport	171
5.6.1	Accumulation Mode and Effective Hygroscopicity	171

5.6.2	Dust Mode	172
5.6.3	Moderate Changes?	173
6	Summary	175
7	Outlook	181
7.1	Future Research Needs	181
7.2	Advanced Hygroscopicity Studies	182
A	Methods Supplement	193
A.1	OPC Bin Specifications and Calibration Results	193
A.1.1	UHSAS	193
A.1.2	SkyOPCs	194
A.2	CCNC Data	195
A.2.1	Column A <i>SS</i> Calibration	195
A.2.2	CPS Tubing Transit Times	195
A.2.3	CCN Correction Scheme Comparison	199
A.3	Comparison with Ground-Based Measurements	199
A.3.1	Particle NSD Retrieval Results	199
A.3.2	CCN Correction Scheme Comparison for 0.2% SS	199
A.3.3	Particle Hygroscopicity Comparison for other SS	203
B	Results Supplement	207
B.1	Intense Dust Event	207
B.2	Time Course of Vertical Profiles	207
B.3	Impactor Samples for Single Particle Analysis	207
B.4	Dry Deposition of SAL Aerosol During Transport	211
B.5	Entirety of NSD and Hygroscopicity Results	212
B.5.1	Lognormal NSD Parameters	212
B.5.2	CCN Concentration, Activation Diameter and Particle Hygroscopicity	212

List of Figures

1.1.1	Global Occurrence of Major Aerosol Types	3
1.2.1	Summertime Spatial Occurrence of Mineral Dust	5
1.2.2	Time Course of Mineral Dust Concentration in the Caribbean	6
1.3.1	Aerosol-Radiation and Aerosol-Cloud Interactions	7
1.3.2	SAL Aerosol Composition during SAMUM	11
2.1.1	Gibbs Energy Change During Homogeneous Cluster Formation	19
2.1.2	Heterogeneous Cluster Formation on Insoluble Nucleus	21
2.1.3	Equilibrium Supersaturation Köhler Curves	23
2.1.4	Verification of Kappa-Köhler Theory	26
2.1.5	Droplet Activation of Fresh Mineral Dust	27
2.2.1	Geometry of Single Particle Light Scattering	29
2.2.2	Mie Scattering Phase Functions	32
2.2.3	Size Dependence of Mie Scattering Cross Section	32
2.2.4	Size Dependence of Scattering Cross Section for Aspherical Particles	33
2.3.1	Lognormal Size Distribution	36
2.3.2	Particle Number, Surface and Volume Size Distributions	37
2.4.1	Particle Mixing State	39
2.5.1	Particle Sampling Loss Mechanisms	41
2.5.2	Size-Dependence of Particle Sampling Losses	43
2.5.3	Cunningham Slip Correction	44
3.1.1	Equipped Falcon Research Aircraft During SALTRACE	48
3.1.2	Ground-Based Measurements on Barbados	49
3.1.3	SALTRACE Flight Tracks	49
3.1.4	SALTRACE Flight Pattern 130711a	52
3.2.1	Falcon In-Cabin Instrumentation	54
3.2.2	Differential Mobility Analyzer	55
3.2.3	Thermodenuder	56
3.2.4	Thermophoretic Losses in the Thermodenuder	57
3.2.5	CPC Schematic	59
3.2.6	CPC Counting Efficiency Cutoff Curves	61
3.2.7	Differential CPC Plateau Counting Efficiency	64
3.2.8	OPC Kernel Functions	68
3.2.9	UHSAS Architecture and Scattering Geometry	71
3.2.10	UHSAS Calibration Stability	74
3.2.11	UHSAS Calibration Results	75

3.2.12	UHSAS Counting Efficiency	76
3.2.13	SkyOPC Architecture and Scattering Geometry	77
3.2.14	SkyOPC and SkyOPC _{TD} Calibration	79
3.2.15	SkyOPC Counting Efficiencies	80
3.2.16	CCNC Schematic	81
3.2.17	CCNC Calibration	84
3.2.18	Particle Loss at the CPS Inlet	85
3.2.19	Pressure-Dependent Particle Stokes Numbers at the CPS Inlet	86
3.2.20	Pressure-Dependent CPS Inlet Loss Correction	88
3.3.1	Particle NSD Retrieval Flowchart	96
3.3.2	Entirety of Counting Efficiency Functions	98
3.3.3	Flowchart for the Derivation of Size-Dependent Volatility	102
3.3.4	Flowchart for the Derivation of Effective Particle Hygroscopicity	105
3.3.5	Time Interval Selection for Comparison with Ground-Based Measurements	109
3.3.6	Comparison with Ground-Based Measurements 20 June	110
3.3.7	Comparison with Ground-Based Measurements 22 and 26 June	111
3.3.8	Comparison with Ground-Based Measurements 10 and 11 July	112
3.3.9	Comparison with Ground-Based Measurements: Hygroscopicity Results Overview	113
4.1.1	SAL Appearance and Transport 11 July	118
4.1.2	Vertical Profiles of Meteorological Parameters 11 July	119
4.1.3	Vertical Stability 11 July	120
4.1.4	Vertical Aerosol Profiles 11 July	122
4.1.5	Vertical CCN Profile 11 July	123
4.1.6	SAL Appearance 8 July	124
4.1.7	Vertical Profile Comparison 8 and 11 July	125
4.1.8	Particle NSDs in the SAL 10 and 11 July	126
4.1.9	Size-Dependent Particle Volatility in the SAL 10 and 11 July	127
4.1.10	Size-Dependent Particle Composition in the SAL 10 and 11 July	128
4.1.11	Particle Hygroscopicity in the SAL 10 and 11 July	129
4.1.12	Contribution of Different Size Ranges to the CCN Concentration in the SAL 10 and 11 July	130
4.2.1	Vertical Profiles of Meteorological Parameters for the Caribbean Dust Events	133
4.2.2	Vertical Profiles of Total Particle Concentration and Volatility for the Caribbean Dust Events	134
4.2.3	Vertical Profiles of the Concentration of Large Particles for the Caribbean Dust Events	135
4.2.4	Vertical Profiles of the Concentration of CCN and Particles Larger 80 nm for the Caribbean Dust Events	136
4.2.5	Vertical Profiles of Meteorological Parameters at the African Coast	138
4.2.6	Vertical Profiles of Total Particle Concentration and Volatility at the African Coast	139
4.2.7	Vertical Profiles of the Concentration of Large Particles at the African Coast	140

4.2.8	Vertical Profiles of the Concentration of CCN and Particles Larger 80 nm at the African Coast	141
4.2.9	Comparison Between the Concentration of CCN and Particles Larger 80 nm for all Flight Legs	142
4.2.10	Definition of Caribbean and African Coast Location Filters	143
4.2.11	Time Course of Ground-Based Measurements	144
4.2.12	Time Course of Airborne Measurements (Part 1)	145
4.2.13	Time Course of Airborne Measurements (Part 2)	146
4.2.14	SAL Flight Leg Statistics (Part 1)	149
4.2.15	SAL Flight Leg Statistics (Part 2)	150
4.2.16	SAL Flight Leg Statistics (Part 3)	151
4.2.17	Definition of Horizontal Flight Leg Extent	152
4.2.18	Horizontal Variability of Particle Concentrations in the SAL	153
4.2.19	Particle NSDs in the SAL Before and After Transatlantic Transport	155
4.2.20	Size-Dependent Particle Volatility in the SAL Before and After Transatlantic Transport	156
4.2.21	Size-Dependent Particle Composition in the SAL Before and After Transatlantic Transport	157
4.2.22	Contribution of Different Size Ranges to the CCN Concentration in the SAL Before and After Transatlantic Transport	158
7.2.1	Simplified SAL Aerosol Model	183
7.2.2	Simple Backward Integration Method (Part1)	185
7.2.3	Simple Backward Integration Method (Part2)	186
7.2.4	Simple Backward Integration Method (Part3)	187
7.2.5	<i>SS</i> -Scanning Method	189
7.2.6	<i>D</i> -Scanning Method	190
7.2.7	Recommended Future Airborne CCNC Setup	192
A.1.1	SkyOPC Response Model Parameter PDFs	196
A.1.2	SkyOPC _{TD} Response Model Parameter PDFs	197
A.2.1	CCNC Calibration (Column A)	198
A.2.2	Transit Time Difference to CPS Inlet	198
A.3.1	Comparison with Ground-Based Measurements: NSD Retrieval Result 20 June	201
A.3.2	CCNC Thermal Gradient Time Series	204
B.1.1	Vertical Profiles 10 July	208
B.1.2	Particle Hygroscopicity in the SAL 10 and 11 July for Uncorrected n_{CCN}	209
B.2.1	Time Course of Airborne Measurements (Part 3)	209
B.2.2	Time Course of Airborne Measurements (Part 4)	210
B.4.1	Modeled Dry Deposition During SAL Transport	212

List of Tables

1.1.1	Major Atmospheric Aerosol Types	2
2.1.1	Homogeneous Nucleation Rates for Water	20
3.1.1	SALTRACE Flight Objectives	51
3.2.1	TSI CPC Counting Efficiency Parameters	62
3.2.2	Cutoff Diameters of CPSA Modules	62
3.2.3	CPC Count-to-Concentration Conversion Parameters	64
3.2.4	Overview of Measured Parameters	94
3.3.1	Initial Parameter PDFs for the NSD Retrieval	97
3.3.2	Prior Probability Assumptions for the NSD Retrieval	99
3.3.3	Parameter PDFs for the Hygroscopicity Derivation	106
5.4.1	Terminal Particle Settling Velocities	166
7.2.1	Simplified SAL Aerosol Model	183
A.1.1	UHSAS Bin Threshold Values	194
A.1.2	SkyOPC Bin Threshold Values	195
A.2.1	CCN Concentration Comparison	200
A.3.1	Comparison with Ground-Based Measurements: CCN Correction Scheme Comparison	202
A.3.2	Comparison with Ground-Based Measurements: Particle Hygroscopicity Results for Different SS	203
A.3.3	CCNC column A Thermal Gradient Bias Test	205
B.3.1	SAL Impactor Samples 10 and 11 July	210
B.3.2	SAL Impactor Samples Before and After Transatlantic Transport	211
B.5.1	Particle NSD Retrieval Results (Part 1)	214
B.5.2	Particle NSD Retrieval Results (Part 2)	215
B.5.3	Particle NSD Retrieval Results (Part 3)	216
B.5.4	Particle NSD Retrieval Results (Part 4)	217
B.5.5	Particle Hygroscopicity Results for Main SS (Part 1)	218
B.5.6	Particle Hygroscopicity Results for Main SS (Part 2)	219
B.5.7	Particle Hygroscopicity Results for Main SS (Part 3)	220
B.5.8	Other Particle Hygroscopicity Results (Part 1)	221
B.5.9	Other Particle Hygroscopicity Results (Part 2)	222
B.5.10	Other Particle Hygroscopicity Results (Part 3)	223

B.5.11 Other Particle Hygroscopicity Results (Part 4) 224

Nomenclature

Abbreviations

AEJ African easterly jet

AERONET Aerosol Robotic Network

AEW African easterly wave

AMSL above mean sea level

AOD aerosol optical depth

CAS cloud and aerosol spectrometer

CCN cloud condensation nucleus

CCNC cloud condensation nuclei counter

CIMH Caribbean Institute for Meteorology and Hydrology

CIMSS Cooperative Institute for Meteorological Satellite Studies

CLWC cloud liquid water content

COSMO-MUSCAT Consortium for Small-Scale Modeling Multiscale Chemistry Aerosol
Transport Model

CPC condensation particle counter

CPS constant pressure section

CPSA condensation particle size analyser

DDA discrete dipole approximation

DLR German Aerospace Center

DMA differential mobility analyzer

DMT Droplet Measurement Technologies

DOY day of the year

DRH deliquescence relative humidity

- ECMWF European Centre for Medium-Range Weather Forecasts
- EDX energy-dispersive X-ray diffraction
- ERH efflorescence relative humidity
- GAIA Grantley Adams International Airport, Barbados
- GCCN giant cloud condensation nucleus
- GEOS Geostationary Operational Environmental Satellite
- IPCC Intergovernmental Panel on Climate Change
- ITCZ intertropical convergence zone
- LAGRANTO Lagrangian Analysis Tool
- LMU Ludwig-Maximilian University of Munich
- MBL marine boundary layer
- MCMC Markov chain Monte Carlo
- MINI micro inertial impactor
- NPF new particle formation
- NSD number size distribution
- OPC optical particle counter
- PDF probability density function
- PLC particle loss calculator
- POLIS portable lidar system
- PSL polystyrene latex
- rBC refractory black carbon
- SABL Saharan atmospheric boundary layer
- SAL Saharan air layer
- SALTRACE Saharan Aerosol Long-Range Transport and Aerosol-Cloud Interaction Experiment
- SAMUM Saharan Mineral Dust Experiment
- SEM scanning electron microscopy
- STP standard temperature and pressure

TC	tropical cyclone
TD	thermodenuder
TEM	transmission electron microscopy
TROPOS	Leipniz Institute for Tropospheric Research
UNIVIE	University of Vienna
UT	upper troposphere
UTC	Coordinated Universal Time

Key Symbols

δ_v	linear volume depolarization ratio
η	sampling/transmission/counting efficiency
κ	hygroscopicity parameter
λ	wavelength
<i>CMD</i>	count median diameter of lognormal NSD mode
<i>GSD</i>	geometric standard deviation of lognormal NSD mode
<i>mr</i>	water vapor mixing ratio
<i>rh</i>	relative humidity
<i>Sh</i>	vertical wind shear (vertical gradient of horizontal wind velocity)
<i>vf</i>	volatile fraction
<i>vf_{total}</i>	total volatile fraction
Θ	potential temperature
\tilde{C}_{scat}	scattering cross section with respect to OPC detection geometry
C_{scat}	scattering cross section
<i>D</i>	particle diameter (also used for hydrated particles and droplets)
<i>D_{act}</i>	activation diameter (critical dry particle diameter)
$dC_{scat}/d\Omega$	differential scattering cross section
$dn/d\log_{10} D$	particle NSD (logarithmic abscissa)
dn/dD	particle NSD (linear abscissa)
m_{rBC}	refractory black carbon mass concentration

m_{dust}	mineral dust mass concentration
N^2	squared Brunt-Väisälä frequency
n_{80}	particle number concentration for $D \gtrsim 80$ nm
n_{CCN}	CCN number concentration
n_{acc}	particle number concentration for $80 \lesssim D \lesssim 300$ nm
n_{giant}	particle number concentration for $D \gtrsim 1.5$ μm
n_{large}	particle number concentration for $D \gtrsim 300$ nm
n_{mode}	integral number concentration of lognormal NSD mode
n_{small}	particle number concentration for $D \lesssim 80$ nm
n_{total}	total particle number concentration
p	pressure
S	water vapor saturation
SS	water vapor supersaturation
T	temperature
v_{wind}	horizontal wind velocity
z	altitude

Abstract

Each year large amounts of aeolian dust are exported from Northern Africa towards the Atlantic. During its maximum in summer this export occurs in the surface-detached Saharan air layer (SAL), with which the dust aerosol is transported across the North Atlantic as far as into the Caribbean sea and beyond. Owing to its high particle content and large geographical extent the SAL has important impacts on climate and environment, such as via aerosol-radiation and aerosol-cloud interactions.

A main motivation behind the Saharan Aerosol Long-Range Transport and Aerosol-Cloud Interaction Experiment (SALTRACE) was to improve our current knowledge on the aerosol properties of the SAL. For this purpose, the dust layer was thoroughly probed with an extensive airborne in situ instrumentation to both sides of its transatlantic transport route during the campaign's core phase in June/July 2013. The acquired data set includes information on size-resolved particle concentration, volatility and composition as well as on the concentration of cloud condensation nuclei (CCN) at a water vapor supersaturation of 0.2%. For the first time, the combination of these data permits a comprehensive examination of the CCN properties of the SAL aerosol, specifically in terms of the particle hygroscopicity parameter κ . To derive representative probability distributions for this parameter and other central aerosol properties like particle number size distribution (NSD), new data evaluation methods have been developed in the course of this study. The in situ information are complemented by a suite of ground-based measurements, among others providing insight into the implications of SAL presence on the aerosol properties in the lower Caribbean troposphere.

Thanks to the persistent external stability of the layer, counteracting efficient mixing with the adjacent atmosphere, a distinct coupling between SAL-induced atmospheric stratification and vertical particle concentration profiles is observed both at the Northwest African coast and in the Caribbean. Accordingly, the layer appears as a separate particle reservoir, in which particulate mass concentration and CCN number concentration typically exhibit their maximum (with regard to standard conditions). Internally the layer shows considerable variability in particle concentrations within vertical distances of only a few hundred meters. On the other hand, the layer shows a high degree of horizontal homogeneity over distances of hundred kilometers and more.

Despite the external stability of the layer, the results clearly demonstrate that the presence of the elevated SAL in the Caribbean is always accompanied by a presence of SAL aerosol in the subjacent troposphere. The input of CCN-rich aerosol from the SAL into the cloud-containing lower troposphere leads to an increase of CCN concentration in the latter, thereby affecting cloud formation and properties in the Caribbean trade wind regime. Yet, the contribution of mineral dust to this indirect aerosol effect can be regarded as inferior. This is because dust is the dominant particulate component in

the SAL only for particle diameters larger than about 500 nm and these particles are comparatively rare in number. Instead, the majority of CCN in the SAL are ascribable to particles in the vicinity of the NSD maximum, i.e. particles with diameters smaller than about 100 – 200 nm. This particle size range is strongly influenced by volatile material, primarily associated with soluble ammonium sulfate. Accordingly, the SAL aerosol exhibits a high effective particle hygroscopicity with κ values ranging from 0.3 to 0.7 at an average of about 0.5. These values are similar or even slightly enhanced compared to those of 0.2 to 0.4 in the Caribbean marine boundary layer (MBL) during the same period. The particulate sulfate carried with the dust layer, accountable for its high κ values and CCN concentration, is commonly attributed to anthropogenic sources. Taken together, these findings suggest an anthropogenic climate impact of the SAL, which has so far (if at all) not been sufficiently treated.

In addition to the omnipresent amounts of volatile material in the SAL, there is strong evidence for occasional further enhancement of such material in the upper part of the layer via aerosol entrainment from the upper troposphere (UT). The air masses above the dust layer are found to contain high concentrations of volatile particles that are predominantly smaller than 80 nm in diameter. These concentrations are so high that, in spite of a significant drop in the concentration of larger particles, the total particle number concentration maximum is encountered above the SAL. The most obvious source of these volatile particles is new particle formation (NPF) in the UT, which is often associated with the production of particulate soluble sulfates. Cases where the enhancement in volatile small particles extends into the upper SAL come along with increased relative CCN concentrations and effective particle hygroscopicities in the latter. Such an influence of UT-born particles on the (CCN) properties of the SAL aerosol has remained unconsidered up to now.

Except for a slight average enhancement of volatile material in the SAL, the aerosol properties of the dust layer are approximately preserved with transatlantic transport. This holds for the shape of the particle NSD in the investigated diameter range below about 2 μm as well as for the effective particle hygroscopicity and the aerosol composition. Particularly, no significant “dust processing”, i.e. no accumulation of soluble material on the dust particles occurs.

Zusammenfassung

Jedes Jahr kommt es zum Export großer Mengen luftgetragenen Staubes aus Nordafrika in Richtung des atlantischen Ozeans. Während dessen Hochphase im Sommer findet dieser Export in einer abgehobenen Schicht, dem Saharan Air Layer (SAL) statt. In dieser Schicht wird das Staubaerosol über den Nordatlantik bis in die Karibik und darüber hinaus transportiert. Aufgrund seines hohen Partikelgehalts und der großflächigen geographischen Ausbreitung hat der SAL wichtige Auswirkungen auf Klima und Umwelt, wie beispielsweise über Aerosol-Strahlungs und Aerosol-Wolken Wechselwirkungen.

Eine der Hauptmotivationen hinter dem Saharan Aerosol Long-Range Transport and Aerosol-Cloud Interaction Experiment (SALTRACE) war die Erweiterung des derzeitigen Wissensstandes über die Aerosoleigenschaften des SAL. Während der Kernphase der Kampagne im Juni/Juli 2013 wurde die Staubschicht zu diesem Zwecke mit einer umfangreichen flugzeuggetragenen Messinstrumentierung zu beiden Seiten des transatlantischen Transports ausführlich beprobt. Der dabei gewonnene Datensatz umfasst Informationen zu größenabhängiger Partikelkonzentration, -volatilität und -zusammensetzung, sowie zur Konzentration an Wolkenkondensationskeimen (CCN) bei einer Wasserdampfübersättigung von 0.2%. Die Kombination dieser Daten erlaubt erstmalig eine vollumfängliche Untersuchung der CCN Eigenschaften des SAL Aerosols, speziell in Form des Partikelhygroskopizitätsparameters κ . Zur Herleitung repräsentativer Wahrscheinlichkeitsverteilungen für diesen Parameter und andere zentrale Aerosoleigenschaften, wie Anzahlgrößenverteilung (NSD) der Partikel, wurden im Zuge dieser Studie neue Datenauswertemethoden entwickelt. Ergänzt werden die in situ Informationen durch eine Reihe von bodenbasierten Messungen, welche u.a. Einblick in die Auswirkungen der Präsenz des SAL auf die Aerosoleigenschaften in der unteren karibischen Troposphäre gewähren.

Dank der anhaltenden äußeren Stabilität des SAL, die einer effektiven Mischung mit der angrenzenden Atmosphäre entgegensteht, wird sowohl an der nordwestafrikanischen Küste als auch in der Karibik eine deutliche Kopplung zwischen der durch den SAL bedingten atmosphärischen Schichtung und den vertikalen Partikelkonzentrationsprofilen beobachtet. Entsprechend tritt der SAL als separiertes Partikelreservoir auf, in dem Partikelmassenkonzentration und CCN Anzahlkonzentration typischerweise ihr Maximum aufweisen (in Bezug auf Standardbedingungen). Intern zeigt die Schicht erhebliche Partikelkonzentrationsvariabilitäten innerhalb vertikaler Distanzen von nur wenigen hundert Metern. Demgegenüber weist sie ein hohes Maß an horizontaler Homogenität auf über Entfernungen von hundert Kilometern und mehr.

Trotz der äußeren Stabilität der Staubschicht zeigen die Ergebnisse deutlich, dass das Auftreten des abgehobenen SAL in der Karibik stets mit einer Präsenz von SAL Aerosol in der darunterliegenden Troposphäre einhergeht. Der Eintrag CCN-reichen Aero-

sols aus dem SAL in die wolkenenthaltende untere Troposphäre führt zu einem Anstieg der dortigen CCN Konzentration und damit zu einer Beeinflussung der Wolkenbildung und -eigenschaften im karibischen Passatwindregime. Der Beitrag von Mineralstaub zu diesem indirekten Aerosoleffekt ist jedoch als nachrangig einzuordnen. Grund hierfür ist, dass sich der Staub im SAL lediglich für Partikeldurchmesser größer ca. 500 nm als dominante Partikelkomponente erweist und die Partikelanzahl in diesem Größenbereich vergleichsweise gering ist. Stattdessen wird die Mehrheit an CCN im SAL von Partikeln in der Nähe des Maximums der Partikel NSD gestellt, d.h. von Partikeln mit Durchmessern kleiner ca. 100 – 200 nm. Dieser Partikelgrößenbereich ist stark von volatilem Material beeinflusst, welches hauptsächlich wasserlöslichem Ammoniumsulfat zuzuschreiben ist. Dementsprechend weist das SAL Aerosol eine hohe effektive Partikelhygroskopizität auf, mit κ Werten im Bereich von 0.3 bis 0.7 bei einem Mittelwert von ca. 0.5. Diese Werte sind ähnlich bis leicht erhöht im Vergleich zu denen (0.2 bis 0.4) in der karibischen marinen Grenzschicht (MBL) im selben Zeitraum. Das mit der Staubschicht transportierte partikelförmige Sulfat, welches für dessen hohe κ Werte und CCN Konzentration verantwortlich ist, wird gemeinhin anthropogenen Quellen zugeordnet. Zusammengenommen legen diese Befunde einen bislang (wenn überhaupt) unzureichend behandelten anthropogenen Klimaeffekt des SAL nahe.

Zusätzlich zum allgegenwärtigen Anteil an volatilem Material im SAL, gibt es vereinzelt starke Indizien für eine zusätzliche Erhöhung solchen Materials im oberen Teil der Schicht durch Aerosoleintrag aus der oberen Troposphäre (UT). Die die Staubschicht überlagernden Luftmassen enthalten eine hohe Konzentration an volatilen kleinen Partikeln mit Durchmessern überwiegend unterhalb 80 nm. Diese Konzentration ist so hoch, dass, trotz des signifikanten Abfallens der Konzentration großer Partikel, das Maximum der Gesamtpartikelkonzentration überhalb des SAL angetroffen wird. Die naheliegendste Quelle dieser volatilen Partikel ist Partikelneubildung (NPF) in der UT, welche oft mit der Erzeugung von partikelförmigen löslichen Sulfaten in Verbindung gebracht wird. Die Fälle in denen die Anreicherung an volatilen kleinen Partikeln bis in den oberen Teil des SAL hineinreicht gehen einher mit einer dortigen Erhöhung der relativen CCN Konzentration und effektiven Partikelhygroskopizität. Ein solcher Einfluss von aus der UT stammenden Partikeln auf die (CCN) Eigenschaften des SAL Aerosols wurde bislang noch nicht berücksichtigt.

Mit Ausnahme einer leichten durchschnittlichen Erhöhung des volatilen Materials im SAL bleiben die Aerosoleigenschaften der Staubschicht über den transatlantischen Transport näherungsweise erhalten. Dies gilt sowohl für die Form der Partikel NSD im untersuchten Durchmesserbereich unterhalb ca. 2 μm als auch für die effektive Partikelhygroskopizität und Aerosolzusammensetzung. Insbesondere tritt keine signifikante "Staubprozessierung", d.h. keine Anhäufung löslichen Materials auf den Staubpartikeln auf.

Chapter 1

Introduction

1.1 Atmospheric Aerosols and the Role of North African Mineral Dust

Atmospheric aerosol¹ particles play a key role for Earth's climate. Among others, they affect its radiation budget directly via light scattering and absorption, and are vital for cloud formation (e.g. Seinfeld and Pandis, 2006). The degree to which an airborne particle takes effect, e.g. how effectively it scatters light, depends on its intrinsic properties such as size and composition. As aerosol particles originate from a wide variety of sources, these properties can vary substantially. Particulate matter is emitted into the atmosphere in the form of pre-existing particles (primary aerosol) or forms in situ via gas-to-particle conversion processes (secondary aerosol). The origin of this matter may be natural or anthropogenic. Once airborne, a particle can undergo modification, i.e. change its size and/or composition. Possible processes for such modification are coagulation/coalescence with other particles or condensation of gaseous material onto the particle. When the product particle is a combination of distinct materials it is termed internally mixed. On the other hand, different particle types can coexist separately in an atmospheric aerosol, which is referred to as an external mixture. The atmospheric lifetime of aerosol particles determining the scale of their temporal and spatial influence strongly depends on the acting removal processes. These processes often favor certain particle types or sizes. Particles are, for instance, washed out via precipitation or sediment due to gravitational settling, both typically most efficient for the largest sizes.

Table 1.1.1 summarizes some of the major atmospheric aerosol types together with their sources, estimated global mass emission fluxes and atmospheric mass loads for the year 2000 (Andreae and Rosenfeld, 2008). Important natural sources for primary aerosol particles include windblown mineral dust from soils in arid and semi-arid regions, sea salt released from the oceans, pollen and spores from the biosphere, ash from volcanic eruptions and soot from forest fires. Exemplary sources for anthropogenic direct emissions are industrial dust and black carbon from fossil fuel combustion. Precursor vapors for the formation of secondary aerosol particles include sulfates, nitrates,

¹By definition, the term "aerosol" refers to the combination of suspended particulate matter and the gas it is suspended in.

Aerosol types (and sources)	Mass emission [Tg/yr]		Mass burden [Tg]
	Best estimate	Range	
Carbonaceous aerosols			
<i>Primary organic</i>	95	40 - 150	1.2
Biomass burning	54	26 - 70	
Fossil fuel	4	3 - 9	
Biogenic	35	15 - 70	
<i>Black carbon</i>	10	8 - 14	0.1
Open burning and bio fuel	6	5 - 7	
Fossil fuel	4.5	3 - 6	
<i>Secondary organic</i>	28	2.5 - 83	0.8
Biogenic	25	2.5 - 79	
Anthropogenic	3.5	0.05 - 4.0	
Sulfates	200	107 - 374	2.8
Biogenic	57	28 - 118	
Volcanic	21	9 - 48	
Anthropogenic	122	69 - 214	
Nitrates	18	12 - 27	0.49
Industrial dust^a	100	40 - 130	1.1
Sea salt	10130	3000 - 20000	15
Mineral (soil) dust	1600	1000 - 2150	18

Values are based on a list of publications given in Andreae and Rosenfeld (2008). The actual range of uncertainty may encompass values both larger and smaller than those reported here.

^a Includes a broad variety of anthropogenic primary aerosols, particularly those from transportation (e.g., tire and brake abrasion, road dust, etc.), coal combustion (fly ash, etc.), cement manufacturing, metallurgical industries, and waste incineration

Table 1.1.1: Sources, global mass emission fluxes and atmospheric mass burdens for various aerosol types estimated for the year 2000. Adopted from Andreae and Rosenfeld (2008).

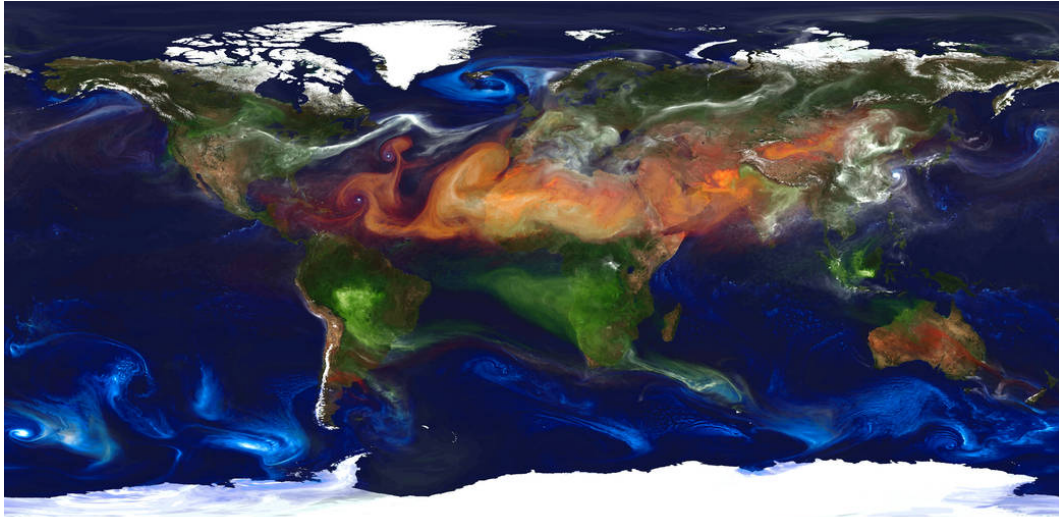


Figure 1.1.1: GEOS-5 model simulation, showing four essential aerosol types and their global occurrence: mineral dust from deserts (red), sea salt (blue), soot and smoke from fires (green) and sulfate particles from volcanoes and fossil fuel combustion (white). Image from: <http://svs.gsfc.nasa.gov/30017>

ammonia and organic hydrocarbons, which can originate from both natural or anthropogenic sources. Sulfates, for example, can be emitted as sulfur dioxide from combustion, biomass burning and volcanoes, as dimethyl sulfide from oceans, and as hydrogen sulfide from biological activities (Andreae, 1995). As with sulfate, for many aerosol types a unique classification into natural or anthropogenic origin is impossible. Yet, in the present-day atmosphere, the majority of black carbon, sulfate, nitrate and ammonium is thought to arise from anthropogenic sources, whereas sea salt, mineral dust and primary biological particles are predominantly of natural origin (Boucher et al., 2013). The variety of sources and emission processes involved complicate the quantification of mass fluxes, which reflects in large uncertainty ranges and considerable scatter between estimates derived by different studies (cf. Tab. 1.1.1). However, publications unanimously agree that sea salt and mineral soil dust dominate global aerosol mass emissions. Although sea salt emissions likely even exceed those of mineral dust, the former is more effectively removed from the atmosphere and thus shorter-lived (Textor et al., 2006). In consequence, mineral dust contributes to approximately 50% or even more (Cakmur et al., 2006) to the total atmospheric aerosol mass burden.

Naturally, emissions and atmospheric occurrences for different particle types are not equally distributed across the globe, but follow characteristic spatial patterns (Fig. 1.1.1). Major sources of mineral dust particles are found in the Northern Hemisphere in a region that is referred to as the “global dust belt” (Prospero et al., 2002), including the Sahara and Sahel regions of Africa, the Arabian Peninsula, Central Asia and desert basins in China. Further sources are located in Australia, North- and South America, and South Africa (e.g. Goudie and Middleton, 2006). Based on an intercomparison of 15 global aerosol models within the AeroCom project, Huneus et al. (2011) estimate the contribution of the North African sources to the global dust emissions to be about 70%, followed by Middle East and Asian sources with approximately 10% each.

These numbers illustrate that North African mineral dust is one of the most important atmospheric aerosol types.

It must be expected that changes in climate and land cover will alter dust emission fluxes and atmospheric dust loads. Due to the complexity of possible feedbacks, future projections are highly uncertain and different estimates for both increasing and decreasing dust burdens exist (Tegen et al., 2004; Woodward et al., 2005; Mahowald et al., 2006). However, latest assessments show that, primarily by agricultural soil modification, the anthropogenic contribution to North African and global dust emissions already amounts to around 8% and 25%, respectively (Ginoux et al., 2012), connoting a significant present-day human influence on this major atmospheric constituent.

1.2 Transatlantic Transport of North African Dust

Owing to atmospheric transport the influence of dust aerosol can extend far beyond its area of origin. One major example for this is the transatlantic transport of North African dust, which is most pronounced in Northern Hemispheric summer. During this time strong solar heating causes a vast low pressure system over the Western Sahara, called the the Saharan heat low. The result is a dry deep mixed layer, the Saharan atmospheric boundary layer (SABL), that often extents from the surface up to about 500 hPa (6 km) (Carlson and Prospero, 1972; Cuesta et al., 2009). Various dynamical processes, of which the breakdown of nocturnal low level jets after sunrise apparently is the dominant one (Schepanski et al., 2009, 2017), lead to mobilization and upward mixing of soil particles feeding the SABL with large quantities of mineral dust (Knippertz and Todd, 2012). Easterly mid-tropospheric winds with a maximum between 15 and 20°N at a pressure level of around 700 hPa, termed the African easterly jet (AEJ), evolve in response to the strong baroclinic zone between the Sahara and the cooler equatorial Africa and export the dust-laden air towards the Northwest African coast where it is undercut by cool, moist low-level marine air and builds the surface-detached Saharan air layer (SAL) (Carlson and Prospero, 1972; Khan et al., 2015). Significantly exceeding the temperature of the normal tropical atmosphere, the warm SAL base strongly enhances the so-called trade wind inversion that caps the moist lower troposphere. The resulting strong temperature inversion suppresses vertical exchange between the layers and, consequently, hinders the removal of SAL aerosol particles (Prospero and Carlson, 1972). The ceiling of the SAL is characterized by a second inversion, which is attributable to large-scale subsidence in the region (Weinzierl, 2007; Gamo, 1996).

The horizontal temperature gradient between the warm SAL and the cooler tropical air to its south promotes its easterly flow and permits its further progress across the North Atlantic (Dunion and Velden, 2004). Meridional instabilities developing over Northeast Africa south of the AEJ core, called tropical or African easterly waves² (AEWs), cause this transatlantic SAL transport to not occur uniformly, but in wave-like episodic outbreaks that are interrupted by phases with southerly wind components (Burpee, 1972; Savoie and Prospero, 1977). During its transport longwave radiative

²AEWs account for approximately half of the tropical cyclones that form in the Atlantic (Burpee, 1972) and over 80% of all intense hurricanes (Landsea, 1993)

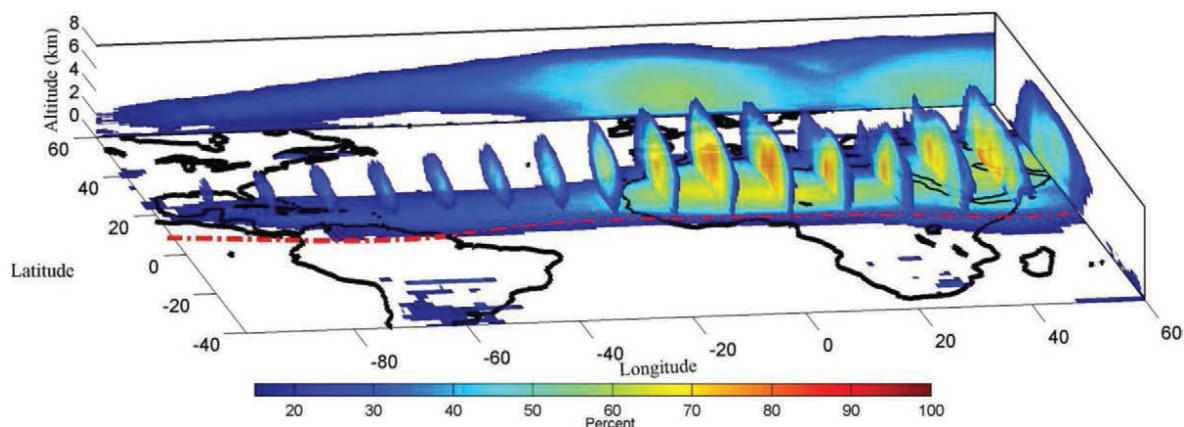


Figure 1.2.1: Average spatial occurrence of mineral dust in the summer months June-August 2006-2010. The colors indicate the frequency of dust occurrence, classified by the vertical feature mask of the CALIPSO satellite lidar measurements, as a percentage of the number of total retrievals during that period. The red dashed line marks the center of the intertropical convergence zone (ITCZ). Adopted from Adams et al. (2012)

cooling energetically equilibrates the SAL's base with its cooler environment, thereby weakening the inversion that inhibits the SAL aerosol from being effectively mixed down into the moist lower troposphere. However, daytime heating via light absorption by the mineral dust particles counteracts the cooling and reinforces the stability at the base of the SAL (Carlson and Benjamin, 1980; Davidi et al., 2012) enabling it to survive and maintain its characteristics during the 5 to 7 days that are required to pass the more than 4500 km distance from the West African coast to the Caribbean sea (Prospero and Carlson, 1972; Huang et al., 2010). Yet, the suppressive trade wind inversion does not imply a complete sealing of the SAL so that gravitational sedimentation and convective mixing events can still lead to input of SAL particles into the subjacent layers (Liu et al., 2008). Turbulent mixing might also take place at the upper end of the SAL during transport. Here, the internal heating has a destabilizing effect on the inversion between the SAL and overlying troposphere. The large-scale subsidence present along the transport route (Colarco et al., 2003), however, can work against this effect and help to preserve the stability at the ceiling of the layer (Weinzierl, 2007). Over the course of the transatlantic long range transport the top of the SAL descends by up to 1-2 km due to this large-scale subsidence, whereas the trade wind inversion and, correspondingly, the SAL's base rises from about 0.5-1 km offshore the North African coast to about 2 km in the Caribbean (Hastenrath, 1991; Karyampudi et al., 1999; Colarco et al., 2003; Weinzierl et al., 2017). Satellite based lidar studies (Liu et al., 2008; Adams et al., 2012) and airborne in situ measurements (e.g. Reid et al., 2002) show that, after reaching the Caribbean and the Gulf of Mexico, the inversion barrier between the SAL and the lower troposphere often is sufficiently attenuated to allow for efficient downward mixing of the SAL aerosol, recognizable by more frequent dust occurrence near the surface (see Fig. 1.2.1). Saharan dust transport across the tropical North Atlantic has a clear seasonal cycle, with most northerly transport into the Caribbean coinciding with maximum dust emissions from North Africa in Northern Hemispheric summer (Prospero and Lamb, 2003; Engelstaedter and Washington, 2007),

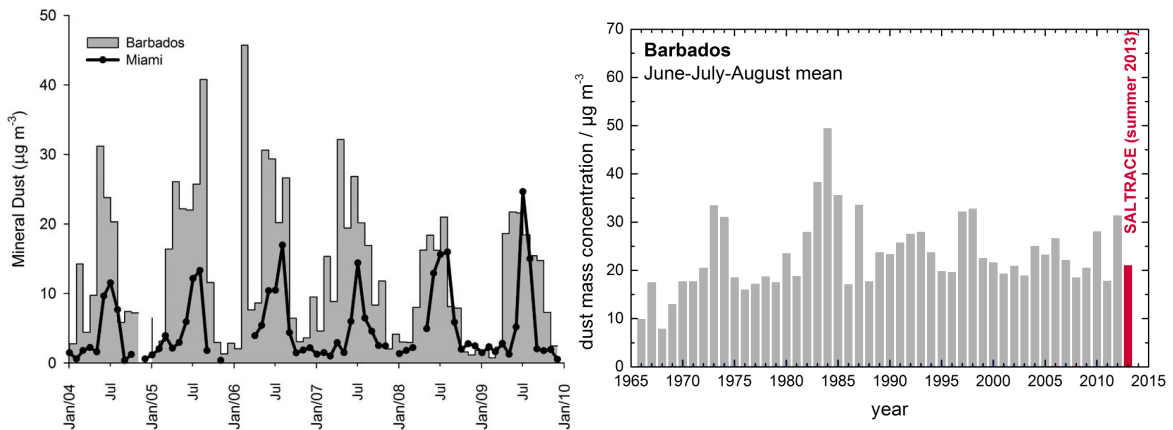


Figure 1.2.2: Seasonality and long-term record of mineral dust mass concentrations measured at ground level in the Caribbean. The left-hand side shows monthly mean dust concentrations at Barbados and Miami from 2004 to 2009. The right-hand side displays the average dust concentrations at Barbados during the summer months June, July and August in a long-term record starting from the mid 60s. Adopted and modified from Prospero and Mayol-Bracero (2013) and Weinzierl et al. (2017)

as can be seen from Fig. 1.2.2, and more southerly transport routes during the rest of the year (e.g. Tsamalis et al., 2013). Nevertheless, the export and transatlantic transport of Saharan dust is an all year phenomenon making it a major global dust transport pathway (Goudie and Middleton, 2001).

1.3 Impact of North African Dust

In summary, the SAL does not only carry one of the highest aerosol loads worldwide but also covers vast global areas, including some of most remote oceanic regions, due to its transport features. Accordingly, it is obvious that the impacts of the SAL on climate and environment are far-reaching and manifold.

Tropical Cyclogenesis

SAL presence affects the meteorological conditions over the tropical North Atlantic, which is a region essential for tropical cyclone (TC) development. The warm dry air and mid-level easterly jet the layer introduces into this region can suppress TC evolution by several means. First of all, deep convection, a prerequisite for TC development, is hampered by the reinforced stability in the lower troposphere. Enhanced vertical wind shear further increases the horizontal dissipation of convective energy. Moreover, intrusion of dry air into the TC circulation can reduce the convective available potential energy (Dunion and Velden, 2004; Zipser et al., 2009). Albeit the complex interactions between the SAL and TCs are still subject to research, observations indeed suggest a strong anti-correlation between TC activity and SAL events over the Atlantic (Evan et al., 2006).

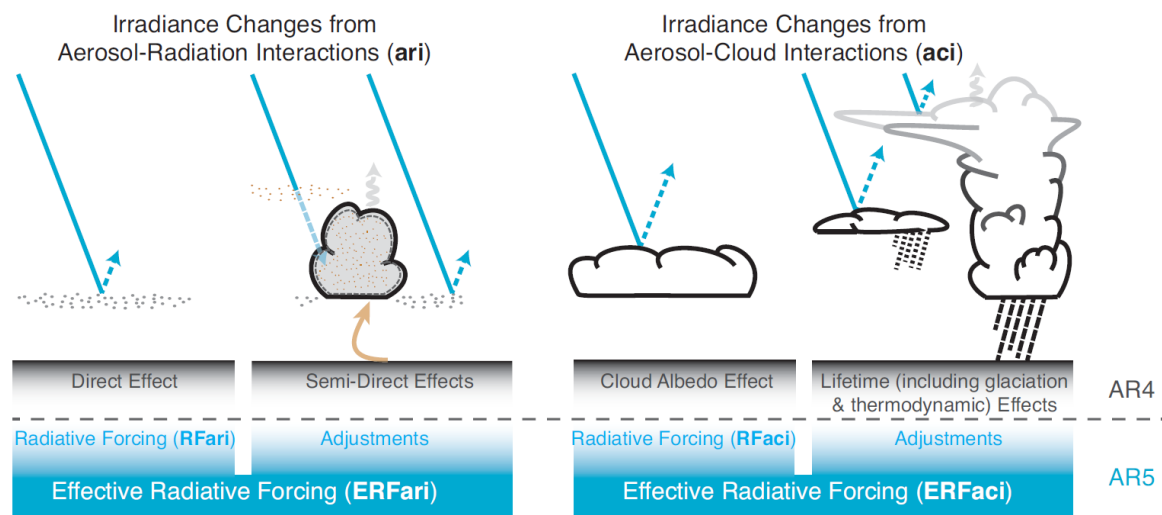


Figure 1.3.1: Schematic view of aerosol radiative forcing effects including their corresponding terminologies following the fourth and fifth assessment reports (AR4 and AR5) of the Intergovernmental Panel on Climate Change (IPCC). The blue and gray arrows visualize short- and longwave radiation, respectively. The brown arrow symbolizes couplings between surface and cloud layer. Adopted from Boucher et al. (2013)

Biosphere

Besides its role for meteorological processes, the SAL may impact the biosphere via input of particulate matter. The high additional particle concentrations with which the SAL supplies the marine background aerosol of the Caribbean islands are of concern for human health, as they can cause an exceedance of air quality standards (Prospero and Lamb, 2003). The inhalation of mineral dust is known to produce a wide range of physiological responses, of which the possible role on asthma is of particular interest (Gyan et al., 2005; Morman and Plumlee, 2013). Although local anthropogenic emissions are low, asthma rates throughout the Caribbean are comparable to polluted urban and/or industrial environments. The dust particles in the SAL further carry important micronutrients like iron and phosphorus. Upon deposition these nutrients fertilize large areas of the Atlantic Ocean, the Caribbean islands and even the Amazon Basin impacting many biochemical cycles (Jickells et al., 2005; Bristow et al., 2010; Niedermeier et al., 2014).

Aerosol-Radiation Interactions

Apart from direct impacts on the biosphere, the SAL aerosol — like any other aerosol — influences local (and global) climate via aerosol-radiation and aerosol-cloud interactions (Fig. 1.3.1). Its particles, and mineral dust in particular, modify both incoming solar shortwave and outgoing terrestrial longwave radiation by scattering and absorption (Sokolik et al., 2001; Balkanski et al., 2007). In the shortwave spectrum dust aerosols affect radiative transfer mainly via light scattering (Fouquart et al., 1987; Sokolik and Toon, 1999; Otto et al., 2007). Consequently, increasing particle concentrations in the SAL result in an increase in solar radiation scattered back to space

and, hence, in a decreasing shortwave irradiance at the surface. Especially over the dark ocean surface this causes a lowering of surface temperature with important implications on interannual to decadal timescales (Lau and Kim, 2007; Evan et al., 2011). To some extent in the shortwave but primarily in the longwave part of the spectrum dust particles also absorb radiation. This leads to a warming of the dust-containing layers, with the discussed consequences for atmospheric stability (Carlson and Benjamin, 1980; Davidi et al., 2012). Moreover, since thermal radiation emitted by the heated layers is undirected, a part of the energy absorbed from terrestrial longwave radiation is sent back towards the surface. This reduces the longwave flux leaving the atmosphere and enhances the longwave irradiance at the surface, similar to the effect of greenhouse gases. Over more reflective land surfaces such as the Saharan desert, where the cooling due to shortwave scattering is less pronounced (Ansmann et al., 2011), this effect even leads to a net warming at ground level (Otto et al., 2007; Bierwirth et al., 2009). The magnitude of the SAL's radiative forcing depends on the aerosol particle size distribution and optical properties, its vertical structure, and the albedo of the underlying surface or clouds (Liao and Seinfeld, 1998; Myhre and Stordal, 2001; Tegen et al., 2010). Although the combination of airborne in situ measurements, satellite- and ground-based remote sensing, and radiative transfer modeling (see Ryder et al. (2013b) and Weinzierl et al. (2017) for a list of previous campaigns) has led to improvements in quantifying the SAL's radiative forcing over the last decades, considerable uncertainties remain (Formenti et al., 2011b; Ansmann et al., 2011; Highwood and Ryder, 2014). Aside from the difficulty of retrieving reliable in situ particle size distributions (Reid et al., 2003a; Wendisch et al., 2004; Fiebig et al., 2005) and the complexity of aerosol composition (Capes et al., 2008; Kandler et al., 2009), an important source of uncertainty is the spatial and particularly the vertical distribution of the aerosol (Kahn et al., 2004; Osborne et al., 2011). Reports about the vertical structure of the SAL are partly divergent. Whereas some studies, including airborne in situ and especially satellite-based lidar measurements, describe the SAL aerosol's vertical structure as homogeneous and well-mixed both before and during long-range transport (Liu et al., 2008; Ryder et al., 2013a; Tsamalis et al., 2013), others point out the substantial variability in the vertical distribution and find complex sublayer structures on either side of the Atlantic (Maring et al., 2003a; Johnson and Osborne, 2011; Formenti et al., 2011a). Further efforts in improving our knowledge of the vertical distribution of SAL aerosol properties and its evolution during transport are thus essential.

Aerosol-Cloud Interactions

In addition to their interaction with radiation, aerosol particles affect the climate via their role in cloud formation processes. To date, these aerosol-cloud interactions (see Fig. 1.3.1) represent the main source of uncertainty in the assessment of climate sensitivity to changes in atmospheric aerosol burden (Boucher et al., 2013; Carslaw et al., 2013). Mineral dust particles have been identified as one of the most important aerosol species with the rare capability of nucleating ice crystals in both mixed-phase and cirrus clouds (DeMott et al., 2003; Kamphus et al., 2010; Cziczo et al., 2013). For the warm low-level clouds characteristic for the North Atlantic trade wind regime beneath the SAL, mainly appearing as cumuli at a lifting condensation level around

700 m (Nuijens et al., 2014), the transported particles are further of importance as potential cloud condensation nuclei (CCN). Globally, the contribution of mineral dust to CCN concentrations is estimated to be up to 40% (Karydis et al., 2011). The formation of liquid cloud droplets via water vapor condensation on preexisting aerosol particles depends on whether the particles allow for unconstrained water uptake from the vapor phase and on the available vapor itself. The ability to act as a CCN at a given ambient water vapor pressure is determined by a particle's size and chemical affinity for water, termed hygroscopicity. The so-called activation of aerosol particles into cloud droplets starts from large hygroscopic particles at lower water vapor supersaturations³ and continues to smaller less hygroscopic particles with rising supersaturation (Köhler, 1936; Petters and Kreidenweis, 2007). Increasing concentrations of CCN principally lead to higher cloud droplet concentrations and, as the CCN compete for the available water vapor, result in smaller droplet sizes. In consequence, the shortwave albedo of clouds influenced by high aerosol loads is usually enhanced compared to that of clouds developing under more pristine conditions (Twomey, 1977; Lohmann and Feichter, 2005). Named after the author, this effect is often referred to as the Twomey effect. Especially for marine clouds in tropical environments with high solar radiation flux and low surface albedo, the Twomey effect can have a great impact on the planetary radiation budget. Smaller droplet sizes further imply lower coalescence efficiency and, as a result, hamper precipitation and extend cloud lifetime (Albrecht, 1989; Rosenfeld et al., 2008). However, a relative enrichment in large (supermicron) aerosol particles, in this context termed giant CCN (GCCN), can have opposing effects. By activating at smaller water vapor supersaturations, GCCN may deplete the ambient supersaturation in the early stages of cloud formation, thus reducing the concentration of droplets that eventually form (Ghan et al., 1998). Nucleating large drops that rapidly grow by collecting smaller cloud droplets GCCN can promote and accelerate the development of precipitation (Levin and Cotton, 2009; Cheng et al., 2009). The ultimate influence of the SAL aerosol particles on the warm North Atlantic trade wind clouds can thus depend on their size distribution and size-dependent hygroscopicity.

Whereas the mineral dust particles transported in the SAL can be large in size (Maring et al., 2003b; Weinzierl et al., 2009, 2011, 2017; Ryder et al., 2013b; Denjean et al., 2016b), freshly emitted dust is hardly hygroscopic which strongly restricts its CCN ability and causes retarded activation kinetics (Herich et al., 2009; Kumar et al., 2011b). Even though field and laboratory studies indicate that fresh mineral dust may nevertheless be able to act as CCN at atmospheric relevant supersaturation via small amounts of soluble material and water adsorption on its surface alone (Twohy et al., 2009; Koehler et al., 2009; Kumar et al., 2011b), dust particles only evolve into effective CCN when they experience atmospheric processing and become internally mixed with hygroscopic material. Such enhancements of mineral dust hygroscopicity can occur upon coagulation with soluble particles such as sea salt (Levin et al., 2005; Denjean et al., 2015), via heterogeneous condensation of soluble gas species onto the dust particles (Sullivan et al., 2007) and in-cloud processing (Yin et al., 2002; Fitzgerald et al., 2015). The latter means that dust particles once incorporated into a subsequently

³A vapor is called supersaturated if its partial pressure exceeds the equilibrium partial pressure over a flat surface of the corresponding condensate. Accordingly, water vapor supersaturation means that relative humidity is greater than 100%.

re-evaporating droplet can be left coated with layers of soluble material (e.g. sulfate) due to aqueous-phase chemistry in the cloud droplet. If and to what extent North African mineral dust experiences atmospheric processing can be central to the role of the SAL as a reservoir of CCN and GCCN. Findings in the literature so far do not show a clear picture of the evolution of mineral dust hygroscopicity with transatlantic long-range transport. Whereas a recent study by Denjean et al. (2015) found African dust particles transported into the Caribbean to be mainly unprocessed and unaltered in hygroscopicity compared to fresh dust, others report increased amounts of soluble material associated with mineral dust particles, which they attribute to in-cloud processing (Matsuki et al., 2010; Fitzgerald et al., 2015). This might appear to be in contrast at first sight. Latter studies, however, were conducted directly in low-level cloud environments over the African continent and the Caribbean and may, hence, not be representative of the main SAL long-range transport itself. Indeed, Fitzgerald et al. (2015) attribute the changes in mineral dust composition they observe to local in-cloud processing at the sampling site rather than to the previous transport. Since the main part of this transport takes place in the interior of the SAL that is separated from the moist cloud layer beneath and is, contrary to continental transport over urban/industrial areas, spared from input of fresh anthropogenic gas emissions, it is not unreasonable that Saharan dust particles can stay unprocessed.

Nevertheless, studies on Caribbean cumulus clouds show that under SAL presence cloud droplet number concentrations are significantly enhanced, meaning that the SAL supplies the cloud-containing lower troposphere with notable numbers of CCN (Siebert et al., 2013; Kristensen et al., 2016; Wex et al., 2016). Some studies further demonstrate that this increase in droplet concentration is accompanied by a reduction in effective droplet radii resulting in higher cloud albedos, i.e. the Twomey effect (Siebert et al., 2013; Werner et al., 2014). Particle composition measurements in the same environment during SAL presence, on the other hand, reveal that mineral dust particles are too low in abundance to significantly contribute to CCN concentrations (Kristensen et al., 2016). The missing link, that often seems to go unnoticed or remains undiscussed in the literature concerning the impact of dust-laden aerosols on clouds, might be that mineral dust particles regularly appear in external mixtures with other particle types, although dust-containing aerosols as a whole are often referred to as “dust”. While few studies indirectly suggest that mineral dust is the dominant particle type in the SAL throughout the complete size range (Zipser et al., 2009; Jung et al., 2013), more commonly it is found that a substantial fraction of particles are not mineral dust. Particularly pronounced in winter during dry season in the Sahel, when dust transport occurs further to the south, biomass burning aerosol can become embedded in the dust layer (Capes et al., 2008; Ansmann et al., 2011; Adams et al., 2012). Moreover, airborne and ground-based measurements of the summertime aerosol composition in Northern Africa during the Saharan Mineral Dust Experiment (SAMUM) in 2006 showed a (predominantly external) mixture between sulfates and mineral dust with a transition at particle diameters around 500 nm (Kandler et al., 2009; Kaaden et al., 2009; Schladitz et al., 2009; Weinzierl et al., 2009). Here, as can be seen from Fig. 1.3.2, smaller particles were mainly comprised of hygroscopic ammonium sulfate, whereas the larger particles were dominated by non-hygroscopic mineral dust (primarily silicates), with only minor fractions of internal mixtures between dust and sulfates. The few publi-

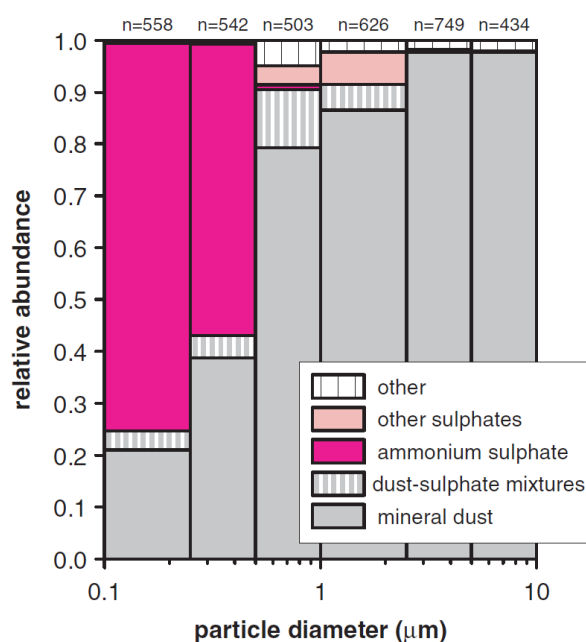


Figure 1.3.2: Size-resolved aerosol composition in Northwest Africa (Marocco) during the SAMUM campaign in early summer 2006. Adopted from Kandler et al. (2009)

cations addressing the presence of sulfate particles in the Saharan dust aerosol link these particles to anthropogenic emissions from European and North African sources (Raes et al., 1997; Kaaden et al., 2009; Rodríguez et al., 2011; Boose et al., 2016). The high degree of external mixture could be explained by the sulfate particles being already aged and low in reactivity before they mix with the mineral dust particles, contrary to fresh sulfate plumes that would rather form internal mixtures with the dust (Raes et al., 1997). When present and exported with the desert dust to the North Atlantic, these particles (of anthropogenic origin) could have a severe influence on the CCN properties of the SAL aerosol in consideration of their hygroscopicity and the fact that they occupy a size range that usually dominates the total particle number concentration. Yet, this potential influence has not been investigated.

Aircraft measurements in the upper troposphere (UT) have further consistently shown elevated concentrations of small particles, including highly hygroscopic species as sulfuric acid, that are associated with new particle formation (NPF) from gas phase precursors (Clarke et al., 1999; Twohy et al., 2002; Hermann et al., 2008; Borrmann et al., 2010). Although not explicitly discussed in the literature, these particles could additionally enhance the number of hygroscopic particles in the SAL upon (large-scale) downward transport from the UT towards the SAL top edge and entrainment into the upper SAL during its formation and/or long range transport, thereby altering its vertical aerosol (CCN) properties.

In 2005, the cloud condensation nuclei counter (CCNC), a tool to study CCN activation in situ at supersaturated conditions, thus allowing to measure CCN concentrations and indirectly infer effective particle hygroscopicity, was introduced to the field (Roberts and Nenes, 2005). Yet, airborne in situ CCN data in general and vertically resolved measurements for the SAL in particular are very rare. While ground-based

studies for the Caribbean marine boundary layer (MBL) are available (Kristensen et al., 2016; Wex et al., 2016), to date the only CCN measurements in the interior of the Caribbean SAL after long-range transport were carried out by Jung et al. (2013) and were limited to altitudes below about 3 km. Jung et al. (2013) derived effective particle hygroscopicities for the SAL aerosol similar to laboratory values for fresh/unprocessed African dust samples (cf. Koehler et al., 2009; Herich et al., 2009; Kumar et al., 2011b). This finding is somewhat surprising since it excludes the presence of any hygroscopic material both externally or internally mixed with the dust, which is not in line with the SAMUM results. As the measurements of Jung et al. (2013) took place in a different year than SAMUM, and in spring rather than during the main dust transport period in summer, this might indicate a strong seasonal and/or interannual variability in the SAL aerosol composition and CCN properties. More comprehensive measurements within the SAL, particularly during the summer season, are urgently needed to gain further insight into its role as a reservoir of CCN. Advanced understanding of the hygroscopic properties of the SAL aerosol is crucial to improve ground- and satellite-based remote sensing CCN retrievals (Mamouri and Ansmann, 2016; Stier, 2016) that are required to extend the in situ measurements limited in space and time to larger scales, and to ultimately improve aerosol-cloud interactions in models (Pringle et al., 2010; Schmale et al., 2017).

1.4 The SALTRACE Campaign and Thesis Objectives

One major disadvantage of previous airborne in situ campaigns studying the SAL's structure and physiochemical aerosol properties was that they were restricted to one side of the North Atlantic. Conducted in different years and/or (transport) seasons, and employing dissimilar measurement methods/instrumentation it is difficult to directly compare their results and to conclude on the role of transatlantic transport on potential differences found. In addition, especially in the Caribbean, in situ data from the SAL interior are scarce and often limited to altitudes far below the SAL top.

To overcome these shortcomings was one of the main motivations behind the Saharan Aerosol Long-Range Transport and Aerosol-Cloud Interaction Experiment (SALTRACE), a German-led initiative involving scientists from Europe, Cabo Verde, the Caribbean and the United States (Weinzierl et al., 2017). During its core phase in June and July 2013, the SALTRACE campaign included airborne in situ measurements over the Northwest African coast in the vicinity of Cabo Verde and, with the same instrumentation, in the Caribbean between the islands of Barbados and Puerto Rico. The platform for the airborne measurements was the Falcon research aircraft of the German Aerospace Center (Deutsches Zentrum für Luft- und Raumfahrt, DLR), that was equipped with an extensive aerosol payload⁴. Besides basic information on aerosol microphysics, such as total particle number concentration and particle number size distribution (NSD), the airborne in situ setup included size-resolved measurements of particle volatility and impactor sampling for offline analysis of single particle composi-

⁴For a complete list of instruments/measurements involved in SALTRACE see Weinzierl et al. (2017, supplement)

tion. Additionally, the campaign involved the first-time operation of a CCNC onboard a German research aircraft. The combination of CCN measurements with information on the aerosol particle size distribution and composition provides new insights into the hygroscopic properties of the SAL aerosol. Moreover, the operational ceiling of the Falcon by far exceeds the maximum SAL top height, thus permitting to assess its full vertical range on either side of the Atlantic. With 86 out of a total of 110 hours of flight time dedicated to sample several consecutive North African dust outbreaks, the SALTRACE airborne measurements represent the largest effort ever made in the investigation of SAL aerosol properties and on long-range transported dust in general.

Figure 1.2.2 puts the SALTRACE core period in the context of the long-term record of summertime mineral dust mass concentrations measured at ground level on Barbados. Unlike for years with exceptionally enhanced dust loads, as for example in the early to mid 80s, that coincided with pronounced droughts in North Africa (Prospero and Lamb, 2003; Prospero et al., 2014), 2013 can be considered as a year representative of long-term average conditions (Weinzierl et al., 2017). In summary, the SALTRACE in situ data set permits to study the SAL aerosol under representative summertime conditions in a more comprehensive way than ever before. Particularly, it allows to examine the layer's physiochemical aerosol properties, including its role as a reservoir of CCN, throughout its entire vertical extent both before and after transatlantic transport without potential biases introduced by differences in instrumentation etc. The airborne in situ data are supplemented by a suite of ground-based measurements, among others giving insight into the aerosol conditions in the Caribbean MBL both during SAL presence and absence. On the basis of this unique data set this thesis aims to address the following scientific questions:

- What is the characteristic vertical (and horizontal) aerosol structure during North African dust events on either side of the Atlantic? How does this structure relate to SAL-induced atmospheric stratification?
- What are the properties, particularly the CCN properties of the SAL aerosol? Do these properties (significantly) change with with long-range transport?
- Does SAL presence affect CCN concentrations in the cloud-containing lower troposphere in the Caribbean?

1.5 Thesis Structure

The thesis is organized as follows: Chapter 2 first introduces the theoretical background necessary to understand the operating principles behind the instruments central to this study, namely nucleation and Köhler theory for the condensation-based particle counters and scattering theory for the optical particle counters (OPCs). In addition, particle NSD and aerosol mixing state (with respect to volatility), two essential aerosol properties, are discussed. Finally, the theory of particle loss in sampling lines is covered, including causes and corrective actions for this source of systematic error in aerosol measurements.

Chapter 3 then presents all measurement and data evaluation methods deployed in this work. The SALTRACE campaign is introduced in more detail with focus on the

airborne setup and sampling strategy. Moreover, the (relevant) ground-based instruments and sampling sites are presented. The central airborne instruments are treated in-depth including their operating principles, associated data processing steps and efforts made to ensure a high data quality. Particularly, an advanced method to model the response of OPCs and to calibrate these instruments in a self-consistent way is presented. This method is published in Walser et al. (2017). For the derivation of some important aerosol properties like particle NSD and hygroscopicity from the combination of different airborne measurements, further novel approaches are introduced. They are designed to guarantee accurate solutions and realistic uncertainty estimates for these key aerosol properties. The validity of the solutions is demonstrated by means of suitable comparison measurements. For the external data used in this study, e.g. those from the ground-based measurements, basic information and references are given.

The results obtained from this extensive data set are presented in Ch. 4. Here, first the intense dust event affecting Barbados on 10 and 11 July 2013 is utilized as a benchmark case to study SAL appearance and the layer's aerosol properties in the Caribbean in full detail. Subsequently, the scope is widened to the overall picture of the SAL met during SALTRACE on both sides of the North Atlantic. Among others, the time-resolved structure of the SAL, transport-induced differences in SAL aerosol properties and the impact of SAL presence on the lower Caribbean troposphere are examined carefully. A few of these results are contained in Weinzierl et al. (2017).

In Ch. 5 the results are interpreted regarding their implications and discussed in the light of the current literature. In this chapter the initial scientific questions are answered at length. A summary of this work is given in Ch. 6, followed by a treatment of pending research needs and possible methodical improvements for future measurements in Ch. 7.

1.6 External Data

The realization of the study required input from a number of collaborators from the SALTRACE project. These contributions and the persons to credit these contributions to are summarized below. More detailed information are given in the corresponding text passages in Ch. 3.

Ambient meteorological data for the airborne measurements were provided by A. Giez, V. Dreiling, M. Zöger and Ch. Mallaun, DLR. Additional airborne in situ aerosol data, namely number concentration of giant (supermicron) particles and refractory black carbon mass concentration were made available by D. Sauer, K. Heimerl and B. Weinzierl⁵, DLR. CCN data were pre-processed by M. Dollner⁶, DLR. K. Kandler of the Technical University of Darmstadt contributed single particle compositional information for the SAL aerosol.

Ground-based in situ data from Barbados, including particle NSD, mineral dust mass concentration and CCN number concentrations were provided by T. Müller and T. Kristensen⁷, Leipzig Institute for Tropospheric Research (TROPOS). Further, ground-based remote sensing data, i.e. lidar profiles from Barbados and sun photometer data

⁵K. Heimerl and B. Weinzierl now at: University of Vienna (UNIVIE)

⁶M. Dollner now at: UNIVIE

⁷T. Kristensen now at: Lund University

from Barbados and Cabo Verde were supplied by V. Freudenthaler, Ludwig-Maximilian University of Munich (LMU) and C. Toledano, University of Valladolid, respectively.

To study the large-scale appearance of the dust layer, in addition to the local remote sensing measurements, the SAL tracking satellite product of the University of Wisconsin-Madison was consulted. The entirety of measurements are supplemented by aerosol transport modeling and trajectory analysis results. These results were made available by B. Heinold, TROPOS and A. Schäfer and T. Götsch, DLR, respectively. Finally, supportive scattering cross section calculations for aspherical particles, used for the OPC-based particle NSD retrievals, were performed by J. Gasteiger⁸, LMU.

⁸J. Gasteiger now at: UNIVIE

Chapter 2

Theory

The following chapter provides the theoretical basis for the methods introduced in Ch. 3 and the interpretation of the results presented in Ch. 4. The first section that deals with the basics of nucleation and Köhler theory is primarily guided by the text books of Hinds (1999) and Seinfeld and Pandis (2006). The subsequent overview over scattering theory is mainly based on Bohren and Huffman (1983). The chapter closes with fundamentals on aerosol particle size distributions, aerosol mixing state (with respect to particle volatility) and particle loss in sampling lines. Detailed information for the former can be found in Hinds (1999) and Seinfeld and Pandis (2006). For further information on aerosol mixing state and particle sampling losses the interested reader is referred to Wendisch and Brenguier (2013) and Kulkarni et al. (2011), respectively. Additional references are given in the respective sections.

2.1 Nucleation and Köhler Theory

The formation of atmospheric liquid phase aerosol particles and water droplets¹ occurs via homogeneous or heterogeneous nucleation from molecules in the gaseous phase. An important quantity deciding whether nucleation can take place or not is the vapor saturation ratio S , also simply called saturation. It is given by the ratio of the ambient vapor partial pressure p_v and the saturation vapor pressure p_s , which is a function of temperature T .

$$S = \frac{p_v}{p_s(T)}$$

The saturation vapor pressure is defined as the equilibrium vapor pressure over a flat surface of the corresponding liquid and can be derived from the energetic balance at the phase transition. The total differential of the suitable thermodynamic potential, i.e. the Gibbs free energy G with the independent variables temperature, pressure and number of molecules N writes as

$$dG = -\hat{S}dT + Vdp + \mu dN \quad (2.1.1)$$

where \hat{S} and V are the entropy and volume of the system, and μ is the chemical potential, that can be defined as the Gibbs free energy per molecule. For the two-phase

¹Although strictly being aerosol particles, too, according to the definition, water droplets are usually not termed as such due to their special role.

system, the vapor and the (flat) liquid, equilibrium means that the rate of molecules leaving the liquid by evaporation equals the rate of molecules condensing, so that no net molecule transfer remains ($dN = 0$). The change in Gibbs energy of the vapor phase dG_v must further correspond to that of the liquid phase dG_l resulting in

$$(\hat{S}_v - \hat{S}_l) dT = (V_v - V_l) dp$$

which can be further rearranged to

$$\frac{dp}{dT} = \frac{\hat{S}_v - \hat{S}_l}{V_v - V_l} = \frac{\Delta\hat{S}}{\Delta V} = \frac{L}{T\Delta V} \quad (2.1.2)$$

with the substance specific latent heat (or enthalpy) of vaporization L . This equation is widely known as the Clausius-Clapeyron equation in its thermodynamic representation. Substitution of the volume difference term ΔV in Eq. (2.1.2) by means of the ideal gas law and subsequent integration yields the corresponding integral form

$$p_s(T) = p_{s,0} \exp\left(-\frac{L}{R} \left(\frac{1}{T} - \frac{1}{T_0}\right)\right)$$

with the universal gas constant R and a reference doublet $(p_{s,0}, T_0)$. Whereas over a flat liquid surface equilibrium is given at $p_v = p_s$, i.e. at saturation $S = 1$ the situation changes in the free atmosphere under the absence of flat surface phase transitions. Atmospheric liquid aerosol particles and water droplets have curved vapor-liquid interfaces which affects the thermodynamic energy budget.

In the following, the classical theory of homogeneous nucleation and the concepts of heterogeneous nucleation involving preexisting aerosol particles as condensation nuclei will be briefly introduced. Although nucleation theory is generally valid for any vapor species, the subsequent sections will mainly focus on the nucleation of water droplets.

2.1.1 Homogeneous Nucleation

Classical nucleation theory is based on the so-called capillary approximation, where clusters containing small numbers of molecules are assumed to exhibit the same physical properties as the bulk liquid. In this approach, the additional energy necessary to form a curved interface is determined by a macroscopic surface tension σ . The formation of a (liquid) cluster containing i molecules from the gaseous phase at constant temperature and vapor pressure leads to a change in Gibbs free energy of

$$\Delta G = (\mu_l - \mu_v) i + 4\pi\sigma r^2 \quad (2.1.3)$$

given by i times the difference in the chemical potentials of the vapor and liquid phase and an additional surface term $4\pi\sigma r^2$ defined by the surface tension σ and the cluster radius r . According to Eq. (2.1.1), for a constant temperature the change in single molecule Gibbs free energy dg , i.e. a change in chemical potential, can be expressed as

$$dg = d\mu = v dp$$

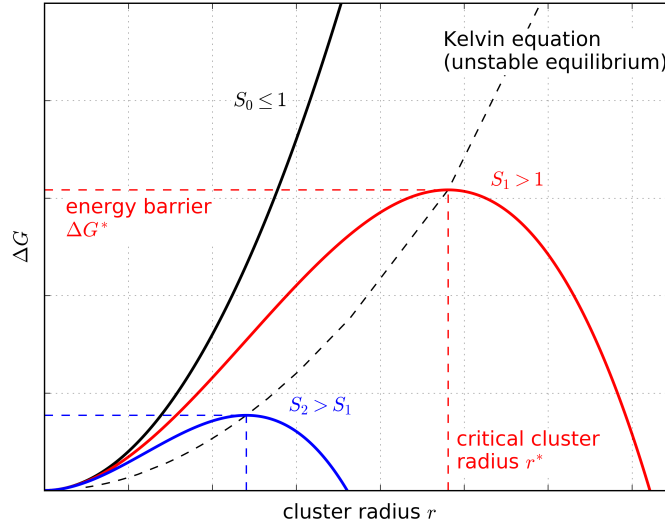


Figure 2.1.1: Change in Gibbs free energy for the formation of a (liquid) cluster from molecules in the gaseous phase in dependence of the cluster radius and for different vapor saturations.

with v denoting the volume occupied by a single molecule in the particular phase. Taking into account that this volume is much larger in the gas than in the liquid phase, the difference in the chemical potentials in Eq. (2.1.3) satisfies

$$d(\mu_l - \mu_v) = (v_l - v_v) dp \approx -v_v dp$$

Assuming ideal gas conditions $v_p = kT$ with the Boltzmann constant k and considering that $\mu_l = \mu_v$ for $p_v = p_s$, this results in

$$\mu_l - \mu_v \approx -kT \int_{p_s}^p \frac{d\tilde{p}}{\tilde{p}} = -kT \ln S$$

Including this result and replacing the number of molecules in the cluster by v_l and the cluster radius r , Eq. (2.1.3) turns into

$$\Delta G = 4\pi\sigma r^2 - \frac{4\pi}{3} \frac{kT \ln S}{v_l} r^3 \quad (2.1.4)$$

Figure 2.1.1 shows the change in Gibbs free energy as a function of cluster radius for different saturations. For small r the first term in Eq. (2.1.4), i.e. the energy required to form a cluster surface dominates and leads to an increase in ΔG with r regardless of the saturation. Positive values of ΔG generally imply that cluster formation is energetically unfavorable for the system and, as a result, molecules will tend to stay in the gaseous phase. An increase in ΔG with r further means that this energetic unprofitability becomes more pronounced with growing cluster size. For saturations $S \leq 1$ also the second term in Eq. (2.1.4) contributes positively to ΔG and the increasing trend continues for all r . Consequently, the formation of macroscopic clusters and, hence, homogeneous nucleation is impossible for $S \leq 1$.

For so-called supersaturated conditions ($S > 1$), on the other hand, the second term in Eq. (2.1.4) becomes negative so that for cluster radii larger than a certain

saturation S	critical cluster size i^*	nucleation rate J [$\text{cm}^{-3}\text{s}^{-1}$]
2	523	5.02×10^{-54}
3	131	1.76×10^{-6}
4	65	1.05×10^6
5	42	1.57×10^{11}

Table 2.1.1: Homogeneous nucleation rates and critical cluster sizes (in terms of molecule number) for different water vapor saturations at $T = 293$ K. Adopted from Seinfeld and Pandis (2006).

threshold, called the critical cluster radius r^* , a further increase in cluster size leads to a decrease in ΔG and is thus energetically promoted. At r^* the ΔG curves experience a maximum representing an unstable equilibrium state, which is given by the Kelvin equation as

$$r^* = \frac{2\sigma v_l}{kT \ln S} \quad (2.1.5)$$

$$\Delta G^* = \frac{4\pi}{3} \sigma r^{*2} = \frac{16\pi}{3} \frac{\sigma^3 v_l^2}{(kT \ln S)^2}$$

Due to the decrease in ΔG for $r > r^*$, for supersaturated conditions clusters will experience unrestricted growth into macroscopic droplets once they surmount the energy barrier ΔG^* . Both ΔG^* and r^* drop with rising saturation S , meaning that the onset of homogeneous nucleation is less hindered and arises at smaller cluster sizes. Although being in an energetically unfavorable state for $r < r^*$, where the system drags the molecules towards the gaseous phase, random collisions between molecules still form short-lived clusters. The finite probability for the occurrence of such a cluster containing i molecules is given by Boltzmann statistics and exponentially decreases with ΔG . As inter-cluster collisions can be neglected due to their rarity, the growth and shrinking of the short-lived clusters takes place via uptake and loss of single molecules. The rate at which homogeneous nucleation occurs is, hence, determined by the probability to find a cluster at r^* and the net single molecule acquisition rate helping the critical cluster to grow into the $r > r^*$ range. At steady state the number of clusters containing i molecules must be conserved. Consequently, the net rate at which they grow to size $i + 1$ must be compensated by the net growth rate of clusters of size $i - 1$. As this holds for all i , all net growth rates J_i must be identical to a common rate J , called the nucleation rate. Several approaches exist for the (rather lengthy) derivation of J that involves the Boltzmann statistics, molecule-cluster collision rates given by the kinetic theory of gases, and the assumption that each cluster is in thermal and pressure equilibrium with its surrounding vapor. The classical derivation (see Seinfeld and Pandis, 2006) yields

$$J \propto \frac{1}{S} \exp\left(-\frac{\Delta G^*}{kT}\right) = \frac{1}{S} \exp\left(-\frac{C}{(\ln S)^2}\right) \quad \text{with} \quad C = \frac{16\pi}{3} \frac{\sigma^3 v_l^2}{(kT)^3}$$

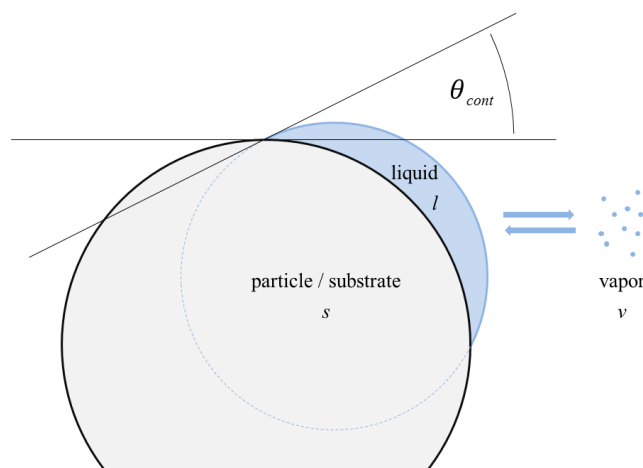


Figure 2.1.2: Schematic of heterogeneous liquid cluster formation on an insoluble spherical particle (substrate). θ_{cont} is the contact angle between the cluster and the substrate.

Table 2.1.1 lists the number of molecules in critical cluster sizes $i^* = 4\pi r^{*3}/3v_l$ and the resulting nucleation rates for water and saturations from $S = 2$ to $S = 5$. Accordingly, within this saturation range J strongly increases with S by more than 60 orders of magnitude. The absolute values of the nucleation rates further reveal that homogeneous nucleation of water droplets can only effectively occur for high saturations. For instance, at $S = 3$ (meaning at a relative humidity of 300%) it would still take about a week for one droplet to form in a volume of 1 cm^3 . As heterogeneous nucleation of water droplets on pre-existing aerosol particles requires far smaller saturations, homogeneous nucleation and, therewith, cloud formation without aerosol particle involvement is practically not taking place in the atmosphere.

2.1.2 Heterogeneous Nucleation

When present, insoluble aerosol particles offer a pre-existing surface to the vapor molecules. The binding energy between the molecules and this surface, or in other words the interfacial tension, determines the contact angle θ_{cont} between a forming (liquid) cluster and the substrate (see Fig. 2.1.2). The contact angle is defined as

$$\cos \theta_{cont} = \frac{\sigma_{sv} - \sigma_{sl}}{\sigma}$$

with σ_{sv} and σ_{sl} denoting the interfacial tensions between particle surface (substrate) and vapor, and between surface and liquid phase, respectively. Since the energy necessary to form the cluster surface depends on the interfacial tensions, the Gibbs free energy barrier ΔG^* is a function of θ_{cont}

$$\Delta G^* = \Delta G_{hom}^* \cdot f(\theta_{cont})$$

where ΔG_{hom}^* is the energy barrier for homogeneous nucleation given by Eq. (2.1.5). Besides the strength of binding between the molecules and the substrate, $f(\theta_{cont})$ also depends on the particle surface geometry, for instance on its curvature and roughness.

In any case, for a completely non-wettable particle $\theta_{cont} = 180^\circ$ and $f(\theta_{cont}) = 1$, meaning that $\Delta G^* = \Delta G_{hom}^*$, i.e. the particle has no effect on cluster formation. However, for a wettable particle the contact angle is smaller than 180° and $f(\theta_{cont}) < 1$. As a result, $\Delta G^* < \Delta G_{hom}^*$, which connotes that the onset of nucleation arises at smaller saturations and that the nucleation rate for a given saturation is increased compared to the homogeneous nucleation process.

Although even insoluble particles can promote droplet nucleation, atmospheric aerosol particles are usually not completely insoluble. In general, they contain both water-soluble and insoluble material. By affecting the chemical potential of the liquid phase, the water-soluble substances lead to a decrease in saturation vapor pressure over the solution compared to that over pure water. The solution saturation vapor pressure can be written as

$$p_{s,sol} = a_w p_s$$

with the saturation vapor pressure for pure water p_s and the water activity a_w . For dilute solutions a_w is given by

$$a_w = \frac{n_w}{n_w + n_{sol}}$$

with n_w and n_{sol} representing the number of moles of water and solute in the solution, respectively. The resulting equation, describing the reduction in saturation vapor pressure over dilute solutions is known as Raoult's law

$$p_{s,sol} = \frac{n_w}{n_w + n_{sol}} p_s$$

Inserting this modified saturation vapor pressure into Eq. (2.1.5) and solving for the logarithm of the saturation yields

$$\ln S = \frac{2\sigma v_l}{kTr^*} + \ln a_w = \frac{4\sigma M_w}{RT\rho_w D} + \ln a_w \quad (2.1.6)$$

with the molar mass and density of water M_w and ρ_w , and the (Kelvin) equilibrium droplet diameter $D = 2r^*$. Assuming that, aside from the amounts of water and solutes, the droplet contains an insoluble (spherical) core of diameter D_u , the total drop volume will satisfy

$$\frac{\pi}{6} D^3 = n_w \frac{M_w}{\rho_w} + n_{sol} \frac{M_{sol}}{\rho_{sol}} + \frac{\pi}{6} D_u^3$$

which can be used to express a_w as

$$a_w^{-1} = 1 + \frac{n_{sol}}{n_w} = 1 + \frac{M_w}{\rho_w} \frac{n_{sol}}{\frac{\pi}{6} (D^3 - D_u^3) - n_{sol} \frac{M_{sol}}{\rho_{sol}}}$$

For the approximation of dilute solutions both $n_{sol} \frac{M_{sol}}{\rho_{sol}}$ and $n_{sol} \frac{M_w}{\rho_w}$ are much smaller than $\frac{\pi}{6} (D^3 - D_u^3)$ such that

$$\ln S \approx \frac{A}{D} - \frac{B}{(D^3 - D_u^3)} \quad (2.1.7)$$

with

$$A = \frac{4\sigma M_w}{RT\rho_w} \quad B = \frac{6n_{sol}M_w}{\pi\rho_w} \quad (2.1.7a)$$

Equation (2.1.7) is known as the Köhler equation and combines the two components that determine equilibrium saturation over an aqueous solution droplet, i.e. the Kelvin effect (first term) and the solute effect (second term). In most cases, however, it is inconvenient to use a particle's insoluble core diameter D_u and the number of moles of solute n_{sol} , but it is more meaningful to use the total dry particle diameter D_{dry} and the mass fraction of soluble material ϵ_m giving

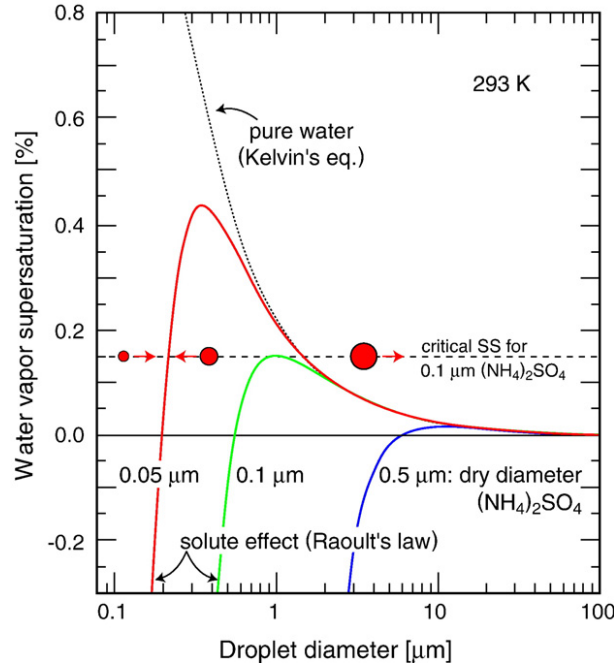


Figure 2.1.3: Köhler curves showing the equilibrium vapor supersaturation ($S - 1$) as a function of water droplet diameter at $T = 293$ K for water-soluble ammonium sulfate particles of varying initial dry diameters. Adopted from Andreae and Rosenfeld (2008).

$$D_u^3 = D_{dry}^3 \left(\frac{\rho_u}{\rho_{sol}} \frac{\epsilon_m}{1 - \epsilon_m} + 1 \right)^{-1} \quad n_{sol} = \frac{\epsilon_m}{M_{sol}} \frac{\iota \pi D_{dry}^3}{6 \left(\frac{\epsilon_m}{\rho_{sol}} + \frac{1 - \epsilon_m}{\rho_u} \right)} \quad (2.1.7b)$$

with the density of the insoluble material ρ_u and the number of ions resulting from dissolution of one solute molecule ι . Figure 2.1.3 exemplarily shows a set of so-called Köhler curves satisfying Eq. (2.1.7) for different initial dry diameters of (completely) water-soluble ammonium sulfate particles. It further shows the equilibrium supersaturation $SS = S - 1$ for pure water droplets. For the latter the solute term in Eq. (2.1.7) is zero and it would require very high supersaturations for small droplet diameters to be in (unstable) equilibrium with the surrounding vapor. For larger pure water droplets the equilibrium supersaturation may decrease, but as discussed in Sect. 2.1.1 at the same time the Gibbs free energy barrier for homogeneous nucleation increases and, consequently, nucleation rates become vanishingly small.

For droplets containing soluble particles the solute term in Eq. (2.1.7) dominates over the Kelvin term for small droplet diameters, leading to a strong lowering of the equilibrium SS . Moreover, the gradient of the equilibrium $SS(D)$ changes from negative to positive. This implies that aqueous solution droplets in this size range are now in stable equilibrium, meaning that a small change in diameter via random loss or uptake of water molecules leads to a restoring force. If, for instance, an aqueous solution droplet that is beforehand in equilibrium with the surrounding vapor slightly shrinks due to random loss of water molecules the ambient SS is larger than the new equilibrium SS of the shrunken droplet. This provokes a net transfer of vapor molecules back towards the droplet until equilibrium with the environment is restored. In contrast to pure water droplets, aqueous solution droplets further allow for equilibrium with the vapor phase also for unsaturated conditions ($S < 1$ or $SS < 0$). By convention, aqueous solution droplets in the ascending branch of the Köhler curves, i.e. in stable equilibrium are commonly referred to as hydrated particles rather than droplets, particularly for unsaturated conditions. Unlike for droplets in unstable equilibrium, the random acquisition of water molecules by hydrated particles in stable equilibrium does not initiate (unrestricted) accelerated growth. On the other hand, for larger diameters where the Kelvin term dominates over the solute term the aqueous solution droplets behave like pure water droplets and the equilibrium state changes back to unstable. This means that any further uptake of water molecules again leads to what so far was been termed nucleation and will hereafter be referred to as droplet “activation”.

Between the two regimes the Köhler curves exhibit a maximum that is defined by the so-called critical supersaturation SS_c , which depends on the properties of the dry aerosol particle. For positive supersaturations with $SS < SS_c$ the Köhler curves feature two equilibrium states, the discussed stable equilibrium at smaller and the unstable equilibrium at larger diameters. Similar to the case of homogeneous nucleation, aqueous solution droplets have to surmount an energy barrier to reach the unstable equilibrium state from the stable equilibrium state and to finally activate by random net uptake of water molecules. This energy barrier rapidly grows the farther SS falls below SS_c , so that droplet activation rates for $SS \ll SS_c$ become negligible. When the supersaturation approaches SS_c , however, a stable hydrated particle needs only few additional water molecules to be pushed towards the unstable descending Köhler curve branch and, accordingly, to trigger its unrestricted water uptake. In summary, if for a certain aerosol particle the ambient SS fulfills $SS \approx SS_c$ or even $SS > SS_c$, then this particle will activate into a droplet. For a given particle composition (soluble content etc.), the dry diameter for which the critical supersaturation equals the ambient supersaturation ($SS_c = SS$) is called the critical dry diameter or activation diameter D_{act} .

From Eq. (2.1.7), (2.1.7a) and (2.1.7b) it is apparent that a number of hardly accessible intrinsic parameters, such as $D_u, \rho_u, \rho_{sol}, \epsilon_m, M_{sol}$ and ν , are necessary to determine SS_c for a given D_{dry} , and vice versa D_{act} for a given SS . For practical use it would, hence, be of advantage to find a simpler parametrization for the ability of a certain particle type to activate into a droplet, i.e. to act as a CCN at a given size and ambient supersaturation.

2.1.3 Kappa-Köhler Theory

Petters and Kreidenweis (2007) introduced such a simplified approximation to classical Köhler theory by expressing the water activity a_w as

$$a_w^{-1} = 1 + \kappa \frac{V_{dry}}{V_w} \quad (2.1.8)$$

where V_{dry} is the volume of the initial dry particle, V_w the volume of water attached to the particle and κ is the so-called hygroscopicity parameter. Representing the dry volume by its spherical equivalent dry diameter D_{dry} , Eq. (2.1.8) turns into

$$a_w^{-1} = 1 + \kappa \frac{D_{dry}^3}{D^3 - D_{dry}^3}$$

with D again denoting the equilibrium droplet diameter. Inserting this into Eq. (2.1.6) yields the new “ κ -Köhler” equation

$$\ln S = \frac{A}{D} + \ln \left(\frac{D^3 - D_{dry}^3}{D^3 - (1 - \kappa) D_{dry}^3} \right) \quad (2.1.9)$$

with A defined as before. The new solute term (second term) in Eq. (2.1.9) is now solely determined by D , D_{dry} and κ . This means that all intrinsic particle properties important for droplet activation are condensed into the single parameter κ . Petters and Kreidenweis (2007) further assume that particles composed of a mixture of substances with individual hygroscopicity parameter values κ_j exhibit a collective κ that is given by their volume weighted average

$$\kappa = \sum_j \frac{V_{dry,j}}{V_{dry}} \kappa_j \quad (2.1.10)$$

with the individual dry volume fractions $V_{dry,j}/V_{dry}$.

However, this parametrization only makes sense if κ really proves to be a characteristic particle property that is independent of the dry diameter and supersaturation. For a certain particle type, κ can be experimentally derived using Eq. (2.1.9) either by studying the growth of hydrated particles with increasing S , called hygroscopic growth, or by finding the supersaturation for the onset of droplet activation, i.e. SS_c . Figure 2.1.4a) shows experimental results for the latter method, i.e. measured pairs of D_{dry} and SS_c for various aerosol particle types. It further displays theoretical isolines for constant values of the hygroscopicity parameter κ fitted to these data. In addition, Fig. 2.1.4b) compares κ fit values for the measurements of multi-component particle types with κ values predicted from the volume mixing rule in Eq. (2.1.10). Obviously, κ -Köhler theory indeed is an adequate approximation that allows to describe heterogeneous droplet formation for a wide range of substances and mixtures thereof. Values for the hygroscopicity parameter range from $\kappa \rightarrow 0$ for insoluble material to $\kappa \approx 1.3$ for sodium chloride (Petters and Kreidenweis, 2007).

Nevertheless, it needs to be mentioned that there are a few exceptions to the applicability of the presented basic κ -Köhler theory. If surface active compounds (surfactants) are present in particles, depending on their amount they may effect the critical

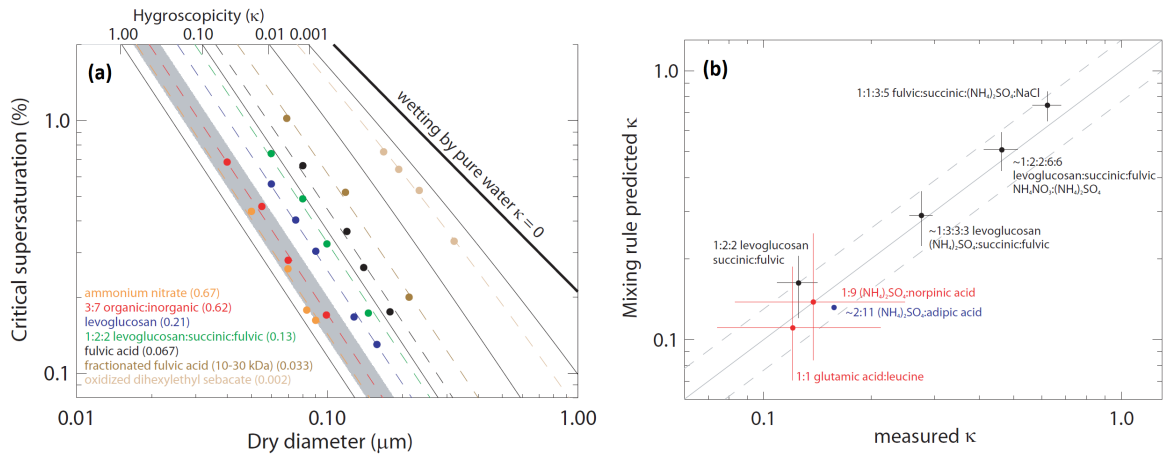


Figure 2.1.4: Experimental results verifying the adequacy of the approximations and assumption made in κ -Köhler theory. The left graph (a) shows measured critical supersaturations as a function of dry particle diameter for several particle types (markers) that are in close match with fitted isolines for constant values of κ (dashed lines). The right graph (b) presents the comparison between fitted (measured) κ and their counterparts predicted by a volume mixing rule from the pure substances. All values fall inside the $\pm 30\%$ deviation range (dashed lines) from the one-to-one relation (solid line). Adopted from Petters and Kreidenweis (2007).

supersaturation and lead to deviations from the simple mixing rule in Eq. (2.1.10) (Petters and Kreidenweis, 2013). Further, the basic theory only considers completely soluble and completely insoluble components. Real soluble materials usually do not take up water until a so-called deliquescence relative humidity (DRH). For highly or moderately soluble materials this DRH is below 95% ($S < 0.95$) and Eq. (2.1.9) still is applicable to the relevant saturation range. Sparingly soluble materials, however, have DRHs larger than 95% and some even do not take up water until the vapor becomes supersaturated. As deliquescence must occur before droplet growth is possible, it can control droplet activation and lead to off- κ -isoline behavior for some of these materials (Petters and Kreidenweis, 2008). Whereas this off-isoline behavior has been experimentally shown for a few specific substances, for most atmospheric aerosols it is presumably irrelevant (Petters and Kreidenweis, 2008, and references therein). Principally, Köhler theory considers the soluble content of a particle as the decisive factor for droplet activation. For particles dominated by insoluble material such as fresh mineral dust, yet, adsorption onto the insoluble surface may also reduce the water activity, as briefly discussed in the first part of Sect. 2.1.2. Figure 2.1.5 shows that, consequently, critical supersaturations for such particles are better described by water adsorption theory (Sorjamaa and Laaksonen, 2007; Kumar et al., 2009, 2011b) than by Köhler theory, although the deviations from a constant κ behavior are non-severe.

Despite these (minor) limitations, in the main κ -Köhler theory proves to be a suitable framework to describe the droplet activation of atmospheric aerosol particles. Due to the simplicity of this approach, the hygroscopicity parameter κ is a widely used way to express the CCN properties of an aerosol.

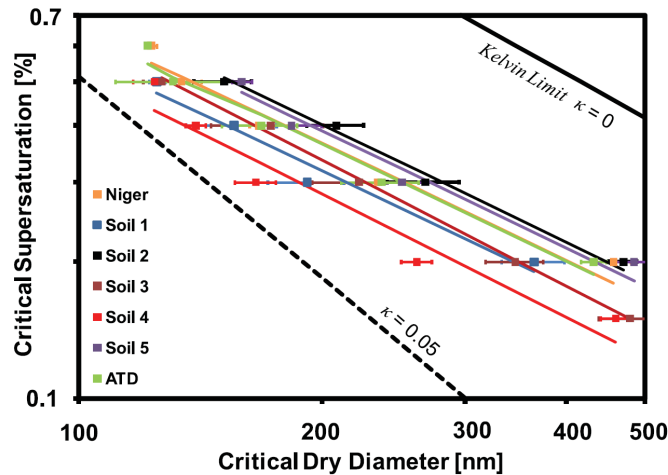


Figure 2.1.5: Relationship between critical supersaturation and dry particle diameter for several (fresh) mineral dust samples. The measurements (markers) slightly deviate from the expected behavior for a constant κ that is illustrated by an isoline at $\kappa = 0.05$ (dashed line). The less steep relation can be reproduced when water adsorption at the particle surface is considered (colored lines). Adopted from Kumar et al. (2011b).

2.2 Scattering Theory

Apart from their vital role in water droplet formation, aerosol particles also impact Earth's radiation budget directly via their interaction with light. When an electromagnetic wave meets an aerosol particle the electric charges within the particle's constituent molecules are excited into oscillatory motion. The oscillation of the electron cloud results in a periodic separation of charge within each molecule, which is called an induced dipole moment. A part of the energy related to these induced oscillations can be absorbed by the particle, e.g. converted into thermal energy. The residual energy is re-emitted in all directions as a superposition of secondary electromagnetic waves from all dipole oscillators, which is termed scattering. When the wave number k (and, accordingly, the wavelength λ) of the scattered light equals that of the incident light, the scattering is called elastic. For a light beam of initial irradiance I_{inc} , i.e. impinging power per unit area, passing through an aerosol volume the combined effects of light absorption and light scattering away from its initial direction lead to an attenuation of the beam. This attenuation in the direction of the incident light is described by the Lambert-Beer law as

$$I_{out} = I_{inc} \exp(-\tau_o) = I_{inc} \exp\left(-\sum_i C_{ext,i} \int n_i dl\right) \quad (2.2.1)$$

with the outgoing irradiance I_{out} and the optical thickness or depth of the aerosol volume τ_o . The optical depth depends on the number density n_i of each particle type i along the path through the aerosol volume, having a total length of $l = \int dl$. It further depends on the particle extinction cross sections $C_{ext,i}$ quantifying the degree of single-particle absorption and scattering ($C_{ext,i} = C_{abs,i} + C_{scat,i}$). The following section will focus on the aspect of light scattering and will introduce the basic theory of elastic scattering. Besides its importance for Earth's climate, light scattering by

aerosol particles also provides a basis for the indirect measurement of particle size (see Sect. 3.2.2.2).

2.2.1 The Scattering Problem

The energy flux density of an electromagnetic wave, i.e. the transported energy per unit time and unit area is given by the Poynting vector

$$\vec{S} = \vec{E} \times \vec{H}$$

with the electric and magnetic field vectors \vec{E} and \vec{H} . As a solution to the Maxwell equations in source-free space \vec{E} and \vec{H} can be written as

$$\begin{aligned}\vec{E}(\vec{r}, t) &= \vec{E}_0 \exp(i(\vec{k}\vec{r} - \omega t)) \\ \vec{H}(\vec{r}, t) &= \sqrt{\frac{\varepsilon}{\mu}} \frac{\vec{k} \times \vec{E}}{k}\end{aligned}$$

with the space and time coordinates \vec{r} and t , the electric field amplitude vector \vec{E}_0 , the wave vector \vec{k} and wave number $k = |\vec{k}| (= 2\pi/\lambda)$, the angular frequency ω , and the electric permittivity ε and magnetic permeability μ of the medium the wave is propagation in (e.g. Jackson, 1998). In the following, the time-dependent factor $\exp(-i\omega t)$ is omitted. For a surface orthogonal to the wave's propagation direction, i.e. orthogonal to $\vec{S}/|\vec{S}| = \vec{k}/k$, the impinging power per unit area is given by the absolute value of the time-averaged Poynting vector and is called the irradiance I

$$I = |\langle \vec{S} \rangle| = \left| \frac{1}{2} \vec{E} \times \vec{H}^* \right| = \left| \frac{1}{2} \vec{E} \times \sqrt{\frac{\varepsilon}{\mu}} \frac{(\vec{k} \times \vec{E})^*}{k} \right| \quad (2.2.2)$$

where $*$ denotes the complex conjugate. A particle that experiences an incident irradiance I_{inc} scatters a total power of

$$P_{scat} = C_{scat} I_{inc} \quad (2.2.3)$$

with the proportionality factor C_{scat} , which is called the particle scattering cross section. The key parameters determining C_{scat} are the dimensionless size parameter α defined by the product of the wave number and the particle size — in case of spherical particles $\alpha = kD/2$ with the particle diameter D — and the particle's complex refractive index relative to the surrounding medium² m . As no particle scatters light equally in all directions, the angular dependence of scattering is an important quantity, too. It is specified by the differential scattering cross section $dC_{scat}/d\Omega$ which satisfies

$$C_{scat} = \int_{4\pi} \frac{dC_{scat}}{d\Omega} d\Omega \quad (2.2.4)$$

,i.e. the integral of $dC_{scat}/d\Omega$ over the complete solid angle $d\Omega$ must equal the total scattering cross section. The normalized differential cross section $C_{scat}^{-1} dC_{scat}/d\Omega$ is

²For scattering in air the relative refractive index m basically is the refractive index of the particle, since that of air in good approximation equals unity. The refractive index itself is a function of the wave number k .

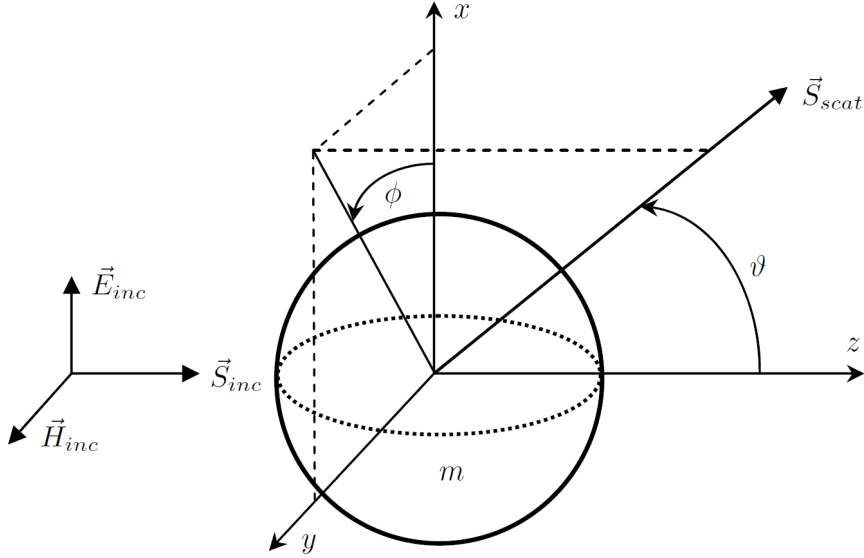


Figure 2.2.1: Geometry for the scattering of a plane electromagnetic wave by a single particle. The incident wave is represented by its Poynting vector \vec{S}_{inc} and its electric and magnetic field vectors \vec{E}_{inc} and \vec{H}_{inc} . The particle scatterer is depicted by a sphere with a refractive index m relative to its surrounding medium. The scattered wave is characterized by its Poynting vector \vec{S}_{scat} . Its direction deviates from that of the incident wave by the scattering angle ϑ . The azimuth angle ϕ describes the rotation of the scattering plane spanned by \vec{S}_{inc} and \vec{S}_{scat} from the direction of \vec{E}_{inc} .

called the scattering phase function³. To derive C_{scat} and $dC_{scat}/d\Omega$ it is necessary to define the scattering geometry first. Figure 2.2.1 shows an example scattering process for an incident plane electromagnetic wave propagating in \vec{e}_z direction that is linearly polarized (meaning its electric field vector oscillates) in \vec{e}_x direction

$$\vec{E}_{inc} = E \vec{e}_x = E_0 \exp(ikz) \vec{e}_x \quad (2.2.5)$$

The outgoing wave, scattered at the coordinate origin $(0, 0, 0)$, is represented by its Poynting vector \vec{S}_{scat} . The plane spanned by \vec{S}_{inc} and \vec{S}_{scat} is called the scattering plane, the angle between the two is the scattering angle ϑ . The azimuth angle ϕ defines the rotation between the polarization direction of the incident light and the scattering plane. Like the incident electric field, at sufficiently large distance r from the scatterer ($kr \gg 1$) the scattered field is transverse, so that both \vec{E}_{inc} and \vec{E}_{scat} can be decomposed into two orthogonal components with respect to the scattering plane, allowing to write the single particle scattering problem as (Bohren and Huffman, 1983)

$$\begin{pmatrix} E_{\parallel scat} \\ E_{\perp scat} \end{pmatrix} = \frac{\exp(ikr)}{-ikr} \begin{pmatrix} S_2 & S_3 \\ S_4 & S_1 \end{pmatrix} \begin{pmatrix} E_{\parallel inc} \\ E_{\perp inc} \end{pmatrix} \quad (2.2.6)$$

where the parallel and perpendicular components of the scattered electric field $E_{\parallel scat}$ and $E_{\perp scat}$ depend on r , the incident field components $E_{\parallel inc}$ and $E_{\perp inc}$ and the so-called

³Often, the scattering phase function is also defined as $4\pi \cdot C_{scat}^{-1} dC_{scat}/d\Omega$ to normalize its integral over the complete solid angle to 4π rather than to 1.

scattering amplitudes S_1 to S_4 , that are complex-valued functions of the scattering direction. Basis transformation in Eq. (2.2.6) yields

$$\vec{E}_{scat} = \frac{\exp(ikr)}{-ikr} \vec{X} E = \frac{\exp(ikr)}{-ikr} \begin{pmatrix} S_2 \cos \phi + S_3 \sin \phi \\ S_4 \cos \phi + S_1 \sin \phi \end{pmatrix} E \quad (2.2.7)$$

with the scattering amplitude vector \vec{X} , and E defined by Eq. (2.2.5). The total scattered power is given by the time-averaged Poynting vector of the light scattered in all directions integrated over the complete sphere with radius r and the scattering particle in its center

$$P_{scat} = \int_{4\pi} \langle \vec{S}_{scat} \rangle \vec{e}_r r^2 d\Omega = \int_{4\pi} |\langle \vec{S}_{scat} \rangle| r^2 d\Omega$$

With Eq. (2.2.2), (2.2.5) and (2.2.7) this can be rewritten as

$$P_{scat} = \frac{1}{2} \sqrt{\frac{\varepsilon}{\mu}} E_0^2 \int_{4\pi} \frac{|\vec{X}|^2}{k^2} d\Omega = I_{inc} \int_{4\pi} \frac{|\vec{X}|^2}{k^2} d\Omega$$

and upon comparison with Eq. (2.2.3) and (2.2.4) results in

$$\begin{aligned} \frac{dC_{scat}}{d\Omega} &= \frac{|\vec{X}|^2}{k^2} = \frac{1}{k^2} (|S_2 \cos \phi + S_3 \sin \phi|^2 + |S_4 \cos \phi + S_1 \sin \phi|^2) \quad (2.2.8) \\ C_{scat} &= \int_{4\pi} \frac{|\vec{X}|^2}{k^2} d\Omega \end{aligned}$$

Accordingly, the scattering problem, i.e. to find C_{scat} and $dC_{scat}/d\Omega$ confines to the determination of the complex-valued functions S_1 to S_4 .

2.2.2 Scattering by Spherical Particles

For spherical particles the scattering problem can be analytically solved by means of Mie theory (Mie, 1908). Here, due to rotational symmetry S_3 and S_4 become zero and the azimuthal dependence of S_1 and S_2 vanishes, so that these complex functions henceforth merely depend on m , α and ϑ . The solutions for S_1 and S_2 can be obtained by expanding the electric fields of the incident and scattered waves, and the wave inside the particle in a series of spherical harmonics. Provided that the tangential components of the electric and magnetic fields are continuous across the particle surface, the coefficients of these expansion functions can be derived, leading to the following series expressions for S_1 and S_2 (Bohren and Huffman, 1983)

$$\begin{aligned} S_1(m, \alpha, \vartheta) &= \sum_n \frac{2n+1}{n(n+1)} (a_n(m, \alpha) \pi_n(\vartheta) + b_n(m, \alpha) \varpi_n(\vartheta)) \quad (2.2.9) \\ S_2(m, \alpha, \vartheta) &= \sum_n \frac{2n+1}{n(n+1)} (a_n(m, \alpha) \varpi_n(\vartheta) + b_n(m, \alpha) \pi_n(\vartheta)) \end{aligned}$$

with the scattering angle-dependent functions π_n and ϖ_n

$$\begin{aligned} \pi_n(\vartheta) &= \frac{P_n(\cos \vartheta)}{\sin \vartheta} \\ \varpi_n(\vartheta) &= \frac{dP_n(\cos \vartheta)}{d\vartheta} \end{aligned}$$

expressed in terms of the Legendre polynomials P_n , and the refractive index and size parameter-dependent coefficient functions a_n and b_n

$$\begin{aligned} a_n(m, \alpha) &= \frac{\psi_n(\alpha) \psi'_n(m\alpha) - m\psi_n(m\alpha) \psi'_n(\alpha)}{\zeta_n(\alpha) \psi'_n(m\alpha) - m\psi_n(m\alpha) \zeta'_n(\alpha)} \\ b_n(m, \alpha) &= \frac{m\psi_n(\alpha) \psi'_n(m\alpha) - \psi_n(m\alpha) \psi'_n(\alpha)}{m\zeta_n(\alpha) \psi'_n(m\alpha) - \psi_n(m\alpha) \zeta'_n(\alpha)} \end{aligned}$$

defined by the Riccati-Bessel functions ψ_n and ζ_n , and their first derivatives (see Seinfeld and Pandis, 2006). The spherical harmonics for the scattered wave can interfere constructively or destructively depending on ϑ and ϕ . The number of terms needed for convergence of the series for S_1 and S_2 is in the order of the value of α .

For small size parameters $\alpha \ll 1$ only the first term in the series is relevant and a particle behaves like a single dipole. The resulting scattering phase function and total scattering cross section for this limiting case of Mie scattering, also called Rayleigh scattering, are

$$\begin{aligned} \left[\frac{dC_{scat}}{d\Omega} \right]_{RI} &= \left| \frac{\alpha^3}{k} \left(\frac{m^2 - 1}{m^2 + 2} \right) \cos \vartheta \cos \phi \right|^2 + \left| \frac{\alpha^3}{k} \left(\frac{m^2 - 1}{m^2 + 2} \right) \sin \phi \right|^2 \quad (2.2.10) \\ [C_{scat}]_{RI} &= \frac{8\pi}{3} \frac{\alpha^6}{k^2} \left| \frac{m^2 - 1}{m^2 + 2} \right|^2 \end{aligned}$$

Accordingly, for particle sizes that are small compared to the wavelength of the incident light the total scattering cross section and, therewith, the total scattered power strongly increases with particle size $[C_{scat}]_{RI} \propto \alpha^6$.

For larger size parameters higher order terms in Eq. (2.2.9) take effect and lead to deviations from the Rayleigh scattering behavior. Figure 2.2.2 shows the scattering angle dependence of differential cross sections calculated via Eq. (2.2.8) and (2.2.9) for unpolarized incident light, a real refractive index (similar to that of ammonium sulfate), and a visible red wavelength. Unpolarized means that the incident light consists of a superposition of plane waves with different polarizations without a fixed phase relation. In this case the azimuthal dependence completely cancels out so that Eq. (2.2.8) and (2.2.10) simplify to

$$\frac{dC_{scat}}{d\Omega} = \frac{|S_2|^2 + |S_1|^2}{2k^2} \quad \left[\frac{dC_{scat}}{d\Omega} \right]_{RI} = \frac{\alpha^6}{2k^2} \left| \frac{m^2 - 1}{m^2 + 2} \right|^2 (1 + \cos^2 \vartheta)$$

In contrast to the Rayleigh single dipole-like behavior at small α where forward and backward scattering are equally pronounced, with advancing magnitude of the size parameter the scattering increasingly favors the forward direction. Due to the growing influence of higher order terms in Eq. (2.2.9) interference patterns further become more complex and small-scaled (see Fig. 2.2.2). In addition to this angular dependence, Fig. 2.2.3 presents the behavior of the total scattering cross section with α for varying refractive indices. Starting from the mentioned α^6 relation, the size-dependence of the total scattering cross sections flattens when leaving the ‘‘Rayleigh regime’’. Moreover, for larger α the degree of overall constructive or destructive interference of the spherical harmonics changes with size leading to wave-like structures (‘‘Mie resonances’’).

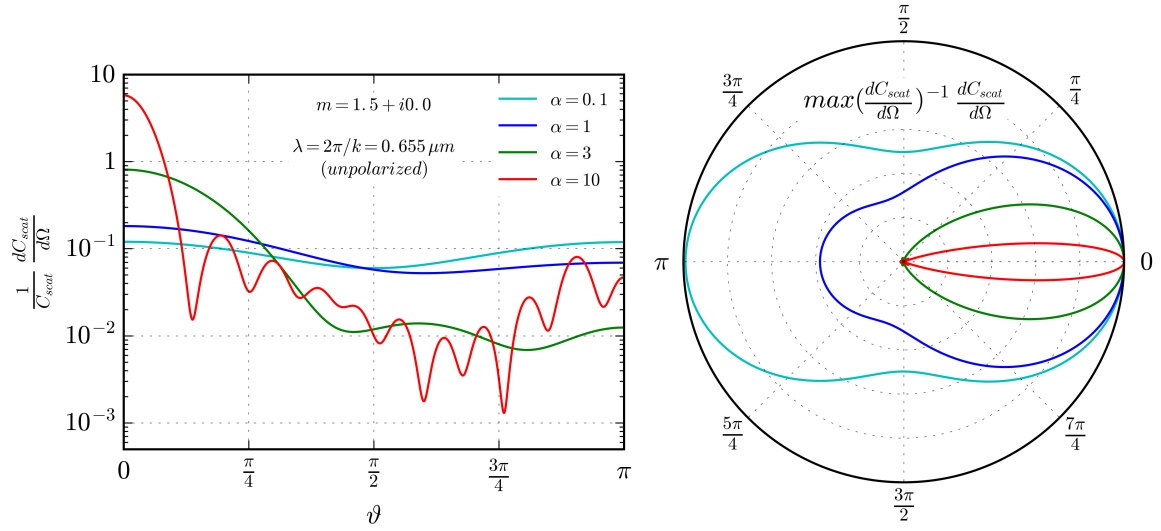


Figure 2.2.2: Normalized differential scattering cross sections for Mie scattering of unpolarized light. The left plot shows the phase functions $C_{scat}^{-1} dC_{scat}/d\Omega$ for several values of the size parameter α in dependence of the scattering angle ϑ on a logarithmic scale. The right plot displays the corresponding differential scattering cross sections $dC_{scat}/d\Omega$ normalized by their maximum in polar coordinates on a linear scale. The calculations are performed at a wavelength of $\lambda = 655 \text{ nm}$ and for a refractive index of $m = 1.5 + i0$ by means of the software *MiePlot* (<http://www.philiplaven.com/mieplot.htm>).

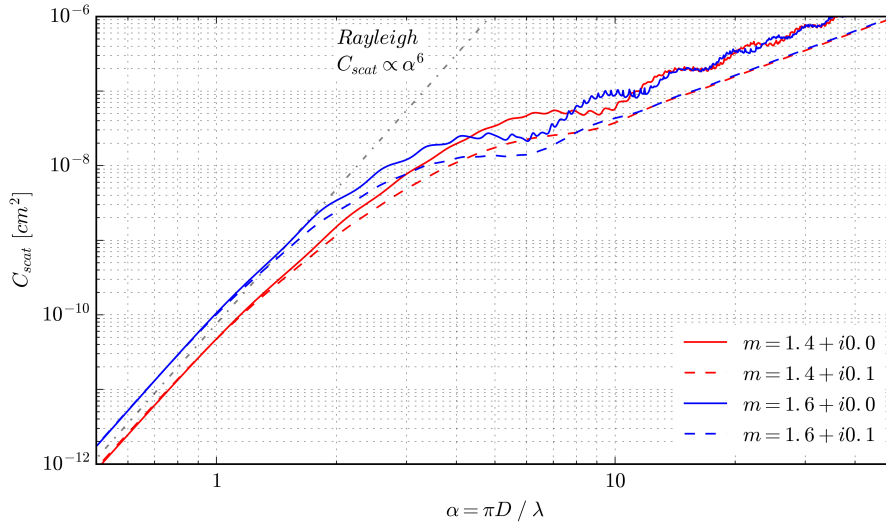


Figure 2.2.3: Behavior of total scattering cross section with the particle size parameter for Mie scattering. The solid lines show results for particles exhibiting an exclusively real refractive index, while the dashed lines represent particles with an additional imaginary part of the refractive index. The line color marks the real part of the refractive index. The dashed gray line symbolizes the characteristic Rayleigh scattering size-dependency of the cross section. The calculations are performed with *MiePlot* and are based on a light wavelength of $\lambda = 655 \text{ nm}$.

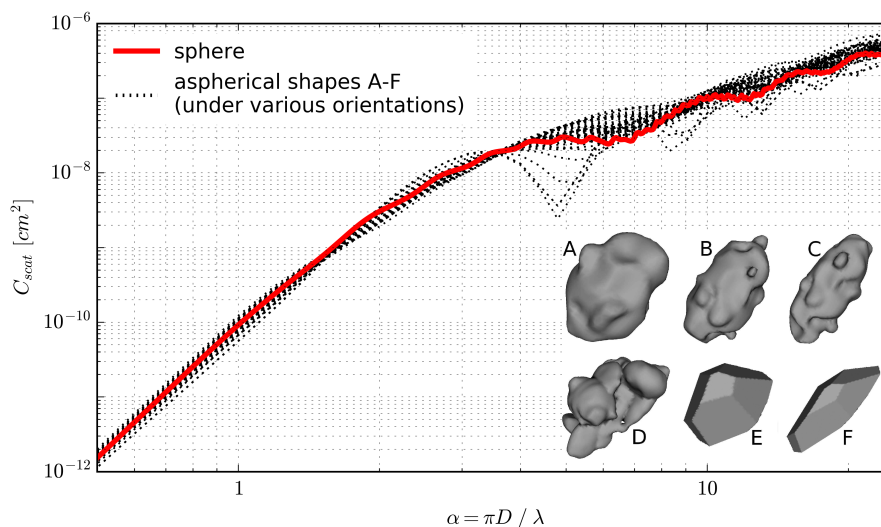


Figure 2.2.4: Behavior of total scattering cross section with particle size parameter for a sphere (red solid line) and a set of aspherical volume-equivalent particles under various orientations with respect to the incident light (black dotted lines). All calculations are based on a refractive index of $m = 1.56 + i0$ and a light wavelength of $\lambda = 655$ nm. The DDA results for the aspherical particles are provided by courtesy of J. Gasteiger, LMU. The visualization of the used shapes A to F is adopted from Gasteiger et al. (2011).

These wiggles occasionally even imply a local decrease in scattering cross section with increasing size and can, hence, cause deviations from a monotonic gradient. They are, however, attenuated when the complex part of the refractive index (i.e. light absorption) becomes sufficiently large.

2.2.3 Scattering by Aspherical Particles

For some atmospheric particles Mie theory is not an adequate formalism, since they at least slightly deviate from a spherical shape. Several methods have been introduced to extend scattering theory to aspherical particles, with the T-Matrix method (Waterman, 1965) and the discrete dipole approximation (DDA) (Purcell and Pennypacker, 1973), also referred to as the Purcell-Pennypacker method, being the most prominent examples. The DDA has the advantage of being more flexible concerning particle shape, while the T-Matrix method is typically faster in terms of computation time. In the DDA, a particle of arbitrary shape is approximated by a three-dimensional lattice of N dipoles that is fine compared to the light wavelength but still wide enough so that a single dipole embodies many molecules. Each of these dipoles is excited by the incident field and the fields of all other dipoles, so that the resulting total field is described by a set of $3N$ linear equations. These equations can be solved iteratively (Purcell and Pennypacker, 1973) or by inverting the $3N \times 3N$ coefficient matrix (Singham and Salzman, 1986). Figure 2.2.4 shows size-dependent total scattering cross sections resulting from DDA calculations for a set of aspherical particles under different orientations to the incident light. The sizes of the aspherical particles are represented by the size

parameter of a volume-equivalent sphere. For comparison, Fig. 2.2.4 features the Mie theory result for the volume-equivalent spherical particle. It can be seen, that particle asphericity in conjunction with varying orientation in first approximation leads to a (size-dependent) spread of the family of $C_{scat}(\alpha)$ curves around the midway Mie solution. Although this simplified perspective on the effect of particle asphericity on $C_{scat}(\alpha)$ is sufficient for the purposes of this study (cf. Sect. 3.3.2), it is not entirely accurate. The orientation average of the $C_{scat}(\alpha)$ curves for an aspherical particle deviates from the Mie result and the direction of this deviation for a certain particle size is the same for all possible aspherical shapes (Mugnai and Wiscombe, 1989).

2.3 Aerosol Particle Size Distributions

The size of an aerosol particle is a central parameter in view of its CCN properties and its impact on radiative transfer. The range of particle sizes found in the atmosphere can span more than five orders of magnitude, starting from small molecular clusters of just a few nm and reaching up to coarse particles of about 100 μm . Although the definitions are not unique or strict, this size range is commonly divided into sub-ranges or modes, namely the nucleation mode covering particle sizes smaller than about 10 nm, the Aitken mode typically peaking around 50 nm, the accumulation mode with a maximum around 100 – 200 nm, and the coarse mode containing all particles larger about 0.5 – 1 μm (e.g. Seinfeld and Pandis, 2006). This classification is based on differences in these modes' sources and atmospheric life cycles. The finest (nucleation mode) particles are secondary particles formed in situ via gas-to-particle conversion processes. The nucleation mode is of transient nature as the small particles quickly coagulate with larger ones, so that it is only observable in the vicinity of sources. The largest particles are mainly of primary nature and are typically generated by mechanical processes such as wind erosion. Because of their high mass/inertia, coarse particles settle out via gravitation or impact on obstacles more effectively than smaller particles. Hence, their atmospheric lifetime is limited, too. In consequence, the majority of particles are usually found in the Aitken and accumulation mode size ranges where removal processes are most ineffective and coagulation is too slow to enable growth into the coarse mode. Here, both primary and secondary particles are present as well as mixtures formed by coagulation of smaller particles or heterogeneous condensation.

Particle size is typically expressed in terms of so-called equivalent diameters D , as for instance the electric mobility diameter or the optical diameter. For a spherical particle the equivalent diameters usually correspond to its geometric diameter⁴, whereas for an aspherical particle they represent the diameter of a sphere with identical physical properties with respect to a certain process. The electric mobility diameter, for example, is the diameter of a sphere with the same electric mobility, i.e. the same terminal velocity in an electric field as the particle in question. The optical diameter describes the diameter of a sphere scattering the same amount of light into a certain solid angle range as the actual particle. As different equivalent diameters do not nec-

⁴Exceptionally, the equivalent diameter for a spherical particle can also represent the geometric diameter of a sphere with different intrinsic properties (refractive index, density, mobility etc.). An example for this is the representation of particle diameter in optical measurements in terms of the diameter of a polystyrene latex (PSL) sphere with the same optical properties.

essarily correspond to each other, it is important to note which size representation is used.

The number occurrence of particles in an aerosol as a function of diameter is described by the particle NSD. The most straightforward way to present the NSD is to somehow count the concentration of particles per unit volume Δn in finite diameter intervals of width ΔD and to plot the normalized values $\Delta n/\Delta D$ as histogram data. Normalization by ΔD is necessary in order to make the histogram a discrete density function, thus allowing to compare different bar heights in terms of a probability to find a particle per fixed reference diameter interval. In the limit of infinitesimal interval widths the discrete histogram proceeds into a differential NSD $F(D)$ that satisfies

$$n(D') = \int_0^{D'} F(D) dD \quad (2.3.1)$$

with $n(D')$ being the cumulative number concentration for particles diameters smaller D' . From Eq. (2.3.1) it directly follows that $F(D)$ can be interpreted as the derivative of the cumulative particle number concentration with the particle diameter

$$F(D) = \frac{d}{dD} n(D)$$

In the atmosphere, NSDs are commonly polydisperse, meaning that an aerosol usually contains a vast spectrum of particle diameters, covering several orders of magnitude. Therefore, it is often inconvenient to use D but rather advantageous to use its logarithm to express the distribution of particle sizes. Using the base 10 logarithm Eq. (2.3.1) can be rewritten as

$$n(D') = \int_{-\infty}^{\log_{10} D'} \frac{dn}{d \log_{10} D} d \log_{10} D$$

with the logarithmic NSD $dn/d \log_{10} D$.

Frequently, NSDs are expressed in terms of analytical functions allowing to parametrize them with a few parameters only. It is an empirical finding that aerosol particle number size distributions are well-approximated by a superposition of lognormal functions. First introduced by Whitby (1978), this lognormal approximation accordingly is the most common way to present aerosol NSDs. A quantity, the particle diameter in this case, is called lognormally distributed with respect to base b when its logarithm to base b is normally distributed

$$\mathcal{N}(\log_b D) = \frac{1}{\sqrt{2\pi} \log_b GSD} \exp\left(-\frac{1}{2} \left(\frac{\log_b D - \log_b CMD}{\log_b GSD}\right)^2\right)$$

with the count median diameter CMD and the geometric standard deviation GSD . Following this, a monomodal lognormal NSD to base 10 can be written as

$$\begin{aligned} \frac{dn}{d \log_{10} D}(D) &= n_{mode} \mathcal{N}(\log_{10} D) \\ \frac{dn}{dD}(D) &= \frac{n_{mode}}{D \ln 10} \mathcal{N}(\log_{10} D) \end{aligned} \quad (2.3.2)$$

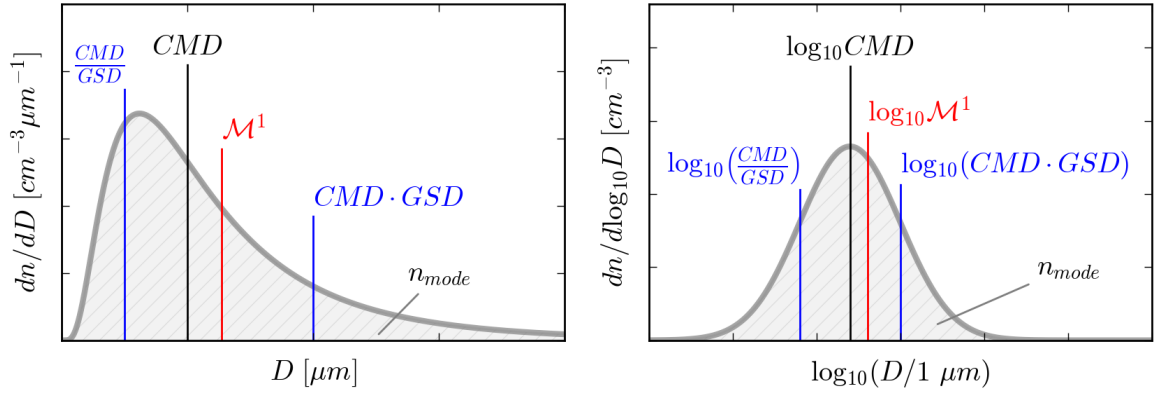


Figure 2.3.1: A monomodal lognormal NSD plotted over a linear (left graph) and logarithmic abscissa (right graph). The area under the curves corresponds to the integral particle number concentration n_{mode} . In addition to the (count) median diameter CMD (black line), the first moment (mean) \mathcal{M}^1 (red line) and the 16 and 84th percentiles of the distribution (blue lines) are indicated.

with the integral mode particle number concentration n_{mode} . A hypothetical, completely monodisperse aerosol that contains only particles of identical size is characterized by $GSD = 1$. For small values of the GSD close to 1 ($GSD \lesssim 1.25$) an aerosol is termed quasi-monodisperse, whereas it is called polydisperse for larger values. The q -th moment of a monomodal lognormal NSD is given by

$$\mathcal{M}^q = \frac{\int_0^{\infty} D^q \frac{dn}{dD}(D) dD}{\int_0^{\infty} \frac{dn}{dD}(D) dD} = CMD^q \exp\left(\frac{(q \ln GSD)^2}{2}\right) \quad (2.3.3)$$

Figure 2.3.1 shows an example of such a NSD satisfying Eq. (2.3.2) over a linear and logarithmic D abscissa. In the former representation, the lognormal NSD is skewed and the distribution's mode, i.e. the particle diameter at which the occurrence of particles within an interval of fixed infinitesimal size dD is maximal, is located to the left of the CMD . In logarithmic representation, the distribution shows the expected normal shape and the mode, this time meaning the diameter at which the occurrence of particles within a logarithmic interval of fixed infinitesimal size $d \log_{10} D$ is maximal, corresponds to the CMD . For a normal distribution the 16 and 84th percentiles encompassing 68% of the total area, here meaning number concentration, are given approximately by the mean \pm one standard deviation. For a lognormal distribution these percentiles, i.e. $D_{16\%}$ and $D_{84\%}$ are represented by⁵

$$\log_{10} D_{16,84\%} \approx \log_{10} CMD \pm \log_{10} GSD$$

or in terms of particle diameter

$$D_{16\%} \approx \frac{CMD}{GSD} \quad D_{84\%} \approx CMD \cdot GSD$$

⁵To be precise, the range between mean \pm one standard deviation for a normal distribution, and $\log_{10} CMD \pm \log_{10} GSD$ for a lognormal distribution (to base 10), encompass about 68.27% of the total probability, so that these values marginally deviate from the 16 and 84th percentiles.

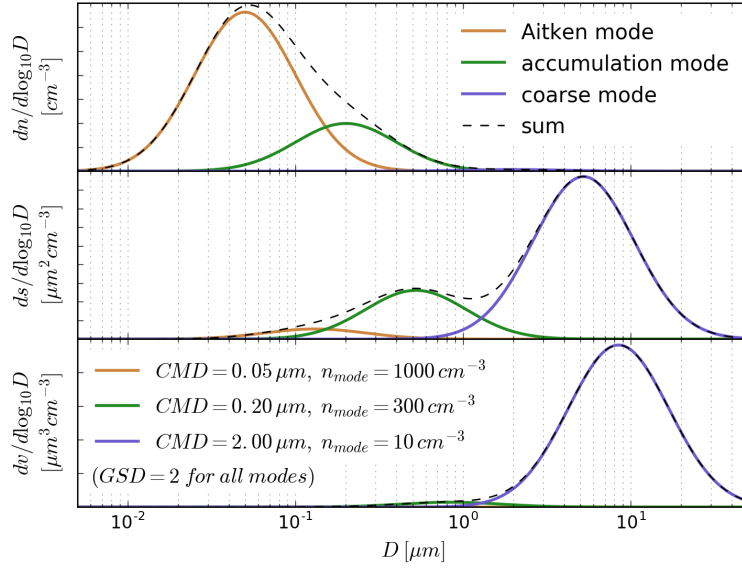


Figure 2.3.2: Particle number, surface and volume size distributions for an exemplary set of lognormal parameters representing an Aitken (brown), an accumulation (green) and a coarse mode (blue). The resulting total distributions are shown by the dashed black lines.

In Fig. 2.3.1 these percentiles are indicated by the blue lines. The lognormal distribution's mean (or first moment) \mathcal{M}^1 given by Eq. (2.3.3) lies to the right of the CMD and is depicted by the red line.

Sometimes, e.g. for mass-determined aerosol processes, not the NSD but higher moment size distributions are relevant, particularly the aerosol particle surface and volume size distributions. For spherical particles (and to some degree also for moderately aspherical particles) the surface and volume size distributions can be derived from the particle NSD as

$$\begin{aligned} \frac{ds}{d\log_{10} D}(D) &= \pi D^2 \frac{dn}{d\log_{10} D}(D) \\ \frac{dv}{d\log_{10} D}(D) &= \frac{\pi}{6} D^3 \frac{dn}{d\log_{10} D}(D) \end{aligned} \quad (2.3.4)$$

with s and v representing the total surface area and volume of all particles contained in a reference aerosol volume. Vice versa, some measurement methods yield higher order moment size distributions and one might want to use them to infer the particle NSD. The use of the lognormal representation of the NSD proves to be quite beneficial in this respect, since when the NSD is lognormal all higher moment size distributions are also lognormal with the same GSD and a shifted median diameter CMD_k that relates to CMD (the median diameter of the NSD) as

$$CMD_k = CMD \exp\left(k (\ln GSD)^2\right) \quad (2.3.5)$$

with k being the moment of the distribution ($k = 2$ for surface and $k=3$ for volume). Figure 2.3.2 shows an exemplary NSD as a superposition of three lognormal modes,

an Aitken, an accumulation and a coarse mode with median diameters of 0.05, 0.2 and 2 μm and a common $GSD = 2$. Further shown are the corresponding surface and volume size distributions. It is apparent that, while the particle number concentration is dominated by the small Aitken and accumulation mode particles, the surface and especially the volume size distribution are governed by the coarse particles. This demonstrates that it is crucial to choose the appropriate moment size distribution when studying a particular aerosol feature. However, due to their direct relationship, the whole information given by the different moment distributions is already contained in the lognormal parameters of a single moment size distribution. For instance, for a N -modal distribution all information is included in the $3N$ parameters determining the NSD, i.e. the set of n_{mode} , CMD and GSD of the individual modes. From this NSD parameter set (or the parameter set of any other moment distribution) the moments of all other distributions can be directly calculated. Inserting Eq. (2.3.5) into Eq. (2.3.3) yields the q -th moment of the k -th moment distribution

$$\mathcal{M}_k^q = CMD_k^q \exp\left(\frac{(q \ln GSD)^2}{2}\right) = CMD^q \exp\left(\left(kq + \frac{q^2}{2}\right) (\ln GSD)^2\right)$$

The mean particle diameter for the volume size distribution, for instance, results from $k = 3$ and $q = 1$. This study concentrates on particle NSD. Yet, by means of the previous formulae the NSD results presented later on (cf. Tab. B.5.1 to B.5.3) can easily be converted into higher order distributions.

It should be mentioned that in practice the NSD and the other moment size distributions are often plotted not only on a logarithmic abscissa but also on a logarithmic ordinate to reveal all details of the distributions. The area under such a curve no longer represents the integral quantity, such as particle number concentration, but the logarithm thereof. Moreover, to guarantee comparability between size distributions that are measured under different pressure and temperature conditions, concentrations are regularly expressed in reference to standard temperature and pressure (STP) conditions. Any concentration size distribution recorded at pressure p and temperature T , determining the aerosol parcel volume V , is converted to STP conditions by multiplication with the factor

$$f_{STP} = \frac{V}{V_{STP}} = \frac{p_{STP}}{p} \frac{T}{T_{STP}} \quad (2.3.6)$$

with the standard pressure p_{STP} , temperature T_{STP} and corresponding parcel volume V_{STP} . In physics, p_{STP} and T_{STP} are usually defined as 1013.25 hPa and 273.15 K. Accordingly, a STP size distribution corresponds to the size distribution that would be measured upon bringing the aerosol parcel to these reference conditions (assuming an ideal gas).

2.4 Aerosol Mixing State and Volatility

Whereas the distribution of particle sizes might be the most fundamental property of an aerosol, its radiative and CCN properties depend also on the intrinsic composition of individual particles. Aerosols can exclusively feature a single particle type, but usually

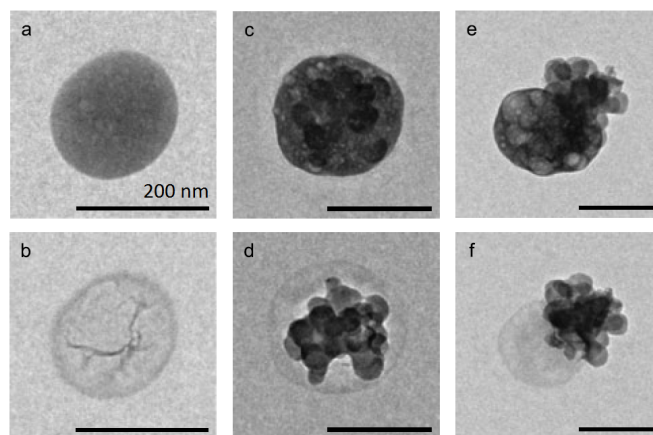


Figure 2.4.1: Transmission electron microscopy images of different aerosol particle mixing states. The upper and lower row show particles before and after electron bombardment (heating), respectively. Images (a) and (b) display a rather pure non-refractory sulfate particle. Images (c) and (d) present an internal mixture of sulfate and refractory soot, where the soot is embedded within a sulfate coating. Images (e) and (f) show another internal mixture of these components, this time in form of a coagulation product. Adopted from Kandler et al. (2011).

the situation is more complex and several particulate components are present. How different components/materials are distributed among the particles is described by the aerosol mixing state. One extreme case is a completely externally mixed aerosol where individual particles are made up of one single component only. An example would be an aerosol with particles that are either pure ammonium sulfate or pure mineral dust. The other extreme is an entirely internally mixed aerosol in which all components are equally distributed among the particles. Sticking to the previous example, this would mean that all particles carry the same (volumetric) amount of mineral dust and ammonium sulfate. Internal mixtures can arise from coalescence or coagulation of particles, heterogeneous condensation of vapor molecules onto particles and chemical reactions at the particle surface. Figure 2.4.1 shows exemplary transmission electron microscopy images for possible mixing states, i.e. a pure sulfate particle and two examples for internal mixtures of soot and sulfate, one where the soot is coated, i.e. situated in the particle core with a sulfate shell, and another where the particle is a coagulation product of these two components.

It is evident that the mixing state can have important implications. Assuming again a two-component mixture between hygroscopic ammonium sulfate and hardly hygroscopic mineral dust and recalling Sect. 2.1, an external mixture would imply differences in the CCN ability of equally sized particles. This means that at certain sizes the ammonium sulfate particles would activate into droplets at a given water vapor supersaturation while mineral dust particles of the same size would remain non-activated. In contrast, in an internal mixture all particles would exhibit the same hygroscopicity, so that particles of equal size would all activate at the same supersaturation. Mixtures also affect the optical properties of particles via the refractive index. Erlick (2006) compares refractive indices for two-component mixtures predicted by various mixing

rules and demonstrates that obtaining a representative refractive index can be complicated even for such simple scenarios. However, when the shape and spatial distribution of the different materials within a particle are unknown, a simple linear volume mixing rule often provides sufficiently good estimates (Erlick, 2006; Michel Flores et al., 2012).

In the majority of cases, aerosols are neither strictly externally nor internally mixed but have an intermediate mixing state, which means that both pure components and particle mixtures of various degrees are present. The mixing state can further be size-dependent since, as mentioned in Sect. 2.3, aerosols regularly feature distinct size modes arising from different sources and particles from the individual modes are not necessarily blending. For example, the measurements of Kandler et al. (2009) in Northwest Africa (see Fig. 1.3.2) show a joint occurrence of internal and external mixtures of dust and sulfate, and a pronounced size-dependence of particle composition. The mixing state might also be a function of aerosol lifetime. If particle coagulation/coalescence rates are low and no vapor is present that could induce heterogeneous processes, the aerosol mixing state can stay rather constant with time. On the other hand, the opposite might be the case when reactive particles and vapors are present. In consequence, information on the size-dependent aerosol mixing state provides important insights into the physiochemical particle properties and their evolution.

One way to assess the aerosol mixing state is to measure the so-called volatility of the particles, i.e. their stability upon exposure to high temperatures. When an aerosol is heated to a certain temperature particle components that are non-refractory will pass over into the gaseous phase by evaporation/sublimation. For a completely internally mixed aerosol containing a non-refractory (volatile) particle component this would cause a uniform relative shrinkage of all particles. The total particle number is conserved in this case but the size distribution shifts towards smaller diameters. An externally mixed aerosol, on the other hand, would lose its volatile particles connoting a reduction in total particle number to the refractory fraction. Particle volatility information can be gained either by microscopic techniques or by a combination of size distribution measurements using heating methods. The former is demonstrated in Fig. 2.4.1. Here, single particle images before and after heating are compared with each other to derive a refractory particle volume fraction rf that is defined by the initial and remnant particle volumes V_i and V_r as

$$rf = \frac{V_r}{V_i} \quad (2.4.1)$$

V_i and V_r are usually estimated from the projected area equivalent diameters. For single-component particles rf is either 0 (non-refractory, volatile) or 1 (refractory, non-volatile), while it is in between these limits for particle mixtures. The other way to determine the aerosol mixing state in terms of particle volatility is to compare the NSD before and after exposure to high temperature, i.e. the total NSD $F(D)$ and the NSD of the refractory remainder $F_r(D)$. From these size distributions a size-dependent volatile particle fraction $vf(D)$ can be defined as

$$vf(D) = 1 - \frac{F_r(D)}{F(D)} \quad (2.4.2)$$

To obtain $F_r(D)$, the aerosol particle population is commonly passed through a heated tube previous to the measurement (see Sect. 3.2.1). Although $vf(D) \leq 1$ for most

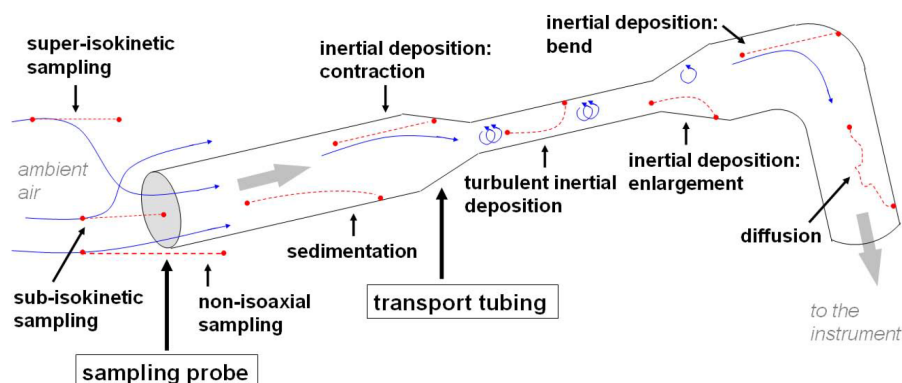


Figure 2.5.1: Illustration of mechanisms occurring during aerosol sampling and transport that lead to a distortion of aerosol measurements. Adopted from von der Weiden et al. (2009).

realistic scenarios, the volatile fraction can theoretically also exceed unity since the loss of particles with diameter D by shrinkage or complete vaporization is counteracted by the gain of shrunken particles with larger initial diameters.

Certainly, particle volatility can only provide indirect information about the important intrinsic particle properties, such as particle hygroscopicity. Nevertheless, especially in combination with additional information on the aerosol's chemical composition, the mixing state with respect to volatility proves to be a useful measurand (e.g. Brooks et al., 2007).

2.5 Particle Sampling Losses

The measurement of aerosol properties, e.g. particle size distributions or mixing state, frequently requires that an aerosol sample is withdrawn from the environment and guided towards a measurement device through some kind of tubing. During the extraction and transport various mechanisms can lead to size-dependent particle losses and can, thereby distort the measurements as illustrated in Fig. 2.5.1. To guarantee representative results it is important to assess and eventually correct for these losses. In the following, a brief description of some of the relevant physical processes occurring during sample extraction and transport is given.

As shown in Fig. 2.5.1, the first obstacle for representative aerosol measurements is the sample extraction, which is characterized by the size-dependent sampling efficiency η_{extr} . It depends on the speed of the ambient air U_0 , the speed inside the sample extraction system U , and the corresponding directions of these velocity vectors. When both velocity vectors point in the same direction the sampling is termed isoaxial, while it is termed anisoaxial otherwise. For $U_0 = U$ the sampling is further called isokinetic, whereas it is called sub-isokinetic for $U_0 > U$ and super-isokinetic for $U_0 < U$. In the ideal case of isoaxial isokinetic extraction the air streamlines, and therewith also the particles, enter the sampling system completely unaffected⁶. For sub-isokinetic

⁶In a strict sense, this holds only for thin-walled sampling nozzles, where the nozzle wall itself does not cause streamline displacement.

conditions, however, the lower speed inside the sampling system leads to a divergence of the streamlines. Whereas particles with low inertia are able to follow the resulting curved streamlines, larger particles with high inertia are not and, in consequence, become enriched in the extracted sample. In contrast, at super-isokinetic conditions the streamlines converge when entering the sampling system, so that high inertia particles become depleted. When the sampling additionally is anisoaxial the streamlines collectively change direction with further consequences for particles with high inertia. For instance, large particles may be lost upon inertial impaction on the inner wall of extraction nozzle. Inertial impaction will be discussed in more detail below.

Once a sample is extracted, it must subsequently pass through a (commonly cylindrical) transport tubing prior to the measurement. The flow conditions in the tubing can be either laminar or turbulent depending on the dimensionless flow Reynolds number Re_f given by

$$Re_f = \frac{d_t U}{\nu}$$

with the tubing diameter d_t and the kinematic viscosity of the air ν . For large $Re_f \gtrsim 2000$ the flow is turbulent, while it is laminar for $Re_f \lesssim 1000$. For most aerosol measurement device inlet tubing systems, the latter is fulfilled, so that the resulting flow profile in the cylindrical geometry is of parabolic shape. Aerosol particles carried along with the flow are permanently bombarded from all directions by a great number of gas molecules. When the particles are large compared to the mean distance between the gas molecules, called the mean free path λ_g , the interaction with the gas can be described in macroscopic terms. For smaller particles, on the other hand, the individual collisions with the gas molecules become more important for the particle's motion. The quantity defining the ratio between the mean free path and the particle diameter D is the Knudsen number Kn

$$Kn = \frac{2\lambda_g}{D}$$

For large particles $Kn \ll 1$ and the corresponding regime is called the continuum regime. When $Kn \gg 1$ a particle's motion resembles the random Brownian motion of the gas molecules, wherefore the corresponding regime is termed free molecule regime (or slip regime). Small particles in the free molecule regime that undergo Brownian motion experience a net flux from regions of high concentration to regions of low concentration via diffusion as defined by Fick's law

$$J_x = -K_{diff} \frac{\partial n}{\partial x} \quad (2.5.1)$$

where the diffusion coefficient K_{diff} and the concentration gradient $\partial n / \partial x$ (in direction x) determine the corresponding diffusion flux density J_x . Upon impingement on the tubing wall in the course of their random walk diffusive particles will deposit. The tubing wall, hence, acts as a sink for these particles and their concentration in the direct vicinity of the wall can be taken as zero. This causes a radial concentration gradient in the tubing and, according to Eq. (2.5.1), results in a net diffusive flux of the small particles towards the wall. The tubing transmission efficiency for particle experiencing this size-dependent net diffusive flux can be expressed as

$$\eta_{diff} = \exp\left(-\frac{\pi d_t l_t v_{diff}}{Q}\right) = \exp(-\xi Sh) \quad (2.5.2)$$

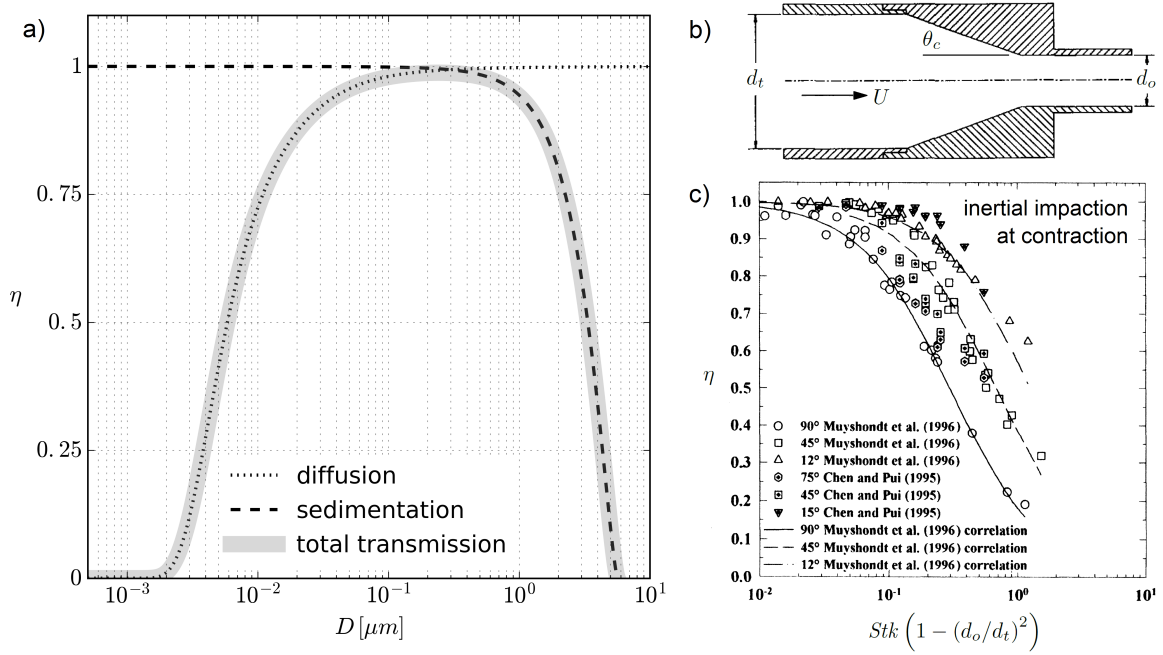


Figure 2.5.2: Particle transmission efficiencies for different sampling line assemblies. Graph (a) shows the particle diameter dependent transmission efficiency for a straight flat tubing ($Q = 1$ l/min, $d_t = 4$ mm, $l_t = 5$ m, $\rho_p = 1.2$ g/cm³, $T = 20^\circ\text{C}$, $p = 1013$ mbar). Here, small and large particles deposit on the tubing wall owing to diffusion and sedimentation, respectively. Graph (b) illustrates a conical tubing contraction at which particles of high inertia are lost via impaction. Graph (c) shows measurement results for the transmission efficiency at such a contraction for different contraction angles θ_c in dependence of the particle Stokes number. Graphs (b) and (c) are adopted from Muyschondt et al. (1996) and Kulkarni et al. (2011). Data in the latter is extracted from Chen and Pui (1995) and Muyschondt et al. (1996).

where l_t is the tubing length, v_{diff} the size-dependent net particle diffusion velocity towards the wall, Q the volumetric air flow rate, $\xi = \pi l_t K_{diff} Q^{-1}$ a dimensionless parameter and Sh the Sherwood number. For laminar flow conditions Holman (1972) gives

$$Sh = 3.66 + \frac{0.2672}{\xi + 0.10079\xi^{1/3}} \quad (2.5.2a)$$

An exemplary size-dependent transmission efficiency curve satisfying Eq. (2.5.2) and (2.5.2a) is shown in Fig. 2.5.2a) by the dotted line. As can be seen, diffusional losses typically only affect the small particles with diameters $D \lesssim 10 - 100$ nm.

Although larger particles remain mostly unaffected by this loss mechanism, they may deposit by other means such a gravitational settling (sedimentation). In the continuum regime, the settling of a particle in still air can be described by the force balance between gravitation F_{grav} and the counteracting drag force F_{drag} at the terminal particle settling velocity V_{ts} given by Stokes law

$$F_{grav} = \frac{\pi}{6} D^3 (\rho_p - \rho_g) g \quad F_{drag} = 3\pi\nu\rho_g D V_{ts} \quad (2.5.3)$$

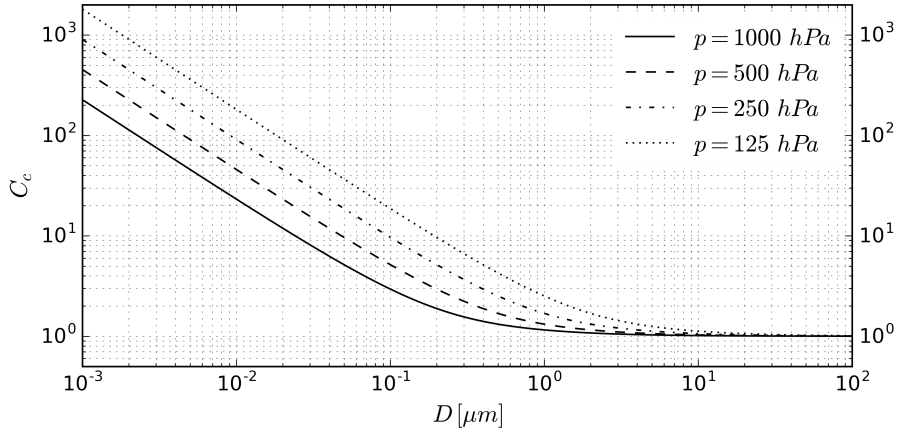


Figure 2.5.3: Size-dependence of the Cunningham slip correction factor C_c for different values of the ambient air pressure.

where g is the gravitational constant, ρ_p and ρ_g the densities of the particle and gas, respectively. Leaving the continuum regime with decreasing particle diameters, the free space between individual collisions with gas molecules leads to an increase in V_{ts} . To account for this effect the drag force is modified by an empirical size-dependent correction factor, called the Cunningham slip correction $C_c(D, \lambda_g)$

$$F_{drag} = 3\pi\nu\rho_p D \frac{V_{ts}}{C_c(D, \lambda_g)} \quad (2.5.3a)$$

Equating this modified drag force with the gravitational force in Eq. (2.5.3) yields

$$V_{ts} = \frac{g(\rho_p - \rho_g)}{18\nu\rho_g} C_c(D, \lambda_g) D^2 \quad (2.5.4)$$

Figure 2.5.3 shows the Cunningham slip correction for particles in air for different values of the ambient pressure p (that linearly relates to λ_g) following the formula given in Hinds (1999)

$$C_c(D, p) = 1 + \frac{\text{hPa } \mu\text{m}}{pD} \left(156 + 70 \exp\left(-0.0059 \frac{pD}{\text{hPa } \mu\text{m}}\right) \right) \quad (2.5.5)$$

As can be seen, while C_c converges to unity for particle diameters $D \gtrsim 1 - 10 \mu\text{m}$, it leads to significant deviations for smaller particles, which become more pronounced for larger mean free paths, i.e. smaller pressure values.

Coming back to the problem of particles transported through a tubing, the gravitational settling described by V_{ts} is superposed by the laminar (parabolic) air flow profile. Particles that manage to travel the vertical distance to the lower tubing wall before passing the tubing length l_t deposit and, hence, get lost via gravitational settling. For a pipe with an angle of inclination to the horizontal θ_i and a resulting horizontally projected tubing length $l_t \cos \theta_i$ Heyder and Gebhart (1977) derived the following expression for the transmission efficiency with respect to sedimentational particle loss

$$\eta_{grav} = 1 - \frac{2}{\pi} \left[2\chi\sqrt{1 - \chi^{2/3}} - \chi^{1/3}\sqrt{1 - \chi^{2/3}} + \arcsin(\chi^{2/3}) \right] \quad (2.5.6)$$

where

$$\chi = \frac{3 l_t \cos \theta_i V_{ts}}{4 d_t U} = \frac{3\pi d_t l_t \cos \theta_i V_{ts}}{16 Q} \quad (2.5.7)$$

with the air flow velocity U . A corresponding transmission efficiency curve is shown by the dashed line in Fig. 2.5.2a). Accordingly, sedimentational losses solely affect particles with diameters $D \gtrsim 0.5 - 1 \mu\text{m}$.

The total transmission efficiency for an aerosol measurement device inlet system is determined by the product of the single transmission efficiencies for all mechanisms in all parts of the system including the extraction and the tubing

$$\eta_{total} = \prod_{parts} \prod_{mechanisms} \eta_{part,mechanism} \quad (2.5.8)$$

Figure 2.5.2a) displays the total transmission for a straight tubing, determined by the product of the individual transmission efficiencies with respect to diffusional and sedimentational particle loss. The qualitative shape of this total transmission is characteristic for any inlet system, with particle losses being significant towards the lower and upper end of the particle size spectrum whereas the size range between ($D \approx 100 - 500 \text{ nm}$) is only marginally afflicted.

When a tubing is not completely straight, large particles may also be lost owing to mechanisms other than gravitational settling. With increasing inertia particles are less coupled to the flow, so that they cannot immediately react to transient changes in the flow field. The characteristic time a particle needs to adapt to such changes, for instance an increase in flow velocity or a change in flow direction, is called the relaxation time τ . It is defined by the time a particle takes to reach $(1 - 1/e) \approx 0.63$ of its terminal velocity from standstill when subjected to an external force field. Utilizing the previous case of a particle settling in still air via gravitation the relaxation time is $\tau = V_{ts}/g$. Vice versa, in the absence of an external force field a particle with the initial velocity V_0 needs the same time τ to decelerate to V_0/e . The product τV_0 is called the stopping distance and the Stokes number Stk relates this stopping distance to a characteristic system dimension L as

$$Stk = \frac{\tau V}{L}$$

The Stokes number is an important parameter to describe particle losses due to inertial impaction at the transport tubing walls, for instance at sharp tubing bends or contractions. At a tubing contraction, as illustrated in Fig. 2.5.2b), the flow streamlines are forced to change direction. With the initial particle velocity corresponding to the flow velocity $V_0 = U$ and the characteristic system dimension given by the orifice radius $d_o/2$ (the smallest radius of the contraction) the Stokes number writes as $Stk = 2\tau U d_o^{-1}$. Using the expression for the terminal settling velocity in Eq. (2.5.4) and considering $\rho_p \gg \rho_g$ yields

$$Stk = \frac{g\rho_p U}{9\nu\rho_g d_o} C_c D^2 \quad (2.5.9)$$

Based on this Stokes number, the orifice diameter d_o , the initial tubing diameter d_t , and the contraction angle θ_c Muyschondt et al. (1996) empirically determined the trans-

mission efficiency for inertial impaction at a tubing contraction to

$$\eta_{contr} = 1 - \frac{1}{1 + \left(Stk \frac{1 - (d_o/d_t)^2}{3.14 \exp(-0.0185\theta_c)} \right)^{-1.24}} \quad (2.5.10)$$

Resulting transmission efficiency curves and corresponding laboratory measurements for a set of contraction angles are shown in Fig. 2.5.2c) as a function of $Stk \left(1 - (d_o/d_t)^2\right)$. In addition to impaction at the front side of a sudden contraction, inertial particle losses may also occur behind the contraction. When the tubing enlargement after the contraction is not smooth turbulence may develop in an otherwise laminar flow. Resulting eddies involve curved streamlines in this region which in turn cause inertial deposition of particles with large Stokes numbers. For these turbulent losses no suitable parametrized equation is given in the literature (von der Weiden et al., 2009). Hence, if such enlargements cannot be avoided the corresponding losses need to be experimentally determined or numerically simulated for the individual geometry (Chen et al., 2007). However, as for sedimentational losses all inertial impaction mechanisms primarily lead to a removal of large particles while leaving the small ones with a closer coupling to the flow field unaffected.

A potential loss mechanism relevant to the complete particle size range is thermophoresis that occurs in the event of temperature gradients. When the gas temperature at the tubing center axis exceeds that at the tubing wall radial heat diffusion will cause a net aerosol velocity towards the wall, thereby leading to particle deposition. As for turbulent losses at sudden enlargements, no expression is given for thermophoretic deposition losses in laminar tube flow (Kulkarni et al., 2011).

For all loss mechanisms with available verified expressions the size-dependent transmission efficiencies can be calculated. An easy-to-use software tool that can be used for this purpose is the *particle loss calculator* (PLC), which includes all established transmission formulae (von der Weiden et al., 2009). The resulting functions allow to correct measured particle NSDs for corresponding sampling losses.

Chapter 3

Methods

The following chapter will start with a brief overview over the SALTRACE campaign with focus on the measurement platforms/sites relevant to this study. Particularly, the central airborne setup is introduced along with the fundamental in situ sampling strategy. Subsequently, all data acquisition, correction and evaluation methods that underlie the results presented in Ch. 4 are presented. Some of these methods have been developed as part of this work, one of which, i.e. the novel approach to OPC response modeling, calibration and OPC-based NSD retrieval (see Sect. 3.2.2.2 and 3.3.2) is published in Walser et al. (2017).

3.1 SALTRACE

As already mentioned in Ch. 1, the Saharan Aerosol Long-range Transport and Aerosol-Cloud-Interaction Experiment (SALTRACE) was a measurement campaign focusing on the long-range transport of mineral dust from North Africa across the North Atlantic Ocean into the Caribbean. To gain deeper insight into various aspects of this phenomenon, the SALTRACE program combined a suite of ground-based and airborne in situ aerosol measurements with remote-sensing and modeling techniques. Divided into different phases the complete program involved measurements from spring 2013 until summer 2014, with its core phase including the airborne measurements taking place in June/July 2013. A complete overview over the SALTRACE program and the project objectives can be found in Weinzierl et al. (2017). The platform for the airborne measurements was the DLR Falcon research aircraft. During SALTRACE, the Falcon was equipped with an extensive aerosol in situ payload, sampling devices for offline particle analysis, a nadir-looking $2\ \mu\text{m}$ wind lidar (see Chouza et al., 2015), dropsondes and an instrumentation for the measurement of standard meteorological parameters. Pictures of the equipped aircraft and selected parts of the instrumentation are shown in Fig. 3.1.1. The ground-based measurements included aerosol in situ, lidar and sun photometer measurements (e.g. Kristensen et al., 2016; Groß et al., 2015; Mamouri and Ansmann, 2016; Haarig et al., 2017). The ground-based in situ measurements were conducted by TROPOS at Ragged Point, Barbados ($13^{\circ}09'54''\text{N}$, $59^{\circ}25'56''\text{W}$). The ground-based remote sensing setup comprised Aerosol Robotic Network (AERONET) sun photometers (Holben et al., 1998) at Cabo Verde and Barbados, and lidar measurements at the Caribbean Institute for Meteorology and



Figure 3.1.1: The DLR Falcon research aircraft during SALTRACE (a) with close-up images of some vital parts of the airborne measurement setup, namely the wing-mounted optical particle spectrometer UHSAS-A (b), the Falcon isokinetic aerosol inlet guiding the ambient aerosol towards the in-cabin instrumentation (c), and the CCNC as a central in-cabin instrument, mounted in an aircraft rack (d).

Hydrology, Barbados (CIMH, $13^{\circ}8'55''\text{N}$, $59^{\circ}37'29''\text{W}$). The locations of the ground-based measurement sites on Barbados are shown in Fig. 3.1.2.

Before the measurement setup and the involved instruments are discussed in more detail, the following section will briefly present the SALTRACE flights, their objectives and the strategy behind the corresponding flight patterns.

3.1.1 Airborne Campaign

Overall, the Falcon performed 31 research flights within the scope of SALTRACE connoting a total of 110 hours of scientific flight time (Weinzierl et al., 2017). This represents the most comprehensive airborne investigation on long-range transported dust ever made. Figure 3.1.3 features a map with all flight tracks of the SALTRACE airborne measurements in summer 2013. After initial transfer from Oberpfaffenhofen, Germany to the Northwest African coast, the airborne campaign started with sampling of the dust-laden SAL between the Cabo Verde islands and Senegal (11-17 June). In addition to the goal of characterizing the SAL aerosol close to its source region with the same instrumentation that was later used to study the transported layer in the Caribbean, these flights aimed to provide a comparison data set with the previous SAMUM campaigns conducted in 2006 and 2008 (Ansmann et al., 2011). After sub-



Figure 3.1.2: Ground-based measurement sites during SALTRACE and their locations on the island of Barbados. Adopted and modified from Weinzierl et al. (2017).

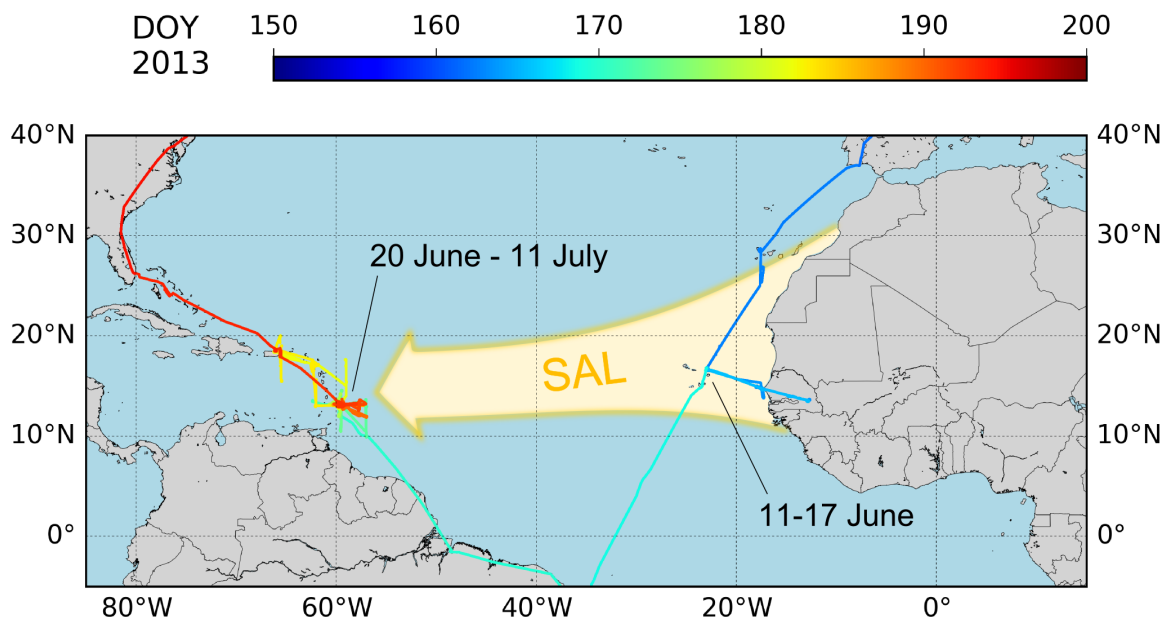


Figure 3.1.3: Flight tracks of all airborne measurements during the SALTRACE core phase in summer 2013. The tracks are color-coded according to their time stamp in day of the year (DOY) 2013 with respect to Coordinated Universal Time (UTC). For illustration purposes, the tracks are underlaid by an outline of the typical average SAL summertime transport corridor.

sequent transfer across Brazil, the first part of the research flights in the Caribbean region in the vicinity of Barbados (20-26 June) were geared towards the study of the horizontal variability of the aerosol properties in the SAL after transatlantic transport. This period also included the first-time airborne in situ sampling of one and the same dust outbreak event on both sides of the Atlantic using an identical instrumentation (17 and 22 June). Following an extension of the horizontal profiling to the region north to Barbados including Antigua and Puerto Rico (30 June and 1 July), the second half of the Caribbean measurements focused more on the vertical profiling of aerosol properties in the transported SAL, again primarily in the proximity of Barbados (5-11 July). Apart from measurements under the presence of high dust loads, the second half of the Caribbean measurements further allowed to study the vertical distribution of aerosol properties in more pristine air masses (8 July) right before the passage of tropical storm Chantal¹. Return transfer to Germany led across the United States where local boreal biomass burning aerosol could be characterized. Table 3.1.1 offers a complete overview over the SALTRACE flights in the Cabo Verde/East Atlantic and the Caribbean/West Atlantic regions together with all individual flight objectives.

Independent of profiling type (horizontal or vertical focus) and flight objective, the typical flight pattern started with an ascent to a high altitude level (about 9 km) far above the SAL upper edge. This allowed to obtain a fast general view of the vertical thermodynamical and aerosol structure by means of the airborne in situ instruments. In the first place, the initial high flight legs were then intended to facilitate a detailed scanning of the vertical and horizontal aerosol structure of the subjacent atmosphere with the nadir-looking onboard lidar. Further, dropsondes launched from these high altitudes provided more profound information about the meteorological parameters in the vertical column. On basis of the real-time information on the spatial aerosol structure, the subsequent strategy was to thoroughly examine different parts of the atmosphere beneath in situ by performing a series of constant altitude flight legs in the course of a stepwise descent. These in situ flight legs were further utilized to collect particle samples for later offline analysis of particle composition. For flights with a focus on horizontal profiling only few but horizontally extended in situ legs were performed, while for vertical profiling the number of vertical steps was enhanced at the expense on horizontal coverage. A typical flight pattern is shown in Fig. 3.1.4 using the example of the vertical profiling flight 130711a, i.e. the first flight on 11 July 2013. The nomenclature for the SALTRACE flights arises from the date of take-off in the format *yymmdd* Coordinated Universal Time (UTC) and an additional letter (a or b) defining the flight order in case of more than one flight per day.

3.2 Instruments and Data

For the airborne in situ measurements, that represent the centerpiece of this study, the Falcon research aircraft has been modified from its original state. As displayed in Fig. 3.1.1, pods installed below the aircraft's wings allow for the operation of optical particle spectrometers outside the cabin. An aerosol inlet system at the plane's fuselage further

¹Chantal evolved on 7 July about 2000 km east-southeast of Barbados and passed the island on 9 July. For detailed information see the TC report at <http://www.nhc.noaa.gov/data/tcr/>

Date	T/O	LDG	From	To	Objectives
Mineral dust characterization off the coast of Africa and in Africa					
2013/06/11	12:51	16:25	La Palma (ES)	Sal (CV)	Mineral dust characterization between Canary Islands and Cabo Verde; detection of the northern SAL edge
2013/06/12	08:52	12:08	Sal (CV)	Dakar (SN)	Mineral dust characterization over Africa
2013/06/12	13:12	16:10	Dakar (SN)	Sal (CV)	Mineral dust characterization over Africa and in the Cabo Verde area; coordinated flight with a CALIPSO overpass of Dakar at 14:45 UTC
2013/06/14	09:06	12:37	Sal (CV)	Dakar (SN)	Mineral dust characterization over Africa
2013/06/14	13:47	15:54	Dakar (SN)	Sal (CV)	Mineral dust characterization over Africa and in the Cabo Verde area
2013/06/17	11:06	12:27	Sal (CV)	Praia (CV)	Mineral dust characterization over the Cabo Verde area; Lagrangian experiment - part 1
2013/06/17	13:24	17:21	Praia (CV)	Natal (BR)	Characterization of mineral dust crossing the Atlantic Ocean
Mineral dust characterization in the Caribbean					
2013/06/20	12:01	15:55	Barbados	Barbados	Characterization of the horizontal (E-W direction) variability of dust properties; detection of anthropogenic plumes including ship exhaust
2013/06/21	18:32	22:01	Barbados	Barbados	Characterization of the mineral dust layer prior to the arrival of the Lagrangian-selected air mass along 57°W
2013/06/22	18:05	21:55	Barbados	Barbados	Mineral dust characterization perpendicular to the main dust outflow along 59.5°W Lagrangian experiment - part 2
2013/06/26	23:25	03:15	Barbados	Barbados	Night flight; wind lidar calibration and mineral dust characterization
2013/06/30	13:03	16:28	Barbados	Antigua	Characterization of the horizontal (N-S direction) variability of dust properties east of Antigua
2013/06/30	19:15	22:00	Antigua	San Juan (PR)	Mineral dust characterization between Antigua and Puerto Rico; wet deposition studies
2013/07/01	14:22	18:12	San Juan (PR)	Antigua	Mineral dust characterization in N-S direction east of Puerto Rico; resampling of the airmass which was detected the day before; wet deposition studies
2013/07/01	19:48	23:30	Antigua	Barbados	Mineral dust characterization in N-S direction west (downstream) of the Caribbean Islands
2013/07/05	12:10	16:01	Barbados	Barbados	Characterization of the horizontal (E-W direction) variability of dust properties under low dust load
2013/07/08	18:55	22:46	Barbados	Barbados	Mineral dust characterization ahead of tropical storm Chantal
2013/07/10	15:07	19:18	Barbados	Barbados	Mineral dust characterization in E-W direction with focus on vertical profiling, measurements after the passage of tropical storm Chantal
2013/07/11	12:37	15:03	Barbados	Barbados	Atmospheric column closure experiment with extended vertical profiling over and near Barbados
2013/07/11	18:04	21:05	Barbados	San Juan (PR)	Mineral dust characterization between Barbados and Puerto Rico

BR: Brazil; CV: Cabo Verde; E: East; ES: Spain; N: North; PR: Puerto Rico; S: South; SN: Senegal; W: West

Table 3.1.1: List of SALTRACE flights including times, locations and flight objectives. Falcon take-off dates are given in the date format yyyy/mm/dd, corresponding take-off (T/O) and landing (LDG) times in the time format hh:mm UTC. Extract from Weinzierl et al. (2017, supplement).

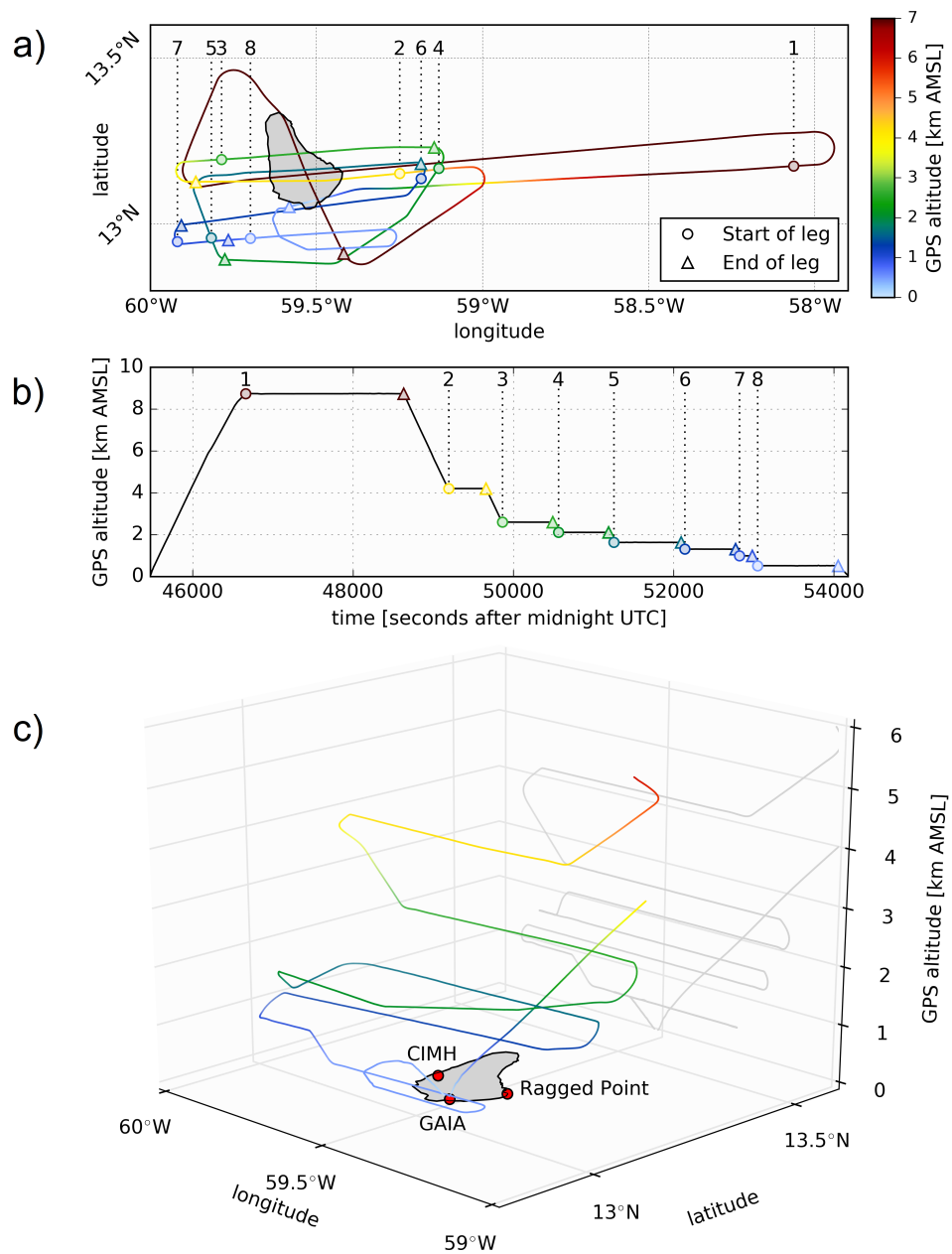


Figure 3.1.4: Flight pattern of SALTRACE flight 130711a. Shown are the top view of the flight path color-coded with the Falcon GPS altitude (a), the corresponding altitude profile (b) and a 3D view of the path for altitudes below 6 km (c). The circle and triangle symbols in plot (a) and (b) indicate beginnings and endings of each constant altitude flight leg. In plot (c), the ground stations on Barbados at CIMH and Ragged Point as well as the location of the Grantley Adams International Airport (GAIA) are highlighted in red.

extracts the ambient aerosol and facilitates a number of aerosol measurements inside the cabin. The aerosol inlet, also shown in Fig. 3.1.1, is oriented in forward direction and is slightly tilted towards the nose of the aircraft to account for its average angle of attack. Accordingly, during flight the apparent wind vector direction is approximately parallel with the inlet's orientation to guarantee near-isoaxial sampling. The diffusor geometry at the front part of the inlet and the in-cabin sampling setup's total flow rate are further adjusted in a way that brings the sampling velocity at the inlet tip into close agreement with the apparent wind velocity, i.e. to establish also near-isokinetic sampling conditions. Whereas, thanks to these settings, the inlet has only negligible effect on submicron particles, possible slight deviations from isoaxial and isokinetic sampling conditions and the inevitable pipe curvature in the rear part of the inlet induce a drop-off in the sampling efficiency η_{extr} for larger particles. The resulting so-called cutoff diameter of the inlet, i.e. the particle diameter at which η_{extr} reduces to 0.5, depends on outside pressure and air speed. It has been determined to range from about $2.5 \mu\text{m}$ near ground level to about $1.5 \mu\text{m}$ at an altitude of 10 km, i.e. close to the aircraft's operational ceiling (Fiebig, 2001; Schumann et al., 2011). Figure 3.2.1 shows a schematic of the in-cabin instrumentation relevant to this study, that was operated behind the Falcon aerosol inlet during SALTRACE. This instrumentation comprised condensation particle counters (CPCs) for the measurement of total aerosol particle number concentration and volatile particle fraction, a CCNC to determine CCN number concentrations, OPCs for the derivation of the aerosol particle NSDs and size-dependent volatility, a soot photometer to infer refractory black carbon mass concentrations, impactors to collect particle samples for offline chemical and volatility analysis, and peripheral equipment. As mentioned in the previous section, the airborne data set obtained by the in-cabin instrumentation and the wing-mounted instruments is supplemented by ground-based measurements. The supplementary ground-based data used in this thesis include sun photometer and lidar products, mineral dust mass concentrations, aerosol particle NSDs and CCN number concentrations.

In the subsequent section first some important auxiliary devices will be introduced. Thereafter, a closer look will be taken at the main instruments that were characterized and evaluated in the scope of this study including details on their operating principles, measured quantities and involved data corrections. Finally, the supplementary instruments, including the ground-based and airborne instruments that were not evaluated as part of this work, will first be briefly addressed with general information on the technique, data products, literature references, and the persons responsible for the data evaluation. A summary of the consulted instruments and corresponding data products is given in Tab. 3.2.4. Additional information about most of the presented instruments can be found in Kulkarni et al. (2011) and Wendisch and Brenguier (2013).

3.2.1 Auxiliary Devices

3.2.1.1 Differential Mobility Analyzer (DMA)

The DMA is a device for particle size filtering that allows to extract (quasi-) monodisperse sub-samples from an initial aerosol (Knutson and Whitby, 1975). It is utilized to provide narrow particle NSDs for the calibration of other aerosol instruments. In combination with a downstream particle counter, e.g. a CPC (see Sect. 3.2.2.1), it

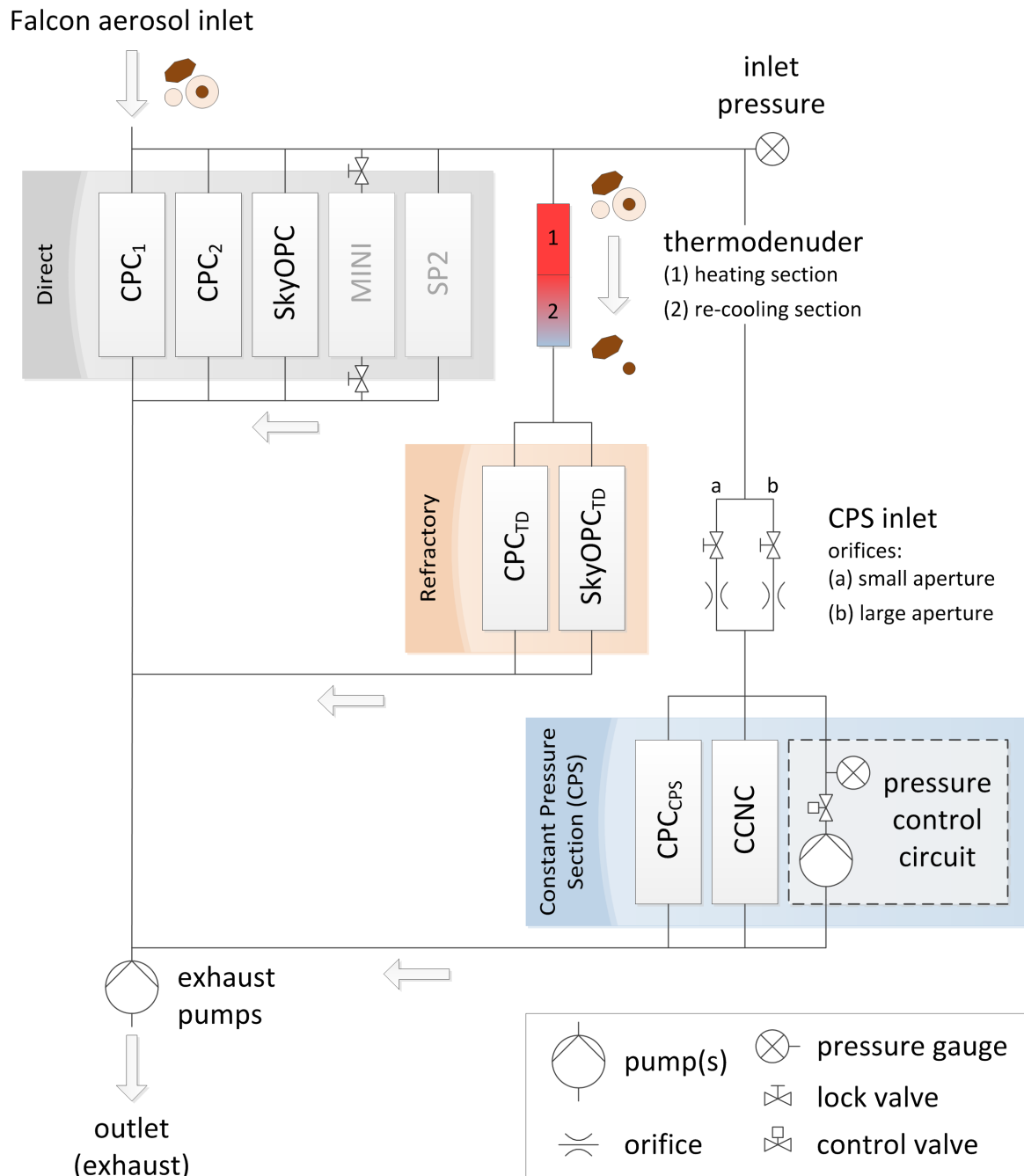


Figure 3.2.1: Schematic flow diagram of the Falcon in-cabin measurement setup used for this study. This setup comprises the condensation particle counters CPC₁, CPC₂, CPC_{TD} and CPC_{CPS}, the optical particle counters SkyOPC and SkyOPC_{TD}, and the cloud condensation nuclei counter CCNC as central instruments. Further indicated are the MINI sampling device (providing the basis for particle offline analysis) and the single particle soot photometer SP2. The exhaust pump symbol is representative for the entirety of external exhaust pumps and the internal CCNC exhaust pump.

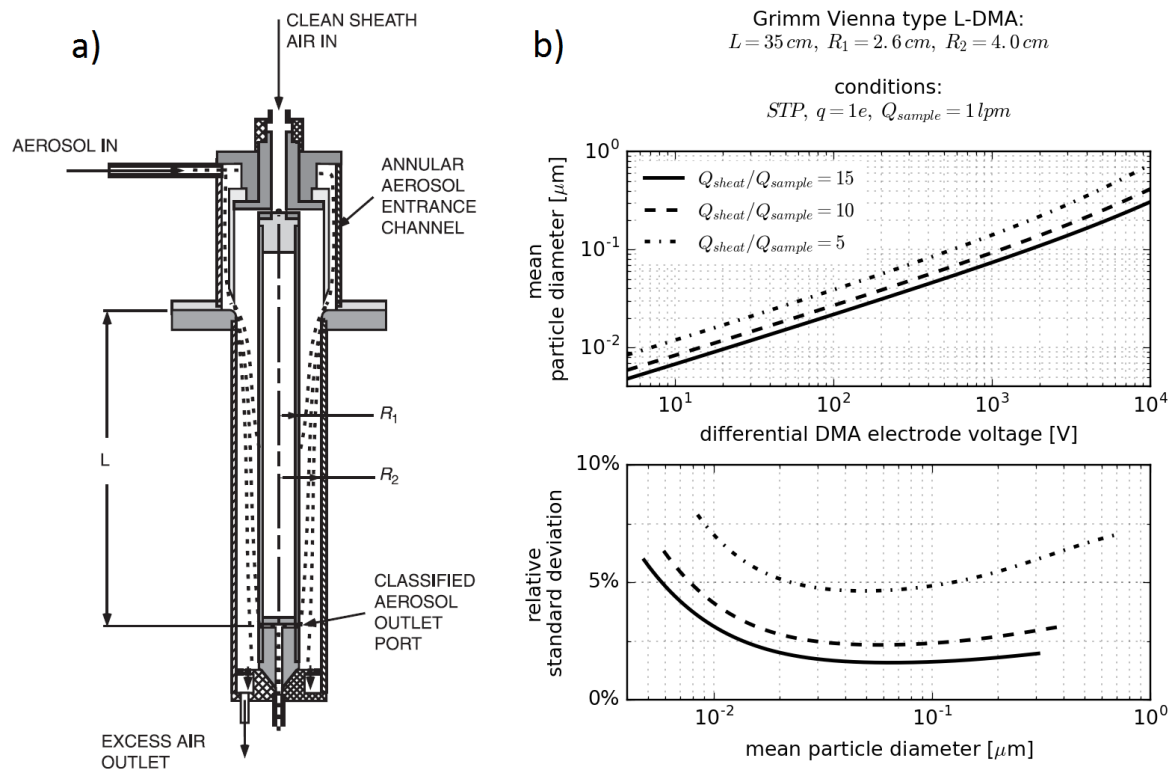


Figure 3.2.2: Schematic of a cylindrical DMA (a) and transfer function parameters, i.e. mean diameter and corresponding relative standard deviation for the Grimm L-DMA (b) in dependence of the differential voltage and the volumetric sheath flow rate at certain boundary conditions. The curves represent calculation results to the formulae given in Reischl et al. (1997). Figure (a) is adopted from Kulkarni et al. (2011).

can further be used to derive the ambient aerosol particle NSD (cf. Sect. 3.2.3.2). Figure 3.2.2a) shows the structure of a cylindrical DMA being the most popular DMA design. It consists of a cylindrical capacitor that is sheathed by a laminar flow of clean air. Previously charged aerosol particles inserted into the electric field via a slot in the outer electrode are accelerated towards the inner electrode by the acting electric force. The distance a particle travels in direction of the cylinder axis before overcoming the sheath flow barrier and striking the inner electrode is determined by the flow velocity along the cylinder axis v_z and the particle's terminal velocity in directing of the electric field v_E . v_E depends on the particle's electrical mobility Z , which can be derived from the force equilibrium between the electric force qE and the drag force given by Eq. (2.5.3a) to

$$Z = \frac{qC_c}{3\pi\nu\rho_g D} \quad v_E = ZE \quad (3.2.1)$$

where E is the electric field strength and q the charge carried by the particle. Downstream of the injection slot, an aerosol sample is extracted through a narrow gap in the inner electrode, so that only particles of a certain electrical mobility range are able to proceed to the device outlet. The transfer functions of a DMA are approximately of Gaussian shape. For the Vienna type cylindrical DMA design these electrical mobility transfer functions are defined by the formulae given in Stolzenburg (1988) and Reischl

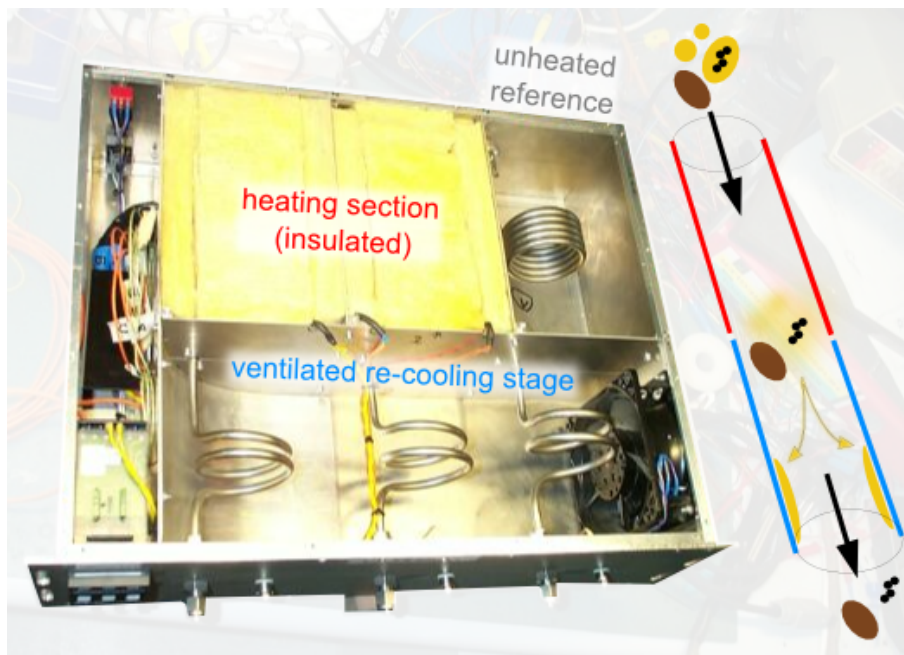


Figure 3.2.3: Photograph of the (opened) DLR Falcon TD with an illustration of its operating principle. The device includes two parallel heating sections with independent temperature controls and an unheated, otherwise identical reference channel. To extent aerosol residence time under the given space constraints, the tubing is spiral-shaped. Volatile particle components evaporated in the initial heating sections are subsequently adsorbed at the tubing wall in the rare (denuder) stage where the aerosol is re-cooled to ambient temperature.

et al. (1997). Their mean and standard deviation can be adjusted by changing the electric field strength via the differential potential between the DMA electrodes or by changing the volumetric flow rates of the sample Q_{sample} and sheath air Q_{sheath} determining v_z . Figure 3.2.2b) shows theoretical calculation results for the particle diameter transfer function parameters of the Grimm L-DMA, the DMA model that was used in this study for the characterization/calibration of the involved instruments. Here, the electrical mobility transfer functions given by Reischl et al. (1997) are converted to diameter via Eq. (3.2.1) assuming singly charged particles ($q = 1e$, where e is the elementary charge).

3.2.1.2 Thermodenuder (TD)

As discussed in Sect. 2.4, the aerosol mixing state with respect to volatility is an informative property. A simple but effective technique to investigate the volatility is to make use of a heated tube installed upstream of a given aerosol particle counting or NSD measurement device (e.g. Clarke, 1991; Burtscher et al., 2001). Heating the aerosol to a defined temperature T_{TD} allows to evaporate a certain range of volatile particle components such as highly volatile organic carbon and sulfuric acid (at $T_{TD} = 30 - 120^\circ\text{C}$), and ammonium sulfate and bisulfate (at $T_{TD} = 125 - 175^\circ\text{C}$) (Burtscher et al., 2001). Refractory aerosol particles such as elemental carbon, mineral dust or sodium chloride remain unaffected for $T_{TD} < 300^\circ\text{C}$. The term thermodenuder

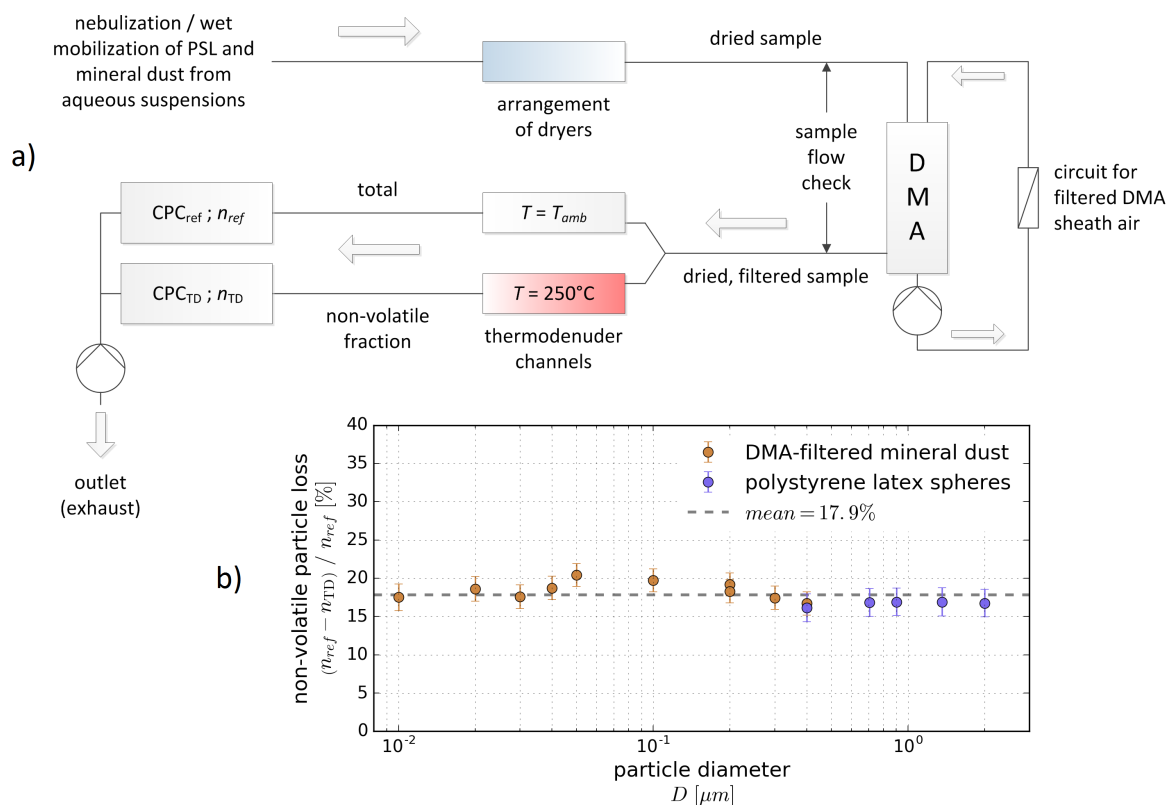


Figure 3.2.4: Laboratory setup for the determination of thermophoretic deposition losses of non-volatile particles in the denuder section of the DLR Falcon TD (a) and the corresponding results (b).

describes the combination of a temperature-controlled heating section and a subsequent re-cooling stage, the so-called denuder section. In the latter, the vapor formed from the volatile components is re-condensed/deposited. Re-condensation may potentially occur as heterogeneous condensation on the remaining refractory particles. However, as the denuder section wall usually by far dominates the available surface, heterogeneous re-condensation on the refractory particles can be regarded as negligible. An initial aerosol that contains both refractory and volatile components (with respect to T_{TD}) will hence be reduced to its refractory remainder upon transit through the TD and the volatile components will be left adsorbed at the denuder section wall². An illustration of this process is shown in Fig. 3.2.3 alongside a photograph of the DLR Falcon TD, which was built and characterized as part of a diploma thesis by Fritzsche (2002). During SALTRACE, all TD channels were operated at $T_{TD} = 250^\circ\text{C}$. This temperature was determined to be the minimum temperature for a complete evaporation of ammonium sulfate (and all species with higher volatility) given the aerosol residence time in the heating section (Fritzsche, 2002).

Unfortunately, owing to thermophoresis (see Sect. 2.5) the TD not only removes volatile particle components but also induces a loss of non-volatile particles in the denuder stage. Fritzsche (2002) measured these losses for particle diameters $50 \leq D \leq 200$ nm and found a size-independent loss factor of approximately 20%. As this

²In order to desorb deposit material from the walls, from time to time the TD needs to be operated at maximum temperature ($T_{TD} \approx 350^\circ\text{C}$) while rinsed with particle-free air.

size range is much narrower than the one covered by the post-TD measurements during SALTRACE, the thermophoretic particle losses were thoroughly investigated over the complete size range as part of this work. Figure 3.2.4a) shows the corresponding laboratory measurement setup. Monodisperse non-volatile particle samples — mineral dust samples and polystyrene latex (PSL) sphere standards were mobilized from aqueous suspensions via nebulization³, subsequently dehumidified by an arrangement of silica gel dryers and size-filtered with a DMA — were passed through the heated TD ($T_{TD} = 250^{\circ}\text{C}$) and the output particle concentration was measured utilizing a CPC. In parallel, a reference particle concentration was determined using a second unheated TD channel. To prevent systematic measurements errors due to differential transport losses (e.g. diffusional loss), the two parallel lines were built in an identical manner. Moreover, systematic biases owing to differential CPC characteristics such as different cutoff diameters and plateau efficiencies (see Sect. 3.2.2.1) were corrected. The results, shown in Fig. 3.2.4b), confirm the uniformity of thermophoretic deposition losses over the complete size range. The constant loss factor is determined to $(1 - \eta_{TD,thermo}) = 17.9 \pm 1.2\%$. Fritzsche (2002) demonstrated that this loss factor is in good approximation pressure-independent, at least for $p \geq 300$ hPa and, therewith, in the pressure range relevant to this study. It was further tested, if the Falcon TD tubing bends provoke significant inertial impaction losses. Both measurements and theoretical calculations for the TD geometry utilizing the PLC (von der Weiden et al., 2009) consistently proved this loss mechanism to be negligible for particles with $D \leq 2$ μm , i.e. in the size range relevant for the Falcon in-cabin instruments.

3.2.2 Main Instruments

3.2.2.1 Condensation Particle Counters (CPCs)

Operating Principle

CPCs, also called condensation nuclei counters, are instruments used to determine the integral aerosol particle number concentration down to small particle sizes, occasionally even down to the lower limit of the occurring size range (particle diameters of just a few nm). By various condensation techniques, small particles are increased in size in order to permit their detection via optical methods. Figure 3.2.5 illustrates the basic principle behind the so-called conductive cooling type CPCs that are employed in this study. An aerosol sample, guided through the device under laminar steady volumetric flow, first enters a saturator section where it becomes saturated with the vapor of a working liquid, i.e. butanol in this case. Leaving the heated saturator section, the aerosol subsequently passes a condenser tube, which is kept at a lower temperature so that the gas is cooled by conduction (heat diffusion). As the diffusivity of heat is much greater than the diffusivity of the large butanol molecules, the working fluid vapor pressure remains high as the surrounding gas is cooled. In consequence, it surpasses its saturation vapor pressure, typically by several hundreds of percent. This immense vapor supersaturation provokes an activation of even the smallest aerosol particles to butanol droplets via heterogeneous condensation. Grown to sizes of several micrometers

³Nebulization of the aqueous suspensions was conducted with the Droplet Measurement Technologies portable aerosol generator running with aerosol-free carrier air.

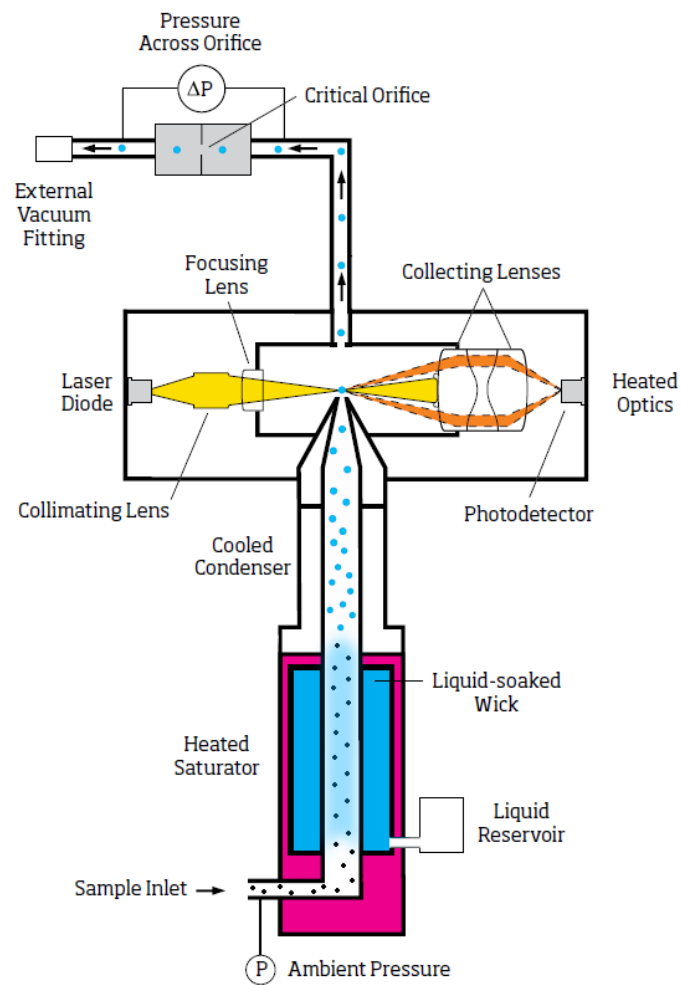


Figure 3.2.5: Schematic of a conductive cooling CPC. Adopted and modified from the TSI Inc. model 3772 CPC brochure.

the particles are injected into an optical detection block where they are identified via their light-scattering ability (cf. Sect. 3.2.2.2). By counting the individual particle scattering pulses per unit time, the raw CPC output is a count rate N . To convert N into a particle number concentration n requires knowledge on the volumetric flow Q through the instrument

$$n = \frac{N}{Q} \quad (3.2.2)$$

As shown in Fig. 3.2.5, for the used CPCs Q is set via a critical orifice. Gas flow through an orifice is called critical or choked, when the gas velocity at the constriction reaches sonic conditions. Slightly depending on the orifice contraction angle, this state is reached when the relative pressure drop over the orifice satisfies $\Delta p/p \gtrsim 0.5$, where p denotes the orifice upstream pressure. Unable to further accelerate, the gas velocity remains constant when the relative pressure drop continues to increase. Hence, as long as the critical flow condition is fulfilled an orifice will passively keep the volume flow rate at a constant value independent of the absolute value of p . The exact value of Q can, hence, easily be determined from volumetric flow measurements at the instrument's inlet at atmospheric or any other ambient pressure.

Counting Efficiency Cutoff

The minimum particle size capable of acting as a condensation nucleus in the CPC is given by an equivalent form of Eq. (2.1.5) as

$$D_{low} = \frac{4\sigma M}{\rho RT \ln S}$$

where σ , ρ and M are the surface tension, density and molecular mass of the working liquid, R is the universal gas constant, and T and S represent the temperature and saturation at the point of activation. However, as T and S are not uniform throughout the condenser but vary slightly, D_{low} is not a sharp value. The actual size-dependent counting efficiency around the lower size limit is an important characteristic of a CPC and described by so-called cutoff curves, that exhibit a sigmoidal shape. Figure 3.2.6 shows such functions in dependence of the absolute pressure p and the temperature difference between saturator and condenser ΔT for a (conductive cooling) CPC using butanol as the working liquid. As can be seen from Fig. 3.2.6a), the drop-off of the sigmoidal curves barely shifts with changing p . While several measurements, such as the ones presented here (Hermann and Wiedensohler, 2001, and references therein), indicate a slight decrease in the 50% counting efficiency diameter $D_{50\%}$ with decreasing pressure, others contrarily report a minor increase (Zhang and Liu, 1990, 1991). However, for the purposes of this study the small potential pressure-dependent variation in $D_{50\%}$ is negligible. As demonstrated in Fig. 3.2.6b), the saturator-condenser temperature difference ΔT , on the other hand, strongly influences the value of $D_{50\%}$. By increasing the supersaturation in the condenser, an enhanced ΔT leads to a decrease in the lower particle diameter cutoff value. For a fixed ΔT setting, the complete trend of the counting efficiency with particle size $\eta(D)$ can in good approximation be described by the following function (Mertes et al., 1995; Wiedensohler et al., 1997)

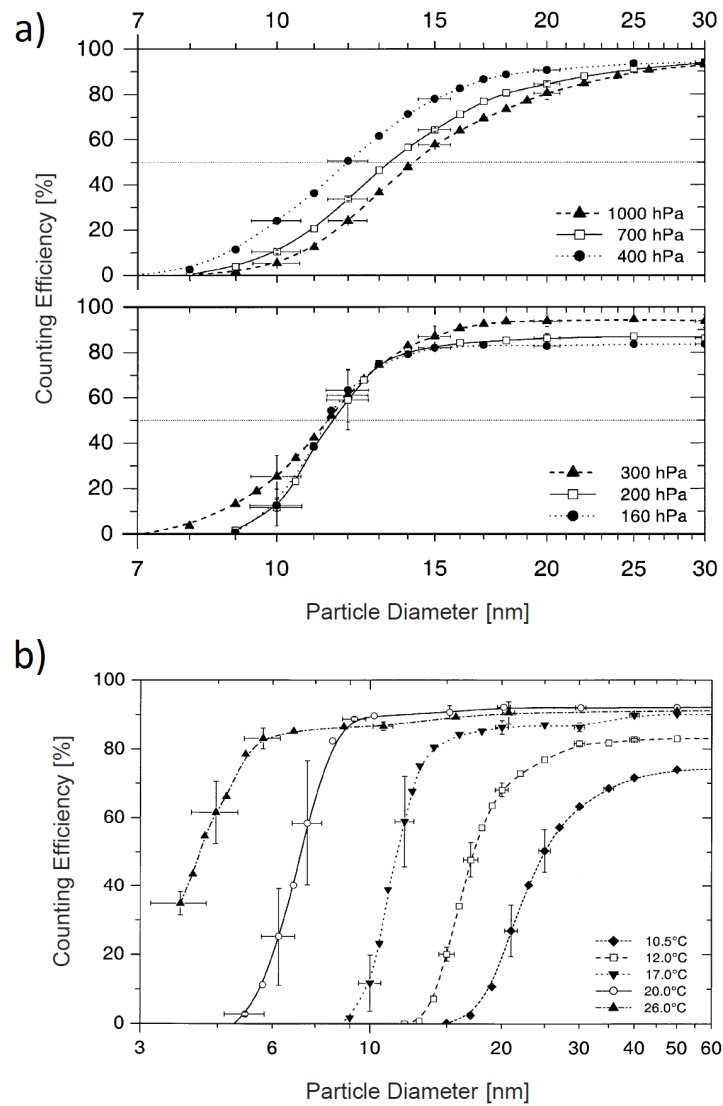


Figure 3.2.6: Counting efficiency cutoff curves for the TSI Inc. model 7610 CPC operated with butanol in dependence of (a) absolute pressure p and (b) saturator-condenser temperature difference ΔT . The TSI 7610 is identical to the model 3670 (CPC₂) used in this study. The presented measurements were performed with either NaCl or Ag particles. Adopted from Hermann and Wiedensohler (2001).

CPC	a	D_1 [nm]	D_2 [nm]	$D_{50\%}$ [nm]
CPC ₁ (TSI 3010)	1.7	4.3	1.5	5.7
CPC ₂ (TSI 3760)	1.07	14.2	2.2	15.07

Table 3.2.1: Counting efficiency function parameter values for the TSI CPCs used in this study, following the parametrization of Mertes et al. (1995). The values are adopted from the extensive measurements of Mertes et al. (1995) and Wiedensohler et al. (1997), and correspond to the operation settings during SALTRACE, i.e. $\Delta T = 25$ K (maximum ΔT) and $Q = 1$ lpm for CPC₁ (TSI 3010), and $\Delta T = 17$ K (standard ΔT) and $Q = 1.5$ lpm for CPC₂ (TSI 3760). From the scatter reported in the intercomparison study by Wiedensohler et al. (1997), the relative accuracies of the values for a , D_1 and D_2 are estimated as $\pm 3\%$, $\pm 7\%$ and $\pm 2\%$, respectively.

ΔT [K]	$D_{50\%}$ [nm] NaCl	$D_{50\%}$ [nm] (NH ₄) ₂ SO ₄
30	4	
21	6	4
18	7	6
15	9	9
11	13	13
9	21	

Table 3.2.2: 50% counting efficiency diameters for the CPSA modules at different ΔT and for different particle materials (NaCl and (NH₄)₂SO₄). Accuracy is specified as ± 0.5 nm. Adopted from Stein et al. (2001).

$$\eta(D) = \begin{cases} 1 - a \left(1 + \exp\left(\frac{D-D_1}{D_2}\right)\right)^{-1} & D \geq D_0 \\ 0 & D < D_0 \end{cases} \quad (3.2.3)$$

with

$$D_0 = D_2 \ln(a - 1) + D_1$$

For the two CPCs that were operated directly⁴ behind the Falcon aerosol inlet, i.e. CPC₁ and CPC₂ (see Fig. 3.2.1) the corresponding parameter values and associated uncertainties are given in Tab. 3.2.1. These values (for the commercially available counters TSI Inc. model 3010 and 3760) are adopted from the comprehensive laboratory measurements from Mertes et al. (1995) and Wiedensohler et al. (1997). Accordingly, during SALTRACE, CPC₁ and CPC₂ were utilized to measure the total particle concentration at slightly different values of $D_{50\%}$. The additional counters, i.e. CPC_{TD} and CPC_{CPS} represent customized CPC architectures, the so-called condensation particle size analyzer (CPSA) modules that were built and characterized at DLR. Table 3.2.2 lists the $D_{50\%}$ values for the CPSA modules at various temperature settings as measured by Stein et al. (2001). For SALTRACE, the values of ΔT were set such that the $D_{50\%}$ values of CPC_{TD} and CPC_{CPS} were approximately corresponding to the ones of CPC₂ and CPC₁, respectively. CPC_{TD} was installed behind the TD to obtain the integral number concentration of non-volatile (refractory) particles n_r and to ultimately derive the total number fraction of (completely) volatile particles as (cf. Eq. (2.4.2))

$$vf_{total} = 1 - \frac{n_r}{n} \quad (3.2.4)$$

CPC_{CPS} was utilized as an auxiliary counter to assess the losses of CCN at the inlet orifices of the constant pressure section (CPS, see Fig. 3.2.1), which is described in detail in Sect. 3.2.2.3. As Tab. 3.2.2 reveals, the lower particle size cutoff of CPCs is material-dependent, although the data suggest that this dependency is insignificant when butanol is used as the working fluid. This finding is supported by a range of other studies (e.g. Kesten et al., 1991; Schröder and Ström, 1997; Hermann and Wiedensohler, 2001). In the following, the particle material impact on the $D_{50\%}$ values is therefore disregarded. The reported cutoff characteristics given in Tab. 3.2.1 and 3.2.2 were verified by laboratory measurements after the SALTRACE campaign.

Concentration Correction

Unmentioned so far, Fig. 3.2.6 shows that not only the cutoff diameter but also the asymptotic CPC counting efficiency for particle diameters $D \gg D_{50\%}$, the so-called plateau counting efficiency may be affected by changes in p and ΔT . The reason for this is that droplet activation is a dynamic process. When the droplet activation kinetics become retarded not all particles are able to grow to detectable sizes any more. Figure 3.2.6a) demonstrates that the plateau counting efficiency of CPC₂ remains unmodified for pressure values $p \geq 300$ hPa (at the standard ΔT setting and using butanol). However, the value of the plateau efficiency and its sensitivity of to p can vary among CPC architectures and different ΔT settings. For the SALTRACE CPCs, the pressure-dependent plateau counting efficiencies were, hence, measured in a series of laboratory

⁴The term “directly” means without additional aerosol modification, such as via the TD.

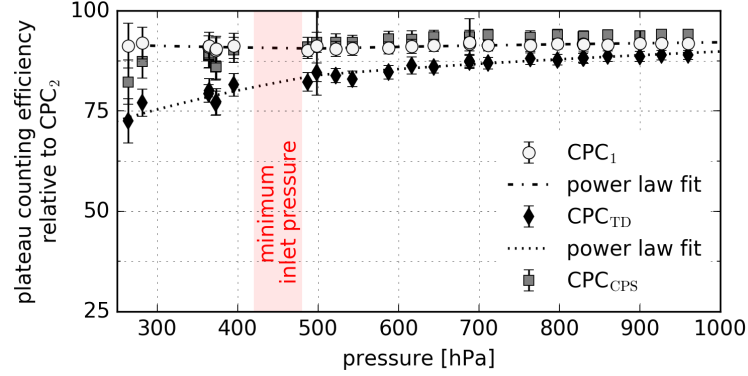


Figure 3.2.7: Pressure-dependent plateau counting efficiencies of the SALTRACE CPCs relative to CPC_2 , along with broken power law fits for CPC_1 and CPC_{TD} . Further indicated is the minimum inlet pressure range for the measurements presented in this study.

CPC	Q [cm^3s^{-1}]	Δt [s]	t_{res} [s]	T [K]	p
CPC_1 (TSI 3010)	16.15	3.5	0.40	306	p_{inlet}
CPC_2 (TSI 3760)	25.53	2.5	0.14	306	p_{inlet}
CPC_{TD} (CPSA 2)	16.17	6.5	0.65	306	p_{inlet}
CPC_{CPS} (CPSA 3)	17.40	7.5	0.85	306	p_{CPS}

CPC	thermophoretic loss correction	plateau counting efficiency correction $f_{corr,pcc}(p; a_0, b_0, a_1, b_1, b_p)$				
	$f_{corr,thermo} = \eta_{TD,thermo}^{-1}$	a_0	b_0	a_1	b_1	b_p
CPC_1 (TSI 3010)	1	7.785×10^{-1}	2.439×10^{-2}	9.921×10^{-1}	-1.466×10^{-2}	499.19
CPC_2 (TSI 3760)	1	1	0	-	-	0
CPC_{TD} (CPSA 2)	1.217	4.571×10^{-1}	9.782×10^{-2}	2.252×10^{-1}	2.118×10^{-1}	500.89
CPC_{CPS} (CPSA 3)	1	0.924	0	-	-	0

Table 3.2.3: List of parameters and corresponding values used to convert the raw CPC count rates into corrected (STP) particle number concentrations.

measurements in order to correct the individual output number concentrations for related biases. For this purpose, side-by-side measurements involving all CPCs were performed at defined pressure conditions using monodisperse aerosol samples with particle diameters $D \gg D_{50\%}$ and in a size range where differential tubing loss impacts can be neglected ($D \approx 200 - 300$ nm). Here, CPC₂ was used as a reference assuming a pressure-independent plateau counting efficiency of 100%, which is legitimized by the literature findings and laboratory comparisons with other instruments. Figure 3.2.7 presents the resulting relative plateau counting efficiencies for CPC₁, CPC_{TD} and CPC_{CPS} as a function of pressure. While for CPC₁ and CPC_{CPS} the counting efficiency is rather constant (though offset) down to the lowest pressure values relevant to this study, CPC_{TD} exhibits a decreasing trend with pressure reduction. To correct for pressure-dependent plateau counting efficiency deviations the measurements are fitted by means of broken power law functions

$$f_{corr,pce}(p) = \begin{cases} (a_0 p^{b_0})^{-1} & p \geq b_p \\ (a_1 p^{b_1})^{-1} & p < b_p \end{cases} \quad (3.2.5)$$

Table 3.2.3 features the associated coefficient values for each CPC and the pressure references for the SALTRACE setup, i.e. $p = p_{inlet}$ (inlet tubing pressure) for CPC₁, CPC₂ and CPC_{CPS} and $p = p_{CPS} \approx 500$ hPa (CPS pressure) for CPC_{CPS}. As CPC_{CPS} was operated at this fixed pressure value, only the corresponding constant value of $f_{corr,pce}$ is reported.

As discussed in Sect. 2.5, transport tubing losses may further lead to systematic biases in measured particle concentrations. For the SALTRACE setup, the differential tubing losses between CPC₁ and CPC₂ can certainly be neglected given the small difference in tubing transport times Δt listed in Tab. 3.2.3. Yet, the absolute transport losses could still shift the measured from the actual ambient particle concentrations. Moreover, for CPC_{TD} the tubing residence time is significantly longer than for CPC₁ and CPC₂, so that in addition to the thermophoretic losses in the TD, differential losses could potentially bias the corresponding concentrations n_r to lower values and, thereby, lead to a systematic overestimation of the total volatile fraction vf_{total} given by Eq. (3.2.4). To evaluate the magnitude of the systematic bias introduced by (differential) tubing losses, all NSDs derived in the scope of this work and pressure-dependent tubing transport efficiency functions calculated with the PLC were combined. According to the results of this sensitivity study, the maximum systematic error in the absolute particle concentrations and the total volatile fractions is below 5%. This is because tubing transport losses impact only the small and large particles but leave the intermediate size range mostly unaffected (cf. Sect. 2.5). This intermediate range, however, entails the majority of particles. Due to the small magnitude of the systematic error and the fact that a time step-wise correction of the (differential) tubing losses is hardly practicable, particularly because the NSD would be needed for each time step, the absolute particle concentrations and the total volatile fractions presented in this study are not corrected for tubing loss effects. The impact of particle transport losses on the particle concentrations determined by CPC_{CPS} is discussed in Sect. 3.2.2.3. The data timestamps of the CPCs and all other instruments used in this study are corrected for Δt to allow for time step-wise comparability.

An additional effect leading to a systematic underestimation of particle concentrations is counting coincidence. Coincident count events occur when two or more particles by chance pass through the volume of detection, called the sampling volume, at the same time. In such a situation the CPC is unable to resolve the individual scattering pulses and falsely detects one aggregate signal. The probability of coincident count events exponentially increases with particle number concentration. It further depends on the sample flow rate Q and the effective time a particle resides in the sampling area t_{res} , both being instrument-specific constants. Taking account of this probability, measured particle concentrations n given by Eq. (3.2.2) can be corrected for counting coincidence as follows

$$n^* = n \cdot f_{corr,coin}(n^*) = n \cdot \exp(n^*Qt_{res}) \quad (3.2.6)$$

where n^* is the corrected concentration. This equation can be solved by recursion. Although the correction for counting coincidence is applied to all SALTRACE data, it is irrelevant until $n \gtrsim 5000 - 10000 \text{ cm}^{-3}$ for the used CPCs, which is a value much larger than the average concentration met in this study (cf. Fig. 4.2.14).

Combining the correction formulae given by Eq. (3.2.5) and (3.2.6), the thermophoretic loss factor derived in Sect. 3.2.1.2, and the STP conversion factor defined by Eq. (2.3.6), the corrected concentrations n_{corr} and $n_{corr,STP}$ result from the coincidence-corrected concentrations n^* measured at pressure p and temperature T as

$$\begin{aligned} n_{corr} &= n^* \cdot f_{corr,pce}(p) \cdot f_{corr,thermo} \\ n_{corr,STP} &= n_{corr} \cdot f_{STP}(p, T) \end{aligned} \quad (3.2.7)$$

All correction parameters are summarized in Tab. 3.2.3. As the actual temperature T at the decisive point, i.e. each CPC's critical orifice, is not available, $T = 306 \text{ K}$ being the average Falcon in-cabin temperature during SALTRACE is assumed to be a representative value for all instruments. Propagating all individual uncertainty estimates for the parameters listed in Tab. 3.2.3, a realistic total accuracy of the presented particle concentrations (excluding the systematic bias adjunct to tubing transport losses) is assumed to be 5%, which is supported by the accuracy experienced during laboratory measurements.

3.2.2.2 Optical Particle Counters (OPCs)

Operating Principle

Like for CPCs, the basic principle underlying OPC measurements is the detection of scattered light. The difference is that, in addition to a simple counting of scattered light pulses, OPCs gain indirect particle size information. A particle passing through the OPC sampling volume illuminated by light, usually coming from a monochromatic laser, scatters part of this light away from its initial direction into a photosensitive detector. As discussed in Sect. 2.2, the detected irradiance (scattering signal amplitude voltage) is directly proportional to the particle scattering cross section (with respect to the detector's spatial coverage), which itself is a function of particle size. An OPC counts the scattering pulses and sorts them into different bins according to their amplitudes. Therefore, the resulting measurement data are histograms of scattering signal

amplitudes. Although it is common practice to express the voltage thresholds defining the OPC bins in terms of particle diameters in order to directly obtain a discrete particle NSD from such a histogram (cf. Sect. 2.3), this ultimately is an incorrect approach when the scattering cross section is a non-monotonic function of particle size (e.g. Szymanski and Liu, 1986; Szymanski et al., 2009; Walser et al., 2017). The actual mathematical problem of retrieving a particle NSD from an OPC count histogram is of inverse nature and is described by a set of so-called Fredholm integral equations of the first kind

$$n_i = \int_0^{\infty} \Upsilon_i(D) \frac{dn}{dD}(D) dD \quad (+\Delta n_i) \quad (3.2.8)$$

where n_i ($= N_i/Q$, with the count rate N_i and the volumetric sample flow Q) is the particle number concentration of OPC bin i , $\Upsilon_i(D)$ the corresponding kernel function giving the probability for each particle diameter D to be sorted into bin i , $\frac{dn}{dD}(D)$ the NSD, and Δn_i a potential systematic error term (Kandlikar and Ramachandran, 1999; Fiebig et al., 2005). As they link the measured set of bin concentrations $\{n_i\}$ with the desired information, i.e. the particle NSD, an accurate characterization of the kernel functions $\Upsilon_i(D)$ (including associated uncertainties) is crucial. Deriving the $\Upsilon_i(D)$ requires knowledge on the OPC bin threshold voltages, the instrument-specific relationship between signal peak voltage and particle scattering cross section, and the theoretical relationship between scattering cross section and particle size. When the OPC detection geometry, the incident light characteristics and the particle properties (e.g. refractive index) are known, the latter can be explicitly calculated as described in Sect. 2.2. The purpose of an OPC calibration is to determine the relationship between this theoretical particle scattering cross sections and measured signal amplitudes.

As described in detail in Walser et al. (2017), prevailing methods do not provide a satisfactory description of the $\Upsilon_i(D)$, both regarding their absolute shape and their uncertainty. A particular reason for this is the disregard of instrument-induced broadening of scattering signal spectra. To improve the accuracy of OPC-derived NSDs but principally to provide a basis for thorough NSD uncertainty estimates and their further propagation (e.g. for the derivation of aerosol hygroscopicity, see Sect. 3.3), within the scope of this study a new OPC data evaluation framework has been developed. Along with a more fundamental parametrization of the $\Upsilon_i(D)$, this framework comprises self-consistent ways to evaluate OPC calibration measurements and to retrieve particle NSDs. In the following, the OPC response model and the associated calibration evaluation method will be briefly explained. In Sect. 3.3 it will further be outlined how the framework is used to properly propagate all initial uncertainties underlying OPC measurements into realistic particle NSD uncertainties (and beyond). A more comprehensive discussion of the new method and its advantages over existing concepts is given in Walser et al. (2017).

New OPC Response Model and Calibration Evaluation

A spherical particle with diameter D and complex refractive index m has a defined scattering cross section $\tilde{C}_{scat,m}$ with respect to the incident light and OPC detection geometry (i.e. the solid angle range covered by the detector). For an ideal OPC, an ensemble of such particles passing through the sampling volume would engender a sharp

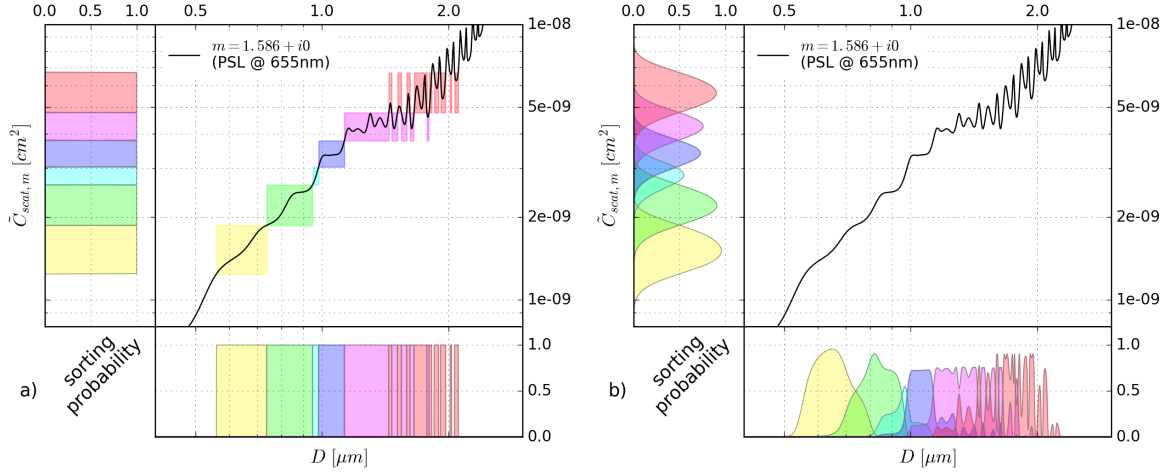


Figure 3.2.8: Exemplary subset of kernel functions for the Grimm SkyOPC for (a) an ideal case without instrument-induced broadening of scattering signal spectra and (b) a more realistic case where this broadening is modeled by a Gaussian distribution. The different OPC bins are visualized by the different colors. The theoretical scattering cross section $\tilde{C}_{scat,m}(D)$ for spherical particles with a refractive index $m = 1.586$ (PSL) is represented by the black curve.

distribution of signal peak voltages at U_m . Assuming a linear signal amplification in the detector, this single U_m is directly proportional to $\tilde{C}_{scat,m}$ with the linear coefficients for slope s and intercept c giving

$$U_m = \tilde{C}_{scat,m} \cdot s + c$$

According to this linear relationship, the OPC bin threshold voltages U_i can be directly expressed in terms of scattering cross sections and the OPC bin kernel functions are given by

$$\Upsilon_i(D) = \int_0^D \delta\left(\tilde{C}_{scat,m}(D') - \frac{U_i - c}{s}\right) - \delta\left(\tilde{C}_{scat,m}(D') - \frac{U_{i+1} - c}{s}\right) dD' \quad (3.2.9)$$

meaning that the probability for a particle of diameter D to be sorted in to bin i equals one if the corresponding scattering cross section $\tilde{C}_{scat,m}$ falls between $(U_i - c)/s$ and $(U_{i+1} - c)/s$, and is zero otherwise. Such kernel functions for an idealized OPC are illustrated in Fig. 3.2.8a).

As discussed in Sect. 2.2.3, for an ensemble of identical aspherical particles with a volume-equivalent diameter equal to D , varying orientations with respect to the incident light cause a scatter of the individual particle scattering cross sections around $\tilde{C}_{scat,m}$ and, thereby, lead to a widening of the beforehand sharp signal peak voltage distribution (orientation-induced signal broadening). For real OPCs, however, the broadening of signal spectra is not limited to aspherical particles. Particularly due to the non-uniformity of incident light irradiance in the sampling volume, even an ensemble of identical spherical particles (with constant $\tilde{C}_{scat,m}$) is associated with a blurred signal peak voltage distribution (instrument-specific signal broadening). Therefore, the

single value U_m must be substituted by a probability density function (PDF) for a set of possible $\{U_m\}$. In a first approach, this PDF can be assumed to be of Gaussian shape with a constant relative standard deviation b , which is equivalent to a replacement of the previously sharp scattering cross section values for the bin thresholds, i.e. the delta functions in Eq. (3.2.9), with Gaussian distributions exhibiting the same relative standard deviation b . Following this, an updated expression for the OPC kernel functions is given by

$$\Upsilon_i(D) = \frac{1}{\sqrt{2\pi}b} \int_0^D \frac{1}{U_i} \exp\left(-\frac{\left(\tilde{C}_{scat,m}(D') - \frac{U_i-c}{s}\right)^2}{2b^2U_i^2}\right) - \frac{1}{U_{i+1}} \exp\left(-\frac{\left(\tilde{C}_{scat,m}(D') - \frac{U_{i+1}-c}{s}\right)^2}{2b^2U_{i+1}^2}\right) dD' \quad (3.2.10)$$

with the extended parameter triplet (b, s, c) defining the instrument response. Figure 3.2.8b) shows an exemplary set of kernel functions satisfying Eq. (3.2.10). As can be seen, taking account of instrument-specific signal broadening the new OPC kernel functions overlap. Consequently, a particle of diameter D can be sorted into different bins and a direct diameter-to-bin assignment is not possible any more, even for spheres of known refractive index.

The extended parametrization not only allows for a realistic description of OPC response but also provides access to a more fundamental way to evaluate calibration measurements and, thereby, gain proper uncertainty estimates for the instrument parameters. OPC calibration measurements involve a set of particle standards with well-defined optical properties and NSDs. Prominent examples are monodisperse samples of PSL spheres or glass beads, both of spherical shape and familiar refractive index. Knowing the particle NSD and the optical properties (therewith $\tilde{C}_{scat,m}$), the OPC model response \hat{n}_{ij} (concentration in bin i) to such a particle standard sample j is given by Eq. (3.2.8) and (3.2.10). With the (real) measured response n_{ij} the task is to inversely find the instrument parameter values that bring \hat{n}_{ij} and n_{ij} into best agreement. For stable measurement conditions, i.e. constant sample flow etc., the uncertainties of the measured bin counts follow the Poisson counting statistics, so that with increasing number of counts (increasing sampling time), the relative uncertainty of the n_{ij} decreases with $N_{ij}^{-1/2} \propto n_{ij}^{-1/2}$. Naturally, the simplified model will not be able to reproduce the measurements perfectly, since there will be additional deviations that are not parametrized. Provided sufficiently high numbers of bin counts in the course of the sampling, the relative bin count uncertainties due to Poisson counting statistics will become negligible compared to these additional deviations. In consequence, bringing model and measurement into agreement corresponds to maximizing the probability for the \hat{n}_{ij} afflicted with unknown uncertainties σ_{ij} , that cover the additional model deviations, to occur given the measured n_{ij} . Both experimental findings and theoretical considerations (e.g. the effect of small fluctuations in light source intensity) justify expressing the remaining (time-dependent) model deviations by relative deviations of the true scattering cross section from the theoretical $\tilde{C}_{scat,m}$ (Walser et al., 2017). A relative scattering cross section shift corresponds to a multiplication of

$\tilde{C}_{scat,m}$ by a factor $\varepsilon \neq 1$ and leads to a modified model response $\hat{n}_{ij,\varepsilon}$ ⁵. Assuming the PDF for the shift factor ε to be a Gaussian distribution centered at 1 with a standard deviation of σ_ε allows to derive the associated PDFs for the $\hat{n}_{ij,\varepsilon}$, which can themselves be well-approximated by Gaussian distributions centered at the \hat{n}_{ij} with the standard deviations σ_{ij} given by

$$\sigma_{ij}^2 = \frac{1}{\sqrt{2\pi}\sigma_\varepsilon} \int_0^\infty (\hat{n}_{ij,\varepsilon} - \hat{n}_{ij})^2 \exp\left(-\frac{\varepsilon^2}{2\sigma_\varepsilon^2}\right) d\varepsilon \quad (3.2.11)$$

In summary, within the new framework the aim of the calibration evaluation is to obtain the set of OPC model parameters $(b, s, c, \sigma_\varepsilon)$ composed of the response parameter tuple (b, s, c) and the remaining relative uncertainty σ_ε of the (time-dependent) $\tilde{C}_{scat,m}$. A way to meet the challenge of model parameter probability maximization under initially unknown model uncertainties is to make use of Bayesian statistics and Markov chain Monte Carlo (MCMC) methods (e.g. Goodman and Weare, 2010). Following Bayes' theorem (Bayes and Price, 1763) the (posterior) probability P for a set of modeled $\{\hat{n}_{ij}\}$ to occur under a set of measured $\{n_{ij}\}$ can be expressed as

$$P(\{\hat{n}_{ij}\} | \{n_{ij}\}) \propto P(\{n_{ij}\} | \{\hat{n}_{ij}\}) \cdot P(b, s, c, \sigma_\varepsilon) \quad (3.2.12)$$

, i.e. the product of the likelihood function determining the probability of the $\{n_{ij}\}$ to occur given the $\{\hat{n}_{ij}\}$ and the so-called prior probability $P(b, s, c, \sigma_\varepsilon)$, including all prior knowledge on the model parameters, for instance from physical constraints or invariance considerations (e.g. Jaynes, 1968). Finding a perfect (uninformative) prior probability can be quite challenging. However, unless the prior probability exhibits a lot of variation in the parameter solution region, it often has a negligible impact on the posterior probability. This was tested and confirmed for the evaluation of the presented OPC calibrations, where different prior probability choices left the parameter solutions unaffected. For simplicity, the results presented in the following, therefore, correspond to flat prior probabilities, i.e. uniform prior parameter PDFs within physically reasonable limits⁶. The proportionality factor equating both sides of Eq. (3.2.12) can be thought of as a normalization constant, which has no impact on the posterior maximization process. With the assumption of Gaussian model bin count PDFs, defined by \hat{n}_{ij} and σ_{ij} , the likelihood function can be expressed as

$$P(\{n_{ij}\} | \{\hat{n}_{ij}\}) = \prod_{ij} \frac{1}{\sqrt{2\pi}\sigma_{ij}} \exp\left(-\frac{(n_{ij} - \hat{n}_{ij})^2}{2\sigma_{ij}^2}\right) \quad (3.2.13)$$

To obtain the posterior model parameter PDFs (solution ensembles), MCMC methods efficiently sample the parameter space to find the region of maximum probability according to Eq. (3.2.12). In this study the Python-based sampler tool *emcee* (Foreman-Mackey et al., 2013) is utilized for this purpose.

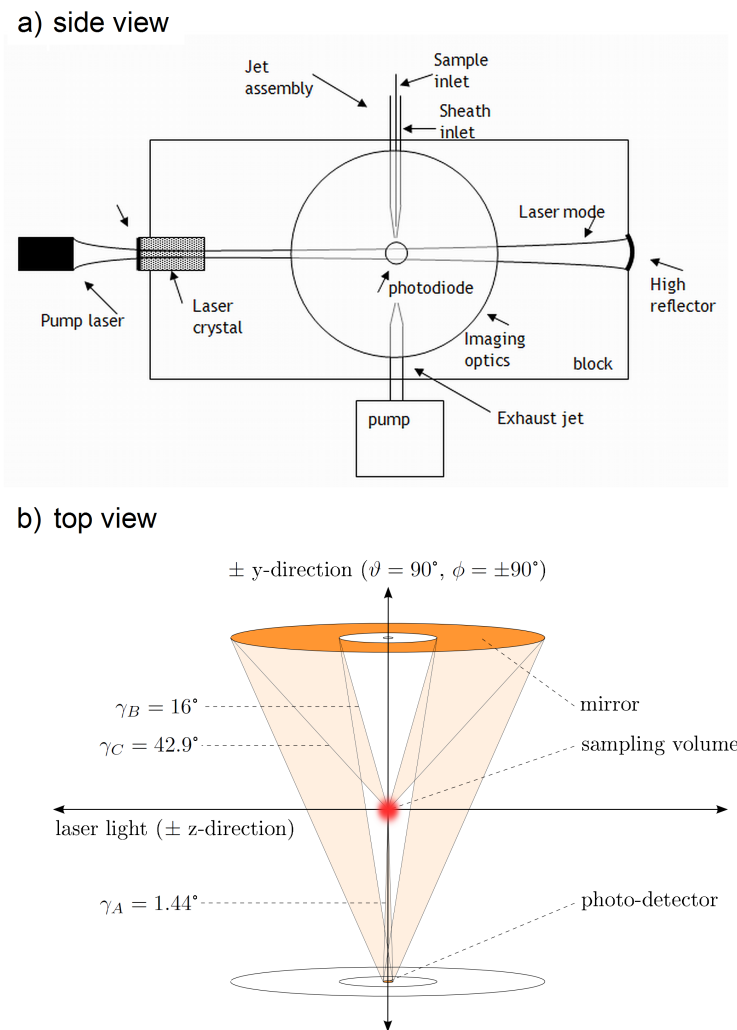


Figure 3.2.9: Schematic of the UHSAS optical block (a) and detailed view of the detection geometry for the scattered light (b). Graph (a) is adopted from the UHSAS manual.

Ultra High Sensitivity Aerosol Spectrometer (UHSAS)

The airborne version of the UHSAS (UHSAS-A) used in this study is an OPC commercially available from Droplet Measurement Technologies (DMT) (Cai et al., 2008; Schmidt, 2009; Brock et al., 2011). It is sensitive to particles with diameters ranging from approximately 0.06 to 1 μm and allows for the classification of corresponding scattering signals by means of 100 customizable bins. Here, only the diameter range of about 80 to 300 nm is utilized with an approximately linear diameter-binning. The reason for discounting the size range $D \gtrsim 300$ nm is that here systematic deviations between the theoretical and measured instrument response could be identified (Schmidt, 2009), presumably linked to a non-linear signal amplification. The UHSAS is mounted in an under-wing pod of the Falcon and is equipped with its own forward facing diffusor inlet (see Fig. 3.1.1). With the aid of this diffusor inlet the ambient aerosol, that has an initial relative velocity to the instrument approximately corresponding to the aircraft speed, is slowed down. The slowed flow is then sub-sampled by a second inlet at (near-)isokinetic conditions. Potential sampling efficiency biases owing to slight deviations from isokinetic sampling are neglected as they hardly affect the particles in the UHSAS size range, especially in the chosen sub-range (cf. Sect. 2.5). As shown in Fig. 3.2.9, subsequent to its extraction the sample is guided into an optical block, where it is aerodynamically focused by means of a sheath air flow to pass the inner OPC sampling volume. Temperature and pressure inside the optical block, and the volumetric sample flow rate are monitored allowing to convert the measured particle count rates into particle (STP) concentrations (for each bin). As for the CPCs, the accuracy for these concentrations is estimated as 5%. The instrument's plateau counting efficiency is assumed to be unity, since the focused particle beam passes the inner sampling volume and, consequently, all particles within the size detection limits induce measurable scattering pulses. This assumption is confirmed by laboratory comparison measurements with CPCs. The drop in counting efficiency to the upper and lower limit of the selected size range results directly from the new OPC response model introduced in the previous paragraph and the UHSAS specifics (scattering geometry and calibration results) discussed below. Particle concentrations of up to 3000 cm^{-3} , a value much larger than the presented concentrations, are recorded without significant counting coincidence losses (Cai et al., 2008). The light source of the UHSAS is a semiconductor-diode-pumped Nd³⁺:YLF solid-state laser with an infrared wavelength of $\lambda = 1054$ nm. The laser light is linearly polarized with the electric field vector parallel to the flow of particles, i.e. in direction of the x-axis with respect to the geometry definitions of Fig. 2.2.1. As shown in Fig. 3.2.9, the solid angle range in which the scattered light is collected is centered in a direction perpendicular to both the direction of the particle flow (x-direction) and the direction of the incident light (z-direction), i.e. in y-direction at a scattering angle of $\vartheta = 90^\circ$ (sideways scattering) and an azimuth angle of $\phi = \pm 90^\circ$. The integral scattering cross section \tilde{C}_{scat} for the collection of light

⁵The $\hat{n}_{ij,\varepsilon}$ are, hence, given by Eq. (3.2.8) and (3.2.10), replacing $\tilde{C}_{scat,m}(D)$ in the latter equation by $\varepsilon \cdot \tilde{C}_{scat,m}(D)$.

⁶Here, "reasonable" for instance connotes a non-negative slope s , non-negative resulting scattering cross section values at the bin thresholds etc.

scattered into a spacial cone with a half-opening angle γ can be expressed as

$$\tilde{C}_{scat} = \int_{\vartheta=0}^{\pi} \int_{\phi=0}^{2\pi} w_{detect}(\vartheta, \phi, \gamma) \frac{dC_{scat}}{d\Omega} \sin \vartheta d\vartheta d\phi \quad (3.2.14)$$

with the differential scattering cross section $dC_{scat}/d\Omega$ given by Eq. (2.2.8). The function $w_{detect}(\vartheta, \phi, \gamma)$ defines the angular weighting, i.e. the angular-dependent detection efficiency. Assuming that all light scattered into the cone is detected ($w_{detect} = 1$) and the residual light is completely blocked ($w_{detect} = 0$), w_{detect} can be derived by simple trigonometry. Following the geometry definitions of Fig. 2.2.1, the solid angle range covered by a cone with the half-opening angle γ centered at $\vartheta = 90^\circ$ and $\phi = 90^\circ$ can be defined by

$$x^2 + z^2 \leq (y \tan \gamma)^2$$

which, by transformation of coordinates

$$\begin{aligned} x &= r \sin \vartheta \cos \phi \\ y &= r \sin \vartheta \sin \phi \\ z &= r \cos \vartheta \end{aligned}$$

yields

$$w_{detect}(\vartheta, \phi, \gamma) = \begin{cases} 1 & \text{for } (1 + \tan^2 \gamma) \sin^2 \vartheta \sin^2 \phi \geq 1 \\ & \text{and } \phi \leq \pi \\ 0 & \text{otherwise} \end{cases} \quad (3.2.15)$$

The exact angular detection range for the UHSAS is given in Fig. 3.2.9b) (cf. Schmidt, 2009). Accordingly, light that is scattered into a cone centered at $\vartheta = 90^\circ$ and $\phi = 90^\circ$ with $\gamma_A = 1.44^\circ$ is directly collected by a photo detector. Additionally, light scattered into the opposite direction ($\phi = -90^\circ$) is collected by a Mangin mirror in the overlap range of two cones with $\gamma_B = 16^\circ$ and $\gamma_C = 42.9^\circ$. Using Eq. (3.2.15), the resulting total angular-dependent detection efficiency for the UHSAS $w_{detect, \text{UHSAS}}$ is given by

$$w_{detect, \text{UHSAS}}(\vartheta, \phi, \gamma) = \begin{cases} 1 & \text{for } (1 + \tan^2 \gamma_A) \sin^2 \vartheta \sin^2 \phi \geq 1 \\ & \text{and } \phi \leq \pi \\ 1 & \text{for } (1 + \tan^2 \gamma_C) \sin^2 \vartheta \sin^2 \phi \geq 1 \\ & \text{and } (1 + \tan^2 \gamma_B) \sin^2 \vartheta \sin^2 \phi < 1 \\ & \text{and } \phi > \pi \\ 0 & \text{otherwise} \end{cases} \quad (3.2.16)$$

Within the optical block the laser light is reflected, so that it incides on the particles from both + and -z-direction, meaning that the total \tilde{C}_{scat} is composed of the overlap of the single \tilde{C}_{scat} given by Eq. (3.2.14) and (3.2.16) and the corresponding solution for a particle mirrored at the x-y plane⁷. Considering this, Eq. (3.2.14) and (3.2.16) allow to calculate the theoretical response of the UHSAS for any particle of

⁷For spherical particles this simply entails a factor of 2 for \tilde{C}_{scat} .

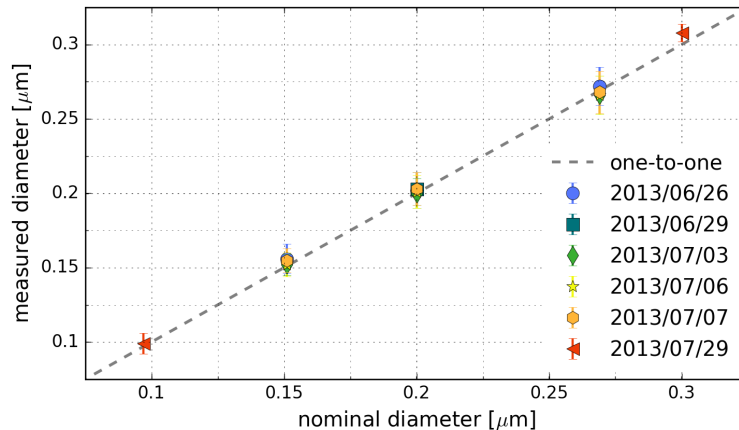


Figure 3.2.10: UHSAS sizing stability tests during SALTRACE. The nominal diameters of PSL standard samples are compared with the mean diameters and their standard deviations measured by the calibrated UHSAS. The different colors represent the different measurement dates. In addition to the measured data, the one-to-one relationship is shown by the dashed line.

given properties, i.e. size, refractive index, shape and orientation. With an implementation of the widely used *bhmie* algorithm (Bohren and Huffman, 1983), providing the solutions to Eq. (2.2.9), these formulae were utilized to calculate a family of instrument-specific $\tilde{C}_{scat,m}(D)$ functions for spherical particles and a range of refractive indices. As legitimized in Sect. 2.2.3, aspherical particles are assumed to follow the $\tilde{C}_{scat,m}(D)$ functions for the volume-equivalent spherical particles on average. The additional orientation-induced broadening of OPC scattering signal spectra for aspherical particles is obtained from DDA calculations (performed by J. Gasteiger⁸, LMU). For the sake of completeness, it should be mentioned that Eq. (3.2.16) might not be entirely accurate, as the UHSAS aerodynamic focusing nozzle might lead to partial shading effects (Schmidt, 2009) and the reflectance of the mirror might deviate from unity. However, the agreement between theoretical and measured UHSAS response for a number of particles with defined sizes and different refractive indices within the scope of this study and in Schmidt (2009) prove the above detection geometry assumptions to be sufficiently good (at least for the chosen particle size sub-range).

During SALTRACE, OPC calibration measurements utilizing PSL spheres were performed on a regular basis, both to allow for a precise bin size assignment for the data evaluation and to monitor (and eventually correct) potential sizing drifts with time, e.g. due to a pollution of optical elements. Figure 3.2.10 demonstrates that such sizing drifts were not observed for the chosen size range, but that the UHSAS response to the particle standards was stable throughout the campaign. For this reason, the UHSAS bin settings were not re-configured and the single set of threshold values given in Tab. A.1.1 applies to the complete campaign period. The threshold values are stored as (apparent) bin diameters in the UHSAS data file headers. In order to apply the beforehand presented calibration evaluation method and obtain the UHSAS response model parameter PDFs, these diameter threshold values were first back-converted into

⁸J. Gasteiger now at: UNIVIE

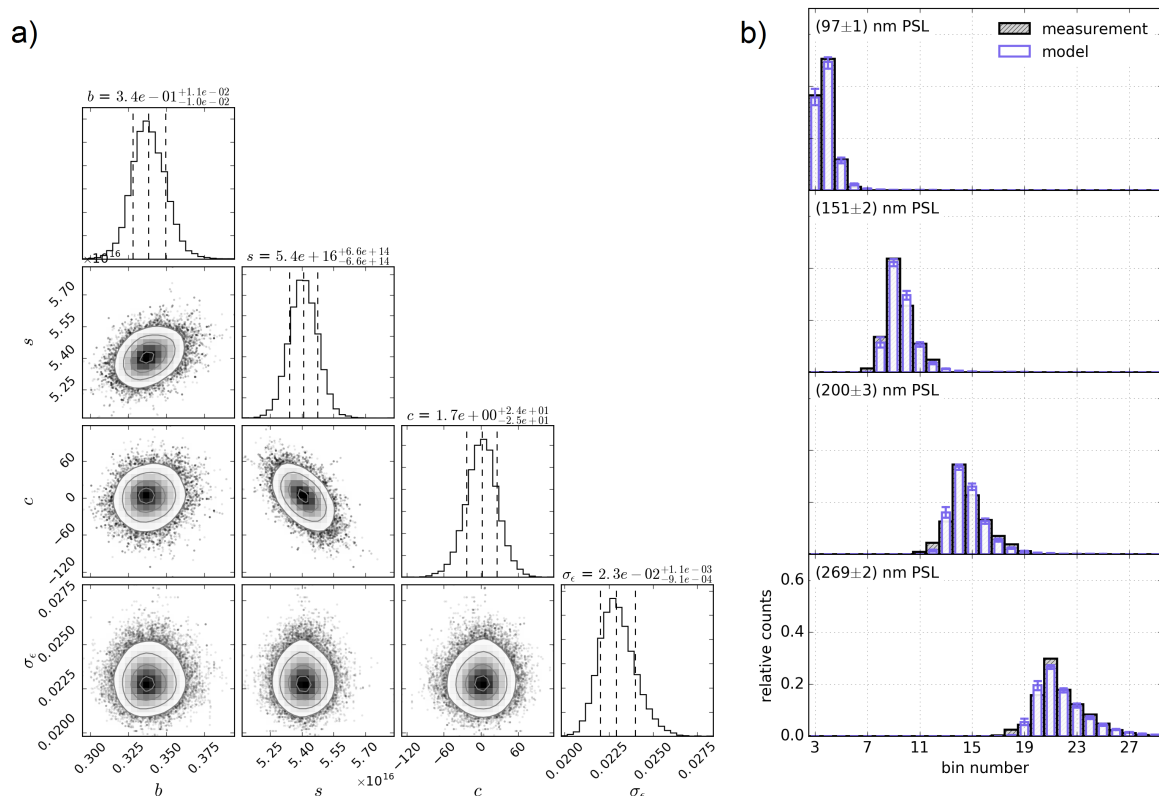


Figure 3.2.11: Results for the UHSAS calibrations during SALTRACE. Plot (a) shows the OPC response model parameter PDFs obtained from the novel MCMC-based calibration evaluation method. The parameter units are $[s] = \text{mV}/\text{cm}^2$ and $[c] = \text{mV}$ (in UHSAS high gain stage equivalent voltages, cf. Sect. A.1.1). The parameters b and σ_ϵ are unitless. The dashed lines in the 1D parameter histograms in plot (a) represent the median, 16 and 84th percentiles. The median values and their distances to the percentiles are additionally noted on top of each histogram. The 2D plots show the solution scatter superposed with 2D histograms and smoothed Gaussian contours at 0.5, 1., 1.5 and 2 sigma. Plot (b) compares the modeled and measured (relative) UHSAS count histograms for the used particle standards. The colored histogram bars represent the modeled bin count medians, the error bars the range between the 16 and 84th percentiles. The mean and standard deviation defining each particle standard's Gaussian NSD are noted in the upper left box corners.

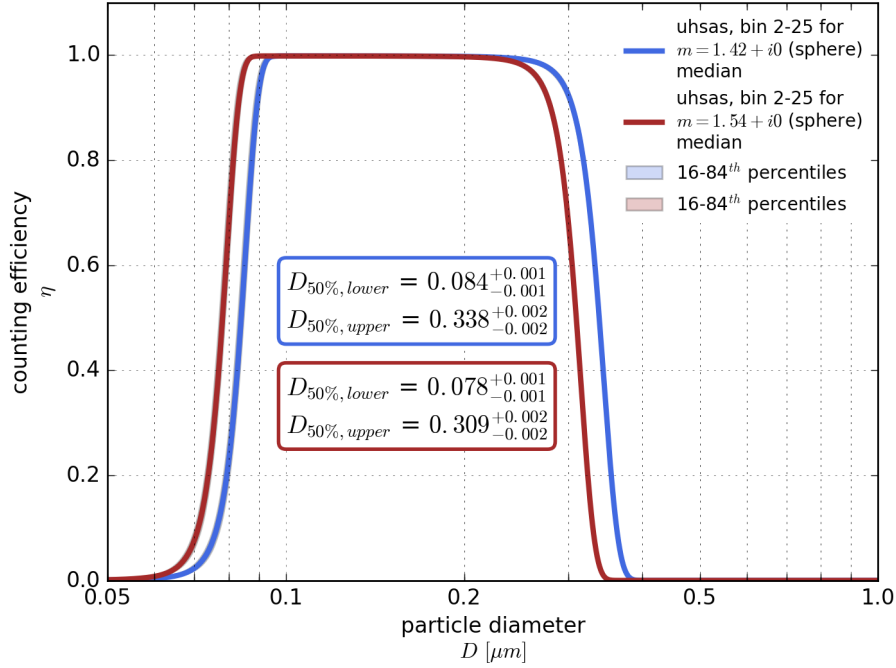


Figure 3.2.12: Collective counting efficiency for the chosen UHSAS size range. The blue and red curves represent spherical particles with (non-absorbing) refractive indices of $m = 1.42$ and $m = 1.54$, respectively.

their actual quantity, i.e. scattering signal peak voltages, as described in Sect. A.1.1. The $\tilde{C}_{scat,m}(D)$ function for the calibration material is calculated from the scattering geometry defined above and the known refractive index of PSL at the UHSAS laser wavelength $m_{\text{PSL},1054\text{nm}} = 1.572 + i0$ (Ma et al., 2003; Sultanova et al., 2009). Figure 3.2.11a) shows the final PDFs for the response model parameters resulting from the evaluation of the collective SALTRACE calibration measurements. In combination with Eq. (3.2.8) and (3.2.10), this parameter solution ensemble provides the basis for the particle NSD retrieval outlined in Sect. 3.3.2. Figure 3.2.11b) demonstrates the accurateness of the new OPC response model by confronting one set of measured PSL calibration histograms with their modeled counterparts.

Besides feeding into the particle NSD retrieval, the UHSAS measurements are presented in the form of an integral particle concentration. This integral concentration (for the selected UHSAS size sub-range) is hereafter referred to as the accumulation mode particle concentration n_{acc} . Figure 3.2.12 depicts the corresponding size-dependent counting efficiency $\eta(D)$ for two exemplary refractive indices. $\eta(D)$ results from the presented OPC response model as

$$\eta(D) = \sum_i \Upsilon_i(D) \quad (3.2.17)$$

with the UHSAS kernel functions Υ_i given by Eq. (3.2.10) and quantified by the parameter PDFs shown in Fig. 3.2.11a). The validity of the counting efficiency resulting from the new OPC response model is demonstrated in Walser et al. (2017).

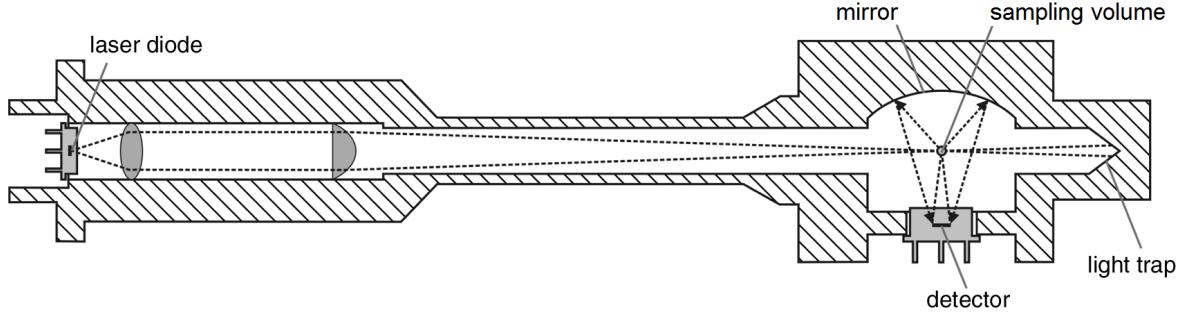


Figure 3.2.13: Schematic of the SkyOPC optical block. The light scattered by particles passing through the sampling volume (in a direction perpendicular to the drawing plane) is collected under a mean scattering angle of $\vartheta = 90^\circ$ by means of a photo detector and an additional opposite parabolic mirror focusing on the detector. Adopted from Bundke et al. (2015).

SkyOPCs

Similar to the UHSAS, the Grimm model 1.129 SkyOPC is a commercially available OPC using a wide-angle light collecting geometry in sideways direction (Bundke et al., 2015). During SALTRACE, both deployed SkyOPCs (cf. Fig. 3.2.1) were operated in “fast mode” (1Hz sampling frequency) covering a nominal diameter range of 0.25 to about $3 \mu\text{m}$ with the associated signal amplitude range separated into 16 predefined bins. Details about the bin threshold definitions can be found in Sect. A.1.2 and Tab. A.1.2. The SkyOPCs were operated inside the aircraft cabin behind the Falcon aerosol inlet, one measuring the total aerosol (hereafter simply named SkyOPC) and the other one the refractory (non-volatile) particles only (SkyOPC_{TD}). As illustrated in Fig. 3.2.13, light emitted by a class 3B laser diode at 655 nm and scattered by the particles (that are aerodynamically focused to the inner sampling volume) is collected directly by a photodiode within a half-opening angle of $\gamma_d = 9^\circ$ around a mean scattering angle of $\vartheta = 90^\circ$, and indirectly by an additional opposite mirror that is defined by $\gamma_m = 60^\circ$. In the same way as for the UHSAS, from these values the angular-dependent detection efficiency for the SkyOPC $w_{detect, \text{SkyOPC}}$ is derived to

$$w_{detect, \text{SkyOPC}}(\vartheta, \phi, \gamma) = \begin{cases} 1 & \text{for } (1 + \tan^2 \gamma_d) \sin^2 \vartheta \sin^2 \phi \geq 1 \\ & \text{and } \phi \leq \pi \\ 1 & \text{for } (1 + \tan^2 \gamma_m) \sin^2 \vartheta \sin^2 \phi \geq 1 \\ & \text{and } \phi > \pi \\ 0 & \text{otherwise} \end{cases} \quad (3.2.18)$$

As explained in the previous paragraph, in combination with Eq. (3.2.14) this function allows to calculate the SkyOPC-specific scattering cross sections $\tilde{C}_{scat}(D)$ for given particle properties. In contrast to the UHSAS, in the SkyOPC light incides on the particles from one direction only, as the unscattered light is not reflected but absorbed in a light trap. As before, it should be mentioned that Eq. (3.2.18) is only an approximation to the true SkyOPC detection efficiency (being unavailable) and slight deviations from the simple cone collection assumption may exist. Yet, Heim et al. (2008) and Walser et al.

(2017) demonstrate that the $\tilde{C}_{scat}(D)$ functions calculated with the above detection geometry are consistent with measurements for different particle materials.

Like for the UHSAS, both SkyOPCs were calibrated utilizing PSL particle standards of defined diameters. With $\tilde{C}_{scat}(D)$ calculated for the refractive index of PSL $m_{\text{PSL},655\text{nm}} = 1.586 + i0$ (Ma et al., 2003; Sultanova et al., 2009), these calibration measurements are evaluated to obtain the response model parameter PDFs for the SkyOPC and the SkyOPC_{TD}. The complete parameter PDFs are shown in Fig. A.1.1 and A.1.2. Figure 3.2.14 compares the resulting model histograms with the ones measured for the used particle standards. Besides the adequacy of the OPC response model, this figure reveals significant differences between the responses of SkyOPC and SkyOPC_{TD}, although they are supposed to be identical instruments. This demonstrates the necessity of the presented thorough response model and calibration evaluation method.

As with the CPCs, the volumetric sample flow rates Q are held constant by means of critical orifices and are measured as 15.67 and 17.67 cm³s⁻¹ for the SkyOPC and SkyOPC_{TD}, respectively. For the orifice upstream pressure p and temperature T it is assumed that $p = p_{inlet}$ and $T = 306$ K (cf. Sect. 3.2.2.1). Again, the accuracy of the resulting (STP) bin concentrations is estimated as 5%. Counting coincidence losses are insignificant for particle concentrations of up to 500 – 1000 cm⁻³ (Heim et al., 2008) and are, hence, neglected for the presented data. The tubing transport times Δt to the instruments are determined as 3.5 and 7.5 s for the SkyOPC and SkyOPC_{TD}, respectively. Whereas diffusional transport losses can certainly be neglected for the size range in question, sedimentational and inertial losses could potentially involve systematic measurement biases for the large particles. For one thing, the latter losses could lead to an underestimation of particle NSD values (derived from the SkyOPC data) at large particle diameters. For another thing, differential losses between SkyOPC and SkyOPC_{TD} could lead to an overestimation of the volatility of large particles calculated via Eq. (2.4.2). While inertial particle losses in the TD are insignificant, as discussed in Sect. 3.2.1, sedimentational tubing losses may indeed be present. To estimate the magnitude of the corresponding systematic error, PLC calculations for pure mineral dust particles (density $\rho_p = 2.5$ g/cm³ and shape factor 1.2, see Kaaden et al. (2009)) were conducted resulting in a maximum loss⁹ of $\lesssim 5\%$ for particles with $D \leq 1$ μm and $\lesssim 20\%$ for $D \approx 2$ μm . The insignificance of losses for $D \leq 1$ μm is confirmed by NSD comparisons between the in-cabin SkyOPC and the loss-unaffected wing-mounted open path spectrometer CAS (see Sect. 3.2.3.1) during SALTRACE (Weinzierl et al., 2017). For the size-resolved volatility measurements (see Sect. 3.3.3), the presented results are confined to the size range $D < 1$ μm . For the presented particle NSDs, the systematic underestimation for $D > 1 - 2$ μm owing to sedimentational tubing losses and the Falcon aerosol inlet sampling efficiency cutoff needs to be kept in mind.

In addition to the usage of the SkyOPC bin concentrations for the NSD retrieval, and the usage of the combined SkyOPC and SkyOPC_{TD} data for the assessment of size-dependent aerosol volatility, the integral SkyOPC concentration is presented as n_{large} . For the same reasons as outlined for the UHSAS, the SkyOPC plateau efficiency is assumed to be unity, meaning that the kernel functions given by Eq. (3.2.10) completely describe the single and collective bin counting efficiencies, with the latter determined by

⁹Absolute particle loss for the SkyOPC and differential particle loss between SkyOPC_{TD} and SkyOPC.

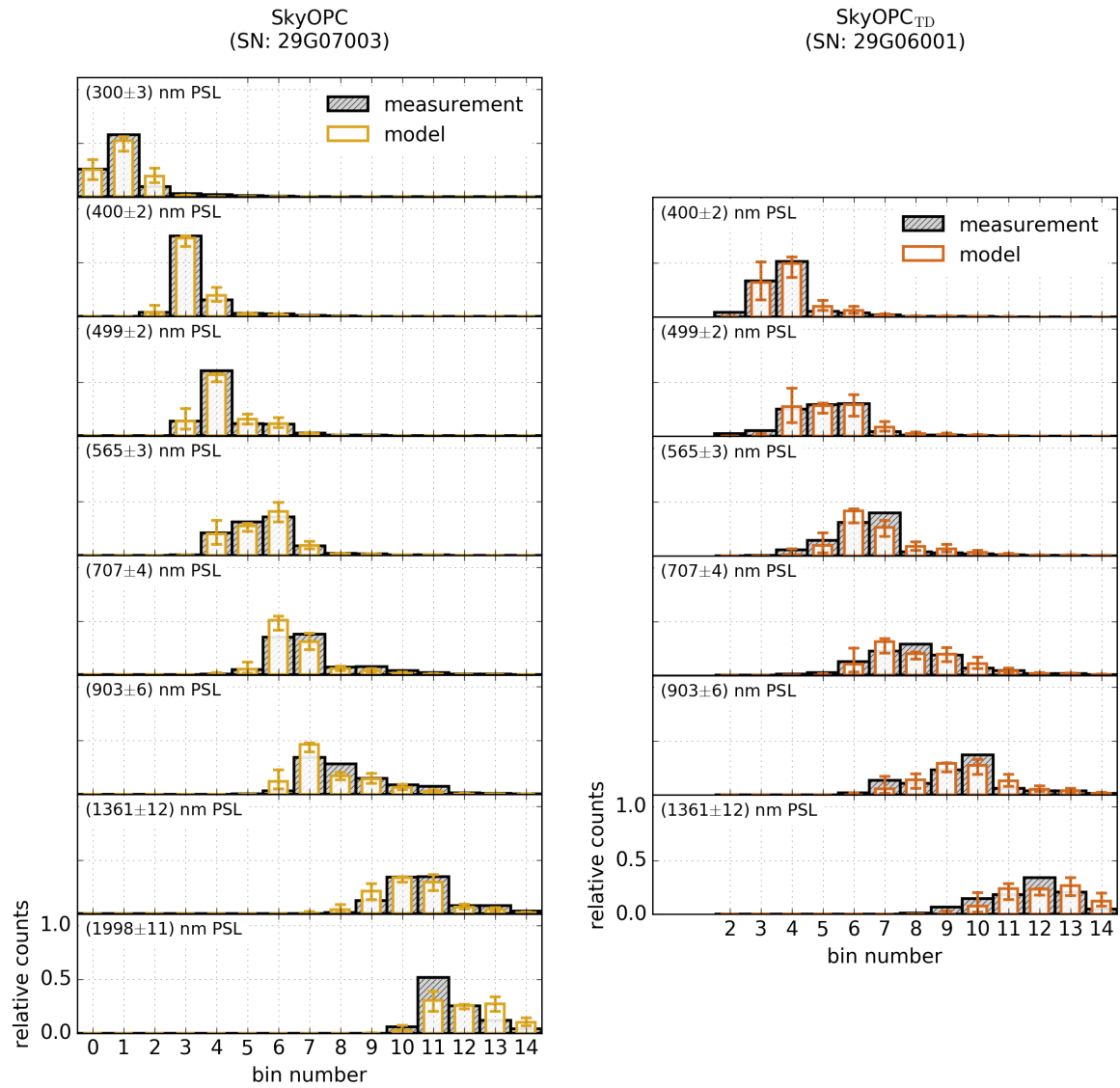


Figure 3.2.14: Comparison of measured and modeled (relative) count histograms for the SkyOPC and the SkyOPC_{TD} and the used PSL particle standards, presented in the same way as in Fig. 3.2.11b).

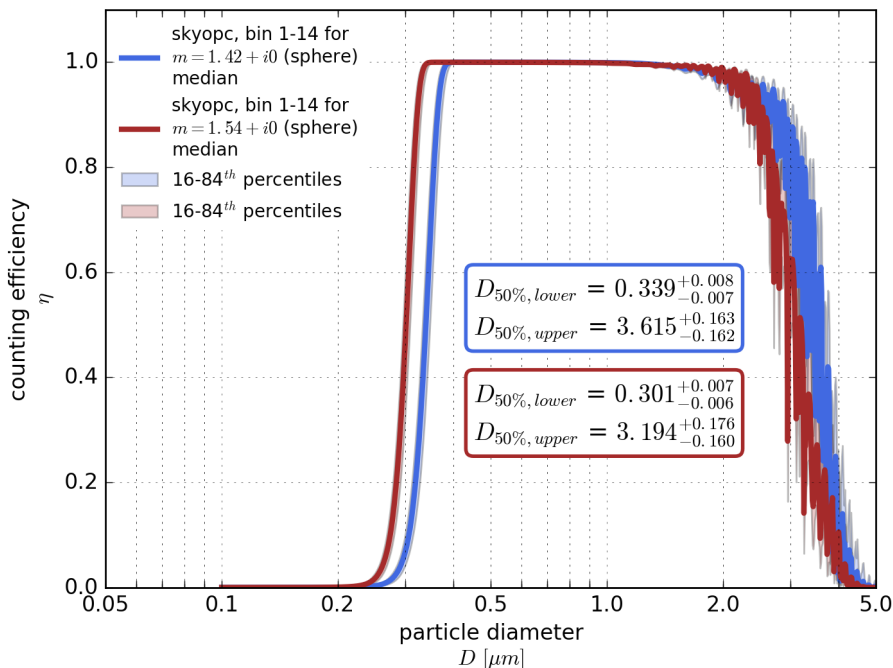


Figure 3.2.15: Collective counting efficiency for the chosen SkyOPC size range (bin 1-14). The blue and red curves represent spherical particles with (real) refractive indices of $m = 1.42$ and $m = 1.54$, respectively.

Eq. (3.2.17). Figure 3.2.15 shows this collective SkyOPC counting efficiency for the two refractive indices used before in Fig. 3.2.12. It is apparent that the collective counting efficiencies of the UHSAS (sub-range) and the SkyOPC blend into each other almost seamlessly (also cf. Fig. 3.3.2). Therefore, the integral particle number concentration for the combined UHSAS and SkyOPC size ranges is approximated by $n_{80} = n_{acc} + n_{large}$.

3.2.2.3 Cloud Condensation Nuclei Counter (CCNC)

Operating Principle

The (DMT) CCNC is an instrument that allows to study aerosol particle droplet activation at defined water vapor supersaturations (Roberts and Nenes, 2005; Lance et al., 2006). As illustrated in Fig. 3.2.16, the aerosol sample enters the cylindrical setup at the center axis confined by a laminar sheath flow layer. The inner CCNC column walls are wetted by a water film connoting water vapor saturation ($SS = 0$) in the direct vicinity of the wall. The temperature at the wall, controlled at the column top (T_1), center (T_2) and bottom (T_3), gradually increases along the sample flow direction ($T_1 < T_2 < T_3$). Together with this increase in wall temperature, the absolute humidity over the water film rises. Since the diffusivity of water vapor exceeds the diffusivity of heat, approaching the centerline an initially saturated vapor originating from a warmer starting point at the wall so to speak “meets” a lower temperature leading to a vapor supersaturation ($SS > 0$). With the thermal gradient ΔT being (approximately) linear, Roberts and Nenes (2005) demonstrate that the centerline SS becomes quasi-

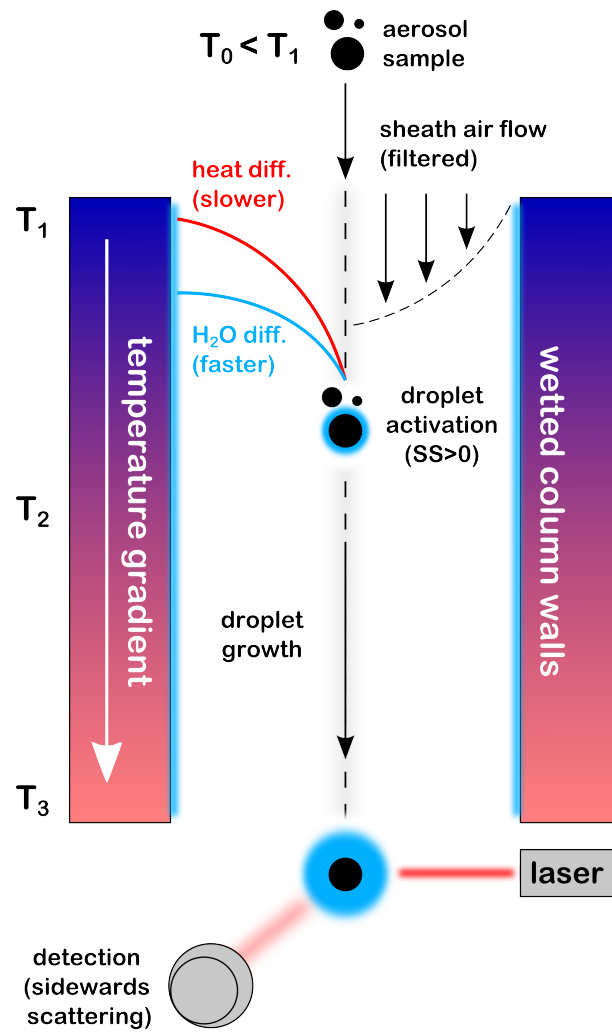


Figure 3.2.16: Operating principle of a (cylindrical) CCNC.

uniform after a certain initial distance. As discussed in detail in Sect. 2.1, when the aerosol sample is exposed the resulting (constant) SS , depending on their individual size and hygroscopicity a subset of the particles in this sample will activate into water droplets. This activation takes place in the upper part of the column at an absolute (activation) temperature of about $T_{act} = (T_2 + T_1) / 2$, where the SS approaches its plateau value (Kristensen et al., 2016). Once activated, the droplets further grow by water uptake in the subsequent part of the column. The grown droplets leaving the column are counted by means of an OPC operating at a wavelength of 660 nm and collecting the scattering pulses in sideways direction. As the sampling volume is chosen large enough to guarantee detection of all activated droplets, and because sample flow, pressure and sample temperature are monitored, the count rate of activated particles can directly be converted into a CCN (STP) number concentration n_{CCN} at the given SS . As for the other instruments, the accuracy of this concentration is estimated to be 5%.

SALTRACE Settings

The CCNC used in this study consists of two parallel individual columns, each having a nominal supersaturation range of $0.07 \leq SS \leq 2\%$. Here, only a sub-range of $0.1 \lesssim SS \lesssim 0.3\%$ is utilized with the main SS chosen as 0.2%, which is found to be a typical value for (Caribbean) trade wind cumuli (Wex et al., 2016). While one of the columns (B) was operated at this fixed main SS value, the other column (A) was run in scanning mode, i.e. changing its SS in a stepwise pattern holding each SS setting for about 5 – 10 min.

As the CCNC OPC sorts the scattering signal peaks into 20 predefined bins, it allows the user to choose the (size) threshold classifying the counts into droplets and non-activated particles. Choosing this threshold too high implies a dismissing of droplets and, thereby, an underestimation of n_{CCN} , whereas a too low threshold could lead to an overestimation of n_{CCN} owing to an additional counting of non-activated particles. Here, the CCNC default threshold value is used, which corresponds to droplet sizes of $D \gtrsim 750$ nm. This value is sufficiently low to capture all activated particles, that typically grow to supermicron sizes. Still, it is legit to wonder if large non-activated particles may lead to a systematic n_{CCN} bias at this threshold. By means of Eq. (2.1.9) it can be tested what hygroscopicities would be necessary for such an erroneous droplet-classification of large non-activated particles. Accordingly, for the above SS sub-range and an activation temperature of $T_{act} \approx 300$ K the hygroscopicity parameter would have to be $\kappa \lesssim 0.003$, which is a value far lower than what is found for African dust ($\kappa \geq 0.02$) in laboratory measurements (Koehler et al., 2009; Herich et al., 2009; Kumar et al., 2011b). For the main SS of 0.2% and a hygroscopicity of $\kappa = 0.02$ (estimated low end of the potential κ range relevant to this study) the maximum diameter for non-activated particles is $D \approx 250$ nm, which is already far from the chosen threshold. This means that for a realistic range of particle hygroscopicities all particles large enough to be erroneously classified as droplets indeed will activate into droplets before. Therefore, no systematic over- or underestimation of n_{CCN} is expected from the chosen droplet classification threshold.

Calibration

As explained above, the CCNC supersaturation is controlled via the vertical thermal gradient ΔT at its column walls. In order to obtain the $SS(\Delta T)$ relationship the CCNC needs to be calibrated. The calibration measurements and their evaluation are performed as suggested in Rose et al. (2008). For a constant ΔT setting, a DMA is utilized to select a set of particle diameters of defined hygroscopic properties — here, ammonium sulfate particles with $\kappa = 0.61$ (Petters and Kreidenweis, 2007) — that are measured in parallel by the CCNC to obtain n_{CCN} and a reference CPC yielding the total particle number concentration n . Figure 3.2.17a) shows the resulting sigmoidal behavior of the size-dependent activated fraction n_{CCN}/n for a calibration measurement during SALTRACE. Here, the thermal gradient, defined as $\Delta T := 2 \cdot (T_2 - T_1)$, is $\Delta T \approx 8$ K. The sigmoidal activation curve is fitted to determine the activation diameter D_{act} (fit function inflection point), i.e. the dry particle diameter for which the CCNC supersaturation is critical (cf. Sect. 2.1). This critical supersaturation corresponding to D_{act} can be calculated theoretically via Eq. (2.1.9), knowing the hygroscopicity parameter κ and the absolute activation temperature T_{act} that determines the water density ρ_w and surface tension σ (Cini et al., 1972). Repeating this procedure for a range of ΔT one finally yields a set of $(SS, \Delta T)$ pairs, as shown in Fig. 3.2.17b) for the entirety of the SALTRACE calibrations for CCNC column B. From these pairs, the linear parameters defining the $SS(\Delta T)$ relationship are derived along with their corresponding (correlated) uncertainties. For the in situ measurements, this relationship then allows to convert the CCNC ΔT readings to the prevailing column supersaturations. The calibration results for the scanning CCNC column A are shown in Fig. A.2.1.

Although ΔT is the controlling parameter, the CCNC supersaturation further depends on the internal column pressure p , because this pressure impacts the heat diffusion velocity. With a decreasing p a reduction in heat diffusivity leads to an increase in SS given a constant ΔT (e.g. Rose et al., 2008). This problem can be solved either by including the pressure-dependence explicitly in the calibration, which is vastly time-consuming and increases the SS uncertainty, or the CCNC can be operated at a fixed p . The latter method is applied for the presented airborne setup, where the CCNC pressure is held constant at $p_{\text{CPS}} \approx 500$ hPa, as illustrated in Fig. 3.2.1 and further outlined in the following paragraph. The beforehand presented calibration results correspond to this pressure value. Rose et al. (2008) further investigated the dependence of SS on the absolute temperature and found a slight decrease of the SS with increasing T_1 . However, this trend is not entirely conclusive in view of their reported SS scatter (low coefficient of determination), wherefore the presented supersaturations are not corrected for an eventual T_1 -dependence. Anyway, the T_1 variations for the in situ data are covered by the T_1 variations met during the calibration measurements, connoting that a potential corresponding (minor) systematic SS bias should be included in the SS calibration uncertainty.

Concentration Correction

The CCNC (plateau) counting efficiency is assumed to be unity for the activation diameter range relevant to this study, which is supported both by the CCNC calibration

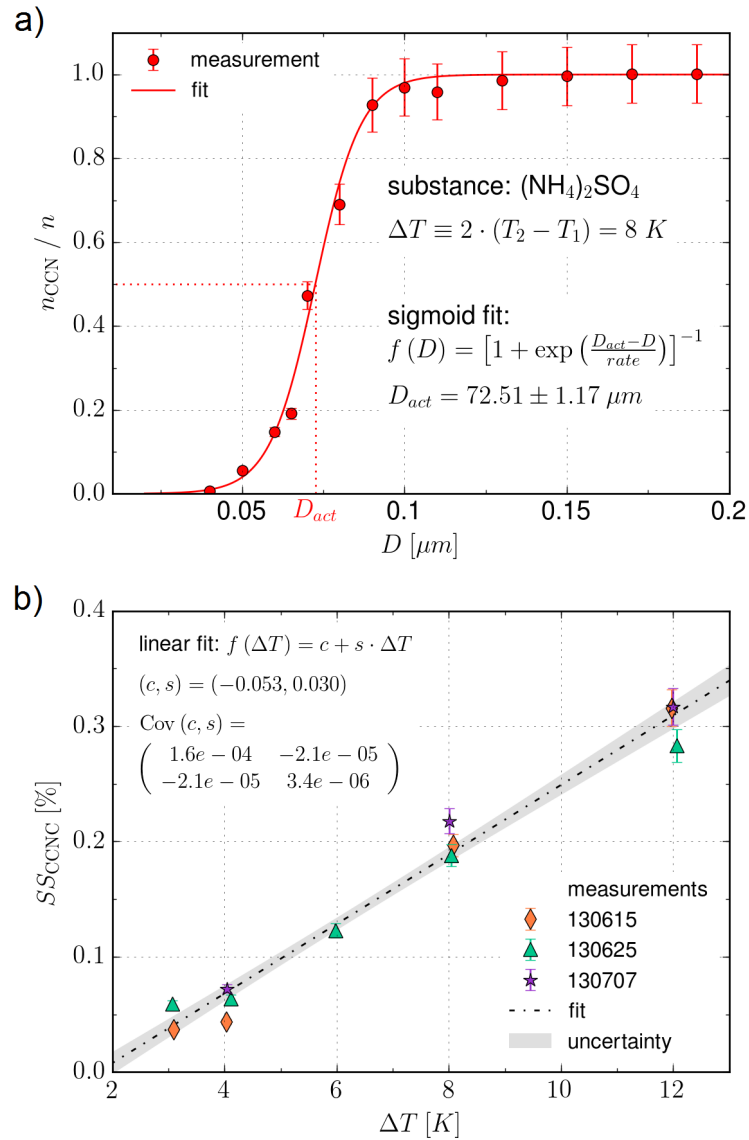


Figure 3.2.17: CCNC (column B) calibration. Plot (a) shows the size-dependent measurement of the activated particle fraction n_{CCN}/n for a certain substance and ΔT setting yielding an activation diameter D_{act} that is translated into a SS using Köhler theory. Plot (b) displays the linear fit to all resulting $(SS, \Delta T)$ pairs for the SALTRACE calibrations. The fit uncertainty range in the bottom plot corresponds to the diameter-wise one sigma standard deviation calculated from the fit parameter covariance matrix. The fit parameters units are $[c] = \%$ and $[s] = \%K^{-1}$.

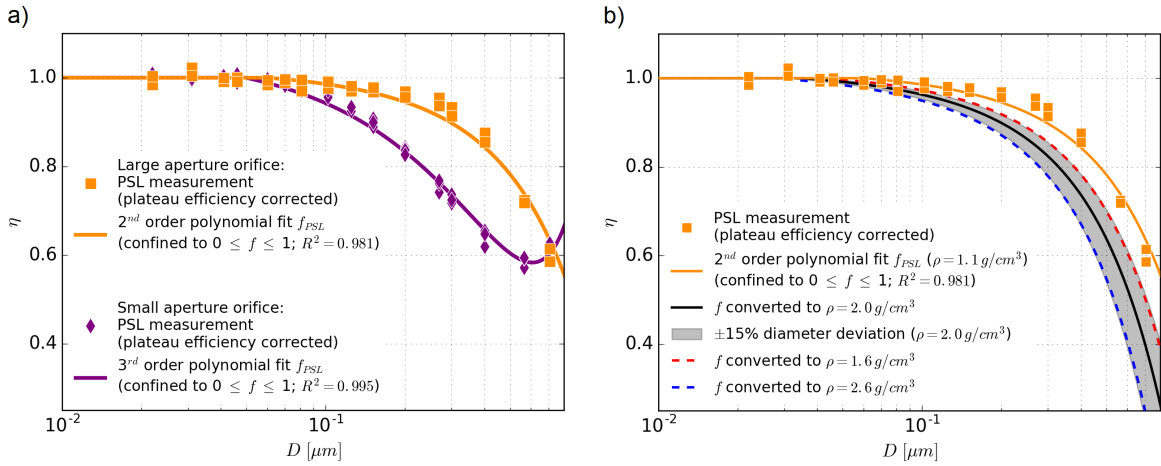


Figure 3.2.18: Size-dependent transmission efficiencies of the CPS inlet orifices. Plot (a) shows the transmission efficiencies of both CPS inlet orifices measured for PSL particle standards. Plot (b) displays the converted transmission efficiency of the large aperture orifice (being the orifice responsible for the SAL heights) for different particle densities. Measurement data are adopted from Dollner (2015).

measurements and other studies (Rose et al., 2008, 2010). According to the latter, diffusional losses of small particles in the CCNC column leading to a decrease in counting efficiency become significant only for sizes $D \lesssim 50$ nm. Similarly, diffusional tubing transport losses that may lead to an underestimation of n_{CCNC} can be neglected as particles in the regarding size range will not activate into droplets for the chosen SS range. However, relevant losses of large particles do occur at the CPS inlet upstream of the CCNC.

As shown in Fig. 3.2.1, the CPS assembly used to ensure CCNC operation at a constant pressure consisted of two selectable inlet orifices of different aperture and a pressure-controlled bypass flow circuit. This final setup is valid for all SALTRACE flights after 16 June 2013. CCNC data for flights prior to this date are partly affected by undefined CPS inlet conditions and/or CCNC malfunctions and are, therefore, disregarded in this study. At the CPS inlet's sudden tubing contraction the air flow experiences a pressure drop that depends on the orifice characteristics (aperture, contraction angle etc.) and the absolute value of the flow. The bypass circuit regulates this flow for varying inlet pressures such that the pressure behind the orifice stays at a constant value. Since the control range is limited, it was necessary to switch between the orifices, one having a smaller aperture to cause a greater pressure drop and another large aperture provoking a more decent pressure reduction. During SALTRACE, the small aperture orifice was utilized for altitudes $z \lesssim 1.5$ km ($p_{inlet} \gtrsim 850$ hPa) and the large aperture orifice for heights above. The CPS assembly's operational ceiling with the large aperture orifice was about 4.5 km ($p_{inlet} \approx 500$ hPa). Above this height p_{CPS} and, thereby, the CCNC SS was no longer constant, wherefore the data presented here are confined to $z \lesssim 4.5$ km.

As mentioned in Sect. 2.5, there is no universally valid parametrization for particle losses occurring at sudden contractions. Therefore these losses need to experimentally determined. For the used orifices and a fixed inlet pressure of $p_{inlet} \approx 930$ hPa,

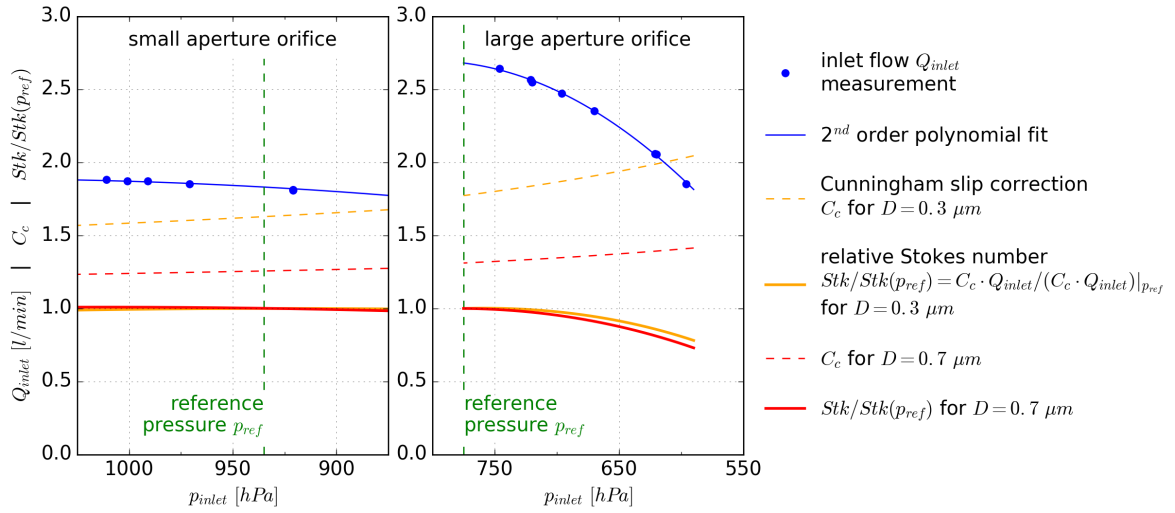


Figure 3.2.19: Pressure-dependence of the volumetric inlet flow upstream the CPS inlet orifices, the Cunningham slip correction for $D = 0.3$ and $0.7 \mu\text{m}$, and the resulting relative particle Stokes numbers.

Dollner (2015) investigated the transmission efficiencies for PSL particles as shown in Fig. 3.2.18. Figure 3.2.18a) features the complete series of data points obtained by side-by-side CPC measurements with a setup similar to that presented in Fig. 3.2.4 (replacing the TD with the CPS inlet assembly). The solid lines represent polynomial fits to these (CPC plateau-efficiency corrected) measurements. Consistent with the literature (e.g. Muyschondt et al., 1996; Chen et al., 2007), the orifices cause significant particle loss only for the larger particle diameters/Stokes numbers and losses are more pronounced for the smaller orifice aperture. The recovery of the transmission efficiency of the small aperture orifice at the largest diameters is also consistent with findings by Chen et al. (2007) and is presumably linked to high turbulence in the enlargement region behind the orifice. In addition to the measurements, Figure 3.2.18b) shows the transmission efficiency function of the large orifice converted to higher particle densities. The conversion is achieved by recalculating the particle diameter scale keeping the decisive parameter, i.e. the particle Stokes number Stk given by Eq. (2.5.9) constant. The gray shaded area that corresponds to a $\pm 15\%$ diameter uncertainty around the converted transmission efficiency for $\rho_p = 2.0 \text{ g/cm}^3$ encompasses a density range of $1.6 \leq \rho_p \leq 2.6 \text{ g/cm}^3$ and, thereby, yields an adequate uncertainty range for the later relevant ambient aerosol ($\rho_p = 2.5 \text{ g/cm}^3$ for mineral dust and 1.8 g/cm^3 for ammonium sulfate). However, the transmission efficiencies presented in Fig. 3.2.18 are only valid for $p_{inlet} \approx 930 \text{ hPa}$, because Stk scales with the flow velocity which in turn depends on p_{inlet} , owing to the varying bypass flow and Cunningham slip correction C_c . To (qualitatively) assess the change in Stk with p_{inlet} , the pressure-dependent total flow upstream the CPS inlet orifices was measured and compared with the pressure trend for C_c calculated via Eq. (2.5.5). The results are shown in Fig. 3.2.19. They reveal that for the small aperture orifice variations in p_{inlet} do not significantly affect Stk . This suggests that the laboratory transmission efficiency curve is valid for the complete pressure range covered by the small aperture orifice. In contrast, for the large aperture orifice Stk significantly declines with decreasing p_{inlet} , which one could

interpret as a shift of the transmission efficiency function to larger diameters. Yet, the turbulent losses behind the orifice may not scale linearly with Stk , so that simply shifting the measured transmission efficiency function could be inadequate. This means that the laboratory transmission efficiency curve cannot be directly used to calculate the particle losses for the large aperture orifice in the respective p_{inlet} range. Nevertheless, with decreasing Stk the total losses at the large aperture orifice must decrease, too. Consequently, the laboratory curve can serve as a lower transmission bound.

To quantify particle losses at the large aperture orifice by means of an experimentally determined transmission efficiency would require repeating the laboratory measurements (shown in Fig. 3.2.18) for a range of p_{inlet} , which would be very time-consuming. Another general problem with particle loss determination via transmission efficiency functions is that the particle NSD is required. However, the particle NSD is not readily available on a time step basis (see Sect. 3.3.2). To overcome this issue a reference CPC, i.e. CPC_{CPS} was operated inside the CPS (cf. Fig. 3.2.1) in order to derive the total particle losses upon comparison with CPC_1 . As described in detail in Dollner (2015), the difference between the corrected STP particle number concentrations Δn determined by CPC_1 and CPC_{CPS} can be equated with the underestimation of n_{CCN} assuming that

- the orifice losses are only significant for particles large enough to activate into droplets in the CCNC, and
- additional differential tubing losses between the CPCs that contribute to Δn but only affect particles irrelevant for n_{CCN} (primarily diffusional losses of small particles) are negligible compared to the orifice losses.

Whereas the former is justified by the measured orifice transmission efficiency functions, the latter is a critical point. Differential diffusional losses between CPC_1 and CPC_{CPS} , that exhibit a tubing transit time difference of $\Delta t = 4$ s (cf. Tab. 3.2.3), will certainly impact Δn the more pronounced the higher the (relative) number concentration of small particles (affected by diffusional loss) is. To minimize this perturbing influence on Δn , Dollner (2015) only corrects the measured n_{CCN} by Δn for time steps with minimum concentrations of small particles. For the remaining data a pressure-dependent relative loss factor derived from the former time steps is used to calculate a corrected Δn_{v1} that is minimized for diffusional loss interference. The raw CCN concentrations corrected via this scheme are symbolized by $n_{CCN,v1}$ in the following. The advantage of this concentration correction scheme is that it provides loss corrected CCN concentrations on a time step basis. Its disadvantage is an unavoidable remaining Δn bias leading to an overestimation of the true CCN concentrations.

For time intervals where the NSD is available an advanced CCN concentration correction scheme was, hence, developed as part of this study. As explained above, the transmission efficiency function $\eta_{os}(D)$ shown in Fig. 3.2.18 allows to directly calculate the NSD behind the small aperture orifice and, thereby, the CCN loss $\Delta n_{v2.1}$ at the orifice as

$$\Delta n_{v2.1} = \int_0^{\infty} (1 - \eta_{os}(D)) \frac{dn}{dD} dD \quad (3.2.19)$$

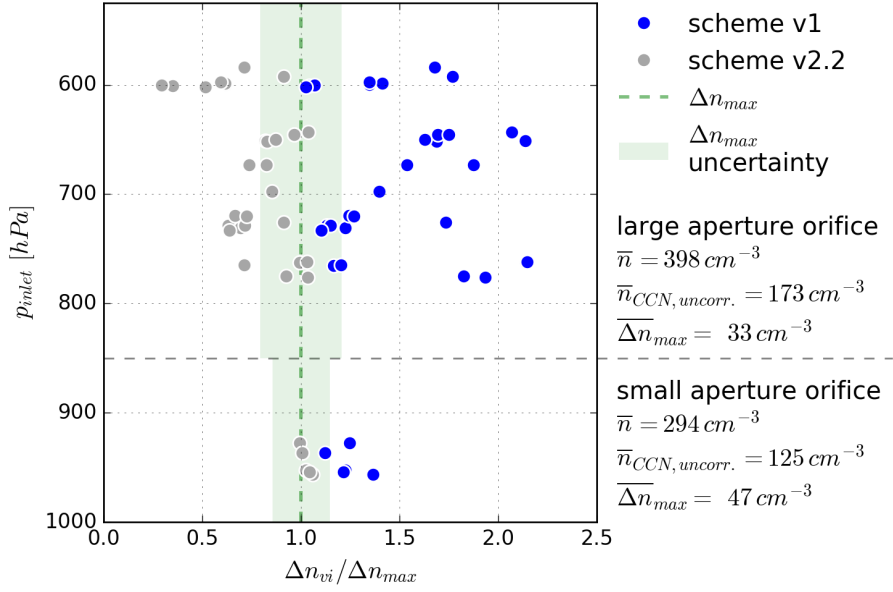


Figure 3.2.20: Corrected CCN losses at the CPS inlet orifices for the two presented schemes, i.e. Δn_{v1} and $\Delta n_{v2.2}$, relative to the maximum losses Δn_{max} derived by means of the measured orifice transmission efficiencies (cf. Fig. 3.2.18).

where dn/dD is the particle NSD upstream the orifice. However, for the discussed reasons it is not possible to calculate the loss of CCN at the large aperture orifice in the same way. Therefore, for the latter orifice the measured CPC concentration difference Δn must still be consulted. As demonstrated in Sect. A.2.2, the tubing transit time difference between CPC_1 and CPC_{CPS} can in good approximation be completely attributed to the exclusive last tubing part upstream the CPC_{CPS} , while the time difference and, therewith, the differential particle losses between CPC_1 and the CPS inlet are negligible. This means that losses occurring in this last CPC_{CPS} tubing part must be subtracted from the measured Δn to obtain the actual loss of CCN occurring at the orifice. With the NSD the tubing transmission efficiency $\eta_t(D)$ (for the given Δt and constant p_{CPS}) can be calculated by means of the PLC yielding the corrected CCN loss $\Delta n_{v2.2}$

$$\Delta n_{v2.2} = \Delta n - \int_0^{\infty} (1 - \eta_t(D)) \frac{dn}{dD} dD \quad (3.2.20)$$

with dn/dD this time denoting the NSD behind the orifice. For the diffusional tubing losses decisive for the integral in Eq. (3.2.20) this NSD can, however, be well-approximated by the NSD upstream the orifice, since the orifice losses do not affect the diffusive small particles. Further, as outlined before, the transmission efficiency of the large aperture orifice $\eta_{ol}(D)$ can be used to calculate an upper loss bound Δn_{max}

$$\Delta n_{max} = \int_0^{\infty} (1 - \eta_{ol}(D)) \frac{dn}{dD} dD \quad (3.2.21)$$

For the time intervals with available NSDs, the different CCN concentration correction

schemes can be directly compared. Figure 3.2.20 contrasts the values of Δn_{v1} and $\Delta n_{v2.2}$ in relation to Δn_{max} ($= \Delta n_{v2.1}$ for the small aperture orifice). It is apparent that the Δn_{v1} neglecting the diffusional losses in the tubing upstream the CPC_{CPS} significantly overestimate the true orifice losses for most of the cases. Particularly for the large aperture orifice at lower p_{inlet} the Δn_{v1} exceed the upper loss bound Δn_{max} by up to a factor of 2. In contrast, the $\Delta n_{v2.2}$ values show the expected (correct) behavior. For the small aperture orifice the $\Delta n_{v2.2}$ calculated via Eq. (3.2.20) almost perfectly agree with the $\Delta n_{max} = \Delta n_{v2.1}$ calculated via Eq. (3.2.19), that are assumed to be accurate following the previous considerations. For the large aperture orifice the $\Delta n_{v2.2}$ on average fall below the Δn_{max} and the fraction $\Delta n_{v2.2}/\Delta n_{max}$ shows a decreasing trend with decreasing p_{inlet} , conform with what is expected from the reduction in Stk (cf. Fig. 3.2.19).

For clarity, Fig. 3.2.20 only features the uncertainty ranges for Δn_{max} resulting from a propagation of the uncertainties in $\eta_{os}(D)$ or $\eta_{ol}(D)$ and the NSD. For the data points ($\Delta n_{vi}/\Delta n_{max}$) only the mean solutions are shown, as the systematic uncertainties for measured Δn can be as large as 50%, thus disturbing the visualization. This is because the Δn values represent a small difference of two large CPC concentration values, each subject to an (assumed) systematic uncertainty of 5% (cf. Sect. 3.2.2.1). Although on average agreeing with the expectations, the $\Delta n_{v2.2}$ values exhibit some scatter. This is, to a large extent, ascribable to small time-dependent variations of the CPC counting efficiencies and/or sample flow rates. Such variations (falling within the range of the 5% accuracy) are regularly observed during CPC laboratory measurements. Especially for the large aperture orifice, where the measured Δn are smallest compared to the absolute concentrations (cf. Fig. 3.2.20), such fluctuations can easily explain the observed scatter. To minimize the uncertainty in the $\Delta n_{v2.2}$ values, the Δn_{max} fraught with less uncertainty are, hence, used as an upper constraint for the derivation of the (v2) corrected CCN concentrations $n_{CCN,v2}$, as outlined in Sect. 3.3.4.

In relation to $n_{CCN,v2}$ the uncorrected $n_{CCN,uncorr}$ underestimate the CCN concentrations (at $SS = 0.2\%$) on average by 27% and 9% for the small and large aperture orifice, respectively. The $n_{CCN,v1}$, on the other hand, overestimate the CCN concentrations on average by 6% and 17% for the two orifices respectively. The complete comparison between the different CCN concentrations is given in Tab. A.2.1. On balance, from the two options available on a time step basis, i.e. $n_{CCN,uncorr}$ and $n_{CCN,v1}$, the latter still offers a better approximation of the (correct) $n_{CCN,v2}$ values with regard to the full altitude range. In Ch. 4, both $n_{CCN,v1}$ and $n_{CCN,v2}$ values are used to present CCN concentrations. Unless otherwise specified, n_{CCN} is used as a synonym for $n_{CCN,v2}$.

3.2.3 Supplementary Instruments

3.2.3.1 Airborne Instruments

Standard Meteorological Instrumentation and Dropsondes

The Falcon standard instrumentation includes measurements of meteorological parameters like ambient pressure, temperature, humidity and 3D wind vector. Table 3.2.4 offers the complete list of parameters used in this study originating from this data set.

In addition, the aircraft is routinely equipped with GPS sensors determining its altitude z above mean sea level (AMSL) and geographic coordinates (longitude and latitude). Detailed information about the aircraft and the standard sensors can be found on the DLR flight experiments homepage¹⁰. For SALTRACE, the Falcon standard data were processed and provided by A. Giez, V. Dreiling, M. Zöger and Ch. Mallaun, DLR.

Complementary meteorological investigations were carried out by means of dropsondes (Govind, 1975; Hock and Franklin, 1999). A dropsonde is a compact device that is released from the aircraft at high altitudes. While descending through the atmospheric column in a moderate speed (about 5 – 10 m/s), measurements of pressure, temperature, humidity, horizontal wind velocity and direction are conducted and transmitted to the aircraft for onboard data processing.

Micro Inertial Impactors (MINIs)

In situ sampling for offline single particle analysis was performed with cascade particle impactors, termed MINIs (Kandler et al., 2007). The sample acquisition was not continuous but manually started and stopped for specific time intervals (typically 5–10 min) by opening and reclosing the lock valves connecting the MINIs to the sampling lines (cf. Fig. 3.2.1). The MINIs consisted of two main impactor stages (equipped with different substrates), i.e. a primary stage A for particle diameters $D \gtrsim 500$ nm and a secondary stage B for particle diameters $D \lesssim 500$ nm. The large particles in stage A were analyzed by scanning electron microscopy (SEM) and energy-dispersive X-ray diffraction (EDX) for size and composition, small particles in stage B by transmission electron microscopy (TEM) and EDX for size, volatility and composition. Whereas the SEM analysis was automated, the TEM analysis for the small particles required manual support, leading to reduced statistical ensemble sizes for the stage B samples. The classification of particle composition follows Kandler et al. (2009) with the exception of quartz being classified as silicate. Volatility for the stage B particles was determined as outlined in Sect. 2.4, and described in detail in Kandler et al. (2011) and Kristensen et al. (2016). It should be noted that these measurements do not yield information on potential organic components. The MINI data set was made available by K. Kandler, Technical University of Darmstadt.

Single Particle Soot Photometer (SP2)

The in-cabin setup used in this study is complemented by an SP2 which is utilized to measure the aerosol refractory black carbon (rBC) mass concentration (Stephens et al., 2003; Laborde et al., 2012). Like for the OPCs, the SP2 guides the aerosol sample through the focus of a laser beam. Particles containing a rBC core absorb the high irradiance laser light, thereby heating up, losing non-refractory coatings and finally incandesce. The peak intensity of the thermal emission from an incandescent rBC core is proportional to its mass. Detecting the distribution of thermal emission signal peaks, thus, allows to derive the rBC mass distribution¹¹. Here, only the integral rBC mass

¹⁰<http://www.dlr.de/fb/en/desktopdefault.aspx/tabid-3714/>

¹¹Strictly speaking, the inferred rBC mass refers to the calibration material. For the presented data, this reference material is fullerene soot.

concentration m_{rBC} within the SP2 size range ($80 \lesssim D \lesssim 480$ nm) is presented. The SP2 data were processed by K. Heimerl and B. Weinzierl, DLR¹².

Cloud and Aerosol Spectrometer (CAS)

Like the UHSAS, the CAS (Baumgardner et al., 2001) was mounted in one of the aircraft's under-wing pods. The centerpiece of the CAS is an OPC having its sampling volume located in an open (forward pointing) large-diameter pipe through which the ambient air flows through passively during flight. The open design has some disadvantages. For instance, as the aerosol sample is not focused to the center of the sampling volume it is necessary to qualify signal pulses by their point of origin in the latter, which complicates data evaluation. However, a major advantage of the open design over inlet-based OPC architectures is that it does not limit the sampling efficiency for larger particles. As a result, the CAS permits the detection of cloud droplets and aerosol particles too large to be efficiently transmitted to the in-cabin instruments (e.g. large mineral dust particles). Apart from utilizing the data for identifying cloud passages, the integral number concentration of particles with $D \gtrsim 1.5 \mu\text{m}$ measured by the CAS n_{giant} is presented as an optimistic estimate¹³ for particles beyond the Falcon inlet size cutoff. The CAS data were processed by D. Sauer, DLR.

3.2.3.2 Ground-Based Instruments

Mobility Particle Size Spectrometer (MPSS) and Aerodynamic Particle Sizer (APS)

The ground-based particle NSD measurements at Ragged Point, Barbados (see Fig. 3.1.2) involved a MPSS (Wiedensohler et al., 2012), covering a particle size range of about 10 to 800 nm, and a (TSI model 3321) APS (e.g. Pfeifer et al., 2016) for particle diameters $D \geq 500$ nm. The MPSS, also commonly referred to as a differential mobility particle sizer (DMPS), consist of an initial section where the aerosol particles become electrically charged (with a defined charge distribution), a DMA used to extract a defined size sub-range from the sample, and a CPC to measure the integral particle number concentration of the transmitted sub-sample. Scanning different size sub-ranges allows to finally infer a NSD by inversion techniques. An APS sizes particles based on their relaxation times. It first accelerates the aerosol sample and then determines the time individual particles need to pass the distance between two subsequent laser beams. This time increases with increasing particle relaxation time and is, hence, longer for larger particles with higher inertia. Calibrating the time-to-size relationship facilitates the derivation of the NSD from the measured distribution of transit times. For the ground-level NSDs the MPSS data were merged with the APS data for sizes larger 800 nm (Kristensen et al., 2016). The ground-level NSD data are provided by T. Müller, TROPOS.

¹²K. Heimerl and B. Weinzierl now at: UNIVIE

¹³In this context, "optimistic" means that the true number concentration of particles that are not efficiently transmitted to the in-cabin instruments can be considered to be $\leq n_{\text{giant}}$.

Cloud Condensation Nuclei Counter (CCNC)

In parallel to the NSD measurement devices, a CCNC was operated at Ragged Point to determine near-ground CCN concentrations for a range of supersaturations. The ground-based CCNC was identical to the one used on the Falcon and calibrated in the same way as the latter. Moreover, direct side-by-side comparison measurements in the laboratory previous to the campaign demonstrated good agreement between the two instruments (Dollner, 2015). In a similar manner to the method presented in Sect. 3.3.4, the Ragged Point NSDs and CCN concentrations were used to derive effective particle hygroscopicities (κ values) for the boundary layer aerosol. Details about the ground-based CCN measurements during SALTRACE are given in Kristensen et al. (2016). T. Kristensen¹⁴, TROPOS made the data available for this study.

Spectral Optical Absorption Photometer (SOAP)

The presented subset of ground-based in situ data is complemented by the time series of mineral dust mass concentration at Ragged Point, which was inferred from spectral attenuation measurements by means of the SOAP (Müller et al., 2009, 2011). The SOAP monitors the transmittance and reflectance of fiber filters being continuously loaded with particles while the sample air is sucked through the device. After correcting the measured attenuation for the light scattering contribution, these measurements yield the spectral run of the absorption coefficient (between 300 and 950 nm). As described in Niedermeier et al. (2014), from these (multi-wavelength) absorption coefficients the mineral dust mass concentration can be derived utilizing estimates for the mineral dust mass absorption coefficients at the corresponding wavelengths. Values for the latter coefficients were obtained following a reanalysis of data from Müller et al. (2009) and Schladitz et al. (2009). The resulting dust mass concentrations m_{dust} were provided by T. Müller, TROPOS.

Sun Photometers

In addition to the airborne and ground-based in situ measurements, the aerosol was studied by remote sensing instruments including a number of sun photometers (e.g. Shaw, 1983). The sun photometer setup comprised AERONET instruments at Cabo Verde, Barbados and Puerto Rico and ancillary instruments located at the CIMH (see Fig. 3.1.2). A detailed overview of this setup is given in Weinzierl et al. (2017). The principal output parameter of sun photometers is the spectral aerosol optical depth (AOD), which is calculated from the extinction of solar radiation based on the Lambert-Beer law. To describe the attenuation of solar radiation in the atmosphere, τ_o in Eq. (2.2.1) is commonly replaced by the product $\tau'_o m_{air}$, where τ'_o refers to the optical depth of the vertical path and m_{air} is called the relative air mass, which is defined as $m_{air} = 1/\cos\theta_z$ with the solar zenith angle θ_z . Contributions to τ'_o from Rayleigh scattering of molecules, and absorption by ozone and other gases are estimated and removed to isolate the aerosol component, i.e. the AOD. Here, only AOD data from the Cabo Verde AERONET station and the CIMH measurements at a wavelength of

¹⁴T. Kristensen now at: Lund University

500 nm are presented. The sun photometer data were extracted from the AERONET database and provided by C. Toledano, University of Valladolid.

Lidar

Height-resolved remote sensing measurements were carried out at CIMH by means of lidar instruments, including the portable lidar system (POLIS) (Freudenthaler et al., 2009) of the LMU. A lidar, short for light detection and ranging, basically consist of a laser emitting light pulses into the atmospheric column and a receiver collecting the backscattered signal power together with information on the signal time delay. Consequently, the fundamental output is a profile of atmospheric scattering versus distance from the instrument. More precisely, the total power received at a given time delay — corresponding to a certain distance to the scattering volume — is a function of the so-called backscatter coefficient including scattering by molecules and aerosol particles, the signal attenuation on the way from the lidar to the scattering volume and back, and the distance itself. Polarization lidars (e.g. Sassen, 1991) extent the basic lidar technique by splitting the backscatter signals into two components, parallel- and cross-polarized with respect to the plane of a linearly polarized laser output. The ratio of the two components, called the linear volume depolarization ratio δ_v is sensitive to the concentration and type (shape) of scatterers — $\delta_v \approx 0$ for spherical particles — and is, hence, among others suitable to trace the vertical structure of mineral dust layers. Here, POLIS vertical δ_v (quicklook) data at a wavelength of 532 nm are presented. These data are made available by V. Freudenthaler, LMU. Periods with low-level clouds interfering the lidar measurements by shielding the overlying dust layer are excluded from the data set.

3.3 Data Evaluation

3.3.1 Cloud Passage Masking

In the course of the airborne in situ measurements, the Falcon occasionally penetrated clouds. During such cloud passages, droplets impacting the aerosol inlets and the aircraft fuselage shatter and generate a large number of smaller particles distorting the aerosol measurements (e.g. Weber et al., 1998; Moharreri et al., 2014). For the airborne in situ instruments including the CPCs, OPCs and the CCNC, this effect results in unrepresentative in-cloud particle concentrations elevated by up to 2-3 orders of magnitude compared to the cloud-free environment. Especially for the CCNC, it is evident that the in-cloud data are erroneous. (Non-shattered) cloud droplets are too large in size to be efficiently sampled by the aerosol inlets, so that without the spurious particles the inlets would sample the non-activated “interstitial” particles only. With the CCNC supersaturation being similar to the ambient cloud supersaturation, these interstitial particles would neither activate in the CCNC (in significant numbers) and, consequently, in-cloud CCN concentrations would have to be minor. As the in-cloud concentrations cannot be corrected for the particle artifacts, all cloud passages have been removed from the SALTRACE data set for this study. For this purpose, the data were screened for time intervals with suspicious concentration peaks in the various in

instrument(s)	data product(s)
<i>Meteorology / Thermodynamics</i>	
Falcon sensors	ambient static pressure p , static temperature T , potential temperature Θ , relative humidity rh , water vapor mixing ratio mr , horizontal wind velocity v_{wind} and direction
<i>Aerosol – Main</i>	
CPC ₁	total particle number concentration n_{total}
UHSAS	“accumulation mode” particle number concentration n_{acc} in the size range $80 \lesssim D \lesssim 300$ nm
SkyOPC	particle number concentration n_{large} in the size range $D \gtrsim 300$ nm ^a
CCNC (+ CPC ₁ + CPC _{CPS})	(loss-corrected) CCN number concentration n_{CCN} at $SS = 0.2\%$ ^b
CPC ₂ + CPC _{TD}	total fraction of (completely) volatile particles vf_{total}
SkyOPC + SkyOPC _{TD}	size-dependent volatile fraction $vf(D)$ in the size range $D \gtrsim 300$ nm ^c
CPC ₁ + UHSAS + SkyOPC	particle number concentrations n_{small} and n_{80} in the size ranges $D \lesssim 80$ and $D \gtrsim 80$ nm, particle NSD $dn/d\log_{10} D$ ^d
CPC ₁ + UHSAS + SkyOPC + CCNC (+ CPC _{CPS})	effective particle hygroscopicity κ ^e
<i>Aerosol – Supplementary – Airborne</i>	
CAS	particle number concentration n_{giant} in the size range $D \gtrsim 1.5 \mu\text{m}^f$
SP2	refractory black carbon mass concentration m_{rBC} in the size range $80 \lesssim D \lesssim 480$ nm
MINIs	single particle chemical composition and/or volatility
<i>Aerosol – Supplementary – Ground-Based</i>	
MPSS + APS	particle NSD $dn/d\log_{10} D$
MPSS + APS + CCNC	effective particle hygroscopicity κ
SOAP	mineral dust mass concentration m_{dust}
sun photometers	AOD at $\lambda = 500$ nm
POLIS	linear volume depolarization ratio δ_v at $\lambda = 532$ nm

All presented concentrations refer to STP conditions.

^a As part of the in-cabin instrumentation, the SkyOPC concentration is affected by the Falcon inlet efficiency cutoff at large diameters.

^b Non-continuous CCN data is available also for other SS (see Sect. B.5.2).

^c See Sect. 3.3.3.

^d The NSD refers to in-cabin conditions, i.e. it may deviate (slightly) from the ambient NSD for the smallest and largest particle diameters (see Sect. 3.3.2).

^e See Sect. 3.3.4.

^f Offers an optimistic estimate for the concentration of large particles beyond the Falcon aerosol inlet cutoff.

Table 3.2.4: Overview of data products used in this study and the various instruments these data products are attributable to.

situ instruments at high relative humidities, coinciding with elevated concentrations of droplet-size particles measured by the CAS. For time intervals where this cloud-screening method led to inconclusive results the Falcon cockpit video material was additionally consulted.

3.3.2 Size Distribution Retrieval

Cloud-free time intervals with homogeneous sampling conditions, i.e. constant altitude flight intervals with homogeneous particle concentrations, are used to derive the aerosol particle NSD from the combination of CPC and OPC measurements. As (most) prevalent methods for the derivation of NSDs from OPC measurements are inadequate, especially concerning a proper uncertainty analysis (Walser et al., 2017), within the scope of this study a new NSD retrieval method has been developed. As explained in detail in the following, this NSD retrieval method is self-consistent with the OPC calibration approach presented in Sect. 3.2.2.2, addresses the actual inverse problem underlying OPC measurements and allows for a thorough propagation of all uncertainties in the underlying parameters.

As illustrated in Fig. 3.3.1 and previously proposed by Fiebig et al. (2005), the NSD retrieval is based on a Monte Carlo method. It starts with drawing random samples from all initial parameters being subject to systematic uncertainty. A complete list of these parameters with associated PDF assumptions is given in Tab. 3.3.1. In Fig. 3.3.1 the parameter PDFs and the Monte Carlo sampling from these PDFs are visualized by dashed boxes and arrows, respectively. For the CPC, the parameters afflicted with systematic uncertainty include a , D_1 and D_2 determining the size-dependent counting efficiency via Eq. (3.2.3), and the potential concentration deviation $(\Delta n/n)_{sys}$, e.g. caused by an eventual small deviation in the sample flow from the value used to convert counts to concentration. Using the Monte Carlo picks from the corresponding PDFs and the measured interval mean concentration \bar{n} , the CPC counting efficiency $\eta_{CPC}(D)$ and a shifted mean concentration $n_{CPC} = \bar{n} \cdot \left(1 + (\Delta n/n)_{sys}\right)$ are calculated. For the OPCs, the uncertainty in the instrument response is given by the model parameter solution ensemble resulting from the evaluation of the calibration measurements, as described in Sect. 3.2.2.2. In contrast to the CPC, additional uncertainty is introduced by the optical properties of the aerosol particles, here taken into account by the bulk refractive index m and an additional OPC signal broadening b_{as} induced by particle asphericity. From the OPC response model parameter pick $(b, s, c, \sigma_\varepsilon)$ and the additional b_{as} a combined response tuple is derived as $(b_{total}, s, c, \sigma_\varepsilon)$, with the total signal broadening $b_{total} = \sqrt{b^2 + b_{as}^2}$ being the standard deviation of the convolution of the two individual (Gaussian) broadening effects. The bulk refractive index pick m is used to calculate the size-dependent theoretical (midway) scattering cross section $\tilde{C}_{scat,m}(D)$ for the specific OPC detection geometry via Mie theory. In a subsequent step, a random shift from this theoretical function is performed according to its potential (time-dependent) systematic deviation, e.g. induced by light source intensity fluctuations. This relative shift ε is drawn from the Gaussian PDF $\mathcal{N}(1, \sigma_\varepsilon^2)$ and yields the shifted $\tilde{C}_{scat,m,\varepsilon}(D) = \varepsilon \cdot \tilde{C}_{scat,m}(D)$. From $\tilde{C}_{scat,m,\varepsilon}(D)$, the instrument parameter tuple (b_{total}, s, c) and the known OPC bin threshold values U_i the OPC kernel functions $\Upsilon_i(D)$ are calculated via Eq. (3.2.10). Under the justified assumption that the OPC sampling efficiencies do not significantly deviate from unity,

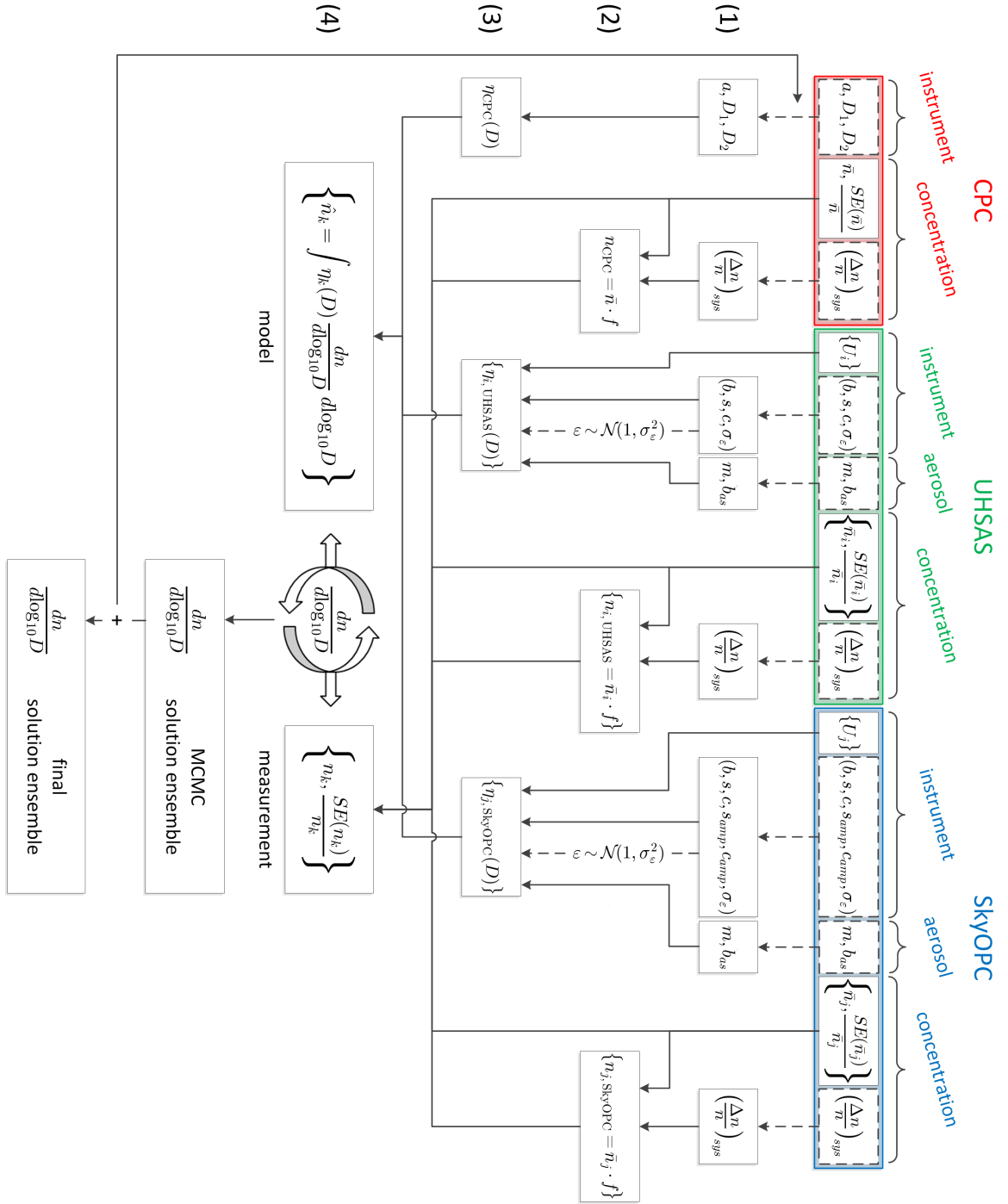


Figure 3.3.1: Flowchart for the NSD retrieval. Each Monte Carlo iteration starts with random samples (picks) from the initial parameter PDFs (1), that are subsequently used to calculate particle concentrations (2) and corresponding counting efficiency functions (3). The results are input to the NSD inversion (4) that is performed by means of a MCMC method. The NSD inversion results for each Monte Carlo iteration are finally merged into a collective NSD solution ensemble. The multiplicand f in step (2) is defined by $f = 1 + \left(\frac{\Delta n}{\bar{n}}\right)_{sys}$.

parameter(s)	description	random Monte Carlo sampling from...
<i>CPC₁</i>		
a, D_1 and D_2	CPC counting efficiency function parameters	(uncorrelated) Gaussian PDFs with 3%, 7% and 2% relative standard deviation for a , D_1 and D_2 , respectively (cf. Tab. 3.2.1)
$(\Delta n/n)_{sys}$	systematic concentration deviation	Gaussian PDF centered at zero with 5% standard deviation $\mathcal{N}(0, 0.05^2)$
<i>UHSAS</i>		
$(b, s, c, \sigma_\varepsilon)$	OPC response model parameters	parameter solution ensemble resulting from the OPC calibration evaluation
ε	systematic scattering cross section deviation	Gaussian PDF $\mathcal{N}(1, \sigma_\varepsilon^2)$ defined by the previous σ_ε pick
b_{as}	additional signal broadening due to particle asphericity	Gaussian PDF $\mathcal{N}(0.06, 0.03^2)$ for the SAL ^a
m	(bulk) particle refractive index	uniform PDF $\mathcal{U}([1.5, 1.6] + i[0, 0.005])$ for the SAL, uniform PDF $\mathcal{U}([1.4, 1.5] + i0)$ for the MBL
$(\Delta n/n)_{sys}$	systematic concentration deviation	Gaussian PDF $\mathcal{N}(0, 0.05^2)$
<i>SkyOPC</i>		
$(b, s, c, s_{amp}, c_{amp}, \sigma_\varepsilon)$	OPC response model parameters	parameter solution ensemble resulting from the OPC calibration evaluation
ε	systematic scattering cross section deviation	Gaussian PDF $\mathcal{N}(1, \sigma_\varepsilon^2)$ defined by the previous σ_ε pick
b_{as}	additional signal broadening due to particle asphericity	Gaussian PDF $\mathcal{N}(0.09, 0.04^2)$ for the SAL ^a
m	(bulk) particle refractive index	uniform PDF $\mathcal{U}([1.5, 1.6] + i[0, 0.005])$ for the SAL, uniform PDF $\mathcal{U}([1.4, 1.5] + i0)$ for the MBL
$(\Delta n/n)_{sys}$	systematic concentration deviation	Gaussian PDF $\mathcal{N}(0, 0.05^2)$

^a Due to hydration particles in the MBL are assumed to be (close to) spherical shape, thus $b_{as} = 0$.

Table 3.3.1: Parameters that are sampled via a Monte Carlo method in the course of the NSD retrieval (see step (1) in Fig. 3.3.1) together with their PDFs, that define the corresponding systematic uncertainties.

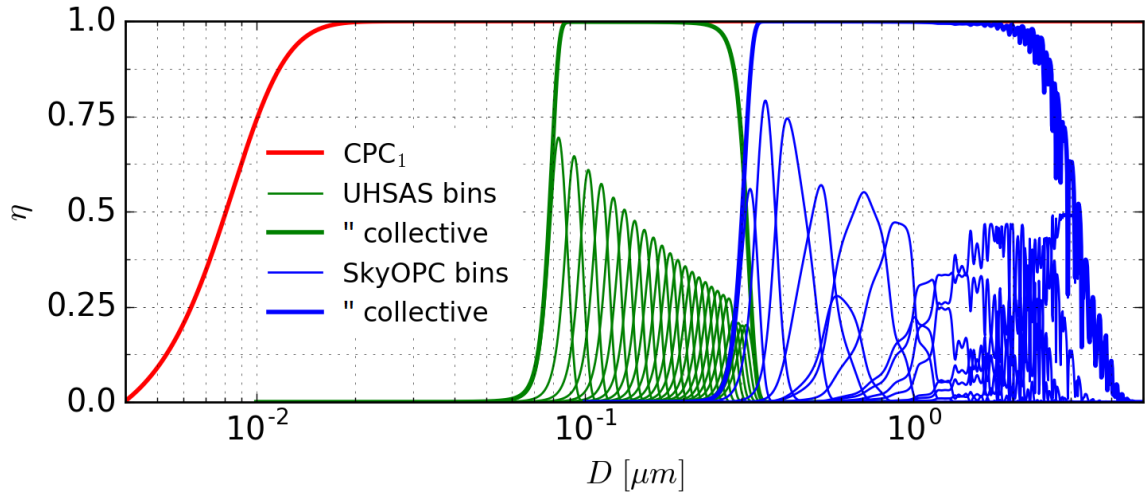


Figure 3.3.2: Exemplary set of counting efficiency functions $\eta_k(D)$ calculated for each NSD retrieval iteration (see step (3) in Fig. 3.3.1). The example represents the entirety of counting efficiency functions for the CPC_1 , the SkyOPC and UHSAS bins using the best estimates for the instrument parameters, assuming spherical particles ($b_{as} = 0$) with a refractive index of $m = 1.54 + i0$ and no relative deviation from the resulting scattering cross sections ($\varepsilon = 0$).

the kernel functions directly correspond to the bin counting efficiency functions, i.e. $\eta_{i,\text{OPC}}(D) = \Upsilon_i(D)$. Like for the CPC, the measured mean OPC bin concentrations are further (collectively) shifted according to the estimated range of potential systematic deviation to obtain the $n_{i,\text{OPC}}$. All resulting CPC and OPC concentrations and counting efficiency functions are then collected to yield the set of $n_k = \{n_{\text{CPC}}, n_{i,\text{OPC}}\}$ and $\eta_k(D) = \{\eta_{\text{CPC}}(D), \eta_{i,\text{OPC}}(D)\}$ for the Monte Carlo iteration. An exemplary set of $\eta_k(D)$ is shown in Fig. 3.3.2. The parameter set is complemented by the relative (statistical) concentration uncertainties $SE(\bar{n}_k)/\bar{n}_k$ calculated by the standard errors of the means $SE(\bar{n}_k)$, i.e. the interval standard deviations of the measured (bin) concentrations divided by the square root of the number of observations (i.e. time steps). These uncertainties are caused by counting variability (Poisson statistics) and any remaining ambient concentration variability¹⁵. The counting variability and, therewith, the relative measurement uncertainty decreases with increasing total number of particle counts. This means that $SE(\bar{n}_k)/\bar{n}_k$ decreases with increasing \bar{n}_k and increasing sampling duration.

The centerpiece of the retrieval is the actual NSD inversion that is realized by means of a nested MCMC process. As for the evaluation of OPC calibration measurements (cf. Sect. 3.2.2.2), the task of this inversion process is to harmonize the measured n_k

¹⁵Further potential causes for measured concentration variability are sample flow or pressure fluctuations in the instruments (around a temporal average), that are unconsidered in the calculation of the (STP) concentrations.

parameter(s)	description	constraint(s)
$n_{mode,0}$, $n_{mode,1}$ and $n_{mode,2}$	integral particle number concentrations of NSD lognormal modes	positive
CMD_0 , CMD_1 and CMD_2	count median diameters of NSD lognormal modes	mode position confinement: $0.01 \leq CMD_l \leq 1 \mu\text{m}$ for $l \in \{0, 1, 2\}$; ascending mode order and mode separation: $(CMD_{l+1} - CMD_l) / CMD_l \geq 0.5$ for $l \in \{0, 1, 2\}$
GSD_0 , GSD_1 and GSD_2	geometric standard deviations of NSD lognormal modes	no (quasi-)monomodal or excessively broad modes: $1.25 \leq GSD_l \leq 3$ for $l \in \{0, 1, 2\}$
$dn/d\log_{10} D$	NSD, i.e. superposition of NSD modes	drop-off to small particle sizes, i.e. no significant occurrence of particles with diameters smaller than the CPC cutoff: $dn/d\log_{10} D \leq 1$ for $D \leq 5 \text{ nm}$

Table 3.3.2: Prior probability assumptions for the parameters defining the multimodal lognormal NSDs.

with their modeled counterparts \hat{n}_k given by Eq. (3.2.8) as

$$\hat{n}_k = \int_{-\infty}^{+\infty} \eta_k(D) \frac{dn}{d\log_{10} D} d\log_{10} D \quad (3.3.1)$$

with the (logarithmic) NSD $dn/d\log_{10} D$. In contrast to the OPC calibration, however, the inversion process in this case aims to find the solutions for $dn/d\log_{10} D$. In this study, the NSD is parametrized by three lognormal modes. One reason for this is that representing the NSD as a superposition of lognormal modes is common practice, particularly in aerosol models, another reason is that in doing so the inverse problem reduces to the determination of the nine lognormal mode parameters, i.e. the NSD mode integral number concentrations $n_{mode,l}$, count median diameters CMD_l and geometric standard deviations GSD_l . Accordingly, Eq. (3.3.1) can be rewritten as (cf. Sect. 2.3)

$$\hat{n}_k = \int_0^{\infty} \eta_k(D) \cdot \frac{1}{D \ln 10} \sum_{l=0}^2 \frac{n_{mode,l}}{\sqrt{2\pi} \log_{10} GSD_l} \exp \left[-\frac{1}{2} \left(\frac{\log_{10} D - \log_{10} CMD_l}{\log_{10} GSD_l} \right)^2 \right] dD \quad (3.3.2)$$

As the measured concentrations n_k follow a Gaussian PDF, the probability $P(\{\hat{n}_k\} | \{n_k\})$ for the model values to occur given the measurements is symmetric in \hat{n}_k and n_k , so that the likelihood function $P(\{n_k\} | \{\hat{n}_k\})$ can be expressed as

$$P(\{n_k\} | \{\hat{n}_k\}) = \prod_k \frac{1}{\sqrt{2\pi}\sigma_k} \exp \left(-\frac{(n_k - \hat{n}_k)^2}{2\sigma_k^2} \right)$$

with the Gaussian standard deviations σ_k of the modeled \hat{n}_k inferred from the measured relative concentration uncertainties $SE(\bar{n}_k)/\bar{n}_k$ as

$$\sigma_k = \hat{n}_k \frac{SE(\bar{n}_k)}{\bar{n}_k}$$

For the same arguments as in Sect. 3.2.2.2, the prior probabilities for the NSD mode parameters $P(n_{mode,l}, CMD_l, GSD_l)$ are assumed flat, i.e. uniform within physically reasonable limits. The prior probability constraints for the NSD (parameters) are listed in Tab. 3.3.2. As before, the MCMC software tool *emcee* (Foreman-Mackey et al., 2013) is utilized for the maximization of the (posterior) probability, or in other words for the determination of the probable range of NSD solutions under the given uncertainties. The number of Markov chain (burn-in) iterations is adjusted to guarantee representative solution ensembles for each maximization process. Repeating the whole retrieval loop many times propagates all initial parameter uncertainties and finally results in a collective (fully correlated) solution ensemble for the nine NSD mode parameters (cf. Fig. A.3.1). This solution ensemble can be seen as a collection of random samples from the final NSD (parameter) PDFs including all systematic and statistical uncertainties.

The initial PDFs for the aerosol optical properties m and b_{as} , specified in Tab. 3.3.1, are based on particle composition measurements, certain assumptions and literature values. For the MBL, Kristensen et al. (2016) show that the majority of particles in the size range $D \leq 500$ nm are completely volatile, with the measurements indicating a dominance of soluble inorganic sulfates (ammonium sulfate) and a non-negligible contribution from organics, likely biogenic secondary organics (K. Kandler and T. Kristensen, personal communication). Contributions from non-volatile particle components such as sea salt, soot or mineral dust are marginal and predominantly appear as small fractions in internal mixtures with the volatile material. For larger particles, sea salt is assumed to play an important role, while the contribution of mineral dust is noteworthy but subordinate¹⁶. Literature values for the refractive index of dry ammonium sulfate (at the used OPC wavelengths) range from about 1.50 to 1.53 (Toon et al., 1976; Tang, 1996; Michel Flores et al., 2012). A similar refractive index is reported for dry sea salt, that is predominantly made up of sodium chloride (e.g. Shettle and Fenn, 1979). While the refractive index for biogenic secondary organics is subject to some degree of uncertainty, Kim and Paulson (2013) give a most representative value of 1.44. As all these particle types are hygroscopic (to a certain extent), it must be assumed that a considerable fraction of the particles in the humid well-mixed MBL have met relative humidities larger than their DRHs and that they approach the sampling inlets at ambient relative humidities larger than their efflorescence relative humidities (ERH). This means that these particles are most likely hydrated. Knowing the temperature in the OPC measurement chamber, the relative humidity of the aerosol sample at the point of measurement can be calculated from the ambient temperature and relative humidity. The resulting range of relative humidities in the OPCs is converted into estimates for the associated particle growth factors $gf = D/D_{dry}$ using hygroscopic growth functions reported in the literature (Tang and Munkelwitz, 1994; Gao et al., 2006; Varutbangkul et al., 2006; Cheng et al., 2015). The estimated range for the (bulk) refractive index then follows from these growth factor estimates ($gf \leq 1.2$), the (dominant) dry particle refractive indices and the refractive index of water (e.g. Daimon and Masumura, 2007) using a volume mixing rule. Fierz-Schmidhauser et al. (2010) and Michel Flores et al. (2012) show that the utilization of a volume mixing rule to calculate the refractive in-

¹⁶According to Groß et al. (2016), despite their large size the contribution of mineral dust particles to the total aerosol particle volume in the MBL is $< 40\%$.

dex of hydrated particles is often a satisfactory assumption for soluble materials. The imaginary part of the refractive index is assumed to be negligible for particles in the MBL. Because the (majority of) particles are assumed to be slightly hydrated at the point of measurement, they are assumed spherical and, hence, b_{as} is neglected, too.

In the SAL, particle composition measurements, that will be discussed in detail in Sect. 4.1.3 and 4.2.3, identify ammonium sulfate and mineral dust as the major particle components. Since, in contrast to the MBL, ambient relative humidities in the SAL are low and the ambient temperatures fall significantly below the temperatures in the OPC chambers, the relative humidities at the point of measurement certainly are below the ERH for all components, i.e. the particles are measured in dry state. The reported range for the refractive index of African mineral dust covers $1.5 \leq m \leq 1.6$ with an imaginary part of ≤ 0.005 (e.g. Petzold et al., 2009; Schladitz et al., 2009; McConnell et al., 2010; Kandler et al., 2011; Formenti et al., 2011a; Ryder et al., 2013b; Denjean et al., 2016a), therewith comprising the refractive index range for the sulfate (see above). OPC signal broadening owing to varying orientations of aspherical particles is estimated from DDA calculations (performed by J. Gasteiger, LMU). These calculations involve a range of particles (cf. Fig. 2.2.4) with aspect ratios ≤ 1.6 , being a realistic upper bound for the particle asphericity in the present size range (Kandler et al., 2011). Although b_{as} can principally be size-dependent, for simplicity only one average b_{as} is utilized for each OPC. Anyhow, b_{as} only has a minor effect on the total signal broadening b_{total} , as the instrument-induced broadening b is significantly stronger.

Despite the fact that the presented NSD retrieval method is one of the most comprehensive methods to date, some remaining imperfections should not be left unmentioned. For simplicity and because no exact information on the optical particle properties is available, a potential size-dependence of m is not considered, but the (bulk) refractive index picked for each Monte Carlo iteration determines $\tilde{C}_{scat,m}(D)$ for the entire size range of each OPC. Moreover, the same m is used for the SkyOPC and the UHSAS, although the two OPCs operate at different wavelengths. Further neglected is the additional signal broadening, that could be induced by external mixtures of particles having the same size but different refractive indices. However, as both in the MBL and the SAL the dominant particle components are assumed to have similar refractive indices (with overlapping uncertainty ranges), the potential size-dependence of m is expected to be only minor, thus having insignificant impact on the NSD solution. For the same reason, additional signal broadening by external particle mixtures is assumed to not cause significant systematic deviations. Last, differences in m owing to the different OPC wavelengths are small compared to the overall refractive index uncertainty. Another potential source of systematic deviation could be the NSD parametrization itself. Although the multimodal lognormal parametrization is a commonly accepted form to express NSDs, the true NSDs might partly deviate from a multimodal lognormal shape. The NSD retrieval results must, hence, be viewed in the context of this approximation.

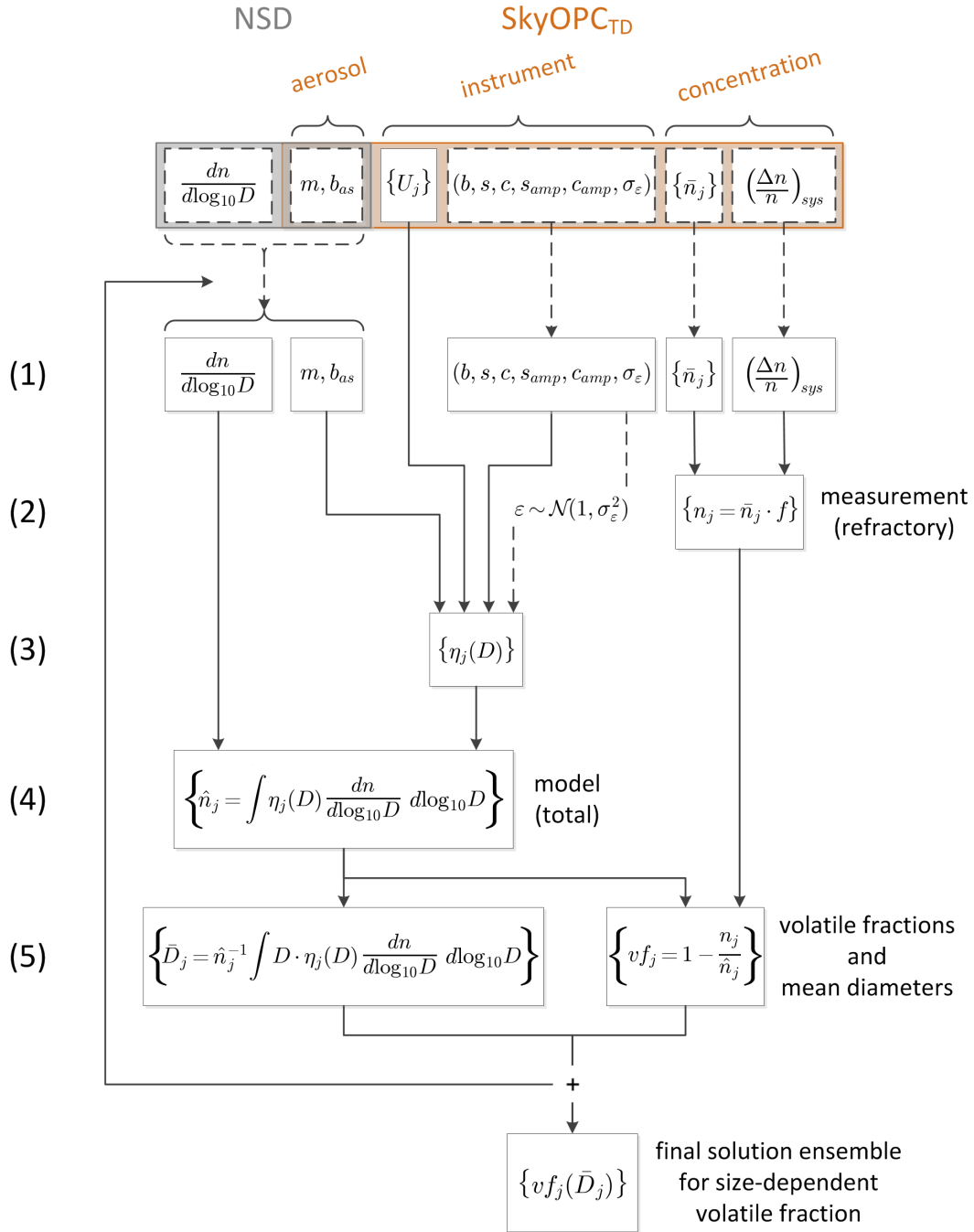


Figure 3.3.3: Flowchart visualizing the derivation of size-dependent particle volatility. Each Monte Carlo iteration starts with random samples (picks) from the initial parameter PDFs (1), that are subsequently used to calculate the refractory particle concentrations for each SkyOPC_{TD} bin (2), the corresponding counting efficiency functions (3) and the (modeled) total particle concentrations (4). The results allow to determine the volatile particle fractions vf_j and mean particle diameters \bar{D}_j for each bin (5). The set of these discrete pairs obtained for each iteration is finally combined to a collective solution ensemble for the size-dependent volatility.

3.3.3 Derivation of Size-Dependent Volatility

To complement the total particle volatility vf_{total} measurements, the combination of SkyOPC_{TD} data and the NSD retrieval solutions are used to infer the size-resolved particle volatility $vf(D)$. $vf(D)$ could be calculated via Eq. (2.4.2) by comparing the total particle NSD, retrieved as explained in Sect. 3.3.2, and a NSD derived in the same manner for the refractory remainder behind the TD. However, for the measurements behind the TD the number of counting efficiency functions and, therewith, the size information is strongly limited. Furthermore, the SkyOPC_{TD} size range does not cover the main part of the NSD, i.e. the accumulation mode size range around $0.1 \mu\text{m}$ containing the majority of particles (cf. Fig. 4.2.19). Accordingly, without an instrument like the UHSAS the post-TD measurements lack a sufficient basis for an informative NSD retrieval. For this reason, $vf(D)$ is derived in an alternative way outlined in Fig. 3.3.3. Like before, the approach is based on a Monte Carlo method. For each iteration a total NSD is randomly picked from the previously retrieved solution ensemble and, in conjunction with this choice, the associated optical particle properties, i.e. the refractive index m and additional signal broadening b_{as} . Simultaneously, the SkyOPC_{TD} instrument response parameters are sampled from the underlying PDFs, just as for the NSD retrieval (cf. Tab. 3.3.1). The resulting set of SkyOPC_{TD} counting efficiency functions $\eta_j(D)$ and the chosen NSD yield the modeled set of bin concentrations \hat{n}_j via Eq. (3.3.1). This set of \hat{n}_j represents the theoretical SkyOPC_{TD} response factoring out the aerosol modification by the TD. The $\eta_j(D)$ and the NSD further allow to calculate a mean particle diameter for each SkyOPC_{TD} bin as

$$\bar{D}_j = \frac{\int_{-\infty}^{+\infty} D \cdot \eta_j(D) \frac{dn}{d \log_{10} D} d \log_{10} D}{\int_{-\infty}^{+\infty} \eta_j(D) \frac{dn}{d \log_{10} D} d \log_{10} D} \quad (3.3.3)$$

In parallel, the set of refractory bin concentrations n_j is calculated for each iteration as follows: First, a set of bin concentrations is sampled from the Gaussian PDFs $\mathcal{N}(\bar{n}_j, SE(\bar{n}_j)^2)$ defined by the measured mean bin concentrations \bar{n}_j and the associated statistical standard errors of these mean values $SE(\bar{n}_j)$. To further account for a potential systematic (collective) concentration bias, this set of bin concentrations is multiplied by $f = 1 + (\Delta n/n)_{sys}$ with the relative systematic concentration deviation $(\Delta n/n)_{sys}$ again sampled from $\mathcal{N}(0, 0.05^2)$. With the resulting refractory bin concentrations n_j and the modeled total concentrations \hat{n}_j the discrete set of volatile fractions vf_j is given by

$$vf_j = 1 - \frac{n_j}{\hat{n}_j}$$

After a large number of iterations, this process finally leads to a representative solution ensemble for the size-dependent volatility $vf_j(\bar{D}_j)$ for $D \gtrsim 0.3 \mu\text{m}$.

In contrast to the total volatility vf_{total} that can in good approximation be interpreted as the number fraction of completely volatile particles, the interpretation of the $vf_j(\bar{D}_j)$ values is more complex. In addition to the fraction of completely volatile particles, these values include the fraction of internally mixed particles leaving the narrow bin size ranges by shrinkage upon losing their volatile components. However, at the

same time each $vf_j(\bar{D}_j)$ value is decreased by the number of internally mixed particles that shrink into the corresponding bin's size range from larger initial diameters. On balance, a $vf_j(\bar{D}_j)$ value must, hence, be interpreted as the net fraction of particles leaving the corresponding bin's size range. Finally, it should be noted that the determined $vf_j(\bar{D}_j)$ values might be afflicted with a minor systematic error. The mean bin particle diameters \bar{D}_j calculated with the total NSD via Eq. (3.3.3) are appropriate for the modeled total bin concentrations \hat{n}_j but might deviate from the actual mean bin particle diameters corresponding to the refractory n_j . This is because both the shape of the NSD and the optical particle properties can change upon passage through the TD. Yet, the corresponding systematic bias in the mean diameters is assumed to be insignificant, first, because the refractive indices of the (dominant) volatile and non-volatile components are similar (see Sect. 3.3.2) and second, because the change in the NSD shape, e.g. its slope within the narrow size range covered by a single bin is certainly moderate.

3.3.4 Derivation of Effective Particle Hygroscopicity

In combination with the NSD retrieval results, the CCNC measurements do not only permit to study the CCN number concentrations n_{CCN} at certain defined water vapor supersaturations, but also provide insight into the aerosol particles' hygroscopic properties. The method used to infer the effective hygroscopicity parameter κ from these combined measurements is introduced in the following and visualized in Fig. 3.3.4. The iterative process starts with a Monte Carlo sampling of all relevant parameters fraught with significant statistical and/or systematic uncertainty. These are the NSD parameters, the measured CCN concentration, the CCNC supersaturation SS_{CCNC} and the variety of parameters determining the loss of CCN at the CPS inlet orifices. While, for the sake of clarity, only a condensed parameter set is shown in Fig. 3.3.4, Tab. 3.3.3 offers a complete list of the relevant parameters and the underlying PDF assumptions. As explained in more detail in Sect. 3.3.3, for the CCNC, the CPC_1 and the CPC_{CPS} the concentration values n_{CCN} , n_{total} and n_{CPS} are sampled from PDFs respecting both the statistical measurement uncertainties and the potential systematic concentration deviations. The difference between n_{total} and n_{CPS} , i.e. $\Delta n = n_{\text{total}} - n_{\text{CPS}}$, the transmission efficiency function for the small or large aperture CPS inlet orifice (determined at $p_{\text{inlet}} \approx 930$ hPa), i.e. $\eta_{\text{os}}(D)$ or $\eta_{\text{ol}}(D)$, and the transmission efficiency function for the exclusive last part of the tubing upstream the CPC_{CPS} , i.e. $\eta_t(D)$, are used to calculate the CCN orifice losses via Eq. (3.2.19) and (3.2.20). The uncertainty of the theoretical $\eta_t(D)$ calculated with the PLC is taken into account by an estimated 10% uncertainty in the underlying diameter grid, being a representative systematic deviation range met when comparing PLC calculations with measurements (e.g. von der Weiden et al., 2009). For $\eta_{\text{os}}(D)$ and $\eta_{\text{ol}}(D)$ this potential systematic diameter deviation is estimated to be 15%, as motivated in Sect. 3.2.2.3. The resulting corrected $\Delta n_{v2.1}$ or $\Delta n_{v2.2}$ must obey the constraint $\Delta n_{v2} \geq 0$, since negative values for the orifice particle losses are non-physical. For the large aperture orifice, a further constraint is given by $\Delta n_{v2.2} \leq \Delta n_{\text{max}}$ with Δn_{max} defined by Eq. (3.2.21) (cf. Sect. 3.2.2.3). If the constraints are met, n_{CCN} is incremented by Δn_{v2} , otherwise the iteration is aborted and the Monte Carlo sampling is repeated. Recalling the fact that size is a

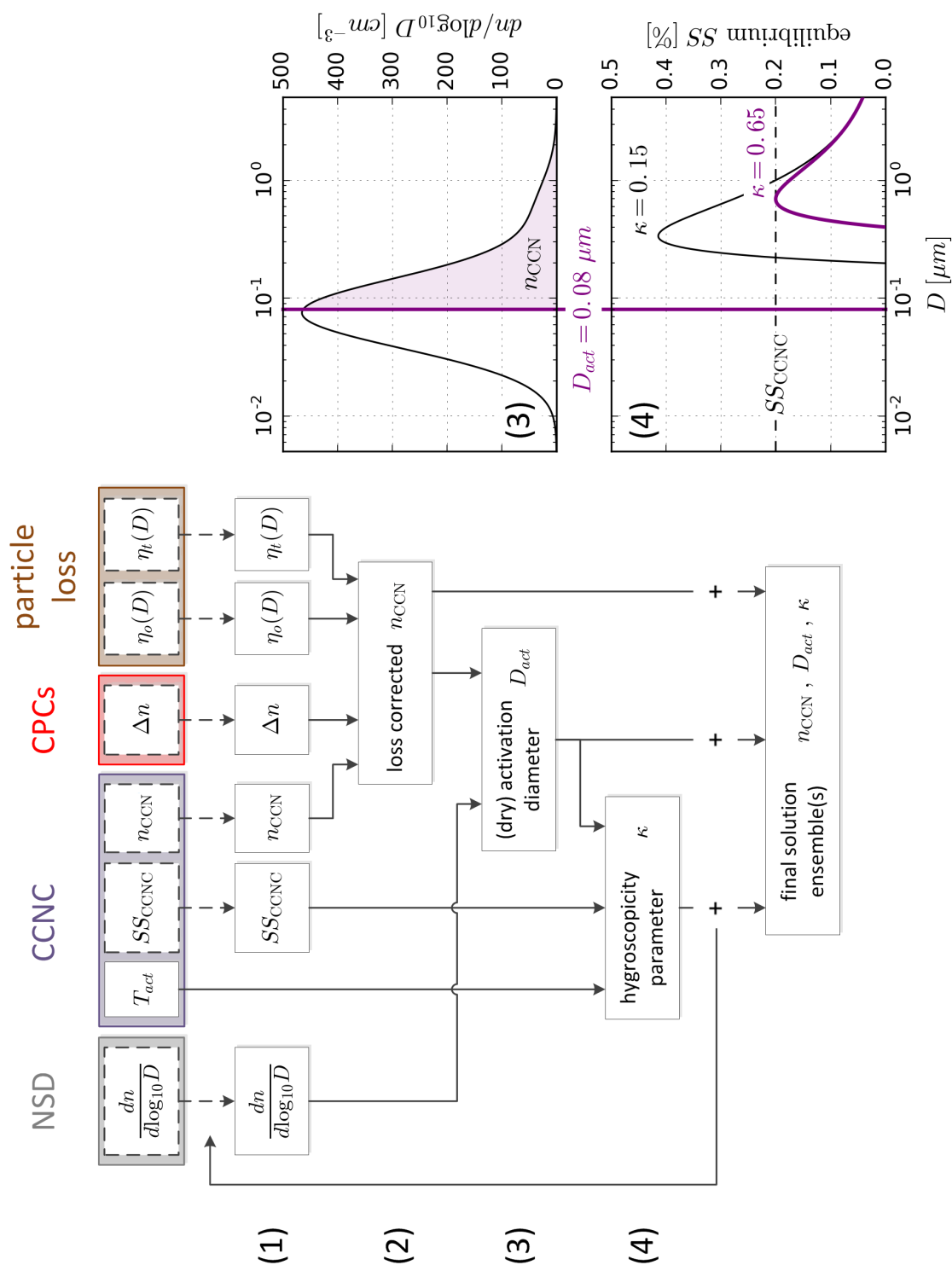


Figure 3.3.4: Flowchart illustrating the derivation of the effective particle hygroscopicity. Each Monte Carlo iteration starts with random samples (picks) from the initial parameter PDFs (1), that are subsequently used to calculate the loss-corrected CCN concentration (2), the (dry) activation diameter (3) and the hygroscopicity parameter (4). The results for each iteration are finally merged into a collective solution ensemble. To the right of the flow diagram, the calculation methods behind steps (3) and (4) are visualized.

parameter(s)	description	random Monte Carlo sampling from...
<i>NSD</i>		
$(n_{mode,l}, CMD_l, GSD_l)$ for $l \in \{0, 1, 2\}$	NSD lognormal mode parameters	NSD retrieval solution ensemble
gf	particle growth factor	$\mathcal{U}([1.0, 1.2])$ for the MBL ^a
<i>CCNC</i>		
n_{CCN}	measured CCN concentration	$\mathcal{N}(\bar{n}_{CCN}, SE(\bar{n}_{CCN})^2)$
$(\Delta n/n)_{sys}$	systematic concentration deviation	$\mathcal{N}(0, 0.05^2)$
SS	supersaturation	$\mathcal{N}(\bar{SS}, \sigma(\bar{SS})^2)$ with the supersaturation mean and standard uncertainty inferred from the $SS(\Delta T)$ calibration curve via the measured ΔT
<i>CPC₁</i>		
n_{total}	measured total particle concentration	$\mathcal{N}(\bar{n}_{total}, SE(\bar{n}_{total})^2)$
$(\Delta n/n)_{sys}$	systematic concentration deviation	$\mathcal{N}(0, 0.05^2)$
<i>CPC_{CPS}</i>		
n_{CPS}	measured particle concentration in CPS	$\mathcal{N}(\bar{n}_{CPS}, SE(\bar{n}_{CPS})^2)$
$(\Delta n/n)_{sys}$	systematic concentration deviation	$\mathcal{N}(0, 0.05^2)$
<i>CPC_{CPS} inlet orifice transmission efficiency $\eta_o(D)$</i>		
$(\Delta D/D)_{sys}$	systematic diameter (grid) deviation	$\mathcal{N}(1, 0.15^2)$
<i>CPC_{CPS} tubing transmission efficiency $\eta_t(D)$</i>		
$(\Delta D/D)_{sys}$	systematic diameter (grid) deviation	$\mathcal{N}(1, 0.1^2)$

^a Inside the SAL the derived NSDs are assumed dry, i.e. $gf = 1$.

Table 3.3.3: List of parameters that are sampled via a Monte Carlo method in the course of the hygroscopicity derivation process and their corresponding PDFs.

very important parameter for whether a particle will activate into a cloud droplet at a given supersaturation (cf. Sect. 2.1.2), the loss-corrected n_{CCN} and the NSD can be used to calculate the activation diameter D_{act} as follows

$$n_{\text{CCN}} = \int_{D_{\text{act}}}^{\infty} \frac{dn}{dD}(D) dD \quad (3.3.4)$$

This means that D_{act} is inferred by integrating the NSD from the upper end of the diameter scale downwards until a particle number concentration equal to n_{CCN} is obtained. An example for such a backward integration is shown in Fig. 3.3.4. The determining factor for droplet activation, however, is the dry particle diameter. Thus, in case that particles around D_{act} are hydrated, D_{act} must first be converted into its dry counterpart before Köhler theory can be applied to study droplet activation. For the MBL, this is done by dividing the D_{act} values calculated via Eq. (3.3.4) by a potential growth factor gf randomly sampled from the uniform PDF $\mathcal{U}([1.0, 1.2])$ (cf. Sect. 3.3.2). With the dry D_{act} and the measured temperature at droplet activation T_{act} , Eq. (2.1.9) allows to calculate the critical supersaturation SS_c (maximum of the Köhler curve) in dependence of the hygroscopicity parameter κ . Here, the influence of T_{act} on the water density ρ_w and surface tension σ (e.g. Cini et al., 1972) is considered. Since the CCNC temperature readings exhibit a high degree of stability, the uncertainty in T_{act} itself is neglected. As shown in Fig. 3.3.4, finding the value for SS_c which satisfies $SS_c = SS_{\text{CCNC}}$ finally yields the effective particle hygroscopicity κ , i.e. the particle hygroscopicity at D_{act} . After a sufficient number of iterations, the presented method propagates all initial parameter PDFs into representative solution ensembles for the loss-corrected n_{CCN} , D_{act} and κ .

The interpretation of the resulting values for D_{act} and κ deserves a more detailed consideration. In the strict sense, D_{act} corresponds to the smallest dry particle diameter able to activate into a cloud droplet only if

- the aerosol is completely internally mixed within a sufficient size range around of the inferred D_{act} , and if
- the assumption that all particles with $D > D_{\text{act}}$ activate holds.

If the former is not the case and the individual particle hygroscopicities in the vicinity of D_{act} vary significantly, there will be activated particles with dry diameters smaller D_{act} and particles larger D_{act} remaining non-activated. Still, D_{act} and the corresponding κ would represent weighted average values. A violation of the second point, on the other hand, potentially introduces a systematic error. When having considerably lower hygroscopicities particles (much) larger than D_{act} could remain non-activated in spite of their size. Backward integration of the complete NSD would not be (entirely) appropriate in such a case and would lead to an overestimation of D_{act} /underestimation of κ . That this error is negligible for the SALTRACE data is justified by the complete information on the size-dependent aerosol properties presented later on (see also Sect. 7.2).

3.3.5 Validation of Results

To verify the validity of the NSD and effective particle hygroscopicity results, they are compared with the ground-based measurements at Ragged Point for suitable low-level flight legs. To guarantee data comparability the comparison intervals are checked for the following requirements:

- The Falcon flight altitude is constant and low enough to fall within the well-mixed boundary layer.
- Both ground-based and airborne measurements are performed in a windward direction from possible local island sources that would contaminate the measurements (differentially). In other words, both measurement platforms sample the same marine air masses.
- The measurements take place under (near-)homogeneous particle concentration conditions.

A total of five airborne in situ sampling intervals during SALTRACE fulfill these criteria. Figure 3.3.5 pictures the detailed situation for 20 June 2013. During the selected comparison interval the Falcon was approaching Barbados from the east at an altitude of 350 m with the in situ wind coming from northeasterly to easterly directions (at a mean speed of about 10 m/s). Northeasterly winds are also reported for the ground station (Kristensen et al., 2016), meaning that both measurement platforms sampled air masses coming from the open ocean only. As can be further seen from Fig. 3.3.5b), the precondition of particle concentration homogeneity is satisfied within the selected in situ sampling interval. Leeward of the island the conditions change and for the same flight level the influence of local pollution is recognizable by considerably increased total particle concentrations n_{total} and an increased total particle volatility vf_{total} . These large amounts of small, highly volatile (secondary) particles can be linked to gaseous precursors from island sources. Figure 3.3.5c) features the vertical profiles of potential temperature Θ and water vapor mixing ratio mr measured by means of the Falcon standard meteorological instrumentation during ascent and descent. These profiles are consistent with the typical situation found for the trade wind boundary layer (e.g. Albrecht et al., 1979; Jung et al., 2013). A humid layer extending from the surface to about 600 m is well-mixed, i.e. exhibits rather constant values of Θ and mr . Following Kristensen et al. (2016), this layer is termed MBL here, while it is also commonly referred to as the sub-cloud layer (Albrecht et al., 1979; Jung et al., 2013). The MBL is capped by a hydrolapse, i.e. a drop in mr . The subsequent layer reaching from the MBL top to the trade wind inversion at about 2 km is referred to as the intermediate layer (Jung et al., 2013) or cloud layer (Albrecht et al., 1979) and features a slight increase in Θ , i.e. moderately stable stratification, and a slight decrease in mr . With a Falcon flight altitude of 350 m, the presented airborne sampling interval evidently falls within the mixed MBL. In summary, these findings demonstrate the suitability of the selected time interval for a comparison between the airborne and ground-based measurements.

The results of the comparison measurement on 20 June are shown in Fig. 3.3.6. Accordingly, the NSD retrieval results are consistent with the ground-based NSD measurements down to diameters of about 70-90 nm. Although still being conform within

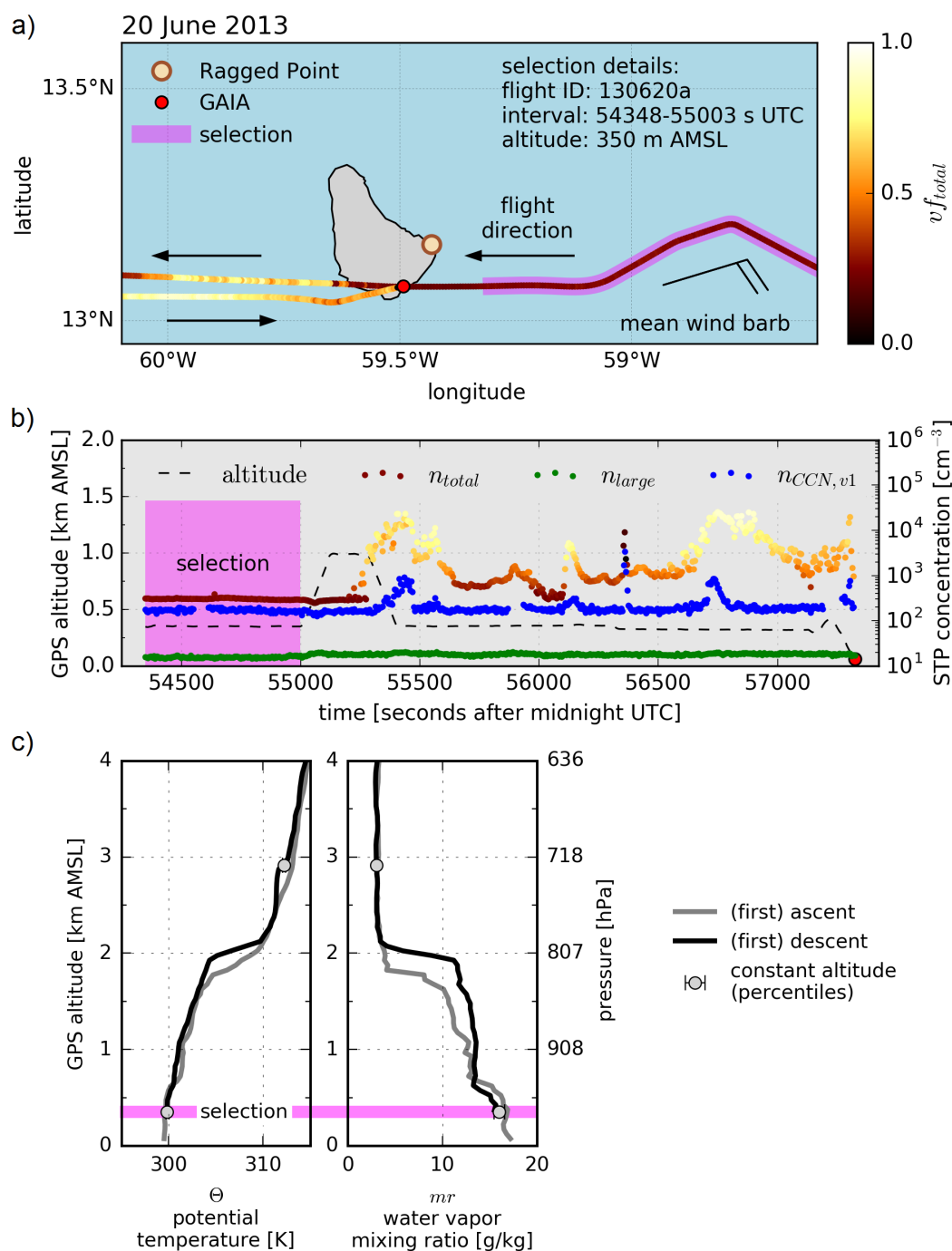


Figure 3.3.5: Falcon sampling interval selection for the comparison with the ground-based measurements at Ragged Point. The upper plot (a) shows the Falcon flight track color-coded with the total particle volatility $v_{f_{total}}$ and further visualizes the average horizontal wind vector for the selected interval by means of a wind barb. The flight track altitude profile and the particle concentration time series for n_{large} , $n_{CCN, v1}$, and n_{total} , color-coded with $v_{f_{total}}$, are featured in the middle plot (b). The two bottom plots (c) show the vertical Falcon measurements of potential temperature and mixing ratio with an indication of the selection altitude. The legend term “percentiles” is short for the median, 16 and 84th percentiles.

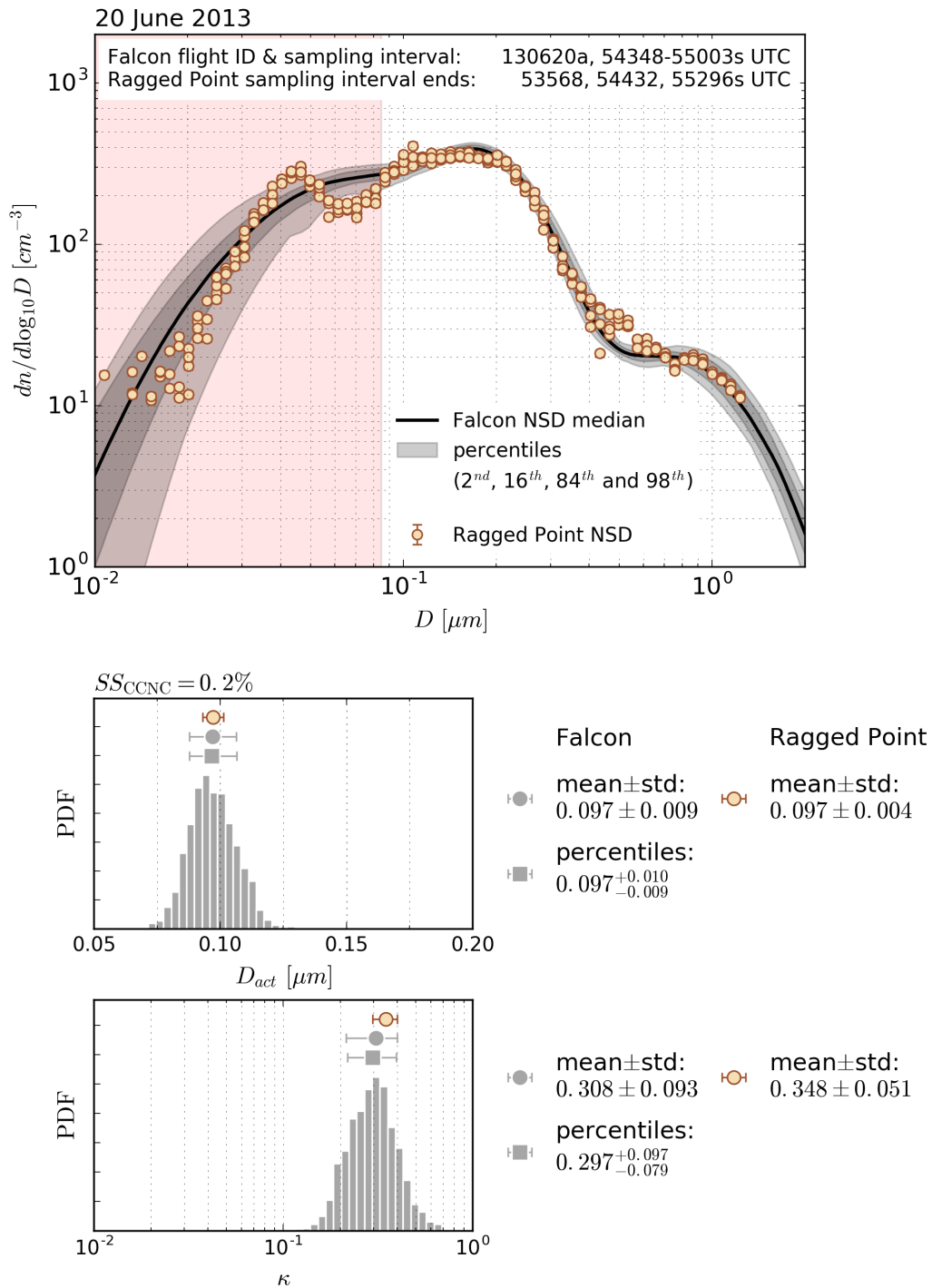


Figure 3.3.6: Comparison of particle NSD (upper plot), activation diameter (middle plot) and effective hygroscopicity (lower plot) derived from the airborne measurements with the corresponding data obtained from the ground-based measurements at Ragged Point on 20 June 2013. The respective sampling interval specifications are noted above the NSDs. Shown concentrations refer to STP conditions. The legend term “percentiles” in the lower two plots is short for the median, 16 and 84th percentiles.

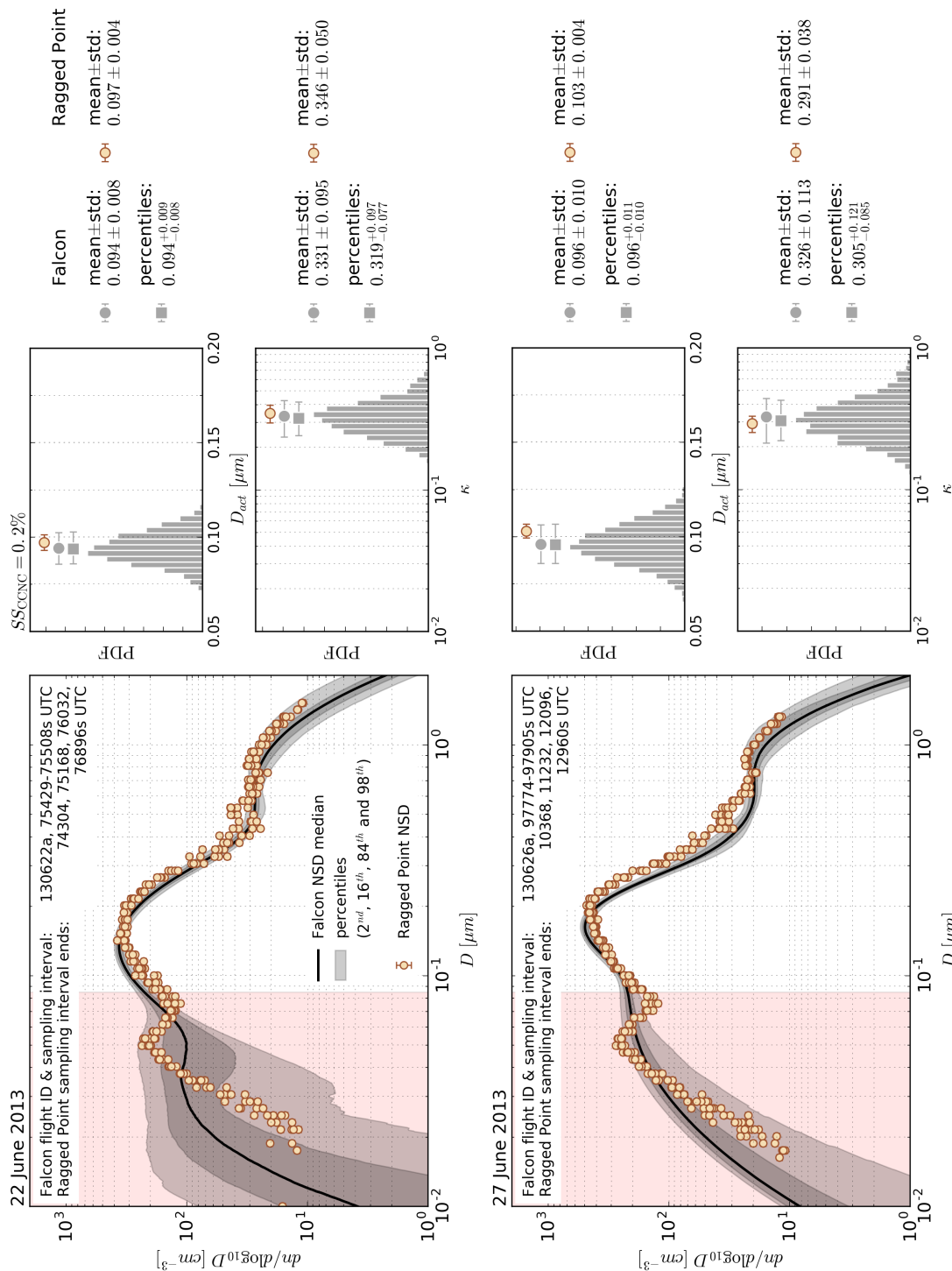


Figure 3.3.7: Same as Fig. 3.3.6 but for the comparison measurements on 22 and 26 June 2013.

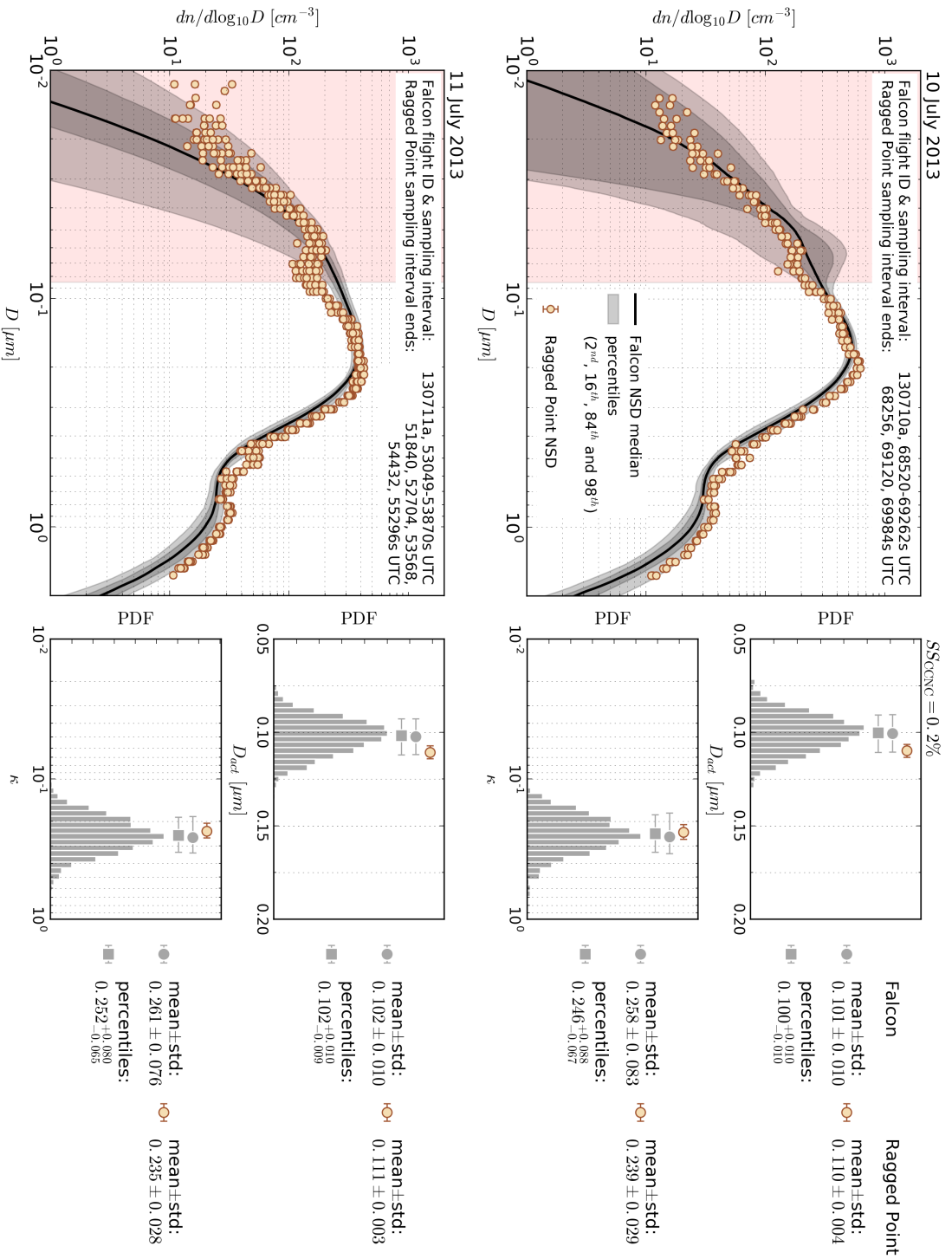


Figure 3.3.8: Same as Fig. 3.3.6 and 3.3.7 but for the comparison measurements on 10 and 11 July 2013.

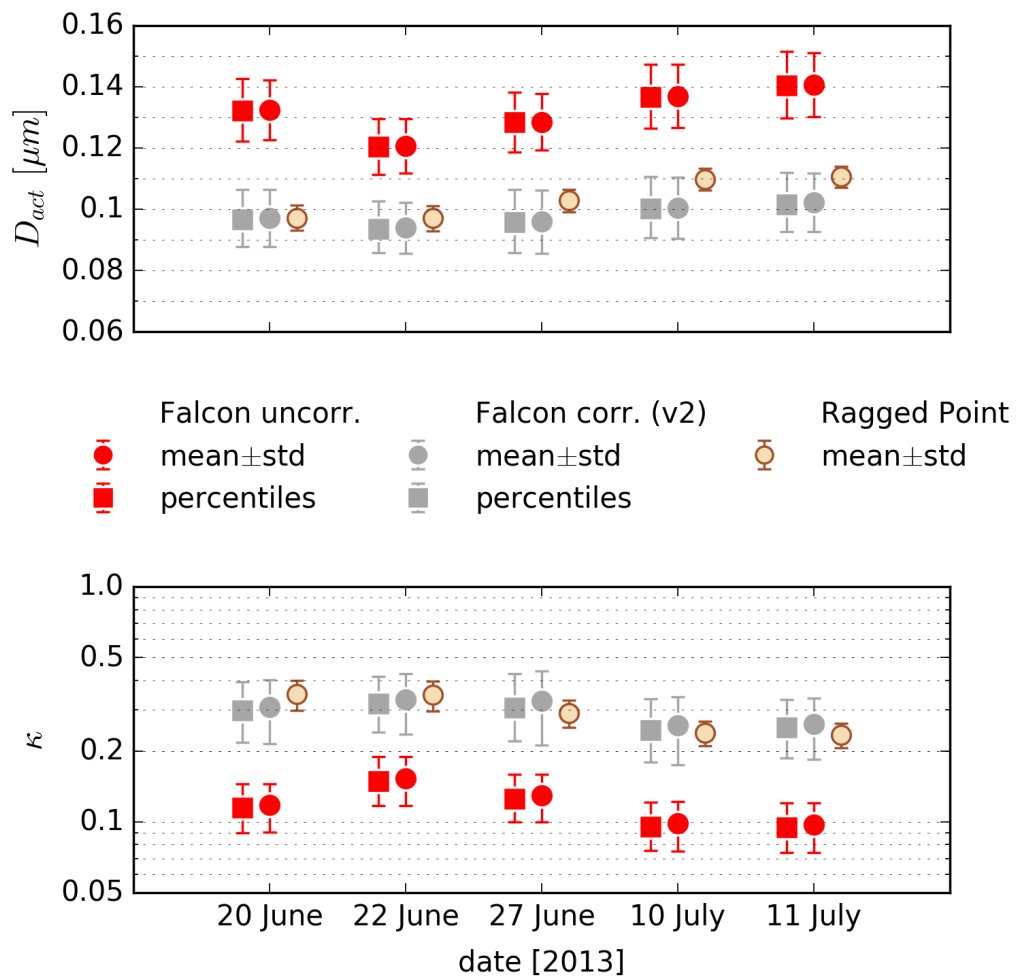


Figure 3.3.9: Overview of all activation diameter (upper plot) and effective hygroscopicity (lower plot) results for the comparison intervals. In addition to the derivation results based on the corrected CCN concentrations (gray markers), the red markers represent the biased results obtained when using the uncorrected CCN concentrations. The legend term “percentiles” is short for the median, 16 and 84th percentiles.

the range of uncertainty, for lower diameters (red-shaded range) some deviations between the NSDs are apparent, namely the retrieval results fail to fully reproduce the Aitken mode peak between 40 and 50 nm that is seen by the Ragged Point measurements. However, this is hardly surprising keeping in mind that no size-resolved information is available for the retrieval process between the lower UHSAS cutoff (about 85 nm for the MBL aerosol) and the CPC cutoff (around 10 nm). In consequence, the retrieval is incapable to resolve any fine NSD structures in this size range, whereas it is capable of fully reproducing the NSD for larger particle diameters. The complete NSD (mode parameter) solution ensemble is shown in Fig. A.3.1. In addition to the NSD, Fig. 3.3.6 features the results for the activation diameter D_{act} and the effective particle hygroscopicity κ . As for the NSD results, the solutions for D_{act} and κ match the ground-based measurements within the range of uncertainty. It should be noted, however, that in contrast to the directly comparable κ values the D_{act} values do not necessarily have to be in exact agreement (even for identical SS), since D_{act} depends on the absolute activation temperature T_{act} , that can slightly differ between the airborne and ground-based measurements. Hence, κ is the more meaningful comparison quantity. Figure 3.3.7 and 3.3.8 show the same results for the other comparison intervals and reveal that good accordance is found for all investigated cases.

The airborne D_{act} and κ values are derived based on the CCN concentrations corrected via Eq. (3.2.19) (v2 correction scheme). As demonstrated in Tab. A.3.1, these results are conform with the ones obtained when using the alternative (v2) CCN concentration correction defined by Eq. (3.2.20), but exhibit less uncertainty. The complete set of derived D_{act} and κ values and their ground-based counterparts is shown in Fig. 3.3.9. Aside from the results for the corrected CCN concentrations, Fig. 3.3.9 displays the solutions for D_{act} and κ based on the uncorrected CCN concentrations. Obviously, the latter significantly overestimate the ground-based (true) values for D_{act} and, hence, significantly underestimate the κ values. For the sake of completeness, Tab. A.3.1 features the D_{act} and κ values using the CCN concentrations corrected by the method described in Dollner (2015). Overestimating the CPS inlet losses, these values slightly under- and overestimate D_{act} and κ , respectively. In conclusion, the presented comparison measurements prove the adequacy of the CCN correction scheme discussed in Sect. 3.2.2.3, the NSD and hygroscopicity derivation processes introduced in Sect. 3.3.2 and 3.3.4, and the appropriateness of the all underlying assumptions.

Whereas, according to the presented results, the κ values derived for the main SS of 0.2% are consistent with the ground-based measurements, systematic deviations are observed for the other SS , i.e. for the airborne scanning CCNC column (A) measurements. While the Ragged Point data show no significant trend in κ with varying SS for $0.1 \lesssim SS \lesssim 0.7\%$ (Kristensen et al., 2016), the values derived for the column A measurements exhibit an increasing trend in κ with decreasing SS . As treated in detail in Sect. A.3.3, there is evidence suggesting that a systematic bias in the ΔT reading for this column induced by too fast changes in the temperature settings is causing these deviations in κ . Owing to this (hardly correctable) measurement bias, only the results for the main SS of 0.2% are presented in the following. However, a complete list of results for all SS is given in Tab. B.5.5 to B.5.11.

3.4 Additional Tools

Apart from the in situ and remote sensing data products introduced in the preceding sections, some further tools are used to visualize SAL appearance and transport in Ch. 4. In the following, these tools will be briefly presented.

CIMSS SAL Product

The SAL satellite product of the Cooperative Institute for Meteorological Satellite Studies (CIMSS, University of Wisconsin-Madison) is an imagery created by differentiating the 12 and 10.7 μm infrared channels on the Geostationary Operational Environmental Satellite (GOES) and the 12 and 10.8 μm infrared channels on the Meteosat satellite¹⁷. The algorithm is sensitive to the presence of dry and/or dusty air masses in the mid-level tropospheric pressure range of $p \approx 600 - 850$ hPa (Dunion and Velden, 2004). 3-hourly product images are available at the CIMSS Homepage (<http://tropic.ssec.wisc.edu/misc/sal/info.html>).

COSMO-MUSCAT

The COSMO-MUSCAT model, short for Consortium for Small-Scale Modeling Multi-scale Chemistry Aerosol Transport Model, is a regional dust model system computing the height- and size-resolved distribution of Saharan dust and its evolution during transport including radiative effects and feedbacks (Heinold et al., 2007, 2011). The model system consists of the non-hydrostatic model COSMO as the meteorological driver, and the online-coupled 3D chemistry tracer transport model MUSCAT. The model results for SALTRACE used in this study were provided by B. Heinold, TROPOS.

LAGRANTO

The Lagrangian Analysis Tool (LAGRANTO) of the Swiss Federal Institute of Technology in Zurich is a tool to compute air parcel trajectories (Wernli and Davies, 1997; Sprenger and Wernli, 2015). The LAGRANTO simulations used here are based on 6-hourly ERA-Interim reanalysis data (Dee et al., 2011) of the European Centre for Medium-Range Weather Forecasts (ECMWF). The ERA-Interim data set is available at the public ECMWF database (apps.ecmwf.int/datasets). The trajectory analysis was carried out by A. Schäfler and T. Götsch, DLR who made their results available for this study.

¹⁷For more recent GOES satellites missing a 12 μm channel, a similar SAL-tracking algorithm was developed substituting the 10.7 and 12 μm channels with 3.9 and 10.7 μm channels, respectively (Dunion and Velden, 2004).

Chapter 4

Results

The following chapter presents all results relevant to this study based on the instruments, data evaluation methods and other tools introduced in Ch. 3. First, Sect. 4.1 investigates the dust layer over Barbados on 10 and 11 July 2013 in full detail as an example of an intense SAL event in the Caribbean. Section 4.2 then widens the scope from this example case to the overall picture of the SAL met during SALTRACE on both sides of the North Atlantic.

4.1 Intense Dust Event in the Caribbean

The North African dust event investigated on 10 and 11 July 2013 represents the most pronounced one in the Caribbean region during the entire campaign. For the associated flights, the airborne sampling strategy was extensive vertical profiling (cf. Tab. 3.1.1). Thanks to the resulting high vertical resolution and the high dust occurrence, these flights are perfectly suited to draw a detailed picture of the Caribbean SAL and its aerosol.

Figure 4.1.1a) gives an overview of the horizontal appearance of the SAL in the temporal proximity of flight 130711a by means of the CIMSS satellite product and COSMO-MUSCAT dust AOD contours (see Sect. 3.4). Both the satellite product and the modeled AOD contours demonstrate that during the period in question high concentrations of dust were present in the Caribbean and, particularly, in the flight track vicinity. The figure further reveals the wave-like structure of SAL transport, which is caused by periodic interruptions of the dusty air masses crossing the North Atlantic by dust-free ones brought in from southeasterly directions (in the course of AEW passages; cf. Sect. 1.2). This is also apparent from the backward trajectories shown in Fig. 4.1.1b). These trajectories, filtered for Saharan origin and ending in the vertical column over Barbados, are pushed northwards along their course over the Atlantic occasionally performing an anticyclonic motion before finally approaching the Caribbean island from northeasterly directions. The history of the SAL air masses, represented by the trajectories reaching Barbados at $p \lesssim 800$ hPa (cf. Sect. 4.1.1.1) shows neither mentionable cloud liquid water content (CLWC) nor near-saturation relative humidities $rh \gtrsim 80\%$. Apart from this main SAL transport, for 12 UTC there seems to be additional (differential) transport of Saharan air masses reaching the Caribbean at lower more humid levels. For 18 UTC, however, no such additional

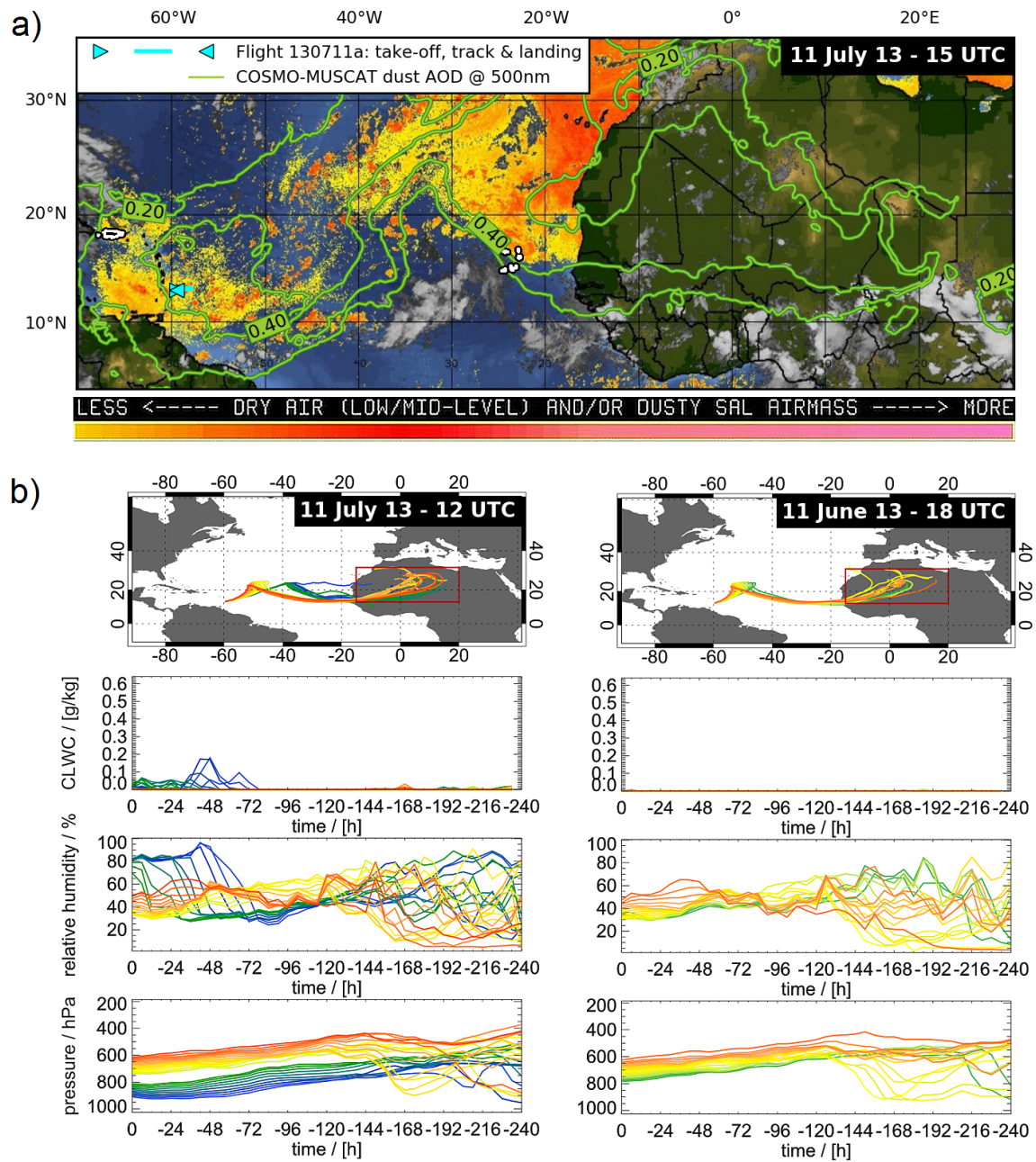


Figure 4.1.1: SAL presence over Barbados during flight 130711a and its previous transport. The top graph (a) shows the CIMSS SAL-tracking satellite product (at 15 UTC) overlaid with dust AOD contours calculated with the COSMO-MUSCAT model (green; also for 15 UTC). Further indicated are the Falcon flight track (cyan; cf. Fig. 3.1.4) and the locations of Barbados (covered by the flight track), Cabo Verde and Puerto Rico (all white-rimmed). The bottom graphs (b) feature LAGRANTO backward trajectories based on ERA-INTERIM data starting from the vertical column over Barbados (at 12 and 18 UTC). The trajectories are color-coded according to their pressure levels over Barbados. The entirety of trajectories is filtered for the ones crossing Northwest Africa (red box) within their 10 days history. In addition to their routes, the graphs exhibit the progress of trajectory cloud liquid water content (CLWC), relative humidity and pressure. Trajectories with $p \lesssim 800$ hPa (light green to red) reach Barbados within the SAL.

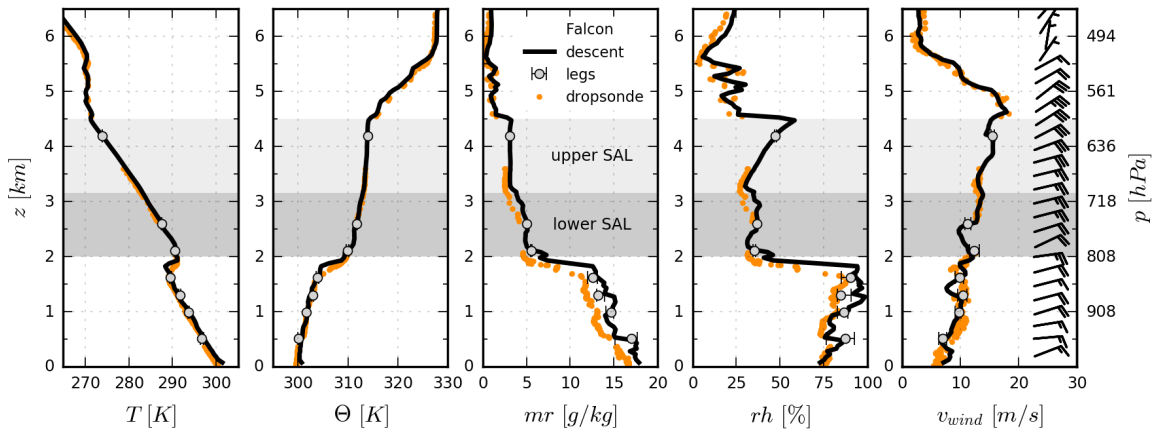


Figure 4.1.2: Vertical profiles of meteorological parameters measured by the Falcon standard instrumentation during flight 130711a in the course of a stepwise descent, and by a dropsonde previously launched from a high altitude. T , Θ , mr , rh and v_{wind} denote temperature, potential temperature, water vapor mixing ratio, relative humidity and horizontal wind velocity, respectively. The data for the constant altitude flight legs are represented by their medians (round markers), 16 and 84th percentiles (error bars). For a Gaussian distribution these percentiles approximately correspond to the mean \pm one standard deviation. In addition to the absolute values for the horizontal wind velocity, the rightmost graph features the horizontal wind barbs (measured by the aircraft instrumentation).

low-level transport occurs. All trajectories consistently exhibit a notable descent from the Northwest African coast towards the Caribbean. These supplementary information provide a background for the following in situ results.

4.1.1 Vertical Profiles

4.1.1.1 Meteorological Parameters

The vertical appearance of the layer in the Caribbean in terms of meteorological parameters like temperature, humidity and wind is shown in Fig. 4.1.2 using the measurements of flight 130711a. These vertical profiles, determined by means of a dropsonde and the aircraft's standard meteorological instrumentation, are (to a large extent) representative for the entire intense dust event on 10 and 11 July (cf. Fig. B.1.1). At an altitude of about 2 km (800 hPa) a distinct temperature inversion leading to a sudden increase in Θ (here, about 5 K within 250 m), the so-called trade wind inversion is apparent. This trade wind inversion coincides with a strong hydrolapse, i.e. a pronounced drop in humidity from near-saturation to $rh < 50\%$. Both trade inversion and hydrolapse define the base of the SAL. At about 4.5 km (600 hPa) a second notable inversion occurs. This inversion capping the SAL is less abrupt while more sustained than the trade wind inversion, with Θ increasing by less than 15 K over a distance of about 1 km. Again, the inversion is accompanied by a decrease in humidity. Between SAL base and ceiling, Θ and mr remain rather constant. Yet, a closer inspection reveals a subdivision of the layer around 3.2 km, with the lower part of the SAL being

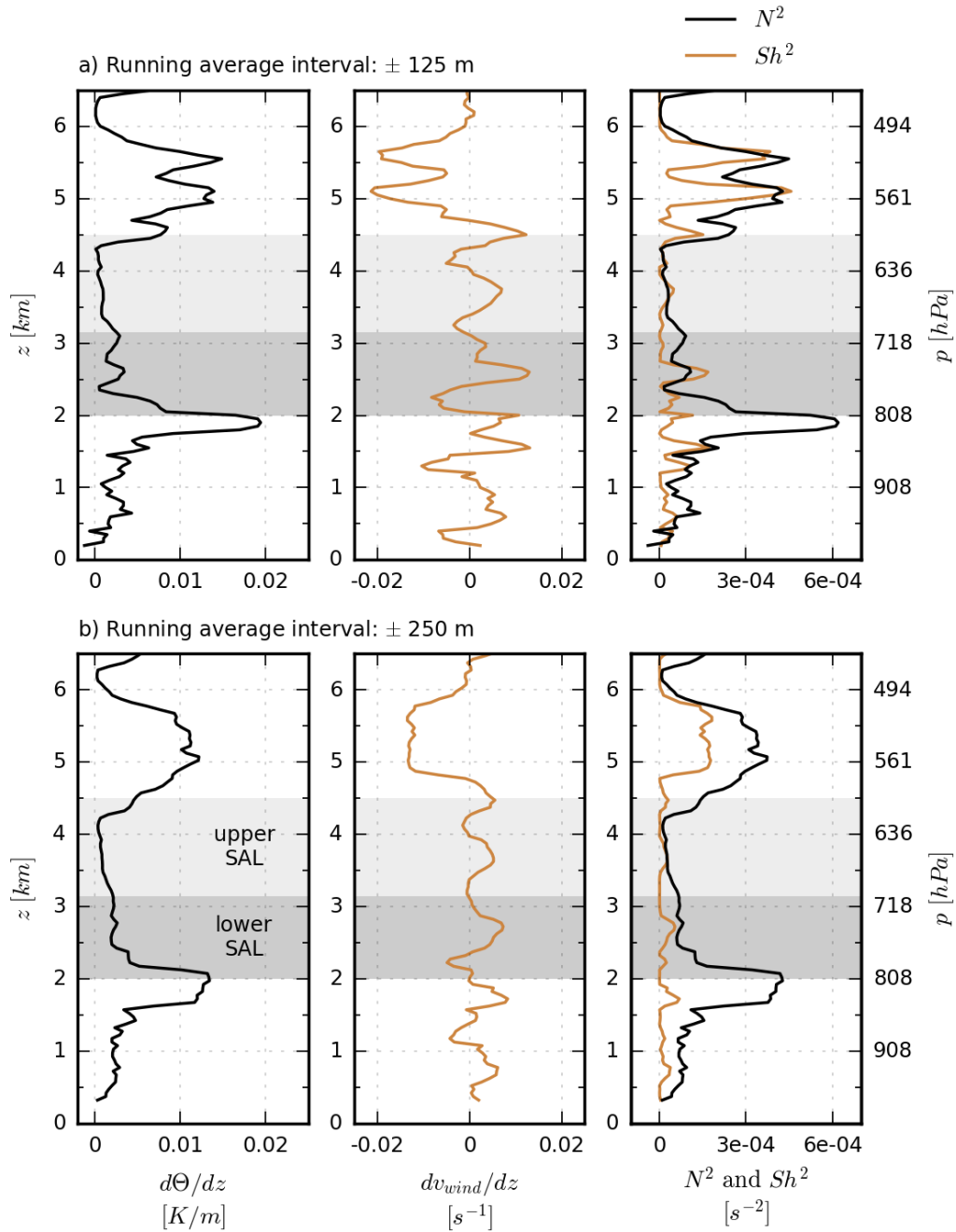


Figure 4.1.3: Vertical stability indicators derived from the meteorological parameter measurements during flight 130711a. The left and middle panels display the vertical profiles of the potential temperature gradient $d\Theta/dz$ and wind shear $Sh = dv_{wind}/dz$, respectively. In the upper and lower rows a running average interval of ± 125 (a) and ± 250 m (b) is applied to smooth the otherwise noise-affected data in order to reveal the general features. In the right panels the squared Brunt Väisälä frequency $N^2 = \frac{g}{\Theta} \frac{d\Theta}{dz}$ is confronted with the squared vertical wind shear Sh^2 .

more humid in terms of mr and colder in terms Θ than the upper part. The vertical profile for the horizontal wind shows an almost monotonic moderate increase in wind speed with altitude up to the SAL top height at near-uniform northeasterly to easterly directions. Coinciding with the increase in Θ at the SAL's capping inversion the wind speed then decreases at a faster rate with the wind barb indicating at turn-over to more northerly directions.

From these meteorological parameters measures for the stability of the SAL can be derived. Figure 4.1.3 shows the vertical profiles for the potential temperature gradient $d\Theta/dz$ and squared Brunt-Väisälä frequency $N^2 = \frac{g}{\Theta} \frac{d\Theta}{dz}$. Positive values of N^2 cause restoring forces to vertical air parcel displacement. The more positive the value of N^2 , the stronger vertical motions are suppressed. Contrarily, vertical wind shear, i.e. the vertical gradient of horizontal wind speed $Sh = dv_{wind}/dz$ induces turbulent vertical mixing. The ratio between these two opposing effects, quantified by N^2 and Sh^2 respectively, ultimately gives an indication for the presence or absence of vertical mixing and the degree of stability, as discussed in Ch. 5. As apparent from Fig. 4.1.3, at the trade wind inversion the highest values of N^2 occur while Sh^2 is negligibly small. On the other hand, at the SAL's capping inversion the values of Sh^2 are relatively enhanced, and the present strong wind shear partially even results in $Sh^2 \geq N^2$. However, also here typically $Sh^2 < N^2$. Inside the SAL, both the values for N^2 and Sh^2 are close to zero (though positive), with a slight enhancement in N^2 and the ratio N^2/Sh^2 in the lower part of the SAL.

4.1.1.2 Particle Concentrations and Total Particle Volatility

The vertical aerosol distribution during the dust event is closely linked to the presented SAL structure. As can be seen from Fig. 4.1.4 the total (STP) particle concentration n_{total} increases at the transition from the lower troposphere to the SAL, from average values of about 275 to 375 cm^{-3} (discounting the peaks attributable to local island pollution at lower levels). Such a concentration increment coinciding with the trade wind inversion is observed also for all other integral particle concentrations, least pronounced for the smallest (n_{small}) and most pronounced for the largest particle sizes (n_{large} and n_{giant}). For instance, n_{large} increases by more than 100% at the base of the SAL from about 20 to above 40 cm^{-3} . Within the SAL altitude range n_{total} remains nearly constant. However, in parallel to the change in mr and Θ from the lower to the upper part of the SAL the particle NSD shifts. n_{large} , n_{giant} and n_{acc} are significantly depleted in the upper SAL to values of about 70% of the respective concentrations in the lower part of the layer. In contrast, n_{small} is enhanced by about 40% in the upper SAL. The relative enhancement in the number of small particles is accompanied by a notable increase in total particle volatility vf_{total} from about 0.15 to 0.3. At the transition from the SAL to the troposphere above another considerable rise in n_{small} and vf_{total} takes place. Despite the simultaneous decrease in n_{acc} , n_{large} and n_{giant} — the latter two size classes completely disappear above the SAL — this rise in n_{small} is so strong that it leads to the maximum of n_{total} occurring above the SAL with values larger 500 – 1000 cm^{-3} (at $vf_{total} \geq 0.5 - 0.6$).

The number concentration of CCN¹ at $SS = 0.2\%$, i.e. n_{CCN} qualitatively follows the vertical profile of n_{80} , as demonstrated in Fig. 4.1.5. Therewith, not only all

¹Here and for all other continuous profiles, n_{CCN} represents the CCN concentration corrected for particle losses via scheme v1, i.e. $n_{CCN,v1}$ (see Sect. 3.2.2.3). It should be recalled that these values are assumed to slightly overestimate the true CCN concentrations (cf. Sect. A.2.3).

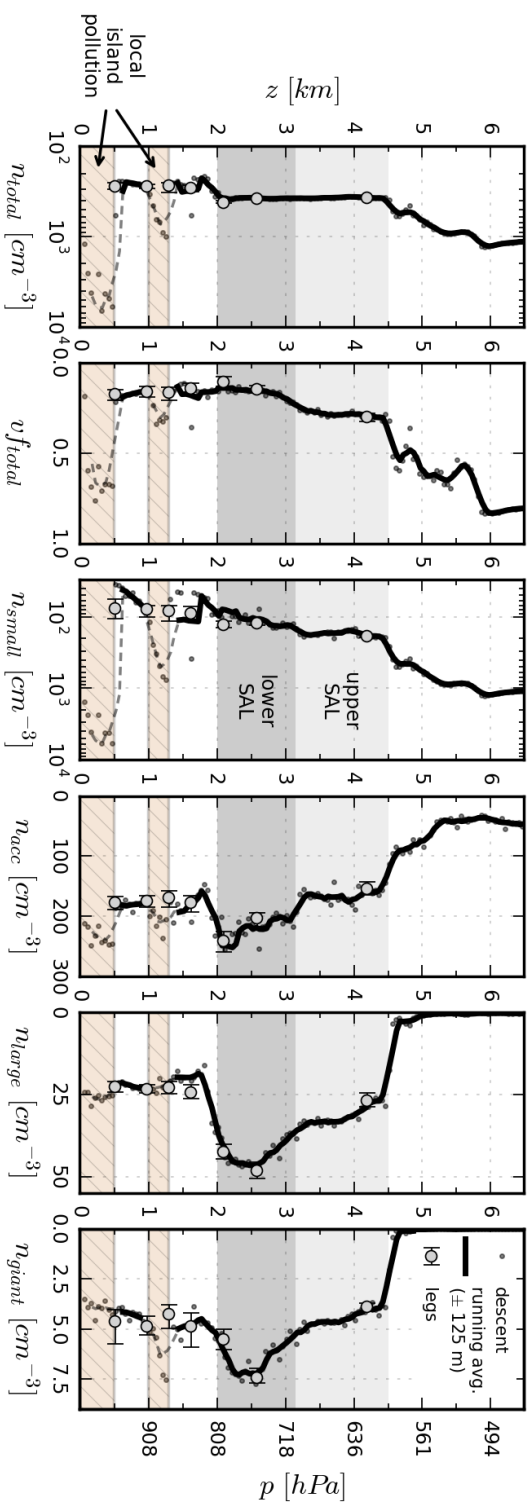


Figure 4.1.4: Vertical profiles of different integral particle concentrations and total particle concentration measured during flight 130711a. n_{total} denotes the total particle concentration, n_{small} , n_{acc} , n_{large} and n_{giant} the integral concentration of particles with diameters $D \lesssim 80$ nm, $80 \lesssim D \lesssim 300$ nm, $0.3 \lesssim D \lesssim 1.5$ μm and $D \gtrsim 1.5$ μm , respectively. The individual data points represent the measurements during aircraft descent, the solid lines running averages of these data (interval ± 125 m). Constant altitude flight leg data are represented by their medians, 16 and 84th percentiles (gray markers and error bars). All concentrations refer to STP conditions. Height intervals influenced by local pollution from Barbados (cf. Fig. 3.3.5) are indicated by brown bars.

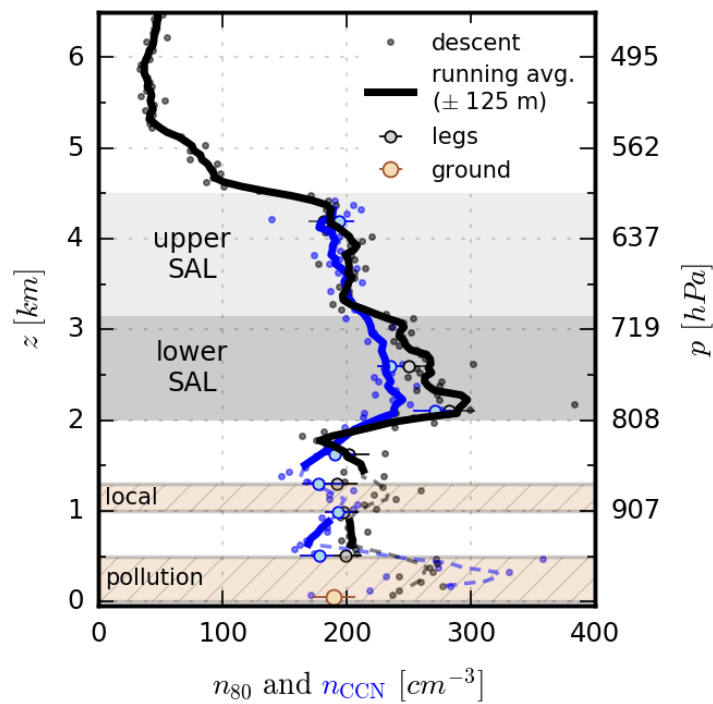


Figure 4.1.5: Vertical profiles of n_{80} (black) and $n_{CCN,v1}$ (blue) measured during flight 130711a. The data are presented in the same way as in Fig. 4.1.4. In addition to the vertical profiles, the mean n_{CCN} for the ground-based measurements (at the same SS of 0.2%) is indicated by the brown marker, together with its \pm one standard deviation range.

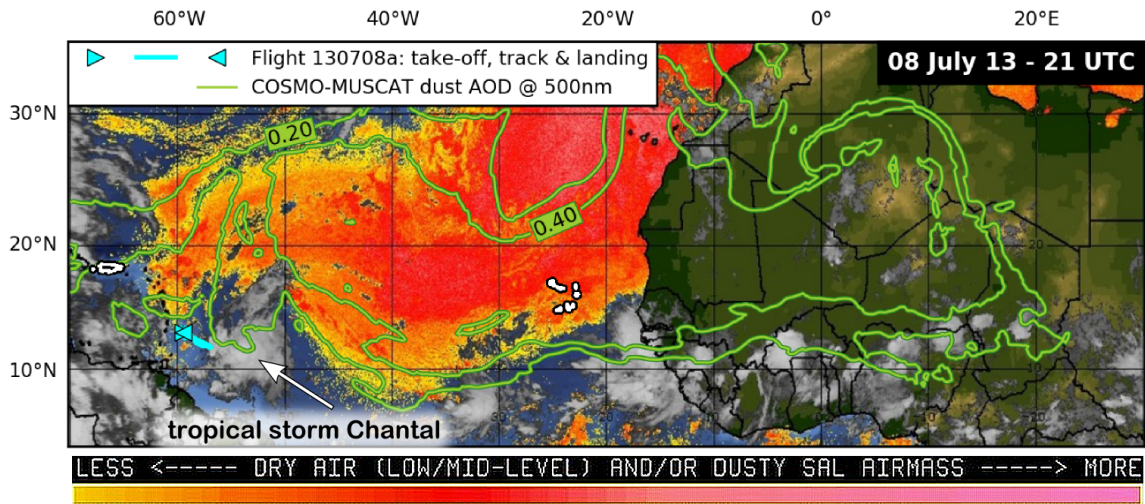


Figure 4.1.6: Appearance of the SAL during flight 130708a, that aimed to sample the dust-free air mass previous to the passage of tropical storm Chantal. Chantal approached Barbados from southeasterly directions, i.e. along the direction of the white arrow before striking the island on 9 July. Details on the satellite product and modeled dust contours are given in Fig. 4.1.1 and Sect. 4.1.

integral particle concentrations in the size range $D \gtrsim 80$ nm but also n_{CCN} experience their maximum within the SAL, precisely in its lower part. Here, n_{CCN} is enhanced by almost 30% compared to the lower troposphere (including the MBL) with average values increasing from about 185 to 235 cm^{-3} . Like all integral particle concentrations except for n_{total} and n_{small} , n_{CCN} then again decreases in the upper part of the SAL. However, compared to the other concentrations this decrease is slightly less pronounced (with a reduction to only about 80%), which is apparent from the convergence of the n_{CCN} and n_{80} profiles. This suggests that, accompanied by the enhancements in n_{small} and vf_{total} , a transition in the CCN properties of the SAL aerosol occurs between its lower and upper part.

As already stated for the meteorological parameter profiles, the presented features of the SAL aerosol during flight 130711a, particularly the SAL subdivision with all its characteristics, are similarly observed for flight 130710a (see Fig. B.1.1). This means that these features are representative for the entire intense dust event impacting the Caribbean area during that period. As discussed in Ch. 5, the subdivision of the layer with the presented vertical features suggests aerosol entrainment into the upper SAL from the overlying troposphere.

4.1.2 Comparison with Dust-Free Air Mass

On 8 July, before the intense dust event, the airborne measurements were intended to investigate the vertical aerosol distribution under SAL absence, i.e. dust-free conditions. Figure 4.1.6 shows the horizontal appearance of the SAL during the corresponding flight 130708a, again using the CIMSS satellite product and COSMO-MUSCAT dust AOD contours. As indicated, during this flight the SAL started to become displaced from the Caribbean region by southeasterly air masses comprising tropical storm Chantal.

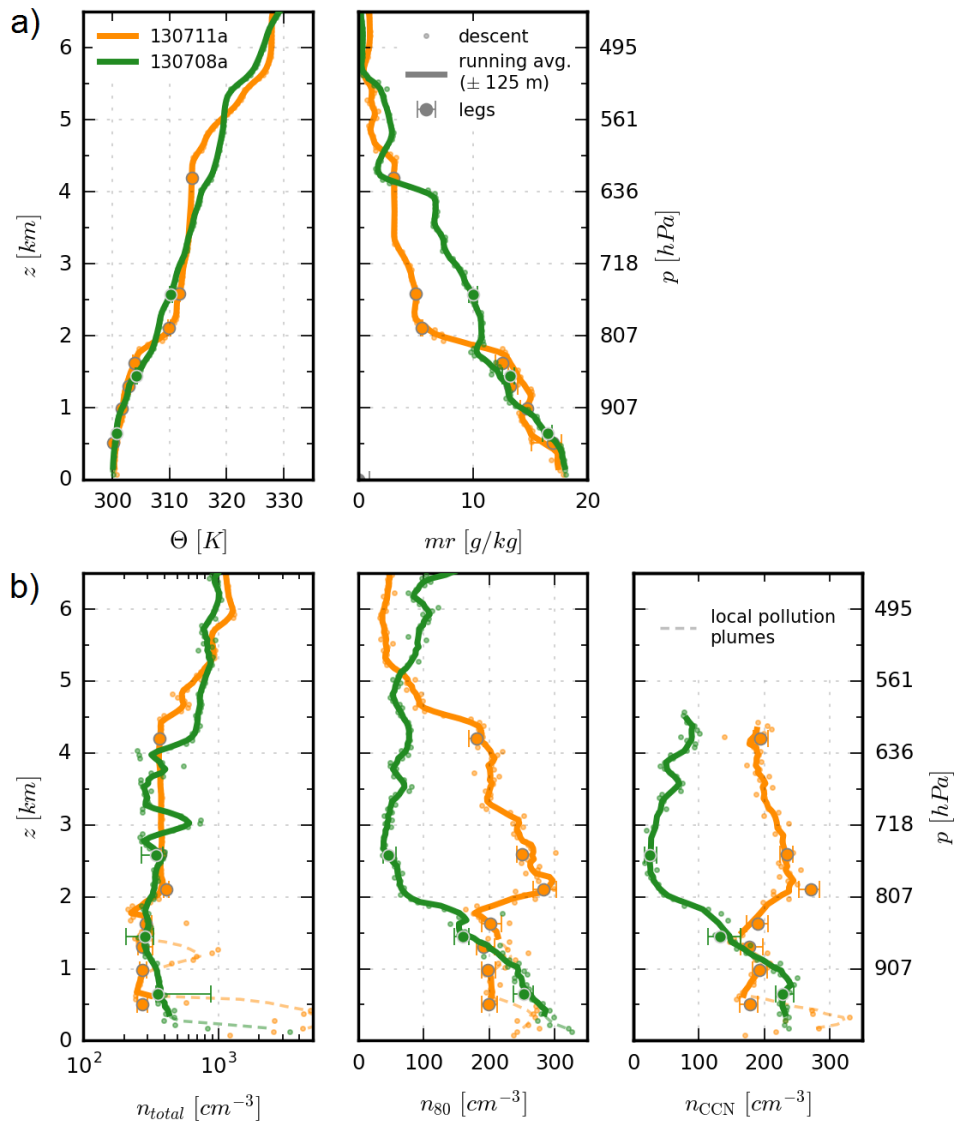


Figure 4.1.7: Comparison between vertical profiles of (a) meteorological parameters and (b) particle concentrations measured in the vicinity of Barbados during flight 130711a (orange) in presence of the SAL and during flight 130708a (green) in a SAL-free atmospheric column. The data are visualized in the same way as before.

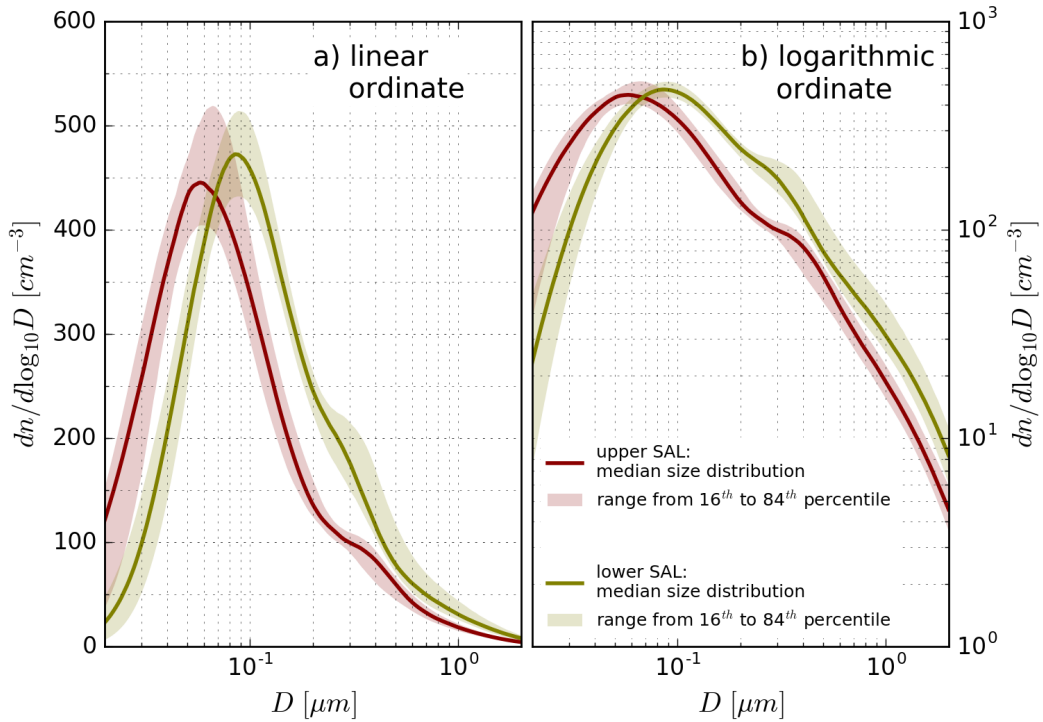


Figure 4.1.8: Particle NSDs inside the SAL over Barbados during the intense dust event on 10 and 11 July. All individual NSD retrieval solutions for the lower and upper SAL (see Fig. B.1.1 and 4.1.2 for the definitions) are merged into respective collective solutions that are represented by their diameter-wise medians, 16 and 84th percentiles. Plot (a) and (b) compare the collective NSDs for the two altitude ranges on a linear and logarithmic ordinate, respectively. Concentrations refer to STP conditions.

In contrast to the situation for SAL presence, in the SAL-free atmospheric column no distinct temperature inversion and associated hydrolapse, meaning no marked stable layering is found around 2 km. Accompanied by this difference in the atmospheric stratification, Fig. 4.1.7 exhibits substantial changes in the vertical aerosol profiles. While the overall course of n_{total} is similar for the two scenarios, during SAL absence n_{80} and n_{CCN} are strongly depleted by up to an order of magnitude in the altitude range $z \gtrsim 2$ km. Hence, whereas n_{80} and n_{CCN} experience their maximum aloft during presence of the dust layer, these concentrations are largest close to the surface during its absence. When these concentrations are compared to n_{total} , it becomes evident that during SAL presence the majority of particles at $z \gtrsim 2$ km can be assigned to the size range $D \gtrsim 80$ nm. On the other hand, during SAL absence the same altitude range is dominated by particles with $D \lesssim 80$ nm and, therewith, by particles mostly too small to act as CCN (at $SS = 0.2\%$).

4.1.3 Detailed Properties of the SAL Aerosol

In the following, the detailed aerosol properties of the SAL, including particle NSD, size-dependent particle volatility, composition and hygroscopicity are presented. These properties are derived on the basis of the constant altitude sampling intervals.

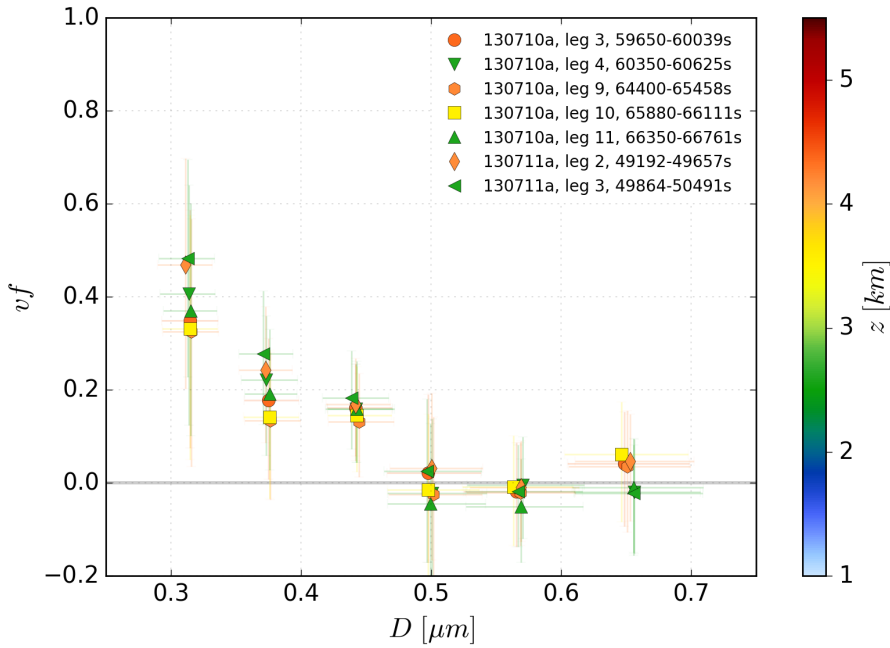


Figure 4.1.9: Size-dependent volatility of the aerosol particles in the SAL on 10 and 11 July. The data points are color-coded with the mean flight leg altitudes and represent the $vf(D)$ solution medians. The error bars indicate the range between the 16 and 84th percentiles of the corresponding PDFs.

As described in Sect. 4.1.1.2, the vertical profiles show an enrichment of small particles with $D \lesssim 80$ nm in the upper SAL at simultaneous depletion of the concentration of larger particles. This is confirmed in a more comprehensive way by the NSDs shown in Fig. 4.1.8. Accordingly, the relative increase in n_{small} appears as a near-collective drift of the entire NSD to smaller diameters with the NSD maximum shifting from² 87 ± 6 to 60 ± 6 nm.

Whereas this NSD alteration is accompanied by a significant increase in vf_{total} in the upper SAL (cf. Fig. 4.1.4), the size-dependent volatility for $D \gtrsim 300$ nm shown in Fig. 4.1.9 remains indistinguishable throughout the layer. The fact that no significant deformation of the $vf(D)$ curves with altitude is observable connotes that the change in total volatility between the lower and the upper part of the SAL is caused solely by particles in the size range $D \lesssim 300$ nm. For both parts of the layer, $vf(D)$ exhibits a transition in aerosol mixing state around $D \approx 500$ nm. Particles in the size range above this value do not carry significant amounts of volatile material and can, hence, be considered completely refractory. On the contrary, for $D \lesssim 500$ nm $vf(D)$ considerably increases with decreasing particle size. At $D \approx 300$ nm the volatile fraction reaches mean values of about 0.4, meaning that at this size already about 40% of the particles are either completely volatile or contain high amounts of volatile material. However, the uncertainties in the absolute values of $vf(D)$ are substantial.

These (rather qualitative) findings are corroborated by the single particle compositional analysis results shown in Fig. 4.1.10. A list of all impactor samples included

²These values represent PDF means and standard deviations for the maxima positions. They are derived via propagation of the NSD parameter solution PDFs.

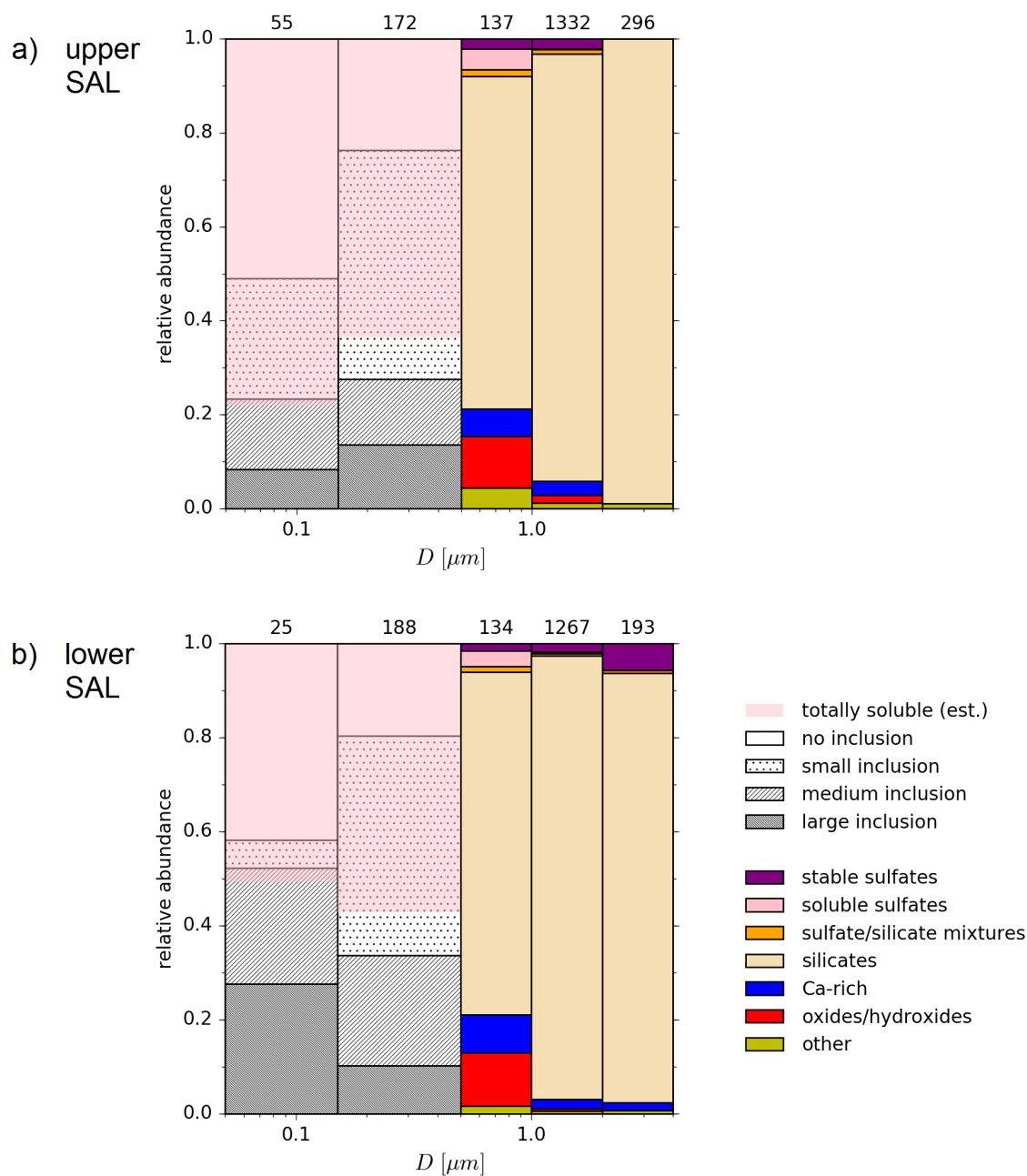


Figure 4.1.10: Single particle analysis results for the collective impactor samples withdrawn on 10 and 11 July in the (a) upper and (b) lower SAL, respectively. Particle sizes are given as projected (circle-equivalent) area diameters. For $D \geq 0.5 \mu\text{m}$ the particles are classified with respect to material type, whereas the smaller particles are sorted according to their volatile volume fractions. Here, “no inclusion” refers to completely volatile particles, “small”, “medium” and “large inclusion” to particles with refractory material contributing less than 30%, 30-90% and more than 90% to the total particle volume, respectively. The volatile component is primarily associated with soluble sulfates (ammonium sulfate). In addition to the volatility classification, an estimate for the fraction of totally soluble particles is shown. Above each size range box the total number of inspected particles is noted.

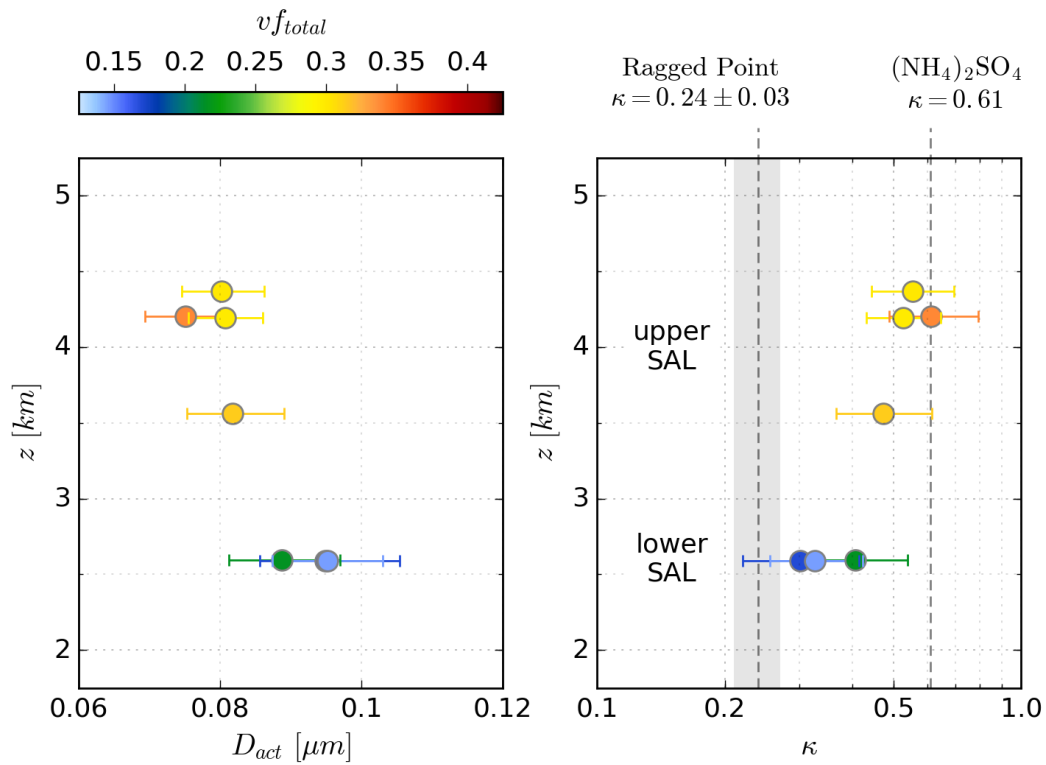


Figure 4.1.11: Derived particle activation diameters (left) and hygroscopicities (right) for the SAL aerosol at different altitudes on 10 and 11 July, color-coded with the total particle volatility. The data points represent the solution PDF medians, the error bars the ranges between the 16 and 84th percentiles. In addition to the κ derivation results for the SAL, the right graph indicates the values of κ (mean \pm standard deviation) for the ground level measurements at Ragged Point during the same period, and the value of κ for pure ammonium sulfate (Petters and Kreidenweis, 2007).

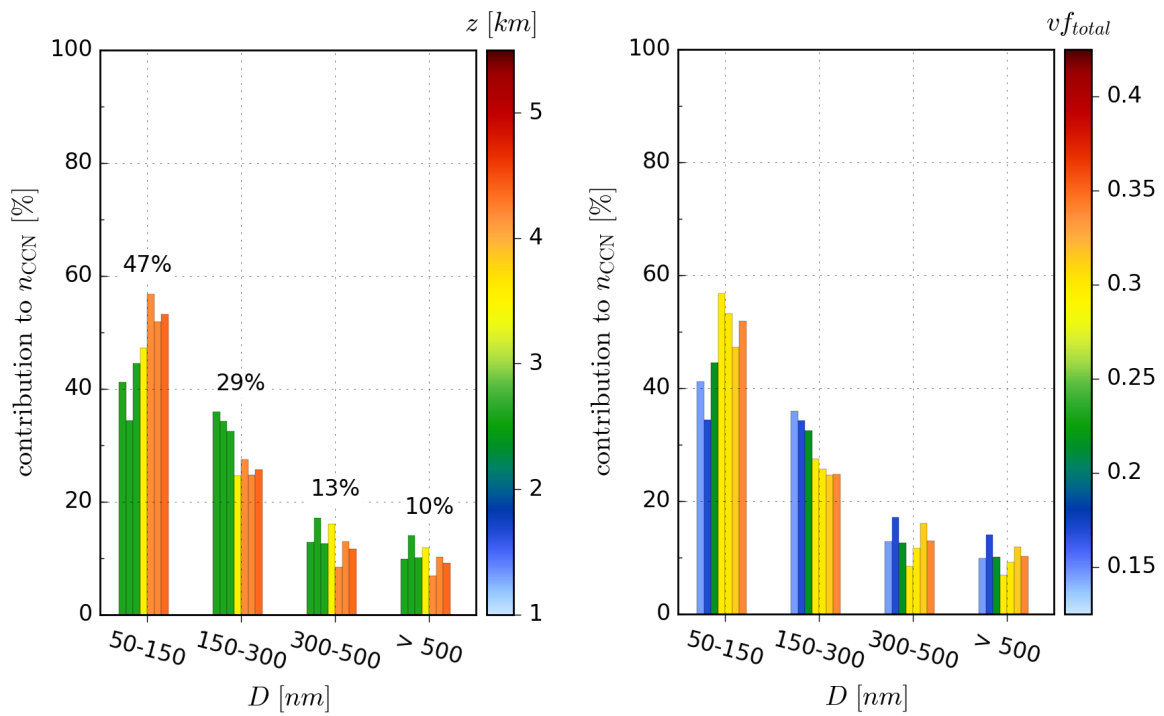


Figure 4.1.12: Contributions of different particle size ranges to n_{CCN} (at $SS = 0.2\%$) in the Caribbean SAL on 10 and 11 July. The different histogram bars represent median values of the contribution PDFs for each size class and derivation case. The bars are color-coded with the corresponding time interval mean altitudes (left) and total volatile fractions (right). In the left graph the overall mean contribution of each size class is noted above the associated bars.

in this analysis is given in Tab. B.3.1. Like for $vf(D)$, a marked transition is found at $D \approx 500$ nm. The particles above this diameter threshold are dominated by mineral dust. Most of these (pure) dust particles are classified as silicates, few others as Fe-oxides/hydroxides and Ca-rich types. The non-dust particle fraction is primarily classified as stable sulfates (predominantly calcium sulfate) and soluble sulfates (predominantly ammonium sulfate). The number of sulfate-silicate mixtures and, in general, internal mixtures between dust and other material is negligible. On the other hand, for $D \lesssim 500$ nm the particulate matter is strongly influenced by volatile material, appearing internally mixed with refractory components and in form of completely volatile particles. This volatile material is primarily identified as ammonium sulfate, deducible from strong sulfur signals in the absence of other potential sulfate partner ions like Na^+ , K^+ , Mg^{+2} or Ca^{+2} . Notable contributions of nitrates are further ruled out from the vaporization behavior of the volatile material under the microscope. Refractory residuals of the particles with $D \lesssim 500$ nm are mainly S-rich components, soot and mineral dust³. A fraction of completely soluble particles is estimated from the number of completely volatile (sulfate) particles and particles with presumably soluble residuals, including the S-rich material, NaCl-like components etc. For the lower and upper part of the SAL differences in the aerosol composition are insignificant for $D \geq 150$ nm. For the smallest size class, i.e. for $D < 150$ nm, however, a significant increase in volatile material — leading to the enhancement in vf_{total} — is apparent from the lower to the upper part of the layer. More precisely, the amount of particles with volatile volume fractions $\geq 70\%$, closely corresponding to the estimated fraction of completely soluble particles, increases from about 50% to 80%.

As already suggested by the (relative) n_{CCN} profiles in Fig. 4.1.5, these compositional changes impact the CCN properties of the SAL aerosol. Figure 4.1.11 demonstrates this effect by presenting the height-dependent values for the activation diameter D_{act} and effective particle hygroscopicity κ . According to the joint PDFs, D_{act} decreases from⁴ 93 ± 9 nm in the lower SAL to 80 ± 6 nm in the upper SAL implying an increase in κ from 0.36 ± 0.11 to 0.56 ± 0.14 . In the lower part of the layer the effective particle hygroscopicity is therewith similar to slightly enhanced compared to the corresponding value of 0.24 ± 0.03 measured in the MBL (at Ragged Point) during the same period. In the upper SAL the κ values are even close to the literature value for pure ammonium sulfate of 0.61 (Petters and Kreidenweis, 2007), thus significantly higher than in the MBL⁵. The overall high κ values in the layer confirm what is suggested from the compositional analysis of the SAL aerosol, i.e. that the volatile material strongly contributing to the particulate volume in the vicinity of the NSD maximum is indeed highly hygroscopic (water soluble).

Combining the individual particle NSDs and the corresponding D_{act} values further allows to conclude how much different size ranges contribute to the total CCN number concentration (at $SS = 0.2\%$). Figure 4.1.12 shows these relative contributions to

³These supplementary information not contained in Fig. 4.1.10 are additionally provided by K. Kandler, TU Darmstadt.

⁴The given values represent means and standard deviations of the respective joint D_{act} and κ PDFs.

⁵As demonstrated in Fig. B.1.2, the height trend in D_{act} and κ is no artifact of the CCN loss correction scheme, as the same features are observed when using the uncorrected CCN concentrations for the derivation of D_{act} and κ .

n_{CCN} for the size classes used in Fig. 4.1.10. It should be mentioned, however, that the presented contribution values do not consider particles larger than the Falcon aerosol inlet cutoff, for which n_{giant} is shown as an optimistic estimate⁶ in Fig. 4.1.4. Thanks to their large size these giant particles certainly act as CCN, too. According to Fig. 4.1.12, the size range $D \geq 500$ nm that is dominated by pure mineral dust particles contributes only about 10% to n_{CCN} . Assuming that n_{giant} is representative of the concentration of additional giant particles this contribution slightly increases but remains $< 14\%$. Anyhow, the major contribution to n_{CCN} comes from the size range $D < 150$ nm, i.e. from the particles in the vicinity of D_{act} that are shown to be governed by hygroscopic volatile material. Owing to the increase in the relative concentration of these particles from the lower to the upper SAL and the simultaneous increase in the fraction of the hygroscopic material, this contribution increases from about 40% to even $> 55\%$ (at an average of 47%).

4.2 Overall Picture of the SAL During SALTRACE

After detailed treatment of the intense Caribbean dust event on 10 and 11 July, in the following the scope of investigation is extended to the entirety of the airborne measurements during SALTRACE. Among others, the goal is to put the results of Sect. 4.1 into the context of the remaining Caribbean SAL measurements and to compare the Caribbean measurements with those in the vicinity of the Northwest African coast. In Sect. 4.2.1 first all (essential) vertical profiles acquired during the presence of dusty air masses on either side of the North Atlantic are presented. Subsequently, Sect. 4.2.2 deals with the full temporal course of observations, including the complementary ground-based measurements. Finally, Sect. 4.2.3 rounds out the investigation of potential transport-induced changes in the SAL aerosol properties by comparing particle NSDs, size-dependent particle volatility and composition between Northwest Africa and the Caribbean.

4.2.1 Entirety of Vertical Profiles in the Presence of the SAL

4.2.1.1 Caribbean

Figure 4.2.1 presents the vertical profiles⁷ of Θ and mr measured during the presence of dusty North African air masses in the Caribbean. In accordance with the findings in Sect. 4.1.1.1, the vast majority of these profiles show a strong trade wind inversion at about 2 km accompanied by a pronounced drop in humidity. The only exception is flight 130701a (near Puerto Rico), where despite the presence of dusty African air masses no such pronounced inversion and hydrolapse are found at this altitude. Whereas for all other cases the height of the trade wind inversion is rather constant, the onset of the second inversion capping the SAL occurs at variable altitudes between

⁶“Optimistic estimate” means that n_{giant} presumably slightly overestimates the number concentration of giant particles that are not efficiently transmitted to the in-cabin instruments.

⁷The shown profiles represent the aircraft descents only. Ascents were typically conducted only in the beginning of each flight and did not include a considerable number of constant altitude sampling intervals, so that the additional information content of these profiles is usually poor.

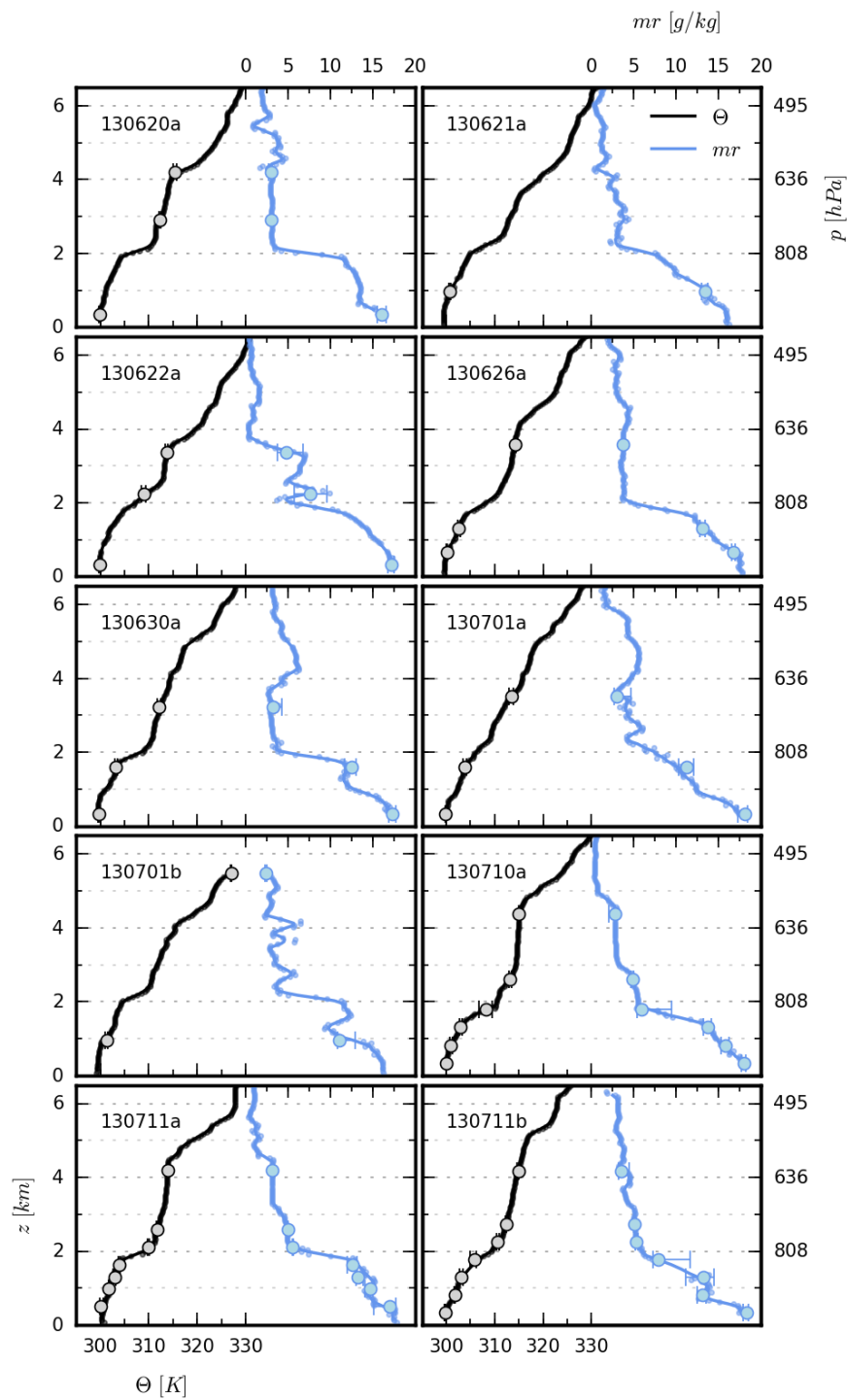


Figure 4.2.1: Vertical profiles of Θ (black) and mr (blue) measured by the Falcon standard meteorological instrumentation during all Caribbean flights with noticeable dust presence. The data are presented in the same way as before.

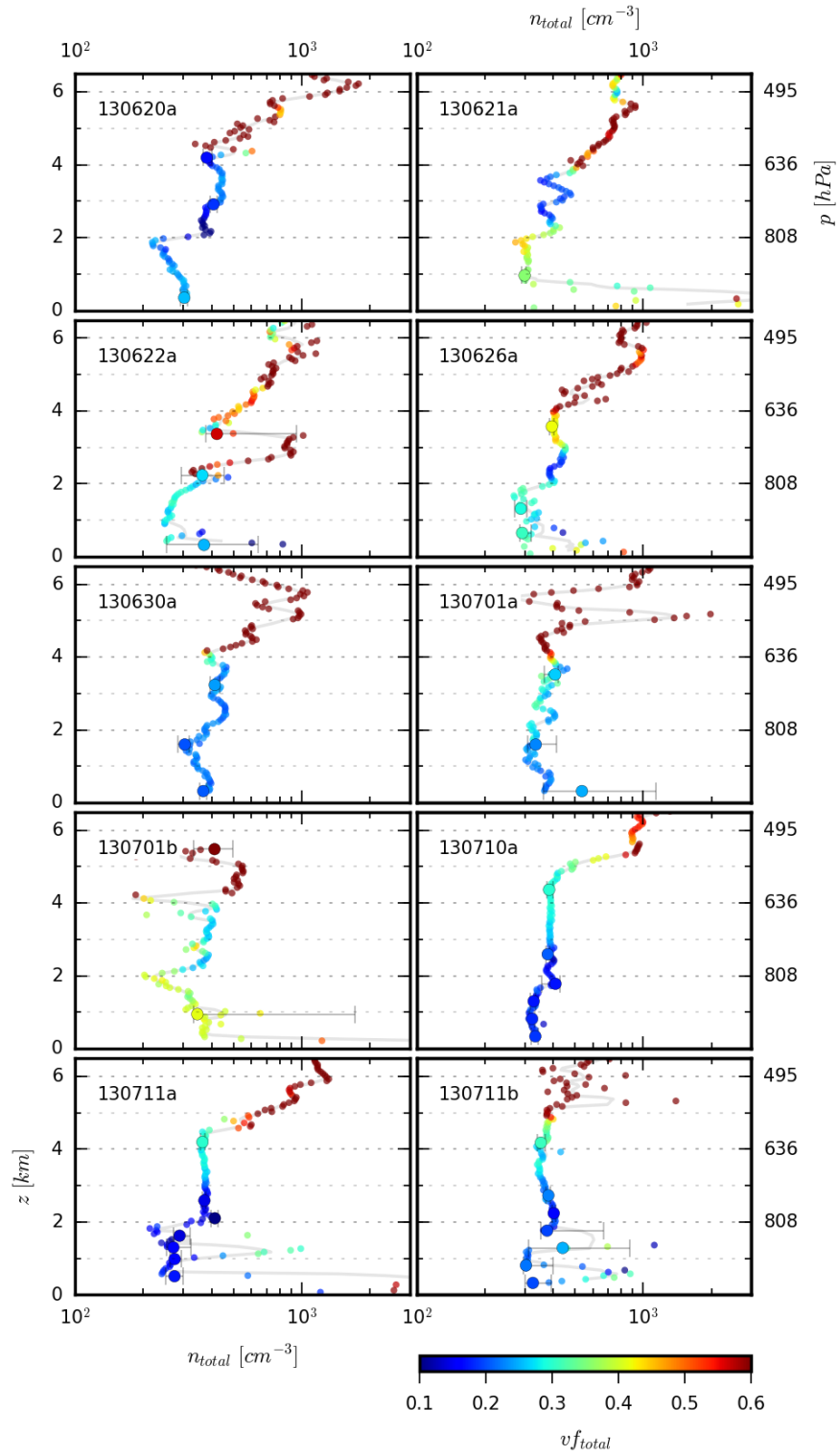


Figure 4.2.2: Same as Fig. 4.2.1 but for n_{total} , color-coded with $v_{f_{total}}$.

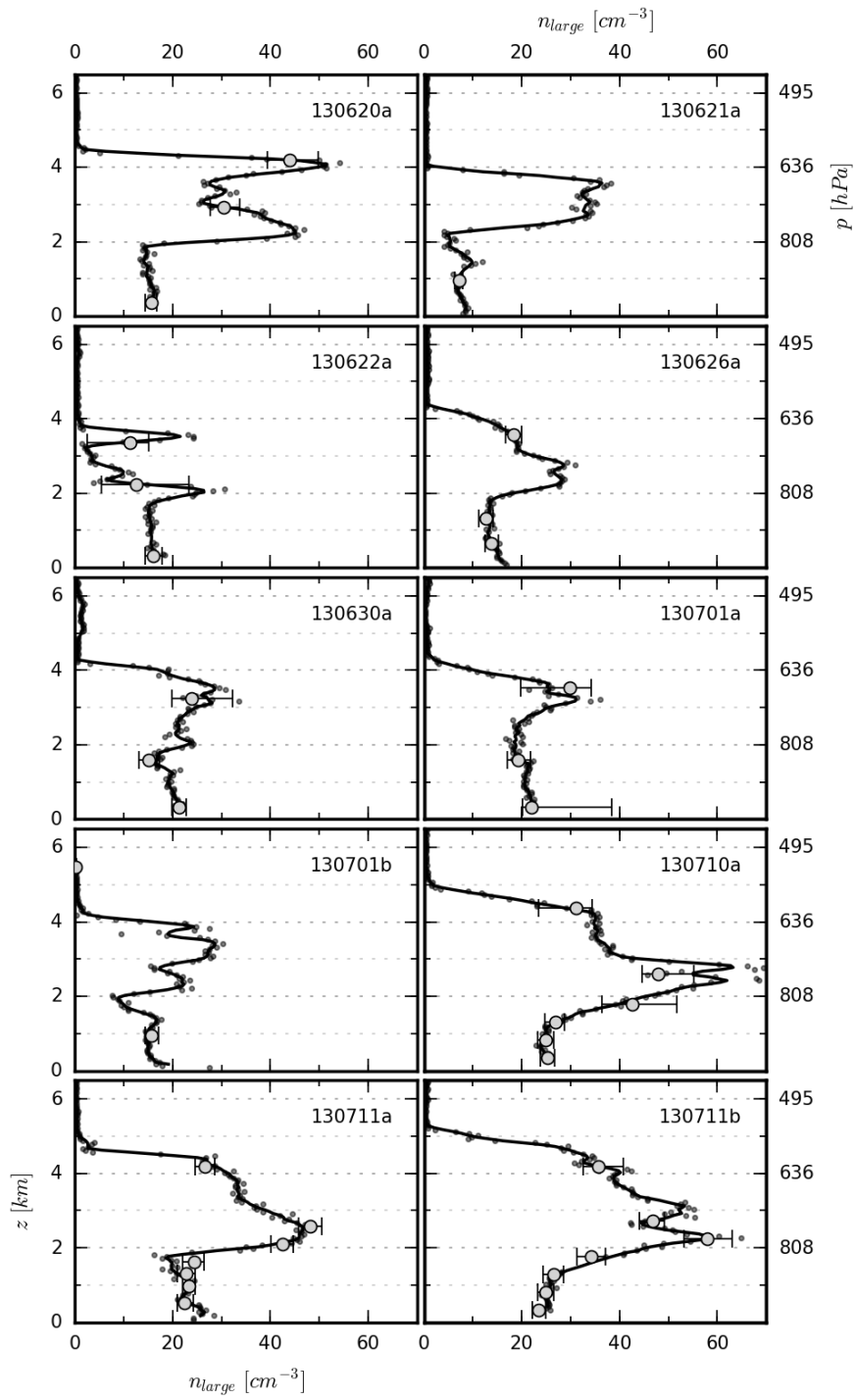


Figure 4.2.3: Same as Fig. 4.2.1 and 4.2.2 but for n_{large} .

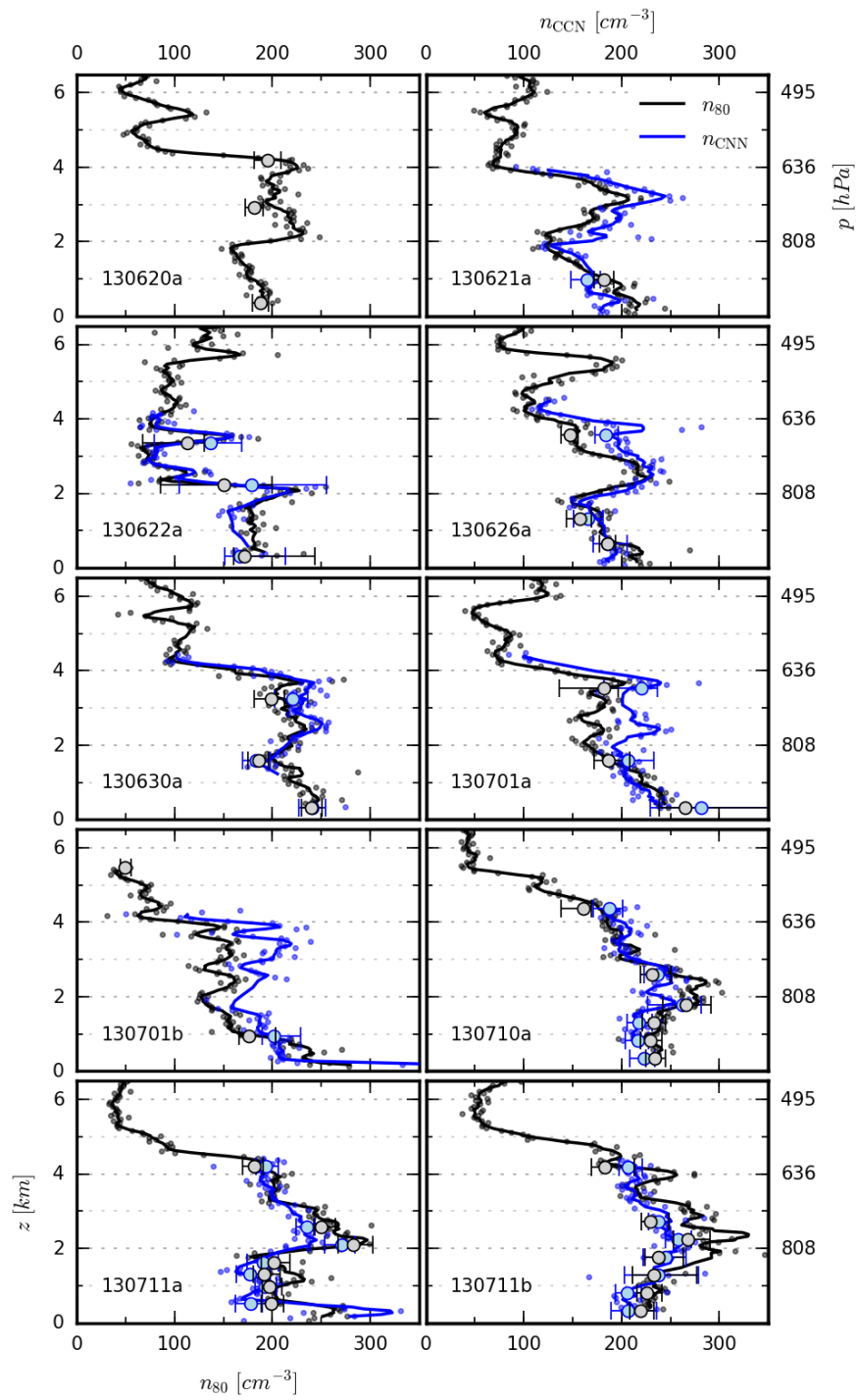


Figure 4.2.4: Same as Fig. 4.2.1 to 4.2.3 but for n_{80} (black) and $n_{CCN,v1}$ (at $SS = 0.2\%$; blue).

about 4 and 5 km. Within the SAL altitude range, defined by the two inversions, typical values for Θ and mr are 310 – 315 K and 2.5 – 5 g/kg, respectively. Yet, these values exhibit noteworthy deviations from uniformity with altitude. Besides the stepped internal Θ and mr structure found for flight 130710a and 130711a (discussed in Sect. 4.1.1.1), some other flights, e.g. 130622a and 130701b, show considerable fluctuations of mr within the layer. Further, Θ often exhibits a moderate increase with altitude in the SAL.

As shown in Fig. 4.2.3, in all cases with a distinct trade wind inversion there is a substantial increase in n_{large} coinciding with this inversion. A similar feature is also found for the majority of n_{80} and n_{CCN} profiles presented in Fig. 4.2.4. Consequently, not only for the intense dust event on 10 and 11 July but also for the other cases, n_{80} , n_{CCN} and n_{large} are typically enhanced in the SAL compared to the lower troposphere. Except for peaks attributable to local pollution encounters in the latter, this typically also holds for the n_{total} profiles displayed in Fig. 4.2.2.

While the profiles mainly agree on these qualitative features, their exact patterns are highly complex and variable. For one, the average particle concentrations in the SAL vary significantly between the different cases. Moreover, also the individual profiles show considerable variation with altitude in the SAL. Particularly, n_{large} regularly exhibits high gradients of $\pm 50\%$ and more within short vertical distances of only a few hundred meters. In addition to this vertical variability in absolute concentrations, some flights even show marked changes in the particle NSD (and volatility) within the SAL. One extreme example is flight 130622a, where a layer enhanced in n_{total} (and vf_{total}) and depleted in n_{large} is obviously interposed into the SAL. Another example is the subdivision of the SAL into an upper and lower part discussed in Sect. 4.1.1.2. Such a notable subdivision of the layer is not an omnipresent but a recurrent feature. Apart from the flights on 10 and 11 July, a similar enhancement of vf_{total} in the upper part of the layer coinciding with a depletion in n_{large} and a relative enhancement in n_{CCN} (compared to n_{80}) is found for flight 130626a. For all flights, a close correlation between the n_{CCN} and n_{80} profiles is observed for the entire vertical range up to $z \approx 4.5$ km, constituting the operational limit for the CCNC setup.

With the onset of the second inversion capping the SAL, n_{large} consistently falls to zero. A similar though not as pronounced decrease is typically encountered for n_{80} and n_{CCN} . Therewith, not only the concentration of the largest particles but usually even that of all particles with CCN-relevant sizes is highest inside the SAL (neglecting low-level local pollution encounters). By contrast, thanks to a strong increase in the concentration of smaller particles (with $D < 80$ nm), n_{total} typically shows its maximum above the SAL. The increase in n_{total} at the SAL's capping inversion is accompanied by a substantial increase in vf_{total} to typically $\gtrsim 60\%$, meaning that the particles above the SAL are predominantly completely volatile.

4.2.1.2 Northwest African Coast

To allow for a direct comparison with the Caribbean measurements, Fig. 4.2.5 to 4.2.8 present the same set of vertical profiles for the flights in the vicinity of the Northwest African coast. As apparent from Fig. 4.2.5, here the lower temperature inversion and simultaneous hydrolapse defining the base of the SAL are typically found between about 0.5 and 1 km. Directly capping the near-ground boundary layer, these transitions in

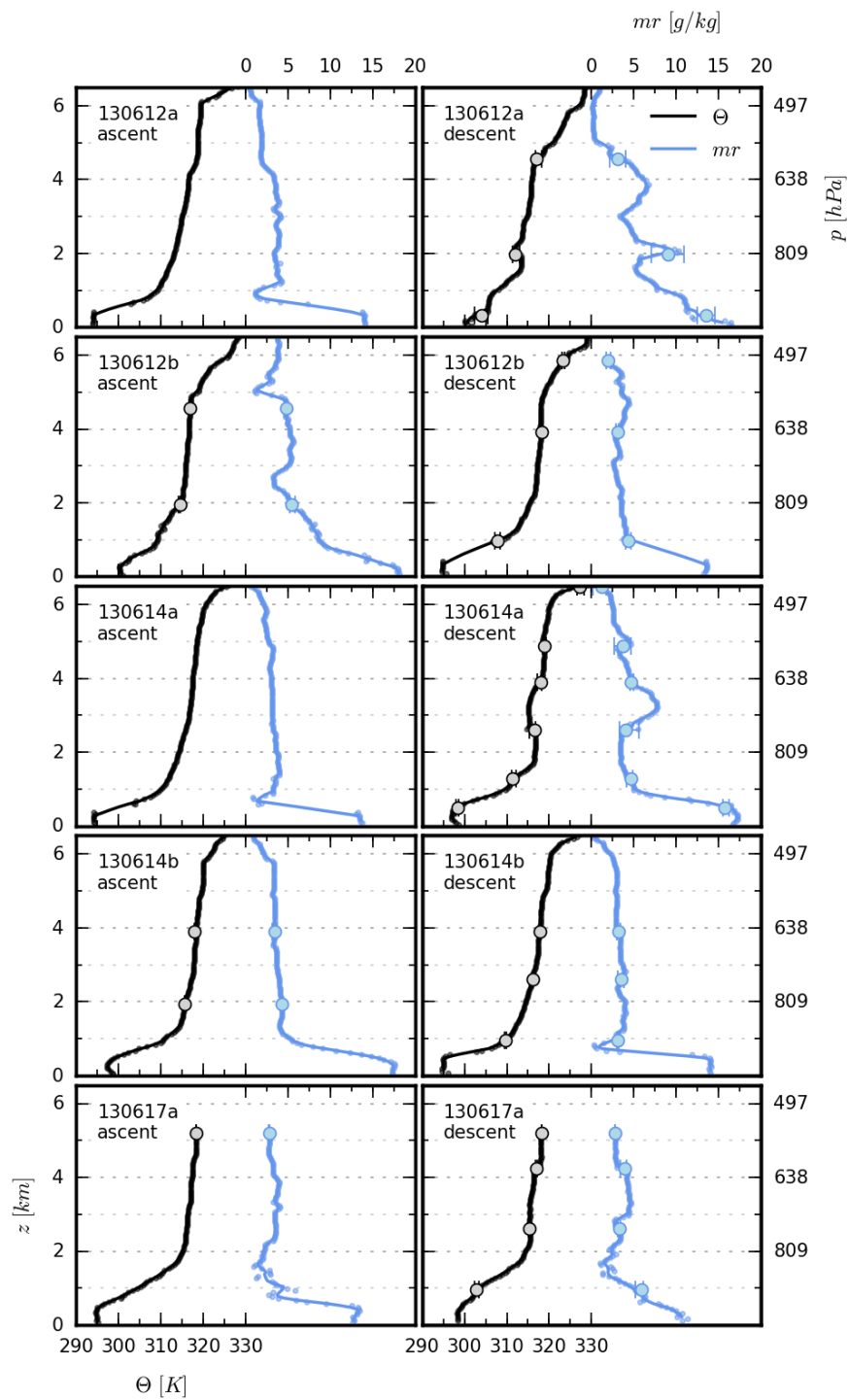


Figure 4.2.5: Vertical profiles of Θ (black) and mr (blue) measured by the Falcon standard meteorological instrumentation during the flights in the vicinity of the Northwest African coast. The data are presented in the same way as before.

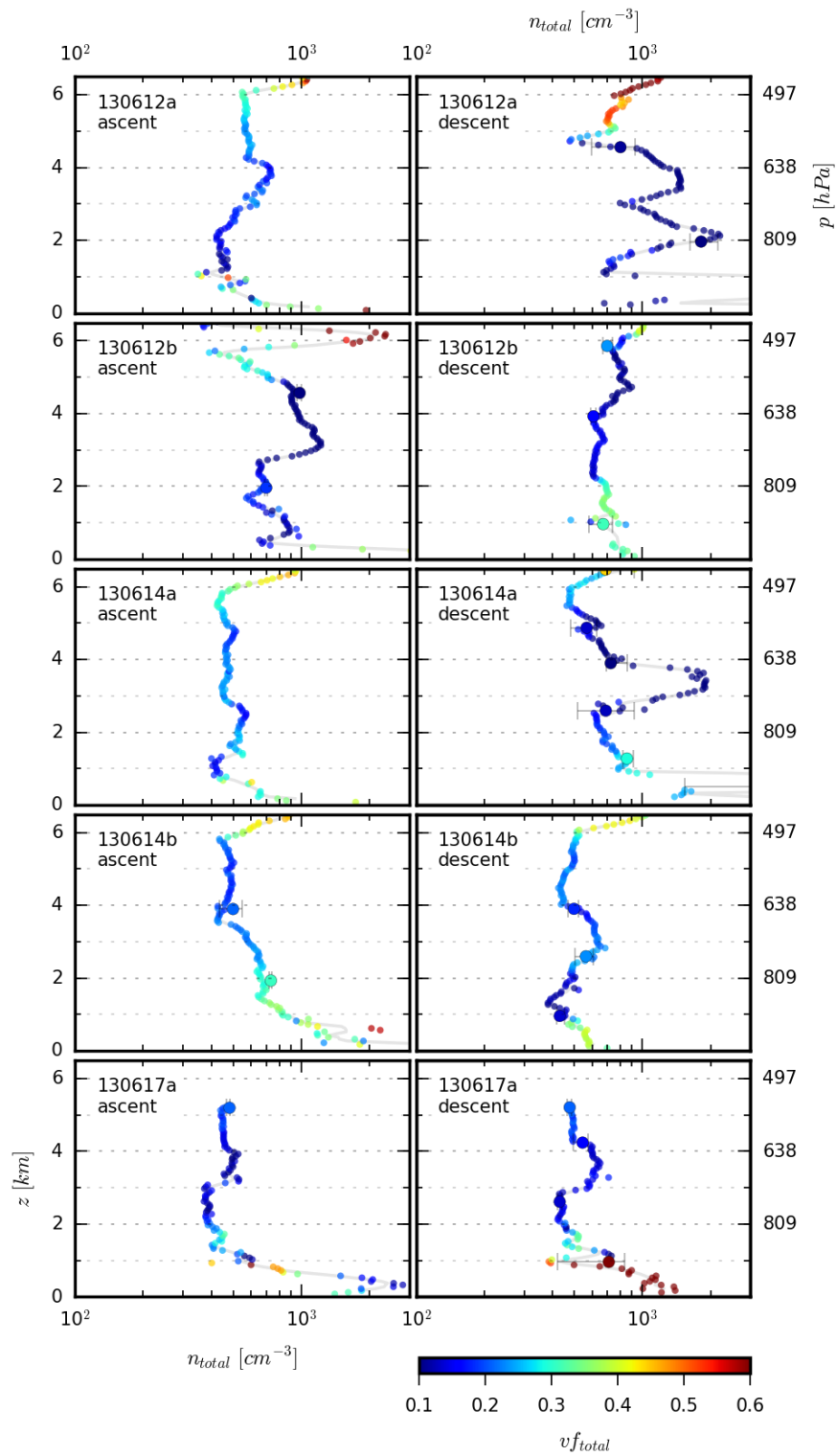


Figure 4.2.6: Same as Fig. 4.2.5 but for n_{total} , color-coded with vf_{total} .

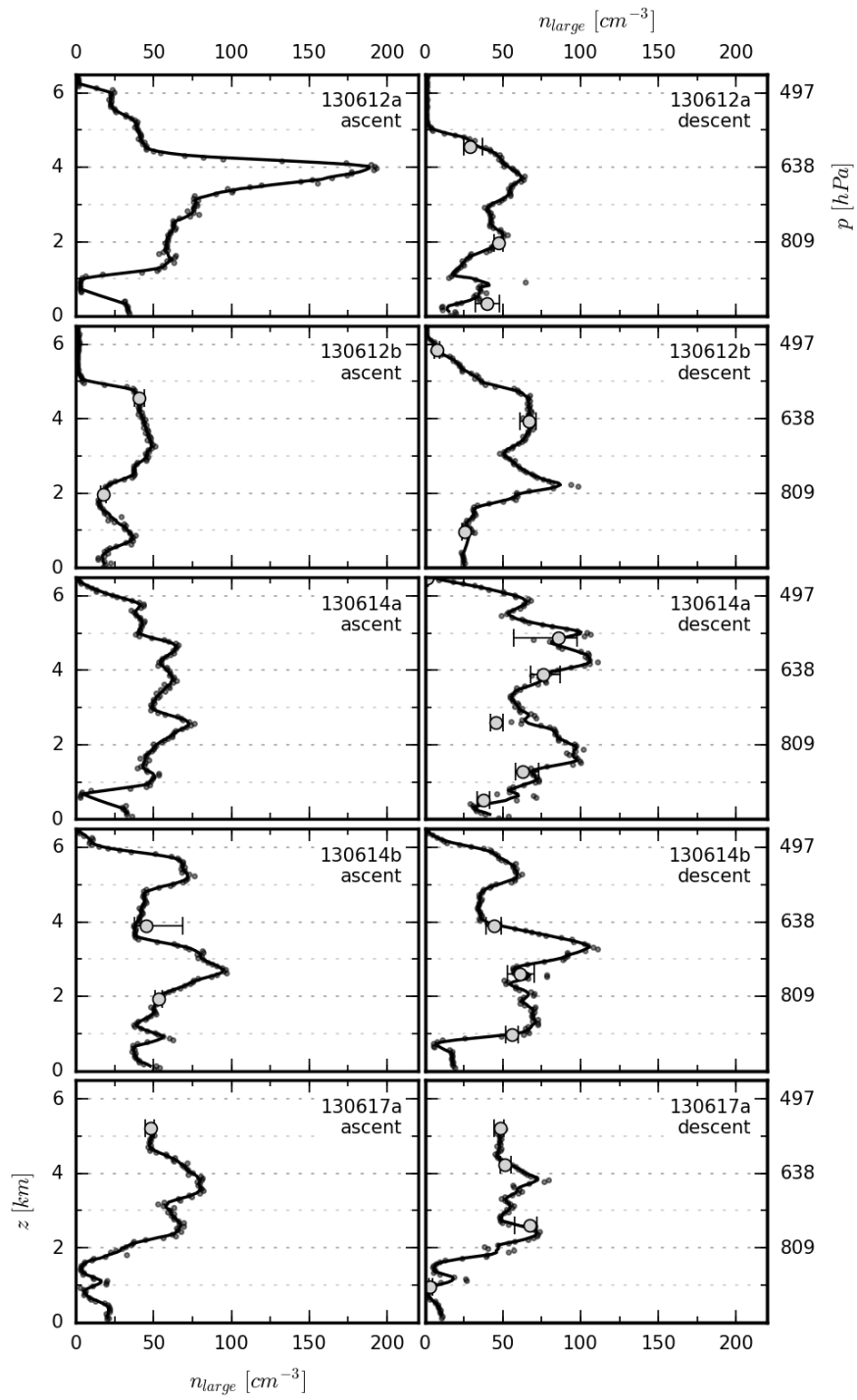


Figure 4.2.7: Same as Fig. 4.2.5 and 4.2.6 but for n_{large} .

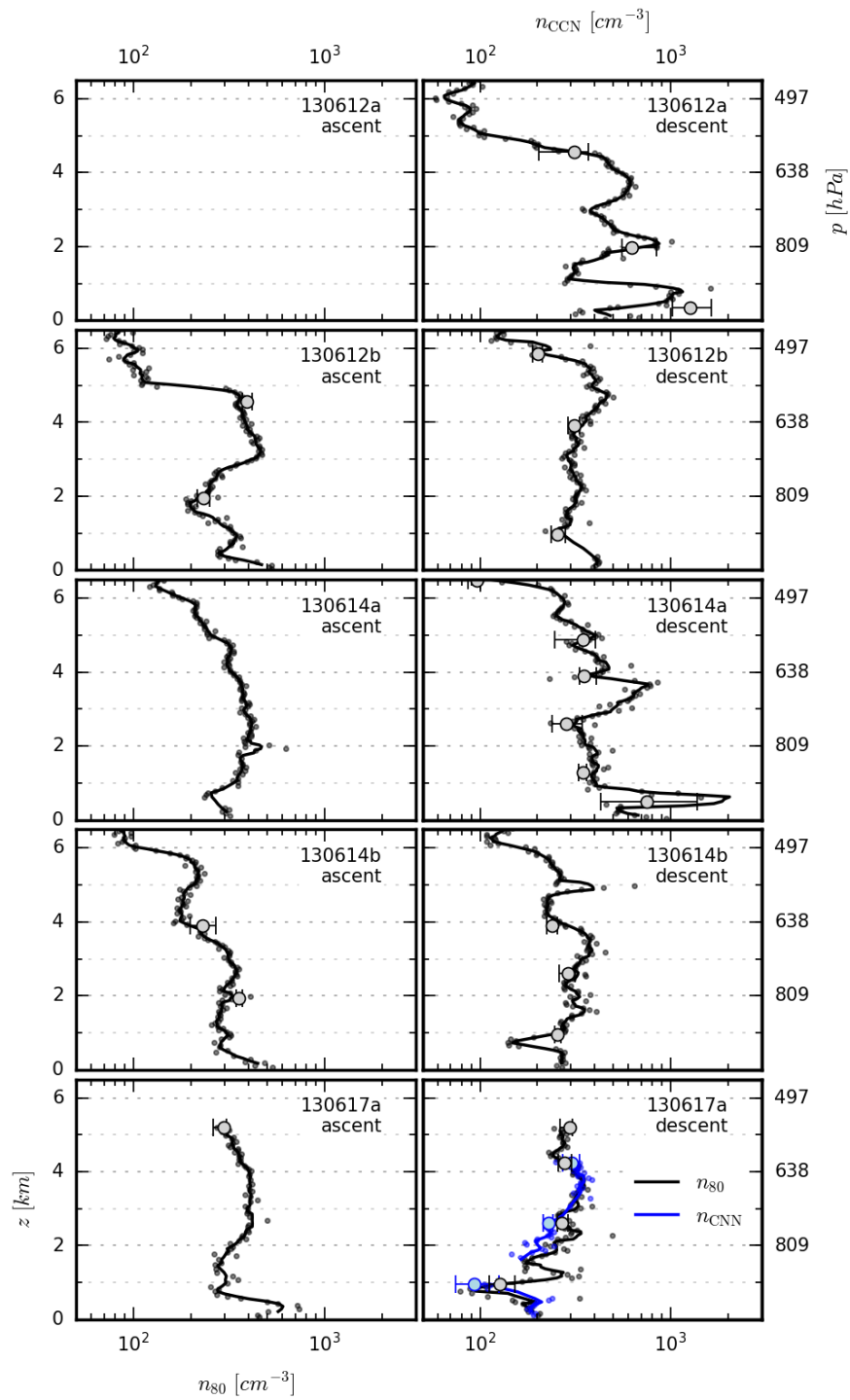


Figure 4.2.8: Same as Fig. 4.2.5 to 4.2.7 but for n_{80} (black) and $n_{\text{CNN},v1}$ (at $SS = 0.2\%$; blue).

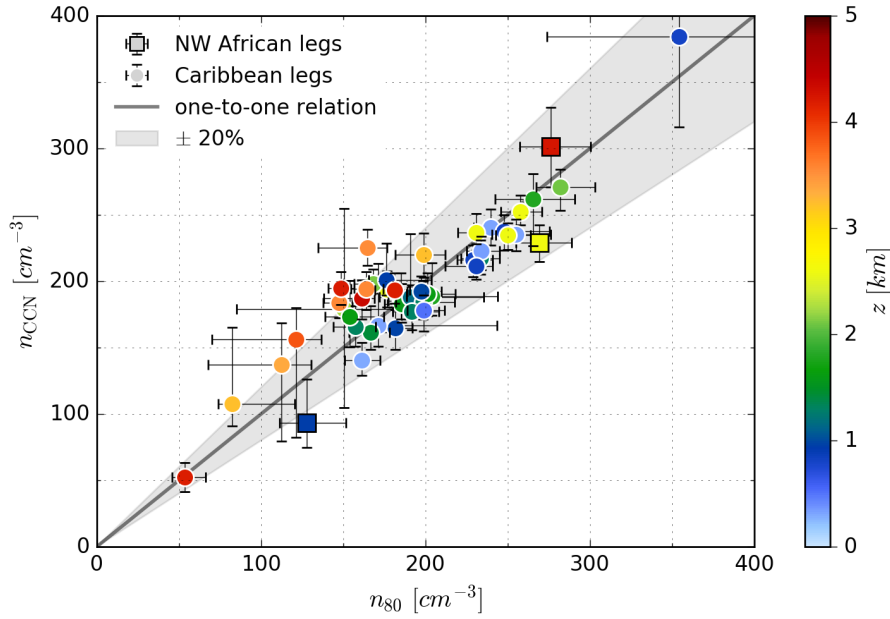


Figure 4.2.9: Comparison between $n_{\text{CCN},v1}$ (at $SS = 0.2\%$) and n_{80} for all flight legs, i.e. constant altitude sampling intervals inside and below the SAL in the Caribbean (round markers) and at the Northwest African coast (squared markers). The data points represent median concentrations for each leg and are color-coded with the flight altitude. The error bars correspond to the ranges between the 16 and 84th percentiles. In addition to the data points, the one-to-one relation (black line) is displayed together with a $\pm 20\%$ deviation range (gray area). Concentrations refer to STP conditions.

Θ and mr are typically even more distinct than in the Caribbean. Whereas the SAL's base is therewith significantly lower than in the Caribbean, the height where the second inversion capping the SAL sets in is elevated to about 5 – 6 km. Taken together, this connotes a considerably larger vertical extent of the SAL. The temperatures inside the SAL at the African coast are slightly (about 5 K) higher than those in the Caribbean. The water vapor mixing ratios inside the layer are comparable for both sides of Atlantic. Consistent with the Caribbean profiles, Θ and mr are typically not uniform within the SAL, but Θ exhibits a moderate increase with altitude and mr occasionally shows significant variations/substructures.

In line with these similarities in the Θ and mr profiles, also the major (qualitative) features of the aerosol profiles are maintained. The maxima of n_{large} and typically also of n_{80} are found inside the SAL. Flight 130617a, i.e. the only flight with quantitatively usable CCN data for the Northwest African coast (cf. Sect. 3.2.2.3), further demonstrates that n_{80} closely follows n_{CCN} . Accordingly, n_{80} constitutes a useful qualitative proxy for n_{CCN} for the entire investigated altitude range on either side of the North Atlantic. Apart from the vertical profiles, this is clearly supported also from the data for the constant altitude flight legs shown in Fig. 4.2.9. Another consistency between the Caribbean and the Northwest African measurements is the drop in n_{large} and n_{80} , and the simultaneous strong increase in n_{total} and vf_{total} at the upper edge of the SAL. The latter means that to both ends of the transatlantic transport the SAL is topped by air masses containing large amounts of small particles ($D \lesssim 80$ nm) that

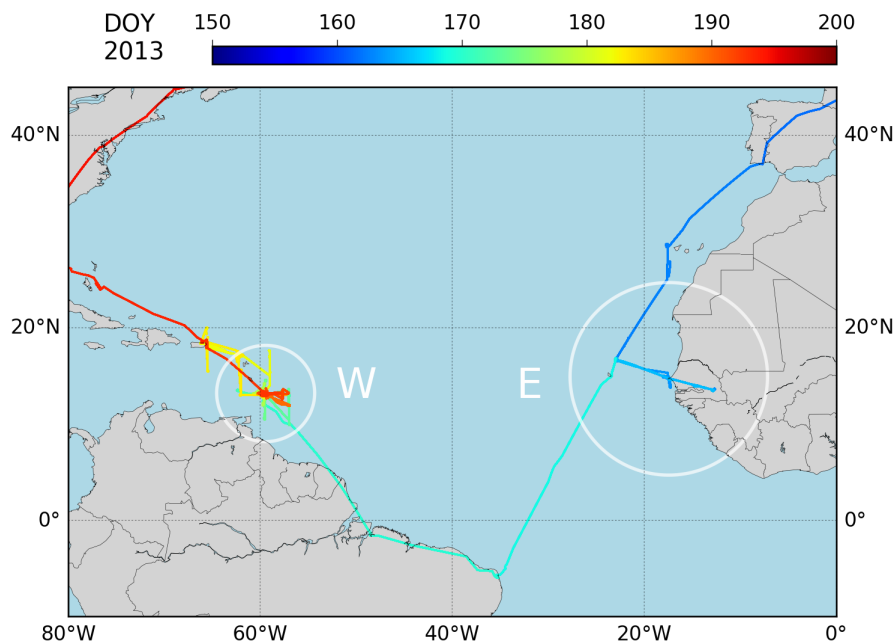


Figure 4.2.10: Visualization of the hereafter used location filters for the Caribbean region in the vicinity of Barbados (W) and the Northwest African coast region (E). The circular areas are defined by latitude-longitude radii of 5° and 10° around Ragged Point, Barbados (13.165°N , 59.432°W) and Dakar, Senegal (14.693°N , 17.447°W), respectively.

are mostly volatile. Like in the Caribbean, there are also cases where the enhancement in particle volatility extends from the troposphere above the SAL into the upper part of the layer (e.g. for flight 130612a and 130614a). However, this occasional feature is not as pronounced as for certain Caribbean profiles (e.g. for flight 130626a, 130710a and 130711a). Also common to both the Caribbean and the Northwest African concentration profiles is the significant vertical variability as well as marked day-to-day differences.

4.2.2 Spatiotemporal Course of Observations

The purpose of the following section is to extend the previous side-by-side comparison of vertical profiles by a more comprehensive spatiotemporal picture of the vertical structures met during SALTRACE and the evolution of important SAL aerosol parameters. In order to correlate the airborne in situ information with the ground-based measurements, especially the extensive ones at Barbados, the complete airborne data set is filtered for intervals sufficiently close to the central ground stations. These location filters are defined in Fig. 4.2.10.

4.2.2.1 Complete Vertical Information from Airborne and Ground-Based Measurements

Figure 4.2.11a) shows the AOD time series derived from the ground-based sun photometer measurements at Cabo Verde and Barbados. Whereas the former measurements

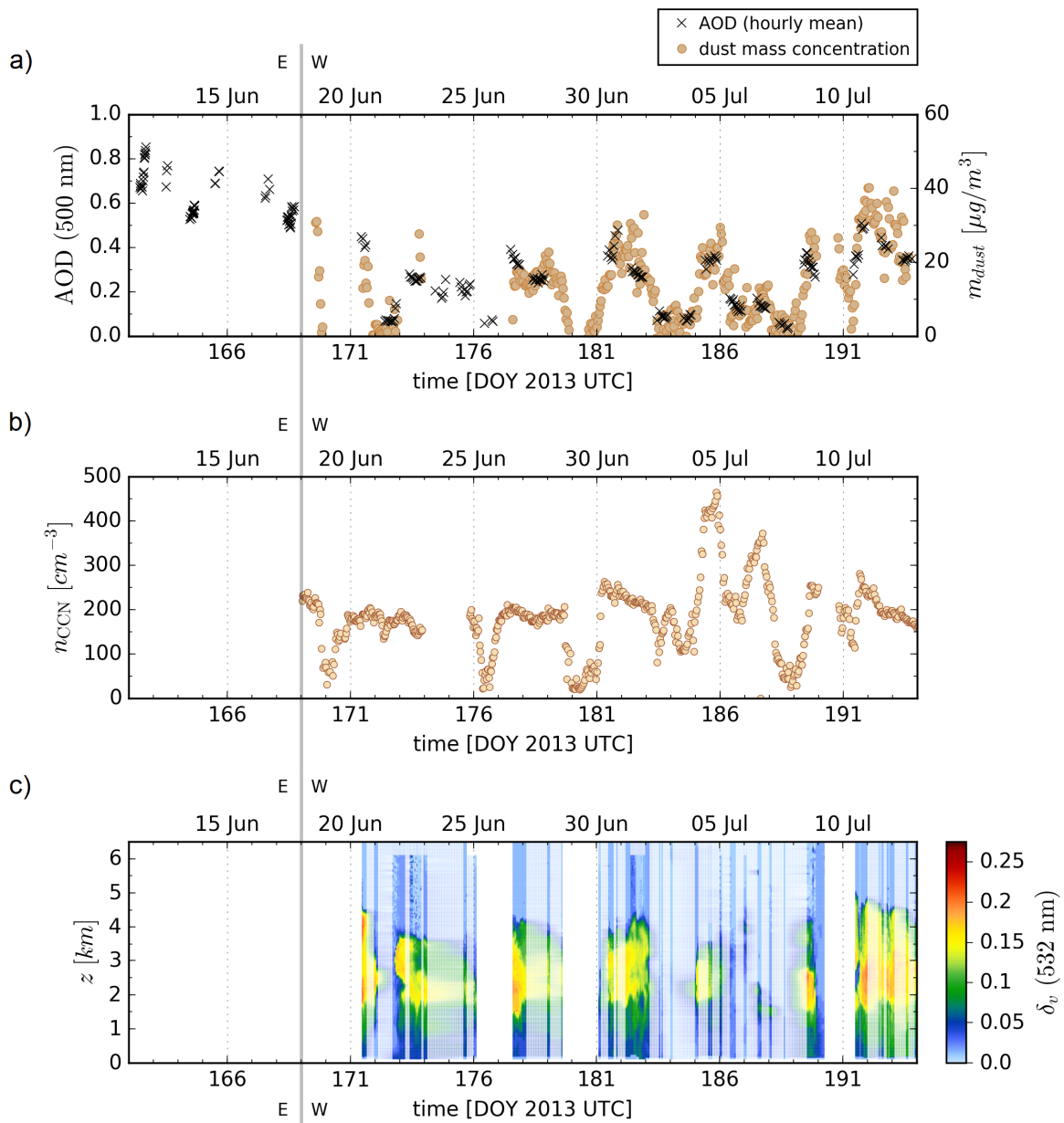


Figure 4.2.11: Time course of (a) AOD and ground-level dust mass concentration m_{dust} , (b) ground-level CCN concentration n_{CCN} (at $SS = 0.2\%$) and (c) the vertical profile of linear volume depolarization ratio δ_v . For an improved visualization of SAL appearance in the Caribbean, the δ_v profiles in graph (c) are linearly interpolated for periods without data (faded colors). Interpolation is only applied when the AOD time course argues against major changes of the SAL between two adjacent lidar measurements. Concentrations refer to STP conditions.

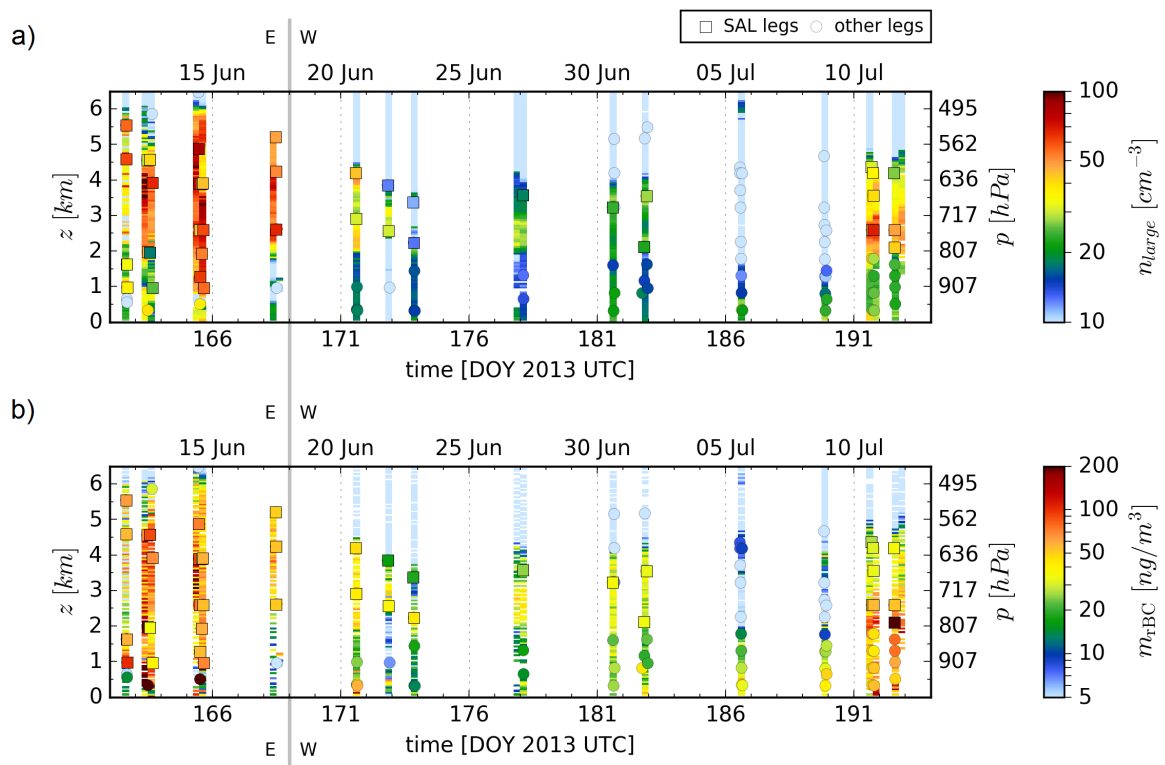


Figure 4.2.12: Time course of the vertical profiles of (a) n_{large} and (b) refractory black carbon mass concentration m_{rBC} . The colors of the vertical profile grid boxes and the flight leg data points (rimmed markers) represent median parameter values. Concentrations refer to STP conditions.

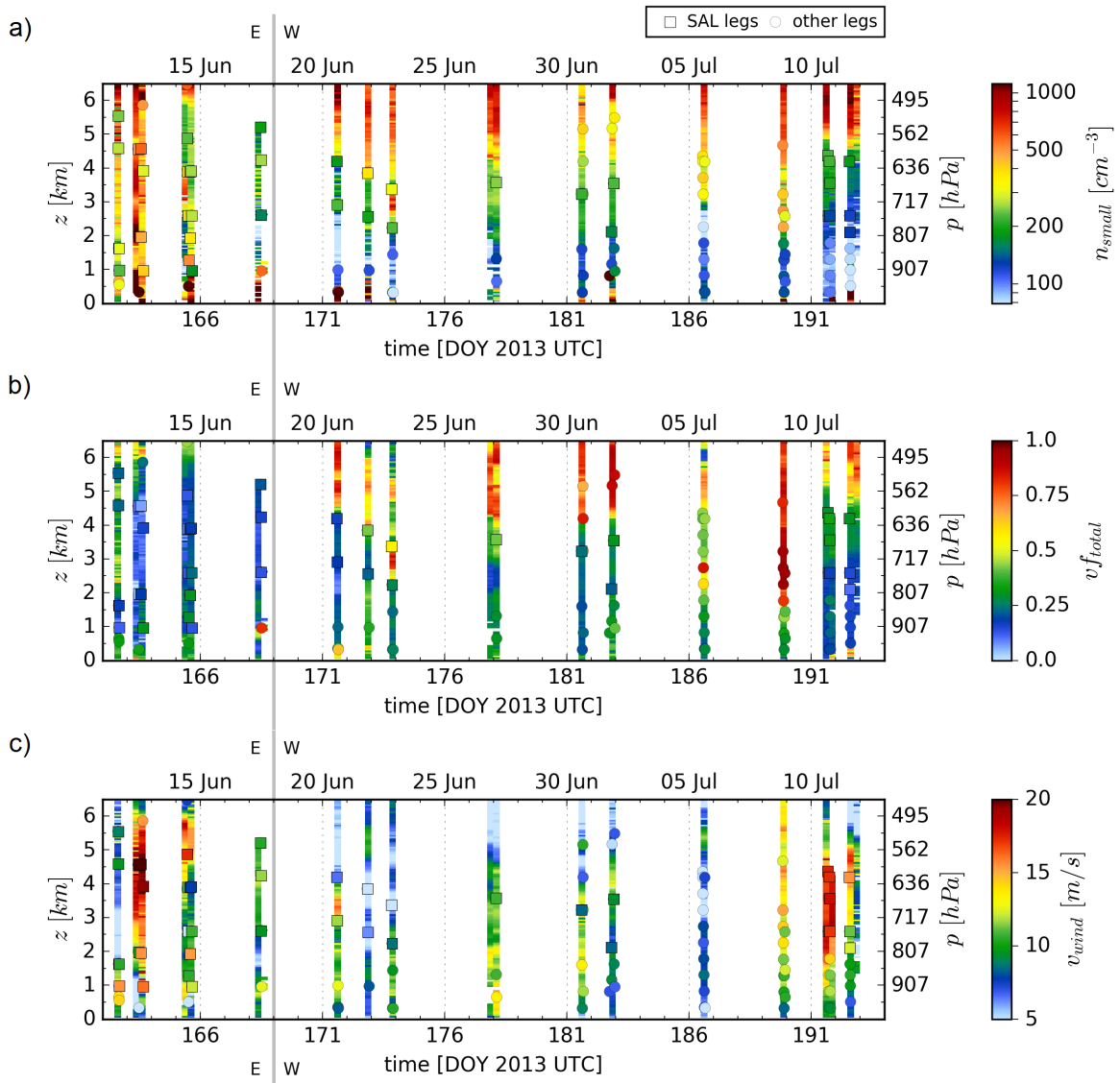


Figure 4.2.13: Time course of the vertical profiles of (a) n_{small} , (b) v_f^{total} and (c) v_{wind} , presented in the same way as in Fig. 4.2.12.

exhibit consistently high values of typically 0.5 – 0.8, the Caribbean measurements shows a pronounced periodical course. Accordingly, at Barbados episodes with enhanced AOD of about 0.3 – 0.6 during SAL presence are interrupted by episodes of near-zero AOD during SAL absence. The periodicity of this cycle, induced by AEWs, is about 3 – 4 days. In addition to the AOD, the dust mass concentration m_{dust} measured at ground level on Barbados is shown. Obviously, this concentration is highly correlated with the AOD showing high values of $m_{dust} \approx 20 - 40 \mu\text{g}/\text{m}^3$ during SAL events and negligible values otherwise. A similar pattern is also observable for the ground-level n_{CCN} (at $SS = 0.2\%$) shown in Fig. 4.2.11b). Periods of enhanced AOD and m_{dust} are accompanied by high values of $n_{CCN} \gtrsim 200 \text{ cm}^{-3}$, while during SAL absence the boundary layer CCN number concentration is typically significantly reduced. This demonstrates that in the Caribbean the presence of the elevated SAL is intrinsically linked to the simultaneous presence of (CCN-relevant) SAL aerosol particles in the lower troposphere. The same feature is also apparent from the POLIS measurements of the linear volume depolarization ratio δ_v shown in Fig. 4.2.11c). Unlike the airborne observations that are strongly limited in temporal coverage, these lidar measurements provide a more continuous picture of the dust events. The values of δ_v , that are sensitive to the concentration of coarse aspherical particles closely reproduce the in situ profiles of n_{large} in Fig. 4.2.12a). Although the highest values of $\delta_v \approx 0.15 - 0.25$ are met inside the SAL, with a distinct transition in δ_v from the layer to the underlying troposphere, δ_v is also consistently enhanced in the latter during SAL presence (from typically $\delta_v < 0.05$ during SAL absence up to ≥ 0.1).

While, according to the typical transition in δ_v at $z \approx 2 \text{ km}$, the dust aerosol in the lower troposphere mainly appears separated from the bulk aerosol mass in the SAL, during short periods in the temporal proximity of 1 July the lidar measurements show notable “filaments” of enhanced δ_v extending from the SAL to lower altitudes. This means that here large particles are efficiently exchanged vertically between the elevated dust layer and the lower troposphere on site. This is consistent with the in situ observations during the same day, namely those of flight 130701a (cf. Sect. 4.2.1). As described earlier, this flight is the only exceptional case where despite dust presence in the Caribbean no discernible SAL separation, i.e. no notable trade wind inversion and no transition in n_{large} at the typical trade wind inversion height of 2 km is encountered.

Figure 4.2.12 is complemented by the vertical profiles of refractory black carbon mass concentration⁸ m_{rBC} . These profiles reveal that in addition to the high concentration of large particles — plus considerable quantities of volatile hygroscopic material (cf. Sect. 4.1.3) — the SAL also carries noteworthy amounts of soot. The only two profiles with negligible values of m_{rBC} in the altitude range above 2 km are ascribable to the flights during SAL absence on 5 and 8 July. Typical values of m_{rBC} in the dust layer are in the range of 30 – 200 ng/m³ with the profiles qualitatively following those of n_{large} (for $z \gtrsim 2 \text{ km}$).

After focusing on the coarse (and refractory) SAL aerosol particles and particularly on their simultaneous appearance in the lower troposphere, Fig. 4.2.13 rivets on the situation at the upper edge of the layer. Whereas n_{large} and m_{rBC} vanish above the SAL, the time course of the n_{small} and vf_{total} profiles (again) demonstrates that this

⁸Precisely, m_{rBC} represents the refractory black carbon mass concentration in the SP2 size range $80 \lesssim D \lesssim 480 \text{ nm}$ (see Sect. 3.2.3.1).

altitude range consistently features high concentrations of volatile small particles (with $D \lesssim 80$ nm) with typical values of $n_{small} \approx 400 - 1000 \text{ cm}^{-3}$ and $vf_{total} \approx 0.5 - 1$. Another characteristic feature at the upper edge of the layer is pronounced wind shear, a potential trigger for vertical turbulence. Like for the example of flight 130711a, discussed in Sect. 4.1.1.1, the majority of v_{wind} profiles exhibit a considerable decrease in horizontal velocity from the SAL, where typically $v_{wind} \approx 10 - 20 \text{ m/s}$, to the rather calm air above the layer, where $v_{wind} \lesssim 5 \text{ m/s}$.

For the Caribbean profiles, it is apparent that n_{small} and vf_{total} are not just jointly enhanced above the layer but are typically correlated within the SAL altitude range as well. This means that enhanced amounts of small particles in the dust layer, usually found near its ceiling, are typically equatable with enhanced amounts of volatile particles. The profiles further illustrate that compared to the lower Caribbean troposphere the SAL is not only enriched in large particles but commonly also in these small particles associated with volatile material.

Additional profiles for the potential temperature gradient $d\Theta/dz$ and mixing ratio mr , and for the particle concentrations n_{80} and n_{CCN} are shown in Fig. B.2.1 and B.2.2, respectively.

4.2.2.2 Aerosol Parameter Statistics for the SAL Flight Legs

While the figures in Sect. 4.2.2.1 provide access to the time-resolved vertical appearance of the SAL, they are of limited utility for the quantitative study of its aerosol parameters. To better serve this task, Fig. 4.2.14 and 4.2.15 present parameter statistics for the constant altitude flight legs inside the dust layer. According to Fig. 4.2.14, with regard to the average values for the respective SAL legs n_{total} and n_{large} decrease from 664 and 51 cm^{-3} to 411 and 32 cm^{-3} from the Northwest African coast to the Caribbean, respectively. This means that on average, after transatlantic transport n_{total} and n_{large} are similarly reduced by about 38% and 37%. The same is also found for n_{small} in Fig. 4.2.15, showing a decrease in average values from 357 to 228 cm^{-3} , i.e. by about 36%. While the particle concentrations are depleted (nearly size-independently), vf_{total} is increased from an average of about 0.17 to 0.29. Evidently, this increase is mainly attributable to the cases of simultaneous vf_{total} and n_{small} enhancements in the upper part of the Caribbean SAL. Here, the overall maxima of vf_{total} in the dust layer are encountered. Whereas vf_{total} and n_{small} are typically correlated throughout the Caribbean measurements, at the Northwest African coast no such correlation is observable.

Figure 4.2.16 complements this quantitative analysis by the time series of n_{CCN} , D_{act} and κ inside the SAL. For these parameters, the shown values are representative of the accurate parameter PDFs derived for the flight leg subintervals specified in Tab. B.5.5 to B.5.7. Accordingly, n_{CCN} decreases by about 26% from an average of 248 to 182 cm^{-3} from the Northwest African coast to the Caribbean, connoting a slightly lower reduction than for the other particle concentrations. However, the limited amount of usable CCN data for the African coast restricts the significance of this finding. For the same reason the measurements are not really conclusive on potential (moderate) differences in D_{act} and κ . What can be stated nevertheless is that for the available data the D_{act} and κ values are comparable to both ends of the long-range transport. According to the respective joint PDFs, the D_{act} values show an insignificant decrease

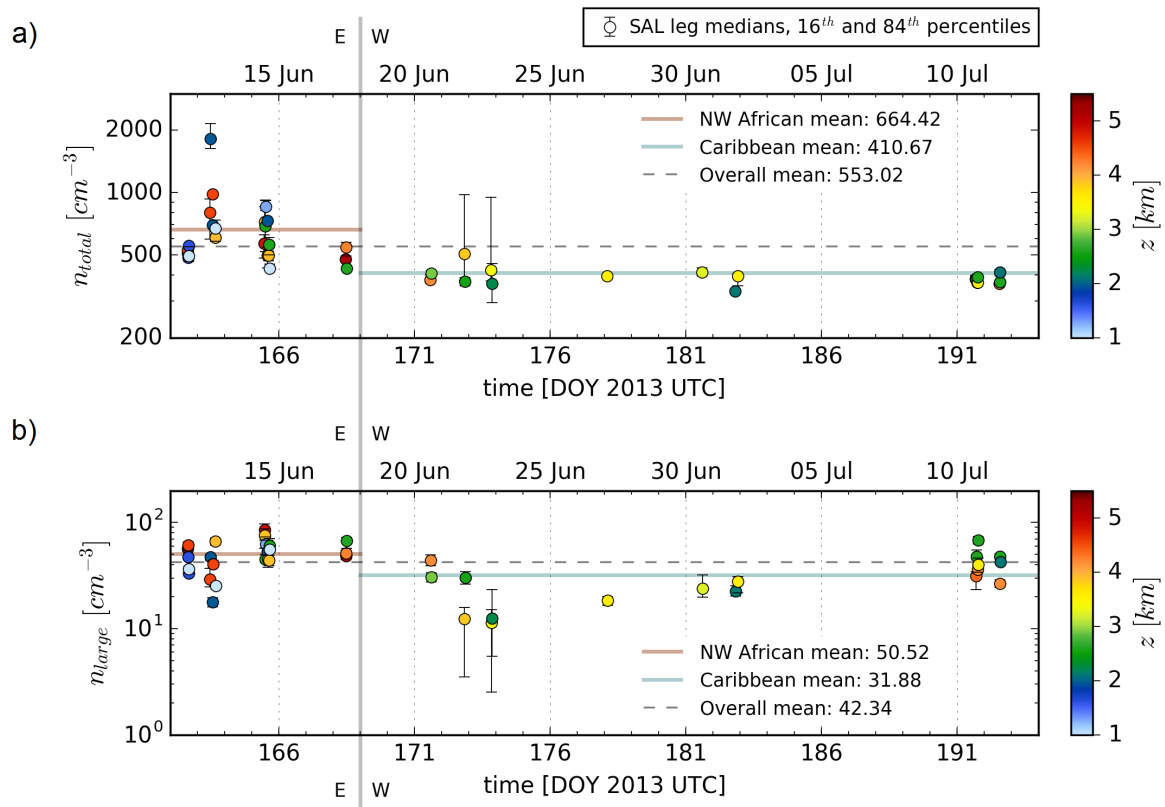


Figure 4.2.14: Time course of (a) n_{total} and (b) n_{large} values measured during the constant altitude flight legs inside the SAL. The markers represent the individual concentration medians, the error bars the range between the 16 and 84th percentiles. The marker colors indicate the leg altitudes. In addition to the individual leg statistics, collective mean values for the Northwest African coast (brown line) and the Caribbean (light blue line), and an overall mean (dashed line) are presented. All concentrations refer to STP conditions.

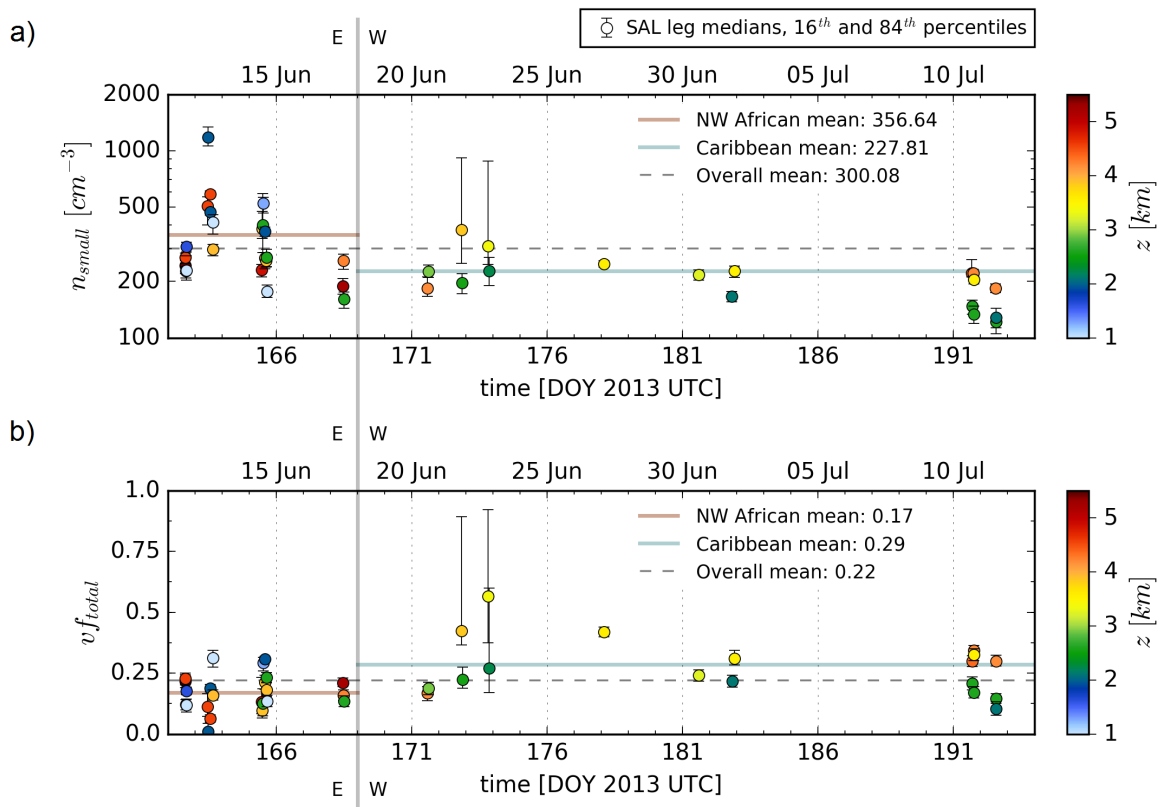


Figure 4.2.15: Same as Fig. 4.2.14 but for (a) n_{small} and (b) $v_{f_{total}}$.

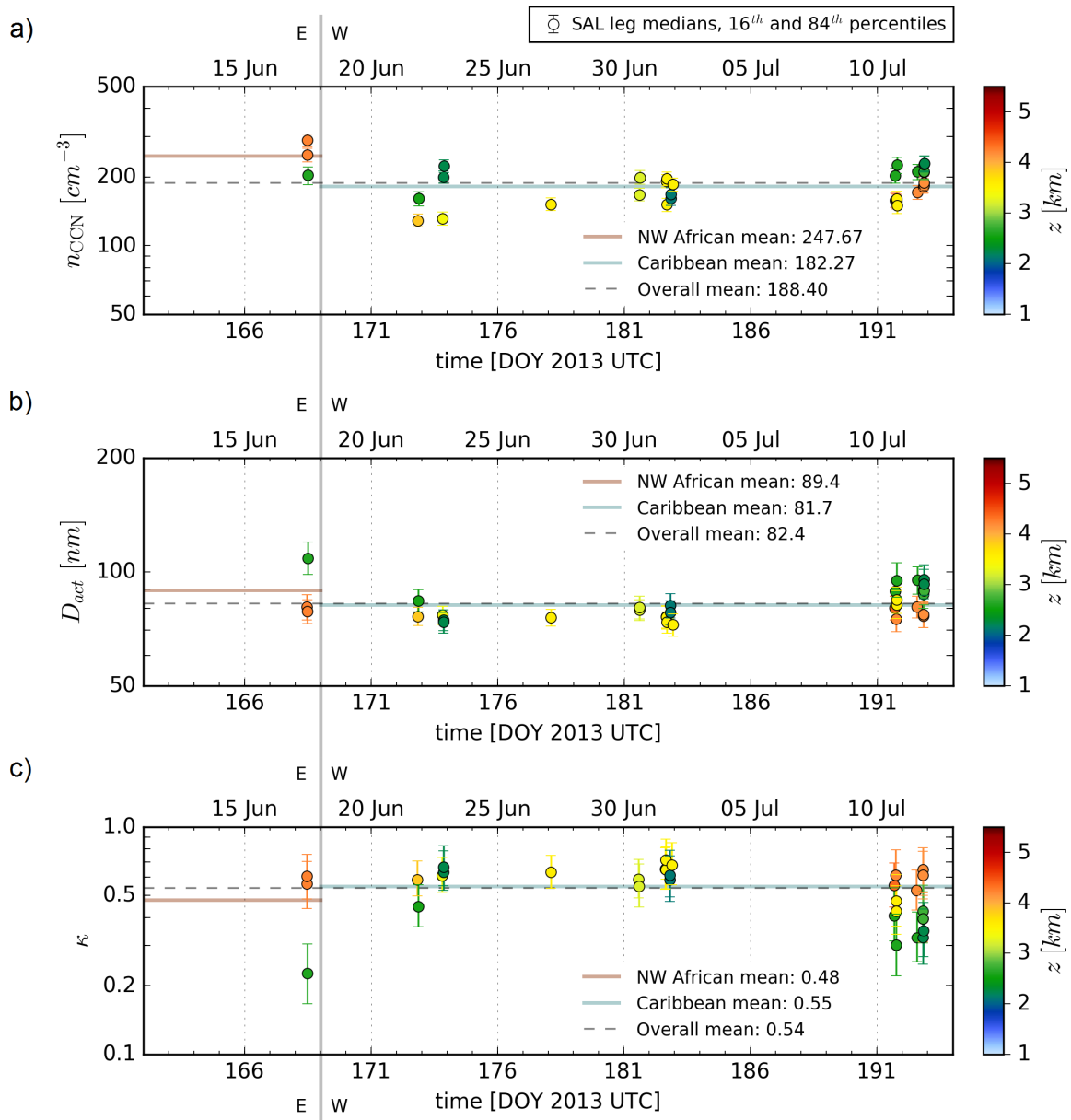


Figure 4.2.16: Time course of (a) n_{CCN} , (b) D_{act} and (c) κ values presented in a similar way as in Fig. 4.2.14 and 4.2.15. Different from before, here the markers and error bars do not visualize the statistics for the entire flight legs, but are representative of the median, 16 and 84th percentiles of the parameter PDFs derived for the subintervals defined in Tab. B.5.5 to B.5.7. n_{CCN} refers to $SS = 0.2\%$ and STP conditions.

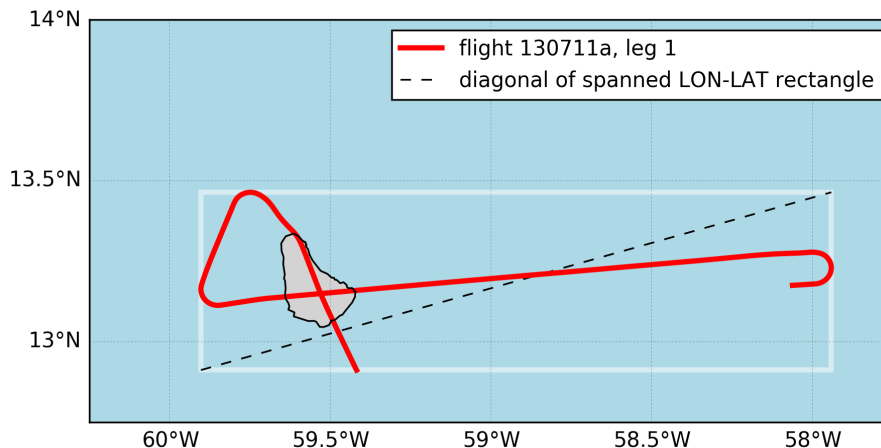


Figure 4.2.17: Definition of the horizontal extent for the constant altitude flight legs. This extent is given by the great-circle distance between the opposing corners of the longitude-latitude rectangle spanned by the corresponding flight track. For the normal case of a straight leg it corresponds to the total length of the track. For the exceptional case of a non-straight flight leg, e.g. the shown example (flight 130711a, leg 1 at about 9 km) the horizontal extent is visualized by the dashed line.

from⁹ 89 ± 16 to 82 ± 9 nm, while the κ values exhibit an insignificant increase from about 0.48 ± 0.21 to 0.55 ± 0.17 . Although the individual κ values exhibit a notable degree of scatter, with mean values ranging from about 0.25 to 0.7, they all imply a considerable particle hygroscopicity in the vicinity of D_{act} . The overall average of $\bar{\kappa} \approx 0.5$ for the SAL aerosol is close to the literature value for ammonium sulfate of 0.61 (Petters and Kreidenweis, 2007). In agreement with the findings for the intense dust event on 10 and 11 July (cf. Fig. 4.1.11), the highest values of κ are typically found for the cases of simultaneous $v_{f_{total}}$ and n_{small} enhancements in the upper SAL.

4.2.2.3 Horizontal Variability of Particle Concentrations in the SAL

The constant altitude flight legs are further utilized to extend the investigation of particle concentration variability in the SAL from the vertical to the horizontal. For this purpose, for each leg a horizontal extent is defined by the great-circle distance¹⁰ between the opposing corners of the longitude-latitude rectangle spanned by the corresponding flight track, as illustrated in Fig. 4.2.17. Flight legs with insufficient horizontal coverage, i.e. those with horizontal extents smaller 25 km are excluded from the analysis. Dividing the ambient relative concentration standard deviation (see Eq. (4.2.1) below) by the horizontal leg extent yields a measure for relative variability per horizontal distance. In Fig. 4.2.18 the resulting values for n_{total} , n_{large} and n_{CCN} are shown.

In order to extract the ambient concentration variability from the total measured variability, the latter must be liberated from interfering (instrument-related) contri-

⁹The given values represent means and standard deviations of the respective joint PDFs. The average standard deviations of the individual values are 6 nm and 0.12, i.e. 7% and 23% for D_{act} and κ , respectively.

¹⁰The great-circle distance is calculated by means of the haversine formula approximating the earth by a sphere with a radius of 6371 km.

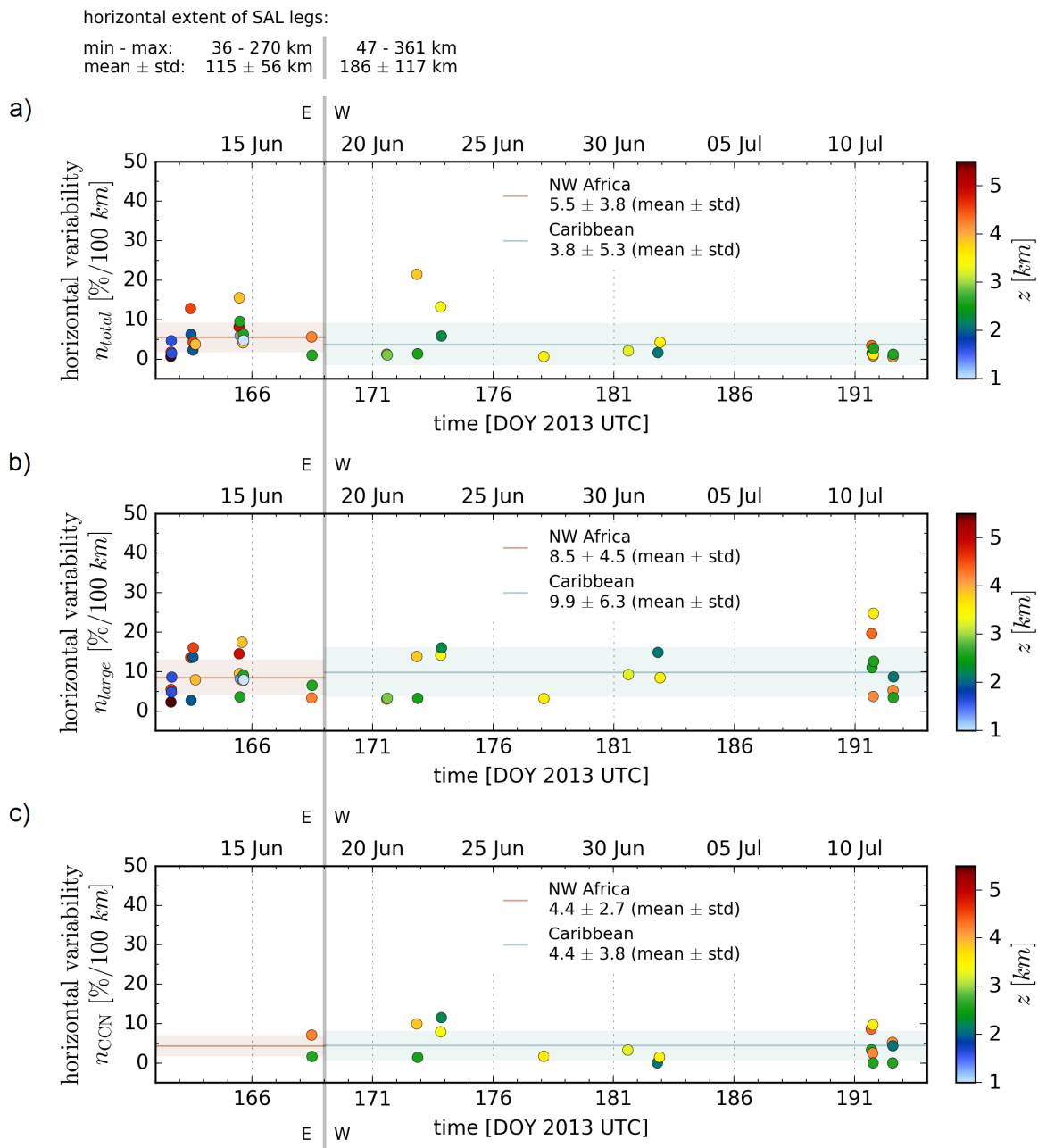


Figure 4.2.18: Horizontal variability of (a) n_{total} , (b) n_{large} and (c) $n_{CCN,v1}$ within the SAL (color-coded with altitude). The variabilities are presented as relative concentration standard deviations per 100 km horizontal distance (cf. Fig. 4.2.17). They are liberated from instrument-related variabilities attributable to Poisson counting statistics. In addition to the individual values, respective means and standard deviations for the Northwest African coast (brown line and range) and the Caribbean (light blue line and range) are presented. Moreover, on top of plot (a) absolute numbers for the total horizontal leg extents are given.

butions first. Here, the dominant source of additional variability is Poisson counting statistics. Assuming that the individual contributions to total variability are independent allows to approximate the total (measured) variance $\text{Var}(n)$ by the sum $\text{Var}_{\text{amb}}(n) + \text{Var}_{\text{Poisson}}(n)$, where $\text{Var}_{\text{amb}}(n)$ is the ambient concentration variance and $\text{Var}_{\text{Poisson}}(n)$ the one due to counting statistics. Following this approximation, the ambient relative concentration standard deviation is given by

$$\frac{\text{Var}_{\text{amb}}^{1/2}(n)}{\bar{n}} = \frac{(\text{Var}(n) - \text{Var}_{\text{Poisson}}(n))^{1/2}}{\bar{n}} = \left(\frac{\text{Var}(n)}{\bar{n}^2} - \frac{1}{\bar{n}Q^*} \right)^{1/2} \quad (4.2.1)$$

with the mean concentration \bar{n} and the instrument-specific particle count-to-concentration conversion factor $Q^* = N/n$ (including volumetric sample flow rate Q and eventual further factors, such as STP correction; e.g. cf. Sect. 3.2.2.1).

As apparent from Fig. 4.2.18, the average (ambient) horizontal variabilities are smaller than 10% per 100 km for all concentrations. With a few exceptions showing slightly increased variabilities of up to about 20 – 25% per 100 km, in the majority of cases the horizontal variability is quite weak, with 75% of the legs showing values smaller 6%, 14% and 8% variability per 100 km for n_{total} , n_{large} and n_{CCN} , respectively. Compared to the high degree of vertical heterogeneity in the SAL, the layer can thus be regarded as near-homogeneous in the horizontal over distances of (several) hundred kilometers. This holds for both the measurements at the Northwest Africa coast and those in the Caribbean, for which no significant differences are found. Moreover, no discernible correlation between horizontal variability and altitude exists.

4.2.3 SAL Aerosol Composition and NSD Before and After Long-Range Transport

By presenting the particle size-resolved information, Fig. 4.2.19 to 4.2.22 complete the comparison of SAL aerosol properties between the Northwest African coast and the Caribbean.

The respective joint particle NSDs in the SAL, shown in Fig. 4.2.19, demonstrate in detail what is already suggested from the particle concentration time series in Sect. 4.2.2.2, namely that on average the decrease in particle concentration with long-range transport is approximately size-independent (within the investigated size range $D \lesssim 2 \mu\text{m}$). This is reflected in the near-parallel course of the median NSDs using a logarithmic ordinate representation. The NSD maxima in the SAL are located at¹¹ 67 ± 11 and 69 ± 13 nm at the Northwest African coast and in the Caribbean, respectively. A list including all individual NSD retrieval results for the SAL is given in Tab. B.5.1 to B.5.3.

The particle volatility measurements for $D \gtrsim 300$ nm in Fig. 4.2.20 show no perceptible changes with transatlantic transport. The features of $vf(D)$, including the transition at $D \approx 500$ nm, are the same as discussed in Sect. 4.1.3. The absence of changes in this size range despite the average increase in vf_{total} (cf. Fig. 4.2.15) implies that particle volatility differences between Northwest Africa and the Caribbean are (primarily) limited to the range $D \lesssim 300$ nm. This is consistent with the observed correlation between vf_{total} and n_{small} .

¹¹As in Sect. 4.1.3, the given values represent the means and standard deviations of the joint PDFs for the maxima positions.

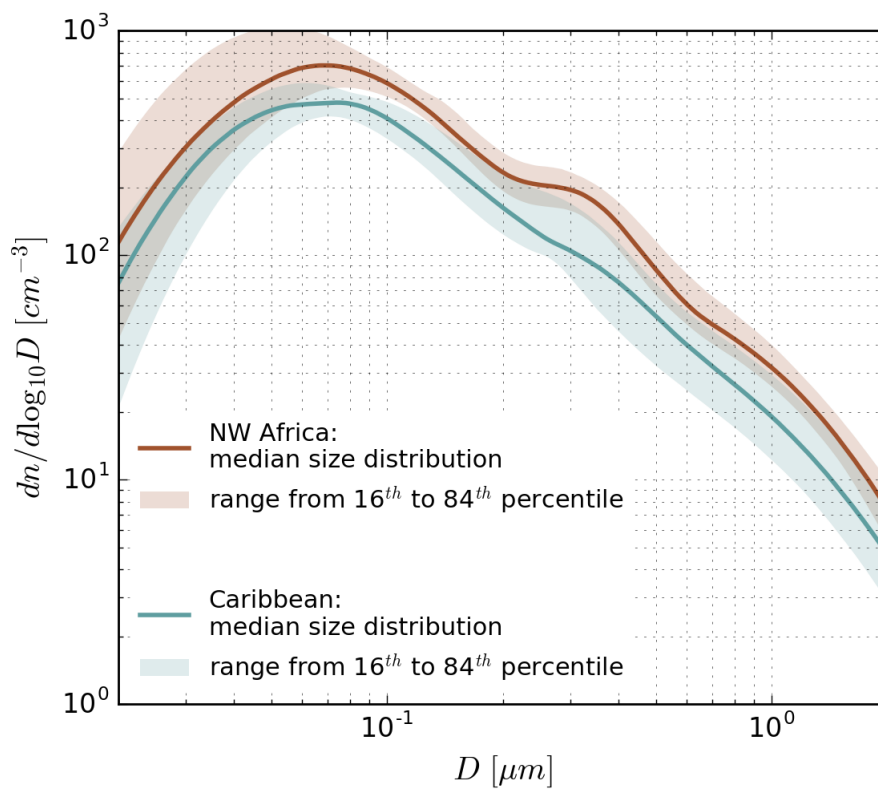
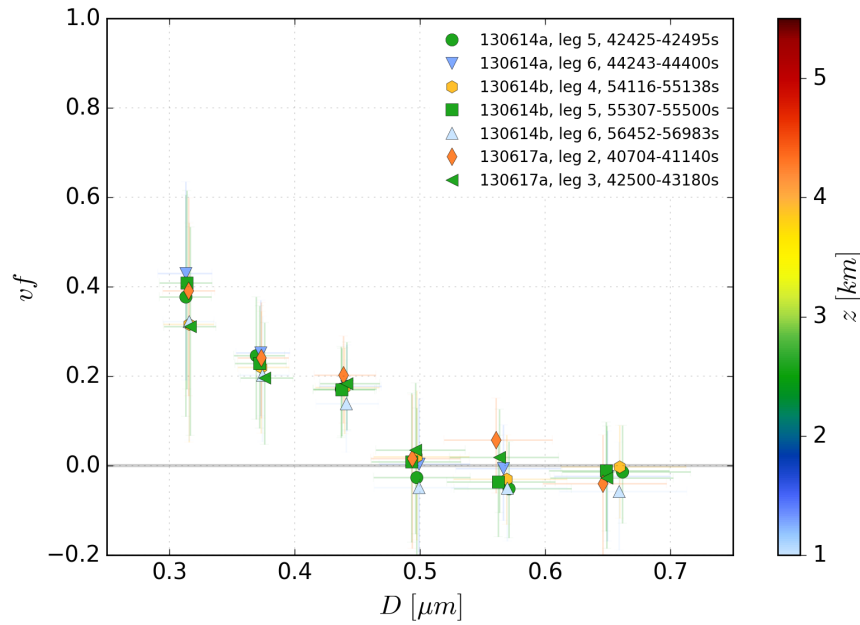


Figure 4.2.19: Comparison of the collective NSDs for the SAL at the Northwest African coast (red) and in the Caribbean (blue). The respective joint NSD retrieval solutions are represented by their diameter-wise medians, 16 and 84th percentiles. Particle concentrations refer to STP conditions.

a) NW Africa



b) Caribbean

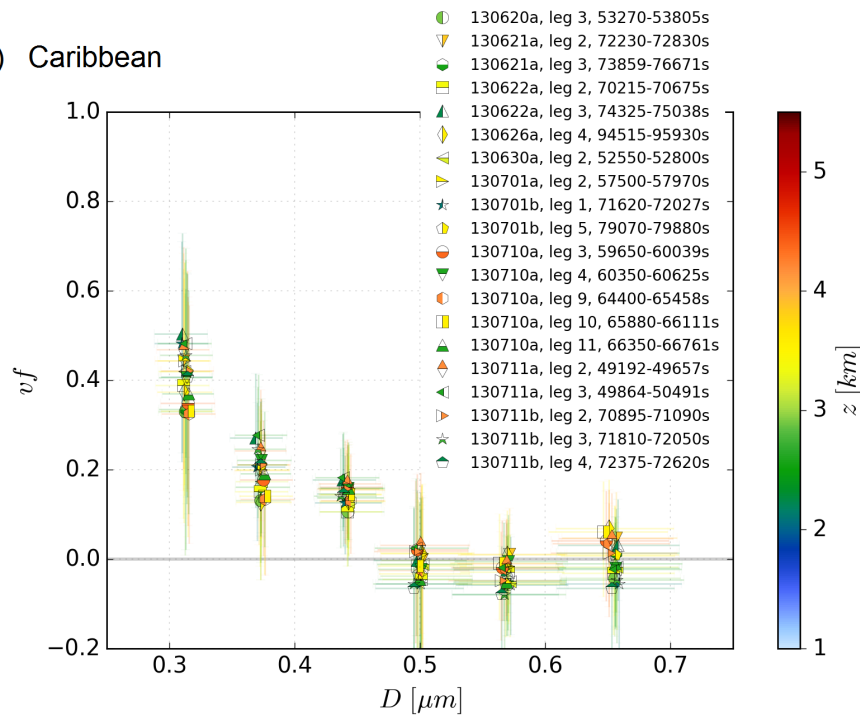


Figure 4.2.20: Size-dependent volatility of aerosol particles in the SAL at (a) the Northwest African coast and (b) in the Caribbean. The results are presented in the same way as in Fig. 4.1.9.

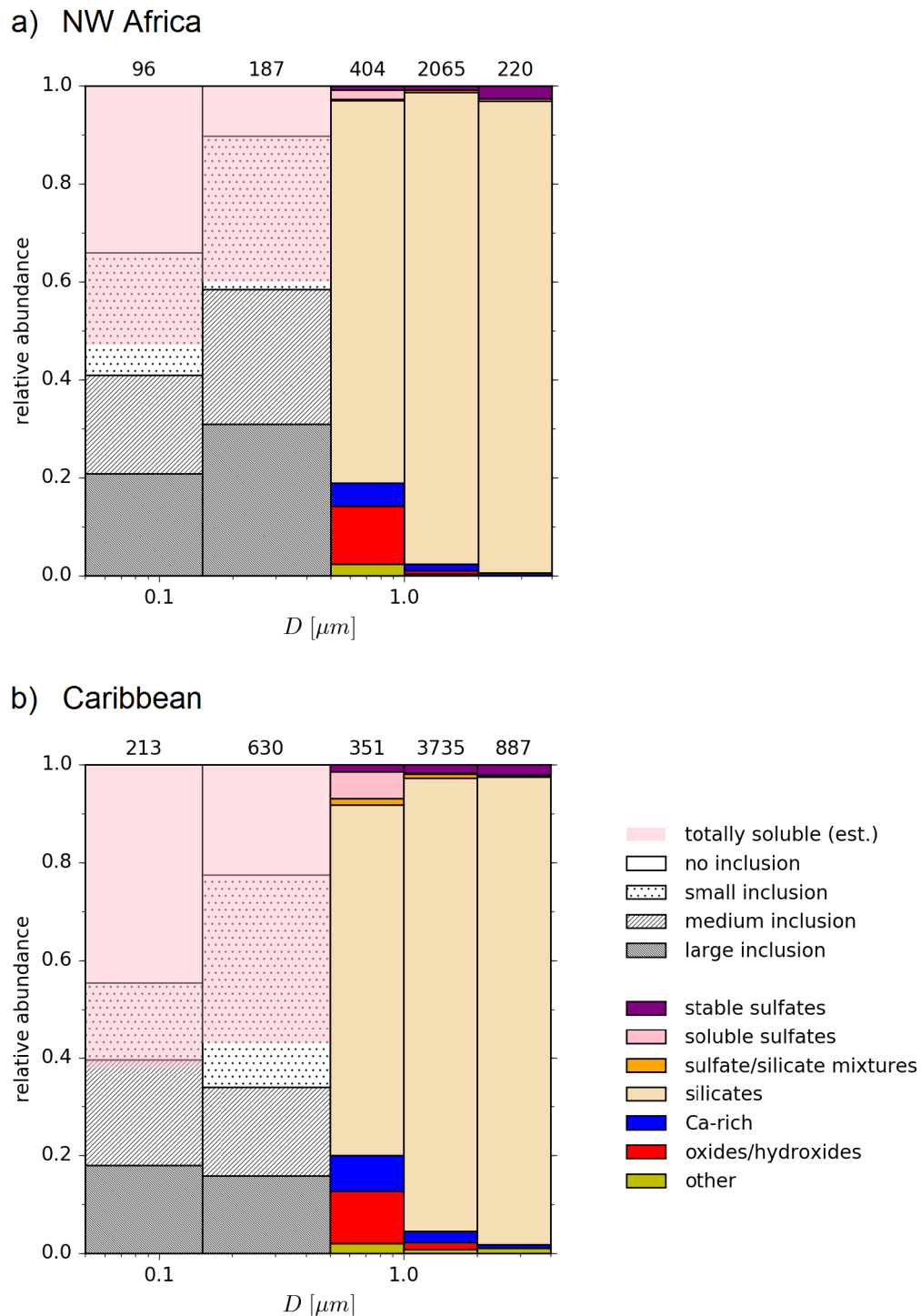
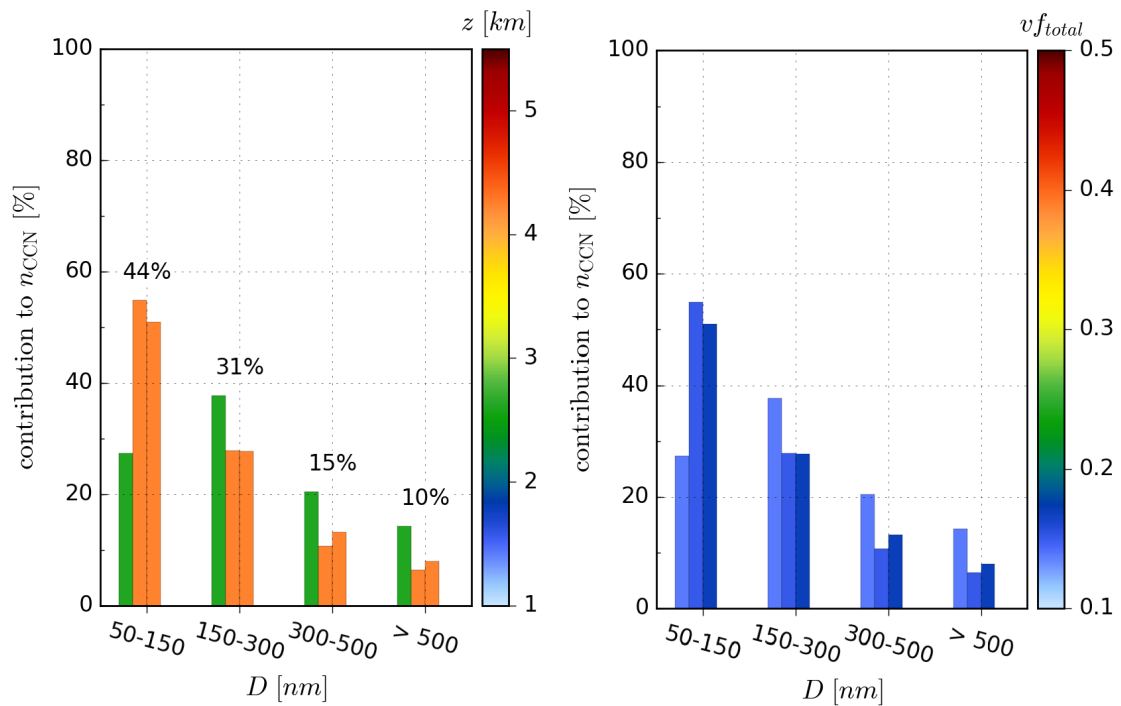


Figure 4.2.21: Single particle analysis results for the collective impactor samples withdrawn from the SAL at (a) the Northwest African coast and (b) in the Caribbean. The results are presented in the same way as in Fig. 4.1.10.

a) NW Africa



b) Caribbean

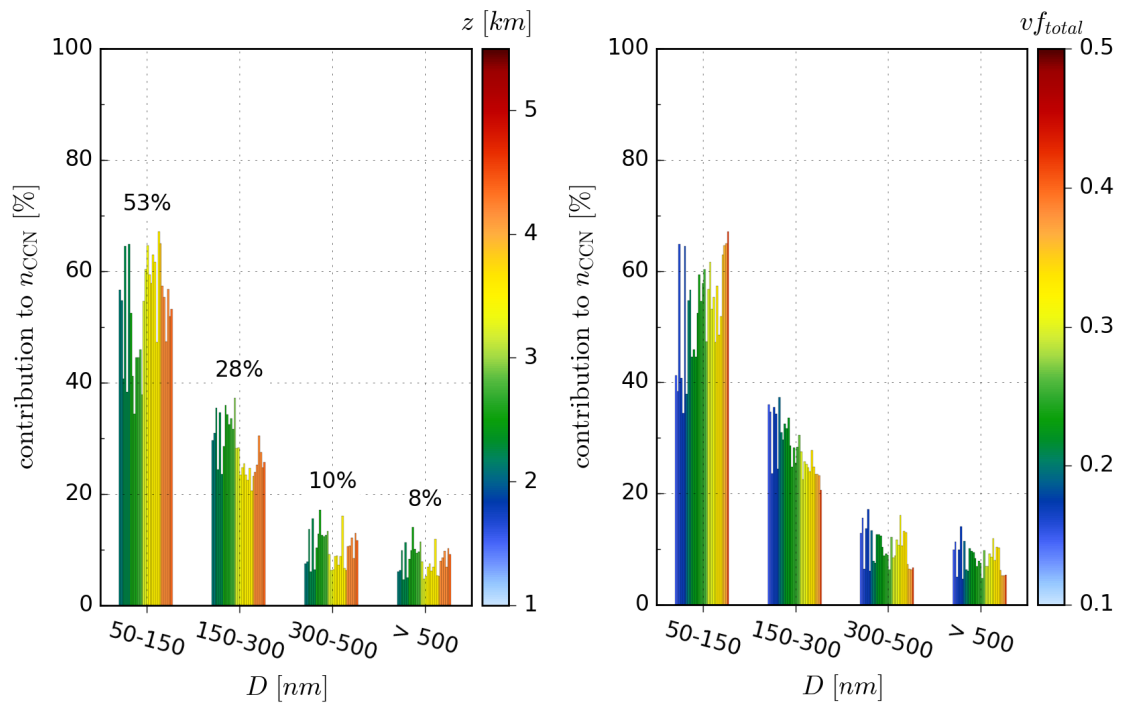


Figure 4.2.22: Contributions of different particle size ranges to n_{CCN} (at $SS = 0.2\%$) in the SAL at (a) the Northwest African coast and (b) in the Caribbean. The results are presented in the same way as in Fig. 4.1.12.

Figure 4.2.21 confronts the collective results of the single particle compositional analysis. A list of all impactor samples included in these results is given in Tab. B.3.2. For either side of the North Atlantic, the general features of the SAL aerosol composition are the same as discussed in Sect. 4.1.3. The size range $D \geq 500$ nm is dominated by mineral dust almost exclusively appearing in the form of pure dust particles. Amounts of internal mixtures between dust and other material, e.g. sulfate-silicate mixtures are negligible. The maximum fraction of such internally mixed dust particles, found for the collective Caribbean samples in the range $0.5 \leq D < 1 \mu\text{m}$, is smaller than 1%. In the latter size range, a slight enhancement in the fraction of soluble sulfates from about 1% to 2.5% seems to present in the Caribbean. However, this enhancement is hardly statistically significant. Similar to the large particles, qualitative agreement between the results is also found for the smallest particles with $D < 150$ nm, i.e. the particles in the vicinity of the NSD maximum. Both at the Northwest African coast and in the Caribbean this size range is dominated by volatile material, with about 60% of the particles having volatile volume fractions $\geq 70\%$. Consistent with the increase in vf_{total} , yet, a moderate increase in the fraction of completely volatile particles from about 35% to 45% is apparent. For the analyzed samples, another increase in volatile material is observed for the intermediate size range $150 \leq D < 500$ nm with a rise in the fraction of completely volatile particles from about 10% to 20%, and a rise in the fraction of particles with volatile volume fractions $\geq 70\%$ from about 40% to 65%.

The approximate preservation of the NSD shape and the features of the aerosol composition, particularly in the vicinity of the D_{act} , finally reflects in the contribution of the different size ranges to n_{CCN} , shown in Fig. 4.2.22. Despite the sparseness of usable CCN data for the Northwest African coast, the available data show results comparable with those in the Caribbean. In either case, the major contribution to n_{CCN} is given by the size range $D < 150$ nm. The corresponding average values for the SAL aerosol before and after long-range transport are 44% and 53%, respectively. In the Caribbean SAL this contribution of the smallest particles exhibits a clear positive correlation with vf_{total} and a less pronounced, though still notable correlation with altitude. This means, that the highest values of up to 60 – 70% are typically found for the (Caribbean) cases with increased volatility in upper part of the dust layer. The average contribution of the dust-dominated particles with $D \geq 500$ nm to n_{CCN} is only¹² 10% and 8%, respectively.

¹²Even when n_{giant} is assumed to be representative for the number concentration of CCN larger than the Falcon aerosol inlet cutoff, the average contribution of particles with $D \geq 500$ nm remains smaller 14% and 11%, respectively.

Chapter 5

Discussion

In the following, the results presented in Ch. 4 are interpreted regarding their implications and discussed in the light of the current literature.

5.1 The SAL as a Separated Particle Reservoir

The investigated Saharan air masses are typically bordered by two discernible temperature inversions, justifying to treat these air masses as an elevated distinct layer, the SAL. As appears from the potential temperature profiles, e.g. shown in Fig. 4.2.1 and 4.2.5, these inversions are not exclusively met at the Northwest African coast but are characteristic for the Saharan air reaching the Caribbean, too. The trade wind inversion defining the base of the SAL is found to rise from altitudes around 0.5 – 1 km at the Northwest African coast to about 2 km in the Caribbean, which is ascribable to a deepening of the moist subjacent troposphere produced by small-scale convection over the ocean (Carlson and Prospero, 1972). While the base inversion occurs at rather constant levels for each respective region, the upper inversion capping the SAL exhibits a greater variability in height, which is likely attributable to differently pronounced vertical growth of the layer during initial formation and/or variable descending rates during transport. The descent of the SAL, leading to the observed decline of its ceiling from about 6 km at the Northwest African coast to approximately 4 – 5 km in the Caribbean (see also Chouza et al., 2016; Weinzierl et al., 2017), is influenced by a present large-scale subsidence between Africa and Central America north of the ITCZ (Colarco et al., 2003) and due to longwave radiative cooling of layer (Huang et al., 2010). A consistent feature of the SAL is a distinct drop in humidity coinciding with its lower inversion, meaning that at its base the SAL interior is not only considerably warmer but also dryer than the subjacent troposphere. All these findings are in close match with former observations (e.g. Carlson and Prospero, 1972; Karyampudi et al., 1999; Reid et al., 2002; Dunion and Marron, 2008), meaning that the observed structure in meteorological parameters associated with the presence of Saharan air masses can be considered representative for the investigated regions in Northern Hemispheric summer.

The existence of strong positive potential temperature gradients at the SAL borders implies a high degree of vertical stability. This external stability limits convective activity and counteracts vertical turbulence (e.g. induced by wind shear), thereby

constituting an obstacle to effective mixing of the SAL with the over- and underlying troposphere. Such a stable tropospheric stratification is not encountered for situations without SAL presence (cf. Fig. 4.1.7), i.e. when the Caribbean SAL is periodically replaced by dust-free air masses from southeasterly directions in the course of AEW passages. The observed conservation of stability at the base of the SAL, facilitating a main transatlantic transport of Saharan air that is separated and dry/cloud-contact free (cf. Fig. 4.1.1), is only possible due to its intrinsic aerosol properties, namely the internal heating caused by light absorbing particles counteracting its radiative cooling (Carlson and Benjamin, 1980; Karyampudi and Carlson, 1988; Davidi et al., 2012). At the same time, the stability at the SAL top is maintained by the large-scale subsidence (Weinzierl, 2007). The resulting long-lasting SAL stratification impacts tropospheric stability over vast areas of the North Atlantic and the adjacent continents and may have important direct implications, as for instance the potential inhibiting effect on TC formation (e.g. Dunion and Velden, 2004) addressed in Sect. 1.3.

Besides its direct relevance for meteorological processes, the stability of the SAL also affects the vertical aerosol structure, particularly by impeding effective downward transport of the high concentrations of SAL aerosol particles into the lower troposphere. This is because low-level clouds that would induce wet particle deposition are hindered from growing into SAL altitudes and vertical mixing is suppressed hampering turbulent dry particle deposition. The result is a marked coupling between SAL-induced atmospheric stratification and particle concentration profiles, observed on both sides of the Atlantic. Especially the (STP) concentration of large particles (with $D \gtrsim 300$ nm) n_{large} typically shows a significant increase at the transition from the lower troposphere into the SAL and a drop-off (to vanishing values) at the SAL's ceiling (cf. Fig. 4.2.3 and 4.2.7). Hence, the maximum of n_{large} and, therewith, the maximum in particulate mass concentration is found inside the elevated SAL. A comparable trend is also observed for the CCN concentration (at $SS = 0.2\%$) n_{CCN} and the closely following number concentration of particles with $D \gtrsim 80$ nm n_{80} . Here as well, a concentration increase is typically met at the base of the SAL and a subsequent decrease is encountered at the SAL's capping inversion¹ (cf. Fig. 4.2.4 and 4.2.8). Accordingly, not only the amount of coarse particles but also the concentration of CCN is commonly most enhanced within the SAL. As can be seen from Fig. 4.1.7, these enhancements in n_{large} , n_{80} and n_{CCN} at altitudes $z \gtrsim 2$ km disappear during the absence of Saharan air masses in the Caribbean, proving that this is a specific SAL feature. The connection between the SAL's bordering inversions and the particle concentration profiles is in line with the vast majority of earlier findings (e.g. Prospero and Carlson, 1972; Maring et al., 2003a; Formenti et al., 2011a; Jung et al., 2013). Only Reid et al. (2002) found temporal deviations from this typical coupling, which they, however, attributed to anomalous SAL formation conditions at the Northwest African coast. In summary, thanks to its preserved external stability and high initial particle content the SAL represents an immense lifted aerosol reservoir both before and after transatlantic transport, especially concerning particulate mass and CCN.

¹For SAL top heights exceeding about 4.5 km, the decrease in n_{CCN} above the layer is not apparent from the presented data, since these data are confined to (inlet) pressures of $p > 500$ hPa. This is because for higher levels (lower pressure) the CCNC supersaturation and flow conditions are no longer defined (cf. Sect. 3.2.2.3). Yet, a decline in n_{CCN} at the SAL's ceiling is still qualitatively observable for these occasions, too (see Dollner, 2015).

5.2 Overlay of the SAL by UT Aerosol

Remarkably, despite the (sharp) decrease in n_{80} , n_{CCN} and especially n_{large} at the upper edge of the SAL, the total particle concentration n_{total} typically shows its maximum above the SAL accompanied by a considerable enhancement in the total fraction of (completely) volatile particles v_{total} (cf. Fig. 4.2.2 and 4.2.6). This means that the SAL is permanently overlaid by air masses containing high concentrations of particles that are predominantly volatile and smaller than 80 nm in diameter, although a minor fraction also occurs at slightly larger sizes. The most obvious source of these particles is located in the UT, where a range of airborne in situ studies consistently reported strong enhancements in such small particles over vast areas, particularly in the tropics and subtropics, over continents as well as over remote oceanic regions (e.g. Clarke et al., 1999; Twohy et al., 2002; Hermann et al., 2008; Borrmann et al., 2010; Weigel et al., 2011; Andreae et al., 2017). The general consensus of these studies is that the high particle concentrations in the UT are the product of NPF from gaseous precursors lifted to these altitudes by deep convection. Owing to high actinic flux, low temperatures and negligible amounts of pre-existing particles that would offer a surface for heterogeneous condensation, the UT represents a promotive environment for such NPF. A prominent particulate product often associated with NPF in the UT is highly volatile and hygroscopic sulfate aerosol, especially in marine and anthropogenically influenced regions supplied with sufficient amounts of sulfur gases (from ocean-emitted dimethyl sulfide or pollution) (Clarke et al., 1999; Twohy et al., 2002; Lee et al., 2003; Merikanto et al., 2009). Provided that NPF aerosol is present above the SAL, large-scale subsidence likely leads to downward transport of this secondary aerosol towards the SAL top explaining the observations. Despite the prominence of NPF aerosol in the UT, to date no reports for the overlay of the SAL by this aerosol exist. Certainly, a main reason for this is that most previous in situ campaigns, particularly in the Caribbean, were either limited to altitudes far below the SAL ceiling and/or lacked an instrumentation allowing to measure particles in this size range. Moreover, remote sensing instruments like lidars are hardly sensitive to such small particles. This is because they usually operate at wavelengths of about 0.5 to 2 μm , i.e. wavelengths much larger than the size of these particles ($\lambda \gg D$). As discussed in Sect. 2.2, in this regime particle scattering efficiency scales with $\alpha^6 = (\pi D/\lambda)^6$ (Rayleigh scattering), i.e. rapidly decreases with the gap between D and λ . Indeed, the airborne wind lidar measurements at $\lambda = 2 \mu\text{m}$ during SALTRACE did not detect this aerosol feature above the SAL (cf. Chouza et al., 2016).

5.3 Internal Structure of the SAL

5.3.1 Vertical Heterogeneity

Unlike at its bottom and top edge where stability suppresses vertical exchange/mixing, the interior of the SAL is often considered well-mixed (Karyampudi et al., 1999; Liu et al., 2008; Ryder et al., 2013a; Tsamalis et al., 2013). Such a well-mixed layer would in a strict sense be characterized by statically neutral air, i.e. a Brunt-Väisälä frequency $N = 0$ (constant potential temperature). Moreover, a well-mixed layer would exhibit

uniform water vapor mixing ratio and STP particle number concentrations. However, the results reveal that during SALTRACE such conditions were rarely met. Typically, slightly positive potential temperature gradients, i.e. moderate stability is found for most part of the SAL interior, and in some cases even small internal inversions seem to be present. Also, the mixing ratio regularly exhibits variations with height, meaning that differently humid, evidently unmixed sublayers coexist within the SAL altitude range, i.e. in the range between the SAL's bordering inversions.

Deviations from homogeneity become even more evident looking at the particle concentration profiles. Especially for n_{large} , high concentration variations of $\pm 50\%$ and more within short vertical distances of only a few hundred meters are frequently observed (cf. Fig. 4.2.3 and 4.2.7). This heterogeneity is also apparent from the lidar measurements (cf. Fig. 4.2.11 and Chouza et al. (2015, 2016)). Moreover, not only pronounced variability in absolute concentrations is observable but occasionally even transitions in the NSD, such as vertically confined relative enhancements in the concentration of small particles n_{small} (with $D \lesssim 80$ nm). For instance, the measurements on 14 (NW Africa) and 22 June (Caribbean) show noticeable intermediate layers of increased n_{small} and simultaneously reduced n_{large} within the SAL altitude range (cf. Fig. 4.2.2 and 4.2.6). Presumably due to the moderate stability of the SAL interior, acting contrary to vertical mixing, there is no significant homogenization of the particle concentration profiles with transatlantic transport. These findings support a number of former airborne in situ studies also reporting high vertical variability in particle concentrations within the SAL on either side of the Atlantic (e.g. Reid et al., 2003b; Maring et al., 2003a; Formenti et al., 2003; Johnson and Osborne, 2011; Formenti et al., 2011a).

Although airborne in situ measurements are strongly limited in space and time, this raises serious doubts on whether the assumption of a well-mixed SAL really is appropriate in the majority of cases. Compared to a homogeneous layer, a heterogeneous vertical distribution of particle concentrations, i.e. of scatterers and absorbers entails a more complex aerosol-radiation interaction. Besides affecting the SAL's direct aerosol radiative effect, the vertical variability in the concentration of (light-absorbing) particles impacts the height-dependent heating rates, in turn influencing the SAL's internal and external stability. The observation of a SAL that is not well-mixed as a whole, however, does not exclude the occurrence of vertical mixing in subparts of the layer. The high abundance of coarse particles ($D \gtrsim 5 - 10 \mu\text{m}$) found in the long-range transported SAL (Maring et al., 2003b; Denjean et al., 2016b; Weinzierl et al., 2017) and their presence near the top edge of the layer (Gasteiger et al., 2017; Haarig et al., 2017) is hardly explainable without (temporary) upward transport by vertical mixing counteracting gravitational settling².

5.3.2 Horizontal Homogeneity

In contrast to the marked vertical heterogeneity of the SAL, only marginal variation in particle concentrations is encountered for the horizontal flight legs inside the SAL (cf. Fig. 4.2.18). Here, the observed concentration standard deviations are explicable

²For mineral dust particles with $D \gtrsim 5 - 10 \mu\text{m}$, the terminal settling velocity is several hundred meters per day (cf. Tab. 5.4.1).

mainly as a result of counting statistics, meaning that the layer shows a high degree of horizontal homogeneity over distances in the order of 100 km. This seems natural considering the large horizontal spread of the dust pulses crossing the North Atlantic, as for instance apparent from the SAL satellite product and the modeled dust AOD contours shown in Fig. 4.1.1. The horizontal homogeneity of the SAL also explains the overall good agreement between the ground-based measurements, particularly the lidar profiles over Barbados, and the sometimes several hundred kilometer distant airborne measurements (cf. Fig. 4.2.11 and 4.2.12).

5.4 Vertical Aerosol Exchange Between the SAL and the Adjacent Troposphere

Despite its distinct bordering inversions letting the SAL appear as the discussed stable/separated aerosol reservoir, there is strong evidence suggesting that the layer is not complete sealed from the under- and overlying troposphere throughout its lifetime.

5.4.1 Entrainment of UT Aerosol

The repeated occurrence of coupled n_{small} and vf_{total} enhancements at simultaneous depletion in larger particles in the upper part of the SAL, e.g. apparent from Fig. 4.2.13 and 4.2.15, leads to the conclusion that, here, the NPF aerosol consistently present above the SAL may occasionally be mixed in. These observations represent the first-time evidence for a contribution of particles originating from the UT to the SAL aerosol. One mechanism that could be responsible for such an entrainment is vigorous vertical mixing with the free troposphere due to strong convection during the initial formation of the SAL (Carlson and Prospero, 1972; Weinzierl, 2007). This is supported by few encounters of vf_{total} enhancements (just) below the SAL's capping inversion already at the Northwest African coast before transatlantic transport, e.g. during flight 130612a and 130614a (cf. Fig. 4.2.6). However, the most explicit examples of this feature are found in the Caribbean, particularly on 26 June and during the last intense dust event on 10 and 11 July (cf. Fig. 4.2.2 and 4.1.4), suggesting that NPF aerosol entrainment into the upper SAL occurs also during transport, despite the presence of the upper (subsidence) inversion. This reasoning is further reinforced by the fact that the overall average vf_{total} (for the entirety of flight legs) is enhanced in the long-range transported Caribbean SAL and that this average enhancement is clearly attributable to measurements in the upper part of the layer at increased n_{small} , as can be seen from Fig. 4.2.15. Such a correlation between enhancements in n_{small} , vf_{total} and altitude is not discernible for the flight legs over the Northwest African coast. A process potentially leading to the entrainment during transport is turbulent mixing due to wind shear. Particularly at the SAL top edge considerable vertical wind shear, i.e. a strong drop in horizontal wind speed from its interior to the troposphere above is consistently observed (cf. Fig. 4.2.13 and Chouza et al. (2016)). Wind shear amplifies vertical air parcel displacements resulting in a growing pattern of Kelvin–Helmholtz

D [nm]	V_{ts} for spherical (NH ₄) ₂ SO ₄ ($\rho_p = 1.8 \text{ g/cm}^3$) [m/day]	V_{ts} for spherical mineral dust ($\rho_p = 2.5 \text{ g/cm}^3$) [m/day]	V_{ts} for aspherical mineral dust (shape factor 1.4) [m/day]
10	0.02	0.02	0.02
50	0.09	0.12	0.09
100	0.19	0.26	0.19
200	0.45	0.63	0.45
500	1.78	2.47	1.77
1000	5.93	8.24	5.88
2000	21.53	29.91	21.36
5000	126.48	175.67	125.48
10000	495.13	687.68	491.20

Table 5.4.1: Size-dependent terminal settling velocities for ammonium sulfate and mineral dust particles. The settling velocities for the spherical particles are calculated by means of Eq. (2.5.4) for a representative SAL ambient pressure of 700 hPa and a dynamic viscosity of $1.75 \times 10^{-5} \text{ kg/ms}$. For the aspherical mineral dust particles, the results of Eq. (2.5.4) are divided by a typical shape factor for coarse dust of 1.4 (cf. Hinds, 1999).

instability motions in situations where restoring forces due to vertical stability³ are no longer able to suppress this growth (e.g. Wallace and Hobbs, 2006). An indicator for the occurrence or absence of wind shear-induced vertical turbulence is the so-called Richardson number $Ri = N^2/Sh^2$, determined by the wind shear Sh and Brunt-Väisälä frequency N . The onset of turbulence requires Ri to drop below a critical value Ri_c , which is usually taken as 0.25, although suggestions in the literature range from 0.2 to 1 (Galperin et al., 2007, and references therein). Once a flow is turbulent, it can stay turbulent even for $Ri > Ri_c$ (hysteresis effect), but usually becomes laminar again for $Ri \gtrsim 1$ (Wallace and Hobbs, 2006). As demonstrated in Fig. 4.1.3 by the example of data from flight 130711a, the vertical wind shear in the altitude range of the SAL's capping inversion indeed seems to be partially strong enough to cause near-critical Richardson numbers, i.e. $Ri < 1$ (although in the main $Ri > 1$). Accordingly, it stands to reason that temporary peaks in Sh may induce turbulent vertical mixing at the upper edge of the SAL in the course of its transport and may, hence, lead to entrainment of NPF aerosol from the UT. However, although the findings underpin this explanatory approach, it cannot be ruled out that changes in the initial vertical structure of the SAL during the campaign contribute to the observed differences.

5.4.2 SAL Aerosol Presence in the Lower Troposphere

Apart from mixing with the overlying troposphere, the results also give strong indications for aerosol exchange at the base of the SAL during transport, particularly for the input of SAL aerosol into the lower troposphere. Whereas there are only small amounts of dust in the MBL at the Northwest African coast during summer, the Caribbean MBL experiences notable dust loads (Weinzierl et al., 2017). The lidar profiles and especially the close correlation between AOD and ground-based dust mass concentrations at Barbados (cf. Fig. 4.2.11 and Groß et al. (2016)) clearly demonstrate that the presence of the elevated SAL in the Caribbean is always accompanied by a presence of dust-laden SAL aerosol in the lower cloud-containing troposphere, which is consistent with earlier studies (e.g. Smirnov et al., 2000).

Since, typically, the vertical wind shear at the base of the SAL is too weak to jeopardize the trade wind inversion's stability (cf. Fig. 4.1.3), shear-induced turbulence can be excluded as a primary cause for this feature. An indisputable mechanism for particle input from the SAL into the lower troposphere is gravitational settling. Particles coarse enough to reach sufficient settling velocities, i.e. particles with $D \gtrsim 5 - 10 \mu\text{m}$ (see Tab. 5.4.1) can fall out through the trade inversion. Such a settling of coarse particles takes place along the entire transport route, which is documented by sedimentation traps across the North Atlantic (van der Does et al., 2016). However, the number concentration of coarse particles in the SAL is far too low to explain the observed enhancements in near-ground particle concentrations in the Caribbean during SAL presence (Kristensen et al., 2016) by gravitational settling alone. The analysis of backward trajectories starting over Barbados, e.g. the ones for 11 July (12 UTC) shown in Fig. 4.1.1, suggests that owing to differential transport some Saharan air masses may reach the Caribbean below the trade wind inversion. This means that there might occasionally be additional transport of Saharan aerosol at lower levels alongside the main SAL transport. Yet, since according to the trajectory analysis such additional transport is absent in many cases where a strong presence of SAL aerosol in the MBL is observed nonetheless, this is unlikely to be the main explanation. SAL transport modeling by means of COSMO-MUSCAT arrives at the conclusion that the most important mechanism leading to the input of SAL aerosol into the lower troposphere is turbulent dry deposition triggered by strong convection events that manage to temporarily overcome the trade wind inversion (Fig. B.4.1 and Heinold et al. (2017, in prep.)). While the model exhibits a rather isolated SAL at the beginning of the transatlantic transport, it shows an incipient occurrence of such convection-induced turbulent deposition events about 1 – 2 days before the arrival of the SAL in the Caribbean. The maximum of SAL aerosol deposition is then reached in the Caribbean sea. These model results are consistent with satellite-based lidar studies of the summertime SAL that also show an minor presence of SAL aerosol in the lower troposphere during the initial phase of transport, but an enhancement of this presence when the SAL approaches and finally reaches the Caribbean sea (Liu et al., 2008; Adams et al., 2012; Tsamalis et al., 2013). For one case during SALTRACE, i.e. on 1 July effective downward mixing of SAL aerosol was apparently directly observed in the Caribbean. Here, the lidar

³Stability, connoting restoring forces to air parcel displacements, requires a squared Brunt-Väisälä frequency of $N^2 > 0$.

measurements at Barbados (Fig. 4.2.11) show clearly recognizable “mixing filaments” extending from SAL altitudes to near the ground, i.e. temporary interruptions of the aerosol separation between the SAL and the underlying atmosphere. This matches with the exceptional vertical in situ profiles for flight 130701a that, contrary to the typical conditions (cf. Sect. 5.1), show a weak to non-existent trade wind inversion accompanied by a missing transition in n_{large} (cf. Fig. 4.2.1 and 4.2.3).

Recalling that the SAL carries large amounts of CCN, it is obvious that the input of SAL aerosol will lead to an enhancement of CCN concentrations in the MBL, meaning in the altitude range providing the aerosol basis for the trade wind regime clouds. Such an increase of n_{CCN} in the Caribbean MBL during SAL presence is apparent from Fig. 4.2.11 and has been demonstrated by other studies (e.g. Wex et al., 2016). By contributing CCN to the MBL, the SAL aerosol unavoidably influences the formation and properties of clouds in the trade wind regime, particularly in the Caribbean sea. This is confirmed by measurements proving that during African dust presence trade wind cumuli experience the Twomey effect, meaning that these clouds exhibit increased droplet number concentrations associated with decreased droplet radii (Siebert et al., 2013; Werner et al., 2014). As discussed in Sect. 1.3, besides the increase in cloud shortwave albedo, the reduction in average droplet size may further impact the climate by extending cloud lifetime.

5.5 CCN Properties of the SAL Aerosol in the Context of Particle Composition

Notwithstanding the influential enhancement of n_{CCN} in the MBL caused by the SAL aerosol, the ground-based analysis of particle composition reveals that the role of mineral dust for the sub-cloud CCN properties is rather negligible (Kristensen et al., 2016). Consequently, it can already be concluded that the SAL must carry CCN-relevant particulate material other than mineral dust.

5.5.1 Role of Soluble Sulfates

Indeed, the results of the compositional analysis of the SAL samples confirm this conclusion. As apparent from Fig. 4.2.21, the composition of the SAL aerosol is substantially changing with particle size. Whereas the size range $D \geq 500$ nm is dominated by mineral dust, significant amounts of volatile material are found at smaller particle diameters. The volatile fraction, more specifically the number fraction of completely volatile particles and particles bearing considerable amounts of volatile material, is typically increasing with decreasing particle size for $D \lesssim 500$ nm. Independent from the single particle analysis, this is confirmed by the in situ measurements of size-resolved volatility (cf. Fig. 4.2.20). Especially for the smallest size class, i.e. $D < 150$ nm, the volatile material plays a dominant role. Here, about 80% of the particles contain volatile volume fractions larger than 10% and about 60% even comprise more than 70% of volatile components by volume. Its chemical signature leads to the conclusion that the volatile material is predominantly ammonium sulfate, a highly water soluble/hygroscopic species. A (qualitatively) consistent size-dependent aerosol com-

position was already observed in the SABL (Kaaften et al., 2009; Kandler et al., 2009; Schladitz et al., 2009) and the initial SAL (Weinzierl et al., 2009) during the SAMUM campaign in 2006, suggesting that this composition may be regarded as characteristic for the (summertime) Saharan aerosol. The significant contribution of soluble sulfate at small particle diameters reflects in the high effective particle hygroscopicity κ in the SAL derived in this study from the combined CCN and particle NSD measurements. The corresponding values range between about 0.3 and 0.7 with an overall mean of $\bar{\kappa} \approx 0.5$ (cf. Fig. 4.2.16), which is close to the laboratory value for pure ammonium sulfate particles of 0.61 (Petters and Kreidenweis, 2007). Therewith, the κ values in the SAL are similar or even slightly enhanced compared to those in the Caribbean MBL during the same period, that are typically found in the range from 0.2 to 0.4 (cf. Kristensen et al. (2016) and Fig. 3.3.9). At least for the SALTRACE period, this finding disproves the prevailing image of a decrease in κ from the MBL to the SAL. Such a decrease in κ , attributed to the hardly hygroscopic dust particles in the SAL, is for example simulated in a model study by Pringle et al. (2010). A potential reason for even enhanced κ values in the SAL compared to the MBL might be a lower concentration of volatile organics in the former. Kristensen et al. (2016) assume that such volatile organic particles, significantly less hygroscopic than sulfates (e.g. Petters and Kreidenweis, 2007), are responsible for the observed deviation of κ from ammonium sulfate-like values in the MBL. However, since volatile organics are not detectable by means of the single particle analysis methods used in this study, this hypothesis remains speculative. The mean κ value of the SAL aerosol corresponds to a mean activation diameter of $\bar{D}_{act} \approx 80$ nm at a water vapor supersaturation of $SS = 0.2\%$, with the latter being a typical ambient value for cloud formation in the trade wind regime (Wex et al., 2016). The integral particle number concentration above this threshold, i.e. n_{80} corroborates the similarities between the hygroscopic properties of the SAL and the MBL aerosol (in the vicinity of D_{act}). So it turns out that n_{80} provides a good qualitative proxy for n_{CCN} (at $SS = 0.2\%$) for the entire vertical column, i.e. for the SAL and the MBL alike (Fig 4.2.4, 4.2.8 and 4.2.9). The fact that the activation diameters are located close to the maximum of the NSD in the SAL (cf. Fig. 4.2.19) further implies that the associated small hygroscopic particles account for the majority CCN. Figure 4.2.22 demonstrates that the size range $D < 150$ nm (presumably) dominated by ammonium sulfate contributes an average of about 50% to n_{CCN} .

The few studies explicitly making the presence of sulfate particles in the SAL a subject of discussion (e.g. Raes et al., 1997, 2000; Kaaften et al., 2009; Rodríguez et al., 2011; Boose et al., 2016) consistently attribute these particles to anthropogenic emissions in Northern Africa and/or Southern Europe. In the absence of an instrumentation allowing to detect anthropogenic gaseous tracers, the SALTRACE airborne measurements cannot directly confirm this link between the sulfates and anthropogenic sources. However, experimental evidence for an anthropogenic contribution to the SAL aerosol is given by the enhanced concentrations of rBC (cf. Fig. 4.2.11 and Schwarz et al. (2017)). Such soot particles are shown to be persistently present along with the sulfates in the summertime “Saharan background aerosol” (Kaaften et al., 2009; Müller et al., 2009) and are likely attributable to anthropogenic pollution as well. At least, a significant contribution of natural biomass burning to the Saharan background and SAL aerosol can be largely excluded, since in summer African biomass burning almost

exclusively occurs south of the ITCZ and interhemispheric exchange is strongly limited (e.g. Kaufman et al., 2005). An anthropogenic origin of the hygroscopic sulfate particles that strongly influence the CCN properties of the SAL aerosol and, consequently, the formation and properties of clouds in the trade wind regime connotes an important, so far not closely examined anthropogenic climate impact of the SAL. To date, the anthropogenic part in changes of the SAL’s climate forcing was discussed primarily in the context of human-induced changes in mineral dust emissions, e.g. caused by alterations in land use (Tegen et al., 2004; Woodward et al., 2005; Mahowald et al., 2006; Ginoux et al., 2012).

5.5.2 Impact of UT Aerosol Entrainment

Besides the high concentration of soluble sulfates in the initial Saharan aerosol observed near dust source regions (e.g. during SAMUM), entrainment at the upper edge of the SAL, that is associated with the input of additional small sulfate particles originating from NPF in the UT, can further increase the amount of hygroscopic material in the layer. That this enhancement in hygroscopic material may not only affect the tiniest particles but also the ones with CCN-relevant sizes, i.e. roughly $D \gtrsim 70 - 80$ nm for $SS = 0.2\%$, is demonstrated by the height-dependent κ values in the SAL that are typically highest in its upper part in cases of simultaneously enhanced vf_{total} and n_{small} (cf. Fig. 4.2.16 and 4.2.15). This is most clearly shown by the example of the measurements during the intense Caribbean dust event on 10 and 11 July. For this “entrainment case”, the increase in volatility with altitude — for $D < 150$ nm the portion of particles with volatile volume fractions larger 70% increases from about 50% to 80% from the lower to the upper part of the SAL (cf. Fig. 4.1.10) — reflects in a notable decrease in D_{act} and an associated increase in κ (cf. Fig. 4.1.11). While the higher fraction of refractory material (including hardly hygroscopic soot and dust) in the lower SAL leads to κ values similar to the ones observed in the MBL (during the same period), the corresponding values in the upper SAL are almost equivalent to pure ammonium sulfate. The high value of κ in the upper SAL combined with the shift of the NSD to smaller diameters (cf. Fig. 4.1.8) results in a markedly increased relative contribution of particles with $D < 150$ nm to n_{CCN} (cf. Fig. 4.1.12). It further provokes a relative increase of n_{CCN} compared to n_{80} (cf. Fig. 4.1.5). These impacts of (apparent) UT aerosol entrainment on the CCN-relevant particle size range in the SAL could be explained by the fact that a minor fraction of the UT-born particles already exhibit sufficient sizes. This is for instance apparent from Fig. 4.1.5, which shows non-vanishing values for n_{80} above the SAL. Additionally, some of the the UT-born particles, predominantly smaller than 80 nm, could internally mix with the pre-existing SAL particles. Either way, the findings strongly suggest that particle input from the troposphere above the SAL can increase the concentration and properties of CCN in the dust layer.

It is highly questionable whether CCN retrievals based on remote sensing methods (e.g. Mamouri and Ansmann, 2016) are capable of tracing such features and, hence, permit to capture the full vertical n_{CCN} profiles adequately, given the already mentioned low sensitivity of such methods to particles significantly smaller than the operating wavelength.

5.5.3 Role of Mineral Dust

Whereas, as mentioned, minor amounts of mineral dust are also present at smaller sizes ($D < 500$ nm), the majority of the dust is found at particle diameters of $D \geq 500$ nm. Here, pure mineral dust particles (mostly silicates) clearly dominate the number concentration in the SAL. Despite their (presumably) low hygroscopicity, these particles are CCN thanks to their sheer size. According to the κ -Köhler equation, i.e. Eq. (2.1.9), at $SS = 0.2\%$ (and $T_{act} = 300$ K) particles with $D \geq 500$ nm only need water activities equivalent to $\kappa \gtrsim 0.002$ to activate into cloud droplets. A range of laboratory studies (Koehler et al., 2009; Herich et al., 2009; Kumar et al., 2011b) demonstrate that this can generally be assumed to be guaranteed for most if not even all kinds of mineral dust particles. With a typical $\kappa \gtrsim 0.02$, North African dust even represents one of the most hygroscopic dust types. Nevertheless, compared to the size range dominated by the volatile material, particularly the accumulation mode, the concentration of coarse dust particles is too small to significantly contribute to the total number of CCN. So these “mineral dust mode” particles only account for about 10% of n_{CCN} at $SS = 0.2\%$ (cf. Fig. 4.2.22). This is consistent with and ultimately explains the negligible role of dust for CCN in the MBL reported by Kristensen et al. (2016).

5.6 Modification of the SAL Aerosol with Transatlantic Transport

Apart from the importance of the SAL aerosol composition itself, a vital question related to dust-containing aerosols is if and how this composition and especially the CCN properties of the particles change with long-range transport (e.g. Sokolik et al., 2001; Formenti et al., 2011b; Denjean et al., 2015; Weinzierl et al., 2017).

5.6.1 Accumulation Mode and Effective Hygroscopicity

On average, in the vicinity of the SAL aerosol’s NSD maximum, i.e. for the accumulation mode no substantial differences are apparent between the Northwest African coast and the Caribbean, despite the cases of apparent entrainment from the UT. So the mean particle composition for $D < 150$ nm (cf. Fig. 4.2.21) and mean effective hygroscopicity in the SAL (cf. Fig. 4.2.16) are approximately preserved with transatlantic transport. On closer inspection, the average Caribbean samples show a slight enhancement in volatility for $D < 150$ nm, although this enhancement manifests itself merely in a relative increase of completely volatile particles at the cost of particles with large volatile volume fractions ($> 70\%$). It seems plausible that such a redistribution has only minor impact on the average particle hygroscopicity as long as the type of volatile material does not change. Like the particle volatility, the mean κ value for the Caribbean SAL aerosol also seems slightly enhanced. However, this enhancement is far from being significant in view of the considerable uncertainties of the derived κ values. Moreover, CCN data are rare for the SAL over the African coast — quantitatively usable data are only available for 17 June — , so that the mean of these data is not a very informative value. Anyway, the results clearly demonstrate that κ values

similar to those in the Caribbean are already found in the SAL before setting out on its transatlantic journey.

5.6.2 Dust Mode

Irrespective of the preserved effective particle hygroscopicity, changes of the NSD and/or the hygroscopicity of particles with $D > D_{act}$ could still have important implications for the CCN properties of the SAL aerosol. This is because cloud formation is a dynamical process where it is not only decisive how many particles may serve as CCN at a given supersaturation but also how the different (differently-sized) CCN compete for the available water vapor. The occurrence or absence of a processing of the coarse mineral dust particles, i.e. their mixing with other (hygroscopic) material during transport might be of particular importance for the SAL, as discussed in Sect. 1.3. Although it has been motivated that even unprocessed coarse Saharan dust particles serve as CCN, an enhancement of hygroscopic material associated with these particles would impact their important role as GCCN (e.g. Levin et al., 2005; Posselt and Lohmann, 2008; Smoydzin et al., 2012). Furthermore, several studies suggest that processing may have a decisive (repressive) influence on the IN activity of mineral dust particles (e.g. Sullivan et al., 2010; Hoose and Möhler, 2012; Wex et al., 2014).

The SALTRACE results, however, exclude the occurrence of significant dust processing with SAL transport. Only negligible amounts of dust mixtures (sulfate-silicate mixtures) are found in the SAL aerosol’s “dust mode”, i.e. in the particle size range $D \geq 500$ nm on either side of the Atlantic (cf. Fig. 4.2.21). Although there might be a minor increase in sulfate-silicate mixtures, differences are marginal and the vast majority of coarse particles are categorized as pure mineral dust both before and after long-range transport. The absence of a significant increase in volatile material associated with the dust particles is also apparent from the size-resolved volatility measurements in Fig. 4.2.20. This finding is supported by previous ground-based studies (Denjean et al., 2015; Li-Jones et al., 1998). From a missing hygroscopic particle growth with increasing relative humidity (below saturation) these studies concluded that no significant amounts of hygroscopic material are associated with North African dust reaching the Caribbean. The absence of notable dust processing is further corroborated by the lidar measurements during SALTRACE, that show only insignificant differences in the depolarization characteristics of the SAL aerosol between Africa and the Caribbean (Groß et al., 2015; Haarig et al., 2017).

Besides particle composition, also the shape of the NSD in the SAL does not exhibit obvious modifications for the average of all respective sampling intervals (cf. Fig. 4.2.19). The near-parallel course of the average NSDs in logarithmic representation implies an approximately size-independent reduction in particle concentration with transatlantic transport for the inspected size range of $D \lesssim 2 \mu\text{m}$. This is further reflected in the almost identical average decrease in the integral particle number concentrations n_{total} , n_{small} and n_{large} of $37 \pm 1\%$ measured for the entirety of all SAL legs (cf. Fig. 4.2.14 and 4.2.15). Apart from its implication for radiative transfer, the conservation of the NSD shape provides additional evidence against significant modification of the dust mode, and significant particle growth via particle mixing (e.g. particle coagulation) in general. If significant particle growth/mixing was occurring in

the SAL, one would expect a relative increase in the concentration of large particles, because particle sedimentation (cf. Tab. 5.4.1) and other removal mechanisms leading to a counteracting preferential loss of large particles (e.g. wet deposition) can be neglected for $D \lesssim 2 \mu\text{m}$ in the separated dry layer. In the absence of pronounced vertical mixing, the likely main reason for the uniform reduction of particle concentrations in the SAL is horizontal dilution.

5.6.3 Moderate Changes?

Although the findings support the picture of a SAL aerosol whose main properties are maintained with long-range transport, they cannot rule out the possibility of moderate changes in the size-dependent hygroscopicity of particles with $D > D_{act}$. The fact that, despite the discussed n_{small} enhancements in the upper SAL associated with entrainment during transport, the average reduction of n_{small} from Africa to the Caribbean is not less pronounced than that of n_{large} suggests that a fraction of the small (predominantly volatile) particles in the layer might indeed grow to larger sizes. A similar indication is given by the compositional analysis showing a moderately enhanced volatility in the intermediate size range, i.e. for $150 < D \leq 500 \text{ nm}$ in the Caribbean SAL (cf. Fig. 4.2.21). Given the large hygroscopicity of the volatile material in the vicinity of D_{act} , it can be assumed that the moderate volatility enhancement connotes an increase in hygroscopicity for these medium-sized particles.

Slight accumulation of soluble material, beyond the detection limit of the single particle analysis, could further lead to moderate changes in the hygroscopicity of the coarse mineral dust particles. For instance, Herich et al. (2009) conclude that an addition of $\gtrsim 3\%$ soluble material (by volume) already considerably enhances dust hygroscopicity. Such small amounts of additional material are insufficient for a classification as “mixed dust” under the microscope. Also the methods based on hygroscopic growth utilized by Denjean et al. (2015) and Li-Jones et al. (1998) are insensitive to changes in mineral dust hygroscopicity as long as no detectable growth takes places at subsaturated conditions. Nevertheless, even if hygroscopic growth remains unaffected, moderate changes in dust hygroscopicity associated with minor additions of soluble material can still have important consequences for droplet activation, i.e. for the role of the dust particles as CCN/GCCN in a supersaturated vapor. Koehler et al. (2009) and Herich et al. (2009) demonstrate that laboratory CCNC measurements (at supersaturation) show considerable differences between dust samples, whereas hygroscopic growth measurements are incapable of doing so in the majority of cases, simply because even moderately hygroscopic dust can remain non-hydrated for relative humidities below 100%.

Yet, differences in the size-dependent particle hygroscopicity for $D > D_{act}$, whether the result of long-range transport or just owing to variability in the initial composition of the SAL aerosol, are unfortunately not accessible by means of the measurement setup used during SALTRACE. In order to allow for an investigation of such potential differences and, in general, the size-dependent aerosol mixing state with respect to particle hygroscopicity in the future, a new method based on available instrumentation has been developed as part of this work. This method will be presented in Sect. 7.2.

Chapter 6

Summary

North African Dust and the SAL

North African mineral dust aerosol is an important aerosol type, contributing about 35%¹ to the total atmospheric particulate mass burden. Primarily in Northern Hemispheric summer, a series of meteorological processes lead to strong mobilization of dust in the Sahara and Sahel regions and an export of the resulting warm dust-laden air masses towards the Northwest African coast, where they form the surface-detached SAL. In this elevated layer the dust aerosol is transported across the North Atlantic reaching as far as into the Caribbean sea and beyond. Influencing such a huge geographic area, it is obvious that the SAL and its aerosol have extensive and manifold impacts on climate and environment, as for instance via aerosol-radiation and aerosol-cloud interactions. In the course of climate change and through direct human actions (e.g. land use changes in Northern Africa) it must be expected that these impacts will change in the future. Not least because of that, it is essential to improve our current knowledge about the SAL aerosol and the anthropogenic contribution to its effects.

Basis of this Study

Some of the decisive properties of the SAL aerosol, such as exact particle NSD, size-dependent particle composition and hygroscopicity, cannot be studied remotely but require elaborate in situ measurements. To date, only a modest number of such (aircraft-based) in situ measurements have been carried out in the SAL and these campaigns were subject to certain restrictions. For one, they were all limited to one side of the Atlantic. Conducted in different years and/or seasons, and employing dissimilar instrumentation, it is impossible to directly conclude on the role of long-range transport on potential aerosol modifications from these measurements. Another major deficit has been the lack of comprehensive investigations of the CCN properties of the SAL aerosol. Among others to close these gaps, during its core phase in June/July 2013 the SALTRACE campaign involved airborne measurements on either side of the Atlantic with an extensive aerosol instrumentation. This instrumentation included devices for

¹According to Cakmur et al. (2006) mineral dust contributes $\geq 50\%$ to the total atmospheric aerosol mass and Huneus et al. (2011) estimate the contribution of North African sources to total dust emissions to about 70%.

the determination of particle NSD, CCN concentration, size-dependent particle volatility and composition. Accumulating more than 86 (out of 110) hours of data sampling several African dust events these in situ measurements represent the largest effort ever made in the investigation of the aerosol properties of the SAL. The airborne sampling of the layer is supplemented by a suite of ground-based measurements, among others providing insight into the aerosol conditions in the lower Caribbean troposphere both during SAL presence and absence. Based on this unique data set this study aimed to examine

- the vertical (and horizontal) aerosol structure during the dust events, and its connection with SAL-induced atmospheric stratification,
- the properties, particularly the CCN properties of the SAL aerosol, and potential changes of these properties with long-range transport, and
- the implication of SAL presence on CCN concentrations in the cloud-containing lower Caribbean troposphere.

From the combination of airborne NSD and CCN measurements particle hygroscopicity information is inferred in form of the particle hygroscopicity parameter κ . At this, a smallest particle diameter capable of nucleating droplets at a given water vapor supersaturation SS , the so-called activation diameter D_{act} is derived and converted to κ by means of κ -Köhler theory. To guarantee accurate NSD and, ultimately, κ solutions with realistic uncertainty estimates new data evaluation methods have been developed. The validity of these methods (and the underlying assumptions) is verified by comparing the solutions to ground-based reference measurements for a set of suitable low-level airborne sampling intervals.

Aerosol Structure During North African Dust Events

Consistent with the common image of summertime North African dust transport, the investigated dust events are typically accompanied by the presence of a distinct SAL, not only at the Northwest African coast but also after transatlantic transport in the Caribbean. In this context, the SAL is defined by two bordering temperature inversions, one at its base and another one at its top, and a considerably reduced humidity compared to the moist lower troposphere. The trade wind temperature inversion constituting the base of the SAL is found to rise from around 0.5–1 km at the African coast to about 2 km in the Caribbean. At the same time, the SAL's ceiling descends from approximately 6 to 4–5 km. The observed preservation of the bordering inversions implies a persistent vertical stability at the edges of the layer counteracting mixing of the dust-laden Saharan air masses with the adjacent atmosphere during transport.

The result is a marked coupling between the SAL-induced atmospheric stratification and the vertical particle concentration profiles. They show considerably enhanced number concentrations of large particles with diameters $D \gtrsim 300$ nm and, therewith, particulate mass in the SAL altitude range (with regard to STP conditions). A comparable enhancement is typically encountered for the number concentration of CCN at $SS = 0.2\%$, being a representative ambient humidity for cloud formation in the trade

wind regime. Hence, thanks to its preserved external stability and high initial particle content the SAL appears as an immense lifted aerosol reservoir both before and after transatlantic transport, particularly concerning particulate mass and CCN.

Internally, this aerosol reservoir exhibits strong vertical heterogeneity expressed in significant variations of the absolute particle concentrations within vertical distances of only a few hundred meters and, occasionally, even notable changes in the NSD with height. This heterogeneity is present in the young SAL over the Northwest African coast and survives transatlantic transport thanks to moderate vertical stability within the layer. The finding of vertical heterogeneity disproves the picture of the SAL as an overall well-mixed layer, as it is sometimes portrayed. Horizontally, on the other hand, the SAL aerosol shows a high degree of homogeneity within flight distances of the order of hundred kilometers.

Despite its separated appearance on either side of the North Atlantic, the results give strong evidence that the SAL is not completely sealed throughout its lifetime but that temporary exchange with the over- and underlying troposphere occurs. For the first time, the dust layer is found to be permanently overlaid by large concentrations of volatile small particles (predominantly with $D \lesssim 80$ nm). The most obvious source of these particles is NPF in the UT, which is often associated with the production of soluble sulfates. In some cases, the concentration enhancement in volatile small particles extends from the troposphere above the SAL down into the upper part of the layer suggesting aerosol entrainment from the UT. One possible mechanism for this entrainment is vigorous vertical mixing with the free troposphere during initial SAL formation. Several indications, such as the fact that the most pronounced examples of this feature are observed in the Caribbean, however, give rise to the conclusion that particle input into the upper SAL also takes place during transport. A potential reason for this is turbulent mixing induced by strong vertical wind shear temporarily defeating the inversion stability at the SAL's ceiling.

Even more important than entrainment of UT aerosol into the upper SAL is input of SAL aerosol into the lower troposphere. The measurements clearly demonstrate that SAL presence in the Caribbean is always accompanied by a presence of SAL aerosol in the MBL (sub-cloud layer). One process leading to particle input from the SAL into the subjacent troposphere during transport is gravitational settling of coarse particles (with $D \gtrsim 5 \mu\text{m}$). Yet, the main mechanism likely is turbulent dry deposition triggered by convection events severe enough to temporarily surmount the trade wind inversion. Carrying significant amounts of CCN, particle input from the SAL leads to a notable enhancement of CCN concentrations in the MBL and, therewith, in the altitude range providing the aerosol basis for cloud formation in the trade wind regime. Enhanced numbers of CCN available during cloud formation essentially result in enhanced cloud droplet number concentrations, engendering an increase in cloud albedo (Twomey effect). Such an impact of North African dust events on the properties of Caribbean trade wind clouds has recently been demonstrated (Siebert et al., 2013; Werner et al., 2014).

CCN Properties and Composition of the SAL Aerosol

However, the contribution of mineral dust to this indirect climate effect is inferior. Compositional analysis of the SAL aerosol reveals that dust solely dominates the particulate material for $D \gtrsim 500$ nm. Owing to the low particle number concentration in this size range, the “dust mode” amounts to only about 10% of the total CCN concentration (at $SS = 0.2\%$). It is the particle size range in the vicinity of the mean activation diameter of $\bar{D}_{act} \approx 80$ nm, near the maximum of the particle NSD, that contributes the lion’s share to CCN number. About 50% of CCN are attributable to particles with $D < 150$ nm. This important size range is dominated by volatile material, for which there is strong evidence for ammonium sulfate to be the key component. Accordingly, high values of $\kappa \approx 0.3 - 0.7$ are found for the effective particle hygroscopicity, i.e. the average particle hygroscopicity at D_{act} . The overall mean of $\bar{\kappa} \approx 0.5$ is close to the laboratory value for pure ammonium sulfate ($\kappa = 0.61$). With these values the particle hygroscopicity in the SAL is similar or even slightly enhanced compared to the MBL, where during the same period $\kappa \approx 0.2 - 0.4$.

Previous studies taking note of the presence of sulfate particles in the SAL consistently attribute these particles to anthropogenic sources in Northern Africa and/or Southern Europe. Such an anthropogenic origin of these particles, apparently having a considerable effect on clouds in the trade wind regime, would connote a so far not closely examined anthropogenic climate impact of the SAL.

In addition to the initial amount of (anthropogenic) sulfates in the SAL, the results suggest that the entrainment of NPF aerosol from the UT may supply the dust layer with further soluble material, influencing its CCN properties. Correspondingly, increased effective particle hygroscopicities and (relative) CCN concentrations are typically encountered for the cases with enhanced amounts of volatile small particles in the upper SAL.

Impact of Long-Range Transport on SAL Aerosol Properties

Except for this (apparent) entrainment-induced modification in individual cases, the main properties of the SAL aerosol, especially its CCN properties, can in good approximation be described as conserved with transatlantic transport. On average, neither the derived κ values nor the aerosol composition in the vicinity of D_{act} exhibit significant differences between the SAL over the Northwest African coast and in the Caribbean. There are just as little considerable changes in the “dust mode”. On either side of the Atlantic, the vast majority of the coarse particles in the latter mode are classified as pure mineral dust (predominantly silicates) with only negligible occurrence of internal mixtures between dust and other material. This particularly means that no significant dust processing, i.e. no accumulation of soluble material on the dust particles that would drastically alter their CCN and/or IN properties, is taking place during SAL long-range transport. Like hygroscopicity and composition, also the shape of the particle NSD remains approximately maintained in the investigated size range of $D \lesssim 2$ μm , providing an additional argument contra significant aerosol transformation.

However, although these findings demonstrate the preservation of the main properties of the SAL aerosol, they cannot rule out the possibility of moderate changes in the size-dependent hygroscopicity of particles with $D > D_{act}$. Such moderate changes, undetectable with the used measurement setup, may still be relevant, particularly regarding the role of coarse dust particles as GCCN and IN. In order to tackle this outstanding issue, new methods to investigate size-dependent particle hygroscopicity and aerosol mixing state with respect to hygroscopicity have been developed for future application.

Chapter 7

Outlook

7.1 Future Research Needs

This study shed light on important features and impacts of the SAL aerosol that have so far not been (sufficiently) treated in the literature. However, for few of these aspects the results can only give indications, but are not entirely conclusive. Hence, further comprehensive investigations are necessary to follow up on these points.

Anthropogenic Sulfates

It has been shown that volatile material, primarily associated with ammonium sulfate, strongly influences the CCN properties of the SAL aerosol. Thorough examination of the assumed anthropogenic origin of this material is, thus, mandatory to learn more about related anthropogenic climate impacts, such as the effect on trade wind clouds. Therefore, it would be advantageous to complement future in situ measurements by trace gas instruments that allow for identification of anthropogenic footprints, e.g. using the ratio of CO/CO₂ as a tracer for different types of fossil fuel combustion (Seinfeld and Pandis, 2006; Djuricin et al., 2010). Comprehensive trajectory and model studies may further provide important insights. For instance, a comparison of measured particulate sulfate concentrations with what is expected based on anthropogenic sulfur emission inventories could help to derive quantitative estimates for the anthropogenic fraction of sulfates in the SAL aerosol. Ultimately, the (indirect) effects of these anthropogenic particles should be quantified and compared to the total climate impact of the SAL aerosol.

Seasonality

The SALTRACE airborne measurements were restricted to the Northern Hemispheric summer months. Although SAL transport is most pronounced during this season, it essentially is an all-year phenomenon. At this, considerable seasonal differences are observable both in vertical aerosol distribution and aerosol composition (Adams et al., 2012; Tsamalis et al., 2013). For instance, during winter African biomass burning aerosol is effectively mixed with the Saharan mineral dust aerosol. Considering this, the results of this study, particularly concerning the CCN properties of the SAL

aerosol, might be representative for summer but not necessarily for the rest of the year. The only other study previously investigating particle hygroscopicity in the Caribbean SAL in situ (Jung et al., 2013) derived significantly lower κ values of about 0.02 to 0.03 for measurements in April (2010). Such values of κ would imply a dominance of pure unprocessed dust (see Sect. 7.2) throughout the entire CCN-relevant size range and would specifically exclude the presence of even minor amounts of soluble material. Provided that these values are not affected by systematic biases, compared to the results of this study, they would connote dramatic seasonal changes in the SAL aerosol properties. To check this in detail and to access the complete seasonal course of particle composition/hygroscopicity in the SAL, SALTRACE-like airborne measurements across all seasons are needed.

UT Aerosol Entrainment

The results of this study give strong indication for an occasional entrainment of volatile particles into the upper part of the SAL. It is further suggested that these particles, likely originating from NPF in the UT, influence the CCN properties of the SAL aerosol by supplying the layer with additional amounts of soluble material. It would be highly interesting to take a closer look at this so far unconsidered phenomenon and to systematically examine its climate effects.

Moderate Changes of Mineral Dust Hygroscopicity

As previously mentioned, the measurement setup used during SALTRACE solely permits to derive an effective particle hygroscopicity, i.e. an average hygroscopicity of the smallest CCN-relevant particles. So far, it has not been possible to additionally utilize the CCNC as a tool to study size-dependent particle hygroscopicity and, even, full aerosol mixing state regarding hygroscopicity for $D > D_{act}$. However, this is a prerequisite in order to investigate potential moderate changes in κ for $D > D_{act}$, especially for the “dust mode” with SAL long-range transport (in situ at supersaturation). To facilitate such investigations in the future, an advanced measurement setup and new data evaluation methods will be introduced in the following.

7.2 Advanced Hygroscopicity Studies

Before the innovations will be presented, first a simplified model of the SAL aerosol is sketched. On the basis of this model aerosol, the incapability of the method used in this study to (even qualitatively) examine changes in mineral dust hygroscopicity is discussed. Subsequently, the benefits of two novel methods are demonstrated. Finally, a possible future CCNC measurement setup and sampling strategy is proposed.

Simplified SAL Aerosol Model

Figure 7.2.1 shows the simplified model of the SAL aerosol that is hereafter utilized for demonstration purposes. In this approximation the particle NSD is described by a bimodal lognormal function. Both modes contain only one single particle type with

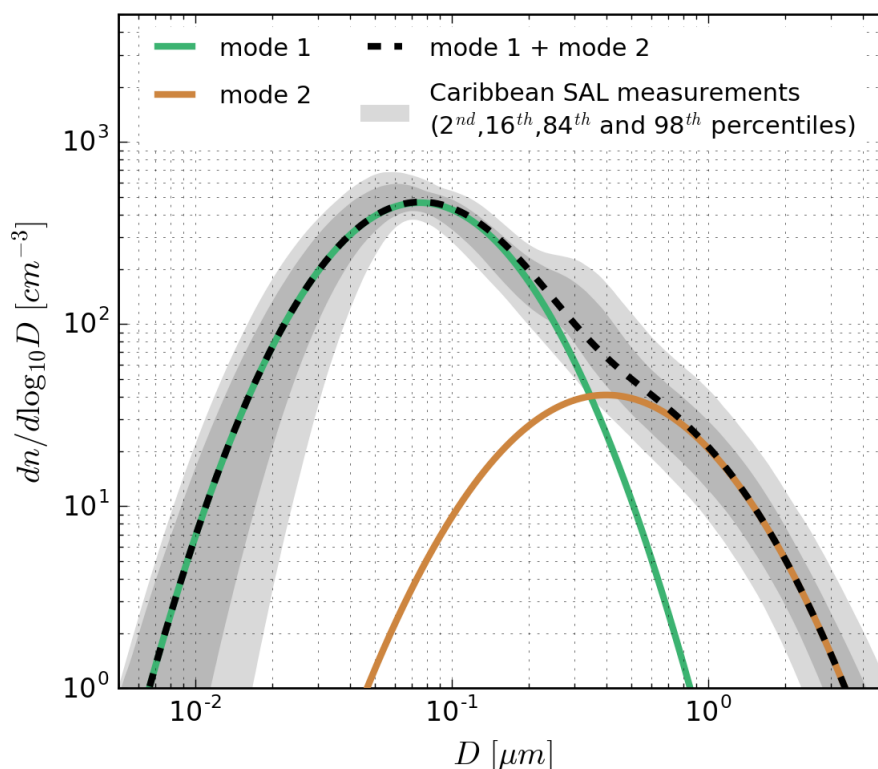


Figure 7.2.1: Approximation of the SAL aerosol by a bimodal lognormal particle NSD, with the two modes being completely externally mixed and made up of a single particle type each. Mode 1 (“sulfate mode”, green) and mode 2 (“dust mode”, brown) contain highly and less hygroscopic particles, respectively. The sum of both modes is shown by the dashed line. For comparison, the diameter-wise percentiles for the entirety of particle NSDs derived from the measurements in the Caribbean SAL (gray colors) are indicated. Concentrations refer to STP conditions.

mode i	$n_{mode,i}$ [cm^{-3} STP]	CMD_i [nm]	GSD_i	κ_i
1	350	75	2.0	0.6
2	35	400	2.2	variable

Table 7.2.1: Parameters defining the bimodal NSD approximation of the SAL aerosol shown in Fig. 7.2.1.

respect to hygroscopicity and the modes are externally mixed with each other. The first mode with a median diameter of 75 nm, constituting the majority of particles, is made up of highly soluble material and is characterized by an ammonium sulfate-like particle hygroscopicity of $\kappa_1 = 0.6$ (“sulfate mode”). The second mode with a median diameter of 400 nm consists of less water-attracting material and is defined by a variable hygroscopicity $\kappa_2 < \kappa_1$ (“dust mode”). For the complete set of mode parameters see Tab. 7.2.1.

Certainly, this simplified model is not completely representative of the actual aerosol in the SAL. However, it still captures some of its main features, such as overall NSD shape, the dominance of hardly hygroscopic (pure dust) particles in the size range $D \gtrsim 500$ nm and highly hygroscopic (sulfate) particles in the vicinity of the NSD maximum ($D \lesssim 150$ nm). Hence, it can be assumed that this model is at least capable of simulating the major CCN properties of the SAL Aerosol in a reasonable way.

Backward Integration Method

Based on this model aerosol, Fig. 7.2.2 and 7.2.3 show the simulation of effective hygroscopicities κ_d that would be obtained by the simple backward integration method (cf. Sect. 3.3.4) for a range of SS and two different values of κ_2 . The value used in Fig. 7.2.2, i.e. $\kappa_2 = 0.02$ represents a lower limit for the hygroscopicity of unprocessed Saharan/Sahelian dust (Koehler et al., 2009; Herich et al., 2009; Kumar et al., 2011b). On the other hand, $\kappa_2 = 0.2$ in Fig. 7.2.3 is a realistic value for considerably processed North African mineral dust (Kumar et al., 2011a). According to the volume mixing rule in Eq. (2.1.10) and assuming a two-component internal mixture between dust (0.02) and sulfate (0.6), $\kappa_2 = 0.2$ would correspond to a sulfate volume fraction of about 31% in the dust mode particles. The detailed procedure¹ for the derivation of κ_d is described in Fig. 7.2.2. Figure 7.2.4 complementary shows the continuous course of κ_d with SS including also the inaccessible SS range below the lower CCNC limit of 0.07%. Here, in addition to κ_d itself a typical uncertainty range for this value is displayed. This uncertainty is estimated as 23% being the average relative standard deviation of the κ values derived from the measurements in the SAL during SALTRACE.

The simulations demonstrate that compared to the sulfate mode CCN concentrations $n_{\text{CCN},1}$, the number of non-activated dust mode particles, precisely the concentration of dust mode particles with $D_{\text{act},1} \leq D < D_{\text{act},2}$, does not lead to significant deviations of κ_d from κ_1 within the CCNC SS range (at least for $SS \gtrsim 0.1\%$). In retrospect to the main study, this supports the approximate adequacy of the backward integration method, particularly for the main SS of 0.2%. Most importantly however, the simulations demonstrate that in consideration of the uncertainties, the backward integration method is incapable of even qualitatively differentiating between unprocessed and considerable processed coarse dust particles within the CCNC SS range. Owing to its superior particle content the sulfate mode is simply masking the dust mode. To quantitatively study κ_2 via the backward integration method — which is impossible until $n_{\text{CCN},2} \gg n_{\text{CCN},1}$ — supersaturations as low as $SS \lesssim 0.01\%$ and $SS \lesssim 0.005\%$ would be necessary for $\kappa_2 = 0.2$ and $\kappa_2 = 0.02$, respectively. These SS fall far below the operational limit of the CCNC.

¹Supplementary information: For the different SS the respective average activation temperatures T_{act} measured during SALTRACE, i.e. $T_{\text{act}} \approx 37^\circ\text{C}$ for $SS = 0.1\%$ to $T_{\text{act}} \approx 39^\circ\text{C}$ for $SS = 0.3\%$ are used for the conversion between activation diameter $D_{\text{act},d}$ and κ_d via Eq. (2.1.9).

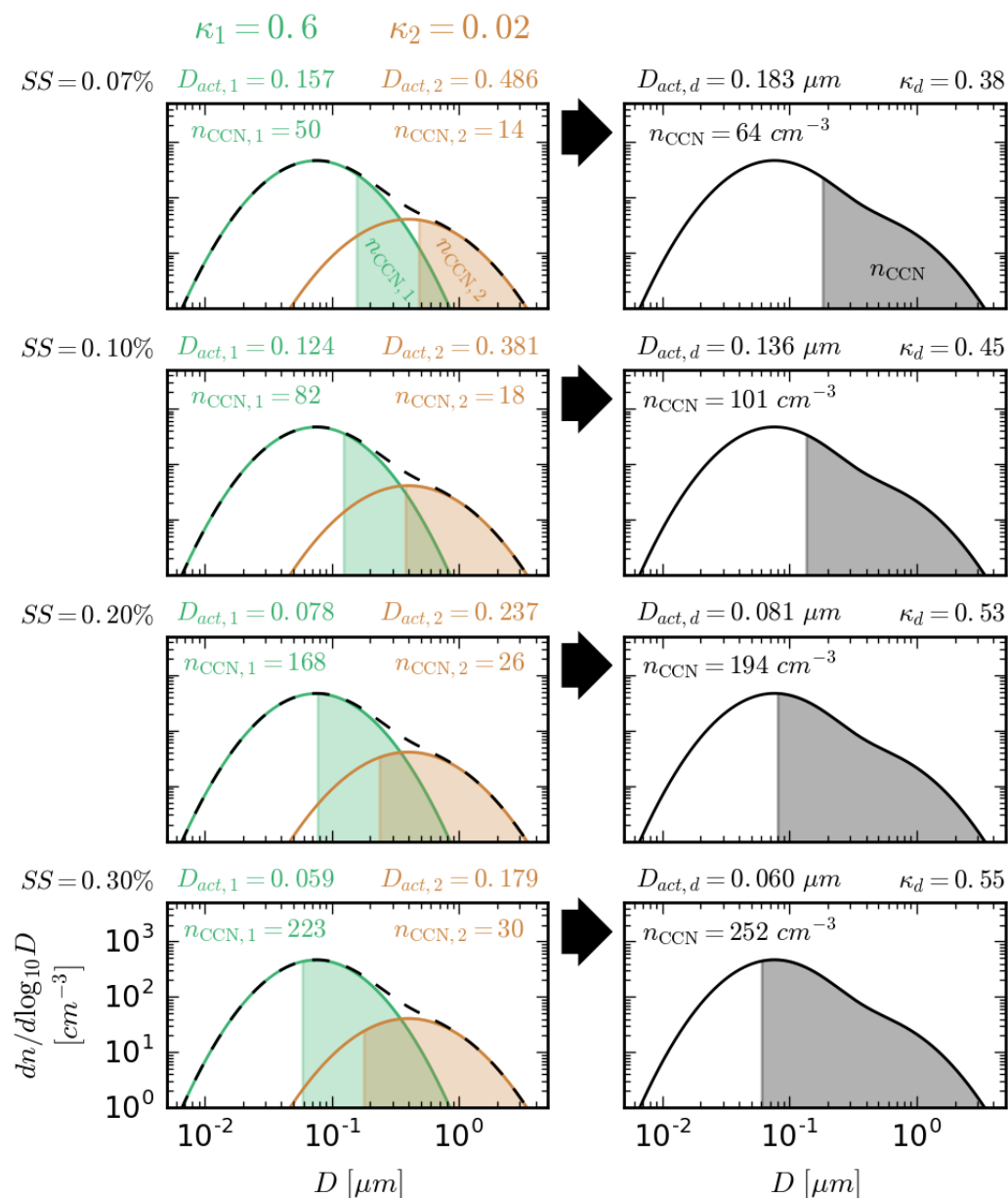


Figure 7.2.2: Simulation of “measured” effective hygroscopicity values κ_d for $\kappa_1 = 0.6$ and $\kappa_2 = 0.02$, and different CCNC supersaturations. Here, κ_2 is representative of fresh/unprocessed Saharan mineral dust. The activation diameters $D_{act,1}$ and $D_{act,2}$ of the individual modes are calculated from κ_1 and κ_2 by means of the κ -Köhler Eq. (2.1.9). The shaded areas below the curves on the left hand side represent the integral particle concentrations for each mode and $D \geq D_{act,i}$. They correspond to the CCN concentrations $n_{CCN,1}$ and $n_{CCN,2}$. From the sum of these CCN concentrations, i.e. the “measured” total concentration $n_{CCN} = n_{CCN,1} + n_{CCN,2}$ an apparent activation diameter $D_{act,d}$ is derived via backward integration of the particle NSD using Eq. (3.3.4). Finally, κ_d is calculated from this $D_{act,d}$ once more making use of Eq. (2.1.9). Shown concentrations refer to STP conditions.

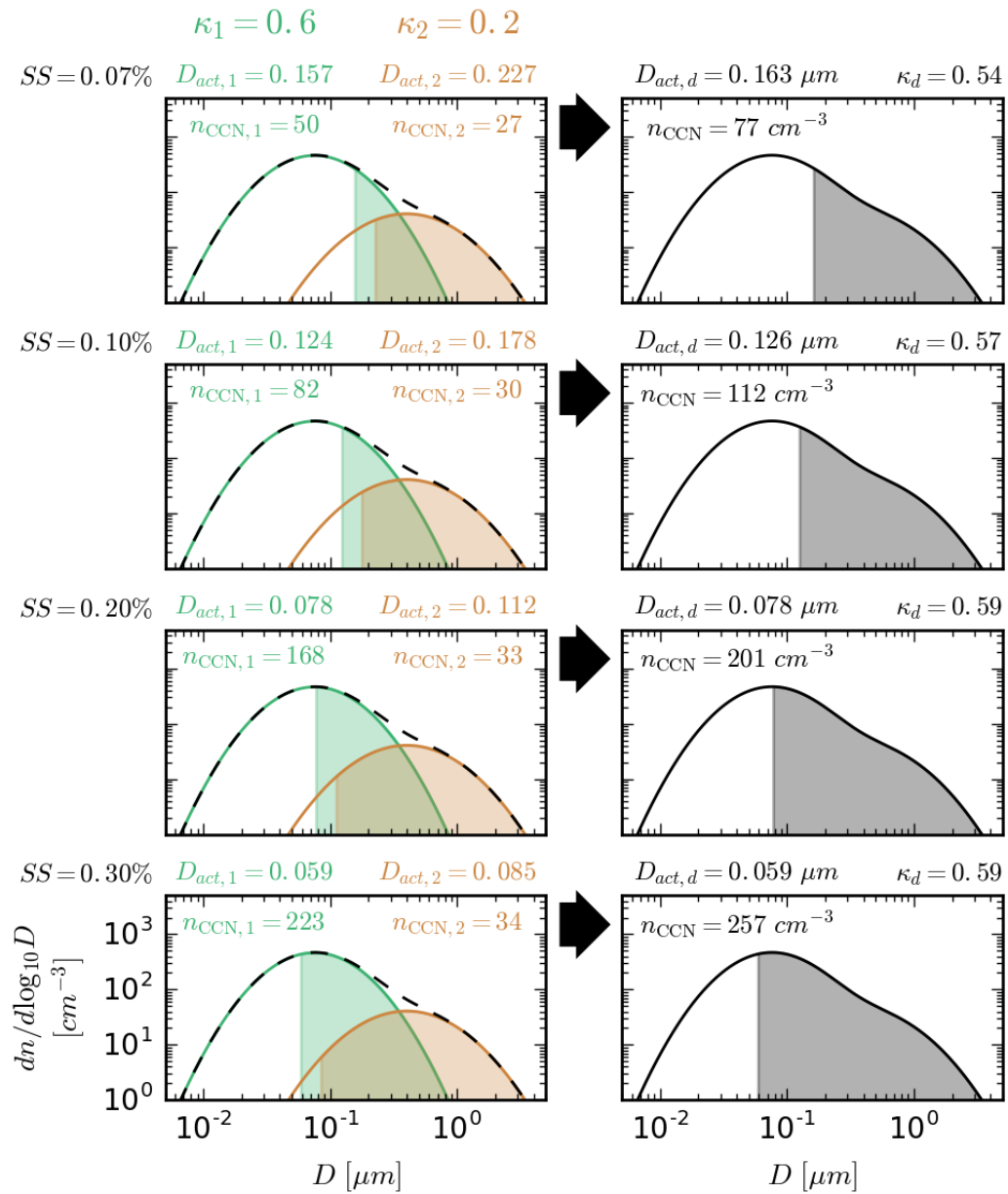


Figure 7.2.3: Same as Fig. 7.2.2 but for $\kappa_2 = 0.2$, representing processed mineral dust with a considerable water-soluble volume fraction.

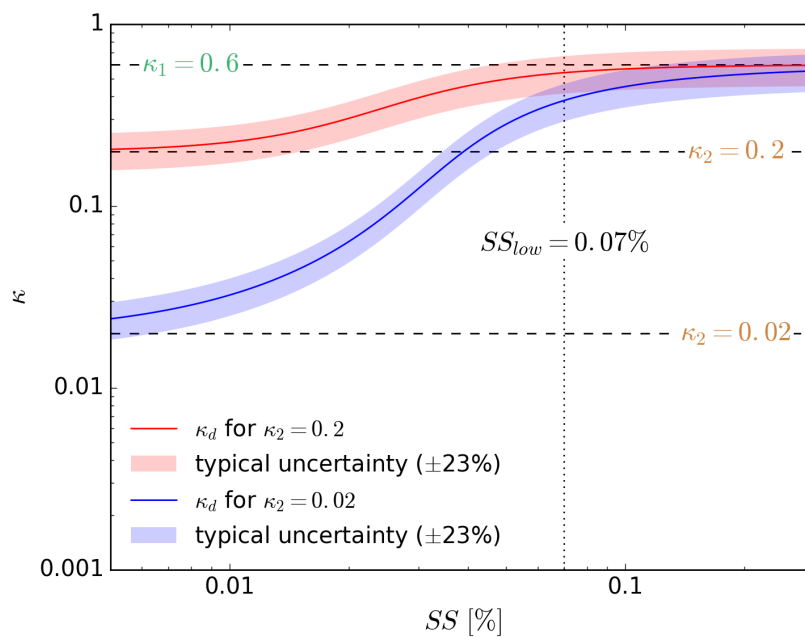


Figure 7.2.4: κ_d values derived via the simple backward integration method for $\kappa_2 = 0.02$ (unprocessed dust, red curve) and $\kappa_2 = 0.2$ (processed dust, blue curve) for a wider (hypothetical) range of supersaturations, extending far beyond the lower CCNC operational limit of $SS = 0.07\%$. The shaded area around each curve represents a relative uncertainty in κ_d of $\pm 23\%$, being the average relative standard deviation of the κ values derived for the measurements in the SAL.

Suggestions for Improvement

For a quantitative investigation of κ_2 within the CCNC SS range, hence, other methods are required. Ideally, such methods should not only allow to distinguish between unprocessed and considerably processed, but also between unprocessed and moderately processed dust. For moderately processed North African mineral dust a hygroscopicity of $\kappa_2 = 0.05$ is assumed. According to the Eq. (2.1.10), this value would correspond to a soluble sulfate volume fraction of about 5%, again assuming a two-component mixture of dust and sulfate with $\kappa = 0.02$ and 0.6, respectively. For both methods introduced in the following, the model aerosol is initially size-filtered. For convenience, this filtering is done by means of Gaussian functions $F_{filter}(D)$ with a fixed relative standard deviation of 5%. For a mean particle diameter D_{filter} the resulting filtered NSD is defined by

$$\left(\frac{dn}{dD}\right)_{filter} = \frac{dn}{dD} \cdot F_{filter} = \frac{dn}{dD} \cdot \mathcal{N}(D_{filter}, (0.05 \cdot D_{filter})^2) \quad (7.2.1)$$

Approximately², such size-filtering (in the hereafter important size range from ca. 100 to 600 nm) can be realized with a DMA, as for instance with the one presented in Sect. 3.2.1.1.

SS -Scanning Method

For a size-filtered NSD the activated particle fraction n_{CCN}/n , i.e. the ratio between CCN concentration and total particle concentration n can be measured in dependence of SS . In Fig. 7.2.5 simulations of such measurements are presented for the model aerosol and a D_{filter} of (a) 150 and (b) 250 nm. For each SS the individual mode's activation diameters $D_{act,1}$ and $D_{act,2}$ are calculated from κ_1 and κ_2 by means of Eq. (2.1.9). Subsequently, $n_{\text{CCN}} = n_{\text{CCN},1} + n_{\text{CCN},2}$ and n are derived via integration of $(dn/dD)_{filter}$. As can be seen from Fig. 7.2.5a), in the present case of an external particle mixture, the course of the activated fraction with SS shows a two-step (generally, a multi-step) behavior. Activation of the highly hygroscopic sulfate mode particles occurs at small SS , whereas equally-sized less hygroscopic dust mode particles need considerable larger SS in order to also serve as CCN. Between these two “activation curves” the course of n_{CCN}/n exhibits a plateau value that corresponds to the number fraction of sulfate mode particles at D_{filter} . In combination with D_{filter} , the inflection point of the second sigmoidal activation curve SS_{ip} can be converted into a hygroscopicity value κ_d via the κ -Köhler equation. This value directly corresponds to κ_2 . This means that for the model aerosol, but theoretically also for more complex aerosol mixtures, this “ SS -scanning method” permits a full quantitative particle hygroscopicity assessment. Not only the hygroscopicity of all externally mixed particle types can be determined (as long as their activation occurs within the available SS range), but also the number fraction of each of those particle types at D_{filter} .

A disadvantage of this method, limiting its applicability to airborne in situ measurements, is that a full SS scan will be extremely time-consuming in reality. Assuming

²Actual DMA filter functions with respect to particle diameter can be more complex than simple monomodal Gaussians, e.g. due to the presence of multiply charged particles.

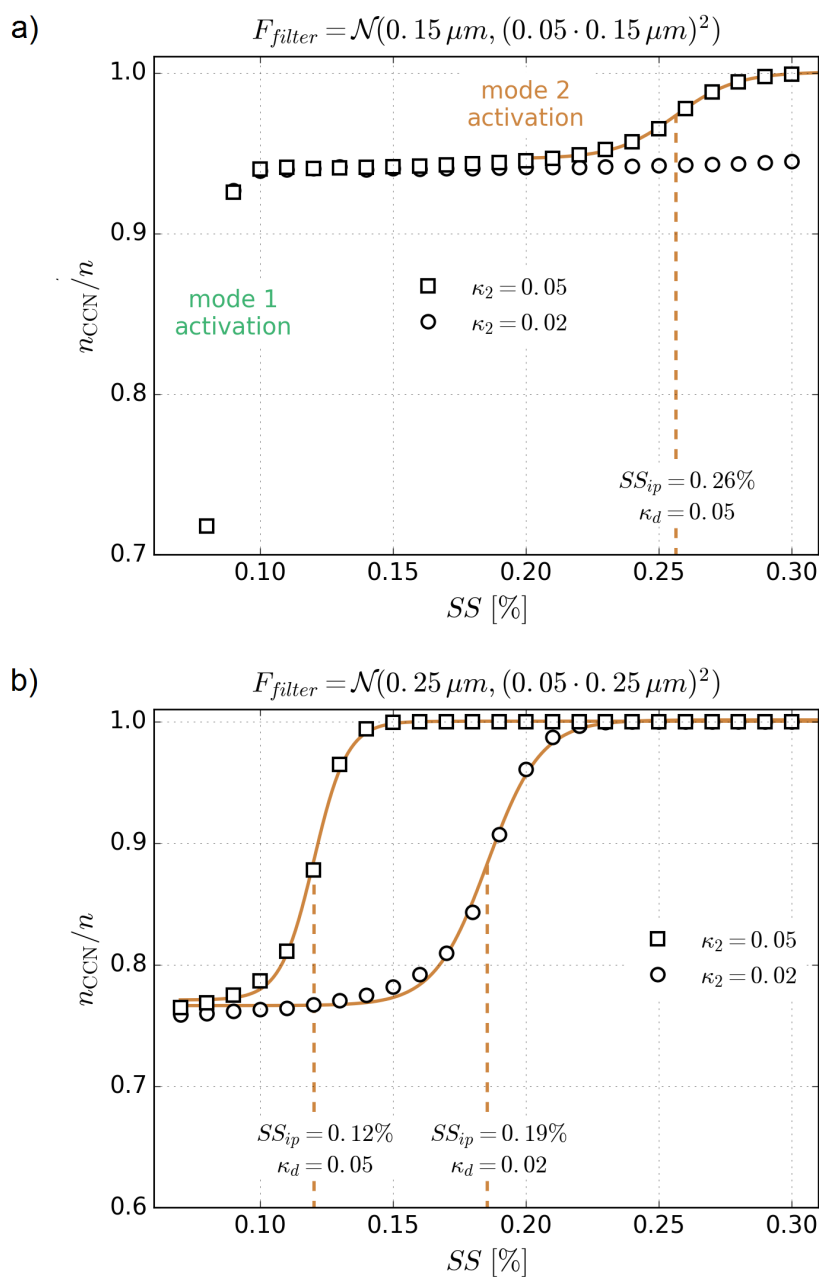


Figure 7.2.5: Quantitative determination of κ_2 utilizing the course of the activated particle fraction n_{CCN}/n with SS . Previous to the “measurements”, the NSD is filtered by Gaussian functions F_{filter} with a relative standard deviation of 5% centered at (a) 150 nm and (b) 250 nm, respectively. As visible in plot (a), the hygroscopic particles (mode 1, $\kappa_1 = 0.6$) activate at significantly lower SS than the dust particles (mode 2, $\kappa_2 \ll \kappa_1$) leading to a two-step structure of the activated fraction. Fitting the second rise in n_{CCN}/n , i.e. the activation of the dust particles by a sigmoid function allows to determine a corresponding inflection point supersaturation SS_{ip} , which represents the critical supersaturation SS_c for the given (mean) dust particle diameter. Via Eq. (2.1.9) these values can be converted into a κ_d that equals the true κ_2 .

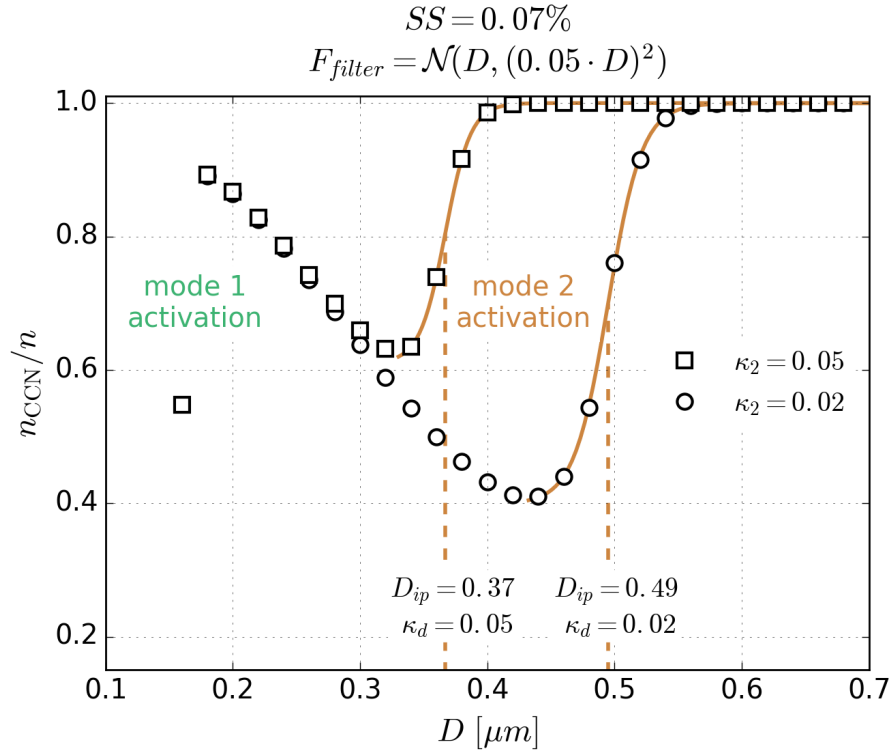


Figure 7.2.6: Quantitative determination of κ_2 utilizing the course of the activated particle fraction n_{CCN}/n with particle diameter for the lowest CCNC supersaturation of 0.07%. To obtain the activated fraction for each particle diameter D , the NSD is filtered by a Gaussian function $F_{\text{filter}} = \mathcal{N}(D, (0.05 \cdot D)^2)$. After its initial rise with the activation of the hygroscopic particles (mode 1, $\kappa_1 = 0.6$) the activated fraction falls off again, which is due to an increasing number fraction of yet non-activated dust particles (mode 2, $\kappa_2 \ll \kappa_1$) at larger D . When the activation of the latter particles then finally occurs, n_{CCN}/n experiences a second rise. A sigmoid fit to this second activation curve yields the inflection point diameter D_{ip} corresponding to the dust particle activation diameter $D_{act,2}$. From this value $\kappa_d = \kappa_2$ can be calculated via Eq. (2.1.9).

that each SS setting must be maintained for about 5 min to guarantee CCNC temperature stabilization (cf. Sect. A.3.3) and the complete scan consists of 10–20 steps, the total duration would add up to 50–100 min, or 25–50 min if both CCNC columns are used simultaneously. This is a lot compared to the average SAL leg duration during SALTRACE of about 17 min.

D-Scanning Method

An alternative to the SS -scanning method is to use a fixed SS and to measure the activated particle fraction while scanning the diameter range instead. Such a “ D -scanning” could be realized comfortably by means of a DMA via stepwise adjustment of its differ-

ential electrode voltage³. Figure 7.2.6 shows the simulation of such a measurement for the model aerosol and $SS = 0.07\%$. Also here, the course of n_{CCN}/n shows a two-step behavior. Subsequent to initial activation of the hygroscopic sulfate mode particles at small D , the activated fraction falls off again. During this decline, n_{CCN}/n equals the number fraction of sulfate mode particles, which decreases with increasing D . When D becomes sufficiently large the dust mode particles finally activate, too, leading to a second rise in n_{CCN}/n to unity. Again, the inflection point of this second activation curve D_{ip} , which corresponds to the activation diameter $D_{act,2}$, can be converted into a $\kappa_d = \kappa_2$ via Eq. (2.1.9).

The D -scanning method can be understood as a reversion of the CCNC calibration method presented in Sect. 3.2.2.3. In contrast to the SS -scanning method, a changeover between the individual scan steps could proceed instantaneously using a DMA. Assuming 30 s sampling duration per step and, again, an identical total number of 10 – 20 steps, the duration for a complete scan would be 5-10 min. This is indeed fast enough to make this method practicable for airborne in situ measurements. Using both CCNC columns, such D scans could further be performed at two different SS values at the same time.

CCNC Setup Revision

Figure 7.2.7 presents a possible future CCNC measurement setup that would facilitate a quantitative investigation of mineral dust hygroscopicity in the SAL — and, in general, size-dependent particle hygroscopicity/hygroscopic mixing state — by means of the methods introduced. A sampling strategy based on this setup could look as follows: In standard operation the DMA⁴ is bypassed and n_{CCN} is measured (at various SS) as before. This would allow to still obtain vertical CCN profiles and to derive effective particle hygroscopicities via NSD backward integration. At this, it would be beneficial to include an additional OPC into the CPS. Doing so would allow to determine the NSD behind the CPS inlet, permitting a direct correction of n_{CCN} for CPS inlet losses and even making CCN loss corrections redundant for the derivation of effective hygroscopicity via NSD backward integration. For particular sampling intervals, e.g. certain flight legs in the SAL, the setup would then be switched to NSD filtering to study size-dependent particle hygroscopicity via the D -scanning method.

³In fact, the relative DMA filter function width is not entirely constant with changing voltage (cf. Fig. 3.2.2), slightly complicating the analysis.

⁴DMA operation inside the CPS avoids one of the main difficulties in the application of these devices onboard of aircrafts, i.e. the sensitivity of DMA filter functions to pressure.

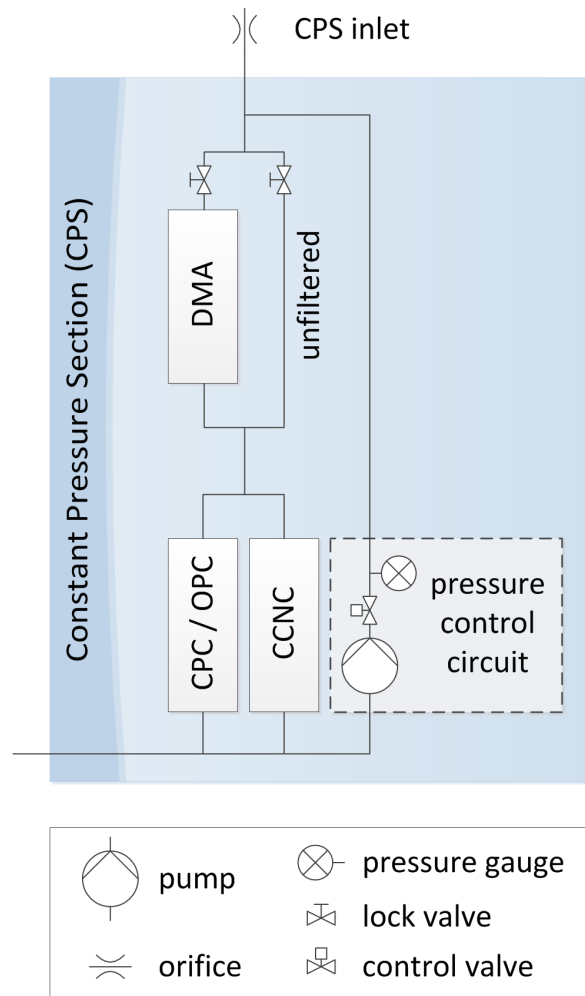


Figure 7.2.7: Recommendation for a future airborne CCNC setup. The current setup shown in Fig. 3.2.1 is complemented by a DMA (and an optional OPC) inside the CPS. Lock valves let the operator decide whether to pass a size-filtered or the unmodified aerosol sample to the measurement devices. This new setup provides the opportunity to quantitatively study size-dependent particle hygroscopicity while maintaining the possibility to measure total CCN number concentrations.

Appendix A

Methods Supplement

A.1 OPC Bin Specifications and Calibration Results

A.1.1 UHSAS

The UHSAS detection system consists of two separate detectors, i.e. an avalanche photodiode for detecting the smallest particles (primary detector) and a low-gain PIN photodiode for detecting particles in the upper size range of the instrument (secondary detector). Each detector itself amplifies the collected scattering pulses by means of two gain stages, named G3 (high gain) and G2 (low gain) for the primary detector, and G1 (high gain) and G0 (low gain) for the secondary detector. The linear relation coefficients for the conversion of the signal peak voltages measured by the individual gain stages (and detectors) are precisely determined in the course of a relative gain calibration (see UHSAS manual). They are stored in the instrument configuration file. With these linear conversion coefficients all signal peak voltages can easily be expressed as G3 equivalent voltages U (in mV). This quantity is directly proportional to the OPC-specific particle scattering cross section $\tilde{C}_{scat}(= (U - c)/s)$ defined in Sect. 3.2.2.2. The bin threshold values, however, are not stored in the data files in terms of the meaningful U_i but as the non-universal (calibration material equivalent) diameter values $D_{i,stored}$. In order to apply the OPC response model presented in Sect. 3.2.2.2, the $D_{i,stored}$ values need to be back-converted into their actual U_i counterparts. For the size range covered by the three highest gain stages G3-G1, the scattering is well-approximated by the Rayleigh solution, i.e. $\tilde{C}_{scat,detect}(D) \propto U(D) \propto D^6$ (linear increase of $\log U$ with $\log D$). Based on an absolute calibration, i.e. (U, D) -tuples (calibration points) of measured mean signal peak voltage and nominal mean calibration standard diameter, the $U(D)$ function used internally by the UHSAS software is, hence, starting with a D^6 extrapolation from the first calibration point and continues with linear $\log U$ ($\log D$)-interpolations between the following calibration points. For G0, the UHSAS uses a hard-coded fit function for $U(D)$ that is adjusted to the calibration points in the corresponding size range. For this size range, not just the calibration points but the (discrete) $U(D)$ function values are explicitly stored in the configuration file. Knowing this, the information included in the configuration file allows to regain the U_i from the $D_{i,stored}$ for the complete size range. For further information on the

bin i	2	3	4	5	6	7	8
$D_{i,stored}$ [μm]	0.079	0.088	0.098	0.107	0.117	0.126	0.136
U_i [mV]	3.89×10^2	7.68×10^2	1.42×10^3	2.49×10^3	4.20×10^3	6.78×10^3	1.06×10^4
	9	10	11	12	13	14	15
	0.145	0.155	0.164	0.174	0.183	0.193	0.202
	1.60×10^4	2.37×10^4	3.44×10^4	4.88×10^4	6.80×10^4	9.31×10^4	1.26×10^5
	16	17	18	19	20	21	22
	0.212	0.221	0.231	0.24	0.25	0.259	0.269
	1.67×10^5	2.20×10^5	2.86×10^5	3.67×10^5	4.68×10^5	5.90×10^5	7.39×10^5
	23	24	25	26			
	0.278	0.288	0.297	0.307			
	8.81×10^5	1.04×10^6	1.23×10^6	1.45×10^6			

Table A.1.1: Lower threshold values defining the UHSAS bins used in this study. Given are the diameter values $D_{i,stored}$ stored in the UHSAS data file headers and the corresponding back-converted G3 equivalent signal peak voltages.

UHSAS gain stages and the internal calibration, the reader is referred to the UHSAS manual. Table A.1.1 lists the $D_{i,stored}$ and back-converted U_i values for the UHSAS configuration (settings and calibration) and the size subrange used in this study.

A.1.2 SkyOPCs

Scattering signals collected by the SkyOPC detector are linearly amplified by two gain stages (hereafter referred to as the low and high gain stage). The high gain stage signal peak voltage U_{high} is first passing a comparator that is set to a fixed voltage of 4.8 V. If U_{high} falls below this threshold, the high gain signal is passed to an A/D converter, that linearly converts U_{high} to a digital value (linear conversion between 0 – 5 V and 0 – 1023). If U_{high} exceeds the comparator threshold, the low gain stage signal peak voltage U_{low} is passed to the converter and the resulting digital value is additionally increased by 1024 to avoid an overlap with the high gain stage digital signals. The nominal relative gain amplification factor and offset between the stages are $s_{amp} = 22$ and $c_{amp} = 0$ V respectively ($U_{high} = U_{low} \cdot s_{amp} + c_{amp}$). However, the actual values for s_{amp} and c_{amp} can (slightly) deviate from the nominal ones and are, hence, included as free parameters in the SkyOPC instrument response model. The SkyOPC digital threshold values x_i , defining the lower borders of each bin i , are fixed and can be read from the instrument log. Table A.1.2 lists these threshold values for the two models used in this study. In order to apply the OPC response model presented in Sect. 3.2.2.2, the x_i need to be converted into voltage values U_i that are directly proportional to the scattering cross sections $\tilde{C}_{scat,i}(= (U_i - c)/s)$. With the above information (by courtesy of M. Richter, Grimm Aerosol Technik), the high gain stage equivalent voltage U_i for each x_i can be calculated by

model	x_0	x_1	x_2	x_3	x_4	x_5	x_6	x_7
SkyOPC (SN: 29G07003)	(36)	62	114	267	531	832	1070	1095
SkyOPC _{TD} (SN: 29G06001)	(38)	(68)	122	267	534	847	1073	1099
	x_8	x_9	x_{10}	x_{11}	x_{12}	x_{13}	x_{14}	x_{15}
	1125	1142	1172	1212	1288	1343	1458	1646
	1126	1146	1180	1229	1284	1337	1445	1621

Table A.1.2: Lower digital threshold values defining the SkyOPC bins for the instrument service state valid for the presented data. The values in parenthesis correspond to bins that are not considered in this study, as they were affected by uncorrectable background noise.

$$U_i = \begin{cases} x_i \frac{5V}{1024} & \text{for } x_i < 983.04 = \frac{4.8 \cdot 1024}{5} \\ (x_i - 1024) \frac{5V}{1024} \cdot s_{amp} + c_{amp} & \text{for } x_i > 1024 \cdot \left(1 + \frac{4.8V - c_{amp}}{5V \cdot s_{amp}}\right) \\ 4.8V & \text{otherwise} \end{cases} \quad (\text{A.1.1})$$

Based on the bin threshold definitions given by Tab. A.1.2 and Eq. (A.1.1), Fig. A.1.1 and A.1.2 show the OPC model parameter solutions to the SALTRACE calibrations for the two SkyOPCs.

A.2 CCNC Data

A.2.1 Column A *SS* Calibration

Figure A.2.1 shows the calibration results for the first CCNC column (A), that was operated in *SS*-scanning mode during SALTRACE, as explained in Sect. 3.2.2.3.

A.2.2 CPS Tubing Transit Times

Figure A.2.2 demonstrates that the tubing transit time difference Δt between CPC₁ and the CPS inlet is negligible ($\Delta t \lesssim \pm 0.5$ s) for both CPS inlet orifices independent of the CPS bypass flow variation adjunct to inlet pressure p_{inlet} changes. This result implies that the differential tubing transit time between CPC₁ and the CCNC reference CPC (CPC_{CPS}), which is determined as 4 s (cf. Tab. 3.2.3), can in good approximation be attributed to the last (exclusive) CPC_{CPS} tubing part (cf. Fig. 3.2.1). The data in Fig. A.2.2 are based on laboratory measurements of the total flow upstream of each CPS inlet orifice for varying p_{inlet} at constant $p_{CPS} = 500$ hPa and the tubing lengths of the SALTRACE setup.

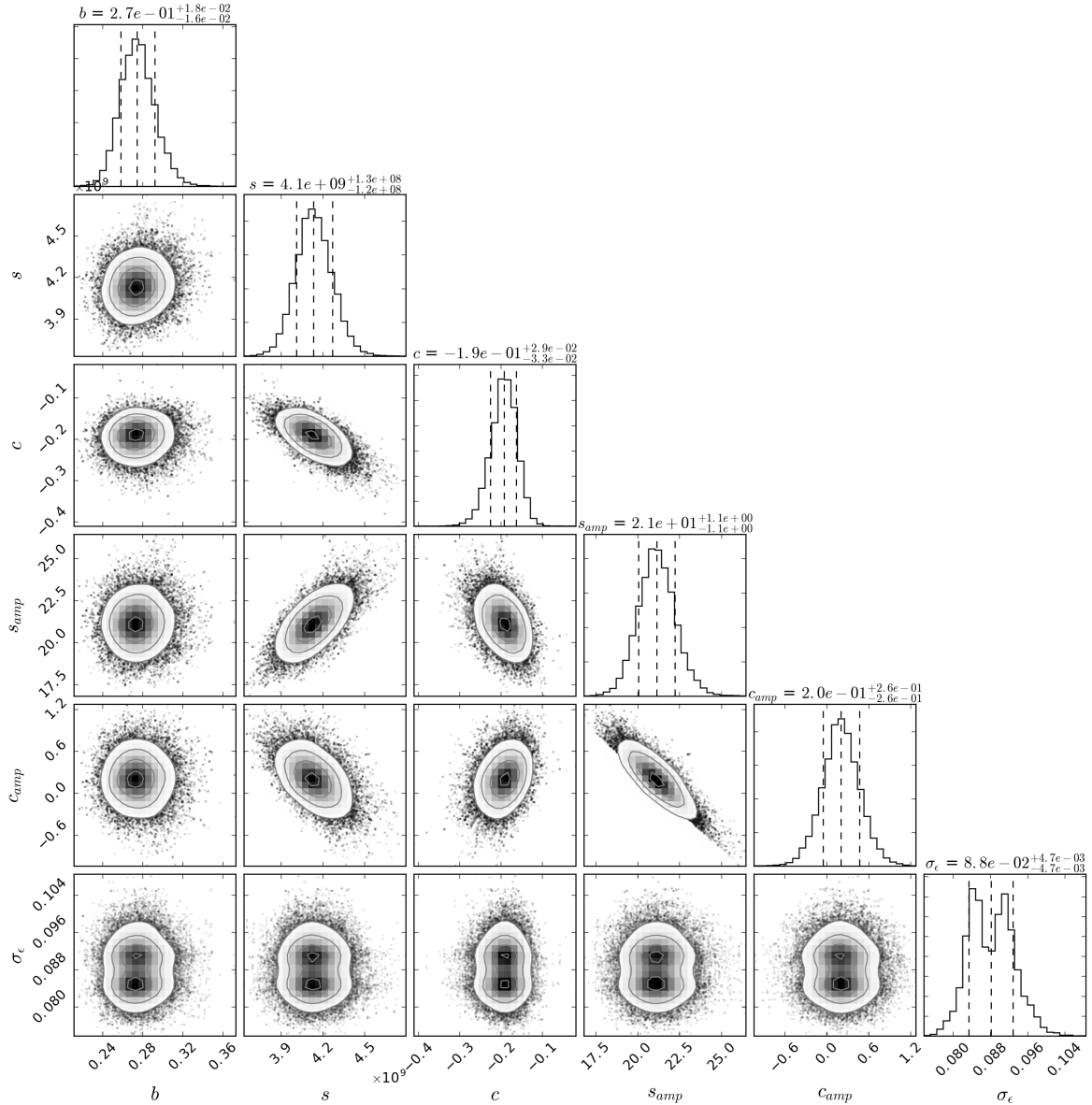


Figure A.1.1: Results for the calibration of the SkyOPC (SN: 29G07003) analogous to Fig. 3.2.11. The additional parameters s_{amp} and c_{amp} define the linear relative signal amplification between the instrument gain stages. The parameter units are $[s] = \text{V}/\text{cm}^2$, $[c] = \text{V}$ and $[c_{amp}] = \text{V}$ (in high gain stage equivalent voltages). Parameters b , s_{amp} and σ_ϵ are unitless.

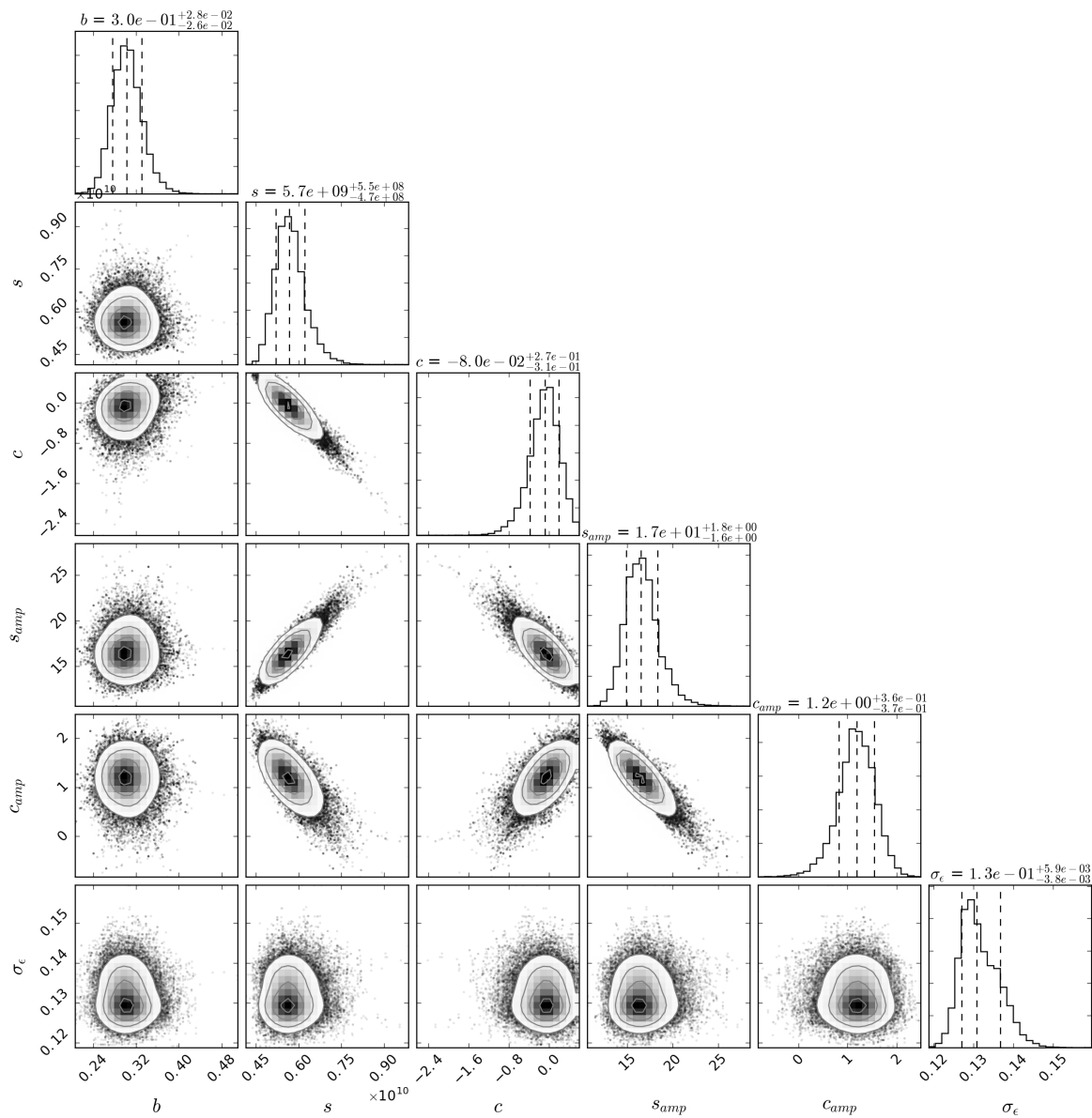


Figure A.1.2: Same as Fig. A.1.1 but for SkyOPC_{TD} (SN: 29G06001).

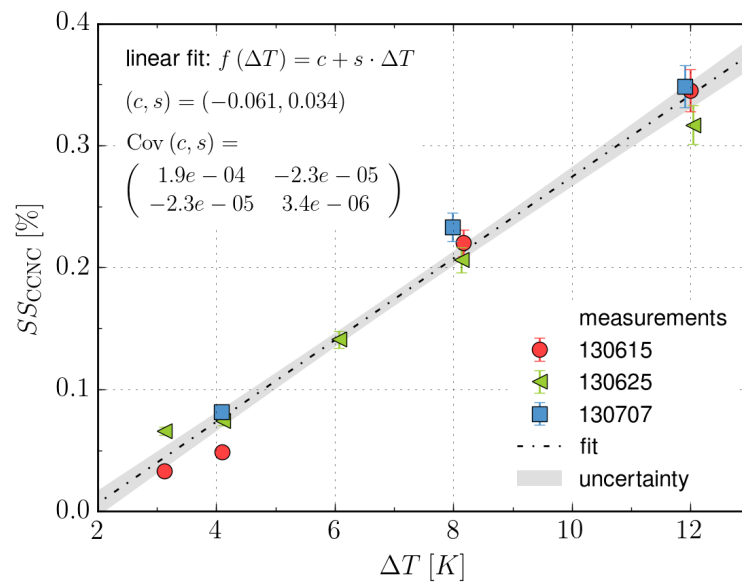


Figure A.2.1: Same as Fig. 3.2.17b) but for CCNC column A.

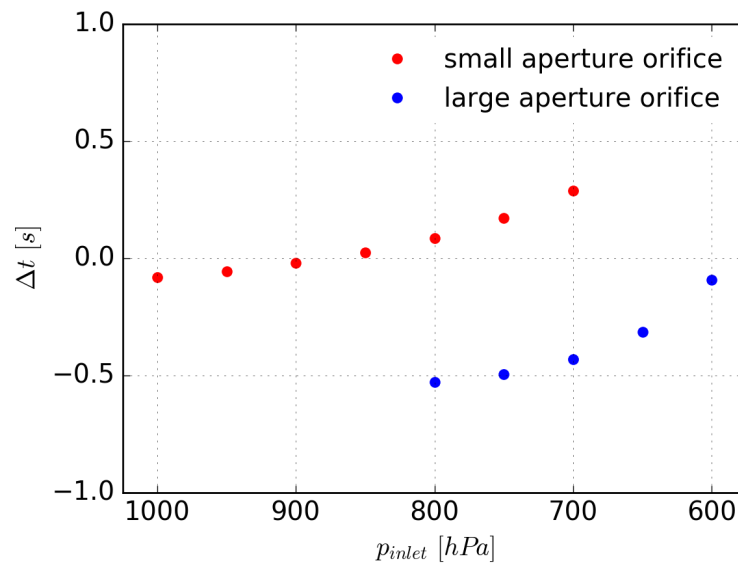


Figure A.2.2: Difference in aerosol tubing transit time Δt between CPC_1 and the CPS inlet in dependence of the inlet pressure p_{inlet} .

A.2.3 CCN Correction Scheme Comparison

Table A.2.1 lists all CCN concentrations (column B, $SS = 0.2\%$) for the different correction stages, i.e. the uncorrected (raw) values $n_{\text{CCN},\text{uncorr}}$, and the ones corrected for particle losses at the CPS inlet orifices following the two correction schemes discussed in Sect. 3.2.2.3, i.e. $n_{\text{CCN},v1}$ and $n_{\text{CCN},v2}$. Accordingly, considering the $n_{\text{CCN},v2}$ values to represent the correct CCN concentrations, for the small aperture orifice the $n_{\text{CCN},\text{uncorr}}$ values underestimate the true concentrations on average by 27%, while the $n_{\text{CCN},v1}$ values slightly overestimate the true concentrations by 6%. For the large aperture orifice the average underestimation of the CCN concentration by $n_{\text{CCN},\text{uncorr}}$ reduces to 9%, whereas the average overestimation by $n_{\text{CCN},v1}$ increases to 17%.

A.3 Comparison with Ground-Based Measurements

A.3.1 Particle NSD Retrieval Results

Figure A.3.1 shows the particle NSD (lognormal mode parameter) solution ensemble for the comparison interval on 20 June 2013 resulting from the NSD retrieval method outlined in Sect. 3.3.2. For the visualization of the NSD result in Fig. 3.3.6 (and, equivalently, in Fig. 3.3.7 and 3.3.8), each member of this solution ensemble, i.e. each solution parameter tuple is used to calculate a full $(dn/d\log_{10} D)$ NSD on a high-resolution diameter grid. Repeating this for all other NSD solution parameter tuples yields ensembles of $dn/d\log_{10} D$ values at each diameter grid point. From the latter ensembles, the displayed diameter-wise $dn/d\log_{10} D$ medians and percentiles are calculated. This way the correlated NSD parameter PDFs are thoroughly propagated into a NSD uncertainty range.

A.3.2 CCN Correction Scheme Comparison for 0.2% SS

A list of all results for n_{CCN} , D_{act} and κ (at $SS = 0.2\%$), obtained from the comparison measurements using the method presented in Sect. 3.3.4, is shown in Tab. A.3.1. This list contains the results for the different CCN concentration correction schemes introduced in Sect. 3.2.2.3. The v2.2 results, where the CCN concentrations are corrected for particle loss at the CPS inlet via Eq. (3.2.20) show good agreement with the v2.1 results corrected by means of Eq. (3.2.19). This finding proves the consistency of these independent approaches. However, owing to the systematic uncertainties of the absolute CPC concentrations used for the former correction, the uncertainties of the v2.2 values are considerably larger than those of the v2.1 values. Therefore, the latter values are used to present the results for D_{act} and κ in Fig. 3.3.6 to 3.3.9. For the v1 CCN concentrations corrected via the method presented in Dollner (2015) an uncertainty of 13% is estimated from error propagation of the individual uncertainties in the (raw) concentrations used for this correction approach. Because this method neglects particle losses in the CPC_{CPS} tubing and, hence, overestimates the losses at the CPS inlet, the v1 results slightly under- and overestimate D_{act} and κ , respectively. Finally, the uncorrected CCN concentrations that completely neglect particle losses at the CPS inlet significantly over- and underestimate D_{act} and κ , respectively.

flight	time interval [s UTC]	$n_{\text{CCN},\text{uncorr}}$ [cm ⁻³ STP]	$n_{\text{CCN},v1}$ [cm ⁻³ STP]	$n_{\text{CCN},v2}$ [cm ⁻³ STP]	$\frac{n_{\text{CCN},\text{uncorr}} - n_{\text{CCN},v2}}{n_{\text{CCN},v2}}$	$\frac{n_{\text{CCN},v1} - n_{\text{CCN},v2}}{n_{\text{CCN},v2}}$
<i>small aperture orifice</i>						
130620a	54348.0 - 55003.0	115.6	170.9	160.7	-0.28	0.06
130622a	75429.0 - 75508.0	107.2	156.8	143.8	-0.25	0.09
130626a	97774.0 - 97905.0	124.8	179.9	169.0	-0.26	0.06
130710a	68520.0 - 69262.0	159.5	234.0	221.5	-0.28	0.06
130711a	53049.0 - 53870.0	120.0	174.6	168.5	-0.29	0.04
					-0.27	0.06
<i>large aperture orifice</i>						
130617a	40920.0 - 41140.0	229.7	272.7	249.9	-0.08	0.09
130617a	41170.0 - 41390.0	268.9	314.9	289.9	-0.07	0.09
130617a	42500.0 - 43180.0	176.4	233.4	203.3	-0.13	0.15
130620a	53425.0 - 53805.0	106.6	148.2	121.9	-0.13	0.22
130621a	72230.0 - 72830.0	119.4	169.0	129.0	-0.07	0.31
130621a	73859.4 - 76671.4	145.7	194.1	160.9	-0.09	0.21
130622a	70215.0 - 70675.0	121.7	165.5	131.2	-0.07	0.26
130622a	74325.0 - 74565.0	186.1	238.4	199.8	-0.07	0.19
130622a	74680.0 - 74945.0	208.0	267.3	223.5	-0.07	0.20
130626a	94515.4 - 95930.4	141.7	184.0	151.9	-0.07	0.21
130630a	51420.0 - 51595.0	155.4	197.4	167.3	-0.07	0.18
130630a	52555.0 - 52800.5	181.6	232.3	199.0	-0.09	0.17
130701a	56514.3 - 57040.0	176.7	226.4	192.0	-0.08	0.18
130701a	57500.0 - 57970.0	180.0	232.2	196.7	-0.08	0.18
130701a	58330.0 - 58650.0	139.8	187.4	151.2	-0.08	0.24
130701b	71620.0 - 71715.0	147.6	193.3	160.9	-0.08	0.20
130701b	71920.0 - 72027.5	154.8	197.8	167.9	-0.08	0.18
130701b	79070.0 - 79880.0	170.8	224.6	185.6	-0.08	0.21
130710a	59650.0 - 60039.4	143.4	188.9	158.3	-0.09	0.19
130710a	60350.0 - 60587.5	182.8	231.2	203.7	-0.10	0.13
130710a	64760.0 - 65458.4	140.6	190.9	156.3	-0.10	0.22
130710a	65553.4 - 65850.0	141.4	195.0	160.1	-0.12	0.22
130710a	65975.5 - 66111.4	134.0	183.2	149.9	-0.11	0.22
130710a	66350.0 - 66761.4	195.7	255.3	225.2	-0.13	0.13
130711a	49192.5 - 49657.5	157.1	194.2	171.0	-0.08	0.14
130711a	49864.5 - 50491.5	189.2	234.3	210.9	-0.10	0.11
130711b	70895.5 - 71090.0	166.2	205.7	181.0	-0.08	0.14
130711b	71150.0 - 71375.0	167.9	207.4	183.6	-0.09	0.13
130711b	71430.0 - 71585.5	171.3	207.0	188.9	-0.09	0.10
130711b	71810.0 - 72050.0	189.8	237.4	210.5	-0.10	0.13
130711b	72065.0 - 72306.5	190.3	238.8	211.5	-0.10	0.13
130711b	72375.5 - 72620.0	201.7	256.4	227.9	-0.11	0.13
130711b	72690.0 - 72885.5	206.0	258.7	230.2	-0.11	0.12
					-0.09	0.17

Table A.2.1: Comparison of CCN concentrations for the different data correction stages and the entirety of time intervals used to derive $n_{\text{CCN},v2}$ and particle hygroscopicity from the CCNC column B measurements (at $SS = 0.2\%$).

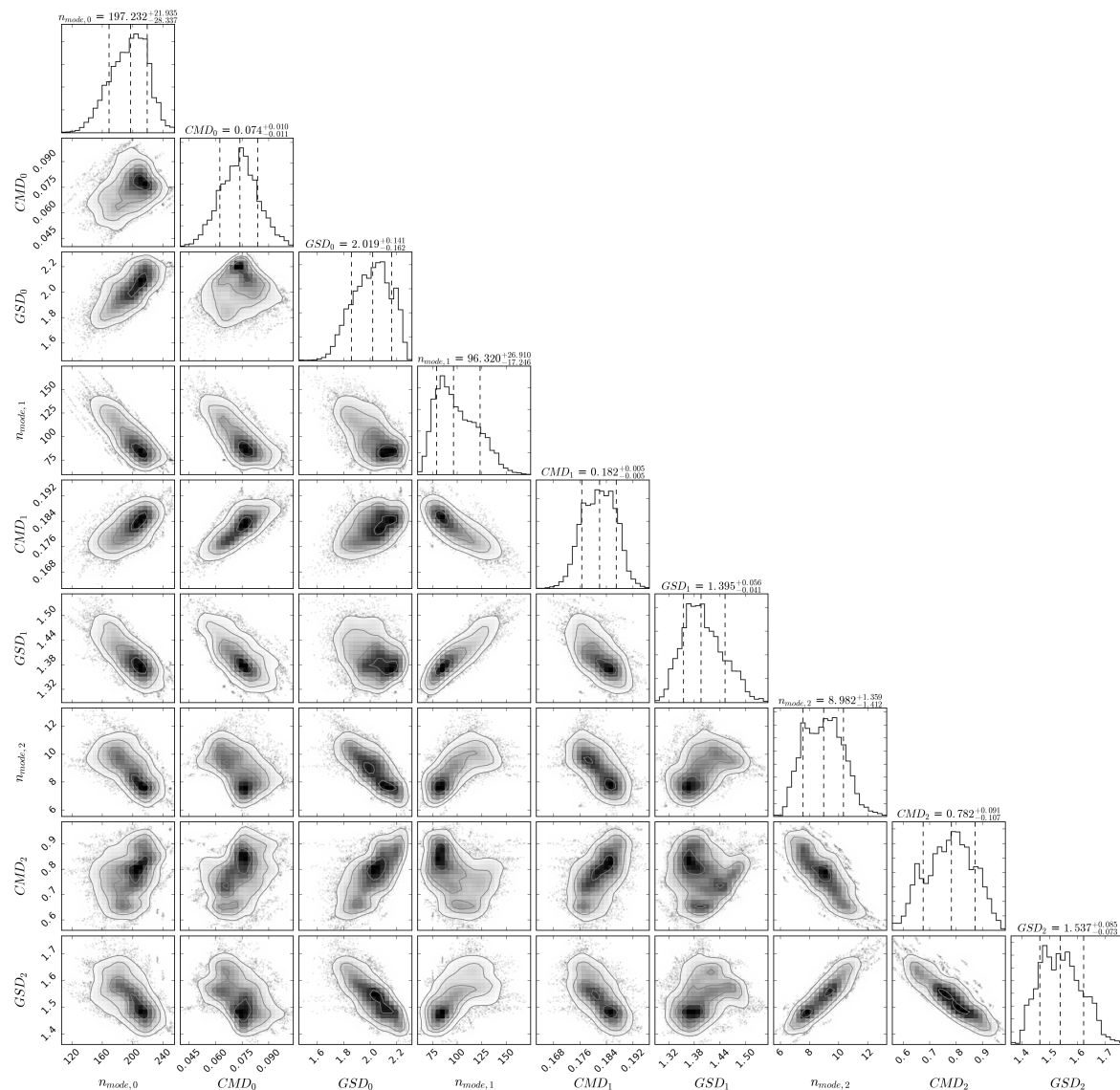


Figure A.3.1: Exemplary NSD retrieval result. Shown is the (trimodal lognormal) NSD mode parameter solution ensemble for flight 130620a and the interval used to compare the airborne with the ground-based measurements (54348-55003 s UTC). The solution ensemble is visualized in the same way as in Fig. 3.2.11. The units for the lognormal modes' integral concentrations $n_{mode,l}$ and count median diameters CMD_l are cm^{-3} (STP) and μm , respectively.

day ^a	n_{CCN} [cm ⁻³ STP]	D_{act} [nm]	κ
<i>Ragged Point</i>			
20 June	168.59	97.18 (± 4.08)	0.348 (± 0.051)
22 June	140.72	97.03 (± 4.11)	0.346 (± 0.050)
26 June	171.79	102.88 (± 3.67)	0.291 (± 0.038)
10 July	235.3	109.83 (± 3.53)	0.239 (± 0.029)
11 July	178.11	110.61 (± 3.47)	0.235 (± 0.028)
<i>Falcon uncorrected</i>			
20 June	115.64 (± 5.87)	132.40 (± 9.75)	0.118 (± 0.028)
22 June	107.23 (± 5.64)	120.62 (± 8.85)	0.153 (± 0.036)
26 June	124.84 (± 6.57)	128.54 (± 9.16)	0.129 (± 0.030)
10 July	159.49 (± 8.05)	136.98 (± 10.38)	0.098 (± 0.024)
11 July	119.99 (± 6.06)	140.68 (± 10.52)	0.097 (± 0.023)
<i>Falcon v1</i>			
20 June	170.90 (± 22.34)	90.18 (± 17.49)	0.464 (± 0.339)
22 June	156.77 (± 20.60)	83.42 (± 18.40)	0.628 (± 0.596)
26 June	179.90 (± 23.64)	87.03 (± 19.91)	0.578 (± 0.513)
10 July	234.03 (± 30.56)	92.76 (± 20.17)	0.433 (± 0.422)
11 July	174.63 (± 22.81)	97.92 (± 18.76)	0.361 (± 0.290)
<i>Falcon v2.1^b</i>			
20 June	160.69 (± 8.97)	97.08 (± 9.31)	0.308 (± 0.093)
22 June	143.84 (± 7.72)	93.99 (± 8.33)	0.331 (± 0.095)
26 June	168.98 (± 9.41)	95.94 (± 10.26)	0.326 (± 0.113)
10 July	221.50 (± 11.86)	100.52 (± 10.04)	0.258 (± 0.083)
11 July	168.53 (± 8.97)	102.20 (± 9.54)	0.261 (± 0.076)
<i>Falcon v2.2</i>			
20 June	162.33 (± 19.92)	96.16 (± 16.35)	0.362 (± 0.226)
22 June	145.70 (± 17.02)	92.21 (± 14.54)	0.400 (± 0.277)
26 June	169.30 (± 19.38)	95.27 (± 17.20)	0.391 (± 0.291)
10 July	223.72 (± 23.80)	98.83 (± 16.46)	0.309 (± 0.213)
11 July	169.20 (± 18.41)	101.72 (± 15.81)	0.294 (± 0.168)

^a For detailed comparison interval times see Fig. 3.3.6 to 3.3.8.

^b Presented as Falcon (v2) results in Fig. 3.3.6 to 3.3.9.

Table A.3.1: List of CCN concentrations, activation diameters and effective particle hygroscopicities (at $SS = 0.2\%$) derived for the intervals used to compare the airborne with the ground-based measurements. The results are obtained by means of the different CCN concentration correction schemes introduced in Sect. 3.2.2.3. The values are represented by the respective PDF means and standard deviations.

day ^a	SS [%]	D_{act} [nm]	κ	SS [%]	D_{act} [nm]	κ
	<i>Ragged Point</i>			<i>Falcon v2^b</i>		
22 June	0.1	172.43 (± 2.53)	0.250 (± 0.038)	0.161	96.95 (± 8.29)	0.468 (± 0.128)
	0.2	97.03 (± 4.11)	0.346 (± 0.050)	0.200	93.99 (± 8.33)	0.331 (± 0.095)
10 July	0.2	109.83 (± 3.53)	0.240 (± 0.029)	0.203	100.52 (± 10.04)	0.258 (± 0.083)
	0.3	89.07 (± 4.16)	0.198 (± 0.032)	0.280	92.43 (± 10.23)	0.175 (± 0.063)
11 July	0.074	203.45 (± 3.50)	0.280 (± 0.059)	0.117	114.69 (± 9.74)	0.560 (± 0.153)
	0.2	110.61 (± 3.47)	0.235 (± 0.028)	0.203	102.20 (± 9.54)	0.261 (± 0.076)
	0.3	89.86 (± 3.91)	0.192 (± 0.030)	0.298	94.63 (± 9.54)	0.151 (± 0.048)

^a For detailed comparison interval times see Fig. 3.3.6 to 3.3.8.

^b Falcon v2 is short for the v2.1 results (cf. Sect. A.3.2 and 3.2.2.3).

Table A.3.2: List of activation diameter and effective particle hygroscopicity results for the (Ragged Point) comparison cases that comprise CCN measurements at different SS . The results are presented in the same way as in Tab. A.3.1. Values for the main SS of 0.2%, corresponding to the airborne measurements with CCNC column B, are printed in bold. For the (scanning) CCNC column A airborne measurements at other SS , the value of SS and the associated results are confronted with the closest “non-0.2%” ground-based measurements.

It should be emphasized that the n_{CCN} and D_{act} values are (in a strict sense) not directly comparable between the airborne and ground-based measurements, since they depend on the exact values of the activation temperature T_{act} and supersaturation SS . These values, particularly T_{act} , can differ for the Falcon and Ragged Point CCNC measurements. As it takes account of T_{act} and SS , the most meaningful comparison quantity is κ .

A.3.3 Particle Hygroscopicity Comparison for other SS

In addition to the values of D_{act} and κ for the main SS of 0.2%, Tab. A.3.2 shows the results for the other SS derived from the (scanning) CCNC column A airborne measurements, and confronts these results with the closest “non-0.2%” ground-based measurements. Although especially the D_{act} values are not directly comparable here, because the SS differ for the airborne and ground-based CCNC measurements, the (qualitative) trend with changing SS can still be compared. Whereas the Ragged Point measurements, assumed to be reliable, see no significant trend in κ with varying SS , i.e. with varying D_{act} — not even for the complete range $0.1 \lesssim SS \lesssim 0.7\%$ (see Kristensen et al., 2016) — the values derived from the airborne column A measurements exhibit a significant increase in κ with decreasing SS . This is not exclusively found for the MBL comparison measurements but the same doubtful features, particularly significantly increased κ values for the lowest SS , are also regularly observed for the measurements inside the SAL (cf. Tab. B.5.8 to B.5.11). In extreme cases, e.g. for flight 130701a at an altitude of about 3.5 km (cf. Tab. B.5.6 and B.5.10), the values for n_{CCN} measured by column A for an apparently low $SS < 0.2\%$ are (almost) identical to the column B n_{CCN} measured for $SS = 0.2\%$. This implies that for (almost) identical D_{act}

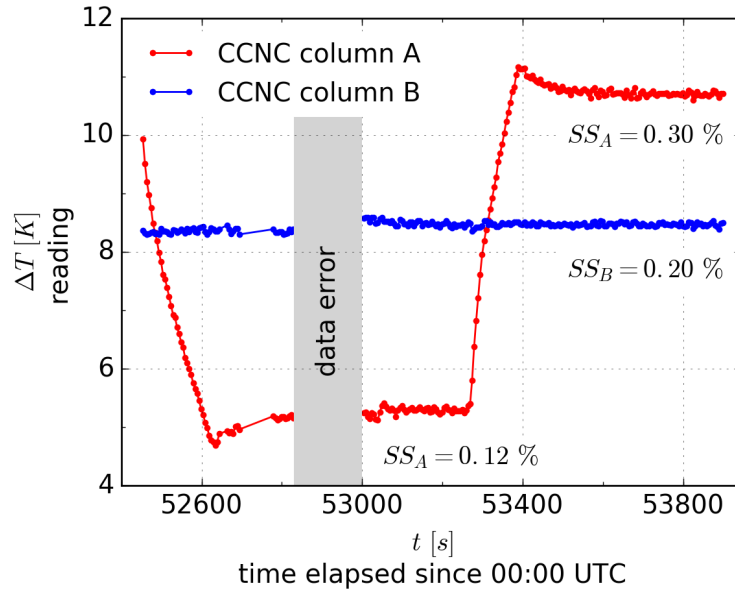


Figure A.3.2: Typical time series of ΔT readings for the constant SS column B and the scanning column A using the example of flight 130711a and the interval utilized to compare the airborne with the ground-based measurements.

considerably different values of κ are derived. These findings immediately suggest a systematic error in the column A measurements. This systematic error is not connected with the CCN concentration correction scheme, as even the uncorrected n_{CCN} exhibit the same features. An obvious explanation for this error is a systematic deviation of the actual column A SS from the value determined via the calibration curve (see Fig. A.2.1) using the measured ΔT reading. In other words, there is evidence for a systematic ΔT reading bias to be the (main) reason for the observed column A measurement abnormalities.

A typical time series for the ΔT readings of the airborne CCNC columns is shown in Fig. A.3.2, using the example of the time interval utilized to compare the airborne and ground-based measurements on 11 July 2013. As appears from this plot, the column A scanning pattern starts with approaching the lower ΔT setting (roughly corresponding to a SS of 0.1%) from larger ΔT , then continues with leveling off at the lower ΔT before jumping to the higher ΔT setting (corresponding to $SS = 0.3\%$). A complete ΔT step takes about 10 min and the ΔT reading suggests that the temperatures settle after approximately 7 min. However, the temperatures are read on the outer column wall, so that the thermal resistance of the column wall itself and the water film wetting the inner column wall may further retard the equalization between the ΔT reading and the actual ΔT inside the column. For (too) fast temperature changes this could lead to a remaining bias of the actual ΔT in the direction of the previous ΔT setting. On the other hand, during the SS calibration (cf. Sect. 3.2.2.3) each ΔT setting is maintained for a long duration, so that here the ΔT reading can be assumed to correspond to the actual ΔT . In consequence, this could imply that for the rather fast in-flight temperature changes the SS determined from the (apparently settled) ΔT reading deviates from the true SS that relates to the ΔT inside the column. For the ground-

CCNC column	time interval [s UTC]	D_{act} [nm]	ΔT [K]	SS [%]	κ	$\Delta T'$ [K]	SS' [%]	κ'
B	53049.0 - 53870.0	102	8.48	0.20	0.26 (± 0.08)			
A	53049.0 - 53270.0	115	5.31	0.12	0.56 (± 0.15)	5.84	0.14	0.37 (± 0.10)
A	53515.0 - 53870.0	95	10.72	0.30	0.15 (± 0.05)	9.64	0.24	0.23 (± 0.07)

Table A.3.3: Testing the impact of a hypothetical systematic deviation between the actual column A thermal gradient and the corresponding reading by the example of flight 130711a and the interval used to compare the airborne with the ground-based measurements. ΔT , SS and κ represent the thermal gradient reading, the resulting supersaturation and hygroscopicity parameter value, respectively. $\Delta T'$ assumes that for the fast column A temperature changes the actual temperature gradient in the CCNC deviates by 15% from the ΔT reading in direction of the previous ΔT setting (see Fig. A.3.2). SS' and κ' denote the associated supersaturation and hygroscopicity parameter value. For κ , in addition to the mean values, the PDF standard deviations are given.

based measurements, the ΔT setting durations were considerable longer — about 15 min with the first ≥ 10 min ruled out (T. Kristensen, personal communication) — and are presumably less or not affected in the same way. Table A.3.3 demonstrates the potential impact of a remaining column A ΔT bias on the results for the hygroscopicity parameter κ . Accordingly, a moderate relative ΔT deviation of 15% in direction of the previous ΔT is already sufficient to remove the significant increase in κ with decreasing SS and to bring the Falcon and Ragged Point measurements into agreement. However, although the combination of the MBL comparison results, the findings inside the SAL and this hypothetical test case argue for this explanation attempt, these indications are not conclusive. For future CCNC scanning column measurements it should, therefore, be tested if remaining ΔT biases are indeed responsible for the observed errors and, in case, if these errors can be removed by increased ΔT setting durations.

Appendix B

Results Supplement

B.1 Intense Dust Event

The most intense dust event occurring in the Caribbean during 10 and 11 July is treated in detail in Sect. 4.1. In the latter section, however, only the vertical profiles for flight 130711a are shown to highlight the important vertical features of the SAL regarding meteorological parameters and aerosol particle concentrations. Figure B.1.1 demonstrates that these main features, e.g. the subdivision of the SAL into a lower and upper part with the discussed properties, are indeed characteristic also for the previous day, i.e. 10 July and, therewith, representative for this entire dust event.

Figure B.1.2 further proves that the differences in D_{act} and κ between the lower and upper SAL connected with the transition in aerosol properties (cf. Fig. 4.1.11) are no artifact of the n_{CCN} correction scheme. Without correcting n_{CCN} for particle losses at the CPS inlet, the D_{act} and κ results shift to (slightly) larger and smaller values, respectively. Yet, the trend with altitude is preserved.

B.2 Time Course of Vertical Profiles

Figure B.2.1 and B.2.2 complement the time course of vertical information (from airborne and ground-based measurements) presented in Sect. 4.2.2.1. The potential temperature gradient and water vapor mixing ratio (Fig. B.2.1) clearly reveal the evolution of the SAL's base and top height and show the breakup of this structure for cases without (notable) SAL presence, i.e. for the flights on 5 and 8 July. The vertical profiles in Fig. B.2.2 once more show the close accordance of n_{CCN} and n_{80} , meaning that the integral number concentration of particles with $D \gtrsim 80$ nm provides a good qualitative proxy for the CCN concentration at $SS = 0.2\%$ throughout the vertical column.

B.3 Impactor Samples for Single Particle Analysis

For traceability of the single particle composition analysis results presented in Fig. 4.1.10 and 4.2.21, Tab. B.3.1 and B.3.2 list all impactor samples providing the data basis for these plots. The listed samples represent all samples with complete size range coverage available for the SAL, i.e. the ones for which both stage A and B have been evaluated up to the date of submission of this thesis.

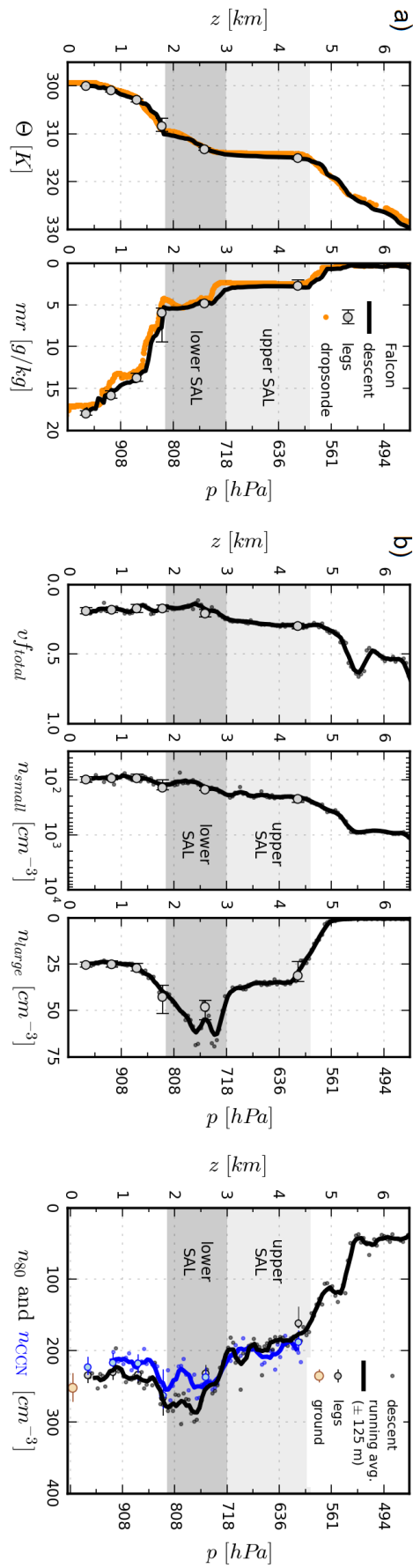


Figure B.1.1: Vertical profiles of (a) meteorological and (b) aerosol parameters measured in the vicinity of Barbados during flight 130710a in the course of a stepwise descent. The data are presented in the same way as in Fig. 4.1.2, 4.1.4 and 4.1.5 for flight 130711a.

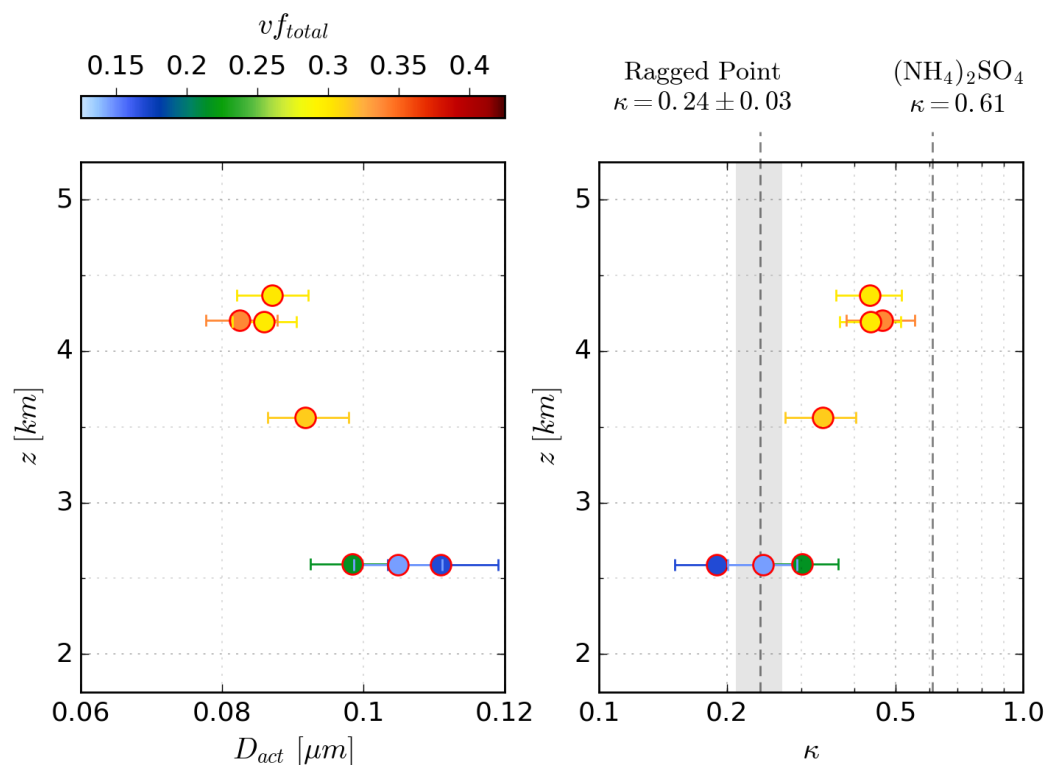


Figure B.1.2: Same as Fig. 4.1.11 but using the uncorrected CCN concentrations for the derivation of D_{act} and κ .

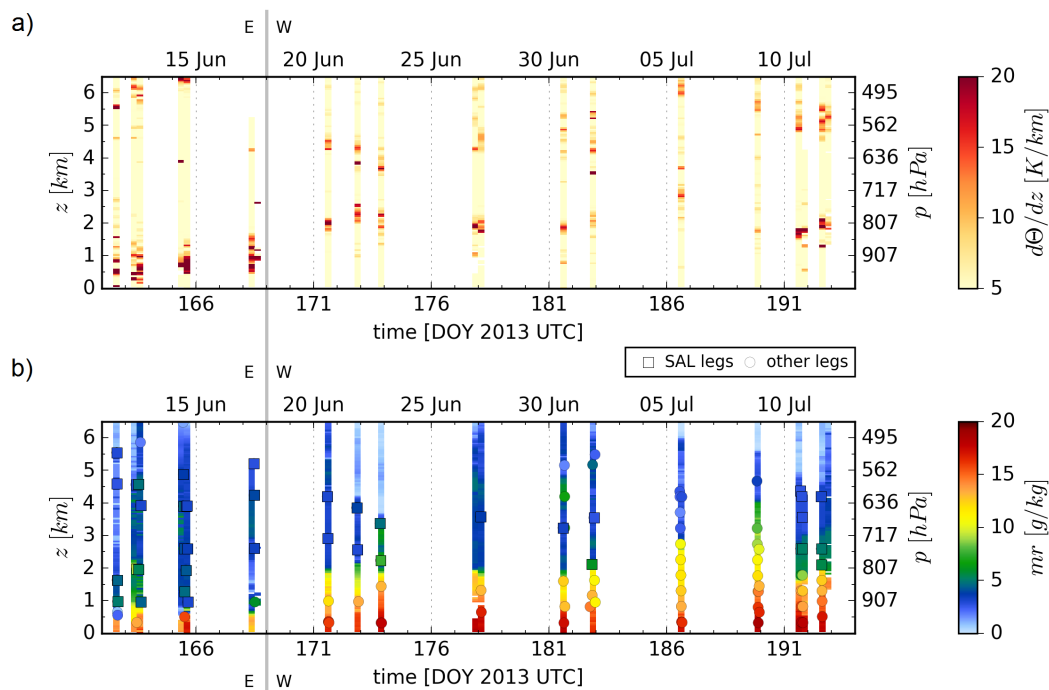


Figure B.2.1: Time course of the vertical profiles of (a) the potential temperature gradient $d\Theta/dz$ and (b) the water vapor mixing ratio mr , presented in the same way as in Fig. 4.2.12 and 4.2.13.

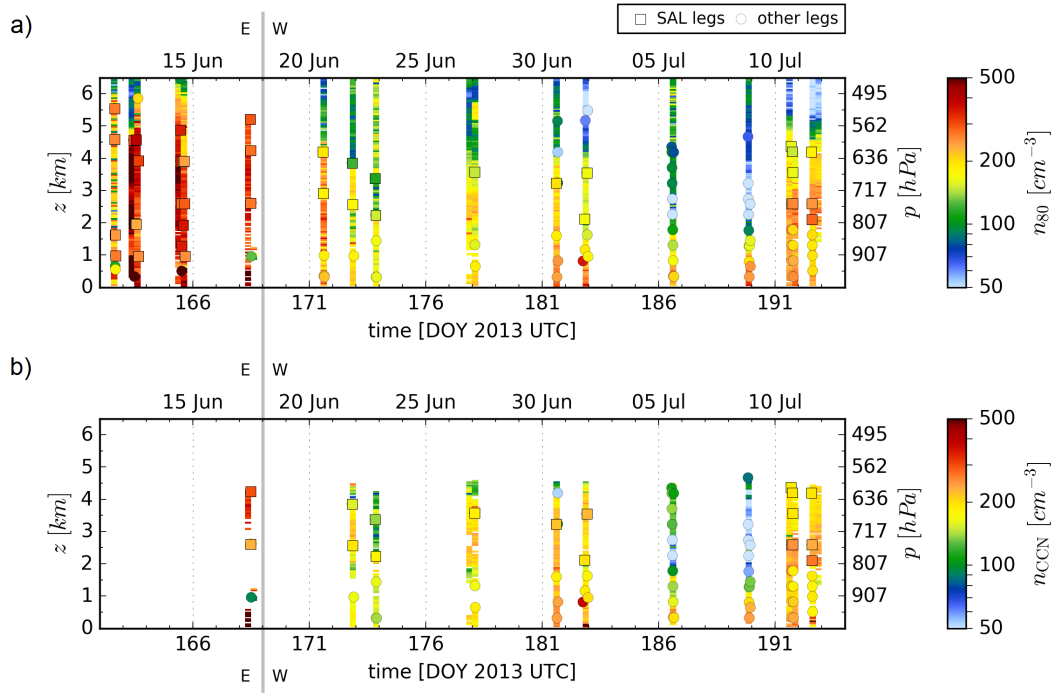


Figure B.2.2: Time course of the vertical profiles of (a) n_{80} and (b) n_{CCN} (at $SS = 0.2\%$), presented in the same way as in Fig. 4.2.12, 4.2.13 and B.2.1.

flight	time interval [s UTC]	altitude [m AMSL]	stage A sample	stage B sample
<i>upper SAL</i>				
130710a	65580.0 - 66030.0	3560	FAE_257a	FAT_257b
130711a	49230.0 - 49560.0	4196	FAE_261a	FAT_261b
<i>lower SAL</i>				
130710a	60300.0 - 60900.0	2595	FAE_255a	FAT_255b
130711a	49950.0 - 50280.0	2590	FAE_263a	FAT_263b

Table B.3.1: List of impactor samples included in Fig. 4.1.10, i.e. the comparison of size-dependent particle composition between the upper and lower part of the SAL on 10 and 11 July. The sampling interval height information is provided in terms of a mean altitude.

flight	time interval [s UTC]	altitude [m AMSL]	stage A sample	stage B sample
<i>Northwest African coast</i>				
130614a	41130.0 - 41730.0	3899	FAE_206a	FAT_206b
130617a	41988.0 - 42506.0	2615	FAE_211a	FAT_211b
<i>Caribbean</i>				
130620a	50700.0 - 51060.0	4198	FAE_215a	FAT_215b
130622a	72810.0, 73170.0	2231	FAE_226a	FAT_226b
130710a	60300.0 - 60900.0	2595	FAE_255a	FAT_255b
130710a	65580.0 - 66030.0	3560	FAE_257a	FAT_257b
130711a	49230.0 - 49560.0	4196	FAE_261a	FAT_261b
130711a	49950.0 - 50280.0	2590	FAE_263a	FAT_263b

Table B.3.2: List of impactor samples included in Fig. 4.2.21, i.e. the comparison of size-dependent particle composition between the SAL aerosol at the Northwest African coast and in the Caribbean. The sampling interval height information is provided in terms of a mean altitude.

B.4 Dry Deposition of SAL Aerosol During Transport

Figure B.4.1 shows an exemplary investigation of SAL aerosol dry deposition during SALTRACE by means of a combination of the COSMO-MUSCAT model and LAGRANTO backward trajectories (cf. Sect. 3.4). In this example a SAL trajectory starting at Cabo Verde on 17 June and passing over Barbados on 22 June is used to study the evolution of the vertical structure of mineral dust concentration and vertical velocity along the trajectory's path. During the first days of transport the trade wind inversion at the base of the SAL (almost) completely suppresses mixing with the underlying atmosphere. Still gravitational settling leads to dry deposition of coarse dust particles. About 1 – 2 days prior to arrival at Barbados (about 20 June) the model shows the occurrence of enhanced convection, i.e. intensified and persistent updrafts below and at the SAL's base. This convection temporarily surmounts the inversion stability and triggers turbulent mixing leading to a strong increase in dry dust deposition and, therewith, in SAL aerosol presence in the lower troposphere. Yet, the main SAL structure is still preserved and the maximum dust concentration remains aloft. The maximum dry deposition is then observed when the trajectory has reached the Caribbean sea, about 1 day after passing over Barbados. Although being just a case study, these features of SAL aerosol dry deposition are representative for the entire SALTRACE campaign (Heinold et al., 2017, in prep.).

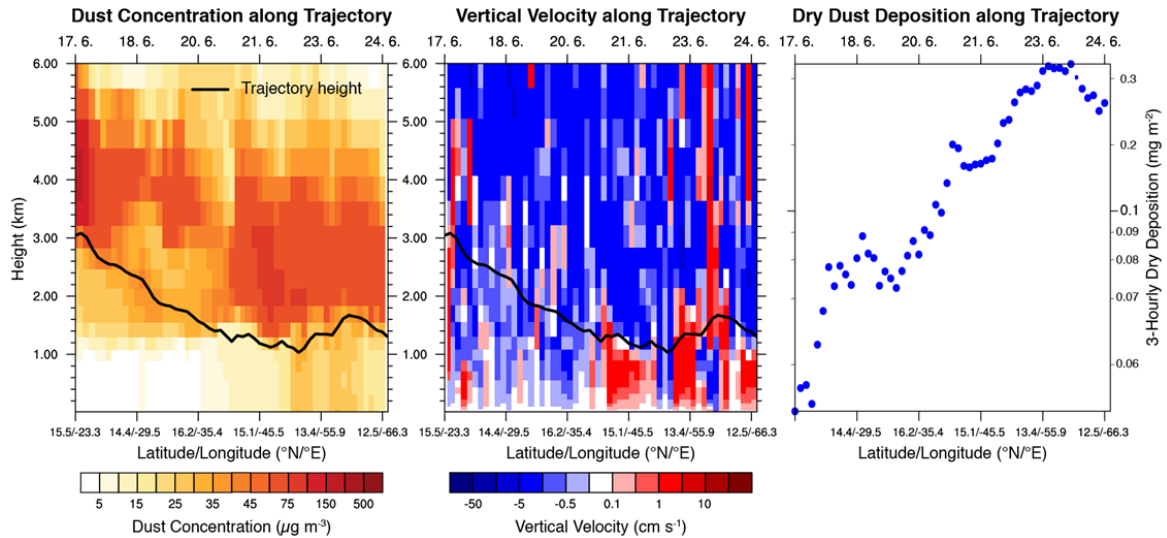


Figure B.4.1: Dry deposition of SAL aerosol particles along the path of a trajectory starting in the SAL over the Northwest African coast on 17 June and passing Barbados on 22 June. Shown are the height profiles of mineral dust concentration (left), clearly displaying the main SAL altitude range, and vertical velocity (center). Additionally, the rightmost plot shows the evolution of dry dust deposition rates. Plot shown by courtesy of B. Heinold, TROPOS.

B.5 Entirety of NSD and Hygroscopicity Results

B.5.1 Lognormal NSD Parameters

Table B.5.1 to B.5.4 provide the complete list of particle NSD retrieval cases used for this study, both for the comparison measurements in the MBL (see Sect. 3.3.5) and the main measurements inside the SAL. For each case, defined by flight number and sampling time interval, the trimodal lognormal NSD solutions (cf. Fig. A.3.1) are given in terms of the (marginalized) individual parameter PDF means and standard deviations (respective top rows) as well as in terms of PDF medians, 16 and 84th percentiles (respective bottom rows). For a Gaussian PDF, the mean should correspond to the median and the mean \pm one standard deviation should roughly correspond to the 16/84th percentile, respectively. Deviations from this behavior indicate parameter PDF skewness.

B.5.2 CCN Concentration, Activation Diameter and Particle Hygroscopicity

Table B.5.5 to B.5.7 show a similar register for all n_{CCN} , D_{act} and κ values derived from the above listed NSDs and the parallel CCNC column B measurements at the main supersaturation of $SS = 0.2\%$. n_{CCN} is short for $n_{\text{CCN},v2}$, i.e. represents the CCN concentration corrected via Eq. (3.2.19) for the MBL measurements and via the combination of Eq. (3.2.20) and (3.2.21) for the SAL measurements (see Sect. 3.2.2.3 and 3.3.4). The (marginalized) solution PDFs for n_{CCN} , D_{act} and κ are presented as described in Sect. B.5.1.

In addition to the results for $SS = 0.2\%$, Tab. B.5.8 to B.5.11 list all n_{CCN} , D_{act} and κ solutions for the scanning CCNC column A measurements. However, it should be once more noted that these values are not fully trustworthy and most probably systematically biased owing to uncorrectable SS deviations (cf. Sect. A.3.3). For this reason, they are not considered for the actual study.

flight	time interval [s UTC]	altitude [m AMSL]	$n_{mode,0}$ [cm ⁻³ STP]	CMD_0 [μ m]	GSD_0	$n_{mode,1}$ [cm ⁻³ STP]	CMD_1 [μ m]	GSD_1	$n_{mode,2}$ [cm ⁻³ STP]	CMD_2 [μ m]	GSD_2
<i>MBL</i>											
130620a	54348.0 - 55003.0	350	191.1 (± 26.3)	0.074 (± 0.011)	1.98 (± 0.16)	100.3 (± 22.7)	0.182 (± 0.005)	1.40 (± 0.05)	9.2 (± 1.4)	0.760 (± 0.090)	1.55 (± 0.08)
			193.6 ^{+24.3} _{-26.6}	0.075 ^{+0.009} _{-0.012}	1.98 ^{+0.19} _{-0.17}	95.4 ^{+29.5} _{-18.3}	0.182 ^{+0.004} _{-0.006}	1.33 ^{+0.06} _{-0.05}	9.0 ^{+1.7} _{-1.3}	0.755 ^{+0.109} _{-0.095}	1.54 ^{+0.11} _{-0.07}
130622a	75429.0 - 75508.0	323	64.9 (± 17.7)	0.035 (± 0.014)	1.55 (± 0.25)	172.3 (± 16.0)	0.137 (± 0.004)	1.56 (± 0.04)	14.4 (± 1.4)	0.671 (± 0.080)	1.64 (± 0.07)
			64.3 ^{+15.7} _{-16.5}	0.034 ^{+0.014} _{-0.012}	1.50 ^{+0.31} _{-0.18}	175.1 ^{+10.9} _{-16.4}	0.137 ^{+0.004} _{-0.003}	1.56 ^{+0.04} _{-0.05}	14.3 ^{+1.4} _{-1.2}	0.671 ^{+0.078} _{-0.088}	1.63 ^{+0.09} _{-0.06}
130626a	97774.0 - 97905.0	650	179.8 (± 20.4)	0.080 (± 0.009)	2.20 (± 0.14)	100.8 (± 14.7)	0.168 (± 0.003)	1.30 (± 0.03)	7.0 (± 1.1)	0.821 (± 0.097)	1.46 (± 0.07)
			180.1 ^{+18.9} _{-17.0}	0.079 ^{+0.010} _{-0.009}	2.24 ^{+0.06} _{-0.14}	100.4 ^{+10.5} _{-11.3}	0.168 ^{+0.003} _{-0.004}	1.29 ^{+0.02} _{-0.02}	6.8 ^{+1.1} _{-0.7}	0.817 ^{+0.101} _{-0.091}	1.45 ^{+0.07} _{-0.06}
130710a	68520.0 - 69262.0	322	124.1 (± 46.1)	0.072 (± 0.019)	1.76 (± 0.39)	210.8 (± 46.1)	0.170 (± 0.009)	1.52 (± 0.06)	13.4 (± 2.5)	0.779 (± 0.094)	1.55 (± 0.09)
			114.7 ^{+61.0} _{-57.3}	0.066 ^{+0.025} _{-0.008}	1.78 ^{+0.41} _{-0.51}	220.3 ^{+36.8} _{-58.5}	0.168 ^{+0.008} _{-0.007}	1.53 ^{+0.04} _{-0.06}	13.8 ^{+1.6} _{-3.0}	0.780 ^{+0.088} _{-0.096}	1.54 ^{+0.11} _{-0.07}
130711a	53049.0 - 53870.0	510	151.5 (± 31.8)	0.093 (± 0.016)	1.80 (± 0.15)	106.8 (± 32.2)	0.196 (± 0.017)	1.45 (± 0.06)	11.9 (± 1.7)	0.763 (± 0.089)	1.59 (± 0.09)
			152.5 ^{+29.3} _{-29.6}	0.093 ^{+0.015} _{-0.014}	1.78 ^{+0.17} _{-0.09}	106.3 ^{+29.6} _{-30.4}	0.191 ^{+0.018} _{-0.008}	1.45 ^{+0.06} _{-0.06}	11.8 ^{+1.8} _{-1.5}	0.765 ^{+0.100} _{-0.096}	1.58 ^{+0.12} _{-0.07}
<i>SAL</i>											
130614a	42425.0 - 42495.0	2597	1070.0 (± 59.0)	0.055 (± 0.003)	1.82 (± 0.04)	30.7 (± 7.7)	0.286 (± 0.014)	1.31 (± 0.06)	42.3 (± 5.7)	0.459 (± 0.041)	2.20 (± 0.16)
			1068.1 ^{+57.4} _{-51.2}	0.055 ^{+0.003} _{-0.003}	1.83 ^{+0.02} _{-0.04}	29.7 ^{+7.7} _{-6.2}	0.289 ^{+0.010} _{-0.014}	1.30 ^{+0.06} _{-0.04}	42.7 ^{+5.3} _{-6.1}	0.450 ^{+0.032} _{-0.021}	2.21 ^{+0.16} _{-0.16}
130614a	42760.0 - 42820.0	2595	692.8 (± 43.0)	0.059 (± 0.003)	1.80 (± 0.07)	35.5 (± 11.1)	0.288 (± 0.021)	1.35 (± 0.08)	39.9 (± 6.8)	0.471 (± 0.050)	2.15 (± 0.18)
			691.5 ^{+40.2} _{-38.0}	0.059 ^{+0.003} _{-0.003}	1.81 ^{+0.05} _{-0.08}	33.2 ^{+11.7} _{-7.7}	0.291 ^{+0.015} _{-0.022}	1.34 ^{+0.08} _{-0.05}	40.1 ^{+6.7} _{-6.6}	0.464 ^{+0.040} _{-0.030}	2.13 ^{+0.20} _{-0.15}
130614a	43670.0 - 43870.0	2589	534.9 (± 31.1)	0.062 (± 0.004)	1.92 (± 0.06)	24.1 (± 6.5)	0.309 (± 0.011)	1.34 (± 0.05)	33.9 (± 6.4)	0.504 (± 0.062)	2.06 (± 0.17)
			532.7 ^{+30.5} _{-26.9}	0.061 ^{+0.004} _{-0.004}	1.93 ^{+0.03} _{-0.08}	23.4 ^{+6.6} _{-5.5}	0.309 ^{+0.011} _{-0.011}	1.33 ^{+0.05} _{-0.05}	34.5 ^{+5.8} _{-7.0}	0.485 ^{+0.060} _{-0.025}	2.07 ^{+0.16} _{-0.16}
130614a	44243.4 - 44400.0	1276	499.6 (± 107.5)	0.048 (± 0.005)	1.74 (± 0.12)	273.7 (± 102.3)	0.154 (± 0.047)	1.99 (± 0.25)	46.4 (± 23.4)	0.502 (± 0.162)	2.17 (± 0.28)
			493.8 ^{+192.2} _{-107.1}	0.048 ^{+0.007} _{-0.004}	1.76 ^{+0.10} _{-0.13}	281.0 ^{+98.8} _{-129.8}	0.143 ^{+0.038} _{-0.035}	2.03 ^{+0.23} _{-0.34}	43.9 ^{+26.1} _{-21.4}	0.469 ^{+0.186} _{-0.109}	2.15 ^{+0.29} _{-0.23}
130614a	44640.0 - 44844.4	1277	669.5 (± 59.1)	0.047 (± 0.004)	1.78 (± 0.07)	173.5 (± 47.5)	0.174 (± 0.026)	1.63 (± 0.11)	69.1 (± 20.8)	0.364 (± 0.103)	2.27 (± 0.26)
			676.0 ^{+45.1} _{-51.7}	0.047 ^{+0.004} _{-0.003}	1.79 ^{+0.06} _{-0.07}	167.0 ^{+51.4} _{-38.4}	0.177 ^{+0.022} _{-0.030}	1.61 ^{+0.12} _{-0.08}	69.0 ^{+20.1} _{-20.7}	0.342 ^{+0.117} _{-0.060}	2.29 ^{+0.24} _{-0.31}
130614b	54116.5 - 55138.5	3905	435.5 (± 26.9)	0.068 (± 0.004)	1.74 (± 0.05)	24.1 (± 5.6)	0.313 (± 0.010)	1.31 (± 0.05)	39.9 (± 5.4)	0.482 (± 0.040)	2.19 (± 0.18)
			432.3 ^{+28.4} _{-22.4}	0.068 ^{+0.003} _{-0.004}	1.75 ^{+0.04} _{-0.06}	23.9 ^{+5.5} _{-5.3}	0.314 ^{+0.009} _{-0.010}	1.31 ^{+0.05} _{-0.05}	40.4 ^{+3.8} _{-4.7}	0.477 ^{+0.015} _{-0.016}	2.18 ^{+0.17} _{-0.15}

Table B.5.1: Complete list of particle NSD retrieval results. For each retrieval time interval the NSD lognormal mode parameter solutions are represented by the (marginalized) PDF means and standard deviations (top rows), and the medians with their distances to the 16 and 84th percentiles (bottom rows). The sampling interval height information is provided in terms of a mean altitude.

flight	time interval [s UTC]	altitude [m AMSL]	$n_{mode,0}$ [cm ⁻³ STP]	CMD_0 [μ m]	GSD_0	$n_{mode,1}$ [cm ⁻³ STP]	CMD_1 [μ m]	GSD_1	$n_{mode,2}$ [cm ⁻³ STP]	CMD_2 [μ m]	GSD_2
<i>SAL</i>											
130614b	55307.5 - 55500.0	2599	528.4 (± 36.9) 528.2 ^{+34.9} _{-34.2}	0.071 (± 0.004) 0.071 ^{+0.004} _{-0.005}	1.96 (± 0.08) 1.99 ^{+0.05} _{-0.11}	30.0 (± 13.3) 27.4 ^{+12.4} _{-7.6}	0.311 (± 0.021) 0.314 ^{+0.015} _{-0.017}	1.34 (± 0.08) 1.32 ^{+0.09} _{-0.05}	41.0 (± 8.6) 40.4 ^{+7.9} _{-7.1}	0.488 (± 0.047) 0.484 ^{+0.034} _{-0.027}	2.04 (± 0.15) 2.03 ^{+0.17} _{-0.14}
130614b	55640.0 - 55790.0	2599	425.6 (± 29.8) 425.1 ^{+29.1} _{-27.8}	0.071 (± 0.004) 0.071 ^{+0.004} _{-0.005}	1.89 (± 0.09) 1.90 ^{+0.08} _{-0.10}	34.5 (± 10.1) 32.6 ^{+11.4} _{-6.9}	0.313 (± 0.014) 0.314 ^{+0.012} _{-0.014}	1.34 (± 0.06) 1.33 ^{+0.06} _{-0.04}	36.1 (± 6.9) 36.5 ^{+5.9} _{-7.1}	0.501 (± 0.059) 0.488 ^{+0.040} _{-0.023}	2.03 (± 0.15) 2.02 ^{+0.16} _{-0.13}
130614b	55900.0 - 56242.5	2599	479.7 (± 32.8) 479.3 ^{+31.1} _{-31.2}	0.070 (± 0.005) 0.070 ^{+0.004} _{-0.005}	1.97 (± 0.09) 2.00 ^{+0.05} _{-0.12}	36.9 (± 12.2) 34.5 ^{+14.4} _{-8.7}	0.325 (± 0.016) 0.326 ^{+0.013} _{-0.015}	1.33 (± 0.06) 1.31 ^{+0.08} _{-0.05}	51.1 (± 8.1) 50.6 ^{+8.6} _{-7.6}	0.500 (± 0.033) 0.497 ^{+0.025} _{-0.023}	2.00 (± 0.14) 1.98 ^{+0.16} _{-0.13}
130614b	56452.5 - 56983.5	960	358.7 (± 25.6) 356.3 ^{+27.5} _{-21.4}	0.079 (± 0.005) 0.080 ^{+0.004} _{-0.005}	1.76 (± 0.08) 1.76 ^{+0.07} _{-0.08}	30.5 (± 6.5) 30.2 ^{+7.1} _{-6.2}	0.318 (± 0.010) 0.318 ^{+0.009} _{-0.009}	1.31 (± 0.04) 1.31 ^{+0.04} _{-0.05}	46.3 (± 7.2) 46.8 ^{+7.5} _{-7.5}	0.490 (± 0.036) 0.482 ^{+0.023} _{-0.014}	2.06 (± 0.15) 2.05 ^{+0.16} _{-0.13}
130617a	40704.5 - 41140.0	4241	429.9 (± 31.3) 431.4 ^{+28.0} _{-31.6}	0.070 (± 0.004) 0.070 ^{+0.003} _{-0.005}	1.91 (± 0.10) 1.92 ^{+0.10} _{-0.11}	41.2 (± 12.5) 38.8 ^{+12.3} _{-8.6}	0.312 (± 0.017) 0.314 ^{+0.012} _{-0.019}	1.37 (± 0.07) 1.35 ^{+0.08} _{-0.05}	31.4 (± 8.5) 32.2 ^{+7.6} _{-9.7}	0.537 (± 0.103) 0.500 ^{+0.105} _{-0.031}	1.93 (± 0.18) 1.93 ^{+0.15} _{-0.16}
130617a	41170.0 - 41661.5	4237	493.7 (± 38.0) 496.0 ^{+32.7} _{-37.6}	0.071 (± 0.004) 0.071 ^{+0.003} _{-0.004}	1.88 (± 0.11) 1.89 ^{+0.10} _{-0.12}	43.8 (± 15.7) 40.3 ^{+16.2} _{-9.9}	0.290 (± 0.022) 0.295 ^{+0.014} _{-0.026}	1.40 (± 0.08) 1.39 ^{+0.08} _{-0.06}	32.0 (± 9.1) 32.8 ^{+8.6} _{-10.3}	0.515 (± 0.113) 0.474 ^{+0.138} _{-0.039}	1.99 (± 0.21) 2.01 ^{+0.16} _{-0.21}
130617a	42300.0 - 42435.0	2615	340.8 (± 35.8) 346.0 ^{+28.4} _{-40.9}	0.081 (± 0.005) 0.081 ^{+0.005} _{-0.005}	1.82 (± 0.14) 1.84 ^{+0.12} _{-0.16}	53.0 (± 22.5) 47.5 ^{+27.5} _{-16.0}	0.314 (± 0.037) 0.323 ^{+0.021} _{-0.043}	1.44 (± 0.11) 1.42 ^{+0.14} _{-0.09}	35.4 (± 13.2) 35.3 ^{+12.1} _{-13.9}	0.617 (± 0.150) 0.567 ^{+0.217} _{-0.073}	1.88 (± 0.20) 1.89 ^{+0.18} _{-0.19}
130617a	42500.0 - 43180.0	2614	357.7 (± 28.2) 358.9 ^{+24.9} _{-30.4}	0.084 (± 0.006) 0.083 ^{+0.005} _{-0.005}	1.95 (± 0.12) 1.95 ^{+0.12} _{-0.12}	37.4 (± 12.5) 35.9 ^{+11.3} _{-9.5}	0.345 (± 0.017) 0.346 ^{+0.015} _{-0.020}	1.33 (± 0.06) 1.32 ^{+0.07} _{-0.05}	42.2 (± 10.0) 41.9 ^{+9.7} _{-9.3}	0.563 (± 0.089) 0.534 ^{+0.081} _{-0.034}	1.89 (± 0.17) 1.90 ^{+0.13} _{-0.15}
130620a	53270.0 - 53805.0	2912	272.8 (± 45.4) 272.1 ^{+47.2} _{-46.6}	0.057 (± 0.004) 0.057 ^{+0.004} _{-0.004}	1.68 (± 0.09) 1.67 ^{+0.09} _{-0.07}	107.8 (± 40.6) 111.2 ^{+38.3} _{-47.6}	0.145 (± 0.054) 0.128 ^{+0.074} _{-0.027}	2.01 (± 0.28) 2.03 ^{+0.25} _{-0.30}	25.2 (± 9.3) 25.0 ^{+9.6} _{-9.1}	0.461 (± 0.152) 0.431 ^{+0.143} _{-0.103}	2.30 (± 0.29) 2.28 ^{+0.33} _{-0.25}
130621a	72230.0 - 72830.0	3850	283.0 (± 40.2) 287.8 ^{+35.2} _{-30.2}	0.050 (± 0.004) 0.050 ^{+0.004} _{-0.004}	1.68 (± 0.17) 1.70 ^{+0.16} _{-0.24}	79.2 (± 36.4) 75.4 ^{+42.6} _{-31.9}	0.118 (± 0.030) 0.110 ^{+0.038} _{-0.019}	1.93 (± 0.33) 1.94 ^{+0.32} _{-0.36}	18.0 (± 7.6) 17.3 ^{+8.4} _{-7.1}	0.357 (± 0.099) 0.346 ^{+0.089} _{-0.073}	2.37 (± 0.25) 2.36 ^{+0.29} _{-0.24}
130621a	73859.4 - 76671.4	2558	307.6 (± 29.4) 315.0 ^{+19.5} _{-34.1}	0.064 (± 0.004) 0.064 ^{+0.004} _{-0.004}	1.78 (± 0.13) 1.77 ^{+0.14} _{-0.11}	35.8 (± 17.8) 32.2 ^{+15.9} _{-12.3}	0.237 (± 0.046) 0.242 ^{+0.045} _{-0.056}	1.56 (± 0.18) 1.54 ^{+0.15} _{-0.14}	31.2 (± 9.8) 31.2 ^{+9.9} _{-9.7}	0.404 (± 0.107) 0.391 ^{+0.076} _{-0.075}	2.32 (± 0.23) 2.33 ^{+0.20} _{-0.24}
130622a	70215.0 - 70675.0	3374	245.1 (± 48.2) 246.8 ^{+48.0} _{-51.6}	0.050 (± 0.004) 0.050 ^{+0.004} _{-0.004}	1.55 (± 0.13) 1.53 ^{+0.17} _{-0.12}	95.9 (± 38.1) 94.8 ^{+38.5} _{-36.9}	0.103 (± 0.029) 0.095 ^{+0.032} _{-0.016}	1.77 (± 0.23) 1.75 ^{+0.26} _{-0.20}	36.6 (± 13.0) 35.8 ^{+14.9} _{-13.2}	0.229 (± 0.087) 0.207 ^{+0.105} _{-0.053}	2.59 (± 0.31) 2.67 ^{+0.23} _{-0.45}

Table B.5.2: Continuation of Tab. B.5.1.

flight	time interval [s UTC]	altitude [m AMSL]	$n_{mode,0}$ [cm ⁻³ STP]	CMD_0 [μm]	GSD_0	SAL					
						$n_{mode,1}$ [cm ⁻³ STP]	CMD_1 [μm]	GSD_1	$n_{mode,2}$ [cm ⁻³ STP]	CMD_2 [μm]	GSD_2
130622a	74325.0 - 74565.0	2241	398.2 (±32.9)	0.064 (±0.004)	1.88 (±0.10)	19.3 (±15.5)	0.240 (±0.035)	1.38 (±0.16)	22.3 (±4.6)	0.409 (±0.069)	2.23 (±0.20)
			400.5 ^{+27.5} _{-27.6}	0.064 ^{+0.003} _{-0.004}	1.90 ^{+0.08} _{-0.12}	13.6 ^{+16.4} _{-4.6}	0.250 ^{+0.021} _{-0.017}	1.33 ^{+0.19} _{-0.07}	22.1 ^{+3.6} _{-3.6}	0.406 ^{+0.053} _{-0.031}	2.22 ^{+0.21} _{-0.19}
130622a	74680.0 - 74945.0	2245	437.5 (±31.5)	0.064 (±0.004)	1.89 (±0.09)	19.7 (±13.1)	0.249 (±0.037)	1.41 (±0.15)	24.7 (±5.3)	0.433 (±0.089)	2.19 (±0.19)
			440.1 ^{+28.0} _{-29.9}	0.064 ^{+0.004} _{-0.004}	1.91 ^{+0.07} _{-0.11}	15.4 ^{+16.1} _{-6.5}	0.261 ^{+0.022} _{-0.019}	1.37 ^{+0.19} _{-0.11}	24.9 ^{+4.3} _{-4.7}	0.426 ^{+0.060} _{-0.060}	2.17 ^{+0.21} _{-0.15}
130626a	94515.4 - 95930.4	3572	16.8 (±31.4)	0.030 (±0.007)	1.63 (±0.37)	295.5 (±36.5)	0.058 (±0.004)	1.71 (±0.10)	85.0 (±18.9)	0.136 (±0.034)	2.78 (±0.19)
			3.5 ^{+27.7} _{-3.0}	0.031 ^{+0.006} _{-0.009}	1.53 ^{+0.37} _{-0.20}	299.2 ^{+28.0} _{-33.6}	0.058 ^{+0.004} _{-0.004}	1.69 ^{+0.09} _{-0.08}	90.3 ^{+12.5} _{-26.6}	0.122 ^{+0.041} _{-0.009}	2.83 ^{+0.12} _{-0.26}
130630a	51420.0 - 51595.0	3233	323.5 (±38.9)	0.062 (±0.004)	1.78 (±0.16)	44.1 (±29.1)	0.192 (±0.037)	1.47 (±0.14)	20.9 (±5.5)	0.391 (±0.099)	2.29 (±0.28)
			329.2 ^{+39.3} _{-42.1}	0.062 ^{+0.004} _{-0.005}	1.78 ^{+0.18} _{-0.17}	37.8 ^{+34.7} _{-22.9}	0.189 ^{+0.042} _{-0.037}	1.47 ^{+0.12} _{-0.15}	20.6 ^{+5.7} _{-5.2}	0.379 ^{+0.110} _{-0.086}	2.29 ^{+0.29} _{-0.29}
130630a	52550.0 - 52800.5	3232	289.5 (±57.4)	0.060 (±0.005)	1.74 (±0.18)	124.8 (±48.3)	0.141 (±0.036)	2.15 (±0.33)	22.3 (±12.4)	0.493 (±0.140)	2.20 (±0.32)
			296.6 ^{+47.9} _{-63.3}	0.060 ^{+0.005} _{-0.005}	1.76 ^{+0.16} _{-0.22}	121.1 ^{+51.3} _{-42.1}	0.132 ^{+0.040} _{-0.022}	2.13 ^{+0.39} _{-0.32}	19.8 ^{+15.3} _{-9.3}	0.468 ^{+0.144} _{-0.103}	2.20 ^{+0.31} _{-0.29}
130701a	56514.3 - 57040.0	3515	330.5 (±38.2)	0.061 (±0.004)	1.76 (±0.11)	52.6 (±27.8)	0.204 (±0.064)	1.73 (±0.30)	32.1 (±11.9)	0.386 (±0.119)	2.28 (±0.28)
			335.3 ^{+33.6} _{-45.5}	0.061 ^{+0.004} _{-0.005}	1.75 ^{+0.14} _{-0.11}	49.4 ^{+32.0} _{-25.6}	0.195 ^{+0.086} _{-0.060}	1.69 ^{+0.32} _{-0.25}	32.2 ^{+11.3} _{-12.0}	0.366 ^{+0.108} _{-0.085}	2.27 ^{+0.29} _{-0.26}
130701a	57500.0 - 57970.0	3522	280.1 (±59.3)	0.058 (±0.005)	1.70 (±0.12)	99.5 (±53.1)	0.151 (±0.060)	1.91 (±0.31)	38.8 (±14.8)	0.353 (±0.107)	2.41 (±0.28)
			283.3 ^{+58.6} _{-63.5}	0.058 ^{+0.005} _{-0.005}	1.68 ^{+0.14} _{-0.09}	96.9 ^{+53.6} _{-51.6}	0.131 ^{+0.090} _{-0.033}	1.93 ^{+0.25} _{-0.30}	37.6 ^{+14.0} _{-12.9}	0.332 ^{+0.121} _{-0.080}	2.40 ^{+0.31} _{-0.27}
130701a	58330.0 - 58650.0	3527	280.1 (±30.1)	0.053 (±0.004)	1.80 (±0.10)	81.7 (±23.0)	0.139 (±0.027)	2.22 (±0.29)	8.4 (±4.9)	0.679 (±0.166)	1.98 (±0.28)
			281.3 ^{+30.1} _{-29.2}	0.053 ^{+0.004} _{-0.004}	1.81 ^{+0.09} _{-0.12}	80.3 ^{+23.6} _{-20.4}	0.134 ^{+0.031} _{-0.021}	2.20 ^{+0.33} _{-0.27}	7.5 ^{+5.3} _{-3.6}	0.658 ^{+0.224} _{-0.145}	1.96 ^{+0.25} _{-0.19}
130701b	71620.0 - 72027.5	2118	316.2 (±16.4)	0.074 (±0.005)	2.13 (±0.06)	16.3 (±9.2)	0.364 (±0.077)	2.63 (±0.33)	3.9 (±2.6)	0.694 (±0.122)	1.55 (±0.29)
			315.5 ^{+16.2} _{-12.3}	0.074 ^{+0.005} _{-0.005}	2.14 ^{+0.04} _{-0.06}	14.4 ^{+10.2} _{-6.9}	0.372 ^{+0.069} _{-0.092}	2.71 ^{+0.20} _{-0.30}	3.5 ^{+3.2} _{-2.2}	0.679 ^{+0.148} _{-0.088}	1.49 ^{+0.30} _{-0.18}
130701b	79070.0 - 79880.0	3547	358.4 (±24.6)	0.061 (±0.004)	1.91 (±0.09)	18.9 (±11.3)	0.292 (±0.038)	1.43 (±0.19)	25.0 (±6.2)	0.460 (±0.066)	2.10 (±0.18)
			359.4 ^{+29.5} _{-22.2}	0.061 ^{+0.003} _{-0.004}	1.94 ^{+0.05} _{-0.11}	16.5 ^{+8.5} _{-5.7}	0.303 ^{+0.016} _{-0.036}	1.39 ^{+0.14} _{-0.10}	24.8 ^{+4.6} _{-4.9}	0.464 ^{+0.033} _{-0.042}	2.08 ^{+0.19} _{-0.15}
130710a	59650.0 - 60039.4	4369	305.3 (±24.8)	0.057 (±0.004)	1.91 (±0.07)	70.2 (±14.6)	0.218 (±0.034)	2.63 (±0.23)	7.3 (±3.7)	0.376 (±0.059)	1.30 (±0.17)
			306.4 ^{+23.7} _{-21.6}	0.057 ^{+0.004} _{-0.004}	1.92 ^{+0.05} _{-0.08}	67.5 ^{+16.9} _{-11.4}	0.222 ^{+0.027} _{-0.039}	2.63 ^{+0.25} _{-0.23}	6.8 ^{+3.1} _{-3.0}	0.368 ^{+0.027} _{-0.018}	1.26 ^{+0.05} _{-0.01}
130710a	60350.0 - 60625.0	2596	295.7 (±38.5)	0.079 (±0.006)	1.82 (±0.14)	43.1 (±25.8)	0.266 (±0.063)	1.55 (±0.24)	39.0 (±13.2)	0.478 (±0.117)	2.13 (±0.23)
			298.9 ^{+34.4} _{-44.6}	0.079 ^{+0.006} _{-0.006}	1.81 ^{+0.16} _{-0.14}	37.5 ^{+32.6} _{-19.6}	0.277 ^{+0.057} _{-0.084}	1.51 ^{+0.26} _{-0.20}	38.2 ^{+12.2} _{-12.3}	0.475 ^{+0.083} _{-0.109}	2.12 ^{+0.25} _{-0.20}

Table B.5.3: Continuation of Tab. B.5.1 and B.5.2.

flight	time interval [s UTC]	altitude [m AMSL]	$n_{mode,0}$ [cm ⁻³ STP]	CMD_0 [μ m]	GSD_0	$n_{mode,1}$ [cm ⁻³ STP]	CMD_1 [μ m]	GSD_1	$n_{mode,2}$ [cm ⁻³ STP]	CMD_2 [μ m]	GSD_2
<i>SAL</i>											
130710a	64400.0 - 65458.4	4204	313.8 (± 16.7) 313.7 ^{+16.3} _{-13.5}	0.054 (± 0.004) 0.054 ^{+0.005} _{-0.003}	1.98 (± 0.05) 1.98 ^{+0.05} _{-0.05}	37.0 (± 14.8) 34.6 ^{+15.4} _{-11.2}	0.298 (± 0.039) 0.301 ^{+0.035} _{-0.039}	1.59 (± 0.23) 1.55 ^{+0.20} _{-0.13}	21.5 (± 8.4) 23.0 ^{+5.9} _{-11.8}	0.561 (± 0.164) 0.503 ^{+0.203} _{-0.061}	2.08 (± 0.23) 2.10 ^{+0.19} _{-0.28}
130710a	65553.4 - 65850.0	3560	320.5 (± 18.3) 318.4 ^{+19.0} _{-14.9}	0.061 (± 0.004) 0.061 ^{+0.003} _{-0.004}	2.03 (± 0.04) 2.04 ^{+0.03} _{-0.04}	24.0 (± 5.3) 23.5 ^{+4.9} _{-4.1}	0.360 (± 0.013) 0.360 ^{+0.013} _{-0.012}	1.32 (± 0.06) 1.31 ^{+0.06} _{-0.05}	27.2 (± 4.2) 27.3 ^{+3.8} _{-4.1}	0.563 (± 0.056) 0.552 ^{+0.028} _{-0.021}	1.91 (± 0.13) 1.91 ^{+0.12} _{-0.14}
130710a	65880.0 - 66111.4	3559	322.1 (± 19.5) 325.2 ^{+15.6} _{-22.9}	0.061 (± 0.005) 0.062 ^{+0.004} _{-0.005}	2.03 (± 0.06) 2.04 ^{+0.04} _{-0.07}	28.0 (± 16.0) 22.6 ^{+19.5} _{-7.8}	0.336 (± 0.044) 0.346 ^{+0.029} _{-0.050}	1.52 (± 0.26) 1.43 ^{+0.29} _{-0.14}	18.1 (± 5.6) 18.6 ^{+5.0} _{-6.6}	0.590 (± 0.116) 0.562 ^{+0.104} _{-0.051}	2.01 (± 0.21) 1.99 ^{+0.20} _{-0.16}
130710a	66350.0 - 66761.4	2591	304.8 (± 33.8) 310.8 ^{+24.7} _{-40.0}	0.088 (± 0.006) 0.088 ^{+0.005} _{-0.007}	1.90 (± 0.13) 1.91 ^{+0.12} _{-0.15}	36.9 (± 18.8) 32.2 ^{+19.9} _{-11.5}	0.323 (± 0.032) 0.329 ^{+0.019} _{-0.026}	1.38 (± 0.12) 1.36 ^{+0.12} _{-0.07}	52.5 (± 13.7) 52.0 ^{+13.1} _{-11.8}	0.529 (± 0.101) 0.511 ^{+0.055} _{-0.037}	2.06 (± 0.17) 2.05 ^{+0.17} _{-0.14}
130711a	49192.5 - 49657.5	4196	200.4 (± 56.1) 204.4 ^{+58.7} _{-71.9}	0.060 (± 0.004) 0.060 ^{+0.004} _{-0.004}	1.55 (± 0.16) 1.58 ^{+0.14} _{-0.25}	122.8 (± 45.5) 120.4 ^{+49.5} _{-42.3}	0.119 (± 0.033) 0.109 ^{+0.036} _{-0.015}	1.89 (± 0.23) 1.87 ^{+0.20} _{-0.18}	42.6 (± 18.1) 39.1 ^{+21.9} _{-13.2}	0.287 (± 0.089) 0.270 ^{+0.087} _{-0.064}	2.57 (± 0.27) 2.60 ^{+0.26} _{-0.33}
130711a	49864.5 - 50491.5	2590	285.6 (± 35.1) 292.0 ^{+23.5} _{-34.4}	0.088 (± 0.005) 0.088 ^{+0.005} _{-0.005}	1.70 (± 0.11) 1.71 ^{+0.09} _{-0.13}	42.1 (± 21.3) 38.6 ^{+22.2} _{-16.1}	0.266 (± 0.033) 0.274 ^{+0.023} _{-0.041}	1.43 (± 0.11) 1.41 ^{+0.13} _{-0.08}	44.7 (± 9.8) 45.0 ^{+9.0} _{-8.4}	0.440 (± 0.087) 0.431 ^{+0.036} _{-0.053}	2.23 (± 0.20) 2.21 ^{+0.26} _{-0.16}
130711b	70895.5 - 71090.0	4176	321.6 (± 21.8) 322.2 ^{+19.2} _{-23.5}	0.067 (± 0.004) 0.067 ^{+0.003} _{-0.004}	1.86 (± 0.09) 1.87 ^{+0.07} _{-0.11}	22.5 (± 7.9) 20.8 ^{+9.0} _{-5.3}	0.310 (± 0.021) 0.314 ^{+0.016} _{-0.022}	1.39 (± 0.08) 1.37 ^{+0.11} _{-0.06}	24.5 (± 5.4) 24.5 ^{+5.6} _{-4.9}	0.512 (± 0.076) 0.497 ^{+0.047} _{-0.031}	2.05 (± 0.16) 2.04 ^{+0.16} _{-0.13}
130711b	71130.0 - 71375.0	4178	309.1 (± 22.2) 308.6 ^{+21.8} _{-19.9}	0.071 (± 0.004) 0.071 ^{+0.004} _{-0.005}	1.90 (± 0.09) 1.91 ^{+0.09} _{-0.09}	18.3 (± 7.8) 16.7 ^{+7.0} _{-4.6}	0.321 (± 0.024) 0.323 ^{+0.018} _{-0.016}	1.36 (± 0.11) 1.34 ^{+0.08} _{-0.06}	27.3 (± 5.2) 27.0 ^{+5.5} _{-5.1}	0.508 (± 0.046) 0.503 ^{+0.041} _{-0.028}	2.06 (± 0.16) 2.05 ^{+0.17} _{-0.15}
130711b	71430.0 - 71585.5	4179	278.2 (± 29.5) 283.4 ^{+18.8} _{-29.6}	0.085 (± 0.004) 0.085 ^{+0.004} _{-0.005}	1.73 (± 0.11) 1.74 ^{+0.08} _{-0.13}	26.9 (± 16.8) 20.7 ^{+19.0} _{-5.7}	0.305 (± 0.038) 0.319 ^{+0.016} _{-0.054}	1.37 (± 0.13) 1.32 ^{+0.19} _{-0.05}	33.6 (± 6.7) 33.4 ^{+6.8} _{-5.7}	0.504 (± 0.076) 0.499 ^{+0.037} _{-0.044}	2.09 (± 0.18) 2.08 ^{+0.20} _{-0.14}
130711b	71810.0 - 72050.0	2732	315.6 (± 24.9) 315.0 ^{+23.9} _{-22.2}	0.082 (± 0.005) 0.082 ^{+0.004} _{-0.005}	1.83 (± 0.10) 1.83 ^{+0.09} _{-0.10}	25.1 (± 9.8) 22.6 ^{+12.4} _{-6.1}	0.299 (± 0.016) 0.303 ^{+0.009} _{-0.019}	1.32 (± 0.08) 1.29 ^{+0.09} _{-0.04}	40.3 (± 7.0) 40.9 ^{+7.8} _{-7.8}	0.472 (± 0.044) 0.465 ^{+0.032} _{-0.025}	2.14 (± 0.16) 2.14 ^{+0.17} _{-0.15}
130711b	72065.0 - 72306.5	2730	316.0 (± 28.7) 316.1 ^{+29.7} _{-27.5}	0.083 (± 0.005) 0.084 ^{+0.004} _{-0.006}	1.84 (± 0.13) 1.83 ^{+0.14} _{-0.13}	27.6 (± 13.8) 23.8 ^{+17.1} _{-8.7}	0.286 (± 0.023) 0.294 ^{+0.009} _{-0.031}	1.34 (± 0.10) 1.32 ^{+0.13} _{-0.06}	40.8 (± 6.7) 41.2 ^{+5.9} _{-6.2}	0.447 (± 0.045) 0.449 ^{+0.020} _{-0.037}	2.20 (± 0.17) 2.18 ^{+0.20} _{-0.16}
130711b	72375.5 - 72620.0	2242	314.3 (± 29.0) 315.7 ^{+25.4} _{-30.3}	0.089 (± 0.005) 0.089 ^{+0.004} _{-0.005}	1.76 (± 0.11) 1.77 ^{+0.10} _{-0.12}	39.1 (± 12.7) 36.8 ^{+14.4} _{-9.5}	0.306 (± 0.018) 0.309 ^{+0.012} _{-0.020}	1.35 (± 0.06) 1.34 ^{+0.07} _{-0.05}	48.5 (± 8.8) 48.5 ^{+8.1} _{-8.5}	0.482 (± 0.048) 0.475 ^{+0.033} _{-0.025}	2.10 (± 0.16) 2.09 ^{+0.18} _{-0.14}
130711b	72690.0 - 72885.5	2241	329.6 (± 31.8) 331.7 ^{+27.7} _{-32.6}	0.089 (± 0.005) 0.089 ^{+0.004} _{-0.005}	1.83 (± 0.14) 1.83 ^{+0.12} _{-0.12}	31.2 (± 14.3) 26.8 ^{+19.2} _{-8.3}	0.295 (± 0.020) 0.301 ^{+0.009} _{-0.024}	1.32 (± 0.09) 1.29 ^{+0.11} _{-0.04}	45.2 (± 6.5) 45.0 ^{+7.0} _{-6.7}	0.458 (± 0.031) 0.460 ^{+0.017} _{-0.026}	2.23 (± 0.17) 2.21 ^{+0.20} _{-0.14}

Table B.5.4: Continuation of Tab. B.5.1 to B.5.3.

flight	time interval [s UTC]	altitude [m AMSL]	n_{CCN} [cm^{-3} STP]	D_{act} [μm]	κ
<i>MBL</i>					
130620a	54348.0 - 55003.0	350	160.7 (± 9.0)	0.097 (± 0.009)	0.308 (± 0.093)
			160.7 $^{+8.8}_{-8.7}$	0.097 $^{+0.010}_{-0.009}$	0.297 $^{+0.097}_{-0.079}$
130622a	75429.0 - 75508.0	323	143.8 (± 7.7)	0.094 (± 0.008)	0.331 (± 0.095)
			143.9 $^{+7.6}_{-7.6}$	0.094 $^{+0.009}_{-0.008}$	0.319 $^{+0.097}_{-0.077}$
130626a	97774.0 - 97905.0	650	169.0 (± 9.4)	0.096 (± 0.010)	0.326 (± 0.113)
			169.2 $^{+9.1}_{-9.5}$	0.096 $^{+0.011}_{-0.010}$	0.305 $^{+0.121}_{-0.085}$
130710a	68520.0 - 69262.0	322	221.5 (± 11.9)	0.101 (± 0.010)	0.258 (± 0.083)
			221.4 $^{+12.2}_{-11.3}$	0.100 $^{+0.010}_{-0.010}$	0.246 $^{+0.088}_{-0.067}$
130711a	53049.0 - 53870.0	510	168.5 (± 9.0)	0.102 (± 0.010)	0.261 (± 0.076)
			168.6 $^{+9.0}_{-8.8}$	0.102 $^{+0.010}_{-0.009}$	0.252 $^{+0.080}_{-0.065}$
<i>SAL</i>					
130617a	40920.0 - 41140.0	4240	249.9 (± 17.2)	0.081 (± 0.006)	0.576 (± 0.145)
			249.7 $^{+18.1}_{-17.4}$	0.081 $^{+0.006}_{-0.006}$	0.562 $^{+0.142}_{-0.124}$
130617a	41170.0 - 41390.0	4239	289.9 (± 18.9)	0.079 (± 0.006)	0.625 (± 0.150)
			289.9 $^{+18.8}_{-19.2}$	0.079 $^{+0.006}_{-0.006}$	0.609 $^{+0.150}_{-0.125}$
130617a	42500.0 - 43180.0	2614	203.3 (± 17.2)	0.109 (± 0.010)	0.235 (± 0.069)
			203.3 $^{+17.7}_{-18.5}$	0.108 $^{+0.011}_{-0.010}$	0.226 $^{+0.078}_{-0.060}$
130621a	72230.0 - 72830.0	3850	129.0 (± 8.2)	0.076 (± 0.004)	0.599 (± 0.105)
			128.8 $^{+8.7}_{-8.1}$	0.076 $^{+0.004}_{-0.004}$	0.587 $^{+0.122}_{-0.090}$
130621a	73859.4 - 76671.4	2558	160.9 (± 11.2)	0.084 (± 0.006)	0.457 (± 0.097)
			160.7 $^{+11.7}_{-11.3}$	0.084 $^{+0.006}_{-0.006}$	0.446 $^{+0.109}_{-0.082}$
130622a	70215.0 - 70675.0	3374	131.2 (± 8.6)	0.077 (± 0.004)	0.625 (± 0.109)
			131.0 $^{+9.2}_{-8.5}$	0.077 $^{+0.004}_{-0.004}$	0.612 $^{+0.121}_{-0.095}$
130622a	74325.0 - 74565.0	2241	199.8 (± 12.2)	0.075 (± 0.005)	0.651 (± 0.127)
			199.4 $^{+13.0}_{-11.9}$	0.075 $^{+0.005}_{-0.005}$	0.634 $^{+0.149}_{-0.107}$

Table B.5.5: Complete list of results for the (corrected) CCN concentrations, activation diameters and effective particle hygroscopicities for the CCNC column B measurements at the constant main supersaturation of $SS = 0.2\%$. For each time interval the solutions are represented by the (marginalized) PDF means and standard deviations (top rows), and the medians with their distances to the 16 and 84th percentiles (bottom rows). The sampling interval height information is provided in terms of a mean altitude.

flight	time interval [s UTC]	altitude [m AMSL]	n_{CCN} [cm ⁻³ STP]	D_{act} [μm]	κ
<i>SAL</i>					
130622a	74680.0 - 74945.0	2245	223.5 (±13.8)	0.074 (±0.005)	0.682 (±0.135)
			223.1 ^{+14.6} _{-13.7}	0.074 ^{+0.005} _{-0.005}	0.667 ^{+0.157} _{-0.115}
130626a	94515.4 - 95930.4	3572	151.9 (±9.5)	0.076 (±0.004)	0.643 (±0.108)
			151.6 ^{+9.9} _{-9.3}	0.076 ^{+0.004} _{-0.004}	0.634 ^{+0.115} _{-0.097}
130630a	51420.0 - 51595.0	3233	167.3 (±10.7)	0.079 (±0.005)	0.604 (±0.122)
			167.0 ^{+11.1} _{-10.4}	0.079 ^{+0.005} _{-0.005}	0.589 ^{+0.130} _{-0.101}
130630a	52555.0 - 52800.5	3232	199.0 (±13.6)	0.081 (±0.006)	0.565 (±0.127)
			198.5 ^{+14.3} _{-13.1}	0.080 ^{+0.006} _{-0.005}	0.547 ^{+0.138} _{-0.103}
130701a	56514.3 - 57040.0	3515	192.0 (±12.6)	0.076 (±0.005)	0.669 (±0.143)
			191.7 ^{+13.4} _{-12.9}	0.076 ^{+0.005} _{-0.005}	0.652 ^{+0.157} _{-0.121}
130701a	57500.0 - 57970.0	3522	196.7 (±13.2)	0.076 (±0.005)	0.672 (±0.145)
			196.3 ^{+13.7} _{-13.2}	0.076 ^{+0.005} _{-0.005}	0.650 ^{+0.166} _{-0.117}
130701a	58330.0 - 58650.0	3527	151.2 (±9.7)	0.074 (±0.005)	0.733 (±0.146)
			151.0 ^{+10.2} _{-10.0}	0.074 ^{+0.005} _{-0.005}	0.714 ^{+0.168} _{-0.124}
130701b	71620.0 - 71715.0	2119	160.9 (±10.8)	0.082 (±0.006)	0.606 (±0.141)
			161.0 ^{+11.0} _{-11.1}	0.081 ^{+0.006} _{-0.006}	0.585 ^{+0.160} _{-0.115}
130701b	71920.0 - 72027.5	2117	167.9 (±10.9)	0.078 (±0.006)	0.636 (±0.151)
			167.7 ^{+11.4} _{-10.9}	0.078 ^{+0.006} _{-0.006}	0.614 ^{+0.176} _{-0.121}
130701b	79070.0 - 79880.0	3547	185.6 (±11.9)	0.073 (±0.005)	0.698 (±0.147)
			185.5 ^{+12.5} _{-12.2}	0.072 ^{+0.005} _{-0.005}	0.680 ^{+0.171} _{-0.124}
130710a	59650.0 - 60039.4	4369	158.3 (±11.2)	0.080 (±0.006)	0.570 (±0.129)
			157.9 ^{+11.6} _{-10.7}	0.080 ^{+0.006} _{-0.006}	0.554 ^{+0.140} _{-0.110}
130710a	60350.0 - 60587.5	2596	203.7 (±14.9)	0.089 (±0.008)	0.426 (±0.116)
			203.1 ^{+15.7} _{-15.0}	0.089 ^{+0.008} _{-0.008}	0.407 ^{+0.133} _{-0.093}

Table B.5.6: Continuation of Tab. B.5.5.

flight	time interval [s UTC]	altitude [m AMSL]	n_{CCN} [cm ⁻³ STP]	D_{act} [μ m]	κ
<i>SAL</i>					
130710a	64760.0 - 65458.4	4204	156.3 (\pm 11.2) 156.2 ^{+11.8} _{-11.3}	0.075 (\pm 0.006) 0.075 ^{+0.006} _{-0.006}	0.635 (\pm 0.151) 0.613 ^{+0.179} _{-0.125}
130710a	65553.4 - 65850.0	3560	160.1 (\pm 12.3) 160.2 ^{+12.9} _{-12.9}	0.082 (\pm 0.007) 0.082 ^{+0.007} _{-0.006}	0.490 (\pm 0.126) 0.472 ^{+0.144} _{-0.107}
130710a	65975.5 - 66111.4	3558	149.9 (\pm 11.3) 150.0 ^{+11.6} _{-11.7}	0.084 (\pm 0.007) 0.084 ^{+0.007} _{-0.007}	0.440 (\pm 0.105) 0.426 ^{+0.126} _{-0.089}
130710a	66350.0 - 66761.4	2591	225.2 (\pm 17.7) 225.1 ^{+18.2} _{-18.3}	0.095 (\pm 0.010) 0.095 ^{+0.011} _{-0.009}	0.317 (\pm 0.102) 0.301 ^{+0.112} _{-0.081}
130711a	49192.5 - 49657.5	4196	171.0 (\pm 11.5) 170.8 ^{+12.0} _{-11.3}	0.081 (\pm 0.005) 0.081 ^{+0.005} _{-0.005}	0.539 (\pm 0.111) 0.526 ^{+0.120} _{-0.095}
130711a	49864.5 - 50491.5	2590	210.9 (\pm 15.3) 210.7 ^{+16.0} _{-15.8}	0.095 (\pm 0.008) 0.095 ^{+0.008} _{-0.008}	0.338 (\pm 0.087) 0.326 ^{+0.097} _{-0.071}
130711b	70895.5 - 71090.0	4176	181.0 (\pm 12.2) 180.8 ^{+12.8} _{-11.8}	0.076 (\pm 0.005) 0.076 ^{+0.006} _{-0.005}	0.663 (\pm 0.153) 0.648 ^{+0.161} _{-0.134}
130711b	71150.0 - 71375.0	4178	183.6 (\pm 12.4) 183.6 ^{+12.7} _{-12.3}	0.077 (\pm 0.006) 0.077 ^{+0.006} _{-0.006}	0.635 (\pm 0.159) 0.613 ^{+0.170} _{-0.131}
130711b	71430.0 - 71585.5	4179	188.9 (\pm 13.3) 188.9 ^{+13.3} _{-13.3}	0.090 (\pm 0.007) 0.090 ^{+0.007} _{-0.007}	0.407 (\pm 0.098) 0.396 ^{+0.104} _{-0.085}
130711b	71810.0 - 72050.0	2732	210.5 (\pm 15.1) 210.3 ^{+15.5} _{-15.8}	0.087 (\pm 0.007) 0.087 ^{+0.007} _{-0.007}	0.443 (\pm 0.117) 0.426 ^{+0.127} _{-0.094}
130711b	72065.0 - 72306.5	2730	211.5 (\pm 15.2) 210.9 ^{+16.0} _{-15.4}	0.089 (\pm 0.008) 0.089 ^{+0.008} _{-0.007}	0.414 (\pm 0.113) 0.395 ^{+0.123} _{-0.088}
130711b	72375.5 - 72620.0	2242	227.9 (\pm 17.3) 227.3 ^{+18.2} _{-17.3}	0.095 (\pm 0.009) 0.095 ^{+0.009} _{-0.009}	0.341 (\pm 0.095) 0.326 ^{+0.110} _{-0.078}

Table B.5.7: Continuation of Tab. B.5.5 and B.5.6.

flight	time interval [s UTC]	altitude [m AMSL]	SS [%]	n_{CCN} [cm ⁻³ STP]	D_{act} [μm]	κ
<i>MBL</i>						
130622a	75429.0 - 75508.0	323	0.16	139.7 (±7.6)	0.097 (±0.008)	0.468 (±0.128)
				139.8 ^{+7.4} _{-7.6}	0.097 ^{+0.009} _{-0.008}	0.452 ^{+0.132} _{-0.106}
130710a	68890.0 - 69097.5	319	0.28	235.0 (±12.4)	0.092 (±0.010)	0.175 (±0.063)
				234.9 ^{+12.7} _{-11.9}	0.092 ^{+0.011} _{-0.010}	0.164 ^{+0.068} _{-0.047}
130711a	53049.0 - 53270.0	511	0.12	152.1 (±8.6)	0.115 (±0.010)	0.560 (±0.153)
				152.2 ^{+8.3} _{-8.4}	0.114 ^{+0.011} _{-0.009}	0.546 ^{+0.161} _{-0.138}
130711a	53515.0 - 53870.0	509	0.30	178.8 (±9.4)	0.095 (±0.010)	0.151 (±0.048)
				178.9 ^{+9.3} _{-9.1}	0.094 ^{+0.010} _{-0.009}	0.145 ^{+0.051} _{-0.039}
<i>SAL</i>						
130617a	41030.0 - 41115.0	4240	0.16	223.9 (±16.5)	0.089 (±0.007)	0.691 (±0.170)
				223.6 ^{+17.2} _{-16.4}	0.089 ^{+0.007} _{-0.007}	0.674 ^{+0.169} _{-0.146}
130617a	41170.0 - 41390.0	4239	0.21	308.7 (±19.6)	0.074 (±0.006)	0.704 (±0.175)
				308.8 ^{+19.7} _{-20.1}	0.074 ^{+0.006} _{-0.005}	0.685 ^{+0.178} _{-0.145}
130617a	42500.0 - 42735.0	2614	0.21	214.9 (±17.6)	0.103 (±0.010)	0.256 (±0.075)
				215.2 ^{+17.8} _{-19.4}	0.102 ^{+0.010} _{-0.009}	0.246 ^{+0.084} _{-0.063}
130617a	42900.0 - 43035.0	2614	0.30	242.1 (±18.5)	0.090 (±0.009)	0.181 (±0.056)
				242.0 ^{+19.2} _{-19.4}	0.090 ^{+0.010} _{-0.009}	0.172 ^{+0.063} _{-0.045}
130621a	72230.0 - 72355.0	3849	0.21	132.5 (±8.5)	0.075 (±0.004)	0.606 (±0.108)
				132.2 ^{+9.1} _{-8.3}	0.075 ^{+0.004} _{-0.004}	0.593 ^{+0.126} _{-0.091}
130621a	72510.0 - 72657.5	3851	0.30	165.4 (±9.7)	0.064 (±0.004)	0.461 (±0.092)
				165.1 ^{+10.1} _{-9.6}	0.064 ^{+0.004} _{-0.004}	0.450 ^{+0.103} _{-0.081}
130621a	72695.0 - 72830.0	3851	0.26	148.7 (±9.1)	0.069 (±0.004)	0.498 (±0.093)
				148.5 ^{+9.7} _{-8.8}	0.069 ^{+0.004} _{-0.004}	0.486 ^{+0.108} _{-0.079}
130621a	73859.4 - 73977.5	2563	0.30	196.1 (±12.6)	0.071 (±0.005)	0.344 (±0.080)
				195.9 ^{+13.2} _{-12.8}	0.071 ^{+0.005} _{-0.005}	0.332 ^{+0.093} _{-0.065}
130621a	74120.0 - 74272.5	2564	0.23	179.7 (±12.0)	0.077 (±0.005)	0.470 (±0.103)
				179.3 ^{+12.7} _{-12.0}	0.077 ^{+0.005} _{-0.005}	0.456 ^{+0.118} _{-0.086}
130621a	74415.0 - 74687.5	2562	0.16	136.4 (±10.5)	0.096 (±0.006)	0.485 (±0.104)
				136.3 ^{+11.3} _{-10.9}	0.096 ^{+0.007} _{-0.007}	0.471 ^{+0.120} _{-0.087}

Table B.5.8: Complete list of results for the (corrected) CCN concentrations, activation diameters and effective particle hygroscopicities for the CCNC column A, i.e. the scanning SS measurements. For each time interval the solutions are represented by the (marginalized) PDF means and standard deviations (top rows), and the medians with their distances to the 16 and 84th percentiles (bottom rows). The sampling interval supersaturation and height information are provided in terms of respective mean values. Note that the results are assumed to be affected by systematic SS biases (cf. Sect. A.3.3).

flight	time interval [s UTC]	altitude [m AMSL]	SS [%]	n_{CCN} [cm ⁻³ STP]	D_{act} [μm]	κ
<i>SAL</i>						
130621a	74775.0 - 74992.5	2560	0.21	172.6 (±11.7) 172.3 ^{+12.6} _{-12.1}	0.079 (±0.005) 0.079 ^{+0.006} _{-0.006}	0.506 (±0.111) 0.491 ^{+0.125} _{-0.091}
130621a	75165.0 - 75297.5	2557	0.30	191.4 (±12.5) 191.0 ^{+13.1} _{-12.7}	0.072 (±0.005) 0.072 ^{+0.005} _{-0.005}	0.320 (±0.075) 0.309 ^{+0.084} _{-0.060}
130621a	75480.0 - 75592.5	2557	0.23	169.0 (±11.7) 168.8 ^{+12.3} _{-11.9}	0.081 (±0.006) 0.080 ^{+0.006} _{-0.005}	0.409 (±0.089) 0.398 ^{+0.100} _{-0.074}
130621a	75730.0 - 76012.5	2556	0.16	124.6 (±10.2) 124.4 ^{+11.1} _{-10.6}	0.103 (±0.007) 0.102 ^{+0.008} _{-0.007}	0.393 (±0.086) 0.385 ^{+0.097} _{-0.075}
130621a	76095.0 - 76312.5	2554	0.21	178.0 (±12.1) 177.7 ^{+12.9} _{-12.2}	0.077 (±0.005) 0.077 ^{+0.006} _{-0.005}	0.545 (±0.121) 0.529 ^{+0.138} _{-0.101}
130621a	76490.0 - 76617.5	2553	0.30	203.8 (±13.0) 203.7 ^{+13.4} _{-13.2}	0.068 (±0.005) 0.068 ^{+0.005} _{-0.005}	0.378 (±0.089) 0.363 ^{+0.106} _{-0.072}
130622a	70252.0 - 70347.5	3377	0.16	117.8 (±8.2) 117.4 ^{+9.0} _{-7.9}	0.082 (±0.004) 0.082 ^{+0.005} _{-0.005}	0.806 (±0.142) 0.789 ^{+0.163} _{-0.127}
130622a	70375.0 - 70642.5	3374	0.21	139.5 (±8.9) 139.1 ^{+9.7} _{-8.6}	0.074 (±0.004) 0.074 ^{+0.004} _{-0.004}	0.645 (±0.113) 0.631 ^{+0.130} _{-0.098}
130622a	74325.0 - 74565.0	2241	0.21	213.1 (±12.7) 212.7 ^{+13.4} _{-12.6}	0.071 (±0.004) 0.071 ^{+0.005} _{-0.005}	0.705 (±0.140) 0.687 ^{+0.165} _{-0.119}
130622a	74782.5 - 74907.5	2245	0.30	262.7 (±15.4) 262.4 ^{+16.0} _{-15.3}	0.064 (±0.004) 0.064 ^{+0.004} _{-0.005}	0.470 (±0.103) 0.457 ^{+0.117} _{-0.087}
130626a	94560.0 - 94690.0	3572	0.30	188.9 (±11.1) 188.8 ^{+11.3} _{-10.8}	0.065 (±0.004) 0.065 ^{+0.004} _{-0.003}	0.472 (±0.086) 0.465 ^{+0.090} _{-0.078}
130626a	95350.0 - 95405.0	3571	0.16	109.1 (±8.3) 108.8 ^{+9.1} _{-8.1}	0.093 (±0.005) 0.093 ^{+0.005} _{-0.005}	0.566 (±0.100) 0.562 ^{+0.105} _{-0.095}
130626a	95545.0 - 95710.0	3573	0.21	153.6 (±9.6) 153.3 ^{+10.2} _{-9.4}	0.075 (±0.004) 0.075 ^{+0.004} _{-0.004}	0.624 (±0.104) 0.615 ^{+0.111} _{-0.095}
130626a	95875.0 - 95930.4	3573	0.30	179.6 (±10.8) 179.5 ^{+10.9} _{-10.8}	0.067 (±0.004) 0.067 ^{+0.004} _{-0.004}	0.414 (±0.073) 0.408 ^{+0.077} _{-0.067}

Table B.5.9: Continuation of Tab. B.5.8.

flight	time interval [s UTC]	altitude [m AMSL]	SS [%]	n_{CCN} [cm^{-3} STP]	D_{act} [μm]	κ
<i>SAL</i>						
130630a	51457.5 - 51595.0	3233	0.11	106.0 (± 8.5)	0.110 (± 0.007)	0.718 (± 0.154)
				105.6 $^{+9.3}_{-8.2}$	0.110 $^{+0.007}_{-0.007}$	0.701 $^{+0.165}_{-0.132}$
130630a	52660.0 - 52800.5	3232	0.39	243.2 (± 15.3)	0.067 (± 0.005)	0.253 (± 0.064)
				242.7 $^{+15.9}_{-14.3}$	0.067 $^{+0.005}_{-0.005}$	0.243 $^{+0.069}_{-0.050}$
130701a	56514.3 - 56785.0	3514	0.21	205.3 (± 13.1)	0.072 (± 0.005)	0.759 (± 0.168)
				204.8 $^{+13.8}_{-13.0}$	0.072 $^{+0.005}_{-0.005}$	0.734 $^{+0.186}_{-0.135}$
130701a	56930.0 - 57040.0	3516	0.30	227.6 (± 14.1)	0.066 (± 0.005)	0.463 (± 0.110)
				227.2 $^{+14.8}_{-13.8}$	0.066 $^{+0.005}_{-0.005}$	0.446 $^{+0.121}_{-0.087}$
130701a	57700.0 - 57805.0	3522	0.11	134.6 (± 11.1)	0.103 (± 0.007)	0.883 (± 0.213)
				134.2 $^{+12.0}_{-11.2}$	0.103 $^{+0.008}_{-0.007}$	0.856 $^{+0.229}_{-0.180}$
130701a	57840.0 - 57970.0	3523	0.16	191.0 (± 12.9)	0.078 (± 0.005)	0.957 (± 0.204)
				190.9 $^{+13.6}_{-13.1}$	0.078 $^{+0.005}_{-0.005}$	0.927 $^{+0.239}_{-0.171}$
130701a	58330.0 - 58400.0	3528	0.20	156.2 (± 10.2)	0.072 (± 0.005)	0.762 (± 0.155)
				156.0 $^{+10.4}_{-10.3}$	0.072 $^{+0.005}_{-0.005}$	0.744 $^{+0.178}_{-0.133}$
130701a	58597.5 - 58650.0	3525	0.30	180.2 (± 11.4)	0.064 (± 0.004)	0.504 (± 0.111)
				179.7 $^{+12.3}_{-11.2}$	0.064 $^{+0.004}_{-0.005}$	0.488 $^{+0.127}_{-0.090}$
130701b	71620.0 - 71700.0	2119	0.21	171.5 (± 11.2)	0.077 (± 0.006)	0.663 (± 0.158)
				171.4 $^{+11.6}_{-11.1}$	0.076 $^{+0.006}_{-0.006}$	0.640 $^{+0.177}_{-0.129}$
130701b	71940.0 - 71997.5	2117	0.30	187.4 (± 11.8)	0.070 (± 0.006)	0.407 (± 0.105)
				187.2 $^{+12.3}_{-11.7}$	0.069 $^{+0.006}_{-0.005}$	0.391 $^{+0.119}_{-0.082}$
130701b	79240.0 - 79495.0	3546	0.16	171.5 (± 11.4)	0.078 (± 0.005)	0.917 (± 0.190)
				171.3 $^{+12.3}_{-11.7}$	0.078 $^{+0.005}_{-0.005}$	0.894 $^{+0.223}_{-0.162}$
130701b	79530.0 - 79792.5	3548	0.21	198.9 (± 12.6)	0.068 (± 0.005)	0.804 (± 0.175)
				198.8 $^{+13.2}_{-12.8}$	0.068 $^{+0.005}_{-0.005}$	0.779 $^{+0.210}_{-0.142}$
130710a	59920.0 - 60039.4	4371	0.11	118.1 (± 10.1)	0.103 (± 0.008)	0.892 (± 0.225)
				117.4 $^{+11.0}_{-9.8}$	0.102 $^{+0.008}_{-0.007}$	0.866 $^{+0.252}_{-0.193}$
130710a	60352.5 - 60517.5	2597	0.11	160.0 (± 13.6)	0.112 (± 0.009)	0.661 (± 0.180)
				159.5 $^{+14.4}_{-13.9}$	0.111 $^{+0.010}_{-0.009}$	0.638 $^{+0.210}_{-0.154}$

Table B.5.10: Continuation of Tab. B.5.8 and B.5.9.

flight	time interval [s UTC]	altitude [m AMSL]	SS [%]	n_{CCN} [cm ⁻³ STP]	D_{act} [μ m]	κ
<i>SAL</i>						
130710a	64400.0 - 64530.0	4204	0.29	192.5 (\pm 12.7)	0.061 (\pm 0.005)	0.556 (\pm 0.137)
				192.6 ^{+13.2} _{-12.9}	0.061 ^{+0.005} _{-0.005}	0.536 ^{+0.161} _{-0.112}
130710a	65142.5 - 65245.0	4204	0.12	87.2 (\pm 9.6)	0.130 (\pm 0.015)	0.385 (\pm 0.133)
				87.2 ^{+10.2} _{-10.6}	0.128 ^{+0.017} _{-0.013}	0.368 ^{+0.153} _{-0.116}
130710a	65387.5 - 65458.4	4203	0.21	178.4 (\pm 12.2)	0.066 (\pm 0.005)	0.873 (\pm 0.212)
				178.1 ^{+12.7} _{-12.3}	0.066 ^{+0.005} _{-0.005}	0.848 ^{+0.233} _{-0.180}
130710a	65637.5 - 65760.0	3562	0.30	192.9 (\pm 13.4)	0.068 (\pm 0.006)	0.391 (\pm 0.103)
				193.0 ^{+14.0} _{-13.9}	0.068 ^{+0.006} _{-0.006}	0.377 ^{+0.115} _{-0.085}
130710a	66022.5 - 66111.4	3558	0.12	81.1 (\pm 9.6)	0.144 (\pm 0.016)	0.286 (\pm 0.095)
				81.0 ^{+10.0} _{-10.5}	0.142 ^{+0.018} _{-0.014}	0.274 ^{+0.108} _{-0.084}
130710a	66350.0 - 66470.0	2592	0.12	169.1 (\pm 16.5)	0.131 (\pm 0.014)	0.378 (\pm 0.127)
				169.1 ^{+17.3} _{-17.5}	0.130 ^{+0.016} _{-0.013}	0.361 ^{+0.143} _{-0.109}
130710a	66712.5 - 66761.4	2589	0.30	249.1 (\pm 18.5)	0.084 (\pm 0.009)	0.210 (\pm 0.074)
				249.0 ^{+19.0} _{-18.9}	0.084 ^{+0.010} _{-0.009}	0.198 ^{+0.079} _{-0.055}
130711a	49285.0 - 49445.0	4196	0.30	200.0 (\pm 12.6)	0.071 (\pm 0.005)	0.363 (\pm 0.080)
				199.8 ^{+13.0} _{-12.3}	0.071 ^{+0.005} _{-0.005}	0.351 ^{+0.089} _{-0.065}
130711a	49864.5 - 50110.0	2591	0.11	153.4 (\pm 13.7)	0.126 (\pm 0.010)	0.467 (\pm 0.122)
				153.5 ^{+14.1} _{-14.7}	0.125 ^{+0.011} _{-0.010}	0.455 ^{+0.134} _{-0.113}
130711a	50360.0 - 50491.5	2589	0.30	224.2 (\pm 15.7)	0.090 (\pm 0.008)	0.181 (\pm 0.049)
				224.1 ^{+16.2} _{-16.5}	0.090 ^{+0.008} _{-0.008}	0.173 ^{+0.054} _{-0.038}
130711b	70895.5 - 71090.0	4176	0.30	211.0 (\pm 13.3)	0.066 (\pm 0.005)	0.455 (\pm 0.115)
				211.0 ^{+13.5} _{-13.1}	0.066 ^{+0.005} _{-0.005}	0.439 ^{+0.124} _{-0.094}
130711b	71430.0 - 71585.5	4179	0.11	126.6 (\pm 11.5)	0.125 (\pm 0.009)	0.486 (\pm 0.120)
				126.2 ^{+12.4} _{-11.6}	0.124 ^{+0.010} _{-0.009}	0.477 ^{+0.128} _{-0.111}
130711b	71810.0 - 72050.0	2732	0.11	148.6 (\pm 13.2)	0.120 (\pm 0.010)	0.541 (\pm 0.144)
				148.5 ^{+13.8} _{-14.1}	0.119 ^{+0.011} _{-0.009}	0.524 ^{+0.160} _{-0.128}
130711b	72375.5 - 72620.0	2242	0.30	250.0 (\pm 18.0)	0.086 (\pm 0.008)	0.205 (\pm 0.061)
				249.6 ^{+18.9} _{-18.1}	0.086 ^{+0.008} _{-0.008}	0.194 ^{+0.071} _{-0.048}

Table B.5.11: Continuation of Tab. B.5.8 to B.5.10.

Bibliography

- Adams, A. M., Prospero, J. M., and Zhang, C.: CALIPSO-Derived Three-Dimensional Structure of Aerosol over the Atlantic Basin and Adjacent Continents, *Journal of Climate*, 25, 6862–6879, doi:10.1175/JCLI-D-11-00672.1, 2012.
- Albrecht, B. A.: Aerosols, Cloud Microphysics, and Fractional Cloudiness, *Science*, 245, 1227–1230, doi:10.1126/science.245.4923.1227, 1989.
- Albrecht, B. A., Betts, A. K., Schubert, W. H., and Cox, S. K.: Model of the Thermodynamic Structure of the Trade-Wind Boundary Layer: Part I. Theoretical Formulation and Sensitivity Tests, *Journal of the Atmospheric Sciences*, 36, 73–89, doi:10.1175/1520-0469(1979)036<0073:MOTTSO>2.0.CO;2, 1979.
- Andreae, M. O.: Chapter 10 - Climatic effects of changing atmospheric aerosol levels, in: *World Survey of Climatology*, edited by Henderson-Sellers, A., vol. 16 of *Future climates of the world: a modelling perspective*, pp. 347–398, Elsevier, DOI: 10.1016/S0168-6321(06)80033-7, 1995.
- Andreae, M. O. and Rosenfeld, D.: Aerosol–cloud–precipitation interactions. Part 1. The nature and sources of cloud-active aerosols, *Earth-Science Reviews*, 89, 13–41, doi:10.1016/j.earscirev.2008.03.001, 2008.
- Andreae, M. O., Afchine, A., Albrecht, R., Holanda, B. A., Artaxo, P., Barbosa, H. M. J., Bormann, S., Cecchini, M. A., Costa, A., Dollner, M., Fütterer, D., Järvinen, E., Jurkat, T., Klimach, T., Konemann, T., Knote, C., Krämer, M., Krisna, T., Machado, L. A. T., Mertes, S., Minikin, A., Pöhlker, C., Pöhlker, M. L., Pöschl, U., Rosenfeld, D., Sauer, D., Schlager, H., Schnaiter, M., Schneider, J., Schulz, C., Spanu, A., Sperling, V. B., Voigt, C., Walser, A., Wang, J., Weinzierl, B., Wendisch, M., and Ziereis, H.: Aerosol characteristics and particle production in the upper troposphere over the Amazon Basin, *Atmos. Chem. Phys. Discuss.*, 2017, 1–95, doi:10.5194/acp-2017-694, 2017.
- Ansmann, A., Petzold, A., Kandler, K., Tegen, I., Wendisch, M., Müller, D., Weinzierl, B., Müller, T., and Heintzenberg, J.: Saharan Mineral Dust Experiments SAMUM–1 and SAMUM–2: what have we learned?, *Tellus B*, 63, 403–429, doi:10.1111/j.1600-0889.2011.00555.x, 2011.
- Balkanski, Y., Schulz, M., Claquin, T., and Guibert, S.: Reevaluation of Mineral aerosol radiative forcings suggests a better agreement with satellite and AERONET data, *Atmos. Chem. Phys.*, 7, 81–95, doi:10.5194/acp-7-81-2007, 2007.
- Baumgardner, D., Jonsson, H., Dawson, W., O’Connor, D., and Newton, R.: The cloud, aerosol and precipitation spectrometer: a new instrument for cloud investigations, *Atmospheric Research*, 59, 251–264, doi:10.1016/S0169-8095(01)00119-3, 2001.

- Bayes, M. and Price, M.: An Essay towards Solving a Problem in the Doctrine of Chances. By the Late Rev. Mr. Bayes, F. R. S. Communicated by Mr. Price, in a Letter to John Canton, A. M. F. R. S., Royal Society of London, 1763.
- Bierwirth, E., Wendisch, M., Ehrlich, A., Heese, B., Tesche, M., Althausen, D., Schladitz, A., Müller, D., Otto, S., Trautmann, T., Dinter, T., Von HOYNINGEN-HUENE, W., and Kahn, R.: Spectral surface albedo over Morocco and its impact on radiative forcing of Saharan dust, *Tellus B*, 61, 252–269, doi:10.1111/j.1600-0889.2008.00395.x, 2009.
- Bohren, C. F. and Huffman, D. R.: Absorption and scattering of light by small particles, 1983.
- Boose, Y., Sierau, B., García, M. I., Rodríguez, S., Alastuey, A., Linke, C., Schnaiter, M., Kupiszewski, P., Kanji, Z. A., and Lohmann, U.: Ice nucleating particles in the Saharan Air Layer, *Atmos. Chem. Phys.*, 16, 9067–9087, doi:10.5194/acp-16-9067-2016, 2016.
- Borrmann, S., Kunkel, D., Weigel, R., Minikin, A., Deshler, T., Wilson, J. C., Curtius, J., Volk, C. M., Homan, C. D., Ulanovsky, A., Ravegnani, F., Viciani, S., Shur, G. N., Belyaev, G. V., Law, K. S., and Cairo, F.: Aerosols in the tropical and subtropical UT/LS: in-situ measurements of submicron particle abundance and volatility, *Atmos. Chem. Phys.*, 10, 5573–5592, doi:10.5194/acp-10-5573-2010, 2010.
- Boucher, O., Randall, D., Artaxo, P., Bretherton, C., Feingold, G., Forster, P., Kerminen, V.-M., Kondo, Y., Liao, H., Lohmann, U., Rasch, P., Satheesh, S., Sherwood, S., Stevens, B., and Zhang, X.: Clouds and Aerosols, in: *Climate Change 2013: The Physical Science Basis. Contribution of Working Group I to the Fifth Assessment Report of the Intergovernmental Panel on Climate Change*, Cambridge University Press, Cambridge, United Kingdom and New York, NY, USA, 2013.
- Bristow, C. S., Hudson-Edwards, K. A., and Chappell, A.: Fertilizing the Amazon and equatorial Atlantic with West African dust, *Geophysical Research Letters*, 37, L14807, doi:10.1029/2010GL043486, 2010.
- Brock, C. A., Cozic, J., Bahreini, R., Froyd, K. D., Middlebrook, A. M., McComiskey, A., Brioude, J., Cooper, O. R., Stohl, A., Aikin, K. C., de Gouw, J. A., Fahey, D. W., Ferrare, R. A., Gao, R.-S., Gore, W., Holloway, J. S., Hübler, G., Jefferson, A., Lack, D. A., Lance, S., Moore, R. H., Murphy, D. M., Nenes, A., Novelli, P. C., Nowak, J. B., Ogren, J. A., Peischl, J., Pierce, R. B., Pilewskie, P., Quinn, P. K., Ryerson, T. B., Schmidt, K. S., Schwarz, J. P., Sodemann, H., Spackman, J. R., Stark, H., Thomson, D. S., Thornberry, T., Veres, P., Watts, L. A., Warneke, C., and Wollny, A. G.: Characteristics, sources, and transport of aerosols measured in spring 2008 during the aerosol, radiation, and cloud processes affecting Arctic Climate (ARCPAC) Project, *Atmos. Chem. Phys.*, 11, 2423–2453, doi:10.5194/acp-11-2423-2011, 2011.
- Brooks, B. J., McQuaid, J. B., Smith, M. H., Crosier, J., Williams, P. I., Coe, H., and Osborne, S.: Intercomparison of VACC- and AMS-derived nitrate, sulphate and ammonium aerosol loadings during ADRIEX, *Quarterly Journal of the Royal Meteorological Society*, 133, 77–84, doi:10.1002/qj.90, 2007.
- Bundke, U., Berg, M., Houben, N., Ibrahim, A., Fiebig, M., Tettich, F., Klaus, C., Franke, H., and Petzold, A.: The IAGOS-CORE aerosol package: instrument design, operation and performance for continuous measurement aboard in-service aircraft, *Tellus B*, 67, doi:10.3402/tellusb.v67.28339, 2015.

- Burpee, R. W.: The Origin and Structure of Easterly Waves in the Lower Troposphere of North Africa, *Journal of the Atmospheric Sciences*, 29, 77–90, doi:10.1175/1520-0469(1972)029<0077:TOASOE>2.0.CO;2, 1972.
- Burtscher, H., Baltensperger, U., Bukowiecki, N., Cohn, P., Hüglin, C., Mohr, M., Matter, U., Nyeki, S., Schmatloch, V., Streit, N., and Weingartner, E.: Separation of volatile and non-volatile aerosol fractions by thermodesorption: instrumental development and applications, *Journal of Aerosol Science*, 32, 427–442, doi:10.1016/S0021-8502(00)00089-6, 2001.
- Cai, Y., Montague, D. C., Mooiweer-Bryan, W., and Deshler, T.: Performance characteristics of the ultra high sensitivity aerosol spectrometer for particles between 55 and 800 nm: Laboratory and field studies, *Journal of Aerosol Science*, 39, 759–769, doi:10.1016/j.jaerosci.2008.04.007, 2008.
- Cakmur, R. V., Miller, R. L., Perlwitz, J., Geogdzhayev, I. V., Ginoux, P., Koch, D., Kohfeld, K. E., Tegen, I., and Zender, C. S.: Constraining the magnitude of the global dust cycle by minimizing the difference between a model and observations, *Journal of Geophysical Research: Atmospheres*, 111, D06 207, doi:10.1029/2005JD005791, 2006.
- Capes, G., Johnson, B., McFiggans, G., Williams, P. I., Haywood, J., and Coe, H.: Aging of biomass burning aerosols over West Africa: Aircraft measurements of chemical composition, microphysical properties, and emission ratios, *Journal of Geophysical Research: Atmospheres*, 113, D00C15, doi:10.1029/2008JD009845, 2008.
- Carlson, T. N. and Benjamin, S. G.: Radiative Heating Rates for Saharan Dust, *Journal of the Atmospheric Sciences*, 37, 193–213, doi:10.1175/1520-0469(1980)037<0193:RHRFSD>2.0.CO;2, 1980.
- Carlson, T. N. and Prospero, J. M.: The Large-Scale Movement of Saharan Air Outbreaks over the Northern Equatorial Atlantic, *Journal of Applied Meteorology*, 11, 283–297, doi:10.1175/1520-0450(1972)011<0283:TLSMOS>2.0.CO;2, 1972.
- Carslaw, K. S., Lee, L. A., Reddington, C. L., Pringle, K. J., Rap, A., Forster, P. M., Mann, G. W., Spracklen, D. V., Woodhouse, M. T., Regayre, L. A., and Pierce, J. R.: Large contribution of natural aerosols to uncertainty in indirect forcing, *Nature*, 503, 67–71, doi:10.1038/nature12674, 2013.
- Chen, D. R. and Pui, D. Y. H.: Numerical and experimental studies of particle deposition in a tube with a conical contraction-Laminar flow regime, *Journal of Aerosol Science*, 26, 563–574, doi:10.1016/0021-8502(94)00127-K, 1995.
- Chen, S.-C., Tsai, C.-J., Wu, C.-H., Pui, D. Y. H., Onischuk, A. A., and Karasev, V. V.: Particle loss in a critical orifice, *Journal of Aerosol Science*, 38, 935–949, doi:10.1016/j.jaerosci.2007.06.010, 2007.
- Cheng, W. Y. Y., Carrió, G. G., Cotton, W. R., and Saleeby, S. M.: Influence of cloud condensation and giant cloud condensation nuclei on the development of precipitating trade wind cumuli in a large eddy simulation, *Journal of Geophysical Research: Atmospheres*, 114, D08 201, doi:10.1029/2008JD011011, 2009.

- Cheng, Y., Su, H., Koop, T., Mikhailov, E., and Pöschl, U.: Size dependence of phase transitions in aerosol nanoparticles, *Nature Communications*, 6, 5923, doi:10.1038/ncomms6923, 2015.
- Chouza, F., Reitebuch, O., Groß, S., Rahm, S., Freudenthaler, V., Toledano, C., and Weinzierl, B.: Retrieval of aerosol backscatter and extinction from airborne coherent Doppler wind lidar measurements, *Atmos. Meas. Tech.*, 8, 2909–2926, doi:10.5194/amt-8-2909-2015, 2015.
- Chouza, F., Reitebuch, O., Benedetti, A., and Weinzierl, B.: Saharan dust long-range transport across the Atlantic studied by an airborne Doppler wind lidar and the MACC model, *Atmos. Chem. Phys.*, 16, 11 581–11 600, doi:10.5194/acp-16-11581-2016, 2016.
- Cini, R., Loglio, G., and Ficalbi, A.: Temperature dependence of the surface tension of water by the equilibrium ring method, *Journal of Colloid and Interface Science*, 41, 287–297, doi:10.1016/0021-9797(72)90113-0, 1972.
- Clarke, A. D.: A thermo-optic technique for in situ analysis of size-resolved aerosol physicochemistry, *Atmospheric Environment. Part A. General Topics*, 25, 635–644, doi:10.1016/0960-1686(91)90061-B, 1991.
- Clarke, A. D., Eisele, F., Kapustin, V. N., Moore, K., Tanner, D., Mauldin, L., Litchy, M., Lienert, B., Carroll, M. A., and Albercook, G.: Nucleation in the equatorial free troposphere: Favorable environments during PEM-Tropics, *Journal of Geophysical Research: Atmospheres*, 104, 5735–5744, doi:10.1029/98JD02303, 1999.
- Colarco, P. R., Toon, O. B., Reid, J. S., Livingston, J. M., Russell, P. B., Redemann, J., Schmid, B., Maring, H. B., Savoie, D., Welton, E. J., Campbell, J. R., Holben, B. N., and Levy, R.: Saharan dust transport to the Caribbean during PRIDE: 2. Transport, vertical profiles, and deposition in simulations of in situ and remote sensing observations, *Journal of Geophysical Research: Atmospheres*, 108, 8590, doi:10.1029/2002JD002659, 2003.
- Cuesta, J., Marsham, J. H., Parker, D. J., and Flamant, C.: Dynamical mechanisms controlling the vertical redistribution of dust and the thermodynamic structure of the West Saharan atmospheric boundary layer during summer, *Atmospheric Science Letters*, 10, 34–42, doi:10.1002/asl.207, 2009.
- Cziczo, D. J., Froyd, K. D., Hoose, C., Jensen, E. J., Diao, M., Zondlo, M. A., Smith, J. B., Twohy, C. H., and Murphy, D. M.: Clarifying the Dominant Sources and Mechanisms of Cirrus Cloud Formation, *Science*, 340, 1320–1324, doi:10.1126/science.1234145, 2013.
- Daimon, M. and Masumura, A.: Measurement of the refractive index of distilled water from the near-infrared region to the ultraviolet region, *Applied Optics*, 46, 3811, doi:10.1364/AO.46.003811, 2007.
- Davidi, A., Kostinski, A. B., Koren, I., and Lehahn, Y.: Observational bounds on atmospheric heating by aerosol absorption: Radiative signature of transatlantic dust, *Geophysical Research Letters*, 39, L04 803, doi:10.1029/2011GL050358, 2012.
- Dee, D. P., Uppala, S. M., Simmons, A. J., Berrisford, P., Poli, P., Kobayashi, S., Andrae, U., Balmaseda, M. A., Balsamo, G., Bauer, P., Bechtold, P., Beljaars, A. C. M., van de Berg, L., Bidlot, J., Bormann, N., Delsol, C., Dragani, R., Fuentes, M., Geer, A. J., Haimberger,

- L., Healy, S. B., Hersbach, H., Hólm, E. V., Isaksen, I., Kållberg, P., Köhler, M., Matriardi, M., McNally, A. P., Monge-Sanz, B. M., Morcrette, J.-J., Park, B.-K., Peubey, C., de Rosnay, P., Tavolato, C., Thépaut, J.-N., and Vitart, F.: The ERA-Interim reanalysis: configuration and performance of the data assimilation system, *Quarterly Journal of the Royal Meteorological Society*, 137, 553–597, doi:10.1002/qj.828, 2011.
- DeMott, P. J., Sassen, K., Poellot, M. R., Baumgardner, D., Rogers, D. C., Brooks, S. D., Prenni, A. J., and Kreidenweis, S. M.: African dust aerosols as atmospheric ice nuclei, *Geophysical Research Letters*, 30, 1732, doi:10.1029/2003GL017410, 2003.
- Denjean, C., Caquineau, S., Desboeufs, K., Laurent, B., Maille, M., Quiñones Rosado, M., Vallejo, P., Mayol-Bracero, O. L., and Formenti, P.: Long-range transport across the Atlantic in summertime does not enhance the hygroscopicity of African mineral dust, *Geophysical Research Letters*, 42, 2015GL065693, doi:10.1002/2015GL065693, 2015.
- Denjean, C., Cassola, F., Mazzino, A., Triquet, S., Chevaillier, S., Grand, N., Bourrienne, T., Momboisse, G., Sellegri, K., Schwarzenbock, A., Freney, E., Mallet, M., and Formenti, P.: Size distribution and optical properties of mineral dust aerosols transported in the western Mediterranean, *Atmos. Chem. Phys.*, 16, 1081–1104, doi:10.5194/acp-16-1081-2016, 2016a.
- Denjean, C., Formenti, P., Desboeufs, K., Chevaillier, S., Triquet, S., Maillé, M., Cazaunau, M., Laurent, B., Mayol-Bracero, O. L., Vallejo, P., Quiñones, M., Gutierrez-Molina, I. E., Cassola, F., Prati, P., Andrews, E., and Ogren, J.: Size distribution and optical properties of African mineral dust after intercontinental transport, *Journal of Geophysical Research: Atmospheres*, 121, 2016JD024783, doi:10.1002/2016JD024783, 2016b.
- Djuricin, S., Pataki, D. E., and Xu, X.: A comparison of tracer methods for quantifying CO₂ sources in an urban region, *Journal of Geophysical Research: Atmospheres*, 115, D11 303, doi:10.1029/2009JD012236, 2010.
- Dollner, M.: Vertical distribution of CCN properties in the Caribbean during SALTRACE, master thesis, Ludwig-Maximilians-Universität München, 2015.
- Dunion, J. P. and Marron, C. S.: A Reexamination of the Jordan Mean Tropical Sounding Based on Awareness of the Saharan Air Layer: Results from 2002, *Journal of Climate*, 21, 5242–5253, doi:10.1175/2008JCLI1868.1, 2008.
- Dunion, J. P. and Velden, C. S.: The Impact of the Saharan Air Layer on Atlantic Tropical Cyclone Activity, *Bulletin of the American Meteorological Society*, 85, 353–365, doi:10.1175/BAMS-85-3-353, 2004.
- Engelstaedter, S. and Washington, R.: Atmospheric controls on the annual cycle of North African dust, *Journal of Geophysical Research: Atmospheres*, 112, D03 103, doi:10.1029/2006JD007195, 2007.
- Erlick, C.: Effective Refractive Indices of Water and Sulfate Drops Containing Absorbing Inclusions, *Journal of the Atmospheric Sciences*, 63, 754–763, doi:10.1175/JAS3635.1, 2006.
- Evan, A. T., Dunion, J., Foley, J. A., Heidinger, A. K., and Velden, C. S.: New evidence for a relationship between Atlantic tropical cyclone activity and African dust outbreaks, *Geophysical Research Letters*, 33, L19 813, doi:10.1029/2006GL026408, 2006.

- Evan, A. T., Foltz, G. R., Zhang, D., and Vimont, D. J.: Influence of African dust on ocean-atmosphere variability in the tropical Atlantic, *Nature Geoscience*, 4, 762–765, doi:10.1038/ngeo1276, 2011.
- Fiebig, M.: Das troposphärische Aerosol in mittleren Breiten - Mikrophysik, Optik und Klimaantrieb am Beispiel der Feldstudie LACE 98, Ph.D. thesis, Ludwig-Maximilians-Universität München, 2001.
- Fiebig, M., Stein, C., Schröder, F., Feldpausch, P., and Petzold, A.: Inversion of data containing information on the aerosol particle size distribution using multiple instruments, *Journal of Aerosol Science*, 36, 1353–1372, doi:10.1016/j.jaerosci.2005.01.004, 2005.
- Fierz-Schmidhauser, R., Zieger, P., Wehrle, G., Jefferson, A., Ogren, J. A., Baltensperger, U., and Weingartner, E.: Measurement of relative humidity dependent light scattering of aerosols, *Atmos. Meas. Tech.*, 3, 39–50, doi:10.5194/amt-3-39-2010, 2010.
- Fitzgerald, E., Ault, A. P., Zauscher, M. D., Mayol-Bracero, O. L., and Prather, K. A.: Comparison of the mixing state of long-range transported Asian and African mineral dust, *Atmospheric Environment*, 115, 19–25, doi:10.1016/j.atmosenv.2015.04.031, 2015.
- Foreman-Mackey, D., Hogg, D. W., Lang, D., and Goodman, J.: emcee: The MCMC Hammer, *Publications of the Astronomical Society of the Pacific*, 125, 306–312, doi:10.1086/670067, arXiv: 1202.3665, 2013.
- Formenti, P., Elbert, W., Maenhaut, W., Haywood, J., and Andreae, M. O.: Chemical composition of mineral dust aerosol during the Saharan Dust Experiment (SHADE) airborne campaign in the Cape Verde region, September 2000, *Journal of Geophysical Research: Atmospheres*, 108, 8576, doi:10.1029/2002JD002648, 2003.
- Formenti, P., Rajot, J. L., Desboeufs, K., Saïd, F., Grand, N., Chevaillier, S., and Schmechtig, C.: Airborne observations of mineral dust over western Africa in the summer Monsoon season: spatial and vertical variability of physico-chemical and optical properties, *Atmos. Chem. Phys.*, 11, 6387–6410, doi:10.5194/acp-11-6387-2011, 2011a.
- Formenti, P., Schütz, L., Balkanski, Y., Desboeufs, K., Ebert, M., Kandler, K., Petzold, A., Scheuven, D., Weinbruch, S., and Zhang, D.: Recent progress in understanding physical and chemical properties of African and Asian mineral dust, *Atmos. Chem. Phys.*, 11, 8231–8256, doi:10.5194/acp-11-8231-2011, 2011b.
- Fouquart, Y., Bonnel, B., Brogniez, G., Buriez, J. C., Smith, L., Morcrette, J. J., and Cerf, A.: Observations of Saharan Aerosols: Results of ECLATS Field Experiment. Part II: Broadband Radiative Characteristics of the Aerosols and Vertical Radiative Flux Divergence, *Journal of Climate and Applied Meteorology*, 26, 38–52, doi:10.1175/1520-0450(1987)026<0038:OOSARO>2.0.CO;2, 1987.
- Freudenthaler, V., Esselborn, M., Wiegner, M., Heese, B., Tesche, M., Ansmann, A., Müller, D., Althausen, D., Wirth, M., Fix, A., Ehret, G., Knippertz, P., Toledano, C., Gasteiger, J., Garhammer, M., and Seefeldner, M.: Depolarization ratio profiling at several wavelengths in pure Saharan dust during SAMUM 2006, *Tellus B*, 61, 165–179, doi:10.1111/j.1600-0889.2008.00396.x, 2009.

- Fritzsche, L.: Untersuchung der thermischen Stabilität von künstlich generierten Aerosolen mit einer Kombination aus einem Differential Mobility Analyser und einem thermischen Partikeldiskriminator, diploma thesis, Fachhochschule Mittweida, 2002.
- Galperin, B., Sukoriansky, S., and Anderson, P. S.: On the critical Richardson number in stably stratified turbulence, *Atmospheric Science Letters*, 8, 65–69, doi:10.1002/asl.153, 2007.
- Gamo, M.: Thickness of the dry convection and large-scale subsidence above deserts, *Boundary-Layer Meteorology*, 79, 265–278, doi:10.1007/BF00119441, 1996.
- Gao, Y., Chen, S. B., and Yu, L. E.: Efflorescence Relative Humidity for Ammonium Sulfate Particles, *The Journal of Physical Chemistry A*, 110, 7602–7608, doi:10.1021/jp057574g, 2006.
- Gasteiger, J., Wiegner, M., Groß, S., Freudenthaler, V., Toledano, C., Tesche, M., and Kandler, K.: Modelling lidar-relevant optical properties of complex mineral dust aerosols, *Tellus B*, 63, 725–741, doi:10.1111/j.1600-0889.2011.00559.x, 2011.
- Gasteiger, J., Groß, S., Sauer, D., Haarig, M., Ansmann, A., and Weinzierl, B.: Particle settling and vertical mixing in the Saharan Air Layer as seen from an integrated model, lidar, and in situ perspective, *Atmos. Chem. Phys.*, 17, 297–311, doi:10.5194/acp-17-297-2017, 2017.
- Ghan, S. J., Guzman, G., and Abdul-Razzak, H.: Competition between Sea Salt and Sulfate Particles as Cloud Condensation Nuclei, *Journal of the Atmospheric Sciences*, 55, 3340–3347, doi:10.1175/1520-0469(1998)055<3340:CBSSAS>2.0.CO;2, 1998.
- Ginoux, P., Prospero, J. M., Gill, T. E., Hsu, N. C., and Zhao, M.: Global-scale attribution of anthropogenic and natural dust sources and their emission rates based on MODIS Deep Blue aerosol products, *Reviews of Geophysics*, 50, RG3005, doi:10.1029/2012RG000388, 2012.
- Goodman, J. and Weare, J.: Ensemble samplers with affine invariance, *Communications in Applied Mathematics and Computational Science*, 5, 65–80, doi:10.2140/camcos.2010.5.65, 2010.
- Goudie, A. S. and Middleton, N. J.: Saharan dust storms: nature and consequences, *Earth-Science Reviews*, 56, 179–204, doi:10.1016/S0012-8252(01)00067-8, 2001.
- Goudie, A. S. and Middleton, N. J.: *Desert Dust in the Global System*, Springer Berlin Heidelberg, doi: 10.1007/3-540-32355-4, 2006.
- Govind, P. K.: Dropwindsonde Instrumentation for Weather Reconnaissance Aircraft, *Journal of Applied Meteorology*, 14, 1512–1520, doi:10.1175/1520-0450(1975)014<1512:DIFWRA>2.0.CO;2, 1975.
- Groß, S., Freudenthaler, V., Schepanski, K., Toledano, C., Schäfler, A., Ansmann, A., and Weinzierl, B.: Optical properties of long-range transported Saharan dust over Barbados as measured by dual-wavelength depolarization Raman lidar measurements, *Atmos. Chem. Phys.*, 15, 11 067–11 080, doi:10.5194/acp-15-11067-2015, 2015.

- Groß, S., Gasteiger, J., Freudenthaler, V., Müller, T., Sauer, D., Toledano, C., and Ansmann, A.: Saharan dust contribution to the Caribbean summertime boundary layer – a lidar study during SALTRACE, *Atmos. Chem. Phys.*, 16, 11 535–11 546, doi:10.5194/acp-16-11535-2016, 2016.
- Gyan, K., Henry, W., Lacaille, S., Laloo, A., Lamsee-Ebanks, C., McKay, S., Antoine, R. M., and Monteil, M. A.: African dust clouds are associated with increased paediatric asthma accident and emergency admissions on the Caribbean island of Trinidad, *International Journal of Biometeorology*, 49, 371–376, doi:10.1007/s00484-005-0257-3, 2005.
- Haarig, M., Ansmann, A., Althausen, D., Klepel, A., Groß, S., Freudenthaler, V., Toledano, C., Mamouri, R.-E., Farrell, D. A., Prescod, D. A., Marinou, E., Burton, S. P., Gasteiger, J., Engelmann, R., and Baars, H.: Triple-wavelength depolarization-ratio profiling of Saharan dust over Barbados during SALTRACE in 2013 and 2014, *Atmos. Chem. Phys.*, 17, 10 767–10 794, doi:10.5194/acp-17-10767-2017, 2017.
- Hastenrath, S.: *Climate Dynamics of the Tropics*, Springer Netherlands, 1991.
- Heim, M., Mullins, B. J., Umhauer, H., and Kasper, G.: Performance evaluation of three optical particle counters with an efficient “multimodal” calibration method, *Journal of Aerosol Science*, 39, 1019–1031, doi:10.1016/j.jaerosci.2008.07.006, 2008.
- Heinold, B., Helmert, J., Hellmuth, O., Wolke, R., Ansmann, A., Marticorena, B., Laurent, B., and Tegen, I.: Regional modeling of Saharan dust events using LM-MUSCAT: Model description and case studies, *Journal of Geophysical Research: Atmospheres*, 112, D11 204, doi:10.1029/2006JD007443, 2007.
- Heinold, B., Tegen, I., Schepanski, K., Tesche, M., Esselborn, M., Freudenthaler, V., Gross, S., Kandler, K., Knippertz, P., Müller, D., Schladitz, A., Toledano, C., Weinzierl, B., Ansmann, A., Althausen, D., Müller, T., Petzold, A., and Wiedensohler, A.: Regional modelling of Saharan dust and biomass-burning smoke, *Tellus B: Chemical and Physical Meteorology*, 63, 781–799, doi:10.1111/j.1600-0889.2011.00570.x, 2011.
- Heinold, B., Schepanski, K., Gieseler, D., and Tegen, I.: Mixing and Deposition Processes during Transatlantic Transport of Saharan Dust, *Atmos. Chem. Phys. Discuss.*, in preparation, 2017.
- Herich, H., Tritscher, T., Wiacek, A., Gysel, M., Weingartner, E., Lohmann, U., Baltensperger, U., and Cziczo, D. J.: Water uptake of clay and desert dust aerosol particles at sub- and supersaturated water vapor conditions, *Physical Chemistry Chemical Physics*, 11, 7804–7809, doi:10.1039/B901585J, 2009.
- Hermann, M. and Wiedensohler, A.: Counting efficiency of condensation particle counters at low-pressures with illustrative data from the upper troposphere, *Journal of Aerosol Science*, 32, 975–991, doi:10.1016/S0021-8502(01)00037-4, 2001.
- Hermann, M., Brenninkmeijer, C. a. M., Slemr, F., Heintzenberg, J., Martinsson, B. G., Schlager, H., Van Velthoven, P. F. J., Wiedensohler, A., Zahn, A., and Ziereis, H.: Submicrometer aerosol particle distributions in the upper troposphere over the mid-latitude North Atlantic—results from the third route of ‘CARIBIC’, *Tellus B*, 60, 106–117, doi:10.1111/j.1600-0889.2007.00323.x, 2008.

- Heyder, J. and Gebhart, J.: Gravitational deposition of particles from laminar aerosol flow through inclined circular tubes, *Journal of Aerosol Science*, 8, 289–295, doi:10.1016/0021-8502(77)90048-9, 1977.
- Highwood, E. J. and Ryder, C. L.: Radiative Effects of Dust, in: *Mineral Dust*, edited by Knippertz, P. and Stuut, J.-B. W., pp. 267–286, Springer Netherlands, doi: 10.1007/978-94-017-8978-3_11, 2014.
- Hinds, W. C.: *Aerosol Technology: Properties, Behavior, and Measurement of Airborne Particles*, Wiley, 1999.
- Hock, T. F. and Franklin, J. L.: The NCAR GPS Dropwindsonde, *Bulletin of the American Meteorological Society*, 80, 407–420, doi:10.1175/1520-0477(1999)080<0407:TNGD>2.0.CO;2, 1999.
- Holben, B. N., Eck, T. F., Slutsker, I., Tanré, D., Buis, J. P., Setzer, A., Vermote, E., Reagan, J. A., Kaufman, Y. J., Nakajima, T., Lavenu, F., Jankowiak, I., and Smirnov, A.: AERONET—A Federated Instrument Network and Data Archive for Aerosol Characterization, *Remote Sensing of Environment*, 66, 1–16, doi:10.1016/S0034-4257(98)00031-5, 1998.
- Holman, J. P.: *Heat transfer*, New York : McGraw-Hill, 3d ed edn., 1972.
- Hoose, C. and Möhler, O.: Heterogeneous ice nucleation on atmospheric aerosols: a review of results from laboratory experiments, *Atmos. Chem. Phys.*, 12, 9817–9854, doi:10.5194/acp-12-9817-2012, 2012.
- Huang, J., Zhang, C., and Prospero, J. M.: African dust outbreaks: A satellite perspective of temporal and spatial variability over the tropical Atlantic Ocean, *Journal of Geophysical Research: Atmospheres*, 115, D05 202, doi:10.1029/2009JD012516, 2010.
- Huneeus, N., Schulz, M., Balkanski, Y., Griesfeller, J., Prospero, J., Kinne, S., Bauer, S., Boucher, O., Chin, M., Dentener, F., Diehl, T., Easter, R., Fillmore, D., Ghan, S., Ginoux, P., Grini, A., Horowitz, L., Koch, D., Krol, M. C., Landing, W., Liu, X., Mahowald, N., Miller, R., Morcrette, J.-J., Myhre, G., Penner, J., Perlwitz, J., Stier, P., Takemura, T., and Zender, C. S.: Global dust model intercomparison in AeroCom phase I, *Atmos. Chem. Phys.*, 11, 7781–7816, doi:10.5194/acp-11-7781-2011, 2011.
- Jackson, J. D.: *Classical Electrodynamics*, 3rd Edition, 1998.
- Jaynes, E. T.: Prior Probabilities, *IEEE Transactions on Systems Science and Cybernetics*, 4, 227–241, doi:10.1109/TSSC.1968.300117, 1968.
- Jickells, T. D., An, Z. S., Andersen, K. K., Baker, A. R., Bergametti, G., Brooks, N., Cao, J. J., Boyd, P. W., Duce, R. A., Hunter, K. A., Kawahata, H., Kubilay, N., laRoche, J., Liss, P. S., Mahowald, N., Prospero, J. M., Ridgwell, A. J., Tegen, I., and Torres, R.: Global Iron Connections Between Desert Dust, Ocean Biogeochemistry, and Climate, *Science*, 308, 67–71, doi:10.1126/science.1105959, 2005.
- Johnson, B. T. and Osborne, S. R.: Physical and optical properties of mineral dust aerosol measured by aircraft during the GERBILS campaign, *Quarterly Journal of the Royal Meteorological Society*, 137, 1117–1130, doi:10.1002/qj.777, 2011.

- Jung, E., Albrecht, B., Prospero, J. M., Jonsson, H. H., and Kreidenweis, S. M.: Vertical structure of aerosols, temperature, and moisture associated with an intense African dust event observed over the eastern Caribbean, *Journal of Geophysical Research: Atmospheres*, 118, 4623–4643, doi:10.1002/jgrd.50352, 2013.
- Kaaden, N., Massling, A., Schladitz, A., Müller, T., Kandler, K., Schütz, L., Weinzierl, B., Petzold, A., Tesche, M., Leinert, S., Deutscher, C., Ebert, M., Weinbruch, S., and Wiedensohler, A.: State of mixing, shape factor, number size distribution, and hygroscopic growth of the Saharan anthropogenic and mineral dust aerosol at Tinfou, Morocco, *Tellus B*, 61, 51–63, doi:10.1111/j.1600-0889.2008.00388.x, 2009.
- Kahn, R. A., Ogren, J. A., Ackerman, T. P., Bösenberg, J., Charlson, R. J., Diner, D. J., Holben, B. N., Menzies, R. T., Miller, M. A., and Seinfeld, J. H.: Aerosol Data Sources and Their Roles within PARAGON, *Bulletin of the American Meteorological Society*, 85, 1511–1522, doi:10.1175/BAMS-85-10-1511, 2004.
- Kamphus, M., Ettner-Mahl, M., Klimach, T., Drewnick, F., Keller, L., Cziczo, D. J., Mertes, S., Borrmann, S., and Curtius, J.: Chemical composition of ambient aerosol, ice residues and cloud droplet residues in mixed-phase clouds: single particle analysis during the Cloud and Aerosol Characterization Experiment (CLACE 6), *Atmos. Chem. Phys.*, 10, 8077–8095, doi:10.5194/acp-10-8077-2010, 2010.
- Kandler, K., Benker, N., Bundke, U., Cuevas, E., Ebert, M., Knippertz, P., Rodríguez, S., Schütz, L., and Weinbruch, S.: Chemical composition and complex refractive index of Saharan Mineral Dust at Izaña, Tenerife (Spain) derived by electron microscopy, *Atmospheric Environment*, 41, 8058–8074, doi:10.1016/j.atmosenv.2007.06.047, 2007.
- Kandler, K., Schütz, L., Deutscher, C., Ebert, M., Hofmann, H., Jäckel, S., Jaenicke, R., Knippertz, P., Lieke, K., Massling, A., Petzold, A., Schladitz, A., Weinzierl, B., Wiedensohler, A., Zorn, S., and Weinbruch, S.: Size distribution, mass concentration, chemical and mineralogical composition and derived optical parameters of the boundary layer aerosol at Tinfou, Morocco, during SAMUM 2006: BOUNDARY LAYER AEROSOL AT TINFOU, MOROCCO, *Tellus B*, 61, 32–50, doi:10.1111/j.1600-0889.2008.00385.x, 2009.
- Kandler, K., Lieke, K., Benker, N., Emmel, C., Küpper, M., Müller-Ebert, D., Ebert, M., Scheuven, D., Schladitz, A., Schütz, L., and Weinbruch, S.: Electron microscopy of particles collected at Praia, Cape Verde, during the Saharan Mineral Dust Experiment: particle chemistry, shape, mixing state and complex refractive index, *Tellus B*, 63, 475–496, doi:10.1111/j.1600-0889.2011.00550.x, 2011.
- Kandlikar, M. and Ramachandran, G.: INVERSE METHODS FOR ANALYSING AEROSOL SPECTROMETER MEASUREMENTS: A CRITICAL REVIEW, *Journal of Aerosol Science*, 30, 413–437, doi:10.1016/S0021-8502(98)00066-4, 1999.
- Karyampudi, V. M. and Carlson, T. N.: Analysis and Numerical Simulations of the Saharan Air Layer and Its Effect on Easterly Wave Disturbances, *Journal of the Atmospheric Sciences*, 45, 3102–3136, doi:10.1175/1520-0469(1988)045<3102:AANSOT>2.0.CO;2, 1988.
- Karyampudi, V. M., Palm, S. P., Reagen, J. A., Fang, H., Grant, W. B., Hoff, R. M., Moulin, C., Pierce, H. F., Torres, O., Browell, E. V., and Melfi, S. H.: Validation of the Saharan Dust Plume Conceptual Model Using Lidar, Meteosat, and ECMWF Data, *Bulletin of the American Meteorological Society*, 80, 1045–1075, doi:10.1175/1520-0477(1999)080<1045:VOTSDP>2.0.CO;2, 1999.

- Karydis, V. A., Kumar, P., Barahona, D., Sokolik, I. N., and Nenes, A.: On the effect of dust particles on global cloud condensation nuclei and cloud droplet number, *Journal of Geophysical Research: Atmospheres*, 116, D23 204, doi:10.1029/2011JD016283, 2011.
- Kaufman, Y. J., Koren, I., Remer, L. A., Tanré, D., Ginoux, P., and Fan, S.: Dust transport and deposition observed from the Terra-Moderate Resolution Imaging Spectroradiometer (MODIS) spacecraft over the Atlantic Ocean, *Journal of Geophysical Research: Atmospheres*, 110, D10S12, doi:10.1029/2003JD004436, 2005.
- Kesten, J., Reineking, A., and Porstendörfer, J.: Calibration of a TSI Model 3025 Ultrafine Condensation Particle Counter, *Aerosol Science and Technology*, 15, 107–111, doi:10.1080/02786829108959517, 1991.
- Khan, B., Stenchikov, G., Weinzierl, B., Kalenderski, S., and Osipov, S.: Dust plume formation in the free troposphere and aerosol size distribution during the Saharan Mineral Dust Experiment in North Africa, *Tellus B*, 67, 2015.
- Kim, H. and Paulson, S. E.: Real refractive indices and volatility of secondary organic aerosol generated from photooxidation and ozonolysis of limonene, α -pinene and toluene, *Atmos. Chem. Phys.*, 13, 7711–7723, doi:10.5194/acp-13-7711-2013, 2013.
- Knippertz, P. and Todd, M. C.: Mineral dust aerosols over the Sahara: Meteorological controls on emission and transport and implications for modeling, *Reviews of Geophysics*, 50, RG1007, doi:10.1029/2011RG000362, 2012.
- Knutson, E. O. and Whitby, K. T.: Aerosol classification by electric mobility: apparatus, theory, and applications, *Journal of Aerosol Science*, 6, 443–451, doi:10.1016/0021-8502(75)90060-9, 1975.
- Koehler, K. A., Kreidenweis, S. M., DeMott, P. J., Petters, M. D., Prenni, A. J., and Carrico, C. M.: Hygroscopicity and cloud droplet activation of mineral dust aerosol, *Geophysical Research Letters*, 36, L08 805, doi:10.1029/2009GL037348, 2009.
- Köhler, H.: The nucleus in and the growth of hygroscopic droplets, 32, 1152–1161, doi:10.1039/TF9363201152, 1936.
- Kristensen, T. B., Müller, T., Kandler, K., Benker, N., Hartmann, M., Prospero, J. M., Wiedensohler, A., and Stratmann, F.: Properties of cloud condensation nuclei (CCN) in the trade wind marine boundary layer of the western North Atlantic, *Atmos. Chem. Phys.*, 16, 2675–2688, doi:10.5194/acp-16-2675-2016, 2016.
- Kulkarni, P., Baron, P. A., and Willeke, K.: *Aerosol Measurement: Principles, Techniques, and Applications*, John Wiley & Sons, 3rd edition edn., 2011.
- Kumar, P., Sokolik, I. N., and Nenes, A.: Parameterization of cloud droplet formation for global and regional models: including adsorption activation from insoluble CCN, *Atmos. Chem. Phys.*, 9, 2517–2532, doi:10.5194/acp-9-2517-2009, 2009.
- Kumar, P., Sokolik, I. N., and Nenes, A.: Cloud condensation nuclei activity and droplet activation kinetics of wet processed regional dust samples and minerals, *Atmos. Chem. Phys.*, 11, 8661–8676, doi:10.5194/acp-11-8661-2011, 2011a.

- Kumar, P., Sokolik, I. N., and Nenes, A.: Measurements of cloud condensation nuclei activity and droplet activation kinetics of fresh unprocessed regional dust samples and minerals, *Atmos. Chem. Phys.*, 11, 3527–3541, doi:10.5194/acp-11-3527-2011, 2011b.
- Laborde, M., Schnaiter, M., Linke, C., Saathoff, H., Naumann, K.-H., Möhler, O., Berlenz, S., Wagner, U., Taylor, J. W., Liu, D., Flynn, M., Allan, J. D., Coe, H., Heimerl, K., Dahlkötter, F., Weinzierl, B., Wollny, A. G., Zannatta, M., Cozic, J., Laj, P., Hitzemberger, R., Schwarz, J. P., and Gysel, M.: Single Particle Soot Photometer intercomparison at the AIDA chamber, *Atmos. Meas. Tech.*, 5, 3077–3097, doi:10.5194/amt-5-3077-2012, 2012.
- Lance, S., Nenes, A., Medina, J., and Smith, J. N.: Mapping the Operation of the DMT Continuous Flow CCN Counter, *Aerosol Science and Technology*, 40, 242–254, doi:10.1080/02786820500543290, 2006.
- Landsea, C. W.: A Climatology of Intense (or Major) Atlantic Hurricanes, *Monthly Weather Review*, 121, 1703–1713, doi:10.1175/1520-0493(1993)121<1703:ACOIMA>2.0.CO;2, 1993.
- Lau, K. M. and Kim, K. M.: Cooling of the Atlantic by Saharan dust, *Geophysical Research Letters*, 34, L23 811, doi:10.1029/2007GL031538, 2007.
- Lee, S.-H., Reeves, J. M., Wilson, J. C., Hunton, D. E., Viggiano, A. A., Miller, T. M., Ballenthin, J. O., and Lait, L. R.: Particle Formation by Ion Nucleation in the Upper Troposphere and Lower Stratosphere, *Science*, 301, 1886–1889, doi:10.1126/science.1087236, 2003.
- Levin, Z. and Cotton, W. R.: *Aerosol Pollution Impact on Precipitation - A Scientific Review*, Springer Netherlands, 2009.
- Levin, Z., Teller, A., Ganor, E., and Yin, Y.: On the interactions of mineral dust, sea-salt particles, and clouds: A measurement and modeling study from the Mediterranean Israeli Dust Experiment campaign, *Journal of Geophysical Research: Atmospheres*, 110, D20 202, doi:10.1029/2005JD005810, 2005.
- Li-Jones, X., Maring, H. B., and Prospero, J. M.: Effect of relative humidity on light scattering by mineral dust aerosol as measured in the marine boundary layer over the tropical Atlantic Ocean, *Journal of Geophysical Research: Atmospheres*, 103, 31 113–31 121, doi:10.1029/98JD01800, 1998.
- Liao, H. and Seinfeld, J. H.: Radiative forcing by mineral dust aerosols: Sensitivity to key variables, *Journal of Geophysical Research: Atmospheres*, 103, 31 637–31 645, doi:10.1029/1998JD200036, 1998.
- Liu, Z., Omar, A., Vaughan, M., Hair, J., Kittaka, C., Hu, Y., Powell, K., Treppe, C., Winker, D., Hostetler, C., Ferrare, R., and Pierce, R.: CALIPSO lidar observations of the optical properties of Saharan dust: A case study of long-range transport, *Journal of Geophysical Research: Atmospheres*, 113, D07 207, doi:10.1029/2007JD008878, 2008.
- Lohmann, U. and Feichter, J.: Global indirect aerosol effects: a review, *Atmos. Chem. Phys.*, 5, 715–737, doi:10.5194/acp-5-715-2005, 2005.
- Ma, X., Lu, J. Q., Brock, R. S., Jacobs, K. M., Yang, P., and Hu, X.-H.: Determination of complex refractive index of polystyrene microspheres from 370 to 1610 nm, *Physics in Medicine and Biology*, 48, 4165, doi:10.1088/0031-9155/48/24/013, 2003.

- Mahowald, N. M., Muhs, D. R., Levis, S., Rasch, P. J., Yoshioka, M., Zender, C. S., and Luo, C.: Change in atmospheric mineral aerosols in response to climate: Last glacial period, preindustrial, modern, and doubled carbon dioxide climates, *Journal of Geophysical Research: Atmospheres*, 111, D10 202, doi:10.1029/2005JD006653, 2006.
- Mamouri, R.-E. and Ansmann, A.: Potential of polarization lidar to provide profiles of CCN- and INP-relevant aerosol parameters, *Atmos. Chem. Phys.*, 16, 5905–5931, doi:10.5194/acp-16-5905-2016, 2016.
- Maring, H., Savoie, D. L., Izaguirre, M. A., Custals, L., and Reid, J. S.: Vertical distributions of dust and sea-salt aerosols over Puerto Rico during PRIDE measured from a light aircraft, *Journal of Geophysical Research: Atmospheres*, 108, 8587, doi:10.1029/2002JD002544, 2003a.
- Maring, H., Savoie, D. L., Izaguirre, M. A., Custals, L., and Reid, J. S.: Mineral dust aerosol size distribution change during atmospheric transport, *Journal of Geophysical Research: Atmospheres*, 108, 8592, doi:10.1029/2002JD002536, 2003b.
- Matsuki, A., Schwarzenboeck, A., Venzac, H., Laj, P., Crumeyrolle, S., and Gomes, L.: Cloud processing of mineral dust: direct comparison of cloud residual and clear sky particles during AMMA aircraft campaign in summer 2006, *Atmos. Chem. Phys.*, 10, 1057–1069, doi:10.5194/acp-10-1057-2010, 2010.
- McConnell, C. L., Formenti, P., Highwood, E. J., and Harrison, M. A. J.: Using aircraft measurements to determine the refractive index of Saharan dust during the DODO Experiments, *Atmos. Chem. Phys.*, 10, 3081–3098, doi:10.5194/acp-10-3081-2010, 2010.
- Merikanto, J., Spracklen, D. V., Mann, G. W., Pickering, S. J., and Carslaw, K. S.: Impact of nucleation on global CCN, *Atmos. Chem. Phys.*, 9, 8601–8616, doi:10.5194/acp-9-8601-2009, 2009.
- Mertes, S., Schröder, F., and Wiedensohler, A.: The Particle Detection Efficiency Curve of the TSI-3010 CPC as a Function of the Temperature Difference between Saturator and Condenser, *Aerosol Science and Technology*, 23, 257–261, doi:10.1080/02786829508965310, 1995.
- Michel Flores, J., Bar-Or, R. Z., Bluvshstein, N., Abo-Riziq, A., Kostinski, A., Borrmann, S., Koren, I., Koren, I., and Rudich, Y.: Absorbing aerosols at high relative humidity: linking hygroscopic growth to optical properties, *Atmos. Chem. Phys.*, 12, 5511–5521, doi:10.5194/acp-12-5511-2012, 2012.
- Mie, G.: Beiträge zur Optik trüber Medien, speziell kolloidaler Metallösungen, *Annalen der Physik*, 330, 377–445, doi:10.1002/andp.19083300302, 1908.
- Moharreri, A., Craig, L., Dubey, P., Rogers, D. C., and Dhaniyala, S.: Aircraft testing of the new Blunt-body Aerosol Sampler (BASE), *Atmos. Meas. Tech.*, 7, 3085–3093, doi:10.5194/amt-7-3085-2014, 2014.
- Morman, S. A. and Plumlee, G. S.: The role of airborne mineral dusts in human disease, *Aeolian Research*, 9, 203–212, doi:10.1016/j.aeolia.2012.12.001, 2013.
- Mugnai, A. and Wiscombe, W. J.: Scattering from nonspherical Chebyshev particles. 3: Variability in angular scattering patterns, *Applied Optics*, 28, 3061–3073, doi:10.1364/AO.28.003061, 1989.

- Müller, T., Schladitz, A., Massling, A., Kaaden, N., Kandler, K., and Wiedensohler, A.: Spectral absorption coefficients and imaginary parts of refractive indices of Saharan dust during SAMUM-1, *Tellus B: Chemical and Physical Meteorology*, 61, 79–95, doi:10.1111/j.1600-0889.2008.00399.x, 2009.
- Müller, T., Schladitz, A., Kandler, K., and Wiedensohler, A.: Spectral particle absorption coefficients, single scattering albedos and imaginary parts of refractive indices from ground based in situ measurements at Cape Verde Island during SAMUM-2, *Tellus B*, 63, 573–588, doi:10.1111/j.1600-0889.2011.00572.x, 2011.
- Muysshondt, A., McFarland, A. R., and Anand, N. K.: Deposition of Aerosol Particles in Contraction Fittings, *Aerosol Science and Technology*, 24, 205–216, doi:10.1080/02786829608965364, 1996.
- Myhre, G. and Stordal, F.: Global sensitivity experiments of the radiative forcing due to mineral aerosols, *Journal of Geophysical Research: Atmospheres*, 106, 18 193–18 204, doi:10.1029/2000JD900536, 2001.
- Niedermeier, N., Held, A., Müller, T., Heinold, B., Schepanski, K., Tegen, I., Kandler, K., Ebert, M., Weinbruch, S., Read, K., Lee, J., Fomba, K. W., Müller, K., Herrmann, H., and Wiedensohler, A.: Mass deposition fluxes of Saharan mineral dust to the tropical northeast Atlantic Ocean: an intercomparison of methods, *Atmos. Chem. Phys.*, 14, 2245–2266, doi:10.5194/acp-14-2245-2014, 2014.
- Nuijens, L., Serikov, I., Hirsch, L., Lonitz, K., and Stevens, B.: The distribution and variability of low-level cloud in the North Atlantic trades, *Quarterly Journal of the Royal Meteorological Society*, 140, 2364–2374, doi:10.1002/qj.2307, 2014.
- Osborne, S. R., Baran, A. J., Johnson, B. T., Haywood, J. M., Hesse, E., and Newman, S.: Short-wave and long-wave radiative properties of Saharan dust aerosol, *Quarterly Journal of the Royal Meteorological Society*, 137, 1149–1167, doi:10.1002/qj.771, 2011.
- Otto, S., de Reus, M., Trautmann, T., Thomas, A., Wendisch, M., and Borrmann, S.: Atmospheric radiative effects of an in situ measured Saharan dust plume and the role of large particles, *Atmos. Chem. Phys.*, 7, 4887–4903, doi:10.5194/acp-7-4887-2007, 2007.
- Petters, M. D. and Kreidenweis, S. M.: A single parameter representation of hygroscopic growth and cloud condensation nucleus activity, *Atmos. Chem. Phys.*, 7, 1961–1971, doi:10.5194/acp-7-1961-2007, 2007.
- Petters, M. D. and Kreidenweis, S. M.: A single parameter representation of hygroscopic growth and cloud condensation nucleus activity – Part 2: Including solubility, *Atmos. Chem. Phys.*, 8, 6273–6279, doi:10.5194/acp-8-6273-2008, 2008.
- Petters, M. D. and Kreidenweis, S. M.: A single parameter representation of hygroscopic growth and cloud condensation nucleus activity – Part 3: Including surfactant partitioning, *Atmos. Chem. Phys.*, 13, 1081–1091, doi:10.5194/acp-13-1081-2013, 2013.
- Petzold, A., Rasp, K., Weinzierl, B., Esselborn, M., Hamburger, T., Dörnbrack, A., Kandler, K., Schütz, L., Knippertz, P., Fiebig, M., and Virkkula, A.: Saharan dust absorption and refractive index from aircraft-based observations during SAMUM 2006, *Tellus B*, 61, 118–130, doi:10.1111/j.1600-0889.2008.00383.x, 2009.

- Pfeifer, S., Müller, T., Weinhold, K., Zikova, N., Martins dos Santos, S., Marinoni, A., Bischof, O. F., Kykal, C., Ries, L., Meinhardt, F., Aalto, P., Mihalopoulos, N., and Wiedensohler, A.: Intercomparison of 15 aerodynamic particle size spectrometers (APS 3321): uncertainties in particle sizing and number size distribution, *Atmos. Meas. Tech.*, 9, 1545–1551, doi:10.5194/amt-9-1545-2016, 2016.
- Posselt, R. and Lohmann, U.: Influence of Giant CCN on warm rain processes in the ECHAM5 GCM, *Atmos. Chem. Phys.*, 8, 3769–3788, doi:10.5194/acp-8-3769-2008, 2008.
- Pringle, K. J., Tost, H., Pozzer, A., Pöschl, U., and Lelieveld, J.: Global distribution of the effective aerosol hygroscopicity parameter for CCN activation, *Atmos. Chem. Phys.*, 10, 5241–5255, doi:10.5194/acp-10-5241-2010, 2010.
- Prospero, J. M. and Carlson, T. N.: Vertical and areal distribution of Saharan dust over the western equatorial north Atlantic Ocean, *Journal of Geophysical Research*, 77, 5255–5265, doi:10.1029/JC077i027p05255, 1972.
- Prospero, J. M. and Lamb, P. J.: African Droughts and Dust Transport to the Caribbean: Climate Change Implications, *Science*, 302, 1024–1027, doi:10.1126/science.1089915, 2003.
- Prospero, J. M. and Mayol-Bracero, O. L.: Understanding the Transport and Impact of African Dust on the Caribbean Basin, *Bulletin of the American Meteorological Society*, 94, 1329–1337, doi:10.1175/BAMS-D-12-00142.1, 2013.
- Prospero, J. M., Ginoux, P., Torres, O., Nicholson, S. E., and Gill, T. E.: Environmental Characterization of Global Sources of Atmospheric Soil Dust Identified with the Nimbus 7 Total Ozone Mapping Spectrometer (toms) Absorbing Aerosol Product, *Reviews of Geophysics*, 40, 1002, doi:10.1029/2000RG000095, 2002.
- Prospero, J. M., Collard, F.-X., Molinié, J., and Jeannot, A.: Characterizing the annual cycle of African dust transport to the Caribbean Basin and South America and its impact on the environment and air quality, *Global Biogeochemical Cycles*, 28, 2013GB004802, doi:10.1002/2013GB004802, 2014.
- Purcell, E. M. and Pennypacker, C. R.: Scattering and Absorption of Light by Nonspherical Dielectric Grains, *The Astrophysical Journal*, 186, 705, doi:10.1086/152538, 1973.
- Raes, F., Van Dingenen, R., Cuevas, E., Van Velthoven, P. F. J., and Prospero, J. M.: Observations of aerosols in the free troposphere and marine boundary layer of the subtropical Northeast Atlantic: Discussion of processes determining their size distribution, *Journal of Geophysical Research: Atmospheres*, 102, 21 315–21 328, doi:10.1029/97JD01122, 1997.
- Raes, F., Dingenen, R. V., Vignati, E., Wilson, J., Putaud, J.-P., Seinfeld, J. H., and Adams, P.: Formation and cycling of aerosols in the global troposphere, *Atmospheric Environment*, 34, 4215–4240, doi:10.1016/S1352-2310(00)00239-9, 2000.
- Reid, J. S., Westphal, D. L., Livingston, J. M., Savoie, D. L., Maring, H. B., Jonsson, H. H., Eleuterio, D. P., Kinney, J. E., and Reid, E. A.: Dust vertical distribution in the Caribbean during the Puerto Rico Dust Experiment, *Geophysical Research Letters*, 29, 55–1, doi:10.1029/2001GL014092, 2002.

- Reid, J. S., Jonsson, H. H., Maring, H. B., Smirnov, A., Savoie, D. L., Cliff, S. S., Reid, E. A., Livingston, J. M., Meier, M. M., Dubovik, O., and Tsay, S.-C.: Comparison of size and morphological measurements of coarse mode dust particles from Africa, *Journal of Geophysical Research: Atmospheres*, 108, 8593, doi:10.1029/2002JD002485, 2003a.
- Reid, J. S., Kinney, J. E., Westphal, D. L., Holben, B. N., Welton, E. J., Tsay, S.-C., Eleuterio, D. P., Campbell, J. R., Christopher, S. A., Colarco, P. R., Jonsson, H. H., Livingston, J. M., Maring, H. B., Meier, M. L., Pilewskie, P., Prospero, J. M., Reid, E. A., Remer, L. A., Russell, P. B., Savoie, D. L., Smirnov, A., and Tanré, D.: Analysis of measurements of Saharan dust by airborne and ground-based remote sensing methods during the Puerto Rico Dust Experiment (PRIDE), *Journal of Geophysical Research: Atmospheres*, 108, 8586, doi:10.1029/2002JD002493, 2003b.
- Reischl, G. P., Mäkelä, J. M., and Neced, J.: Performance of Vienna Type Differential Mobility Analyzer at 1.2–20 Nanometer, *Aerosol Science and Technology*, 27, 651–672, doi:10.1080/02786829708965503, 1997.
- Roberts, G. C. and Nenes, A.: A Continuous-Flow Streamwise Thermal-Gradient CCN Chamber for Atmospheric Measurements, *Aerosol Science and Technology*, 39, 206–221, doi:10.1080/027868290913988, 2005.
- Rodríguez, S., Alastuey, A., Alonso-Pérez, S., Querol, X., Cuevas, E., Abreu-Afonso, J., Viana, M., Pérez, N., Pandolfi, M., and de la Rosa, J.: Transport of desert dust mixed with North African industrial pollutants in the subtropical Saharan Air Layer, *Atmos. Chem. Phys.*, 11, 6663–6685, doi:10.5194/acp-11-6663-2011, 2011.
- Rose, D., Gunthe, S. S., Mikhailov, E., Frank, G. P., Dusek, U., Andreae, M. O., and Pöschl, U.: Calibration and measurement uncertainties of a continuous-flow cloud condensation nuclei counter (DMT-CCNC): CCN activation of ammonium sulfate and sodium chloride aerosol particles in theory and experiment, *Atmos. Chem. Phys.*, 8, 1153–1179, doi:10.5194/acp-8-1153-2008, 2008.
- Rose, D., Nowak, A., Achtert, P., Wiedensohler, A., Hu, M., Shao, M., Zhang, Y., Andreae, M. O., and Pöschl, U.: Cloud condensation nuclei in polluted air and biomass burning smoke near the mega-city Guangzhou, China – Part 1: Size-resolved measurements and implications for the modeling of aerosol particle hygroscopicity and CCN activity, *Atmos. Chem. Phys.*, 10, 3365–3383, doi:10.5194/acp-10-3365-2010, 2010.
- Rosenfeld, D., Lohmann, U., Raga, G. B., O’Dowd, C. D., Kulmala, M., Fuzzi, S., Reissell, A., and Andreae, M. O.: Flood or Drought: How Do Aerosols Affect Precipitation?, *Science*, 321, 1309–1313, doi:10.1126/science.1160606, 2008.
- Ryder, C. L., Highwood, E. J., Lai, T. M., Sodemann, H., and Marsham, J. H.: Impact of atmospheric transport on the evolution of microphysical and optical properties of Saharan dust, *Geophysical Research Letters*, 40, 2433–2438, doi:10.1002/grl.50482, 2013a.
- Ryder, C. L., Highwood, E. J., Rosenberg, P. D., Trembath, J., Brooke, J. K., Bart, M., Dean, A., Crosier, J., Dorsey, J., Brindley, H., Banks, J., Marsham, J. H., McQuaid, J. B., Sodemann, H., and Washington, R.: Optical properties of Saharan dust aerosol and contribution from the coarse mode as measured during the Fennec 2011 aircraft campaign, *Atmos. Chem. Phys.*, 13, 303–325, doi:10.5194/acp-13-303-2013, 2013b.

- Sassen, K.: The Polarization Lidar Technique for Cloud Research: A Review and Current Assessment, *Bulletin of the American Meteorological Society*, 72, 1848–1866, doi:10.1175/1520-0477(1991)072<1848:TPLTFC>2.0.CO;2, 1991.
- Savoie, D. L. and Prospero, J. M.: Aerosol concentration statistics for the Northern Tropical Atlantic, *Journal of Geophysical Research*, 82, 5954–5964, doi:10.1029/JC082i037p05954, 1977.
- Schepanski, K., Tegen, I., Todd, M. C., Heinold, B., Bönisch, G., Laurent, B., and Macke, A.: Meteorological processes forcing Saharan dust emission inferred from MSG-SEVIRI observations of subdaily dust source activation and numerical models, *Journal of Geophysical Research: Atmospheres*, 114, D10 201, doi:10.1029/2008JD010325, 2009.
- Schepanski, K., Heinold, B., and Tegen, I.: Harmattan, Saharan heat low, and West African monsoon circulation: modulations on the Saharan dust outflow towards the North Atlantic, *Atmos. Chem. Phys.*, 17, 10 223–10 243, doi:10.5194/acp-17-10223-2017, 2017.
- Schladitz, A., Müller, T., Kaaden, N., Massling, A., Kandler, K., Ebert, M., Weinbruch, S., Deutscher, C., and Wiedensohler, A.: In situ measurements of optical properties at Tinfou (Morocco) during the Saharan Mineral Dust Experiment SAMUM 2006, *Tellus B*, 61, 64–78, doi:10.1111/j.1600-0889.2008.00397.x, 2009.
- Schmale, J., Henning, S., Decesari, S., Henzing, B., Keskinen, H., Paramonov, M., Sellegri, K., Ovadnevaite, J., Pöhlker, M. L., Brito, J., Bougiatioti, A., Kristensson, A., Kalivitis, N., Stavroulas, I., Carbone, S., Jefferson, A., Park, M., Schlag, P., Iwamoto, Y., Aalto, P., Äijälä, M., Bukowiecki, N., Ehn, M., Frank, G., Fröhlich, R., Frumau, A., Herrmann, E., Herrmann, H., Holzinger, R., Kos, G., Kulmala, M., Mihalopoulos, N., Nenes, A., O’Dowd, C., Petäjä, T., Picard, D., Pöhlker, C., Pöschl, U., Poulain, L., Prévôt, A. S. H., Swietlicki, E., Andreae, M. O., Artaxo, P., Wiedensohler, A., Ogren, J., Matsuki, A., Yum, S. S., Stratmann, F., Baltensperger, U., and Gysel, M.: What do we learn from long-term cloud condensation nuclei number concentration, particle number size distribution, and chemical composition measurements at regionally representative observatories?, *Atmos. Chem. Phys. Discuss.*, 2017, 1–51, doi:10.5194/acp-2017-798, 2017.
- Schmidt, L.: Charakterisierung und Erprobung des optischen Aerosolspektrometers UHSAS-A für den Betrieb auf dem Forschungsflugzeug HALO, diploma thesis, Ludwig-Maximilians-Universität München, 2009.
- Schröder, F. and Ström, J.: Aircraft measurements of sub micrometer aerosol particles (> 7 nm) in the midlatitude free troposphere and tropopause region, *Atmospheric Research*, 44, 333–356, doi:10.1016/S0169-8095(96)00034-8, 1997.
- Schumann, U., Weinzierl, B., Reitebuch, O., Schlager, H., Minikin, A., Forster, C., Baumann, R., Sailer, T., Graf, K., Mannstein, H., Voigt, C., Rahm, S., Simmet, R., Scheibe, M., Lichtenstern, M., Stock, P., Rüba, H., Schäuble, D., Tafferner, A., Rautenhaus, M., Gerz, T., Ziereis, H., Krautstrunk, M., Mallaun, C., Gayet, J.-F., Lieke, K., Kandler, K., Ebert, M., Weinbruch, S., Stohl, A., Gasteiger, J., Groß, S., Freudenthaler, V., Wiegner, M., Ansmann, A., Tesche, M., Olafsson, H., and Sturm, K.: Airborne observations of the Eyjafjalla volcano ash cloud over Europe during air space closure in April and May 2010, *Atmos. Chem. Phys.*, 11, 2245–2279, doi:10.5194/acp-11-2245-2011, 2011.

- Schwarz, J. P., Weinzierl, B., Samset, B. H., Dollner, M., Heimerl, K., Markovic, M. Z., Perring, A. E., and Ziemba, L.: Aircraft measurements of black carbon vertical profiles show upper tropospheric variability and stability, *Geophysical Research Letters*, 44, 2016GL071241, doi:10.1002/2016GL071241, 2017.
- Seinfeld, J. and Pandis, S.: *Atmospheric Chemistry and Physics: From Air Pollution to Climate Change*, John Wiley & Sons, New York, 2nd edition edn., 2006.
- Shaw, G. E.: Sun Photometry, *Bulletin of the American Meteorological Society*, 64, 4–10, doi:10.1175/1520-0477(1983)064<0004:SP>2.0.CO;2, 1983.
- Shettle, E. P. and Fenn, R. W.: *Models for the aerosols of the lower atmosphere and the effects of humidity variations on their optical properties*, Tech. rep., 1979.
- Siebert, H., Beals, M., Bethke, J., Bierwirth, E., Conrath, T., Dieckmann, K., Ditas, F., Ehrlich, A., Farrell, D., Hartmann, S., Izaguirre, M. A., Katzwinkel, J., Nuijens, L., Roberts, G., Schäfer, M., Shaw, R. A., Schmeissner, T., Serikov, I., Stevens, B., Stratmann, F., Wehner, B., Wendisch, M., Werner, F., and Wex, H.: The fine-scale structure of the trade wind cumuli over Barbados – an introduction to the CARRIBA project, *Atmos. Chem. Phys.*, 13, 10 061–10 077, doi:10.5194/acp-13-10061-2013, 2013.
- Singham, S. B. and Salzman, G. C.: Evaluation of the scattering matrix of an arbitrary particle using the coupled dipole approximation, *The Journal of Chemical Physics*, 84, 2658–2667, doi:10.1063/1.450338, 1986.
- Smirnov, A., Holben, B. N., Savoie, D., Prospero, J. M., Kaufman, Y. J., Tanre, D., Eck, T. F., and Slutsker, I.: Relationship between column aerosol optical thickness and in situ ground based dust concentrations over Barbados, *Geophysical Research Letters*, 27, 1643–1646, doi:10.1029/1999GL011336, 2000.
- Smoydzin, L., Teller, A., Tost, H., Fnais, M., and Lelieveld, J.: Impact of mineral dust on cloud formation in a Saharan outflow region, *Atmos. Chem. Phys.*, 12, 11 383–11 393, doi:10.5194/acp-12-11383-2012, 2012.
- Sokolik, I. N. and Toon, O. B.: Incorporation of mineralogical composition into models of the radiative properties of mineral aerosol from UV to IR wavelengths, *Journal of Geophysical Research: Atmospheres*, 104, 9423–9444, doi:10.1029/1998JD200048, 1999.
- Sokolik, I. N., Winker, D. M., Bergametti, G., Gillette, D. A., Carmichael, G., Kaufman, Y. J., Gomes, L., Schuetz, L., and Penner, J. E.: Introduction to special section: Outstanding problems in quantifying the radiative impacts of mineral dust, *Journal of Geophysical Research: Atmospheres*, 106, 18 015–18 027, doi:10.1029/2000JD900498, 2001.
- Sorjamaa, R. and Laaksonen, A.: The effect of H₂O adsorption on cloud drop activation of insoluble particles: a theoretical framework, *Atmos. Chem. Phys.*, 7, 6175–6180, doi:10.5194/acp-7-6175-2007, 2007.
- Sprenger, M. and Wernli, H.: The LAGRANTO Lagrangian analysis tool – version 2.0, *Geosci. Model Dev.*, 8, 2569–2586, doi:10.5194/gmd-8-2569-2015, 2015.
- Stein, C., Schröder, F., and Petzold, A.: The Condensation Particle Size Analyzer: A New Instrument for the Measurement of Ultrafine Aerosol Size Distributions, in: *Journal of Aerosol Science*, vol. 32, pp. S381–S382, 2001.

- Stephens, M., Turner, N., and Sandberg, J.: Particle identification by laser-induced incandescence in a solid-state laser cavity, *Applied Optics*, 42, 3726–3736, doi:10.1364/AO.42.003726, 2003.
- Stier, P.: Limitations of passive remote sensing to constrain global cloud condensation nuclei, *Atmos. Chem. Phys.*, 16, 6595–6607, doi:10.5194/acp-16-6595-2016, 2016.
- Stolzenburg, M. R.: An Ultrafine Aerosol Size Distribution System, Ph.D. thesis, University of Minnesota, 1988.
- Sullivan, R. C., Guazzotti, S. A., Sodeman, D. A., and Prather, K. A.: Direct observations of the atmospheric processing of Asian mineral dust, *Atmos. Chem. Phys.*, 7, 1213–1236, doi:10.5194/acp-7-1213-2007, 2007.
- Sullivan, R. C., Petters, M. D., DeMott, P. J., Kreidenweis, S. M., Wex, H., Niedermeier, D., Hartmann, S., Clauss, T., Stratmann, F., Reitz, P., Schneider, J., and Sierau, B.: Irreversible loss of ice nucleation active sites in mineral dust particles caused by sulphuric acid condensation, *Atmos. Chem. Phys.*, 10, 11 471–11 487, doi:10.5194/acp-10-11471-2010, 2010.
- Sultanova, N., Kasarova, S., and Nikolov, I.: Dispersion Properties of Optical Polymers, *Acta Physica Polonica A*, 116, 585–587, doi:10.12693/APhysPolA.116.585, 2009.
- Szymanski, W. W. and Liu, B. Y. H.: On the Sizing Accuracy of Laser Optical Particle Counters, *Particle & Particle Systems Characterization*, 3, 1–7, doi:10.1002/ppsc.19860030102, 1986.
- Szymanski, W. W., Nagy, A., and Czitrovsky, A.: Optical particle spectrometry—Problems and prospects, *Journal of Quantitative Spectroscopy and Radiative Transfer*, 110, 918–929, doi:10.1016/j.jqsrt.2009.02.024, 2009.
- Tang, I. N.: Chemical and size effects of hygroscopic aerosols on light scattering coefficients, *Journal of Geophysical Research: Atmospheres*, 101, 19 245–19 250, doi:10.1029/96JD03003, 1996.
- Tang, I. N. and Munkelwitz, H. R.: Water activities, densities, and refractive indices of aqueous sulfates and sodium nitrate droplets of atmospheric importance, *Journal of Geophysical Research: Atmospheres*, 99, 18 801–18 808, doi:10.1029/94JD01345, 1994.
- Tegen, I., Werner, M., Harrison, S. P., and Kohfeld, K. E.: Relative importance of climate and land use in determining present and future global soil dust emission, *Geophysical Research Letters*, 31, L05 105, doi:10.1029/2003GL019216, 2004.
- Tegen, I., Bierwirth, E., Heinold, B., Helmert, J., and Wendisch, M.: Effect of measured surface albedo on modeled Saharan dust solar radiative forcing, *Journal of Geophysical Research: Atmospheres*, 115, D24 312, doi:10.1029/2009JD013764, 2010.
- Textor, C., Schulz, M., Guibert, S., Kinne, S., Balkanski, Y., Bauer, S., Berntsen, T., Berglen, T., Boucher, O., Chin, M., Dentener, F., Diehl, T., Easter, R., Feichter, H., Fillmore, D., Ghan, S., Ginoux, P., Gong, S., Grini, A., Hendricks, J., Horowitz, L., Huang, P., Isaksen, I., Iversen, I., Kloster, S., Koch, D., Kirkevåg, A., Kristjansson, J. E., Krol, M., Lauer, A., Lamarque, J. F., Liu, X., Montanaro, V., Myhre, G., Penner, J., Pitari, G., Reddy, S., Seland, Ø., Stier, P., Takemura, T., and Tie, X.: Analysis and quantification of the

- diversities of aerosol life cycles within AeroCom, *Atmos. Chem. Phys.*, 6, 1777–1813, doi:10.5194/acp-6-1777-2006, 2006.
- Toon, O. B., Pollack, J. B., and Khare, B. N.: The optical constants of several atmospheric aerosol species: Ammonium sulfate, aluminum oxide, and sodium chloride, *Journal of Geophysical Research*, 81, 5733–5748, doi:10.1029/JC081i033p05733, 1976.
- Tsamalis, C., Chédin, A., Pelon, J., and Capelle, V.: The seasonal vertical distribution of the Saharan Air Layer and its modulation by the wind, *Atmos. Chem. Phys.*, 13, 11 235–11 257, doi:10.5194/acp-13-11235-2013, 2013.
- Twohy, C. H., Clement, C. F., Gandrud, B. W., Weinheimer, A. J., Campos, T. L., Baumgardner, D., Brune, W. H., Faloon, I., Sachse, G. W., Vay, S. A., and Tan, D.: Deep convection as a source of new particles in the midlatitude upper troposphere, *Journal of Geophysical Research: Atmospheres*, 107, 4560, doi:10.1029/2001JD000323, 2002.
- Twohy, C. H., Kreidenweis, S. M., Eidhammer, T., Browell, E. V., Heymsfield, A. J., Bansemer, A. R., Anderson, B. E., Chen, G., Ismail, S., DeMott, P. J., and Van Den Heever, S. C.: Saharan dust particles nucleate droplets in eastern Atlantic clouds, *Geophysical Research Letters*, 36, L01 807, doi:10.1029/2008GL035846, 2009.
- Twomey, S.: The Influence of Pollution on the Shortwave Albedo of Clouds, *Journal of the Atmospheric Sciences*, 34, 1149–1152, doi:10.1175/1520-0469(1977)034<1149:TIOPOT>2.0.CO;2, 1977.
- van der Does, M., Korte, L. F., Munday, C. I., Brummer, G.-J. A., and Stuut, J.-B. W.: Particle size traces modern Saharan dust transport and deposition across the equatorial North Atlantic, *Atmos. Chem. Phys.*, 16, 13 697–13 710, doi:10.5194/acp-16-13697-2016, 2016.
- Varutbangkul, V., Brechtel, F. J., Bahreini, R., Ng, N. L., Keywood, M. D., Kroll, J. H., Flagan, R. C., Seinfeld, J. H., Lee, A., and Goldstein, A. H.: Hygroscopicity of secondary organic aerosols formed by oxidation of cycloalkenes, monoterpenes, sesquiterpenes, and related compounds, *Atmos. Chem. Phys.*, 6, 2367–2388, doi:10.5194/acp-6-2367-2006, 2006.
- von der Weiden, S.-L., Drewnick, F., and Borrmann, S.: Particle Loss Calculator – a new software tool for the assessment of the performance of aerosol inlet systems, *Atmos. Meas. Tech.*, 2, 479–494, doi:10.5194/amt-2-479-2009, 2009.
- Wallace, J. M. and Hobbs, P. V.: *Atmospheric Science, Second Edition: An Introductory Survey*, Academic Press, Amsterdam ; Boston, 2 edition edn., 2006.
- Walser, A., Sauer, D., Spanu, A., Gasteiger, J., and Weinzierl, B.: On the parametrization of optical particle counter response including instrument-induced broadening of size spectra and a self-consistent evaluation of calibration measurements, *Atmos. Meas. Tech.*, 10, 4341–4361, doi:10.5194/amt-10-4341-2017, 2017.
- Waterman, P.: Matrix formulation of electromagnetic scattering, *Proceedings of the IEEE*, 53, 805–812, doi:10.1109/PROC.1965.4058, 1965.
- Weber, R. J., Clarke, A. D., Litchy, M., Li, J., Kok, G., Schillawski, R. D., and McMurry, P. H.: Spurious aerosol measurements when sampling from aircraft in the vicinity of clouds, *Journal of Geophysical Research: Atmospheres*, 103, 28 337–28 346, doi:10.1029/98JD02086, 1998.

- Weigel, R., Borrmann, S., Kazil, J., Minikin, A., Stohl, A., Wilson, J. C., Reeves, J. M., Kunkel, D., de Reus, M., Frey, W., Lovejoy, E. R., Volk, C. M., Viciani, S., D'Amato, F., Schiller, C., Peter, T., Schlager, H., Cairo, F., Law, K. S., Shur, G. N., Belyaev, G. V., and Curtius, J.: In situ observations of new particle formation in the tropical upper troposphere: the role of clouds and the nucleation mechanism, *Atmos. Chem. Phys.*, 11, 9983–10 010, doi:10.5194/acp-11-9983-2011, 2011.
- Weinzierl, B.: Radiatively-driven processes in forest fire and desert dust plumes, Ph.D. thesis, Ludwig-Maximilians-Universität München, 2007.
- Weinzierl, B., Petzold, A., Esselborn, M., Wirth, M., Rasp, K., Kandler, K., Schütz, L., Koepke, P., and Fiebig, M.: Airborne measurements of dust layer properties, particle size distribution and mixing state of Saharan dust during SAMUM 2006, *Tellus B*, 61, 96–117, doi:10.1111/j.1600-0889.2008.00392.x, 2009.
- Weinzierl, B., Sauer, D., Esselborn, M., Petzold, A., Veira, A., Rose, M., Mund, S., Wirth, M., Ansmann, A., Tesche, M., Gross, S., and Freudenthaler, V.: Microphysical and optical properties of dust and tropical biomass burning aerosol layers in the Cape Verde region—an overview of the airborne in situ and lidar measurements during SAMUM-2, *Tellus B*, 63, 589–618, doi:10.1111/j.1600-0889.2011.00566.x, 2011.
- Weinzierl, B., Ansmann, A., Prospero, J. M., Althausen, D., Benker, N., Chouza, F., Dollner, M., Farrell, D., Fomba, W. K., Freudenthaler, V., Gasteiger, J., Groß, S., Haarig, M., Heinold, B., Kandler, K., Kristensen, T. B., Mayol-Bracero, O. L., Müller, T., Reitebuch, O., Sauer, D., Schäfer, A., Schepanski, K., Spanu, A., Tegen, I., Toledano, C., and Walser, A.: The Saharan Aerosol Long-Range Transport and Aerosol–Cloud-Interaction Experiment: Overview and Selected Highlights, *Bulletin of the American Meteorological Society*, 98, 1427–1451, doi:10.1175/BAMS-D-15-00142.1, 2017.
- Wendisch, M. and Brenguier, J.-L.: *Airborne Measurements for Environmental Research: Methods and Instruments*, 2013.
- Wendisch, M., Coe, H., Baumgardner, D., Brenguier, J.-L., Dreiling, V., Fiebig, M., Formenti, P., Hermann, M., Krämer, M., Levin, Z., Maser, R., Mathieu, E., Nacass, P., Noone, K., Osborne, S., Schneider, J., Schütz, L., Schwarzenböck, A., Stratmann, F., and Wilson, J. C.: Aircraft Particle Inlets: State-of-the-Art and Future Needs, *Bulletin of the American Meteorological Society*, 85, 89–91, doi:10.1175/BAMS-85-1-89, 2004.
- Werner, F., Ditas, F., Siebert, H., Simmel, M., Wehner, B., Pilewskie, P., Schmeissner, T., Shaw, R. A., Hartmann, S., Wex, H., Roberts, G. C., and Wendisch, M.: Twomey effect observed from collocated microphysical and remote sensing measurements over shallow cumulus, *Journal of Geophysical Research: Atmospheres*, 119, 1534–1545, doi:10.1002/2013JD020131, 2014.
- Wernli, B. H. and Davies, H. C.: A lagrangian-based analysis of extratropical cyclones. I: The method and some applications, *Quarterly Journal of the Royal Meteorological Society*, 123, 467–489, doi:10.1002/qj.49712353811, 1997.
- Wex, H., DeMott, P. J., Tobo, Y., Hartmann, S., Rösch, M., Clauss, T., Tomsche, L., Niedermeier, D., and Stratmann, F.: Kaolinite particles as ice nuclei: learning from the use of different kaolinite samples and different coatings, *Atmos. Chem. Phys.*, 14, 5529–5546, doi:10.5194/acp-14-5529-2014, 2014.

- Wex, H., Dieckmann, K., Roberts, G. C., Conrath, T., Izaguirre, M. A., Hartmann, S., Herenz, P., Schäfer, M., Ditas, F., Schmeissner, T., Henning, S., Wehner, B., Siebert, H., and Stratmann, F.: Aerosol arriving on the Caribbean island of Barbados: physical properties and origin, *Atmos. Chem. Phys.*, 16, 14 107–14 130, doi:10.5194/acp-16-14107-2016, 2016.
- Whitby, K. T.: The physical characteristics of sulfur aerosols, *Atmospheric Environment* (1967), 12, 135–159, doi:10.1016/0004-6981(78)90196-8, 1978.
- Wiedensohler, A., Orsini, D., Covert, D. S., Coffmann, D., Cantrell, W., Havlicek, M., Brechtel, F. J., Russell, L. M., Weber, R. J., Gras, J., Hudson, J. G., and Litchy, M.: Inter-comparison Study of the Size-Dependent Counting Efficiency of 26 Condensation Particle Counters, *Aerosol Science and Technology*, 27, 224–242, doi:10.1080/02786829708965469, 1997.
- Wiedensohler, A., Birmili, W., Nowak, A., Sonntag, A., Weinhold, K., Merkel, M., Wehner, B., Tuch, T., Pfeifer, S., Fiebig, M., Fjåraa, A. M., Asmi, E., Sellegri, K., Depuy, R., Venzac, H., Villani, P., Laj, P., Aalto, P., Ogren, J. A., Swietlicki, E., Williams, P., Roldin, P., Quincey, P., Hüglin, C., Fierz-Schmidhauser, R., Gysel, M., Weingartner, E., Riccobono, F., Santos, S., Gruning, C., Faloon, K., Beddows, D., Harrison, R., Monahan, C., Jennings, S. G., O'Dowd, C. D., Marinoni, A., Horn, H.-G., Keck, L., Jiang, J., Scheckman, J., McMurry, P. H., Deng, Z., Zhao, C. S., Moerman, M., Henzing, B., de Leeuw, G., Löschau, G., and Bastian, S.: Mobility particle size spectrometers: harmonization of technical standards and data structure to facilitate high quality long-term observations of atmospheric particle number size distributions, *Atmos. Meas. Tech.*, 5, 657–685, doi:10.5194/amt-5-657-2012, 2012.
- Woodward, S., Roberts, D. L., and Betts, R. A.: A simulation of the effect of climate change-induced desertification on mineral dust aerosol, *Geophysical Research Letters*, 32, L18 810, doi:10.1029/2005GL023482, 2005.
- Yin, Y., Wurzler, S., Levin, Z., and Reisin, T. G.: Interactions of mineral dust particles and clouds: Effects on precipitation and cloud optical properties, *Journal of Geophysical Research: Atmospheres*, 107, 4724, doi:10.1029/2001JD001544, 2002.
- Zhang, Z. and Liu, B. Y. H.: Performance of TSI 3760 Condensation Nuclei Counter at Reduced Pressures and Flow Rates, *Aerosol Science and Technology*, 15, 228–238, doi:10.1080/02786829108959530, 1991.
- Zhang, Z. Q. and Liu, B. Y. H.: Dependence of the Performance of TSI 3020 Condensation Nucleus Counter on Pressure, Flow Rate, and Temperature, *Aerosol Science and Technology*, 13, 493–504, doi:10.1080/02786829008959464, 1990.
- Zipser, E. J., Twohy, C. H., Tsay, S.-C., Hsu, N. C., Heymsfield, G. M., Thornhill, K. L., Tanelli, S., Ross, R., Krishnamurti, T. N., Ji, Q., Jenkins, G., Ismail, S., Ferrare, R., Chen, G., Browell, E. V., Anderson, B., Hood, R., Goodman, H. M., Heymsfield, A., Halverson, J., Dunion, J. P., Douglas, M., and Cifelli, R.: The Saharan Air Layer and the Fate of African Easterly Waves—NASA's AMMA Field Study of Tropical Cyclogenesis, *Bulletin of the American Meteorological Society*, 90, 1137–1156, doi:10.1175/2009BAMS2728.1, 2009.

Index

A

- aerosol (particle), 1
 - hydrated, 22
 - mixing state, 37
 - external/internal mixture, 37
 - number size distribution, 33
 - primary/secondary, 1
 - sampling losses, 39
 - settling velocity, 41
 - volatility, 38
- aerosol-cloud interactions, 8
- aerosol-radiation interactions, 7
- African easterly jet (AEJ), 4
- African easterly wave (AEW), 4

C

- cloud condensation nucleus (CCN), 8
 - giant CCN (GCCN), 8
- critical orifice, 60
- critical/choked flow, 60
- Cunningham slip correction, 41

D

- droplet, 18
 - activation, 22
 - activation diameter, 22

H

- hygroscopic growth, 23
- hygroscopicity (parameter) κ , 23
 - effective, 106

K

- Köhler theory, 21
 - κ -Köhler, 22

N

- North African mineral dust, 3
 - (long-range) transport, 4
 - hygroscopicity, 82
 - processing, 9

- nucleation, 16

- heterogeneous, 19
- homogeneous, 16

S

- Saharan air layer (SAL), 4
- scattering, 25
 - cross section, 26
 - discrete dipole approx. (DDA), 31
 - Mie, 29
 - Rayleigh, 29
- standard (STP) conditions, 37
- Stokes number, 44

T

- trade wind inversion, 4
- Twomey effect, 8

W

- water vapor, 15
 - saturation (ratio), 15
 - supersaturation, 21
 - critical, 22

Acknowledgments

Die Durchführung und Ausarbeitung dieser Arbeit wäre nicht möglich gewesen ohne die Unterstützung einer Reihe von Personen, bei denen ich mich hiermit ausdrücklich bedanken möchte.

Mein Dank geht zunächst an Bernadett Weinzierl für die Betreuung und Begutachtung dieser Arbeit, und dafür mir überhaupt erst ermöglicht zu haben in einem fruchtbaren Arbeitsumfeld an diesem interessanten Thema forschen zu können. Ebenso möchte ich mich bei meinem Zweitgutachter Bernhard Mayer bedanken, neben der Begutachtung speziell für die ausserordentliche Hilfsbereitschaft bei meinen Anliegen.

Bedanken möchte ich mich ausserdem bei Josef Gasteiger, Oliver Reitebuch, Maximilian Dollner und Antonio Spanu für das Gegenlesen meiner Manuskripte und die nützlichen Hinweise, die zur Verbesserung der Qualität dieser Arbeit beigetragen haben.

Des Weiteren geht mein Dank an die verantwortlichen Personen am Deutschen Zentrum für Luft- und Raumfahrt, insbesondere Hans Schlager für die Ermöglichung meiner dortigen Studien. Vor allem möchte ich mich auch bei den noch nicht erwähnten Mitgliedern der (ehemaligen) AerCARE Gruppe am DLR, u.a. Daniel Sauer, Daniel Fütterer, Katharina Heimerl und Fernando Chouza für die konstruktive Zusammenarbeit und deren Hilfe im Labor sowie bei fachlichen Themen bedanken.

Die Arbeit in ihrer jetzigen Form wurde darüber hinaus erst möglich durch den Daten- und Wissensaustausch innerhalb der SALTRACE Projektgemeinschaft. Mein Dank geht hier insbesondere an Thomas Kristensen, Thomas Müller, Konrad Kandler, Bernd Heinold, Andreas Schäfler und Carlos Toledano.

Zu guter Letzt möchte ich mich bei meiner Mutter und bei meiner Freundin Sandra bedanken, die mir stets den Rücken gestärkt haben und deren Unterstützung mich durch die vergangenen Jahre getragen hat.